Third Computational Aeroacoustics (CAA) Workshop on Benchmark Problems

Proceedings of a conference held at and sponsored by
Ohio Aerospace Institute
Cleveland, Ohio
November 8–10, 1999

National Aeronautics and
Space Administration

Glenn Research Center

August 2000

Available from

Preface

The Computational Aeroacoustics (CAA) Workshops on Benchmark Problems have been organized to gauge the technological advancement of computational techniques to calculate all aspects of sound generation and propagation in air directly from the fundamental governing equations. The first Workshop, held in 1994, emphasized the basic technical challenges to accurate CAA calculations. Some of these challenges were the extraction of small acoustic quantities from a large magnitude background field, the sensitivity of propagating waves to dissipation and dispersion errors over large distances, the usually higher frequencies of sound versus lower frequency unsteady events, the stability of the calculations over long times to enable spectral calculations, the proper acoustic boundary conditions at open and solid surfaces, and the nonlinear effects at high Mach numbers. The benchmark problems had the simple geometries and the idealized acoustic conditions necessary to test the accuracy and effectiveness of computational algorithms and numerical boundary conditions. For the second Workshop in 1996, benchmark problems with more realistic conditions were designed to show the applicability of CAA to solve practical problems, such as, two- and three-dimensional scattering, radiation from a duct, and gust interaction with a cascade of flat plates. There was also the initial challenge to compute the sound generated by a separating turbulent flow.

The Third CAA Workshop builds on the emphasis in the second Workshop of computing realistic problems. The Workshop was held at the Ohio Aerospace Institute in Cleveland, Ohio, on November 8-10, 1999. This publication documents the numerical predictions and comparisons with solutions to the benchmark problems. Fan noise was chosen as the theme for this workshop with problems in four of the six benchmark problem categories representing issues involved in computing fan noise. Recognition is also given to the fact that as problems become more realistic and more complicated, exact or asymptotic solutions become more difficult to obtain. Thus, an initial step is made here to compare computational results to data from a well-documented experiment. The benchmark problems encompassed the following six categories.

Category 1 - Internal Propagation. The propagation of sound through a narrow passage with flow exists in many applications. One problem models the upstream propagation of sound through a nozzle with near sonic conditions. The computations must account for a ten-fold change in wavelength and out-going waves at each end of the nozzle. In a second problem, a shock is present in the nozzle making nonlinearities important.

Category 2 - Rotor Noise. The sound field generated by a rotor is affected by its environment. An open rotor will radiate noise. When placed in a duct, conditions can be such that no noise is radiated; the cut-off condition.

Category 3 - Sound Generation by Interaction with a Gust. Sound is generated when a vortical gust interacts with an airfoil. This noise source mechanism exists in turbomachinery applications. The three problems in this category were designed to show CAA calculations for a single thick airfoil, a single airfoil with sweep, and a cascade of swept airfoils. In all three cases, a steady mean flow exists.

Category 4 - Fan Stator with Harmonic Excitation by a Rotor Wake. Rotor-stator interaction is a large source of noise in turbofan engines. The wakes from a rotor rotating in a cylindrical annulus are represented as a convecting wave of radial vorticity. This wave interacts with a stator cascade of flat plates to create sound described by its modal content.

Category 5 - Generation and Radiation of Acoustic Waves from a 2-D Shear Layer. In high-speed jets, instability waves become an important source of radiated noise. The problem was designed to show the ability of CAA to compute the source of this radiated noise.

Category 6 - Automobile Noise Involving Feedback. Under certain conditions, the flow over a cavity generates acoustic tones. The phenomenon depends on the thickness of the approaching boundary layer. Thus, viscosity is an important fluid property. The challenge is to compute a sound source that is inherent in the fluid dynamics. Experimental data is provided for comparison to the computed solution in this category.

Solutions are provided for the benchmark problems in Categories 1 to 5. Even though no CAA computations were performed for comparison to the solutions of the Category 3, Problem 2, and the Category 4 problems, their solutions are provided for completeness and in the hope that these problems will be tried in the future.

These proceedings are available on CD-ROM in the PDF document format. In addition, the CD-ROM contains information related to all 6 categories of the benchmark problems including the numerical results from the calculations of the analytical solutions and the experimental data for the Category 6 problem. See the README file in the CD-ROM directory entitled, "caawksp3data" for further details.

Milo D. Dahl, NASA Glenn Research Center

Organizing Committee

This Workshop was organized by:
Jay C. Hardin, Consultant
Dennis Huff, NASA Glenn Research Center
Christopher Tam, Florida State University

Scientific Committee

The benchmark problems were proposed and decided on by a Scientific Committee which consisted of:
Thomas Barber, United Technologies Research Center
Kenneth Brentner, NASA Langley Research Center
Leo Dadone, Boeing Helicopters
Milo Dahl, NASA Glenn Research Center
William Dalton, Rolls-Royce Allison
Sanford Davis, NASA Ames Research Center
Philip Gliebe, GE Aircraft Engines
Kenneth C. Hall, Duke University
Donald Hanson, Consultant
Jay C. Hardin, Consultant
Brenda Henderson, Kettering University
Fang Hu, Old Dominion University
Dennis Huff, NASA Glenn Research Center
Mahendra Joshi, Boeing Commercial Airplane Company
Sanjiva Lele, Stanford University
Lou Povinelli, NASA Glenn Research Center
Philip Morris, The Pennsylvania State University
N.N. Reddy, Lockheed Martin Aeronautical Systems
David Reed, Boeing Commercial Airplane Company
Lakshmi Sankar, Georgia Institute of Technology
Christopher Tam, Florida State University
James L. Thomas, NASA Langley Research Center

Table of Contents

Benchmark Problems

Problem 1: Propagation of Sound Waves through a Transonic Nozzle

In a transonic cascade, the local Mach number of the flow in the narrow passages may be close to sonic. The computation of sound propagating through such regions presents a challenging problem. To reduce the complexity of the problem, but retaining the basic physics and difficulties, we will model such propagation problems by a one-dimensional acoustic wave transmission problem through a nearly choked nozzle.

We will use the following as characteristic scales.

> length scale   = diameter of nozzle in the uniform region downstream of the throat (see figure), D
> velocity scale = speed of sound in the same region, a_∞.
>
> time scale $= \dfrac{D}{a_\infty}$
>
> density scale   = mean density of gas in the same region, ρ_∞.
> pressure scale $= \rho_\infty a^2{}_\infty$.

Consider a one-dimensional nozzle with an area distribution as follows

$$A(x) = \begin{cases} 0.536572 - 0.198086 e^{-(\ln 2)\left(\frac{x}{0.6}\right)^2}, & x > 0 \\[2ex] 1.0 - 0.661514 e^{(-\ln 2)\left(\frac{x}{0.6}\right)^2}, & x < 0 \end{cases}$$

The governing equations in dimensionless form are,

$$\frac{\partial \rho}{\partial t} + \frac{1}{A}\frac{\partial \rho u A}{\partial x} = 0$$

$$\rho\left(\frac{\partial u}{\partial t} + u\frac{\partial u}{\partial x}\right) + \frac{\partial p}{\partial x} = 0$$

$$A\frac{\partial p}{\partial t} + \frac{\partial(puA)}{\partial x} + (\gamma - 1)p\frac{\partial(uA)}{\partial x} = 0$$

The Mach number in the uniform region downstream of the throat is $\gamma = 1.4$.

Small amplitude acoustic waves, with angular frequency $\omega = 0.6\pi$, is generated way downstream and propagate upstream through the narrow passage of the nozzle throat. Let the upstream propagating wave in the uniform region downstream of the nozzle throat be represented by

$$\begin{bmatrix} \rho' \\ u' \\ p' \end{bmatrix} = \varepsilon \begin{bmatrix} 1 \\ -1 \\ 1 \end{bmatrix} \cos\left[\omega\left(\frac{x}{1-M} + t\right)\right]$$

where $\varepsilon = 10^{-5}$. Use a computation domain of size 20, 10 upstream and 10 downstream of the nozzle throat, to calculate the distribution of maximum acoustic pressure inside the nozzle.

This problem can, of course, be calculated accurately if a very large number of mesh points is used. But this is not always practical. It is recommended that no more than 400 mesh points be used. Report the locations of your mesh points and the pressure distribution. Also report the total number of mesh points used.
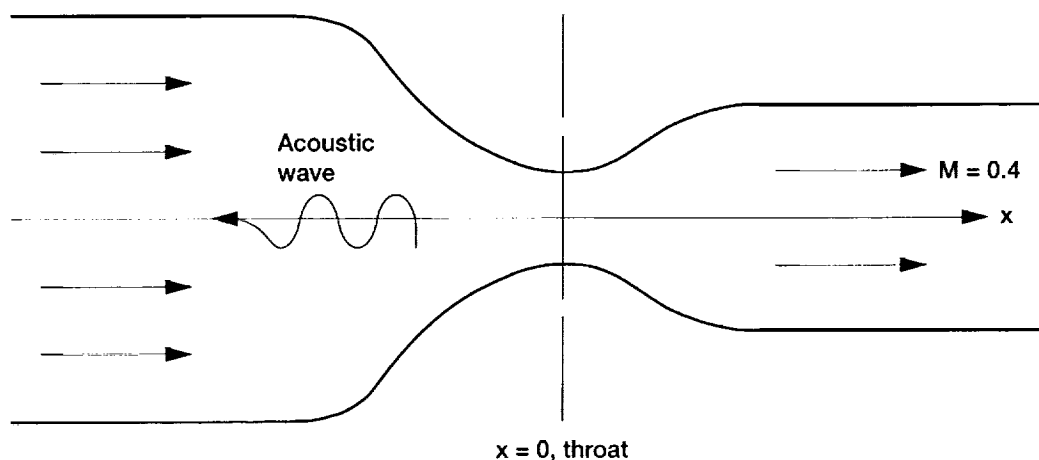
Propagation of sound through a transonic throat of a subsonic nozzle.

Problem 2: Shock-Sound Interaction

In imperfectly expanded supersonic jets, shock-cell structures are formed downstream of the nozzle exit. To simulate the shock-sound interactions, the problem is simplified as a sound wave passing through a shock in a quasi-1-D supersonic nozzle.

This problem uses the same geometry as Problem 1, but now there is a supersonic shock downstream of the throat.

In this problem, the quasi-1-D Euler equations are solved:

$$\frac{\partial}{\partial t}(\rho A) + \frac{\partial}{\partial x}(\rho u A) = 0$$

$$\rho\left(\frac{\partial u}{\partial t} + u\frac{\partial u}{\partial x}\right) + \frac{\partial p}{\partial x} = 0 \tag{1}$$

$$\frac{\partial}{\partial t}(pA) + \frac{\partial}{\partial x}(puA) + (\gamma - 1)p\frac{\partial}{\partial x}(uA) = 0$$

All quantities are nondimensionalized using the upstream values:

$$\text{length scale} = D_{inlet}$$

$$\text{density scale} = \rho_{inlet}$$

$$\text{velocity scale} = a_{inlet} \tag{2}$$

$$\text{pressure scale} = \rho_{inlet}a_{inlet}^2$$

$$\text{time scale} = \frac{D_{inlet}}{a_{inlet}}$$

where D is the nozzle height and a is the speed of sound. $\gamma = 1.4$

As before, the domain is $-10 < x < 10$, and the area of the nozzle is given by:

$$A(x) = \begin{cases} 0.536572 - 0.198086e^{-(\ln 2)\left(\frac{x}{0.6}\right)^2}, & x > 0 \\ 1.0 - 0.661514e^{(-\ln 2)\left(\frac{x}{0.6}\right)^2}, & x < 0 \end{cases} \tag{3}$$

At the inflow boundary, the conditions are:

$$\begin{bmatrix} \rho \\ u \\ p \end{bmatrix} = \begin{bmatrix} 1 \\ M \\ 1/\gamma \end{bmatrix} + \begin{bmatrix} 1 \\ 1 \\ 1 \end{bmatrix} \varepsilon \sin\left[\omega\left(\frac{x}{1+M} - t \right) \right] \tag{4}$$

where:

$$\varepsilon = 1.0 \times 10^{-5}$$

$$\omega = 0.6\pi \tag{5}$$

$$M_{\text{inlet}} = 0.2006533$$

The pressure will be set at the outflow boundary to create a shock:

$$(p)_{\text{exit}} = 0.6071752 \tag{6}$$

The data required for this problem is:

1. Grid used for the problem (i,x)

2. On the domain $-10.0 < x < 10.0$, give
   a. Steady mean distribution $(x, \overline{\rho}(x), \overline{u}(x), \overline{p}(x))$
   b. Perturbation at the start of a period $(x, \rho(x) - \overline{\rho}(x), u(x) - \overline{u}(x), p(x) - \overline{p}(x))$

3. Over the period of the perturbation, give:

4. Pressure perturbation at the exit plane through one period $(t, p(t) - \overline{p}(t))$
   a. The format in FORTRAN is:

format (4(3x, e18.5))
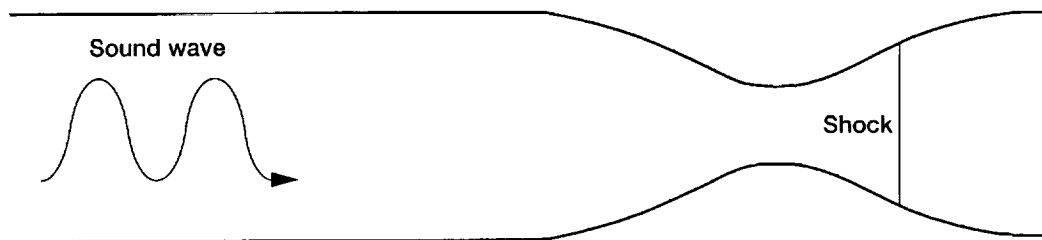
Sound wave—normal shock interaction.

Comparison between the sound field generated by an open rotor and the sound field generated by the same rotor placed inside a semi-infinite duct.

The sound field associated with an open rotor and that associated with the same rotor placed inside a semi-infinite duct (see figures at the end of the problem) can be extremely different. A good understanding of the differences is important in fan noise work.

We will use nondimensional variables with respect to the following scales.

length scale	$= b$ (length of blade)
velocity scale	$= a_\infty$ (ambient sound speed)
time scale	$= \dfrac{b}{a_\infty}$
density scale	$= \rho_\infty$ (ambient gas density)
pressure scale	$= \rho_\infty a_\infty^2$
body force scale (per unit volume)	$= \rho_\infty a_\infty^2$

A rotor exerts a rotating force on the fluid. As a model problem, we will replace the rotor by a distribution of rotating body force. The governing equations are the linearized Euler equations. In cylindrical coordinates (r, ϕ, x), they are,

$$\frac{\partial v}{\partial t} = -\frac{\partial p}{\partial r} + F_r$$

$$\frac{\partial w}{\partial t} = -\frac{1}{r}\frac{\partial p}{\partial \phi} + F_\phi$$

$$\frac{\partial u}{\partial t} = -\frac{\partial p}{\partial x} + F_x$$

$$\frac{\partial p}{\partial t} + \frac{1}{r}\frac{\partial (vr)}{\partial r} + \frac{1}{r}\frac{\partial w}{\partial \phi} + \frac{\partial u}{\partial x} = 0$$

(1)

where (F_r, F_ϕ, F_x) are the components of the body force.

For simplicity, we will let $F_r = 0$ and

$$\begin{bmatrix} F_\phi(r,\phi,x,t) \\ F_x(r,\phi,x,t) \end{bmatrix} = \mathrm{Re}\left\{ \begin{bmatrix} \tilde{F}_\phi(r,x) \\ \tilde{F}_x(r,x) \end{bmatrix} e^{im(\phi-\Omega t)} \right\}$$

(2)

where Re{ } is the real part of. For computation purposes, we will use the following body force distribution in r and x.

$$\tilde{F}_\phi(r,x) = \begin{cases} F(x)rJ_m(\lambda_{mN}r) & r \leq 1 \\ 0 & r > 1 \end{cases} \tag{3}$$

$$\tilde{F}_x(r,x) = \begin{cases} F(x)J_m(\lambda_{mN}r) & r \leq 1 \\ 0 & r > 1 \end{cases} \tag{4}$$

$$F(x) = \exp\left\{-(\ln 2)(10x)^2\right\} \tag{5}$$

where $J_m(\ )$ is the mth-order Bessel function, λ_{mN} is the Nth root of J'_m or $J'_m(\lambda_{mN}) = 0$.

In this model, m is the number of blades, Ω is the angular velocity of the rotor. In the ducted case N is the radial mode number. The choice of the Bessel functions in (3) and (4) has no other significance than making the analytical solution simple.

It is possible to reduce the 3-D problem of (1) to a two-dimensional problem by factoring out the azimuthal dependence. Let

$$\begin{bmatrix} u(r,\phi.x.t) \\ v(r,\phi.x.t) \\ w(r,\phi.x.t) \\ p(r,\phi.x.t) \end{bmatrix} = \text{Re}\left\{ \begin{bmatrix} \tilde{u}(r,x.t) \\ \tilde{v}(r,x.t) \\ \tilde{w}(r,x.t) \\ \tilde{p}(r,x.t) \end{bmatrix} e^{im\phi} \right\} \tag{6}$$

The governing equations for $(\tilde{u},\tilde{v},\tilde{w},\tilde{p})$ are found by substituting (2) to (6) into (1) and factoring out $e^{im\phi}$. They are

$$\frac{\partial \tilde{v}}{\partial t} = -\frac{\partial \tilde{p}}{\partial r}$$

$$\frac{\partial \tilde{w}}{\partial t} = -\frac{im}{r}\tilde{p} + \tilde{F}_\phi(r,x)e^{-im\Omega t}$$

$$\frac{\partial \tilde{u}}{\partial t} = -\frac{\partial \tilde{p}}{\partial x} + \tilde{F}_x(r,x)e^{-im\Omega t} \tag{7}$$

$$\frac{\partial \tilde{p}}{\partial t} + \frac{1}{r}\frac{\partial(\tilde{v}r)}{\partial r} + \frac{im\tilde{w}}{r} + \frac{\partial \tilde{u}}{\partial x} = 0$$

For the open rotor case, it is only necessary to find the outgoing wave solution of (7) in the r-x-plane. In the case of the ducted rotor, the solid wall boundary condition must be satisfied at the surface of the infinitesimally thin duct wall.

Calculate the directivity, $D(\theta)$, of the radiated sound for a 8-blade rotor ($m = 8$). Set $N = 1$ ($\lambda_{8,1} = 9.64742$). In spherical coordinates (R,θ,ϕ), with the x-axis as the polar axis, the directivity is defined by, (for the ducted rotor, center the coordinate system at the end of the duct)

$$D(\theta) = \lim_{R \to \infty} R^2 \overline{p^2(R,\theta,\phi,t)}$$

where $\overline{}$ is the time average.

Consider two rotational speeds in your computation.

(a) $\Omega = 0.85$ (subsonic tip speed)
(b) $\Omega = 1.15$ (supersonic tip speed)

Report the values of $D(\theta)$ at 1 degree intervals.
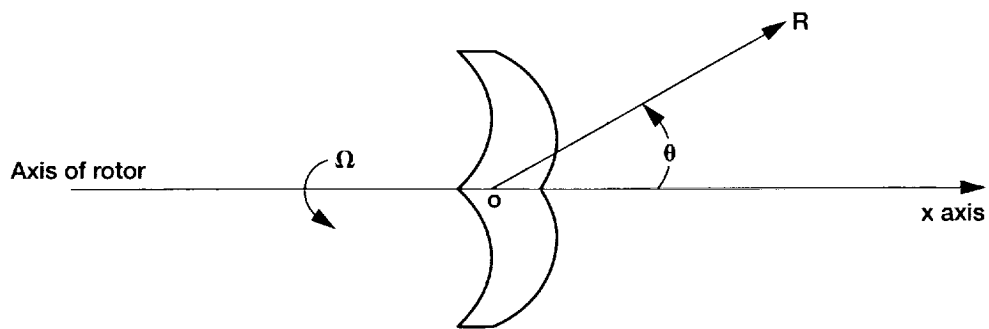
(a) Open rotor.
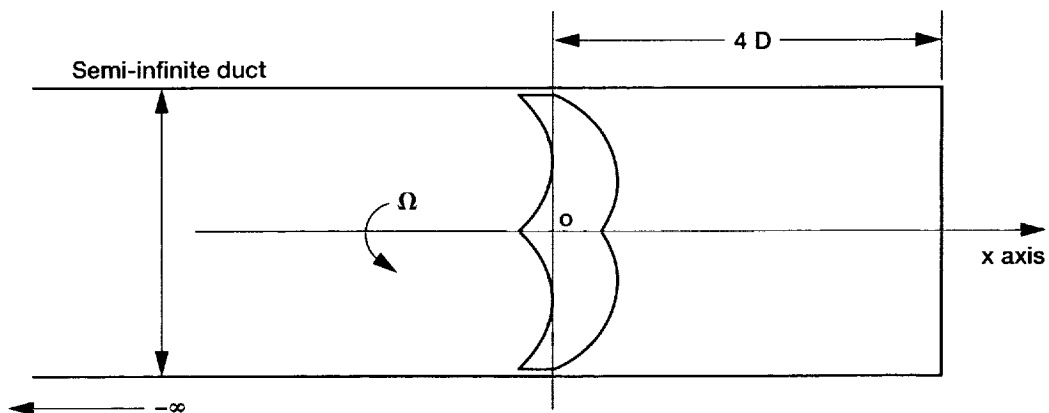
(b) Ducted rotor.

Problem 1: Single Airfoil Gust Response Problem

The purpose of this problem is to test the ability of a CFD/CAA code to accurately predict the unsteady aerodynamic and aeroacoustic response of a single airfoil to a two-dimensional, periodic vortical gust.

Consider the airfoil configuration shown in Figure 1. The airfoil has chord length c and angle of attack α. The upstream velocity is:

$$\mathbf{U} = U_\infty \mathbf{i} + \mathbf{a}\cos\left[\mathbf{k}\cdot\left(\mathbf{x} - iU_\infty t\right)\right] \tag{1}$$

where $\mathbf{x} = (x_1, x_2)$ denotes the spatial coordinates, $\mathbf{a} = (a_1, a_2)$ is the gust amplitude vector with $a_1 = -\varepsilon\, U_\infty k_2/\left|\mathbf{k}\right|$, $a_2 = \varepsilon\, U_\infty k_1/\left|\mathbf{k}\right|$, $\mathbf{k}$ is the wave number vector, and ε is a small parameter satisfying $\varepsilon \ll 1$.

The governing equations are the 2-D Euler equations

$$\frac{\partial\rho}{\partial t} + \frac{\partial}{\partial x}(\rho u) + \frac{\partial}{\partial y}(\rho v) = 0 \tag{2}$$

$$\frac{\partial}{\partial t}(\rho u) + \frac{\partial}{\partial x}(\rho u^2 + p) + \frac{\partial}{\partial y}(\rho uv) = 0 \tag{3}$$

$$\frac{\partial}{\partial t}(\rho u) + \frac{\partial}{\partial x}(\rho uv) + \frac{\partial}{\partial y}(\rho v^2 + p) = 0 \tag{4}$$

$$\frac{\partial E_t}{\partial t} + \frac{\partial}{\partial x}\left[(E_t + p)u\right] + \frac{\partial}{\partial y}\left[(E_t + p)v\right] = 0 \tag{5}$$

where ρ, u, v, p and E_t, denote the fluid density, velocity, pressure, and internal energy per unit volume.

Since the gust amplitude $\mathbf{a}$ satisfies $\left|\mathbf{a}\right| \ll U_\infty$, one can alternatively solve the linearized unsteady Euler equations

$$\frac{D_0\rho'}{Dt} + \rho'\nabla\cdot\mathbf{U}_0 + \nabla\cdot\left(\rho_0\mathbf{u}\right) = 0 \tag{6}$$

$$\rho_0\left(\frac{D_0\mathbf{u}}{Dt} + \mathbf{u}\cdot\nabla\mathbf{U}_0\right) + \rho'\mathbf{U}_0\cdot\nabla\mathbf{U} = -\nabla p' \tag{7}$$

$$\frac{D_0 s'}{Dt} = 0 \tag{8}$$

where $\dfrac{D_0}{Dt} = \dfrac{\partial}{\partial t} + \mathbf{U}_0\cdot\nabla$ is the material derivative associated with the mean flow, $\mathbf{u} = (u',v')$, primed quantities are the unknown perturbation variables, and 0 subscripts denote steady mean flow quantities which must be independently solved for and are assumed to be known.

Nondimensionalize the Euler equations as follows:

x_1, x_2	by	$\dfrac{c}{2}$
$\mathbf{U} = (u, v)$	by	U_∞
c_0 (sound speed)	by	U_∞
ρ	by	ρ_∞
p	by	$\rho_\infty U_\infty^2$
T	by	T_∞
t	by	$\dfrac{c}{2U_\infty}$
$\omega = k_1 U_\infty$	by	$\dfrac{2U_\infty}{c}$
k_1, k_2	by	$\dfrac{2}{c}$

If solving the linearized unsteady Euler equations, nondimensionalize the mean flow variables as above, and the perturbation variable as follows:

$\mathbf{u} = (u', v')$	by	U_∞
ρ'	by	ρ_∞
p'	by	$\rho_\infty U_\infty^2$
T'	by	T_∞
$\mathbf{a}$	by	U_∞

For the following two cases, solve the gust response problem for a Joukowski airfoil in a two-dimensional gust with $k_2 = k_1$ for reduced frequencies $k_1 = 0.1$, 1.0, and 3.0. The nondimensional upstream velocity is $\mathbf{U} = \mathbf{i} + \varepsilon \mathbf{a} \cos(\mathbf{k} \cdot \mathbf{x} - k_1 t)$, where $\mathbf{a} = (a_1, a_2)$ $= \left(-\dfrac{\sqrt{2}}{2}, \dfrac{\sqrt{2}}{2}\right)$. Take $\varepsilon = .02$.

For Case 1, the airfoil has a 12% thickness ratio, free stream Mach number $M_\infty = 0.5$, angle of attack $\alpha = 0°$, and a camber ratio of zero.

For Case 2, change α to 2° and the camber ratio to .02.

The airfoil geometries can be generated as follows. Set

$$\zeta_1 = r_0 e^{i\theta} + \zeta_{0'} \tag{9}$$

where

$$\zeta_{0'} = -\varepsilon_1 + i\varepsilon_2 \tag{10}$$

is a complex constant. Letting $z = x + iy$ denote the airfoil coordinates in the complex z-plane, the transformation

$$z = \left(\zeta_1 + \frac{d^2}{\zeta_1}\right) e^{-i\alpha} \tag{11}$$

transforms the ζ_1 circle defined by equation (9) into the desired airfoil shape.

For Case 1, use $r_0 = 0.54632753$, $\varepsilon_1 = 0.05062004$, $\varepsilon_2 = 0$, $d^2 = 0.24572591$, $\alpha = 0$. Discretize the ζ_1 circle in θ, starting from 0 and going to 2π, and then apply equation (11) to get the airfoil coordinates. The values $\theta = 0$ and $\theta = 2\pi$ map into the trailing edge point.

For Case 2, use $r_0 = 0.54676443$, $\varepsilon_1 = 0.05062004$, $\varepsilon_2 = 0.02185310$, $d^2 = 0.24572591$, $\alpha = 0.034906585$. Discretize the ζ_1 circle in θ, starting from $\theta = -\beta$ and going to $\theta = 2\pi - \beta$, $\beta = 0.039978687$, and then apply equation (11) to get the airfoil coordinates. The values $\theta = -\beta$ and $\theta = 2\pi - \beta$, map into the trailing edge point.

The above procedure for generating the airfoil geometries will generate Joukowski airfoil of chord length 2, situated very nearly between $x = -1$ and $x = 1$, where x is the nondimensional horizontal spatial coordinate. The airfoil geometries for the two cases are shown in figure 2.

For both Case 1 and Case 2, march the discrete equations in time until the solution becomes periodic. On the airfoil surface, calculate the mean pressure p_0 and the RMS pressure $\sqrt{\overline{(p')^2}}$. In the far field, calculate the intensity $\overline{(p')^2}$ on a circle of radius R = 8 (four chord lengths), centered at the origin (the airfoil center). State whether the solution is from the Euler equations or linearized equations. Also state the grid dimensions for each calculation, the number of complete periods computed, the CPU time per period, and the type of machine on which the calculations were run on.

Output Specification

Submitted solutions to the gust response problem will consist of six files. Each file will be presented in the following format. Line 1 will state the problem number, followed by the name(s) of the submitter(s). Line 2 will state a point of contact, phone number, and e-mail address. Line 3 will state, "Computed Airfoil Results for Case I, k1=freq, npoints = N", where $I = 1$ or 2, freq = 0.1, 1.0, or 3.0, and N is the number of data points on the airfoil. Both mean and RMS pressure values will be given as a function of fraction of airfoil chord, $(x-x_{1.e})/c$, where $x_{1.e}$ is the x coordinate of the airfoil leading edge. Lines 4 through $N+3$ will be the airfoil results written out in a format of (f12.8,2x,e16.8,2x, e16.8). The first number of each line will be the fraction of chord value, the second number the corresponding mean pressure, and the third the corresponding RMS pressure value. Write out the upper surface values first, followed by the lower surface values, beginning each time at the leading edge and proceeding to the trailing edge. Line $N+4$ will state "Computed Far-Field Results for Case I, k1=freq, npoints=181". The next 181 lines will be the mean square pressure values as a function of polar angle θ on a circle of radius four chord lengths from the airfoil center (the point on the y-axis midway between the leading and trailing edges). The θ values will begin with $0°$ and

continue up to 360° in two-degree increments. (A different θ discretization is acceptable so long as "npoints" is specified appropriately in line $N+4$.) The far-field results will be written in an (f10.2, 2x, e16.8) format, where the first number is the angle and the second number is the corresponding mean square pressure. The next five lines will state, in order, which equations were solved, the grid dimensions (i.e., $M \times N$), the number of periods computed, the CPU time per period, and the type of machine on which the calculations were run on.
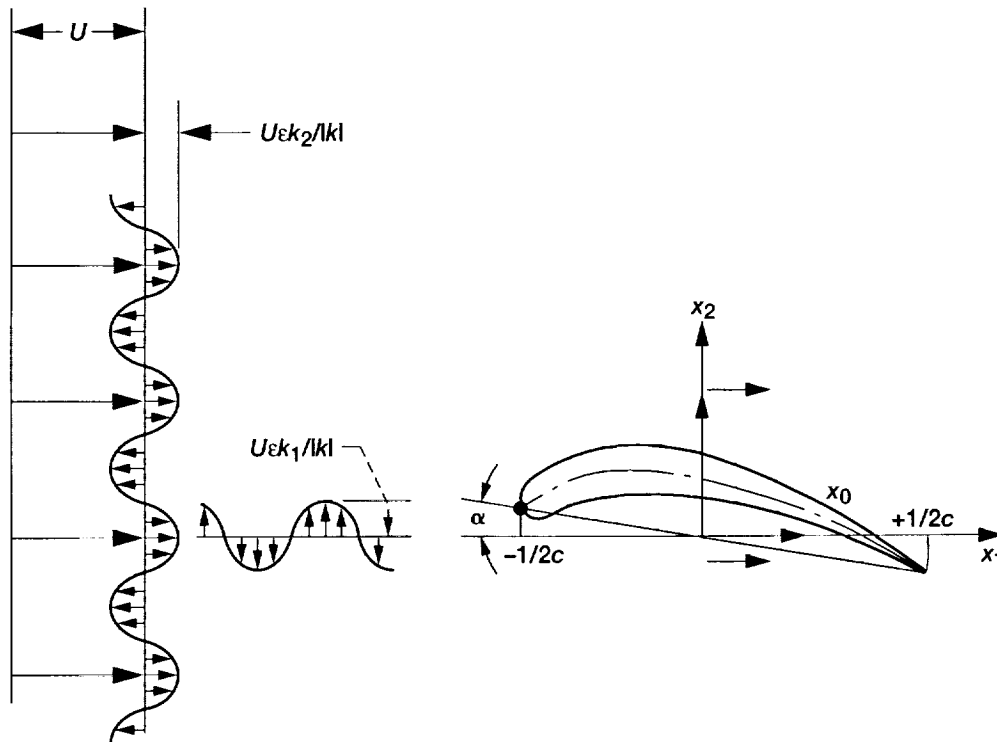
Figure 1.—Airfoil in a gust with parallel and vertical components.
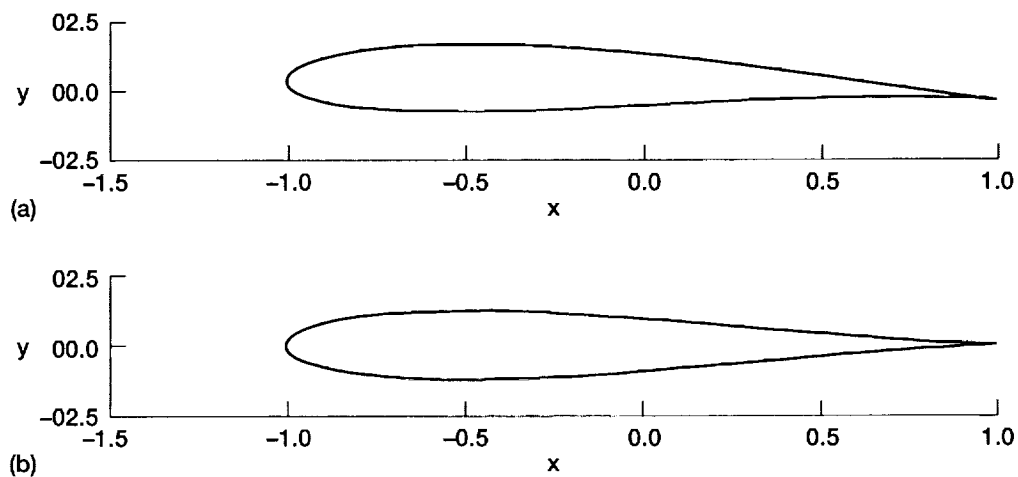
Figure 2.—Joukowski airfoil geometry. (a) Case 1. (b) Case2.

Problem 2: Unsteady Response of an Isolated Finite Span Swept Airfoil to an Incident Gust

This problem is aimed at testing the ability of CAA methods to calculate the acoustic field generated as a result of the interaction of a convected (i.e., frozen) harmonic gust with a finite span, swept, flat plate airfoil bounded by two parallel walls.

The coordinate system is chosen so that the x-axis is aligned with the chord of the airfoil (denoted by c), the y-axis is perpendicular to it and the z-axis is normal to the bounding walls. The origin of the coordinate system is located as shown. The normal distance between the walls is taken to be ℓ. The sweep of the airfoil is measured by α, the angle between the z-axis and the leading edge of the airfoil.

The mean flow is assumed to be uniform, unidirectional and aligned with the x-axis, i.e.,

$$U = (U_0, 0, 0), \qquad U_0 = constant, \qquad p_0 = constant, \qquad \rho_0 = constant, \tag{1}$$

The appropriate physical scales are: a_0 (the speed of sound) for velocity, ρ_0 for density, $\rho_0 a_0^2$ for pressure, c for length and c/a_0 for time. The evolution of small perturbations superimposed on the uniform flow is governed by the three-dimensional linearized Euler equations which, in non-dimensional form, are given by:

$$\frac{\partial}{\partial t}\begin{pmatrix} \rho \\ u \\ v \\ w \\ p \end{pmatrix} + \frac{\partial}{\partial x}\begin{pmatrix} M_0\rho + u \\ M_0 u + p \\ M_0 v \\ M_0 w \\ M_0 p + u \end{pmatrix} + \frac{\partial}{\partial y}\begin{pmatrix} v \\ 0 \\ p \\ 0 \\ v \end{pmatrix} + \frac{\partial}{\partial z}\begin{pmatrix} w \\ 0 \\ 0 \\ p \\ w \end{pmatrix} = 0 \tag{2}$$

where ρ, p, (u,v,w) denote perturbations in density, pressure and velocity components. M_0 is the mean flow Mach number.

The incident gust is a small-amplitude harmonic velocity fluctuation of the form

$$(u, v, w) = (0, A\cos(k_x x + k_y y + k_z z - \omega t), 0) \tag{3}$$

where k_x, k_y, k_z are the streamwise, transverse and normal gust wavenumbers and ω the harmonic frequency. The bounding walls and the airfoil are assumed impermeable. These conditions are supplemented by the Sommerfield radiation condition. The non-dimensional parameters of the problem are given by:

Wall spacing	$\ell/c = 2.6$
Sweep angle	$\alpha = 15°$
Mean flow Mach number	$M_0 = 0.5$
Gust amplitude	$A = 0.05$
Frequency	$\omega c/a_0 = k_x c M_0$
Chordwise gust wavenumber	$k_x c = 5.5$
Transverse gust wavenumber	$k_y c = 0.0$
Spanwise gust wavenumber	$k_z c = 3.6m$

Three cases, corresponding to three different gust orientations, are considered: $m = 0$, $m = 1$, $m = 2$. For each case, determine the rms acoustic pressure (i.e., $p_{rms} = \sqrt{\overline{p^2}}$) halfway between the two bounding walls and along a circle that is centered at the point $(0,0,\ell/2)$ and has a radius of $5c$. The overbar denotes time-averaging over one time period $2\pi/\omega$. Note that the long-time asymptotic solution is required, so run your calculations for sufficiently large t for all the transients to die out. The appropriate FORTRAN output statement should read "WRITE $(IUNIT, *)$ x, y, p_{rms}".
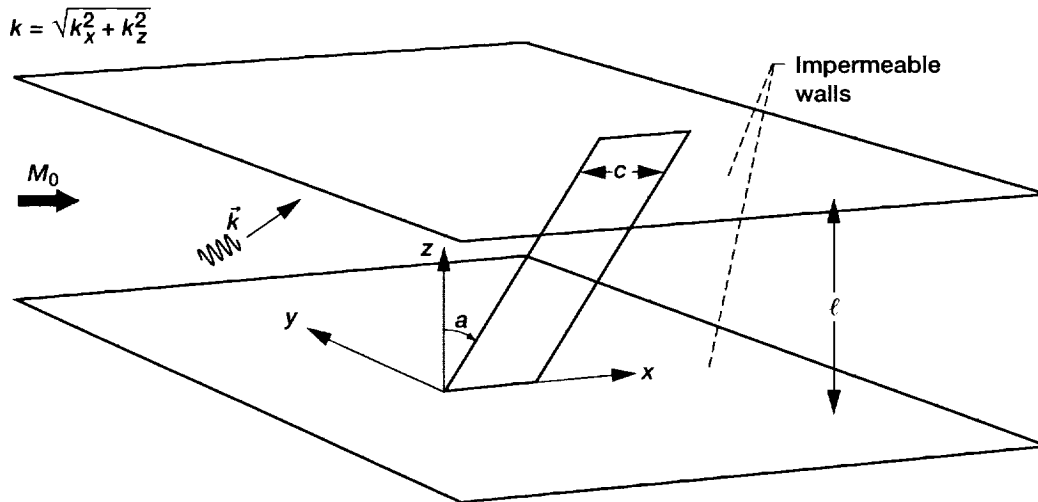
Problem 3: Unsteady Response of a Rectilinear Swept Cascade to an Incident Gust

This problem is aimed at testing the ability of CAA methods to calculate the acoustic pressure field generated as a result of the interaction of a convected harmonic gust with a rectilinear cascade of swept flat plates.

All relevant geometric information is the same as problem 2 with the exception of the sweep angle α which is now taken to be a variable. Assume a cascade stagger angle of zero (with the x-axis aligned with the chord) and a gap-to-chord ratio of $h/c = 1$. The mean flow Mach number M_0, gust frequency ω, gust amplitude A and chordwise wavenumber k_x are the same as in the previous problem. But for the cascade problem take $k_y = \pi$ and $k_z = 0$.

The appropriate physical scales are also the same as problem 2 as is the governing equation and boundary conditions. Naturally, the impermeability condition now applies to the entire cascade.

For this problem, determine the amplitude of upstream-radiated rms acoustic pressure as a function of the sweep angle at the specified frequency. Specifically, show the variations of rms acoustic pressure amplitude at the upstream location $(-5c, 0, \ell/2)$ for sweep angle α in the range $(0.0°, 30.0°)$. Use sweep angle increments no larger than $2.5°$. Express the results in dB using the rms pressure value for $\alpha = 0.0°$ as the reference level. The appropriate FORTRAN output statement should read "WRITE ($IUNIT$, *) α, $20 \log_{10} (p_{rms}(\alpha)/p_{rms}(0))$".
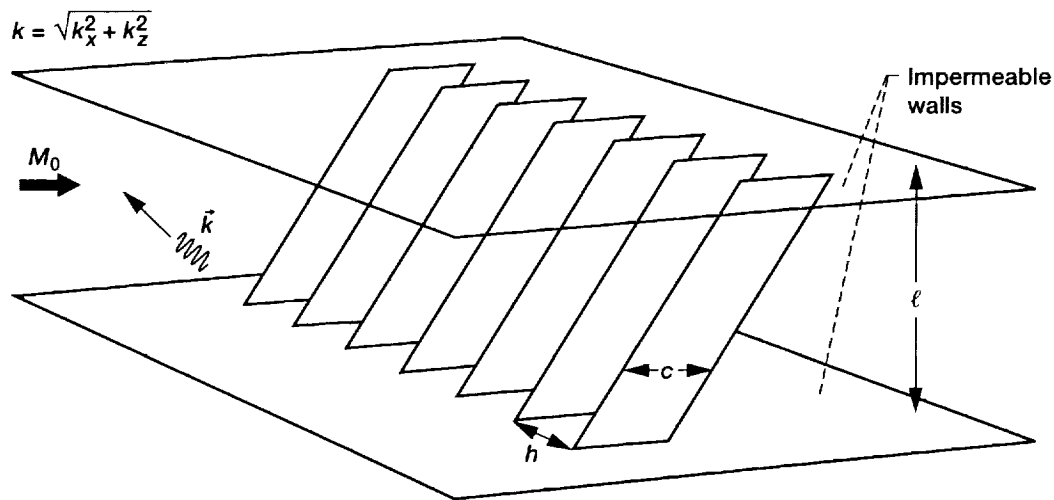
These problems are simple representations of rotor wake/stator interaction in axial flow fans. They include much of the blade row scattering/spinning mode propagation physics of the real problem but are still in the realm of Green's function/panel methods, so that results can be checked. They are problems that anyone developing a CFD/CAA code for fans might do for code checkout and should be doable with several codes in existence today. The vane/blade ratio of 3/2 will make the problems easier for codes based on periodic boundary conditions.

The first cases are for excitation that is nearly 2D (constant along the span). Then, the problem is made progressively more 3-dimensional by varying the phase of the excitation along the span. This simulates the situation (typical of turbofans) where more than one wake from the rotor intersects a vane at the same time. A high hub/tip ratio case has been added for a check against 2D (S.N. Smith) theory.

3D results will be checked by comparison with one or more well known panel methods. In particular, Professor M. Namba from Kyushu University in Japan and Dr. J.B.H.M. Schulten from the National Aerospace Laboratory NLR in the Netherlands will be asked to provide results from their lifting surface codes.

$B = 16$
$V = 24$
$h/R = 0.5$
$(gap/chord)_{tip} = 1.0$
$M = 0.5$
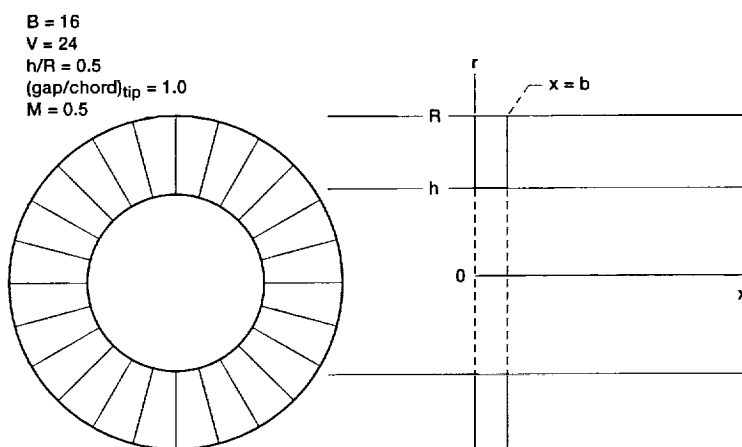
Mean Flow and Geometry

Assume standard day conditions for speed of sound a_0 and pressure p_0 and uniform axial flow at $M_x = 0.5$. The duct is infinite in both directions with constant outer radius R (which need not enter the calculations) and hub/tip ratio h/R. The stator consists of constant chord, zero thickness vanes with chords parallel to the fan axis. (If zero thickness causes problems, use 10th standard cascade airfoils with camber removed. Ordinate information is provided on the CD.) Gap/chord = 1.0 at the tip. Blade/vane counts are $B = 16$ and $V = 24$. The duct and the 24 vanes are the only surfaces.

Wake Representation

In the x, r, ϕ coordinate system, excitation for the problem is a convected wave of radial vorticity representing a harmonic rotor wake. It produces a velocity perturbation in the ϕ direction given by (the real part of)

$$v(r, \phi, x, t) = U \sum_{n=0}^{\infty} V_n e^{inB[\Omega x/U + \phi - \theta(r) - \Omega t]} \tag{1}$$

U is the axial flow speed $a_0 M_x$ and Ω is the rotor (and wake) angular velocity. Consider only the blade passing frequency (BPF) fundamental, $n = 1$, with upwash amplitude equal to 0.1 radian, $V_n = 0.1$. Reduced frequency $\omega b/U = nB \Omega b/U$ is constant over the span. The function giving the radial dependence is

$$\theta(r) = -\frac{2\pi q}{B}\frac{r-h}{R-h} \tag{2}$$

$\theta(R) = -2\pi q/B$ is the phase shift along the stator span. For $q = 0$, the excitation is in phase from root to tip of the stator. When $q = 2$, there are 2 wakes intersecting each stator vane, on average. The minus sign leading (2) causes the wake at the stator root to lead that at the tip as in typical fan designs. In the convention of (1), the inter-vane phase angle is $2\pi nB/V$ (counting vanes in the direction of rotor rotation).

Cases for Computation

Some participants may want to test their codes in a narrow annulus mode first for comparison with the Smith code before moving on to the 3D cases. Results from the Smith code are available on the CD. The appendix provides background from standard fan noise theory (Tyler-Sofrin) that was used to determine the 3D cases.

Narrow Annulus

To approximate 2D, run hub/tip ratio $h/R = 0.98$ and no radial variation, $\theta(r) = 0$. In this case the cutoff ratio of the response waves is given by

$$\xi = \frac{nB}{m}\frac{M_T}{\beta} \tag{3}$$

where $m = nB - kV$ is their spinning mode order and $\beta^2 = 1 - M_x^2$. Run a BPF ($n = 1$) series around cuton plus two cases well above cuton as follows

ξ	M_T	Comments
0.9	0.3897	cut off (sub-resonant)
1.0	0.4330	resonant
1.1	0.4763	m = -8 is cut on
1.5	0.6495	m = -8 is cut on

The chord-based reduced gust frequency $\omega b/U = nB\Omega\, b/(a_0 M) = nB\Omega R/(a_0 M)b/R = (2\pi nB/V)(M_T/M)$ where $V = 24$ is the vane count. The duct radius-based acoustic reduced frequency $\omega R/a_0 = nBM_T$.

To present results, give the complex coefficients A_m, which are defined by the expression for the pressure perturbation

$$p(x,\phi,t) = p_0 \sum_{k=-\infty}^{\infty} A_m(x)e^{i(m\phi - nB\Omega t)} \tag{4}$$

Do this for axial locations one chord upstream and one chord downstream of the stator ($x = -b$ and $+2b$) and present results by filling in the following table with complex values of A_m.

M_T	Upstream Waves, $x = -b$				Downstream Waves, $x = +b$			
	m = 40	m = 16	m = -8	m = -32	m = 40	m = 16	m = -8	m = -32
0.3897								
0.4330								
0.4763								
0.6495								

Full Annulus

These are all for $h/R = 0.5$. The first series is for zero radial phase variation and has the same cutoff ratios as the narrow annulus case above. They pass through cuton via increases in rotor speed.

q	ξ	M_T
0	0.9	0.470
0	1.0	0.522
0	1.1	0.574
0	1.5	0.783

The second series starts with the $\xi = 1.5$ case above and progresses through cutoff by increasing the phase variation of the excitation along the radius. This represents the sweep of a rotor wake.

q	$\xi @ \mu = q$	M_T
0	**1.50**	**0.783**
0.5		0.783
1.0	1.05	0.783
1.5		0.783
2.0	**0.83**	**0.783**
2.5		0.783
3.0	0.65	0.783

The middle column is the cutoff ratio of the acoustic mode with the same number of radial zero crossings as the excitation wave.

Present results as the complex coefficients $A_{nm\mu}$, which are defined by the pressure field modal expansion

$$p_n(r, \phi, x, t) = p_0 \sum_{k=-\infty}^{\infty} \sum_{\mu=0}^{\infty} A_{nm\mu}(x) \Psi_{m\mu}(r) e^{i(m\phi - nB\Omega t)} \tag{5}$$

where $\Psi_{m\mu}(r)$ is the radial mode shape (discussed below) and, again, $m = nB - kV$. Do this for axial locations one chord upstream and one chord downstream of the stator ($x = -b$ and $+2b$). Present results in modal form by filling in tables like the following for each condition run.

Radial mode order μ	Upstream Waves, $x = -b$				Downstream Waves, $x = +b$			
	$m = 40$	$m = 16$	$m = -8$	$m = -32$	$m = 40$	$m = 16$	$m = -8$	$m = -32$
0								
1								
2								
3								
4								

For participants wishing to minimize the number of cases to run, the highest priority should be the $q = 0$ and $q = 2$ cases at $M_T = 0.783$ shown above in bold type.

The mode amplitudes will depend on the convention used for the radial mode shapes $\Psi_{m\mu}(r)$. These are the duct eigenmodes described by Tyler and Sofrin. However, for easy comparison with 2D results, a different normalization is used. The extreme value of each mode is set to $+1$. The FORTRAN routine that allows Fourier analysis of the pressure perturbation in a constant x-plane to determine the complex mode amplitudes $A_{nm\mu}$ is available on the CD.

REFERENCES

1. Smith, S.N., "Discrete Frequency Sound Generation in Axial Flow Turbomachines," Aeronautical Research Council Reports and Memoranda, R. & M. No. 3709, HMSO, London, 1973.
2. Tyler, J.M. & Sofrin, T.G., "Axial Flow Compressor Noise Studies," SAE Trans., Vol. 70, 1962, 308–332.

Appendix—Background from Spinning Mode Theory

In the traditional treatment of acoustic waves in annular ducts with uniform axial flow, the pressure disturbance at the nth harmonic of blade passing frequency can be expressed in the following modal form

$$p_n(r, \phi, x, t) = p_0 \sum_k \sum_\mu A_{nm\mu} \Psi_{m\mu}(r) e^{i\left(\gamma_{nm\mu} x + m\phi - nB\Omega t\right)} \tag{6}$$

where the circumferential order of the spinning mode order is

$$m = nB - kV \tag{7}$$

Ω is the angular speed of the rotor and $\Psi_{m\mu}(r)$ are the radial mode functions, which are combinations of Bessel functions. From the form of the exponential in (6), it can be deduced that the spin Mach number of the mode at the outer wall is

$$M_S = \frac{nB}{m} M_T \tag{8}$$

where $M_T = (\Omega R/a_0)$ is the rotor tip rotational Mach number. Since cuton is determined by the mode spin speed, we must identify the most cut on mode. The following table, for $n = 1$ (BPF)

k	m	nB/m
-1	40	0.40
0	16	1.00
1	-8	-2.00
2	-32	-0.50

shows that the fastest mode is the fundamental interaction mode $m = B - V$. This is an 8 lobe pattern rotating in the direction opposite the rotor at twice the rotor speed.

The cutoff ratio is the ratio of the rpm to the cuton rpm. This is given by

$$\xi = \frac{nB}{m} \frac{M_T}{\beta M_m^*} \tag{9}$$

which is also the ratio of the mode spin speed to the spin speed βM^*_m at which the mode cuts on. $M^*_m = k'\sigma_{m\mu}/m$ can be computed by looking up $k'\sigma_{m\mu}$ in the Tyler-Sofrin paper. The correction for axial Mach number is $\beta^2 = 1 - M_x^2$. Note that $M^*_m = 1.0$ for 2D cases. The required information for our situation at BPF with an $m = -8$ mode in a duct with 0.5 hub/tip ratio and 0.5 axial Mach number is

μ	M^*_m	βM^*_m	M^*_T
0	1.205	1.043	0.522
1	1.725	1.494	0.747
2	2.168	1.877	0.939
3	2.767	2.396	1.198

where M^*_T is the rotor tip Mach number for cuton of the -8,μ mode.

An acoustic source inside of a 2-D jet excites an instability wave in the shear layer resulting in sound radiating away from the shear layer. Solve the linearized Euler equations to predict the sound radiation outside of the jet. The governing equations are given by

$$\frac{\partial \rho'}{\partial t} + U(y)\frac{\partial \rho'}{\partial x} + \rho(y)\frac{\partial u'}{\partial x} + \rho(y)\frac{\partial v'}{\partial y} + v'\frac{\partial \rho(y)}{\partial y} = 0$$

$$\frac{\partial u'}{\partial t} + U(y)\frac{\partial u'}{\partial x} + v'\frac{\partial U(y)}{\partial y} = -\frac{1}{\rho(y)}\frac{\partial p'}{\partial x}$$

$$\frac{\partial v'}{\partial t} + U(y)\frac{\partial v'}{\partial x} = -\frac{1}{\rho(y)}\frac{\partial p'}{\partial y}$$

$$\frac{\partial p'}{\partial t} + U(y)\frac{\partial p'}{\partial x} + \gamma P\frac{\partial u'}{\partial x} + \gamma P\frac{\partial v'}{\partial y} = A\exp\left[-B(\ln 2)\left(x^2 + y^2\right)\right]\cos(\omega t)$$

and the mean flow variables are given by

$$U(y) = U_\infty + \left(U_j - U_\infty\right)\exp\left[-(\ln 2)\left(\frac{y}{b} - \frac{h}{b}\right)^2\right], \quad y \geq h$$

$$= U_j \qquad\qquad\qquad 0 \leq y < h$$

$$\frac{1}{\rho(y)} = -\frac{1}{2}\frac{\gamma - 1}{\gamma P}\left(U(y) - U_j\right)\left(U(y) - U_\infty\right) + \frac{1}{\rho_j}\frac{\left(U(y) - U_\infty\right)}{\left(U_j - U_\infty\right)} + \frac{1}{\rho_\infty}\frac{\left(U_j - U(y)\right)}{\left(U_j - U_\infty\right)}$$

The jet static pressure is assumed to be constant. The jet flow is parallel and symmetric about the x-axis. Use a symmetry boundary condition along the x-axis.

The length scale is given by the half-velocity distance $R_{1/2}$. The velocity is scaled by the jet velocity U_j, the density by ρ_j, the pressure by $\rho_j U^2_j$, and the time and frequency by $R_{1/2}/U_j$. The constants are given as: $P = 101330$ (kg/m s^2), $R = 286.8875$ (m^2/s^{2}K), $U_j = 517.4569$ (m/s), $T_j = 166.6667$ (K), $U_\infty = 0$, $T_\infty = 300$ (K), $M_j = 2$, $T_{j0}/T_\infty = 1$, $\gamma = 1.4$, $R_{1/2} = h + b = 1$ (m), $h = 0.6$ (m), $b = 0.4$ (m), $A = 0.001$ (kg/ms^3), and $B = 8$ (1/m^2). Calculations are to be made at frequencies with St $= 2fR_{1/2}/U_j = 0.14$ and 0.6. The physical domain is $-5 \leq x/R_{1/2} \leq 50$ and $0 \leq y/R_{1/2} \leq 10$.

Benchmark Problems—Category 5

Generation and Radiation of Acoustic Waves from a 2-D Sh...

Calculate $\overline{p'^2}$ along the outer boundary at 101 evenly spaced points along the line $y/R_{1/2} = 10$ over $0 \le x/R_{1/2} \le 50$ and at 16 evenly spaced points along the line $x/R_{1/2} = 50$ over $2 \le y/R_{1/2} \le 9.5$. Also, calculate p' at 101 evenly spaced points along the line $y/R_{1/2} = 1$ over $0 \le x/R_{1/2} \le 50$ at the start of a cycle. Output $x/R_{1/2}$, $y/R_{1/2}$, $\overline{p'^2}$ or p' in FORMAT (3(2X,1P,E14.5)).

Specify the computer used, the total CPU time, the time step size, the total number of time steps, and the total number of grid points.
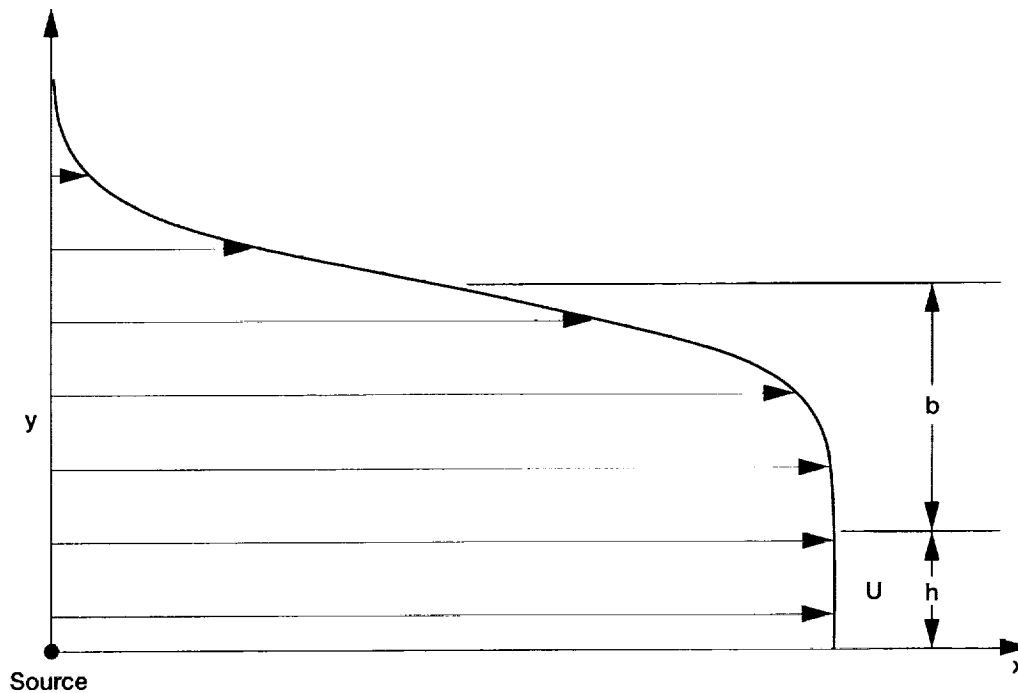
Calculate the frequencies and the sound pressure level in dB of the tones at the center of the left wall associated with the flow of air over a door gap cavity. Data exists for the geometry and velocities shown in Figure 1. It is known experimentally that two edgetone frequencies occur between 0 Hz and 2000 Hz and frequencies associated with longitudinal cavity modes occur between 2000 Hz and 4000 Hz. The boundary layer is turbulent. The boundary layer thickness at the mouth of the cavity is 1.6 cm for U = 26.8 m/s and 2.2 cm for U = 50.9 m/s. For simplicity, you may use the one-seventh power-law velocity profile given by

$$\left\{ \frac{u}{U_0} \right\} = \left(\frac{y}{\delta} \right)^{\frac{1}{7}},$$

where δ is the boundary layer thickness. You may do one or both cases.

A = 15.9 mm
B = 24.7 mm
C = 8.76 mm
D = 3.3 mm
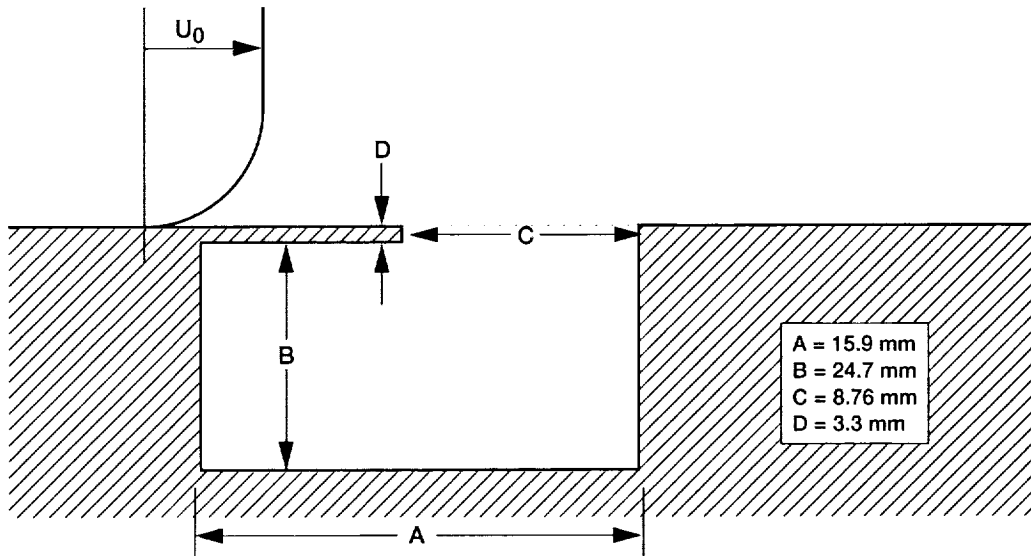
Figure 1.

Analytical Solutions

PROPAGATION OF SOUND THROUGH A TRANSONIC NOZZLE
CATEGORY 1: PROBLEM 1, ANALYTICAL SOLUTION

CHRISTOPHER K.W. TAM

Department of Mathematics

Florida State University

Tallahassee, FL 323064510

Email: tam@math.fsu.edu

Introduction

There are two primary objectives in formulating this benchmark problem. First, most aeroacoustics problems have multiple-length scales. This problem is designed to test the workshop participants' ability to deal with this type of problems computationally. When sound waves propagate against a flow, their wavelengths decrease as they enter into regions with higher and higher subsonic Mach number. In this problem, the Mach number at the nozzle throat reaches a value of 0.94. A simple estimate shows that there is a reduction of acoustic wavelength by a factor of about 10 in propagating through the nozzle throat.

The second objective of this problem is to test the formulation and implementation of numerical boundary conditions. In this problem, there is an incoming sound wave from the downstream side of the nozzle. Because of the constriction imposed by the nozzle throat, a part of the wave train is reflected back. The remaining part propagates through and exits the upstream end of the nozzle as the transmitted wave. Since the computation domain is specified to be from $x = -10$ to $+10$, a radiation boundary condition is needed at the upstream end of the nozzle. At the downstream end of the computation domain an inhomogeneous outflow boundary condition is required. The boundary condition must generate the incoming acoustic wave and at the same time allow the reflected acoustic wave and entropy wave to exit without reflection.

Without solving the problem, the nature of the solution can be easily established by simple physical reasonings. The problem asks one to find the maximum pressure envelope. Upstream of the nozzle throat, essentially there is only the transmitted acoustic wave. So the maximum pressure envelope should be a constant. At the throat, the nozzle area is the smallest and the propagation speed is the slowest. By conservation of acoustic wave energy flux, the sound pressure level must be the highest. One expects a sharp peak at the nozzle throat. Downstream of the throat, there is an upstream propagating acoustic wave as well as a downstream propagating reflected wave. The two wave trains

form an interference pattern. Let the maximum pressure level of the upstream propagating wave be A and that of the reflected wave be B. Then the maximum and minimum level of the interference pattern is approximately $A + B$ and $A - B$, respectively. The average is A, which must be equal to the maximum amplitude of the incoming wave. This is prescribed by the problem as ε.

Exact Solution

The governing equations are the quasi-one-dimensional continuity, momentum and energy equations,

$$\frac{\partial \rho}{\partial t} + \frac{1}{A}\frac{\partial(\rho u A)}{\partial x} = 0 \tag{1}$$

$$\rho\left(\frac{\partial u}{\partial t} + u\frac{\partial u}{\partial x}\right) + \frac{\partial p}{\partial x} = 0 \tag{2}$$

$$A\frac{\partial p}{\partial t} + \frac{\partial(puA)}{\partial x} + (\gamma - 1)p\frac{\partial(uA)}{\partial x} = 0 \tag{3}$$

where $\gamma = 1.4$ and $A(x)$, the nozzle area, is given. The time independent mean flow solution of (1), (2) and (3), denoted by an overbar, is

$$\overline{p}\,\overline{u}\,A = \rho_r u_r A_r \tag{4}$$

$$\frac{\overline{p}}{\overline{\rho}^\gamma} = \frac{p_r}{\rho_r^\gamma} \tag{5}$$

$$\frac{\overline{u}^2}{2} + \frac{\gamma}{\gamma - 1}\frac{p_r}{\rho_r^\gamma}\overline{\rho}^{\gamma-1} = \frac{u_r^2}{2} + \frac{\gamma}{\gamma - 1}\frac{p_r}{\rho_r} \tag{6}$$

where subscript r denotes physical quantities in the reference station. In this case, we use the Mach 0.4 uniform region as the reference station. Thus $\rho_r = 1$, $u_r = 0.4$, $p_r = \frac{1}{\gamma}$ and $A_r = 0.536572$.

The acoustic disturbances in the nozzle are very small. A linear analysis will suffice. The linearized forms of equations (1) to (3) are,

$$\frac{\partial \rho}{\partial t} + \frac{\overline{p}\,u}{A}\frac{dA}{dx} + \overline{p}\frac{\partial u}{\partial x} + u\frac{d\overline{p}}{dx} + \rho\frac{\overline{u}}{A}\frac{dA}{dx} + \rho\frac{d\overline{u}}{dx} + \overline{u}\frac{\partial \rho}{\partial x} = 0 \tag{7}$$

$$\overline{\rho}\frac{\partial u}{\partial t} + \overline{\rho}\,\overline{u}\frac{\partial u}{\partial x} + \rho\,\overline{u}\frac{d\overline{u}}{dx} + \overline{\rho}\,u\frac{d\overline{u}}{dx} + \frac{\partial p}{\partial x} = 0 \tag{8}$$

$$\frac{\partial p}{\partial t} + \overline{u}\frac{\partial p}{\partial x} + u\frac{d\overline{p}}{dx} + \frac{\gamma}{A}(\overline{p}\,u + p\,\overline{u})\frac{dA}{dx} + \gamma\overline{p}\frac{\partial u}{\partial x} + \gamma p\frac{d\overline{u}}{dx} = 0 \tag{9}$$

Interest is on time periodic solution of frequency ω. Let the solution be of the form,

$$\begin{bmatrix} \rho \\ u \\ p \end{bmatrix} = \mathrm{Re} \left\{ \begin{bmatrix} \widehat{\rho}(x) \\ \widehat{u}(x) \\ \widehat{p}(x) \end{bmatrix} e^{-i\omega t} \right\}. \tag{10}$$

On substitution of (10) into (7) to (9), the governing equations for the amplitude functions $(\widehat{\rho}, \widehat{u}, \widehat{p})$ may be found. They are,

$$\overline{u} \frac{d\widehat{\rho}}{dx} + \overline{\rho} \frac{d\widehat{u}}{dx} = i\omega \, \widehat{\rho} - \frac{1}{A}(\overline{\rho} \, \widehat{u} + \overline{u} \, \widehat{\rho}) \frac{dA}{dx} - \widehat{u} \frac{d\overline{\rho}}{dx} - \widehat{\rho} \frac{d\overline{u}}{dx}$$

$$\overline{\rho} \, \overline{u} \frac{d\widehat{u}}{dx} + \frac{d\widehat{p}}{dx} = i\omega \, \overline{\rho} \, \widehat{u} - \overline{\rho} \, \overline{u} \frac{d\overline{u}}{dx} - \overline{\rho} \, \widehat{u} \frac{d\overline{u}}{dx} \tag{11}$$

$$\gamma \, \overline{p} \frac{d\widehat{u}}{dx} + \overline{u} \frac{d\widehat{p}}{dx} = i\omega \, \widehat{p} - \widehat{u} \frac{d\overline{p}}{dx} - \frac{\gamma}{A}(\overline{p} \, \widehat{u} + \widehat{p} \, \overline{u}) \frac{dA}{dx} - \gamma \, \widehat{p} \frac{d\overline{u}}{dx}.$$

In the uniform regions upstream and downstream of the nozzle throat, equations (11) reduce to a system of equations with constant coefficients. Three exact solutions are easily found. They are the upstream propagating acoustic wave, with solution in the form,

$$\begin{bmatrix} \widehat{\rho} \\ \widehat{u} \\ \widehat{p} \end{bmatrix} = \begin{bmatrix} \frac{1}{\overline{a}^2} \\ -\frac{1}{(\overline{\rho} \, \overline{a})} \\ 1 \end{bmatrix} e^{-i\frac{\omega x}{(\overline{a} - \overline{u})}} \tag{12}$$

(where $\overline{a} = (\frac{\gamma \overline{p}}{\overline{\rho}})^{\frac{1}{2}}$ is the speed of sound), the downstream propagating acoustic wave,

$$\begin{bmatrix} \widehat{\rho} \\ \widehat{u} \\ \widehat{p} \end{bmatrix} = \begin{bmatrix} \frac{1}{\overline{a}^2} \\ \frac{1}{(\overline{\rho} \, \overline{a})} \\ 1 \end{bmatrix} e^{i\frac{\omega x}{(\overline{a} + \overline{u})}}, \tag{13}$$

and the entropy wave, which is convected downstream by the mean flow,

$$\begin{bmatrix} \widehat{\rho} \\ \widehat{u} \\ \widehat{p} \end{bmatrix} = \begin{bmatrix} 1 \\ 0 \\ 0 \end{bmatrix} e^{i\frac{\omega x}{\overline{u}}}. \tag{14}$$

There is no simple analytical solution to equation (11). To find a numerical solution to the benchmark problem, one may integrate (11) numerically using the Runge-Kutta or similar method. Suppose (11) is integrated numerically from $x = 10$ to $x = -10$ using (12) as the starting solution. Let us label

this solution as the incoming wave solution. Again, integrate (11) from $x = 10$ to $x = -10$ using (13) and (14) as the starting solutions. We will call these two solutions as the reflected wave and the entropy wave solution. The amplitude of the incoming wave solution is ε as given by the benchmark problem. The amplitude of the reflected wave and the entropy wave are unknown. At $x = -10$ and further upstream there is only one upstream propagating acoustic wave given by (12). This is the transmitted wave. Now, the solutions at $x = -10$ must match. This yields,

$$\varepsilon \begin{bmatrix} \widehat{\rho} \\ \widehat{u} \\ \widehat{p} \end{bmatrix}_{\text{incoming}} + c_1 \varepsilon \begin{bmatrix} \widehat{\rho} \\ \widehat{u} \\ \widehat{p} \end{bmatrix}_{\text{reflected}} + c_2 \varepsilon \begin{bmatrix} \widehat{\rho} \\ \widehat{u} \\ \widehat{p} \end{bmatrix}_{\text{entropy}} = c_3 \varepsilon \begin{bmatrix} \widehat{\rho} \\ \widehat{u} \\ \widehat{p} \end{bmatrix}_{\text{transmitted}} . \tag{15}$$

For the benchmark problem, we find $c_1 = -0.01615 - 0.11636i$, $c_2 = 0.0$, $c_3 = 0.49037 + 0.24309i$. In other words, there is negligible amount of entropy wave. Also about 10% of the incoming acoustic wave energy is reflected back by the nozzle throat. The maximum pressure envelope is shown in figures 1 and 2.
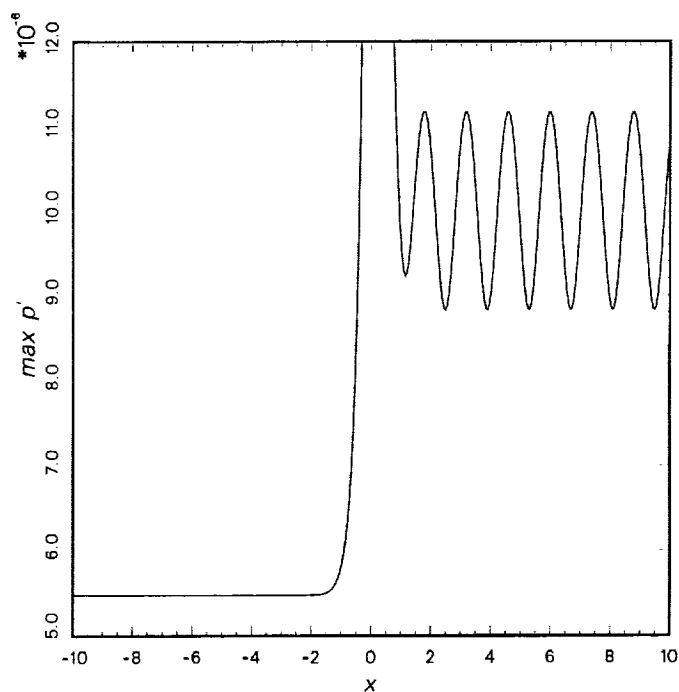
Figure 1. Maximum pressure envelope along the transonic nozzle
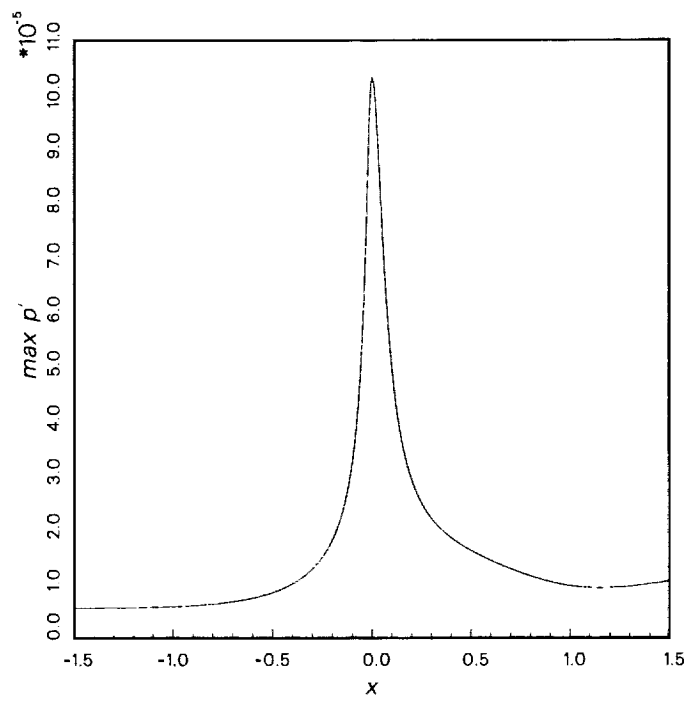
Solution of Category 1 Problem 2

RAY HIXON
CAA Group, ICOMP
NASA Glenn Research Center
Cleveland, OH 44135

J. Wright
Massachusetts Institute of Technology
Cambridge, MA 02139

In Category 1, the problems are solved using the quasi-1-D Euler equations, given in the conserved variables as:

$$\left\{\begin{array}{c} \rho \\ \rho u \\ E \end{array}\right\}_t + \left\{\begin{array}{c} \rho u \\ \rho u^2 + p \\ u(E+p) \end{array}\right\}_x + \frac{1}{A}\frac{dA}{dx}\left\{\begin{array}{c} \rho u \\ \rho u^2 \\ u(E+p) \end{array}\right\} = 0 \qquad (1)$$

The nozzle is the same for both problems, extending from -10<x<10 with the distribution:

$$A(x) = \left\{\begin{array}{ll} 0.536572 - 0.198086e^{-(\ln 2)(x/0.6)^2} & x > 0 \\ 1.0 - 0.661514e^{-(\ln 2)(x/0.6)^2} & x < 0 \end{array}\right. \qquad (2)$$

The problem to be solved is the downstream propagation of an acoustic wave through a shock wave in a convergent-divergent nozzle. The mean flow is set as:

$$\left\{\begin{array}{c} \bar{\rho} \\ \bar{u} \\ \bar{p} \end{array}\right\}_{inflow} = \left\{\begin{array}{c} 1 \\ 0.2006533 \\ 1/\gamma \end{array}\right\} \qquad (3)$$

and

$$p_{outflow} = 0.6071752 \qquad (4)$$

The acoustic wave is set at the upstream boundary as:

$$\left\{ \begin{matrix} \rho' \\ u' \\ p' \end{matrix} \right\}_{inflow} = \varepsilon \left\{ \begin{matrix} 1 \\ 1 \\ 1 \end{matrix} \right\} \sin\left(\omega \left[\frac{x_{inflow}}{(1 + M_{inflow})} + t \right] \right) \tag{5}$$

The variables are linearized about a steady mean flow:

$$\rho = \bar{\rho} + \hat{\rho} e^{i\omega t}$$
$$u = \bar{u} + \hat{u} e^{i\omega t} \tag{6}$$
$$p = \bar{p} + \hat{p} e^{i\omega t}$$

The mean flow is given as a function of the local Mach number as:

$$\bar{\rho} = \bar{\rho}_0 \left(1 + \frac{(\gamma - 1)}{2} \bar{M}^2 \right)^{-\left(\frac{1}{\gamma - 1} \right)}$$

$$\bar{c} = \bar{c}_0 \left(1 + \frac{(\gamma - 1)}{2} \bar{M}^2 \right)^{-\frac{1}{2}} \tag{7}$$

$$\bar{p} = \frac{\bar{\rho} \bar{c}^2}{\gamma}$$

$$\bar{u} = \bar{c} \bar{M}$$

The mean flow is marched in space using:

$$\frac{d}{dx} \bar{M} = \frac{\bar{M} \left(1 + \frac{(\gamma - 1)}{2} \bar{M}^2 \right) \frac{dA}{dx}}{A (\bar{M}^2 - 1)} \tag{8}$$

The characteristic waves are defined as:

$$A_1 = \hat{p} - \bar{c}^2 \hat{\rho}$$
$$A_2 = \hat{p} - \bar{\rho} \bar{c} \hat{u} \tag{9}$$
$$A_3 = \hat{p} + \bar{\rho} \bar{c} \hat{u}$$

where A_1 is the entropy wave, A_2 is the upstream-running acoustic wave, and A_3 is the down-stream-running acoustic wave.

These waves are marched in space using the equations:

$$\frac{dA_1}{dx} = \left(\frac{i\omega\sqrt{1 + \frac{(\gamma-1)}{2}\overline{M}^2}}{\overline{c}_0\overline{M}} + \frac{\gamma\overline{M}}{1-\overline{M}^2} \right) A_1$$

$$\frac{dA_2}{dx} = \left(\frac{-\overline{M}^2\frac{dA}{dx}}{(\overline{M}-1)^2(\overline{M}+1)A} \right) A_1 \qquad\qquad (10)$$

$$+ \left(\frac{i\omega\sqrt{1 + \frac{(\gamma-1)}{2}\overline{M}^2}}{\overline{c}_0(\overline{M}-1)} + \frac{(-2 + 2\overline{M} - (3+\gamma)\overline{M}^2 + (1+3\gamma)\overline{M}^3)\frac{dA}{dx}}{4(\overline{M}-1)^2(\overline{M}+1)A} \right) A_2$$

$$+ \left(\frac{\left(1 - \frac{(\gamma-1)}{2}\overline{M}^2\right)\frac{dA}{dx}}{2(\overline{M}-1)^2 A} \right) A_3$$

$$\frac{dA_3}{dx} = \left(\frac{\overline{M}^2\frac{dA}{dx}}{(\overline{M}+1)^2(\overline{M}-1)A} \right) A_1$$

$$+ \left(\frac{\left(1 - \frac{(\gamma-1)}{2}\overline{M}^2\right)\frac{dA}{dx}}{2(\overline{M}+1)^2 A} \right) A_2$$

$$+ \left(\frac{i\omega\sqrt{1 + \frac{(\gamma-1)}{2}\overline{M}^2}}{\overline{c}_0(\overline{M}+1)} + \frac{(2 - 2\overline{M} - (3+\gamma)\overline{M}^2 - (1+3\gamma)\overline{M}^3)\frac{dA}{dx}}{4(\overline{M}+1)^2(\overline{M}-1)A} \right) A_3$$

For marching in space, the 5-6 optimized fourth-order nonlinear Runge-Kutta method of Stanescu and Habashi is used (ref. 1)

In this calculation, there are three regions to be solved: (1) upstream of the sonic point, (2) between the sonic point and the shock, and (3) downstream of the shock. These regions are illustrated in Figure 1.

Region 1: Upstream of the Sonic Point

In this region, the solution is marched upstream from the sonic point to the upstream boundary. At the sonic point, the equation for the Mach number changes to:

$$\frac{d}{dx}\overline{M}\Big|_{\overline{M}=1} = \pm\sqrt{\frac{(\gamma+1)\dfrac{d^2A}{dx^2}}{4A}} \tag{11}$$

Since the flow goes from subsonic to supersonic at the sonic point, the positive value is used.

There can be no perturbation of the Mach number at the sonic point; thus:

$$A_2\Big|_{\overline{M}=1} = \frac{2}{\gamma+1}\left(-A_1 + \frac{(3-\gamma)}{2}A_3\right)$$

The perturbation equations at the sonic point are:

$$\frac{dA_1}{dx}\Big|_{\overline{M}=1} = \left(\frac{\gamma\dfrac{d^2A}{dx^2}}{2A\dfrac{d}{dx}\overline{M}}\right)A_1$$

$$\frac{dA_2}{dx}\Big|_{\overline{M}=1} = \left(\frac{dA_1}{dx}\Big|_{\overline{M}=1} + \frac{(3-\gamma)}{2}\frac{dA_3}{dx}\Big|_{\overline{M}=1}\right)\left(\frac{\dfrac{\gamma\dfrac{d^2A}{dx^2}}{2A\dfrac{d}{dx}\overline{M}}}{1 + \dfrac{(\gamma-1)}{2}\dfrac{\dfrac{d^2A}{dx^2}}{2A\dfrac{d}{dx}\overline{M}}}\right) \tag{12}$$

$$\frac{dA_3}{dx}\Big|_{\overline{M}=1} = (A_1 - (\gamma+1)A_3)\left(\frac{\dfrac{d^2A}{dx^2}}{4A\dfrac{d}{dx}\overline{M}}\right)$$

Initially, the A_1 wave is set to zero at the sonic point and the A_3 wave is set to one. After marching upstream, the amplitude and phase of the A_3 wave at the sonic point is set such that the value at the upstream boundary matches that of the A_3 wave imposed at the inflow boundary and the solution is then calculated.

Region 2: From the sonic point to the shock

Once the conditions at the sonic point are known, the solution can be marched directly to the shock location. Note that the second derivative of the area is discontinuous at the sonic point; thus, the correct value changes depending on the marching direction.

Region 3: From the shock to the downstream boundary

At the shock itself, there are four specified quantities and three unknowns. The four specified waves are the three upstream waves (A_1, A_2, and A_3) and the upstream-running acoustic wave A_2 from downstream of the shock. The three unknowns are the entropy and downstream-running acoustic waves A_1 and A_3 behind the shock, and the velocity of the shock itself, V (ref. 2)

At the shock, mass, momentum, and energy must be conserved. The equations at the shock itself are thus:
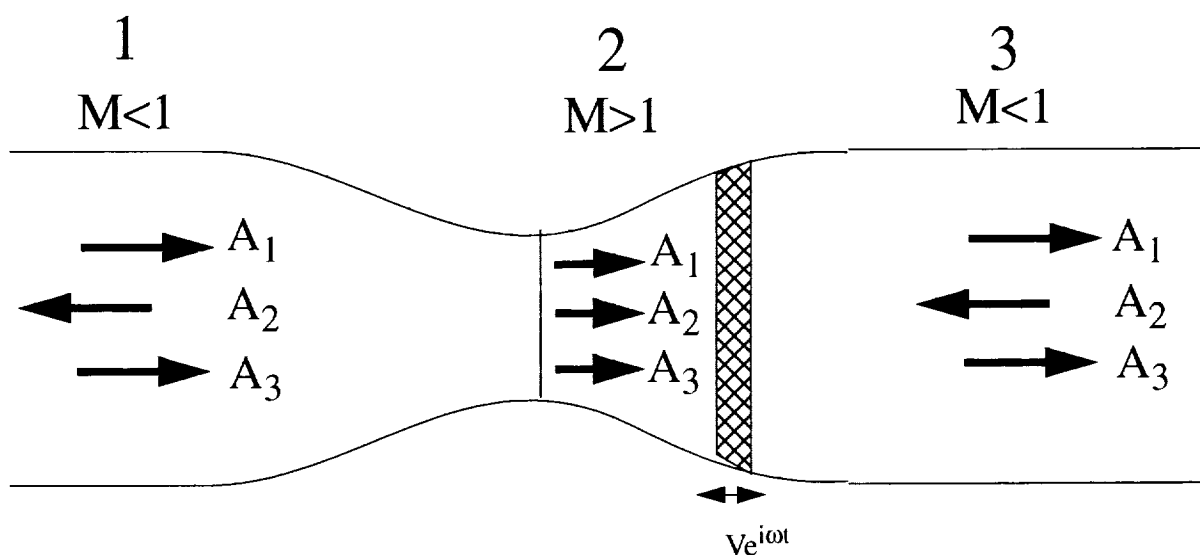
Figure 1: Three Solution Zones of Category 1 Problem 2
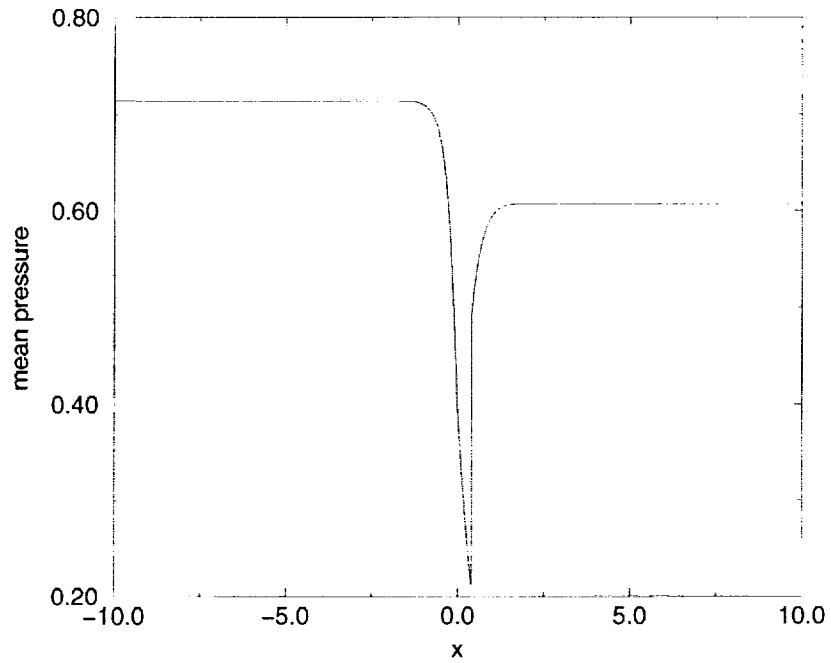
Figure 2: Mean Pressure Solution
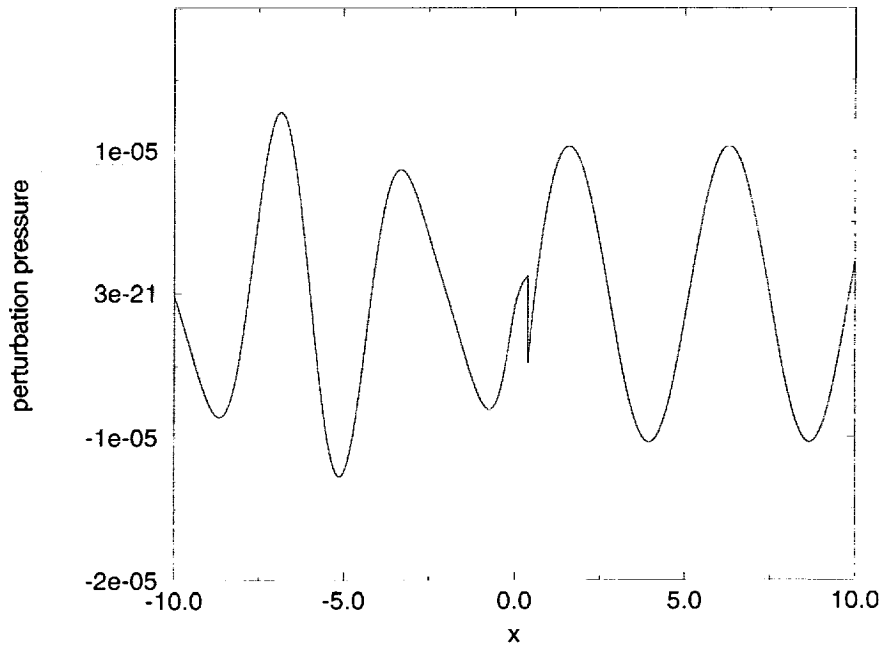
Figure 3: Perturbation Pressure Solution at the Start of a Cycle
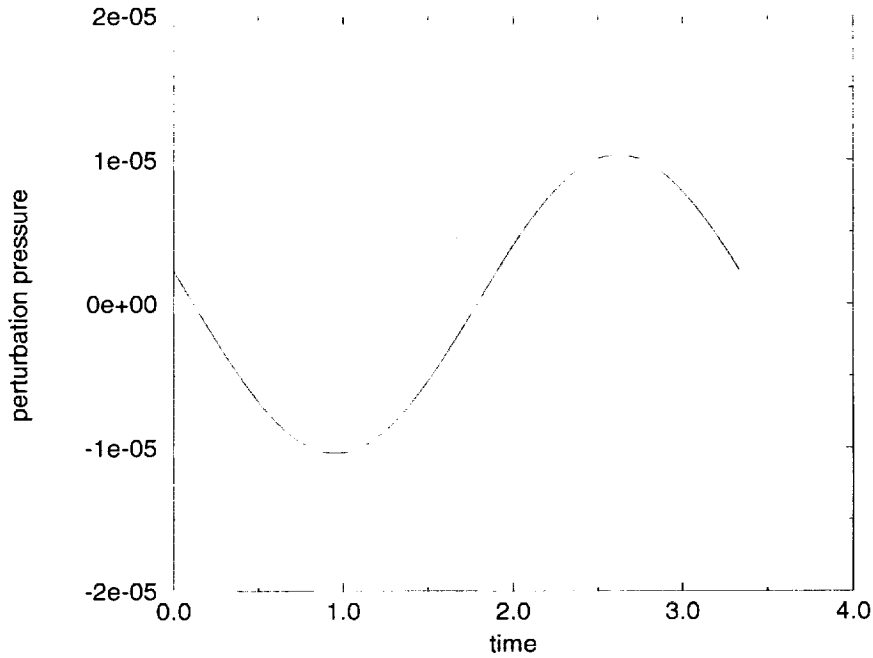
Figure 4: Perturbation Pressure Solution through a Cycle at Exit Plane

$$-\frac{\overline{M}_3}{\bar{c}_3}(A_1)_3 + \left(\frac{\overline{M}_3 - 1}{2\bar{c}_3}\right)(A_2)_3 + \left(\frac{\overline{M}_3 + 1}{2\bar{c}_3}\right)(A_3)_3 - \bar{\rho}_3 \hat{V} = \tag{13}$$

$$-\frac{\overline{M}_2}{\bar{c}_2}(A_1)_2 + \left(\frac{\overline{M}_2 - 1}{2\bar{c}_2}\right)(A_2)_2 + \left(\frac{\overline{M}_2 + 1}{2\bar{c}_2}\right)(A_3)_2 - \bar{\rho}_2 \hat{V}$$

$$-\overline{M}_3^2(A_1)_3 + \left(\frac{(\overline{M}_3 - 1)^2}{2}\right)(A_2)_3 + \left(\frac{(\overline{M}_3 + 1)^2}{2}\right)(A_3)_3 - 2\bar{\rho}_3\bar{u}_3 \hat{V} = \tag{14}$$

$$-\overline{M}_2^2(A_1)_2 + \left(\frac{(\overline{M}_2 - 1)^2}{2}\right)(A_2)_2 + \left(\frac{(\overline{M}_2 + 1)^2}{2}\right)(A_3)_2 - 2\bar{\rho}_2\bar{u}_2 \hat{V}$$

$$\frac{1}{\bar{\rho}_3(\gamma - 1)}(A_1)_3 - \left(\frac{\overline{M}_3 - 1}{2\bar{\rho}_3}\right)(A_2)_3 + \left(\frac{\overline{M}_3 + 1}{2\bar{\rho}_3}\right)(A_3)_3 - 2\bar{u}_3 \hat{V} = \tag{15}$$

$$\frac{1}{\bar{\rho}_2(\gamma - 1)}(A_1)_2 - \left(\frac{\overline{M}_2 - 1}{2\bar{\rho}_2}\right)(A_2)_2 + \left(\frac{\overline{M}_2 + 1}{2\bar{\rho}_2}\right)(A_3)_2 - 2\bar{u}_2 \hat{V}$$

where the subscript '2' refers to zone 2, upstream of the shock; the subscript '3' refers to zone 3, downstream of the shock.

In zone 3, the upstream-running acoustic wave must be set. Since it is known that there is no upstream-running wave from the downstream boundary, the wave is set such that the amplitude is zero at the downstream boundary.

Acknowledgment

References

1) Stanescu, D. and Habashi, W. G., '2N-Storage Low Dissipation and Dispersion Runge-Kutta Schemes for Computational Acoustics', *J. Comp. Phys.*, Vol. 143, No. 2, 1998, p. 674-681.

2) Landau, L. D., and Lifshitz, E. M., *Fluid Mechanics*, Pergamon Press, New York, 1959.

ROTOR NOISE: CATEGORY 2
ANALYTICAL SOLUTION

CHRISTOPHER K.W. TAM
Department of Mathematics
Florida State University
Tallahassee, FL 32306-4510
Email: tam@math.fsu.edu

Introduction

The sound field of an open rotor and that of a ducted rotor can be extremely different. This provides a good example to illustrate the important aeroacoustics principle that the environment, an acoustic source is in, often exerts decisive influence on the acoustic radiation from the source. This is especially important to fan and turbomachinery noise.

A body moving at a constant subsonic velocity will not generate sound. On the other hand, a body undergoing acceleration or deceleration will. In the case of an open rotor, although the force exerted by the blades on the fluid is moving with constant speed yet, because of rotation, there is radial acceleration. One, therefore, expects strong acoustic radiation in and around the plane of rotation.

When the rotor is housed inside a circular duct, acoustic disturbances are continuously reflected back by the walls. This causes cancellations and reinforcements. The net result is that it is possible to have complete cancellation resulting in no acoustic radiation. This is the case even when the blade tip speed is slightly supersonic. The numerical values of the benchmark problem have been chosen so that the ducted rotor effectively has no sound radiation. However, if the rotational speed increases further, there will be sound radiation from the open end of the duct. This is the cut-off phenomenon (see Ref. [1]). Exact solution of the radiation problem from the open end of a long duct can be found by the Wiener-Hopf technique and is well described in Ref. [2].

To compute the radiated sound from the open rotor, one should be aware of the difference in scales between the noise source and the sound field. The source length scale is determined by the geometry and loading of the blades. The length scales of the acoustic field is determined by the acoustic wave length, which, in turn, is determined by the rotational frequency and the number of blades of the rotor (the blade passage frequency). Appropriate spatial resolution must be used in the source region and in the acoustic field to ensure an accurate and efficient numerical solution.

Analytical Solution

The governing equations to be solved are,

$$\frac{\partial \widetilde{v}}{\partial t} = -\frac{\partial \widetilde{p}}{\partial r}$$

$$\frac{\partial \widetilde{w}}{\partial t} = -\frac{im}{r}\widetilde{p} + \widetilde{F}_\phi(r,x)e^{-im\Omega t}$$

$$\frac{\partial \widetilde{u}}{\partial t} = -\frac{\partial \widetilde{p}}{\partial x} + \widetilde{F}_x(r,x)e^{-im\Omega t}$$

$$\frac{\partial \widetilde{p}}{\partial t} + \frac{1}{r}\frac{\partial(\widetilde{v}\,r)}{\partial r} + \frac{im\,\widetilde{w}}{r} + \frac{\partial \widetilde{u}}{\partial x} = 0.$$

(1)

The time period solution must have the same time dependence as the sources. Let

$$\begin{bmatrix} \widetilde{u} \\ \widetilde{v} \\ \widetilde{w} \\ \widetilde{p} \end{bmatrix} = \begin{bmatrix} \widehat{u}(r,x) \\ \widehat{v}(r,x) \\ \widehat{w}(r,x) \\ \widehat{p}(r,x) \end{bmatrix} e^{-im\Omega t}.$$

(2)

Substitution of (2) into (1) leads to a problem in the $x - r$-plane. The equations to be solved are,

$$-im\Omega\,\widehat{v} = -\frac{\partial \widehat{p}}{\partial r}$$

$$-im\Omega\,\widehat{w} = -\frac{im}{r}\widehat{p} + \widetilde{F}_\phi$$

$$-im\Omega\,\widehat{u} = -\frac{\partial \widehat{p}}{\partial r} + \widetilde{F}_x$$

(3)

$$-im\Omega\,\widehat{p} + \frac{1}{r}\frac{\partial}{\partial r}(\widehat{v}\,r) + \frac{im}{r}\,\widehat{w} + \frac{\partial \widehat{u}}{\partial x} = 0.$$

Solution to (3) satisfying the radiation boundary condition may be found by the method of Fourier transform. Let the Fourier transform of $f(x)$ be $\overline{f}(k)$. $f(x)$ and $\overline{f}(k)$ are related by

$$\overline{f}(k) = \frac{1}{2\pi}\int_{-\infty}^{\infty} f(x)e^{-ikx}\,dx, \quad f(x) = \int_{-\infty}^{\infty}\overline{f}(k)e^{ikx}\,dk.$$

(4)

Upon taking the Fourier transform of (3), it is straightforward to obtain, after eliminating all the other variables, a single equation for $\overline{p}$,

$$\frac{d^2\overline{p}}{dr^2} + \frac{1}{r}\frac{d\overline{p}}{dr} + (m^2\Omega^2 - k^2)\overline{p} - \frac{m^2}{r^2}\overline{p} = \begin{cases} \frac{i}{2\pi}\left(\frac{\pi}{100\ln 2}\right)^{\frac{1}{2}} e^{-\frac{k^2}{400(\ln 2)}}(m+k)J_m(\lambda_{mN}r), & r \leq 1 \\ 0, & r > 1 \end{cases}.$$

(5)

For $r > 1$, the solution of (5), which satisfies the radiation condition at $r \to \infty$, is

$$\overline{p} = A(k)H_m^{(1)}(i(k^2 - m^2\Omega^2)^{\frac{1}{2}}r) \tag{6}$$

where $H_m^{(1)}(\ )$ is the mth order Hankel function of the first kind. The branch cuts of the square root function $(k^2 - m^2\Omega^2)^{\frac{1}{2}}$ are taken to be $\text{Re}(k^2 - m^2\Omega^2)^{\frac{1}{2}} > 0$, if $\text{Re}(k^2 - m^2\Omega^2)^{\frac{1}{2}} = 0$ take $\text{Im}(k^2 - m^2\Omega^2)^{\frac{1}{2}} < 0$. The branch cuts are shown in figure 1.
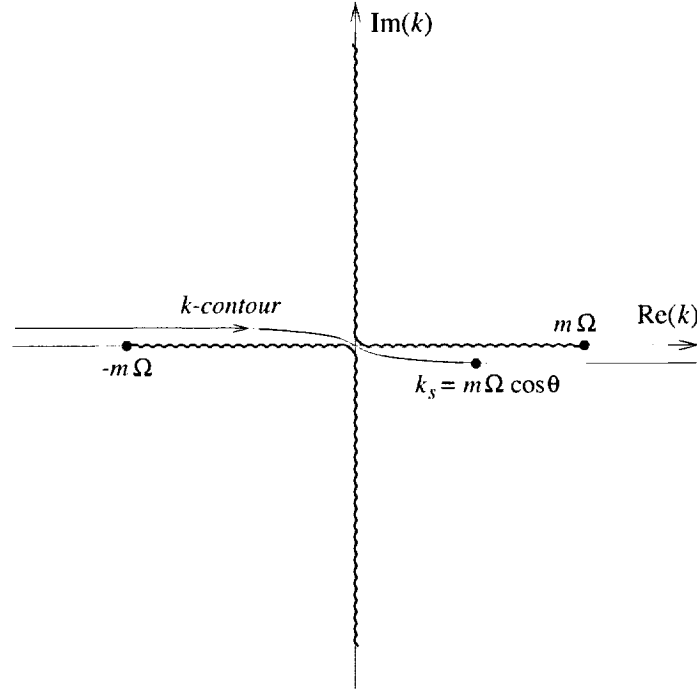
Figure 1. Branch cuts of $(k^2 - m^2\Omega^2)^{\frac{1}{2}}$ in the $k-$plane

For $r < 1$, the solution of (5) consists of a particular solution and a homogeneous solution. The solution that is bounded at $r = 0$ may be written as,

$$\overline{p} = B(k)J_m(i(k^2 - m^2\Omega^2)^{\frac{1}{2}}r) - \frac{i}{2\pi}\left(\frac{\pi}{100\ln 2}\right)^{\frac{1}{2}}\frac{m + k}{k^2 + \lambda_{mN}^2 - m^2\Omega^2}e^{-\frac{k^2}{400(\ln 2)}}J_m(\lambda_{mN}r) \tag{7}$$

where $J_m(\ )$ is the mth order Bessel function.

Now the solution of (5) and its derivative must be continuous at $r = 1$. By imposing these continuity conditions on (6) and (7), the unknown $A(k)$ and $B(k)$ are found. This gives,

$$A(k) = \frac{i}{4}\left(\frac{\pi}{100\ln 2}\right)^{\frac{1}{2}}e^{-\frac{k^2}{400(\ln 2)}}\frac{(k^2 - m^2\Omega^2)^{\frac{1}{2}}(m + k)}{(k^2 - \lambda_{mN}^2 - m^2\Omega^2)}J_m(\lambda_{mN})J_m'(i(k^2 - m^2\Omega^2)^{\frac{1}{2}}) \tag{8}$$

where $J'_m(z) = \frac{d J_m(z)}{d z}$.

By inverting the Fourier transform $\bar{p}$, the pressure in the far field $r \to \infty$ is obtained,

$$p(r,x,t) = e^{-im\Omega t} \int\limits_{-\infty}^{\infty} A(k) H_m^{(1)}(i(k^2 - m^2\Omega^2)^{\frac{1}{2}} r) e^{ikx} dk. \tag{9}$$

For large r, we may replace the Hankel function by its asymptotic form; i.e.,

$$p(r,x,t) \underset{r \to \infty}{\sim} e^{-im\Omega t} \int\limits_{-\infty}^{\infty} A(k) \left(\frac{2}{\pi i (k^2 - m^2\Omega^2)^{\frac{1}{2}} r} \right)^{\frac{1}{2}} e^{-(k^2 - m^2\Omega^2)^{\frac{1}{2}} r + ikx - i\frac{m\pi}{2} - i\frac{\pi}{4}} dk. \tag{10}$$

Let us now switch to a spherical polar coordinate system (R,θ,ϕ) with the x-axis as the polar axis. On noting that

$$x = R\cos\theta, \quad r = R\sin\theta$$

(10) may be written as,

$$p(R,\theta,t) \underset{R \to \infty}{\sim} e^{-im\Omega t} \int\limits_{-\infty}^{\infty} A(k) \left(\frac{2}{i\pi (k^2 - m^2\Omega^2)^{\frac{1}{2}} R\sin\theta} \right)^{\frac{1}{2}}$$

$$\cdot e^{-[(k^2 - m^2\Omega^2)^{\frac{1}{2}} \sin\theta - ik\cos\theta]R - \frac{i}{2}(m+\frac{1}{2})\pi} dk. \tag{11}$$

The k integral of (11) can be evaluated asymptotically by the method of stationary phase. The stationary phase point is at $k_s = m\Omega\cos\theta$. A straightforward implementation of the method of stationary phase yields the following expression for the acoustic pressure field.

$$p(R,\theta,t) \underset{R \to \infty}{\sim} \frac{2}{R} A(k_s) e^{im\Omega(R-t) - \frac{i}{2}(m+1)\pi} \tag{12}$$

where

$$A(k_s) = \frac{1}{4} \left(\frac{\pi}{100\ln 2} \right)^{\frac{1}{2}} \frac{m^2(1 + \Omega\cos\theta)\Omega\sin\theta}{\lambda_{mN}^2 - m^2\Omega^2\sin^2\theta} J_m(\lambda_{mN}) J'_m(mR\sin\theta) e^{-\frac{m^2\Omega^2\cos^2\theta}{400(\ln 2)}}. \tag{13}$$

The directivity, $D(\theta)$, is given by

$$D(\theta) = \lim_{R \to \infty} R^2 \overline{p^2} = 2A^2(k_s). \tag{14}$$

The directivities for the two cases $\Omega = 0.85$ and 1.15 are shown in figures (2) and (3).
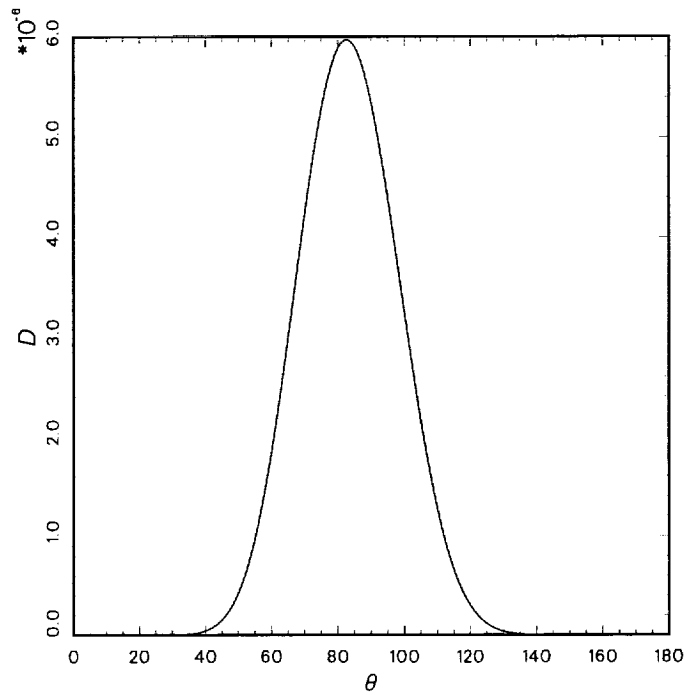
Figure 2. Directivity of rotor noise, $\Omega = 0.85$
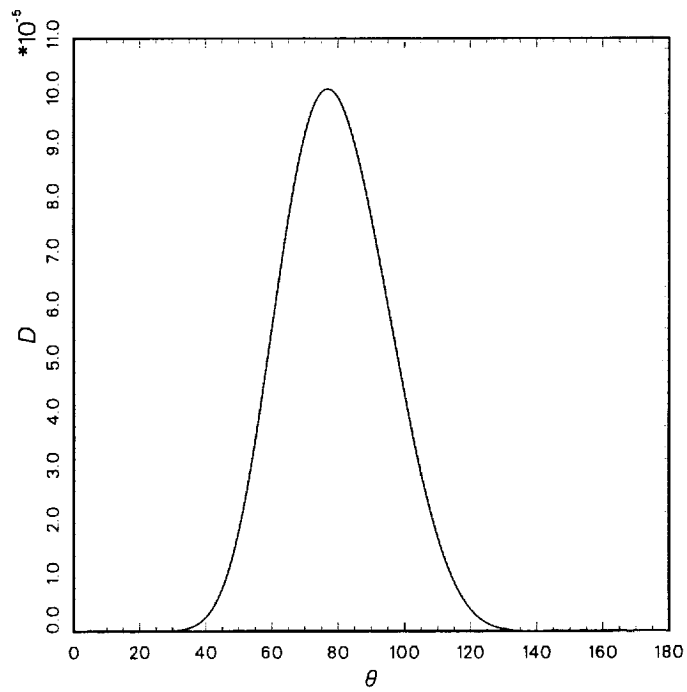
Figure 3. Directivity of rotor noise, $\Omega = 1.15$

Acknowledgment

The author wishes to thank Alexei Aganin for his assistance.

References

1. Eversman, W. "Theoretical models for duct acoustic propagation and radiation", Chapter 13 in Aeroacoustics of Flight Vehicles: Theory and Practice. Vol. 2, ed. H.H. Hubbard, NASA RP 1258, Aug. 1991, pp. 101–163.

2. Cho, Y.C. and Ingard, K.V., "Exact solution for sound radiation from a circular duct", Proceedings of the Second Computational Aeroacoustics Workshop on Benchmark Problems. NASA CP 3352, June 1997, pp. 27–39.

Single Airfoil Gust Response Problem

James R. Scott
NASA Glenn Research Center at Lewis Field
Cleveland, Ohio

The solution to this problem can be obtained by solving the linearized unsteady Euler equations. Let the unsteady flow field be given by

$$\vec{U}(\vec{x},t) = \vec{U}_0(\vec{x}) + \vec{u}(\vec{x},t) \tag{1}$$

$$p(\vec{x},t) = p_0(\vec{x}) + p'(\vec{x},t) \tag{2}$$

$$\rho(\vec{x},t) = \rho_0(\vec{x}) + \rho'(\vec{x},t) \tag{3}$$

$$s(\vec{x},t) = s_0 + s'(\vec{x},t) \tag{4}$$

where the entropy s_0 is constant, and $\vec{u}$, p', ρ', and s' are the unsteady perturbation velocity, pressure, density and entropy, respectively. Zero subscripts denote mean flow quantities which are assumed to be known.

Substituting (1) – (4) into the nonlinear Euler equations and neglecting products of small quantities, one obtains the linearized equations

$$\frac{D_0 \rho'}{Dt} + \rho' \vec{\nabla} \cdot \vec{U}_0 + \vec{\nabla} \cdot (\rho_0 \vec{u}) \;=\; 0 \tag{5}$$

$$\rho_0 \Big(\frac{D_0 \vec{u}}{Dt} + \vec{u} \cdot \vec{\nabla}\vec{U}_0 \Big) + \rho' \vec{U}_0 \cdot \vec{\nabla}\vec{U}_0 \;=\; -\vec{\nabla}p' \tag{6}$$

$$\frac{D_0 s'}{Dt} \;=\; 0, \tag{7}$$

where $\frac{D_0}{Dt} = \frac{\partial}{\partial t} + \vec{U}_0 \cdot \vec{\nabla}$ is the convective derivative associated with the mean flow.

If the mean velocity $\vec{U}_0$ can be expressed as the gradient of a potential Φ_0, then equations (5) - (7) can be reduced to a single, non-constant coefficient, inhomogeneous convective wave equation [1,2]

$$\frac{D_0}{Dt}\Big(\frac{1}{c_0{}^2} \frac{D_0 \phi}{Dt} \Big) - \frac{1}{\rho_0} \vec{\nabla} \cdot (\rho_0 \vec{\nabla}\phi) \;=\; \frac{1}{\rho_0} \vec{\nabla} \cdot (\rho_0 \vec{u}^{(R)}), \tag{8}$$

where the unsteady velocity is decomposed into a known vortical component $\vec{u}^{(R)}$ and an unknown potential component $\vec{\nabla}\phi$,

$$\vec{u}(\vec{x},t) \;=\; \vec{u}^{(R)} + \vec{\nabla}\phi. \tag{9}$$

The unsteady pressure is given by

$$p' = -\rho_0(\vec{x})\frac{D_0\phi}{Dt}.$$

(10)

An unsteady aerodynamic code, called GUST3D [3], has been developed to solve equation (8) for flows with periodic vortical disturbances. The code uses a frequency-domain approach with second-order central differences and a Sommerfeld radiation condition in the far field. It has been extensively validated on model problems with analytical solutions.

GUST3D requires as input certain mean flow quantities which are calculated separately by a potential flow solver. This solver calculates the mean flow using a Gothert's Rule approximation [3]. On the airfoil surface, it uses the solution calculated by the potential code FLO36 [4]. Figure 1 shows the mean pressure along the airfoil surface for Cases 1 and 2.

To calculate the unsteady pressure, GUST3D was run on systematically refined grids to obtain a converged solution at each frequency. It was found that 24 points per wavelength was sufficient for convergence. The location of the outer grid boundary was also varied to check for sensitivity to the far-field boundary condition.

Flat plate results were calculated using the above approach to help assess accuracy. Figure 2 shows the calculated RMS pressure versus analytical results for a flat plate in a transverse gust. Two numerical solutions are shown per frequency, each corresponding to grids with different far-field boundaries. The far-field boundary locations are shown in number of chord lengths on each figure. The maximum error for each case is also shown (omitting the first 1% of chord near the leading edge singularity). The acoustic intensity was calculated using a single-layer-potential Kirchoff method [5]. Kirchoff circles with radii of 2, 2.25, and 2.5 chord lengths were used to propagate the pressure to the circle of radius 4.0. The three Kirchoff calculations for each of the two different far-field boundary locations resulted in six different intensity calculations for each frequency. Figure 3 presents the most accurate and least accurate of the six calculations to give some indication of the numerical uncertainty of the results.

The Joukowski airfoil results for Cases 1 and 2 were calculated in the same manner as the flat plate results. Figure 4 presents the RMS pressures and Figure 5 shows the corresponding intensity results. The relative numerical uncertainty of each calculation is also shown. For the RMS pressures, this uncertainty determination did not include pressure values in the first $\frac{1}{2}$% of airfoil chord near the leading edge nor the last $\frac{1}{2}$% of airfoil chord near the trailing edge. Note that there are no RMS results for Case 2, $k_1 = 3.0$, and no intensity results at this frequency for either Case 1 or Case 2. Work is still ongoing to obtain an acceptably converged solution for these cases.

References

1. M. E. Goldstein, *J. Fluid Mech.* **89**, 433 (1978).

2. H. M. Atassi and J. Grzedzinski, *J. Fluid Mech.* **209**, 385 (1989).

3. J. R. Scott and H. M. Atassi, *J. Comp. Phys.* **119**, 75-93, (1995).

4. A. Jameson and D. A. Caughey, in *Proceedings of the AIAA 3rd Computational Fluid Dynamics Conference*, Williamsburg, Virginia, 1979, 122.

5. S.I. Hariharan, J. R. Scott and K. L. Kreider, "A Potential Theoretic Method for Far Field Sound Radiation Calculations", submitted to *J. Comp. Phys.*
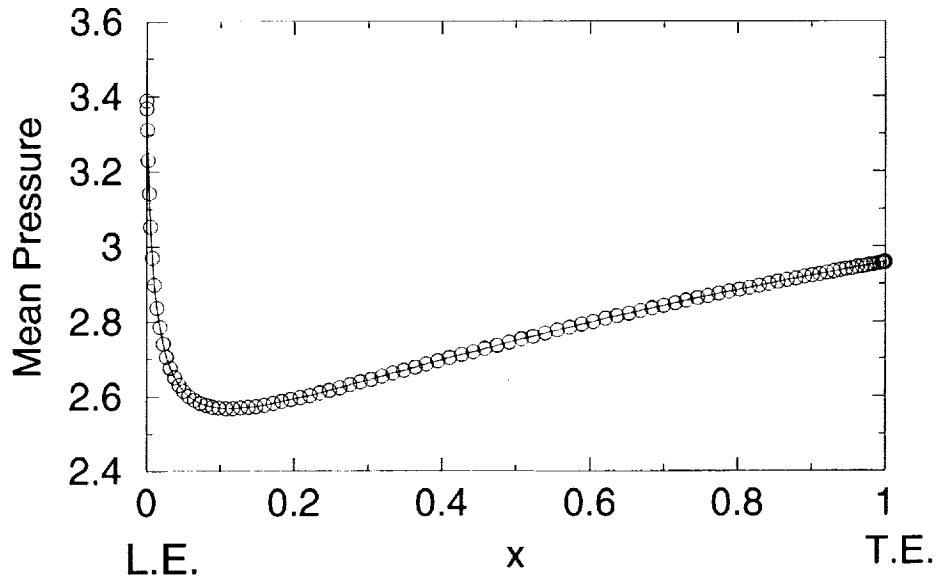
Figure 1.a Mean pressure on airfoil surface – Case 1.
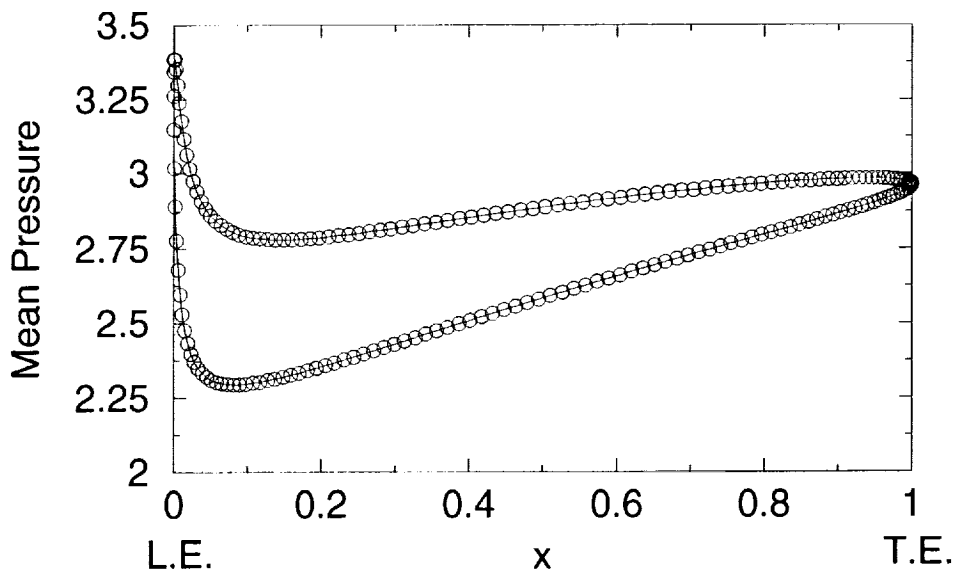
Figure 1.b Mean pressure on airfoil surface – Case 2.
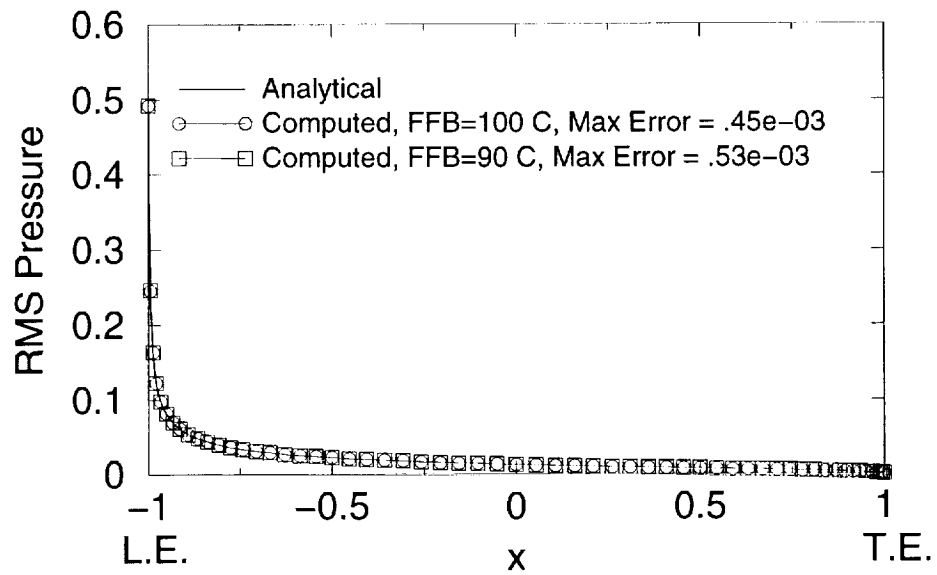
Figure 2.a RMS pressure on a flat plate. M=0.5, k1=0.1
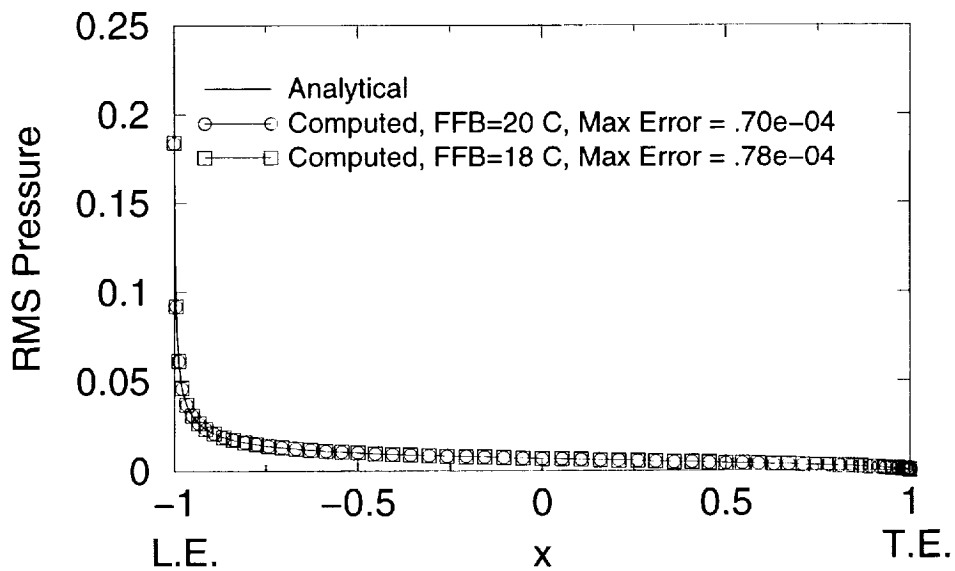
Figure 2.b RMS pressure on a flat plate. M=0.5, k1=1.0
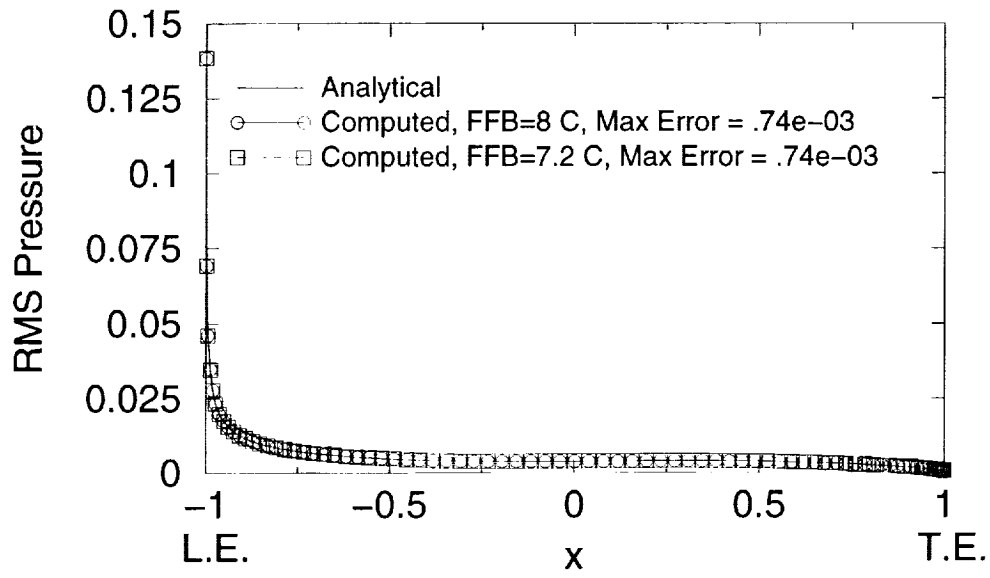
Figure 2.c RMS pressure on a flat plate. M=0.5, k1=3.0
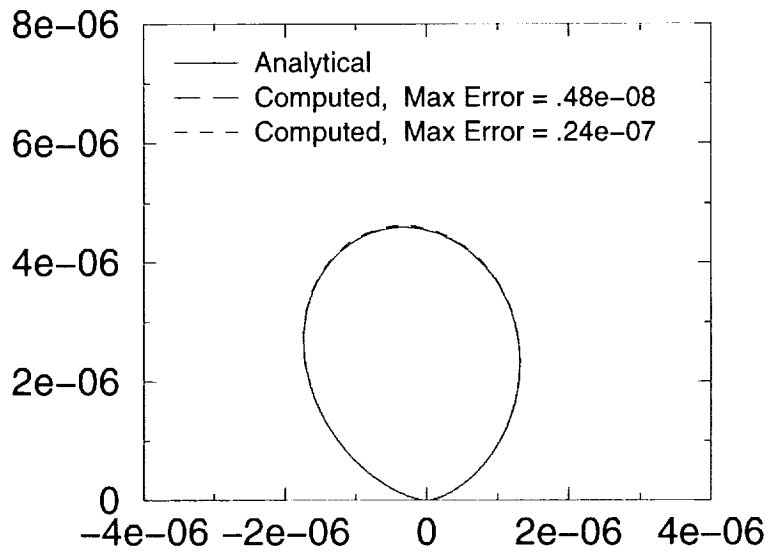
Figure 3.a Acoustic intensity for a flat plate. M=0.5, k1=0.1
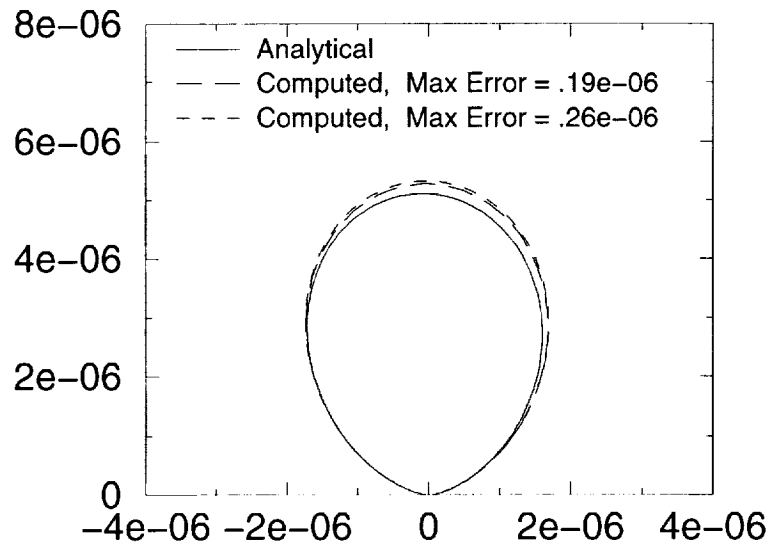
Figure 3.b Acoustic intensity for a flat plate. M=0.5, k1=1.0
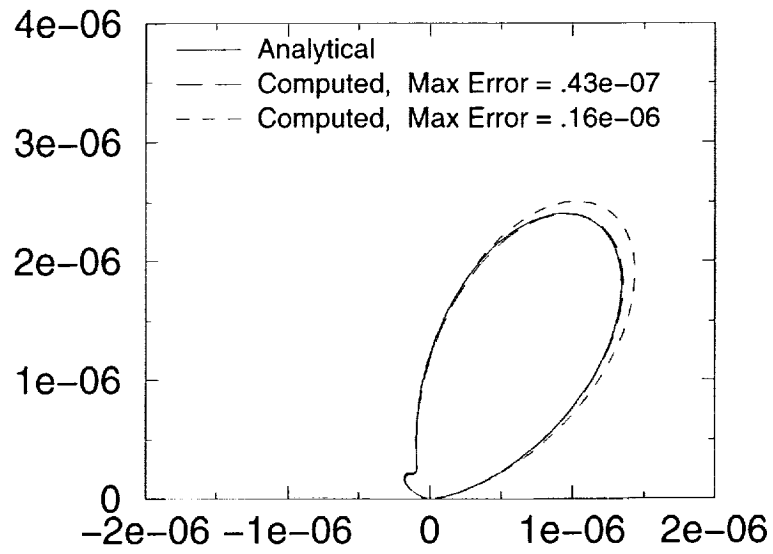
Figure 3.c Acoustic intensity for a flat plate. M=0.5, k1=3.0
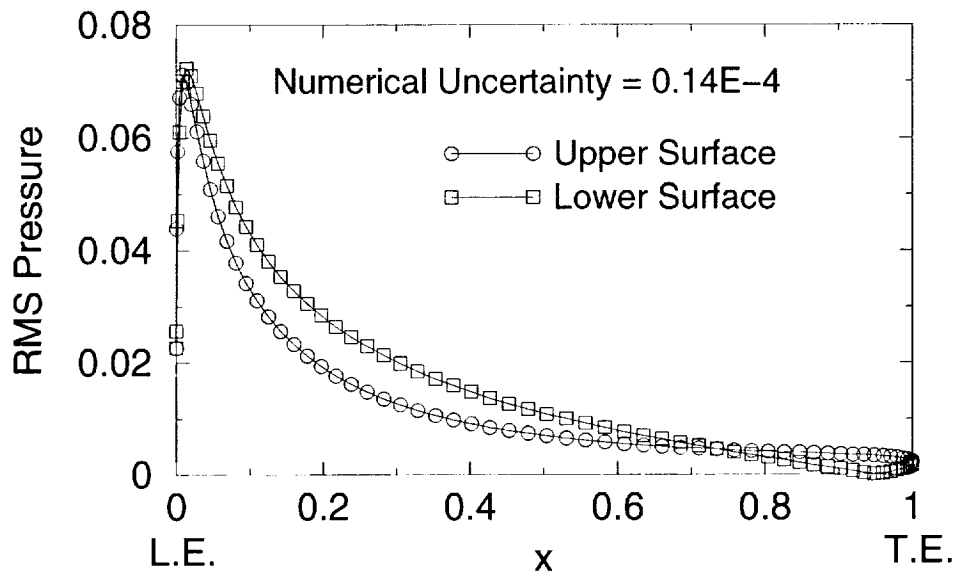
Figure 4.a RMS pressure on airfoil surface, Case 1, k1=k2=0.1
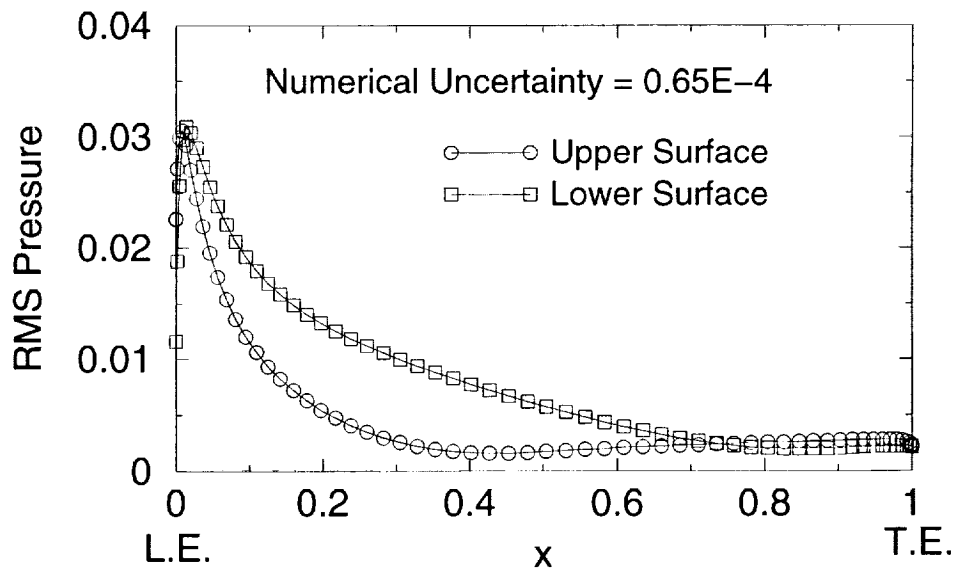
Figure 4.b RMS pressure on airfoil surface, Case 1, k1=k2=1.0
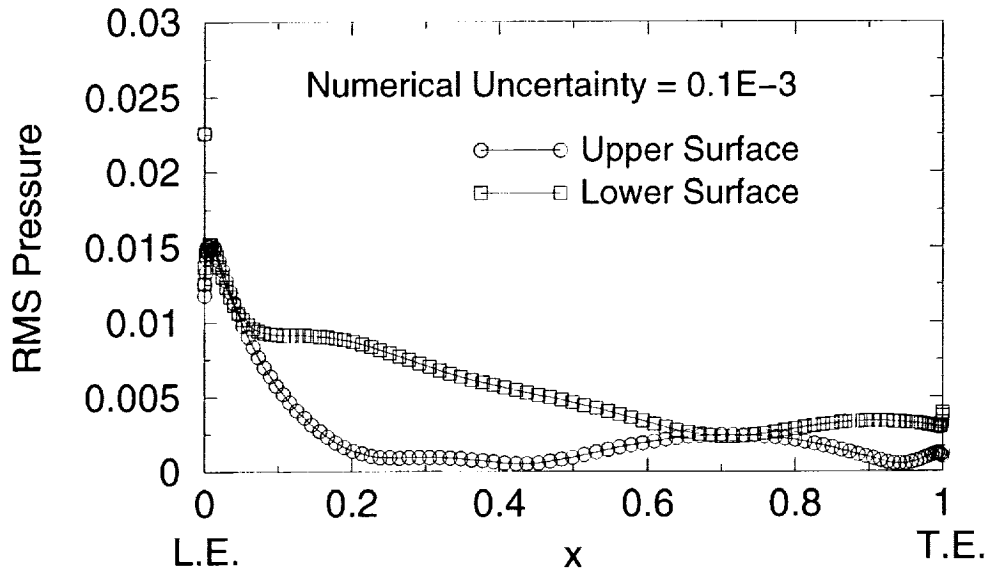
Figure 4.c RMS pressure on airfoil surface, Case 1, k1=k2=3.0
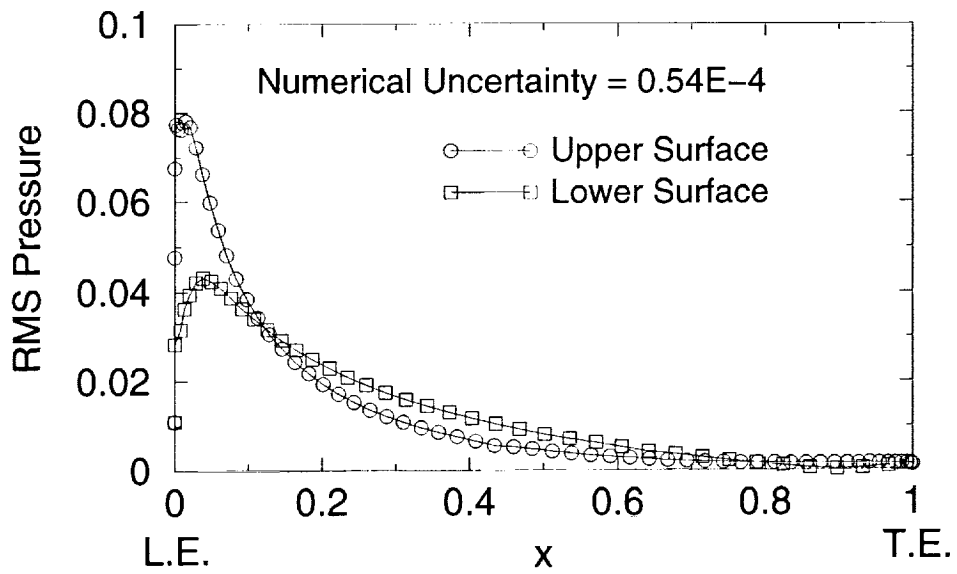
Figure 4.d RMS pressure on airfoil surface, Case 2, k1=k2=0.1

56
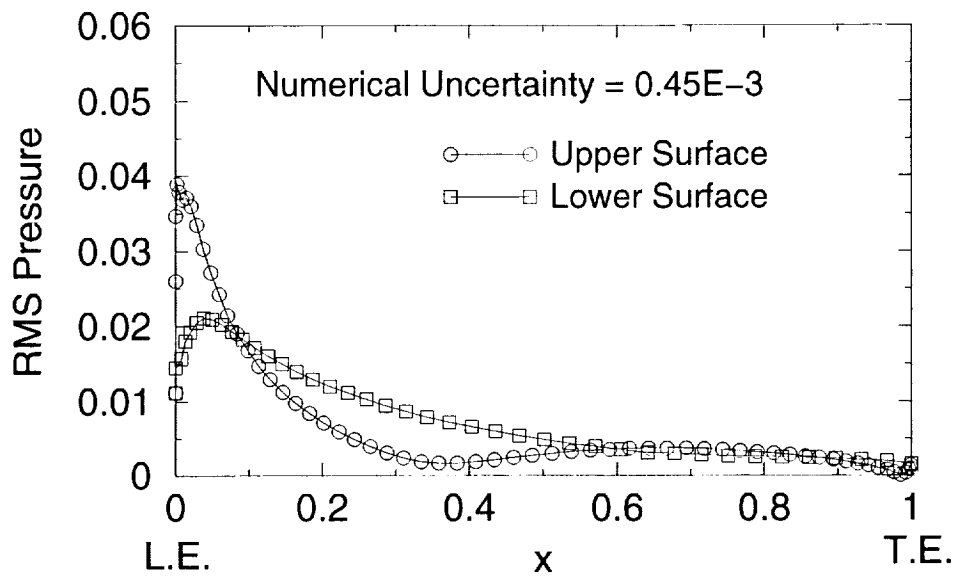
Figure 4.e RMS pressure on airfoil surface, Case 2, k1=k2=1.0
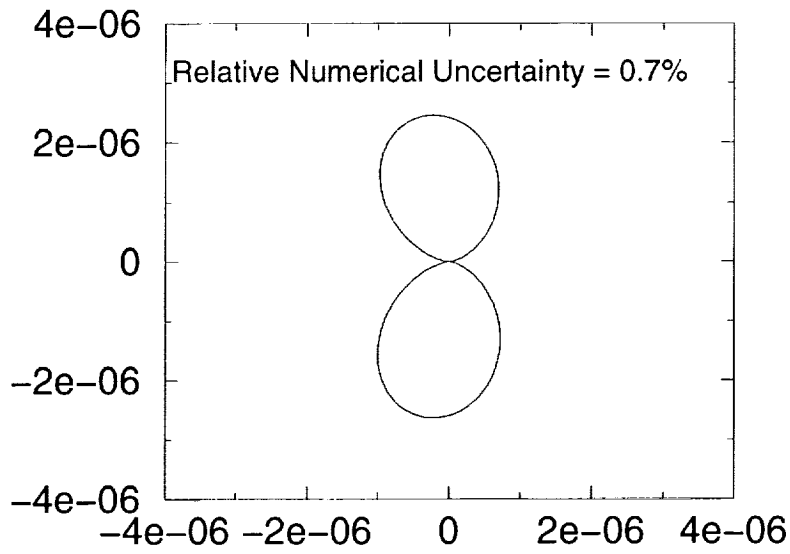
Figure 5.a Acoustic intensity, Case 1, k1=k2=0.1
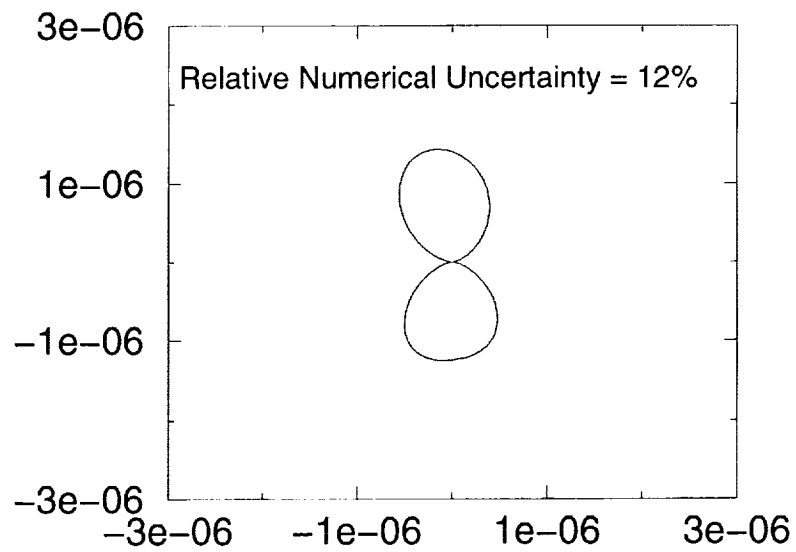
Figure 5.b Acoustic intensity, Case 1, k1=k2=1.0

58
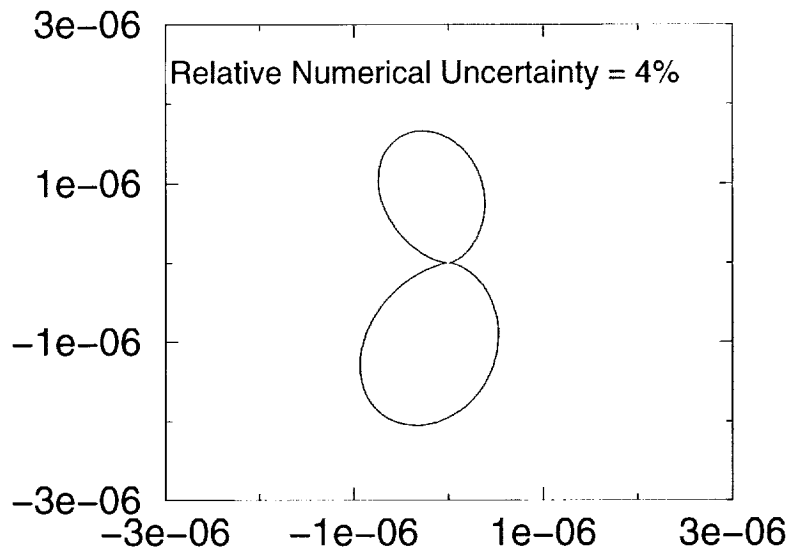
Figure 5.c Acoustic intensity, Case 2, k1=k2=0.1
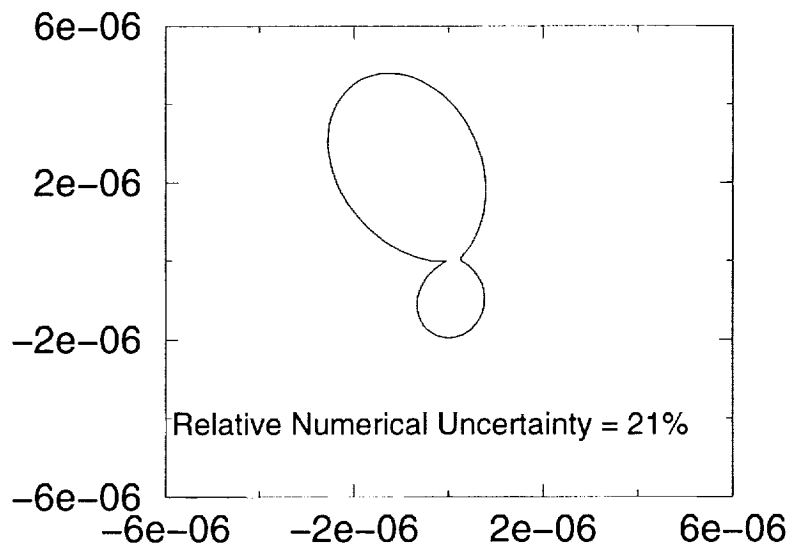
Figure 5.d Acoustic intensity, Case 2, k1=k2=1.0

ANALYTICAL SOLUTION OF THE CATEGORY 3, BENCHMARK PROBLEMS 2 AND 3

EDMANE ENVIA
NASA Glenn Research Center
Cleveland, Ohio

Solution of Problem 2

The solution to this problem is most conveniently obtained by introducing an acoustic velocity potential and eliminating all primitive variables from the governing equations. The end result is the convected wave equation for the acoustic velocity potential ϕ,

$$\left(\nabla^2 - a_0^{-2}\frac{D_0^2}{Dt^2}\right)\phi = 0, \qquad \frac{D_0}{Dt} = \frac{\partial}{\partial t} + U_0\frac{\partial}{\partial x} \tag{1}$$

with $(u,v,w) = \nabla\phi$, $p = -\rho_0(D_0\phi/Dt)$ and $\rho = p/a_0^2$. The corresponding boundary conditions in terms of ϕ are given by

$$\left(\frac{\partial\phi}{\partial y}\right)_{y=0,\,0\leq x-z\tan\alpha\leq c} = Ae^{i(k_x x + k_y y + k_z z - \omega t)} \tag{2}$$

$$\left(\frac{\partial\phi}{\partial z}\right)_{z=0,\,\ell} = 0 \tag{3}$$

$$\left(\left.\frac{D_0\phi}{Dt}\right|_{y=0^-}^{y=0^+}\right)_{x-z\tan\alpha>c} = 0 \tag{4}$$

Eqs. (2) and (3) enforce the impermeability of the airfoil and bounding walls, while Eq. (4) stipulates the continuity of pressure downstream of the airfoil trailing edge. Since ϕ is an odd function of y, $\phi(x,0,z,t) \equiv 0$ upstream of the airfoil. Finally, since we have used an exponential representation for the incident gust and, therefore, only the real part of the final solution is implied.

The analysis outlined here will follow closely that presented in ref. 1. For a convected gust $k_x = \omega/U$. The Sommerfeld radiation condition is enforced indirectly by assuming that k_x has a small positive imaginary part which is set to zero at the end of the analysis. Introduction of a reduced velocity potential via $\phi = \tilde{\phi}\,e^{-i(k_x M^2 x/\beta^2 + \omega t)}$, the Prandtl-Glauert transformation $x' = x/\beta$, and the non-orthogonal coordinate system

$$\xi = x'\cos\alpha' - z\sin\alpha', \quad \zeta = z, \quad \tan\alpha' = \tan\alpha/\beta \tag{5}$$

leads to

$$\left(\frac{\partial^2}{\partial \xi^2} + \frac{\partial^2}{\partial \zeta^2} - 2\gamma_1 \frac{\partial^2}{\partial \xi \partial \zeta} + \frac{\partial^2}{\partial y^2} + \frac{k_x^2 M^2}{\beta^2} \right) \tilde{\phi} = 0 \tag{6}$$

$$\left(\frac{\partial \tilde{\phi}}{\partial y} \right)_{y=0,\, 0 \le \xi \le \gamma_2 c'} = A e^{i\left[\kappa \xi + (\gamma_1 \kappa + k_z)\zeta \right]} \tag{7}$$

$$\left[\left(-i\kappa \tilde{\phi} + \frac{\partial \tilde{\phi}}{\partial \xi} \right)_{y=0^-}^{y=0^+} \right]_{\xi > \gamma_2 c'} = 0 \tag{8}$$

$$\left(\frac{\partial \tilde{\phi}}{\partial \zeta} - \gamma_1 \frac{\partial \tilde{\phi}}{\partial \xi} \right)_{\zeta = 0, \ell} = 0 \tag{9}$$

$$\gamma_1 = \sin \alpha', \quad \gamma_2 = \cos \alpha', \quad \kappa = k_x / \beta \gamma_2, \quad c' = c / \beta \tag{10}$$

A Fourier transform in ξ reduces these equations to

$$\left(\frac{\partial^2}{\partial \zeta^2} + 2i\gamma_1 \lambda \frac{\partial}{\partial \zeta} + \frac{\partial^2}{\partial y^2} + \frac{k_x^2 M^2}{\beta^2} - \lambda^2 \right) \Phi = 0 \tag{11}$$

$$\left(\frac{\partial \Phi}{\partial y} \right)_{y=0,\, 0 \le \xi \le \gamma_2 c'} = \frac{iA e^{i(\gamma_1 \kappa + k_z)\zeta}}{\sqrt{2\pi} (\lambda + \kappa)} \left(1 - e^{i\gamma_2 (\lambda + \kappa) c'} \right) \tag{12}$$

$$\left(\Phi \big|_{y=0^-}^{y=0^+} \right)_{\xi > \gamma_2 c'} = 0 \tag{13}$$

$$\left(\frac{\partial \Phi}{\partial \zeta} + i\gamma_1 \lambda \Phi \right)_{\zeta = 0, \ell} = 0 \tag{14}$$

Separation of variables in y and ζ yields

$$\Phi(\lambda, y, \zeta) = \sum_{n=0}^{\infty} C_n(\lambda) Y_n(y) Z_n(\zeta) \tag{15}$$

$$Y_n(y) = \operatorname{sgn}(y) \, e^{-\gamma_2 \sqrt{\lambda^2 - w_n^2} \, |y|}, \quad w_n = \sqrt{\kappa^2 M^2 - n^2 \pi^2 / \gamma_2^2} \tag{16}$$

$$Z_n(\zeta) = e^{-i\gamma_1 \lambda \zeta} \cos(n\pi \zeta / \ell) \tag{17}$$

A proper choice of the branch cuts for $\sqrt{\lambda^2 - w_n^2}$ will ensure outgoing waves at infinity. It is advantageous to use the linear nature of the governing equation and the boundary conditions and introduce $\Phi = \Phi_1 + \Phi_2 + \cdots$ where Φ_l's represent successive terms in a leading-edge/trailing-edge expansion strategy (see ref. 2). The resulting problems for individual Φ_l's are then easier to solve.

Leading-Edge Problem: Φ_1

Ignoring the trailing edge allows for the chord to be extended to downstream infinity. Substituting for Φ_1 from Eq. (15) in Eq. (12), and applying the orthogonality condition

$$\int_0^{\ell} Z_n(\zeta) Z_k^*(\zeta) d\zeta = \begin{cases} 0 & \text{if} \quad n \neq k \\ \ell/2 & \text{if} \quad n = k \neq 0 \\ \ell & \text{if} \quad n = k = 0 \end{cases} \tag{18}$$

yields

$$-\gamma_2 \sqrt{\lambda^2 - w_n^2} \; C_{1n}^+(\lambda) = D_{1n}^-(\lambda) + \frac{A \varepsilon_n \mathcal{F}_n(\lambda)}{\sqrt{2\pi}(\lambda + \kappa)} \tag{19}$$

$$\mathcal{F}_n(\lambda) = i \int_0^{\ell} e^{i\vartheta\zeta} \cos(n\pi\zeta/\ell) \; d\zeta = \frac{\vartheta\left[(-1)^n e^{i\vartheta} - 1\right]}{\left(\vartheta^2 - n^2\pi^2\right)} \tag{20}$$

$$\varepsilon_n = \begin{cases} 2/\ell & \text{if} \quad n \neq 0 \\ 1/\ell & \text{if} \quad n = 0 \end{cases}, \qquad \vartheta = \gamma_1(\lambda + \kappa) + k_z \tag{21}$$

where C_{1n}^+ and D_{1n}^- denote the unknown functions $\int_0^{\ell} \Phi_1(\lambda, 0, \zeta) Z_n^*(\zeta) d\zeta$ and $\int_0^{\ell} \partial\Phi_1(\lambda, 0, \zeta)/\partial y \; Z_n^*(\zeta) d\zeta$, respectively. The superscripts $+$ and $-$ denote the regions of analyticity of the functions defined according to

$$F^{\pm}(\lambda) = \frac{1}{\sqrt{2\pi}} \int_{-\infty}^{\infty} f(\xi) \, H(\pm\xi) e^{i\lambda\xi} d\xi \tag{22}$$

where H is the unit step function. It should be noted that for the leading-edge problem it is not necessary to enforce Eq. (13). The region of analyticity of C_{1n}^+ is dictated by the requirement that the solution be an odd function of y.

If the terms in Eq. (19) behaved algebraically at infinity (i.e., $|\lambda| \to \infty$), Liouville's theorem could be used to establish the most general function satisfying this equation. However, since C_{1n}^+, D_{1n}^- and $\mathcal{F}_n$ do not behave

algebraically at infinity (see ref. 1), Liouville's theorem does not apply. But, as it turns out, the asymptotic structure of C_{1n}^+ and D_{1n}^- is similar to that of $\mathcal{F}_n$. Thus, if it were assumed that both of these functions contained $\mathcal{F}_n$ as a factor, and that their non-algebraic behavior was entirely due to it, then factoring out $\mathcal{F}_n$ would make Eq. (19) amenable to the application of Liouville's theorem (see ref. 1 for a discussion of the implications of this assumption). The solution of Eq. (19) is then given by

$$C_{1n}^+(\lambda) = -\frac{iA\varepsilon_n \mathcal{F}_n(\lambda)}{\gamma_2 \sqrt{2\pi} \sqrt{\kappa + w_n} \sqrt{\lambda + w_n} (\lambda + \kappa)} \tag{23}$$

The corresponding pressure field, in the Prandtl-Glauert coordinates, is

$$p_{1n}(x',y,z,t) = \text{sgn}(y) \frac{\rho_0 U_0 A\varepsilon_n \cos(n\pi z/\ell)}{2\pi\beta \sqrt{\kappa + w_n}} e^{-i(\gamma_2 \kappa M^2 x' + \omega t)}$$

$$\times \int_{-\infty}^{\infty} \frac{\mathcal{F}_n(\lambda)}{\sqrt{\lambda + w_n}} e^{i\gamma_2\left(-\lambda x' + i\sqrt{\lambda^2 - w_n^2} |y|\right)} d\lambda \tag{24}$$

In the farfield, the integral can be evaluated explicitly via the method of stationary phase. The final form of the leading-edge contribution is given by

$$p_1(r',\theta',z,t) \cong \frac{\rho_0 U_0 A}{\beta \sqrt{\pi \gamma_2 r'}} e^{-i(\gamma_2 \kappa M^2 x' + \omega t + \pi/4)} \cos(\theta'/2)$$

$$\times \sum_{n=0}^{\infty} \frac{\varepsilon_n \mathcal{F}_n(-w_n \cos\theta') \cos(n\pi z/\ell)}{\sqrt{\kappa + w_n}} e^{i\gamma_2 w_n r'} \tag{25}$$

$$r' = \sqrt{x^2/\beta^2 + y^2}, \qquad \theta' = \tan^{-1}(\beta y/x) \tag{26}$$

Trailing-Edge Problem: Φ_2

Having solved for the leading edge contribution, we now let the leading edge move off to upstream infinity and introduce a new coordinate origin via $\hat{x} = x - c$. Continuity of pressure downstream of the trailing edge (i.e., Eq. (13)) stipulates that, on a per mode basis, we must have

$$(\lambda + \kappa)\Phi_{2n}^+(\lambda) = -\frac{iA\varepsilon_n \mathcal{F}_n(-w_n)e^{-i\gamma_2 \kappa M^2 c'}}{\gamma_2 \sqrt{2\pi} \sqrt{\kappa + w_n}} \times \frac{\left[1 - \mathcal{G}_n(\lambda)\right]e^{-i\gamma_2 \lambda c'}}{\sqrt{\lambda + w_n}} \tag{27}$$

$$\mathcal{G}_n(\lambda) = \varepsilon_n \int_0^\ell \text{erf}\left(\sqrt{-i(\lambda + w_n)(\gamma_1 \zeta + \gamma_2 c')}\right)\cos^2(n\pi\zeta/\ell) d\zeta \tag{28}$$

$$\text{erf}(z) = \frac{2}{\sqrt{\pi}} \int_0^z e^{-u^2} \, du \tag{29}$$

to ensure continuity of pressure downstream of the trailing edge. Furthermore, since it is necessary that $\partial \Phi_2 / \partial y|_{y=0} = 0$ for $\hat{\xi} < 0$ for Eq. (12) to remain true, we find that

$$\Phi_{2n}^{+'} = -\gamma_2 \sqrt{\lambda^2 - w_n^2} \left(\underbrace{\Phi_{2n}^- + \Phi_{2n}^+}_{C_{2n}(\lambda)} \right) \tag{30}$$

Substituting the expression for Φ_{2n}^+ in Eq. (30) leads to the following Wiener-Hopf equation for the trailing edge field

$$\frac{(\lambda + \kappa)\Phi_{2n}^{+'}}{\sqrt{\lambda + w_n}} = -\gamma_2 (\lambda + \kappa)\sqrt{\lambda - w_n} \, \Phi_{2n}^-$$

$$+ \frac{iA\varepsilon_n \mathcal{F}_n(-w_n) e^{-i\gamma_2 \kappa M^2 c'}}{\sqrt{2\pi}\sqrt{\kappa + w_n}} \times \frac{\sqrt{\lambda - w_n}\left[1 - \mathcal{G}_n(\lambda)\right]e^{-i\gamma_2 \lambda c'}}{\sqrt{\lambda + w_n}} \tag{31}$$

Splitting the mixed function and solving the "plus" side of the equation yields

$$\Phi_{2n}^{+'} = \frac{iA\varepsilon_n \mathcal{F}_n(-w_n) e^{-i\gamma_2 \kappa M^2 c'}}{\sqrt{2\pi}\sqrt{\kappa + w_n}} \times \frac{\sqrt{\lambda + w_n}\,\mathcal{F}_n(\lambda)\mathcal{H}_n^+(\lambda)}{(\lambda + \kappa)} \tag{32}$$

$$\mathcal{H}_n^+(\lambda) = \frac{1}{2\pi i} \int_{\mathcal{C}} \frac{\sqrt{\eta - w_n}\, e^{-i\gamma_2 \eta c'}}{\sqrt{\eta + w_n}\,\mathcal{F}_n(\eta)(\eta - \lambda)} \, d\eta \tag{33}$$

where the contour $\mathcal{C}$ does not enclose the pole at $\eta = \lambda$. The appearance of $\mathcal{F}_n(\lambda)$ in Eq. (32) is consistent with the assumption stated earlier in connection with Eq. (19). The expression for $C_{2n}(\lambda)$ is, therefore, given by

$$C_{2n}(\lambda) = -\frac{iA\varepsilon_n \mathcal{F}_n(-w_n) e^{-i\gamma_2 \kappa M^2 c'}}{\gamma_2 \sqrt{2\pi}\sqrt{\kappa + w_n}} \times \frac{\mathcal{F}_n(\lambda)\mathcal{H}_n^+(\lambda)}{\sqrt{\lambda - w_n}\,(\lambda + \kappa)} \tag{34}$$

The corresponding trailing-edge pressure field, in Prandtl-Glauert coordinates, is given by

$$p_{2n}(x',y,z) = \mathrm{sgn}(y)\frac{\rho A U \varepsilon_n \mathcal{E}_n(-w_n)}{2\pi\sqrt{\kappa+w_n}}e^{-i(\gamma_2\kappa M^2 x' + \omega t)}\cos(n\pi z/\ell)$$

$$\times \int_{-\infty}^{\infty}\frac{\mathcal{E}_n(\lambda)\mathcal{H}_n^+(\lambda)}{\sqrt{\lambda-w_n}}\,e^{i\gamma_2\left(-\lambda(x'-c')+i\sqrt{\lambda^2-w_n^2}\,|y|\right)}\,d\lambda \qquad (35)$$

The expression for $\mathcal{H}_n^+(\lambda)$ can be computed by closing the contour in the lower-half-plane and expanding near the branch point at $\eta = -w_n$. The result is

$$\mathcal{H}_n^+(\lambda) \cong -\frac{i\sqrt{2w_n}\,e^{-i\gamma_2\lambda c'}}{\sqrt{\gamma_2(\lambda+w_n)c'}\mathcal{E}_n(-w_n)}\left[1 - \mathrm{erf}\left(\sqrt{-i\gamma_2(\lambda+w_n)c'}\right)\right] \qquad (36)$$

Substituting in Eq. (35) and evaluating the remaining integral using the stationary phase method we find that

$$p_2(r',\theta',z,t) \cong -\mathrm{sgn}(\pi-\theta')\frac{\rho_0 U_0 A}{\beta\sqrt{\pi\gamma_2 r'}}e^{-i(\gamma_2\kappa M^2 x' + \omega t + \pi/4)}$$

$$\times \sum_{n=0}^{\infty}\frac{\varepsilon_n \mathcal{E}_n(-w_n\cos\theta')\cos(n\pi z/\ell)}{\sqrt{\kappa+w_n}}\left[1 - \mathrm{erf}\left(\sqrt{-i\gamma_2 w_n(1-\cos\theta')c'}\right)\right]e^{i\gamma_2 w_n r'} \qquad (37)$$

Finally, the complete airfoil solution is given by

$$p(r',\theta',z,t) = \mathrm{Re}\left(p_1(r',\theta',z,t) + p_2(r',\theta',z,t)\right) \qquad (38)$$

It should be noted that, in the expressions for p_1 and p_2, only a finite number of terms in the infinite sums contribute to the radiated field. n's for which w_n is imaginary produce evanescent waves and hence do not contribute to the farfield radiation. The physical and geometric parameters of the benchmark problem are such that only terms for which $n \leq 2$ need be accounted for.

Finally, it is worth noting that if sweep is set to zero (i.e., $\alpha = 0$), Eqs. (25 & 37) reduce to the well-known solution of the 2D gust-airfoil interaction problem (see ref. 3).

Results

The solutions corresponding to the flow and gust parameters defined in the problem statement are summarized in the figure below. The figure shows the analytically predicted rms pressure directivities on a circle centered at $(0,0,\ell/2)$ and a radius of $5c$ as computed from Eq. (38) and normalized by their respective maximum rms pressures.

$m = 0$	$m = 1$	$m = 2$
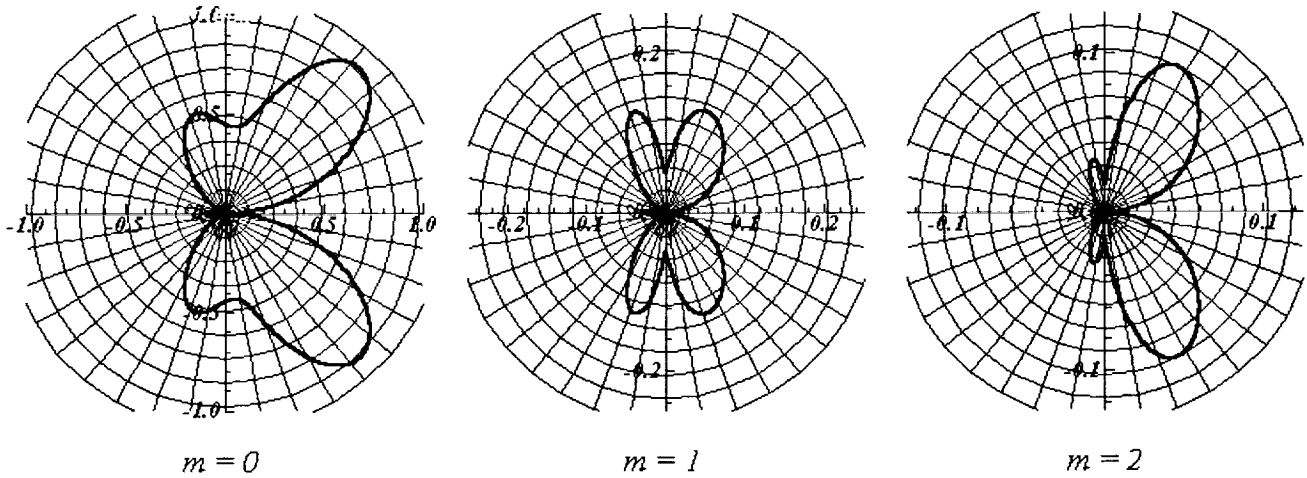
(Note the change in scale in each figure).

Solution of Problem 3

For the cascade problem, the governing equation and the imposed boundary conditions are the same as those for the isolated airfoil problem except for Eq. (2), which now should read

$$\left(\frac{\partial \phi}{\partial y} - A e^{i\left(k_x x + k_y y - \omega t\right)} \right)_{y_q = 0,\ 0 \le x_q - z \tan \alpha \le c} = 0 \tag{39}$$

$$x_q = x - qs, \qquad y_q = y - qh \tag{40}$$

where integer $q = 0,\ \pm 1,\ \pm 2,\ \cdots$ indexes the airfoils in the cascade and s and h denote the cascade stagger and spacing, respectively. For the sake of generality, the solution will be developed for non-zero stagger. The solution to the benchmark problem can be recovered by setting $s = 0$ in the final formula.

Owing to the linearity of the problem we envisage $\phi = \sum\limits_{q=-\infty}^{\infty} \phi^{(q)}$, where $\phi^{(q)}$ is the solution in the qth strip defined by $qh < y < (q+1)h$. Since the incident gust in the qth strip is related to the gust in the 0th strip through the phase shift $e^{iq\left(k_x s + k_y h\right)}$, we stipulate an identical relationship between the solutions in the qth and 0th strips;

$$\phi^{(q)}\left(x, y, z, t\right) = \phi^{(0)}\left(x_q, y_q, z, t\right) e^{iq\left(k_x s + k_y h\right)} \tag{41}$$

Therefore, once the solution in the 0th strip (i.e., $\phi^{(0)}$) is found, the solution everywhere can be obtained via Eq. (41). Following the procedure established for the previous problem, we introduce a reduced velocity potential via $\phi = \tilde{\phi}\, e^{-i\left(k_x M^2 x / \beta^2 + \omega t\right)}$, the Prandtl-Glauert transformation $x' = x / \beta$, and the non-orthogonal coordinate system given by Eq. (5). The phase shift in Eq. (41) when re-expressed in the non-orthogonal coordinates is given by $e^{iq\varpi h}$ where $\varpi = \gamma_2 \kappa s' / h + k_y$. In view of this, we find that the solution of the wave equation for the cascade problem (in the transformed plane) is given by

$$\Phi = \sum_{q=-\infty}^{\infty} \sum_{n=0}^{\infty} C_n^{(0)^+}\left(\lambda\right) Y_{q,n}\left(y_q\right) Z_n\left(\zeta\right) \tag{42}$$

$$Y_{q,n} = \text{sgn}\left(y - qh\right) e^{-\gamma_2 \sqrt{\lambda^2 - w_n^2}\,|y - qh|}\, e^{iq\left(\varpi h + \gamma_2 \lambda s'\right)} \tag{43}$$

where Z_n and w_n were defined in Eqs. (16 & 17) and $s' = s / \beta$.

Again, we take $\Phi = \Phi_1 + \Phi_2 + \cdots$ and solve for leading-edge and trailing-edge responses separately. For the cascade problem, however, we only account for the leading-edge response. This is because, at the reduced frequencies of interest here, the trailing-edge response is quite small upstream of the leading edge (compare

Eqs. (25 & 37)). As a result, in the subsequent development the trailing edge is ignored and the chord is assumed to be semi-infinite.

After a fair amount of algebraic manipulations, Eq. (39) leads to the following Wiener-Hopf equation for the cascade

$$-\mathcal{K}_n(\lambda)C_{1n}^{(0)^+}(\lambda) = D_{1n}^{(0)^-}(\lambda) + \frac{A\varepsilon_n \mathcal{F}_n(\lambda)}{\sqrt{2\pi}(\lambda + \kappa)} \tag{44}$$

where

$$\mathcal{K}_n(\lambda) = \gamma_2 \sqrt{\lambda^2 - w_n^2} \sum_{q=-\infty}^{\infty} e^{-\gamma_2 h \sqrt{\lambda^2 - w_n^2}\,|q|}\, e^{iq(\varpi h + \gamma_2 \lambda s')}$$

$$= \gamma_2 \sqrt{\lambda^2 - w_n^2} \left\{ \frac{\sinh\left(\gamma_2 h \sqrt{\lambda^2 - w_n^2}\right)}{\cosh\left(\gamma_2 h \sqrt{\lambda^2 - w_n^2}\right) - \cos(\varpi h + \gamma_2 \lambda s')} \right\} \tag{45}$$

where the subscript "1" emphasizes that this equation holds for the leading-edge response only. The cascade kernel function $\mathcal{K}_n$ enforces periodicity of the cascade solution. Note that, if the term in the curly bracket is set to unity, $\mathcal{K}_n$ reduces to the kernel for the isolated airfoil (see Eq. 19).

Performing a multiplicative split of the kernel function into terms that are analytic in upper-half-plane (i.e., a "+" function) and lower-half-plane (i.e., a "−" minus function), and assuming that the entire function $\mathcal{F}_n$ is a common factor on both sides of Eq. (44), we find a solution for $C_{1n}^{(0)^+}$ given by

$$C_{1n}^{(0)^+}(\lambda) = -\frac{A\varepsilon_n \mathcal{F}_n(\lambda)}{\sqrt{2\pi}\mathcal{K}_n^-(-\kappa)\mathcal{K}_n^+(\lambda)(\lambda + \kappa)} \tag{46}$$

where

$$\mathcal{K}_n^{\pm}(\lambda) = \sqrt{\mathcal{K}_n(0)}\, e^{\pm i\chi(\lambda)} \frac{\displaystyle\prod_{j=0}^{\infty}\left(1 - \lambda/\tau_{n,j}^{\mp}\right)}{\displaystyle\prod_{j=-\infty}^{\infty}\left(1 - \lambda/\sigma_{n,j}^{\mp}\right)} \tag{47}$$

$$\mathcal{K}_n(0) = -\frac{\gamma_2 w_n \sin(\gamma_2 h w_n)}{\cos(\gamma_2 h w_n) - \cos(\varpi h)} \tag{48}$$

$$\chi(\lambda) = \gamma_2 \left[s'(1/2 + \varphi'/\pi) - (h/\pi)\log(2\sin\varphi')\right]\lambda, \quad \varphi' = \tan^{-1}(h/s') \tag{49}$$

$$\sigma_{n,j}^{\pm} = \frac{(2j\pi - \varpi h)\gamma_2 s' \pm \Delta_{n,j}}{(\gamma_2 d')^2}, \quad \tau_{n,j}^{\pm} = \pm\sqrt{w_n^2 - (j\pi/\gamma_2 h)^2} \tag{50}$$

$$\Delta_{n,j} = \gamma_2 h \sqrt{\left(\gamma_2 w_n d'\right)^2 - \left(2j\pi - \varpi h\right)^2}, \quad d' = \sqrt{s'^2 + h^2} \tag{51}$$

where $\sigma_{n,j}^{\pm}$ and $\tau_{n,j}^{\pm}$ are the roots of the numerator and the denominator in Eq. (45). These correspond to acoustic modes (both propagating and evanescent) generated upstream, downstream and between the plates.

The decomposition of the kernel function is achieved through the use of Weiestrass's factor theorem which allows for infinite product representations of the functions involved. The exponential factor $\chi(\lambda)$, derived by analyzing the asymptotic behavior of the infinite products involved, ensures the convergence of the infinite products at infinity (see ref. 4).

Substituting for $C_{1n}^{(0)^+}$ in Eq. (42), applying an inverse Fourier transform, and reverting to the Prandtl-Glauert coordinates, leads to a representation of the leading-edge pressure field for the cascade given by

$$p_{1n}\left(x',y,z\right) = -\frac{i\rho_0 U_0 A \varepsilon_n}{2\pi\beta \mathcal{K}_n^-\left(-\kappa\right)} e^{-i\left(\gamma_2 \kappa M^2 x' + \omega t\right)} \cos\left(n\pi z / \ell\right)$$

$$\times \int_{-\infty}^{\infty} \frac{\mathcal{A}_n\left(\lambda\right)\mathcal{F}_n\left(\lambda\right)}{\mathcal{K}_n^+\left(\lambda\right)} e^{-i\gamma_2 \lambda x'} d\lambda \tag{52}$$

$$\mathcal{A}_n\left(\lambda\right) = \frac{\cosh\left(\gamma_2\left(y - h\right)\sqrt{\lambda^2 - w_n^2}\right) - e^{i\left(\varpi h + \gamma_2 \lambda s'\right)}\cosh\left(\gamma_2 y\sqrt{\lambda^2 - w_n^2}\right)}{\cosh\left(\gamma_2 h\sqrt{\lambda^2 - w_n^2}\right) - \cos\left(\varpi h + \gamma_2 \lambda s'\right)} \tag{53}$$

Well upstream of the 0th airfoil (i.e., $x' < 0$) the contour in Eq. (52) can be completed in the upper-half-plane and the integral evaluated using the residue theorem. Only $\sigma_{n,m}^+$ that are real contribute to the integral. After a fair amount of algebra, the result is

$$p_1\left(x',y,z,t\right) = \frac{i\rho_0 U_0 A}{\beta} \sum_{n=0}^{\infty} \frac{\varepsilon_n \cos\left(n\pi z / \ell\right)}{\mathcal{K}_n^-\left(-\kappa\right)} \sum_{m=M_1}^{M_2} \frac{\left(2m\pi - \Lambda_{n,m}\right)\mathcal{F}_n\left(\sigma_{n,m}^+\right)}{\Delta_{n,m}\mathcal{K}_n^+\left(\sigma_{n,m}^+\right)}$$

$$\times e^{-i\left[\gamma_2\left(\sigma_{n,m}^+ + \kappa M_0^2\right)x' + \left(2m\pi - \Lambda_{n,m}\right)y/h + \omega t\right]} \tag{54}$$

where

$$\Lambda_{n,m} = \varpi h + \gamma_2 s' \sigma_{n,m}^+ \tag{55}$$

$$M_1 = \min\left[\operatorname{int}\left(\left(\varpi h - \gamma_2 d' w_n\right)/2\pi\right), \operatorname{int}\left(\left(\varpi h + \gamma_2 d' w_n\right)/2\pi\right)\right] \tag{56}$$

$$M_2 = \max\left[\operatorname{int}\left(\left(\varpi h - \gamma_2 d' w_n\right)/2\pi\right), \operatorname{int}\left(\left(\varpi h + \gamma_2 d' w_n\right)/2\pi\right)\right] \tag{57}$$

Recall that due to the periodicity of the solution in y, one need only consider $y \in (0,h)$ in Eq. (54). As in the previous problem, only a finite number of terms in the sum over index n contribute propagating waves to the farfield. When computing the infinite products implied by the terms $\mathcal{K}_n^-(-\kappa)$ and $\mathcal{K}_n^+(\sigma_{n,m}^+)$, however, it is necessary to include a sufficiently large number of evanescent modes in order to ensure convergence of the infinite products.

Finally, the solution for the benchmark problem is given by

$$p(x'y,z,t) = \mathrm{Re}\big(p_1(x',y,z,t)\big) \tag{58}$$

It is worth noting that if sweep is set to zero (i.e., $\alpha = 0$) the 2D-cascade response developed in ref. (5) is essentially recovered from Eq. (54).

Results
The solution corresponding to the flow and gust parameters defined in the problem statement are summarized in the figure below. The figure shows the sound pressure level reduction (in dB) due to introduction of sweep at the upstream location: $(-5c, 0, \ell/2)$ as predicted by Eq. (58).
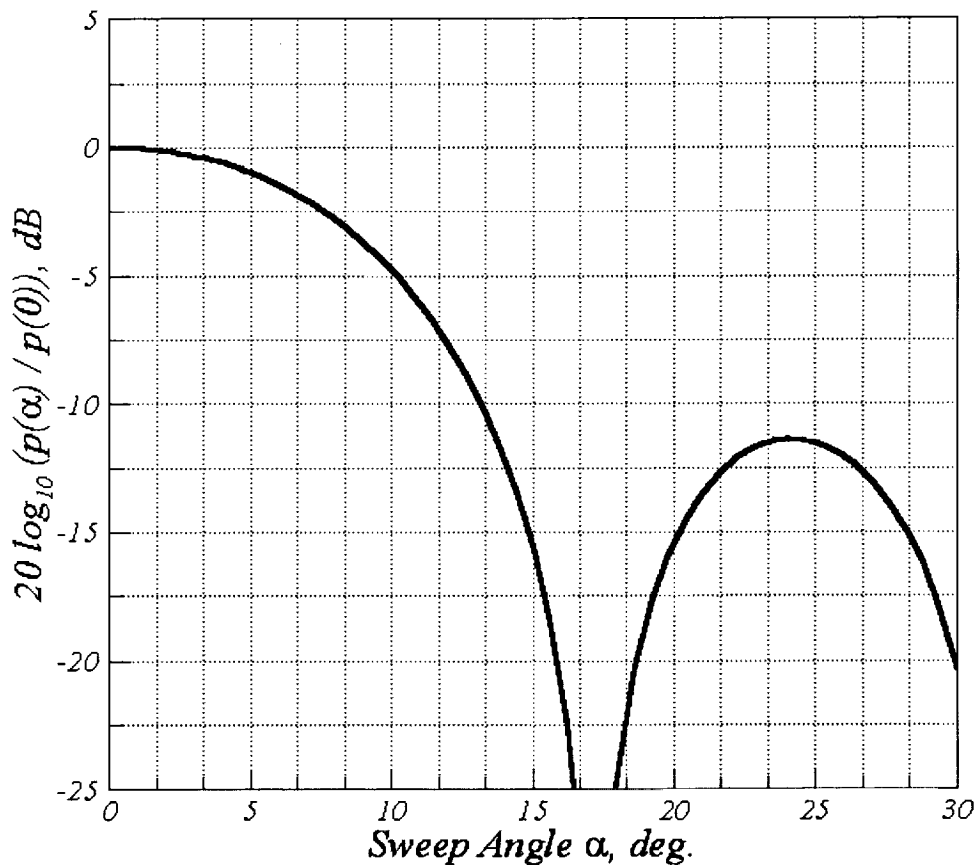
References

1. Envia, E.: Influence of Vane Sweep on Rotor-Stator Interaction Noise, Ph.D. Thesis, The University of Arizona, 1988.

2. Landhal, M.T.: Theoretical Studies of Unsteady Transonic Flow – IV. The Oscillating Rectangular Wing with Control Surface, Aeronautical Research Institute of Sweden (FFA), Report 80, 1958.

3. Matinez, R. and Widnall, S.E.: Unified Aerodynamic-Acoustic Theory for a Thin Rectangular Wing Encountering a Gust, AIAA Journal, Vol. 18, no. 16, 1980, pp. 636-645.

4. Noble, B.: Methods Based on the Wiener-Hopf Technique for the Solution of Partial Differential Equations, Chelsea Publishing Company, 1988.

5. Peake, N.: The Interaction between a High Frequency Gust and a Blade Row, Journal of Fluid Mechanics, 232, 1991, pp. 285-309.

Category 4—Fan Stator with Harmonic Excitation by Rotor Wake

NUMERICAL RESULTS OF LIFTING SURFACE THEORY

Masanobu Namba
Kumamoto Institute of Technology
Kumamoto, Japan

and

Johan B.H.M. Schulten
National Aerospace Laboratory NLR
Emmeloord, The Netherlands

Introduction

The Category 4 problem of the 3rd CAA Workshop is concerned with the noise resulting from rotor wakes impinging on a stator. Traditionally, the solution of the rotor-stator interaction noise problem is obtained by the application of a lifting surface method. These methods are based on the flow equations linearized about a uniform mean flow and have become a well-established technique. A strong point of lifting surface methods is the absence of numerical dissipation and dispersion errors, which prevent the application of regular CFD methods so often for noise problems. Therefore lifting surface results are very suitable as a benchmark test for CAA methods.

This paper gives the outline of the analytical methods based on the linearized lifting surface theory applied to Category 4, and the resulting numerical data. Unfortunately no CAA results for this problem were officially submitted at the 3rd workshop. It will be shown that this problem is worth to be retained as a test case for future CAA work.

Outline of Lifting Surface Theory

The original lifting surface theories by Namba (refs.1,2) and Schulten (refs.3,4) are formulated for a rotating annular cascade of straight or swept blades. Just to avoid unnecessary complexity we describe here the formulation applied to the present problem, i.e., a stator cascade of straight flat plates at zero stagger angle interacting with oncoming sinusoidal gust. We also use the same notations as those used in the problem description by Hanson.

Interaction of the stator vanes with an oncoming sinusoidal gust with a circumferential velocity

$$v(r,\phi,x,t) = UV_1 e^{iB[\Omega x/U + \phi - \theta(r) - \Omega t]} \tag{1}$$

produces an unsteady blade loading. The pressure difference across the ν–th blade surface can be expressed as

$$\ldots \rho_0 U^2 \Delta C_p(r,x) e^{-i\omega t + i2\pi\nu B/V} : \nu = 0,1,\ldots,V-1. \tag{2}$$

Here ρ_0 is the ambient air density and $\omega = B\Omega$. Then the wave equation for the acoustic pressure generated from the blades is given by

$$\left\{ \nabla^2 - \frac{1}{a_0^2}\left(\frac{\partial}{\partial t} + U\frac{\partial}{\partial x}\right)^2 \right\} p(r,\phi,x,t) = -\rho_o U^2 \frac{1}{r}\frac{\partial}{\partial \phi}\sum_{\nu=0}^{V-1}\int_h^R \frac{1}{r}\delta(r - r_0)\,dr_0$$

$$\times \int_0^h \Delta C_p(r_0, x_0) e^{-i\omega t + i2\pi v B/V} \delta(x - x_0) dx_0 \, \delta(\phi - 2\pi v/V). \tag{3}$$

The boundary condition at the duct walls is

$$\partial p / \partial r = 0 \quad \text{at} \quad r = R \quad \text{and} \quad r = h. \tag{4}$$

The formal solution can be expressed as

$$p(r, \phi, x, t) = \rho_0 U^2 \frac{1}{R^2} e^{-i\omega t} \int_h^R dr_0 \int_0^h \Delta C_p(r_0, x_0) K_p(r, \phi, x - x_0 | r_0) dx_0. \tag{5}$$

Here the kernel function is obtained as the solution of the following equations:

$$\left\{ \nabla^2 - \frac{1}{a_0^2} \left(-i\omega + U \frac{\partial}{\partial x} \right)^2 \right\} K_p(r, \phi, x - x_0 | r_0)$$

$$= -\frac{R^2}{r^2} \delta(r - r_0) \delta(x - x_0) \sum_{v=0}^{V-1} e^{i2\pi v B/V} \delta'(\phi - 2\pi v/V), \tag{6}$$

$$\partial K_p / \partial r = 0 \quad \text{at} \quad r = R \quad \text{and} \quad r = h. \tag{7}$$

The solution is expressed as follows:

$$K_p(r, \phi, x | r_0) = \frac{V}{4\pi\beta^2} \sum_{k=-\infty}^{\infty} \sum_{\mu=0}^{\infty} \frac{im}{\Lambda_{m\mu}} \Phi_{m\mu}(r) \, \Phi_{m\mu}(r_0)$$

$$\times \exp\left[im\phi - i(M_x^2/\beta^2)\omega x/U - \Lambda_{m\mu} |x|/R \right] \tag{8}$$

Here

$$m = B - kV, \quad M_x = U/a_0, \quad \beta^2 = 1 - M_x^2.$$

Further $\Lambda_{m\mu}$ is defined by

$$\Lambda_{m\mu} = \begin{cases} \sqrt{A} & : A \geq 0 \\ -i \, \text{sgn}(\omega) \sqrt{-A} & : A \leq 0 \end{cases}, \quad A = \left\{ k_{m\mu}^2 - (\omega R/U)^2 M_x^2/\beta^2 \right\} \beta^2. \tag{9}$$

Here $k_{m\mu}$ and $\Phi_{m\mu}(r)$: $(\mu = 0, 1, 2, ...)$ are radial eigenvalues and eigenfunctions respectively of the following Sturm-Liouville boundary value problem.

$$\frac{R^2}{r} \frac{d}{dr} \left(r \frac{d\Phi_{m\mu}(r)}{dr} \right) + \left(k_{m\mu}^2 - \frac{m^2 R^2}{r^2} \right) \Phi_{m\mu}(r) = 0, \tag{10}$$

$$d\Phi_{m\mu}(r)/dr = 0 \quad \text{at} \quad r = R \quad \text{and} \quad r = h. \tag{11}$$

The eigenfunctions are normalized as follows:

$$\cdots \frac{1}{R^2} \int_h^R r \, \Phi_{m\mu}(r) \Phi_{mv}(r) dr = \delta_{\mu v}. \tag{12}$$

Therefore the mode shape function $\Psi_{m\mu}(r)$ defined in the problem description is given by

$$\cdots \cdots \Psi_{m\mu}(r) = \Phi_{m\mu}(r) / \left[\Phi_{m\mu}(r) \right]_{\max}. \tag{13}$$

The blade loading function $\Delta C_p(r, x)$ can be determined from the flow tangency condition on blade surfaces, which can be expressed by

$$\cdots \frac{1}{R^2} \int_h^R dr_0 \int_0^h \Delta C_p(r_0, x_0) K_v(r, 0, x - x_0 | r_0) dx_0 = -V_1 e^{i\omega x/U - iB\theta(r)}, \tag{14}$$

where $K_v(r,\phi,x \mid r_0)$ is the upwash velocity kernel function given by

$$K_v(r,\phi,x \mid r_0) = -e^{i\omega x/U} \int_{-\infty}^{x} e^{-i\omega x/U} \frac{1}{r} \frac{\partial}{\partial \phi} K_p(r,\phi,x \mid r_0) dx$$

$$= -\frac{V}{4\pi\beta^2} \frac{R}{r} \sum_{k=-\infty}^{\infty} \sum_{\mu=0}^{\infty} \frac{m^2}{\Lambda_{m\mu} \left(i\omega R/(\beta^2 U) + \Lambda_{m\mu} \, \text{sgn}(x) \right)} \Phi_{m\mu}(r) \Phi_{m\mu}(r_0) e^{im\phi - i\left(M_x^2/\beta^2\right)\omega x/U - \Lambda_{m\mu}|x|/R}$$

$$+ H(x) e^{i\omega x/U} \frac{VR}{2\pi r} \sum_{k=-\infty}^{\infty} \sum_{\mu=0}^{\infty} \frac{m^2}{k_{m\mu}^2 + (\omega R/U)^2} \Phi_{m\mu}(r) \Phi_{m\mu}(r_0) e^{im\phi}. \tag{15}$$

The integral equation (14) for $\Delta C_p(r,x)$ should be solved numerically. Various methods are available. The methods used for the present problem by Namba and by Schulten are described in Appendix A and B respectively.

Finally the modal pressure amplitude $A_{m\mu}(x)$ defined by

$$p(r,\phi,x,t) = p_0 \sum_{k=-\infty}^{\infty} \sum_{\mu=0}^{\infty} A_{m\mu}(x) \Psi_{m\mu}(r) e^{i(m\phi - B\Omega t)}, \tag{16}$$

can be calculated from

$$A_{m\mu}(x) = \gamma M_x^2 \frac{imV}{4\pi\beta^2 \Lambda_{m\mu}} \left[\Phi_{m\mu}(r) \right]_{\text{max}}$$

$$\times \frac{1}{R^2} \int_h^R dr_0 \int_0^b \Delta C_p(r_0,x_0) \Phi_{m\mu}(r_0) \exp\left[-\frac{M_x^2}{\beta^2} \frac{\omega}{U}(x - x_0) - \frac{\Lambda_{m\mu}}{R}|x - x_0| \right] dx_0, \tag{17}$$

where $\gamma (= 1.4)$ is the specific heat ratio of air.

Numerical Results

Numerical values of the modal pressure amplitude $A_{m\mu}(x)$ calculated by Namba and Schulten are given in Table 1 and Tables 2.1 – 2.10. To save space, circumferential wave numbers are confined to the smallest two; $m=16$ and $m=-8$. The other modal pressure amplitudes are extremely small. The agreement between Namba's and Schulten's data is fairly good. The discrepancies will come from various numerical processes in solving the integral equation (14) and computing integrals in equation (17). In particular the exceptional large discrepancy observed for $M_T = 0.433$ of the narrow annulus (Table 1) is due to the fact that the condition is very close to the resonance $(\Lambda_{m\mu} = 0)$ of the mode of $m = -8, \mu = 0$.

Table 3 and Figure 1 show a comparison between the unsteady lift coefficient C_L $(= \int_0^b \Delta C_p(r,x)dx/(bV_1))$ at mid-span of the narrow annulus cascade and that of the corresponding 2-dimensional cascade. It is clear that the flow field of the narrow annulus cascade is nearly two-dimensional. On the other hand the validity of the 2D code used to compute the two-dimensional problems was ascertained from the fact that it exactly reproduces Figure 5(a) of Hall and Verdon (ref.5), which was computed with Smith's code.

It should be noted that in the full annulus cases, all modes are cut-off for $M_T = 0.470$, only one mode ($m=-8$, $\mu=0$) is cut-on for $M_T = 0.522$ and $M_T = 0.574$, and two modes ($m=-8$, $\mu = 0$), ($m=-8$, $\mu = 1$) are cut-on for $M_T = 0.783$. Certainly the amplitudes of cut-off modes are smaller than those of cut-on modes, but they are not extremely small. This is because the axial positions one chord away from the leading and trailing edges are not far enough for the cut-off modes to decay out. Therefore at more distant positions the difference in the magnitude between cut-on and cut-off modes will be more pronounced. However to compute pressures at such distant positions by CAA methods may worsen the problem of numerical dissipation and dispersion.

In Figure 2 a comparison is made between the results of Namba and Schulten. The pressure jump distribution (ΔC_p based on $\rho_0 U^2/2$) at mid-span for the full annulus is compared for the highest tip speed of the rotor investigated in the present study ($M_T = 0.783$). It is clear that the agreement between both methods is very good. Only in the aft portion of the chord some small discrepancies are visible.

A three-dimensional view on the pressure jump distribution over the whole reference vane is given in Figure 3. In this case the incident velocity field is in phase along the span ($q = 0.0$) which is clearly reflected by the behavior of the pressure jump in the vicinity of the leading edge. In the aft portion of the vane some mild spanwise variation is discernable which results from the three-dimensionality of the stator.

As shown in Figure 4 the response of the stator is quite sensitive to the spanwise phasing of the impinging field which is characterized by $q = 1.5$ in this case. This spanwise periodicity is only recognized in the pressure jump distribution in the immediate vicinity of the leading edge. Further downstream, the spanwise response is closer to one full wave length. But the most remarkable observation is the very large amplitude of the response, which points to some kind of near-resonance behavior. This may have to do with the (intentional, see problem description) similarity of the excitation with the acoustic radial mode shapes for $\mu = 1$ (cut-on) and $\mu = 2$ (cut-off) ($m = -8$).

The contrast with the results for $q = 3.0$, presented in Figure 4, is striking. It is hardly imaginable that the only difference in the incident field is a spanwise phasing twice as high as in Figure 3. This phasing can still be observed in the leading edge portion of the vane but vanishes downstream. It is reconfirmed even stronger that the spanwise phasing is crucial to the stator response.

The $q = 3.0$ case was taken for another comparison between Namba's and Schulten's results. In Figure 5 the pressure jump is compared along a spanwise line located at 6 percent of the chord. The agreement is quite satisfactory but some slight discrepancies near the hub and the casing can be observed. Figure 6 gives the results along a spanwise line at 20 percent of the chord. Here some more discrepancies are visible, not only at hub and casing but also in the mid-span region. However, it should not be overlooked that the scale is four times larger than in the previous figure. It seems as if the spanwise waviness first starts to disappear in the mid-span region. Note that the pressure jump should have a zero derivative at hub and casing due to the hard wall boundary conditions [Eq.(4)]. Relatively large discrepancies are observed along the 50 percent line in Figure 7. Only one full spanwise wavelength can be observed here. Finally, in Figure 8 the pressure jump along the 90 percent line shows a better, although not a perfect, agreement. In general, it seems that closer to the leading and trailing edges the agreement is better than in the inner portion of the vane. It is noted that seemingly small discrepancies in the pressure jump can affect the modal amplitudes more seriously. This may be the reason that, occasionally, the agreement in the modal amplitudes is not as good as was expected by the authors on beforehand.

Concluding remarks

The Category 4 benchmark problem was successfully computed by two lifting surface methods. The problem definition was well chosen to include some interesting near-resonance effects.

Comparison of the results of both methods showed good agreement on the whole. It appeared that relatively small discrepancies in the pressure jump distribution could lead to relevant discrepancies in the modal amplitudes. It would be helpful if in future CAA benchmarking of the rotor stator interaction problem, attention will also be paid to the prediction of the pressure jump distribution rather than only to the modal amplitudes.

References

1. Namba, M., "Three-Dimensional Flows," *AGARD Manual on Aeroelasticity in Axial Flow Turbomachines, Vol.1, Unsteady Turbomachinery Aerodynamics* (AGARD-AG-298). M.F. Platzer and F.O. Carta, eds., Neuilly sur Seine, France, Chap. 4, 1987.
2. Namba, M. and Ishikawa, A., "Three-Dimensional Aerodynamic Characteristics of Oscillating Supersonic and Transonic Annular Cascades", *ASME J. of Engineering for Power*, **105**, 1983, pp.138-146.
3. Schulten, J.B.H.M., "Sound Generated by Rotor Wakes Interacting with a Leaned Vane Stator", *AIAA J.*, **20-10**, 1982, pp.1352-1358.
4. Schulten, J.B.H.M., "Vane sweep effects on rotor/stator interaction noise," *AIAA Journal*, Vol.35, No.6, June 1997, pp.945-951.
5. Hall, K.C. and Verdon, J.M., "Gust Response Analysis for Cascades Operating in Nonuniform Mean Flows," *AIAA Journal*, **29-8**, 1991, pp.1463-1471.
6. Abramowitz, M., Stegun, I.A., *Handbook of Mathematical Functions*, Dover Publications, New York, 1968.
7. Bender, C.M., Orszag, S.A., *Advanced Mathematical Methods for Scientists and Engineers*, McGraw-Hill, 1978.

Appendix A Namba's Method

The kernel function of the integral equation (14) contains singularities of $1/(x-x_0)$ and $\log|x-x_0|$. It is desirable to calculate the principal values analytically rather than numerically. To do so it is necessary to extract the singular parts from the kernel function. But it is not easy because the eigenfunctions $\Phi_{m\mu}(r)$ do not approach to definite values as m goes to infinity.

To cope with this difficulty Namba (refs.1,2) developed the method of finite radial mode expansion. The essence of the method is to approximate the eigenfunction by a finite series expansion of the form:

$$\Phi_{m\mu}(r) = \sum_{\ell=0}^{L-1} B_{\mu\ell}^{(m)} \Phi_{0\ell}(r). \tag{A1}$$

Then the coefficients $B_{\mu\ell}^{(m)}$ can be determined as eigenvectors of a real symmetric matrix, and we can calculate the limit values of $\lim_{m\to\infty} B_{\mu\ell}^{(m)} = B_{\mu\ell}^{(\infty)}$. Therefore the approximate eigenfunctions have definite limit functions of $\Phi_{\infty\mu}(r)$. Expressing the kernel function in terms of $\Phi_{0\mu}(r)$ or $\Phi_{\infty\mu}(r)$, we can easily extract the singular parts of the kernel function.

The unknown blade loading function is expressed in terms of double mode function series:

$$\Delta C_p(r,x) = \sum_{\ell=0}^{L-1} \Phi_{\infty\ell}(r)\left\{ A_{\ell 0}\cot\frac{\xi}{2} + \sum_{j=1}^{J-1} A_{\ell j}\sin(j\xi) \right\}, \quad x = (1-\cos\xi)b/2, \tag{A2}$$

and the principal values can be analytically calculated. The problem reduces to algebraic equations for the coefficients $A_{\ell j}$. This formulation also enables us to calculate the integrals in equation (17) analytically.

The accuracy of the numerical solution essentially depends on the numbers of retained terms L and J. To solve the present problem $L=21$ and $J=11$ are adopted. It takes about 65 seconds to compute one case on PC of Celeron 350 MHz.

Appendix B Schulten's Method

The first step to the numerical solution of Eq. 14 is the representation of the unknown ΔC_p. The chordwise expansion is identical to Namba's given in Eq. (A2). However, for the spanwise direction a Chebyshev (1st kind) series is adopted. This series can be considered as a Fourier cosine series in the variable ψ where

$$\cos\psi = 2(r-h)/(R-h) - 1 \qquad (B1)$$

To solve the integral equation (14) numerically, a Galerkin procedure is followed. This means that both sides of the equation are projected on a set of orthogonal basis functions. The advantage of a Galerkin method over a collocation method is that the number of points on the vane surface can be taken (much) larger than the number of unknowns . The Galerkin method yields the least squares fit to the point values on the vane. The Galerkin basis functions used are Chebyshev 1st kind for the spanwise direction and 2nd kind for the chordwise direction. Gauss-Lobatto integration formulae (ref. 6) are used to evaluate the integrals.

The number of required projections is taken to be sufficient to capture the right hand side to a preset accuracy. In the present study an accuracy of 0.004 relative to the largest right hand side term was adopted throughout. Further, the expansions are taken sufficiently large to resolve the shortest acoustic wave lengths upstream and downstream as well as in spanwise direction. The final criterion is that also the hydrodynamic wave is accurately resolved. For the most demanding case ($M_T = 0.783$, $q = 3.0$), the maximum number of required projections was 17 spanwise $\times$ 9 chordwise. These numbers were also taken for J and L respectively in the expansion of ΔC_p.

After taking the Galerkin projections the integral equation turns into a matrix equation the left hand side of which contains a series in k which essentially is a Fourier series in the circumferential coordinate. This is a slowly convergent series with terms behaving as $1/k^2$ asymptotically. To obtain an accuracy of, say, $\varepsilon = 0.004$ with respect to the largest element in its row of the matrix would require something in the order of $1/\varepsilon = 250$ terms. This would be very hard computationally. Therefore a 2nd order Richardson extrapolation (ref.7) is applied to the k-series. For the most demanding case (see above) this limits k_{max} to 18. Nevertheless, the total computing time for this matrix is about 40 hours on a 300 MHz PC.

In the present method the evaluation of the infinite radial series over μ as occurring in Eqs. (8) and (15) is handled quite differently from Namba's method. As described in ref.4, the series can be replaced by an integral in the complex α-plane, where α is the wave number in x-direction. By deforming the contour of integration away from the poles, a smooth integrand is obtained that can be accurately integrated numerically. The only difficulty is encountered for a case very close to duct mode resonance (cut-on) when the path of integration has to pass two poles very closely. This integral representation is especially advantageous for vanes of arbitrary shape. For the unswept vanes with constant chord of the present configuration it is considerably more time consuming than Namba's method.

Tables

Table 1. Narrow Annulus q =0

<table>
<tr><td colspan="9">Upstream Waves: $x=-b$</td></tr>
<tr><td rowspan="3">M_T</td><td colspan="4">M=16</td><td colspan="4">m =-8</td></tr>
<tr><td colspan="2">Real</td><td colspan="2">Imag</td><td colspan="2">Real</td><td colspan="2">Imag</td></tr>
<tr><td>Namba</td><td>Schulten</td><td>Namba</td><td>Schulten</td><td>Namba</td><td>Schulten</td><td>Namba</td><td>Schulten</td></tr>
<tr><td>0.3897</td><td>-2.422E-05</td><td>-1.930E-05</td><td>9.174E-06</td><td>8.120E-06</td><td>-5.067E-03</td><td>-5.407E-03</td><td>1.924E-03</td><td>2.231E-03</td></tr>
<tr><td>0.4330</td><td>-9.952E-05</td><td>-8.599E-05</td><td>-1.874E-05</td><td>-5.001E-06</td><td>-1.142E-03</td><td>2.083E-03</td><td>-2.170E-04</td><td>3.459E-04</td></tr>
<tr><td>0.4763</td><td>-1.043E-04</td><td>-1.033E-04</td><td>-7.110E-05</td><td>-6.823E-05</td><td>-7.603E-03</td><td>-7.538E-03</td><td>1.837E-03</td><td>2.055E-03</td></tr>
<tr><td>0.6495</td><td>-8.334E-05</td><td>-1.074E-04</td><td>-4.261E-04</td><td>-4.033E-04</td><td>7.577E-03</td><td>7.364E-03</td><td>-1.814E-03</td><td>-2.453E-03</td></tr>
<tr><td colspan="9">Downstream Waves: $x=+2b$</td></tr>
<tr><td rowspan="3">M_T</td><td colspan="4">m =16</td><td colspan="4">m =-8</td></tr>
<tr><td colspan="2">Real</td><td colspan="2">Imag</td><td colspan="2">Real</td><td colspan="2">Imag</td></tr>
<tr><td>Namba</td><td>Schulten</td><td>Namba</td><td>Schulten</td><td>Namba</td><td>Schulten</td><td>Namba</td><td>Schulten</td></tr>
<tr><td>0.3897</td><td>-6.945E-05</td><td>-7.063E-05</td><td>3.666E-05</td><td>3.999E-05</td><td>8.584E-03</td><td>8.734E-03</td><td>-4.532E-03</td><td>-4.943E-03</td></tr>
<tr><td>0.4330</td><td>-5.302E-05</td><td>-4.718E-05</td><td>1.641E-05</td><td>8.436E-06</td><td>1.715E-02</td><td>3.410E-03</td><td>-5.298E-03</td><td>-6.981E-04</td></tr>
<tr><td>0.4763</td><td>-3.587E-05</td><td>-3.619E-05</td><td>1.999E-05</td><td>2.090E-05</td><td>1.050E-02</td><td>1.061E-02</td><td>1.604E-02</td><td>1.556E-02</td></tr>
<tr><td>0.6495</td><td>2.529E-05</td><td>1.903E-05</td><td>1.282E-05</td><td>5.809E-06</td><td>-1.120E-02</td><td>-9.946E-03</td><td>5.684E-03</td><td>5.870E-03</td></tr>
</table>

Table 2.1 Full Annulus : q=0, M_T =0.470

<table>
<tr><td colspan="9">Upstream Waves, $x=-b$</td></tr>
<tr><td rowspan="3"></td><td colspan="4">m =16</td><td colspan="4">m =-8</td></tr>
<tr><td colspan="2">Real</td><td colspan="2">Imag</td><td colspan="2">Real</td><td colspan="2">Imag</td></tr>
<tr><td>Namba</td><td>Schulten</td><td>Namba</td><td>Schulten</td><td>Namba</td><td>Schulten</td><td>Namba</td><td>Schulten</td></tr>
<tr><td>μ = 0</td><td>-6.635E-05</td><td>-5.482E-05</td><td>1.687E-05</td><td>1.047E-05</td><td>-2.073E-03</td><td>-2.881E-03</td><td>-1.955E-03</td><td>-1.456E-03</td></tr>
<tr><td>μ = 1</td><td>-7.690E-06</td><td>-8.411E-06</td><td>-5.077E-06</td><td>-3.579E-06</td><td>1.894E-04</td><td>2.546E-04</td><td>4.300E-04</td><td>2.595E-04</td></tr>
<tr><td>μ = 2</td><td>-1.500E-06</td><td>-1.950E-06</td><td>-1.921E-06</td><td>-1.272E-06</td><td>2.341E-05</td><td>3.635E-05</td><td>6.261E-05</td><td>4.026E-05</td></tr>
<tr><td>μ = 3</td><td>-3.851E-07</td><td>-5.237E-07</td><td>-5.331E-07</td><td>-4.021E-07</td><td>1.312E-06</td><td>1.958E-06</td><td>2.356E-06</td><td>2.221E-06</td></tr>
<tr><td>μ = 4</td><td>-4.975E-08</td><td>-7.115E-08</td><td>-7.526E-08</td><td>-6.257E-08</td><td>5.220E-08</td><td>8.742E-08</td><td>1.119E-07</td><td>1.097E-07</td></tr>
<tr><td colspan="9">Downstream Waves, $x=+2b$</td></tr>
<tr><td rowspan="3"></td><td colspan="4">m =16</td><td colspan="4">m =-8</td></tr>
<tr><td colspan="2">Real</td><td colspan="2">Imag</td><td colspan="2">Real</td><td colspan="2">Imag</td></tr>
<tr><td>Namba</td><td>Schulten</td><td>Namba</td><td>Schulten</td><td>Namba</td><td>Schulten</td><td>Namba</td><td>Schulten</td></tr>
<tr><td>μ = 0</td><td>-7.287E-05</td><td>-6.680E-05</td><td>3.060E-05</td><td>3.998E-05</td><td>9.484E-03</td><td>9.296E-03</td><td>-4.826E-03</td><td>-5.798E-03</td></tr>
<tr><td>μ = 1</td><td>-2.814E-06</td><td>-3.457E-06</td><td>3.402E-06</td><td>3.081E-06</td><td>-3.249E-06</td><td>9.737E-05</td><td>-2.600E-04</td><td>-1.776E-04</td></tr>
<tr><td>μ = 2</td><td>-7.340E-08</td><td>-3.810E-07</td><td>6.725E-07</td><td>4.967E-07</td><td>-1.264E-05</td><td>-1.055E-07</td><td>-2.353E-05</td><td>-1.290E-05</td></tr>
<tr><td>μ = 3</td><td>3.477E-09</td><td>-5.530E-08</td><td>1.562E-07</td><td>1.054E-07</td><td>-1.534E-07</td><td>-1.315E-07</td><td>-8.371E-07</td><td>-4.555E-07</td></tr>
<tr><td>μ = 4</td><td>3.018E-09</td><td>-2.657E-09</td><td>1.857E-08</td><td>1.123E-08</td><td>-1.415E-08</td><td>-1.294E-08</td><td>-2.883E-08</td><td>-1.219E-08</td></tr>
</table>

Table 2.2 Full Annulus : q =0, M_T =0.522

<table>
<tr><td colspan="9">Upstream Waves, $x=-b$</td></tr>
<tr><td rowspan="3"></td><td colspan="4">m =16</td><td colspan="4">m =-8</td></tr>
<tr><td colspan="2">Real</td><td colspan="2">Imag</td><td colspan="2">Real</td><td colspan="2">Imag</td></tr>
<tr><td>Namba</td><td>Schulten</td><td>Namba</td><td>Schulten</td><td>Namba</td><td>Schulten</td><td>Namba</td><td>Schulten</td></tr>
<tr><td>μ = 0</td><td>-1.224E-04</td><td>-1.190E-04</td><td>-8.522E-05</td><td>-5.906E-05</td><td>1.792E-02</td><td>1.529E-02</td><td>1.153E-02</td><td>5.181E-03</td></tr>
<tr><td>μ = 1</td><td>-3.614E-06</td><td>-6.159E-06</td><td>-7.968E-06</td><td>-1.302E-05</td><td>-4.648E-04</td><td>-1.110E-05</td><td>4.768E-04</td><td>1.032E-03</td></tr>
<tr><td>μ = 2</td><td>1.995E-07</td><td>-5.846E-07</td><td>-1.308E-06</td><td>-3.141E-06</td><td>-5.493E-05</td><td>-1.412E-05</td><td>3.837E-05</td><td>1.073E-04</td></tr>
<tr><td>μ = 3</td><td>5.952E-08</td><td>-4.987E-08</td><td>-2.994E-07</td><td>-8.420E-07</td><td>-1.006E-06</td><td>-9.035E-07</td><td>1.465E-06</td><td>4.692E-06</td></tr>
<tr><td>μ = 4</td><td>9.765E-09</td><td>5.772E-09</td><td>-3.386E-08</td><td>-1.138E-07</td><td>-4.796E-08</td><td>-5.519E-08</td><td>4.262E-08</td><td>1.867E-07</td></tr>
<tr><td colspan="9">Downstream Waves, $x=+2b$</td></tr>
<tr><td rowspan="3"></td><td colspan="4">m =16</td><td colspan="4">m =-8</td></tr>
<tr><td colspan="2">Real</td><td colspan="2">Imag</td><td colspan="2">Real</td><td colspan="2">Imag</td></tr>
<tr><td>Namba</td><td>Schulten</td><td>Namba</td><td>Schulten</td><td>Namba</td><td>Schulten</td><td>Namba</td><td>Schulten</td></tr>
<tr><td>μ = 0</td><td>-6.237E-05</td><td>-7.757E-05</td><td>1.613E-06</td><td>2.344E-05</td><td>3.928E-02</td><td>4.724E-02</td><td>-5.248E-03</td><td>-9.905E-03</td></tr>
<tr><td>μ = 1</td><td>-2.969E-06</td><td>-7.565E-06</td><td>6.235E-06</td><td>4.294E-06</td><td>6.465E-05</td><td>-3.512E-04</td><td>-8.589E-04</td><td>-4.707E-04</td></tr>
<tr><td>μ = 2</td><td>-2.241E-07</td><td>4.121E-07</td><td>1.726E-06</td><td>9.459E-07</td><td>-3.234E-06</td><td>-4.480E-05</td><td>-8.308E-05</td><td>-4.237E-05</td></tr>
<tr><td>μ = 3</td><td>-3.758E-08</td><td>1.651E-07</td><td>4.150E-07</td><td>2.376E-07</td><td>1.173E-07</td><td>-1.916E-06</td><td>-2.440E-06</td><td>-1.623E-06</td></tr>
<tr><td>μ = 4</td><td>-2.497E-09</td><td>2.756E-08</td><td>5.147E-08</td><td>3.011E-08</td><td>-3.218E-09</td><td>-8.002E-08</td><td>-9.167E-08</td><td>-5.717E-08</td></tr>
</table>

Table 2.3 Full Annulus, q =0, M_T =0.574

	Upstream Waves, $x=-b$							
	m =16				m =-8			
	Real		Imag		Real		Imag	
	Namba	Schulten	Namba	Schulten	Namba	Schulten	Namba	Schulten
$\mu = 0$	-8.222E-05	-9.639E-05	-1.274E-04	-1.175E-04	-1.970E-02	-1.725E-02	7.111E-05	4.671E-03
$\mu = 1$	-7.084E-06	-5.057E-06	-8.093E-06	-6.979E-06	-1.293E-05	-4.105E-04	1.297E-04	1.377E-04
$\mu = 2$	-1.488E-06	-8.443E-07	-1.246E-06	-9.783E-07	1.088E-05	-2.539E-05	9.418E-06	4.041E-06
$\mu = 3$	-4.026E-07	-2.110E-07	-3.127E-07	-1.884E-07	1.214E-06	-4.166E-07	1.065E-06	7.052E-08
$\mu = 4$	-5.554E-08	-2.855E-08	-3.953E-08	-1.787E-08	5.876E-08	7.636E-10	3.681E-08	-5.059E-09
	Downstream Waves, $x=+2b$							
	m =16				m =-8			
	Real		Imag		Real		Imag	
	Namba	Schulten	Namba	Schulten	Namba	Schulten	Namba	Schulten
$\mu = 0$	-4.189E-05	-4.431E-05	1.166E-05	1.088E-05	6.598E-03	5.028E-03	2.515E-02	2.561E-02
$\mu = 1$	-4.419E-06	-3.181E-06	5.204E-06	6.692E-06	4.831E-04	2.696E-04	-8.430E-04	-1.146E-03
$\mu = 2$	-8.140E-07	-4.852E-07	1.313E-06	1.633E-06	3.338E-05	1.562E-05	-6.704E-05	-9.173E-05
$\mu = 3$	-1.816E-07	-9.871E-08	3.064E-07	4.253E-07	1.042E-06	4.736E-07	-1.848E-06	-3.356E-06
$\mu = 4$	-2.087E-08	-1.003E-08	3.725E-08	5.548E-08	3.322E-08	1.101E-08	-6.705E-08	-1.176E-07

Table 2.4 Full Annulus q =0, MT =0.783

	Upstream Waves, $x=-b$							
	m =16				m =-8			
	Real		Imag		Real		Imag	
	Namba	Schulten	Namba	Schulten	Namba	Schulten	Namba	Schulten
$\mu=0$	2.541E-04	1.486E-04	-6.945E-04	-6.906E-04	3.493E-03	5.140E-03	1.125E-02	1.056E-02
$\mu=1$	6.726E-06	6.191E-06	-2.322E-05	-2.409E-05	-6.674E-03	-7.631E-03	-1.811E-02	-1.747E-02
$\mu=2$	1.188E-06	8.004E-07	-3.107E-06	-3.231E-06	-1.816E-04	-8.145E-05	1.243E-04	1.072E-04
$\mu=3$	2.634E-07	1.324E-07	-7.104E-07	-7.178E-07	-3.028E-06	-1.370E-06	4.329E-06	4.021E-06
$\mu=4$	2.739E-08	1.044E-08	-8.201E-08	-8.572E-08	-6.474E-08	-2.451E-08	1.053E-07	1.271E-07
	Downstream Waves, $x=+2b$							
	m =16				m =-8			
	Real		Imag		Real		Imag	
	Namba	Schulten	Namba	Schulten	Namba	Schulten	Namba	Schulten
$\mu=0$	2.088E-05	-3.081E-05	-1.024E-04	-1.007E-04	-1.707E-02	-1.497E-02	-1.594E-03	-2.731E-04
$\mu=1$	-1.025E-05	-8.833E-06	5.674E-06	5.207E-06	7.702E-03	8.603E-03	1.731E-02	1.564E-02
$\mu=2$	-1.824E-06	-1.898E-06	1.295E-06	1.428E-06	1.022E-04	1.729E-04	-1.558E-04	-2.034E-04
$\mu=3$	-3.404E-07	-4.196E-07	2.745E-07	3.240E-07	1.589E-06	3.048E-06	-2.310E-06	-3.024E-06
$\mu=4$	-3.730E-08	-4.788E-08	3.130E-08	3.878E-08	6.709E-08	8.474E-08	-6.732E-08	-8.943E-08

Table 2.5 Full Annulus q =0.5, M_T =0.783

	Upstream Waves, $x=-b$							
	m =16				m =-8			
	Real		Imag		Real		Imag	
	Namba	Schulten	Namba	Schulten	Namba	Schulten	Namba	Schulten
$\mu = 0$	2.295E-04	2.607E-04	5.566E-04	5.036E-04	-7.152E-03	-7.285E-03	1.333E-05	2.304E-05
$\mu = 1$	1.703E-05	2.046E-05	5.059E-06	1.080E-05	1.109E-02	1.241E-02	-1.667E-02	-1.951E-02
$\mu = 2$	3.463E-06	3.173E-06	-2.646E-06	-3.587E-06	-5.908E-04	-2.929E-04	5.684E-04	9.876E-04
$\mu = 3$	8.275E-07	6.741E-07	-8.096E-07	-1.316E-06	-8.793E-06	-5.157E-06	8.222E-06	1.661E-05
$\mu = 4$	5.814E-08	6.093E-08	-9.399E-08	-1.778E-07	3.554E-08	-4.438E-08	1.225E-07	3.835E-07
	Downstream Waves, $x=+2b$							
	m =16				m =-8			
	Real		Imag		Real		Imag	
	Namba	Schulten	Namba	Schulten	Namba	Schulten	Namba	Schulten
$\mu = 0$	-1.625E-05	-1.893E-05	-3.463E-05	-2.728E-05	1.132E-02	8.825E-03	-1.370E-02	-1.405E-02
$\mu = 1$	-1.517E-05	-7.840E-06	8.852E-06	1.166E-05	5.529E-03	8.351E-03	2.134E-02	1.706E-02
$\mu = 2$	-1.591E-06	-2.141E-06	-5.765E-07	-8.008E-07	-1.701E-04	2.677E-04	5.495E-04	7.376E-04
$\mu = 3$	-1.457E-07	-5.001E8007	-4.244E-07	-5.714E-07	-2.808E-06	4.390E-06	9.158E-06	1.251E-05
$\mu = 4$	-1.139E-08	-5.981E-08	-5.678E-08	-8.514E-08	-2.334E-09	1.255E-07	1.476E-07	2.690E-07

Table 2.6 Full Annulus $q=1.0\_M_T=0.783$

	Upstream Waves $x=-b$							
	$m=16$				$m=-8$			
	Real		Imag		Real		Imag	
	Namba	Schulten	Namba	Schulten	Namba	Schulten	Namba	Schulten
$\mu=0$	-2.151E-04	-2.711E-04	-2.391E-04	-3.082E-04	1.063E-03	3.948E-03	1.310E-03	1.371E-03
$\mu=1$	-1.491E-05	-2.915E-05	3.802E-06	1.870E-05	8.336E-03	1.860E-02	1.009E-02	1.338E-02
$\mu=2$	5.645E-06	7.245E-06	1.242E-06	-1.626E-09	-1.471E-03	-2.266E-03	-7.834E-04	3.048E-04
$\mu=3$	7.557E-07	1.952E-06	5.352E-07	-1.631E-07	-4.147E-08	-1.947E-05	-1.607E-05	1.823E-07
$\mu=4$	-6.994E-09	1.789E-07	8.519E-08	-1.049E-09	2.238E-07	-2.077E-07	-3.766E-07	-1.231E-07
	Downstream Waves, $x=+2b$							
	$m=16$				$m=-8$			
	Real		Imag		Real		Imag	
	Namba	Schulten	Namba	Schulten	Namba	Schulten	Namba	Schulten
$\mu=0$	1.419E-04	3.216E-05	-1.141E-04	-1.743E-04	1.987E-03	4.907E-03	9.959E-03	8.607E-03
$\mu=1$	-3.118E-05	-3.213E-05	-1.251E-05	7.415E-06	-1.679E-02	-5.257E-03	2.178E-02	2.413E-02
$\mu=2$	1.238E-06	1.370E-06	-4.899E-07	-2.064E-06	-1.635E-03	-1.746E-03	-4.069E-04	8.727E-04
$\mu=3$	1.155E-06	1.267E-06	1.501E-07	-8.691E-07	-2.597E-05	-2.838E-05	-6.972E-06	1.425E-05
$\mu=4$	1.567E-07	1.764E-07	2.462E-08	-1.140E-07	-4.218E-07	-4.800E-07	-9.487E-08	2.750E-07

Table 2.7 Full Annulus $q=1.5$, $M_T=0.783$

	Upstream Waves, $x=-b$							
	$m=16$				$m=-8$			
	Real		Imag		Real		Imag	
	Namba	Schulten	Namba	Schulten	Namba	Schulten	Namba	Schulten
$\mu=0$	2.151E-04	3.234E-04	1.990E-04	1.278E-04	-3.762E-03	-4.124E-03	-2.203E-04	2.379E-03
$\mu=1$	1.652E-06	-1.293E-05	-1.816E-05	-2.847E-05	-8.479E-03	-1.073E-02	-3.723E-03	5.808E-03
$\mu=2$	1.008E-06	2.192E-06	5.194E-06	6.159E-06	3.715E-04	-6.205E-04	-1.112E-03	-1.650E-03
$\mu=3$	7.308E-08	7.286E-07	-5.011E-07	4.380E-07	1.778E-05	2.586E-06	2.463E-05	8.658E-06
$\mu=4$	-2.661E-07	-1.646E-07	-1.873E-07	-3.530E-08	1.840E-06	1.473E-06	2.679E-07	-7.326E-08
	Downstream Waves, $x=+2b$							
	$m=16$				$m=-8$			
	Real		Imag		Real		Imag	
	Namba	Schulten	Namba	Schulten	Namba	Schulten	Namba	Schulten
$\mu=0$	7.441E-05	1.402E-04	1.266E-04	2.861E-05	-1.104E-03	-1.276E-03	-4.053E-03	-1.952E-03
$\mu=1$	1.771E-06	-1.460E-05	-2.379E-05	-2.232E-05	-1.290E-02	-1.342E-02	-1.786E-03	7.195E-03
$\mu=2$	-4.071E-07	9.430E-07	1.695E-06	1.643E-06	2.264E-04	-8.604E-04	-1.431E-03	-1.384E-03
$\mu=3$	-1.939E-07	6.728E-07	1.080E-06	1.071E-06	4.634E-06	-1.351E-05	-2.161E-05	-2.156E-05
$\mu=4$	-2.658E-08	9.155E-08	1.431E-07	1.454E-07	8.860E-08	-2.293E-07	-3.754E-07	-3.841E-07

Table 2.8 Full Annulus $q=2.0$, $M_T=0.783$

	Upstream Waves, $x=-b$							
	$m=16$				$m=-8$			
	Real		Imag		Real		Imag	
	Namba	Schulten	Namba	Schulten	Namba	Schulten	Namba	Schulten
$\mu=0$	-1.655E-04	-1.630E-04	-5.795E-05	-3.128E-05	8.854E-04	8.971E-04	-9.089E-05	-2.980E-04
$\mu=1$	7.105E-06	6.334E-06	-1.076E-06	-3.142E-06	4.251E-03	3.284E-03	-2.294E-03	-1.984E-03
$\mu=2$	-2.101E-06	-1.869E-06	9.234E-07	1.126E-06	-1.020E-06	-4.847E-05	-1.195E-04	-2.211E-04
$\mu=3$	1.139E-06	1.113E-06	5.017E-07	5.386E-07	-2.845E-05	-2.699E-05	9.511E-06	8.071E-06
$\mu=4$	1.707E-07	1.548E-07	-3.971E-07	-3.633E-07	4.429E-07	4.618E-07	2.714E-06	2.503E-06
	Downstream Waves, $x=+2b$							
	$m=16$				$m=-8$			
	Real		Imag		Real		Imag	
	Namba	Schulten	Namba	Schulten	Namba	Schulten	Namba	Schulten
$\mu=0$	-9.715E-06	-6.093E-06	-1.819E-05	-8.570E-06	1.026E-03	1.317E-03	3.203E-03	2.805E-03
$\mu=1$	-8.477E-07	-2.302E-06	-3.636E-06	-4.420E-06	-4.846E-03	-5.003E-03	3.659E-03	4.453E-03
$\mu=2$	-6.190E-07	-5.247E-07	-2.135E-07	-1.204E-07	1.139E-04	3.086E-05	-7.585E-05	-1.458E-04
$\mu=3$	-1.372E-07	-8.094E-08	-6.714E-10	5.737E-08	5.670E-07	-5.327E-07	-3.561E-07	-1.646E-06
$\mu=4$	-1.550E-08	-7.661E-09	-5.687E-10	8.106E-09	3.488E-08	1.104E-08	1.259E-08	-1.193E-08

Table 2.9 Full Annulus q =2.5, M_T =0.783

	Upstream Waves, $x=-b$							
	m =16				m =-8			
	Real		Imag		Real		Imag	
	Namba	Schulten	Namba	Schulten	Namba	Schulten	Namba	Schulten
$\mu=0$	1.120E-04	1.587E-04	8.099E-05	5.307E-05	-2.015E-03	-2.228E-03	2.092E-05	1.137E-03
$\mu=1$	2.381E-06	-2.963E-06	-3.944E-06	-8.550E-06	-2.597E-03	-3.704E-03	-1.874E-03	1.704E-03
$\mu=2$	3.718E-07	7.788E-07	3.257E-07	8.292E-07	1.562E-04	-2.159E-04	-4.155E-04	-6.501E-04
$\mu=3$	-3.968E-07	-1.115E-07	4.161E-07	7.756E-07	6.050E-07	-5.117E-06	-5.274E-06	-1.060E-05
$\mu=4$	2.676E-07	2.871E-07	9.914E-09	5.259E-08	-1.620E-06	-1.612E-06	9.243E-07	8.243E-07
	Downstream Waves, $x=+2b$							
	m =16				m =-8			
	Real		Imag		Real		Imag	
	Namba	Schulten	Namba	Schulten	Namba	Schulten	Namba	Schulten
$\mu=0$	3.383E-05	6.089E-05	4.788E-05	9.554E-06	-4.152E-04	-5.593E-04	-2.263E-03	-1.433E-03
$\mu=1$	6.928E-07	-5.671E-06	-9.390E-06	-9.323E-06	-5.606E-03	-6.059E-03	-4.126E-04	3.095E-03
$\mu=2$	-2.515E-07	2.610E-07	5.447E-07	5.622E-07	1.079E-04	-3.089E-04	-5.412E-04	-5.530E-04
$\mu=3$	-9.519E-08	2.353E-07	4.061E-07	4.230E-07	1.625E-06	-5.251E-06	-8.799E-06	-9.154E-06
$\mu=4$	-1.124E-08	3.304E-08	5.430E-08	5.849E-08	2.289E-08	-9.597E-08	-1.397E-07	-1.539E-07

Table 2.10 Full Annulus q =3.0, M_T =0.783

	Upstream Waves, $x=-b$							
	m =16				m =-8			
	Real		Imag		Real		Imag	
	Namba	Schulten	Namba	Schulten	Namba	Schulten	Namba	Schulten
$\mu=0$	-9.928E-05	-1.031E-04	-3.509E-05	-1.889E-05	5.764E-04	6.058E-04	-9.392E-05	-2.580E-04
$\mu=1$	3.082E-06	2.825E-06	-3.724E-07	-1.612E-06	2.669E-03	2.213E-03	-1.441E-03	-1.365E-03
$\mu=2$	-4.728E-07	-3.774E-07	6.002E-07	7.317E-07	-9.207E-06	-3.803E-05	-6.399E-05	-1.247E-04
$\mu=3$	3.721E-07	3.761E-07	-2.232E-08	1.822E-08	-1.089E-05	-1.089E-05	3.008E-06	2.595E-06
$\mu=4$	4.869E-08	5.559E-08	1.652E-08	1.860E-08	-4.233E-07	-4.470E-07	1.647E-07	1.683E-07
	Downstream Waves, $x=+2b$							
	m =16				m =-8			
	Real		Imag		Real		Imag	
	Namba	Schulten	Namba	Schulten	Namba	Schulten	Namba	Schulten
$\mu=0$	-5.613E-06	-3.755E-06	-1.069E-05	-4.942E-06	6.404E-04	8.712E-04	1.947E-03	1.768E-03
$\mu=1$	-5.973E-07	-1.508E-06	-2.136E-06	-2.709E-06	-2.955E-03	-3.133E-03	2.274E-03	2.865E-03
$\mu=2$	-3.657E-07	-3.265E-07	-1.472E-07	-9.456E-08	6.815E-05	2.212E-05	-4.114E-05	-8.419E-05
$\mu=3$	-8.694E-08	-5.794E-08	-3.965E-09	3.026E-08	5.958E-07	-7.943E-09	-3.561E-07	-1.068E-06
$\mu=4$	-9.828E-09	-6.417E-09	9.234E-11	4.465E-09	1.807E-08	8.769E-09	-1.317E-09	-1.267E-08

Table 3. Comparison of lift coefficient between 3D cascade (narrow annulus)
at mid span and corresponding 2D cascade.

	3D (Narrow annulus)		2D	
MT	Real	Imag	Real	Imag
0.3897	-2.263E-01	1.825E-01	-2.336E-01	1.971E-01
0.4330	-4.209E-02	1.064E-01	-4.030E-02	1.039E-01
0.4763	1.273E-02	1.453E-01	1.816E-02	1.413E-01
0.6495	8.959E-02	1.806E-01	9.709E-02	1.586E-01

Figures
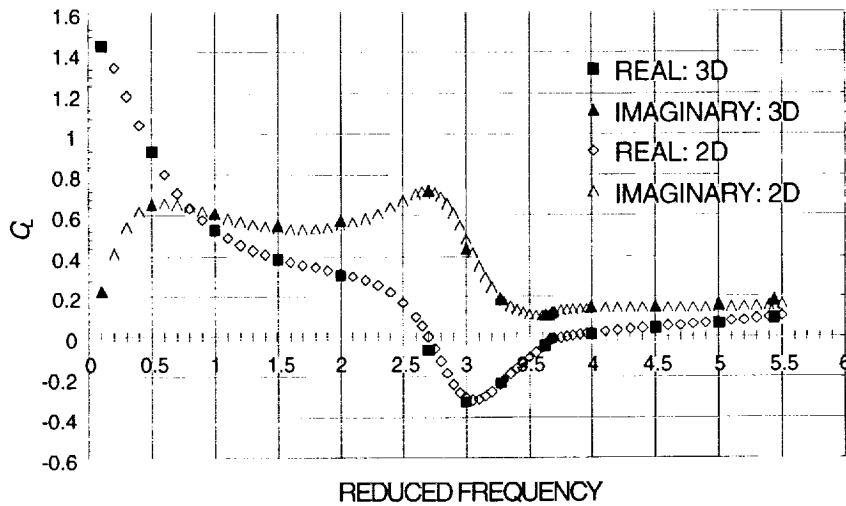
Figure 1 Comparison of lift coefficient between 3D cascade (narrow annulus) at mid span and corresponding 2D cascade. Reduced frequency $=(2\_B/V)(M_T/M)$
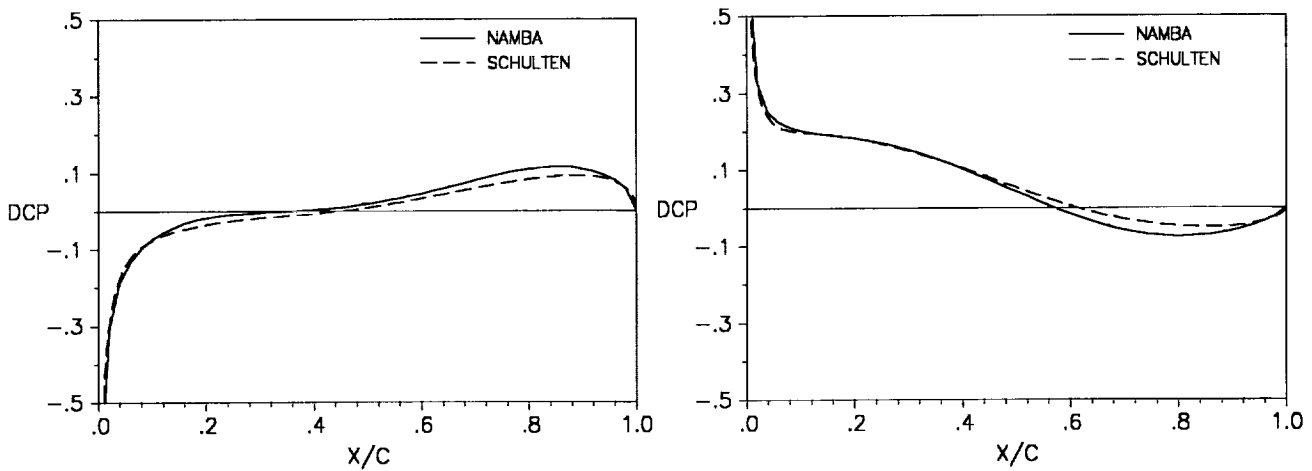
Figure 2 Real (left) and imaginary part of midspan ΔC_p, full annulus, $q = 0$, $M_T = 0.783$.
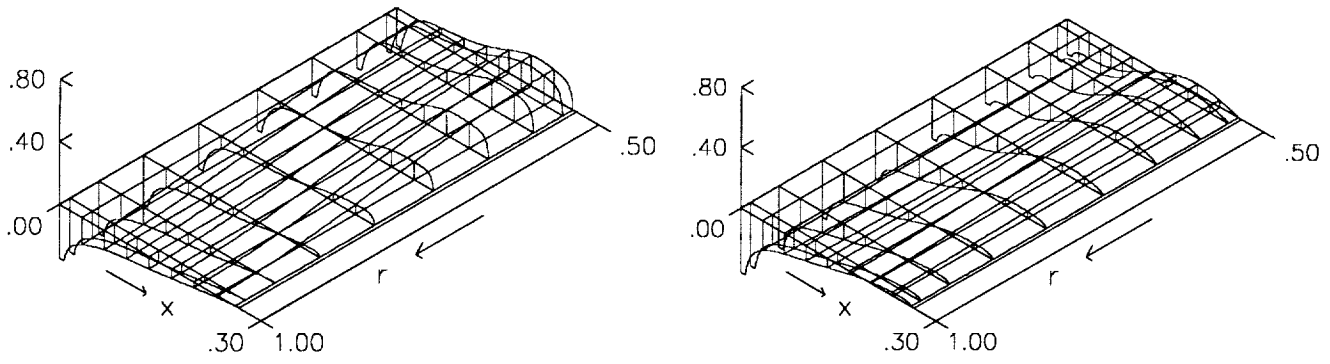
Figure 3 Real (left) and imaginary parts of ΔC_p, $q = 0.0$, $M_T = 0.783$
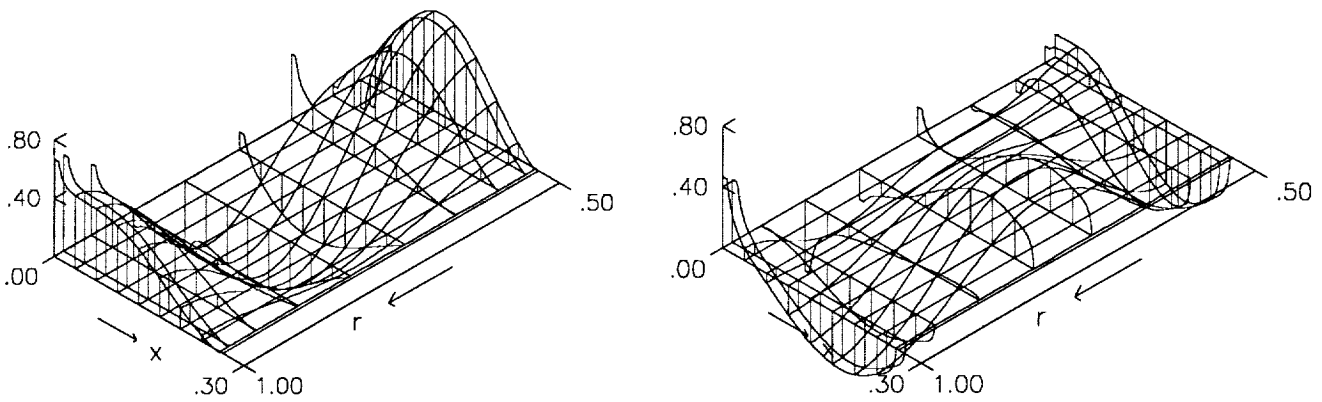
Figure 4   Real (left) and imaginary parts of ΔC_p, $q = 1.5$, $M_T = 0.783$
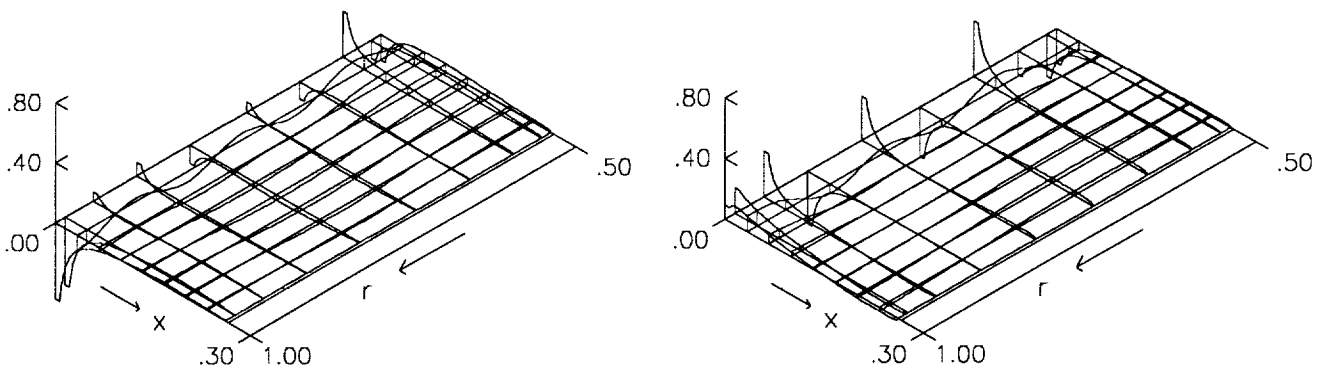
Figure 5   Real (left) and imaginary parts of ΔC_p, $q = 3.0$, $M_T = 0.783$
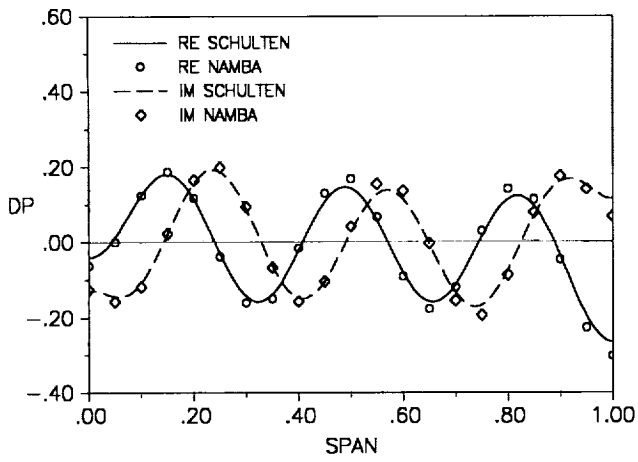
Figure 6 ΔC_p along x/c = 0.06, q = 3.0, M_T = 0.783
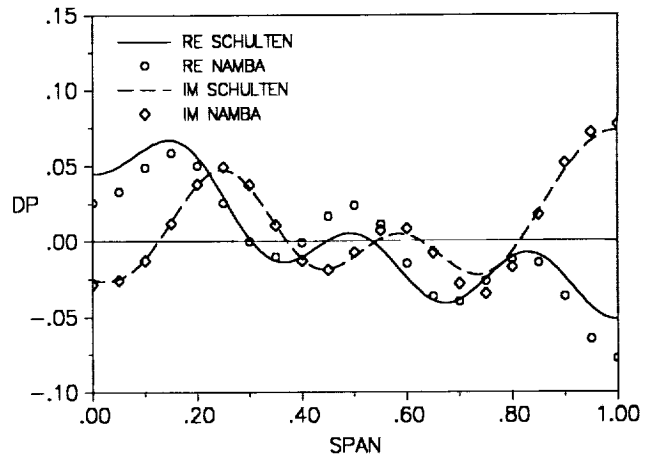
Figure 7 ΔC_p, along x/c = 0.2, q=3.0, M_T = 0.783
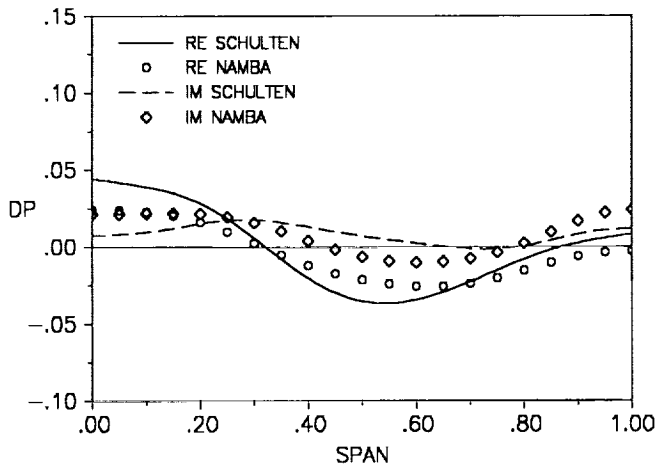
Figure 8 ΔC_p along x/c = 0.5, q = 3.0, M_T = 0.783
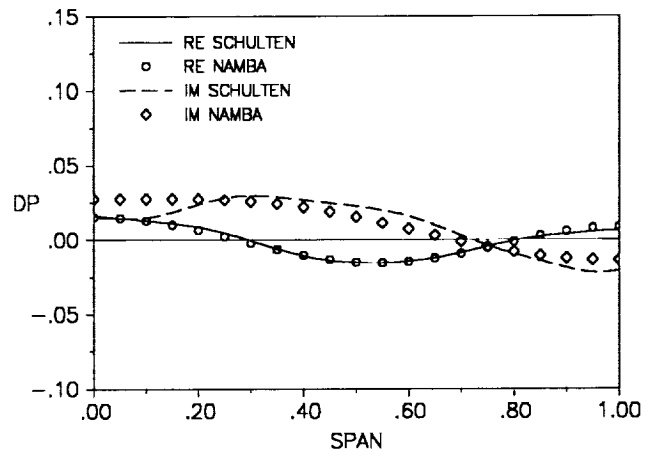
Figure 9 ΔC_p along x/c = 0.9, q = 3.0, M_T = 0.783

SOLUTION TO THE CATEGORY 5 PROBLEM:
GENERATION AND RADIATION OF ACOUSTIC WAVES FROM A 2D SHEAR LAYER

MILO D. DAHL
NASA Glenn Research Center
Cleveland, OH

A thin free shear layer containing an inflection point in the mean velocity profile is inherently unstable. Disturbances in the flow field can excite the unstable behavior of a shear layer, if the appropriate combination of frequencies and shear layer thicknesses exists, causing instability waves to grow. For other combinations of frequencies and thicknesses, these instability waves remain neutral in amplitude or decay in the downstream direction. A growing instability wave radiates noise when its phase velocity becomes supersonic relative to the ambient speed of sound. This occurs primarily when the mean jet flow velocity is supersonic. Thus, the small disturbances in the flow, which themselves may generate noise, have generated an additional noise source. It is the purpose of this problem to test the ability of CAA to compute this additional source of noise.

The problem is idealized such that the exciting disturbance is a fixed known acoustic source pulsating at a single frequency. The source is placed inside of a 2D jet with parallel flow; hence, the shear layer thickness is constant. With the source amplitude small enough, the problem is governed by the following set of linear equations given in dimensional form.

$$\frac{\partial \rho'}{\partial t} + U(y)\frac{\partial \rho'}{\partial x} + \rho(y)\frac{\partial u'}{\partial x} + \rho(y)\frac{\partial v'}{\partial y} + v'\frac{\partial \rho(y)}{\partial y} = 0 \tag{1}$$

$$\frac{\partial u'}{\partial t} + U(y)\frac{\partial u'}{\partial x} + v'\frac{\partial U(y)}{\partial y} = -\frac{1}{\rho(y)}\frac{\partial p'}{\partial x} \tag{2}$$

$$\frac{\partial v'}{\partial t} + U(y)\frac{\partial v'}{\partial x} = -\frac{1}{\rho(y)}\frac{\partial p'}{\partial y} \tag{3}$$

$$\frac{\partial p'}{\partial t} + U(y)\frac{\partial p'}{\partial x} + \gamma P\frac{\partial u'}{\partial x} + \gamma P\frac{\partial v'}{\partial y} = A\exp\left[-B\ln 2\left(x^2 + y^2\right)\right]\cos(\omega t) \tag{4}$$

We begin the analysis to solve for the pressure disturbances by nondimensionalizing the above set of equations. The physical coordinates are scaled by the half-velocity distance $R_{1/2}$. The velocity is scaled by the jet velocity U_j, the density by ρ_j, the pressure by $\rho_j U_j^2$, and the time and frequency by $R_{1/2}/U_j$. The equations are then combined into a single, nondimensional, third-order, inhomogeneous differential equation.

$$\left(\frac{\partial}{\partial t} + \bar{u}\frac{\partial}{\partial x}\right)^3 p - \frac{1}{\bar{\rho}M_j^2}\left[\left(\frac{\partial}{\partial t} + \bar{u}\frac{\partial}{\partial x}\right)\left(\frac{\partial^2 p}{\partial x^2} + \frac{\partial^2 p}{\partial y^2}\right) - \frac{1}{\bar{\rho}}\frac{\partial\bar{\rho}}{\partial y}\left(\frac{\partial}{\partial t} + \bar{u}\frac{\partial}{\partial x}\right)\frac{\partial p}{\partial y}\right.$$
$$\left. - 2\frac{\partial\bar{u}}{\partial y}\frac{\partial^2 p}{\partial x\partial y}\right] = \left(\frac{\partial}{\partial t} + \bar{u}\frac{\partial}{\partial x}\right)^2 S(x,y,t) \tag{5}$$

If the source term in equation (5) is defined as

$$S(x,y,t) = A^* e^{-B^*\ln 2(x^2+y^2)} e^{-i\omega t}, \tag{6}$$

where $A^* = AR_{1/2}/\rho_j U_j^3$ and $B^* = BR_{1/2}^2$, then the solution to equation (5) is given by the real part of the complex disturbance pressure p. (Note that the real part of equation (6) is the source term in equation (4).) The approach that follows constructs an integral equation using a Green's function that solves for p in equation (5).

Assume that the solution is harmonic with the source term. After differentiating with respect to time and dividing through by $e^{-i\omega t}$, equation (5) becomes

$$\left(-i\omega + \bar{u}\frac{\partial}{\partial x}\right)^3 p - \frac{1}{\bar{\rho} M_j^2}\left[\left(-i\omega + \bar{u}\frac{\partial}{\partial x}\right)\left(\frac{\partial^2 p}{\partial x^2} + \frac{\partial^2 p}{\partial y^2}\right) - \frac{1}{\bar{\rho}}\frac{\partial \bar{\rho}}{\partial y}\left(-i\omega + \bar{u}\frac{\partial}{\partial x}\right)\frac{\partial p}{\partial y}\right.$$
$$\left. - 2\frac{\partial \bar{u}}{\partial y}\frac{\partial^2 p}{\partial x \partial y}\right] = \left(-i\omega + \bar{u}\frac{\partial}{\partial x}\right)S_1(x,y) \tag{7}$$

where

$$S_1(x,y) = (-i\omega - 2B'x\bar{u}(y))A^* e^{-B'x^2} e^{-B'y^2} \tag{8}$$

and $B' = B^* \ln 2$.

Defining the Fourier transform of the x variable as

$$\tilde{p}(k,y) = \frac{1}{2\pi}\int_{-\infty}^{\infty} p(x,y)e^{-ikx}dx, \tag{9}$$

the transform is applied to equation (7) and the results rearranged to obtain

$$\frac{\partial}{\partial y}\left[\frac{1}{\bar{\rho} M_j^2(\omega - \bar{u}k)^2}\frac{\partial \tilde{p}}{\partial y}\right] + \tilde{p} - \frac{k^2}{\bar{\rho} M_j^2(\omega - \bar{u}k)^2}\tilde{p} = -\frac{\tilde{S}_1(k,y)}{(\omega - \bar{u}k)^2}. \tag{10}$$

Equation (10) has the form of a Sturm-Liouville equation.

$$\frac{\partial}{\partial y}\left[a\frac{\partial \tilde{p}}{\partial y}\right] + b\tilde{p} - \lambda c\tilde{p} = f(k,y) \tag{11}$$

The solution of this equation is expressed as the integral

$$\tilde{p}(k,y) = \int_0^{\infty} f(k,y_o)\tilde{G}(k,y;y_o)dy_o \tag{12}$$

where $\tilde{G}(k,y;y_o)$ is the Green's function that solves

$$\frac{\partial}{\partial y}\left[a\frac{\partial \tilde{G}}{\partial y}\right] + b\tilde{G} - \lambda c\tilde{G} = \delta(y - y_o) \tag{13}$$

subject to the same boundary conditions as apply to $\tilde{p}$ in equation (11). These conditions are symmetry at $y = 0$ and outgoing waves as $y \rightarrow \infty$.

The Green's function derived from equation (13) has the form

$$\tilde{G}(k,y;y_o) = \frac{A_o(k,y_o)}{\Delta(k,y_o)}[\zeta_2(k,y_o)\zeta_1(k,y)H(y_o - y) + \zeta_1(k,y_o)\zeta_2(k,y)H(y - y_o)] \tag{14}$$

88

where

$$\Delta(k, y_o) = \zeta_1(k, y_o) \frac{\partial \zeta_2(k, y_o)}{\partial y} - \zeta_2(k, y_o) \frac{\partial \zeta_1(k, y_o)}{\partial y}$$

$$= \Delta_o(k)\bar{\rho}(y_o)(\omega - \bar{u}(y_o)k)^2, \tag{15}$$

$$A_o(k, y_o) = \bar{\rho}(y_o)M_j^2(\omega - \bar{u}(y_o)k)^2, \tag{16}$$

and H is the step function defined as

$$H(z) = \begin{cases} 1, & z > 0 \\ \frac{1}{2}, & z = 0 \\ 0, & z < 0. \end{cases}$$

From the boundary condition at $y = 0$, $\partial \zeta_1/\partial y = 0$ and as $y \to \infty$, $\zeta_2 \to \exp(i\nu y)$ where $\nu = \sqrt{k_\infty^2 - k^2}$ and $k_\infty^2 = \bar{\rho}_\infty M_j^2 \omega^2$. The branch cuts associated with ν are chosen such that $-\pi/2 < \arg(\nu) < \pi/2$ to insure outgoing waves.

It is now a matter of substituting both $f(k, y_o)$ and $\tilde{G}(k, y; y_o)$ into equation (12) and applying the inverse Fourier transform

$$p(x, y) = \int_{-\infty}^{\infty} \bar{p}(k, y)e^{ikx}dk \tag{17}$$

to get the general integral solution for the disturbance pressure

$$p_g(x, y) = \frac{iA^*M_j^2}{2\pi}\sqrt{\frac{\pi}{B'}}$$

$$\times \left[\int_{-\infty}^{\infty} e^{-k^2/4B'}\zeta_1(k, y) \left\{ \int_{y}^{\infty} \bar{\rho}(y_o)(\omega - \bar{u}(y_o)k)\frac{\zeta_2(k, y_o)}{\Delta(k, y_o)}e^{-B'y_o^2}dy_o \right\} e^{ikx}dk \right.$$

$$\left. + \int_{-\infty}^{\infty} e^{-k^2/4B'}\zeta_2(k, y) \left\{ \int_{0}^{y} \bar{\rho}(y_o)(\omega - \bar{u}(y_o)k)\frac{\zeta_1(k, y_o)}{\Delta(k, y_o)}e^{-B'y_o^2}dy_o \right\} e^{ikx}dk \right]. \tag{18}$$

To obtain this equation, equation (8) was used to complete the integration in $f(k, y_o)$.

$$f(k, y_o) = -\frac{\tilde{S}_1(k, y_o)}{(\omega - \bar{u}(y_o)k)^2}$$

$$= -\frac{1}{2\pi(\omega - \bar{u}(y_o)k)^2} \int_{-\infty}^{\infty} S_1(x_o, y_o)e^{-ikx_o}dx_o$$

$$= -\frac{iA^*}{2\pi(\omega - \bar{u}(y_o)k)}\sqrt{\frac{\pi}{B'}}e^{-B'y_o^2}e^{-k^2/4B'} \tag{19}$$

One major goal of this problem is to compute the pressure disturbance generated by a growing instability wave excited in the shear layer by the acoustic source. The instability wave comes from the homogeneous solution to equation (10). Hence, we have an eigenvalue problem where a nonzero solution exists at k equal to the eigenvalue α and $\bar{p}$ has the form of the eigenfunction ζ. In the limit as $k \to \alpha$, both ζ_1 and $\zeta_2 \to \zeta$

giving the result in equation (15) that $\Delta(k, y_o) = \Delta_o(k) = 0$ for all y_o. Thus, a simple pole exists at $k = \alpha$ in equation (18) and the solution for the inverse Fourier transform can be determined by residue theory. The instability wave solution for the pressure disturbance is

$$
p_\alpha(x, y) = A^* M_j^2 \sqrt{\frac{\pi}{B'}}
$$

$$
\times \ e^{-\alpha^2/4B'} \zeta(\alpha, y) \left\{ \int_0^\infty \bar{\rho}(y_o)(\omega - \bar{u}(y_o)\alpha) \frac{\zeta(\alpha, y_o)}{\partial\Delta(\alpha, y_o)/\partial y} e^{-B'y_o^2} dy_o \right\} e^{i\alpha x} \qquad (20)
$$

The total solution for the pressure disturbance with a growing instability wave is the sum of $p_g(x, y)$ and $p_\alpha(x, y)$ given by equations (18) and (20). Outside of the jet, this represents the pressure disturbances generated by the instability wave and the disturbances that are generated directly by the source and propagate outward through the jet flow. If the pressure was to be computed in the far field, then the inverse Fourier transform in equation (18) could be found by using asymptotic methods. But the solution is desired close to the jet flow, hence the integrals must be computed numerically.

Solution for St = 0.14

The path of integration to numerically solve for the inverse Fourier transform in equation (18) is shown in Figure 1. The horizontal path slightly deviates from the real axis to avoid the branch cuts and insure that the outgoing wave boundary conditions are satisfied. In addition, this path also attempts to avoid the real axis where $\omega - \bar{u}(y_o)k = 0$. The vertical portion of the path is traversed twice in opposite directions resulting in no contribution from the integration along this section of the path. Thus, the total solution is the sum of the numerical integration of equation (18) along the horizontal path plus the residue solution at $k = \alpha$ given by equation (20).

The problem statement asked for the computed pressure disturbance in the x-direction at $y/R_{1/2} = 1$. As of the workshop, the method of numerically integrating equation (18) has not been proven to converge to a reliable solution. Hence, Figure 2 shows only the growing instability wave solution. The eigenvalue for this instability wave is $\alpha = 0.61489 - i0.067236$.

Outside of the jet, the numerical integration converged to a consistent solution. The computed mean square pressures are shown in Figure 3 in the x-direction at $y/R_{1/2} = 10$ and in the y-direction at $x/R_{1/2} = 50$.

Solution for St = 0.60

At a Strouhal number of 0.60, the flow conditions and the shear layer width do not support a growing instability wave. Thus, only equation (18) is used to compute the pressure disturbance outside of the jet and only the horizontal path of integration is followed in Figure 1. The result for the mean square pressure are shown in Figure 4.

References

Jones, D. S., 1977, "The Scattering of Sound by a Simple Shear Layer," *Phil. Trans. R. Soc. Lond.*, vol. A284, pp. 287–328.

Tam, C. K. W., 1978, "Excitation of Instability Waves in a Two-Dimensional Shear Layer by Sound," *J. Fluid Mech.*, vol. 89, pp. 357–371.
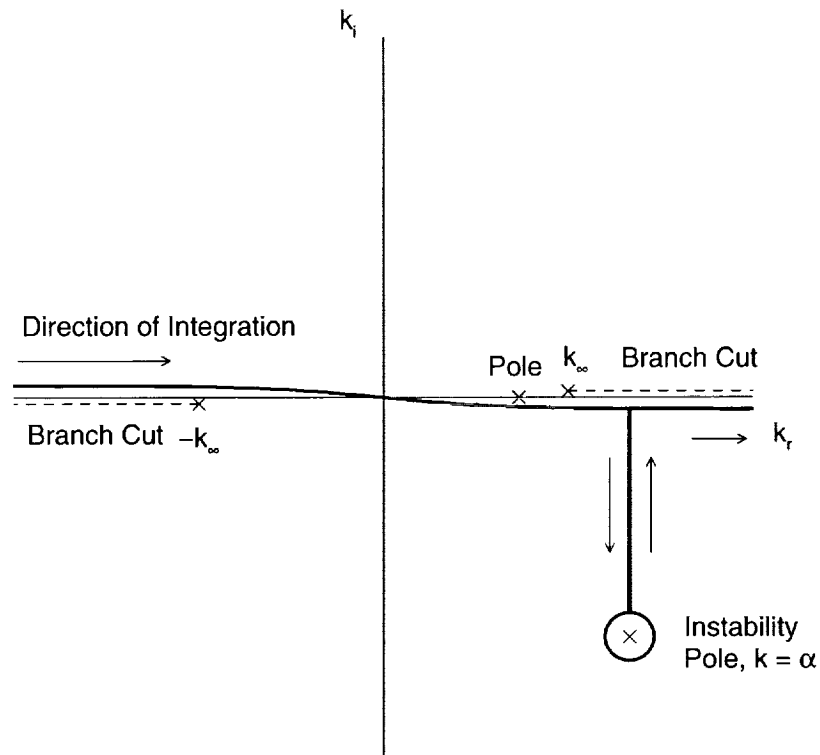
Figure 1: Path of integration in the k-plane for computing the inverse Fourier transform.
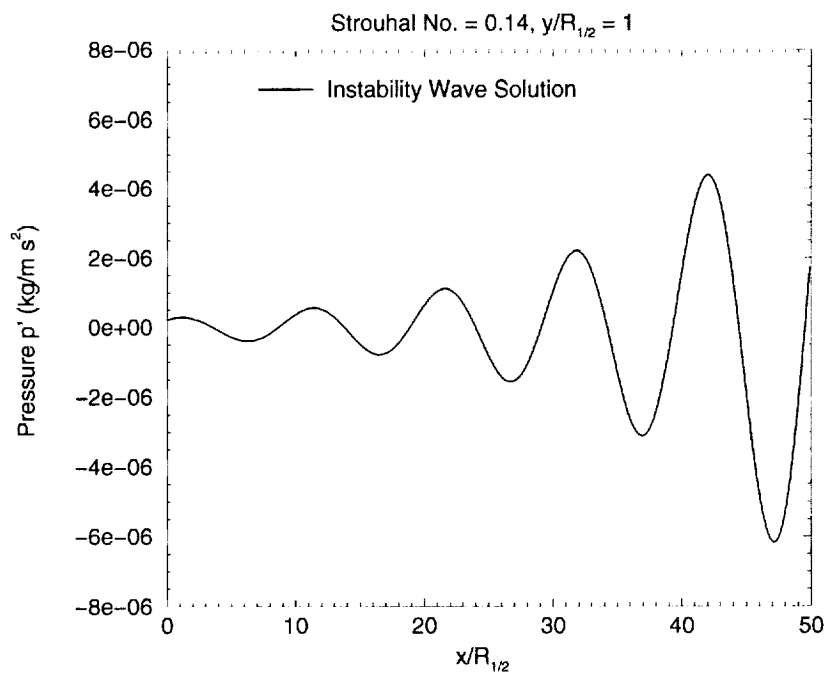
Figure 2: The instability wave solution $\mathrm{Re}\{p_\alpha(x,y)\}$ at $y = 1$.
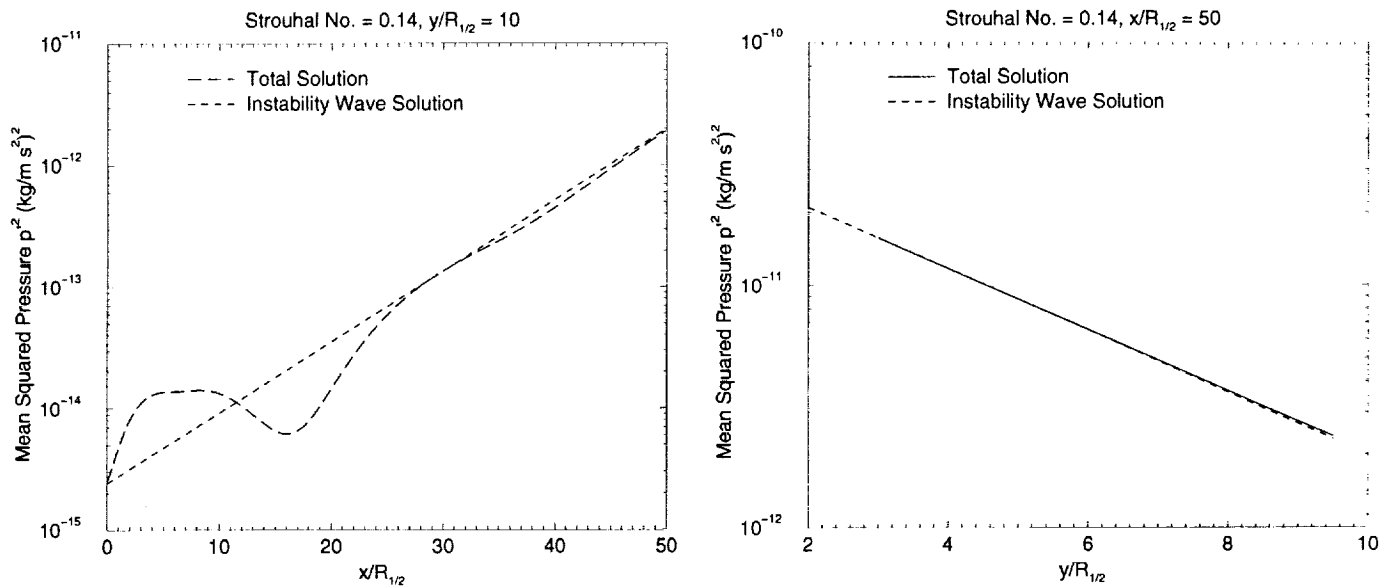
Figure 3: Mean square disturbance pressure outside of the jet at $St = 0.14$ with growing instability wave.
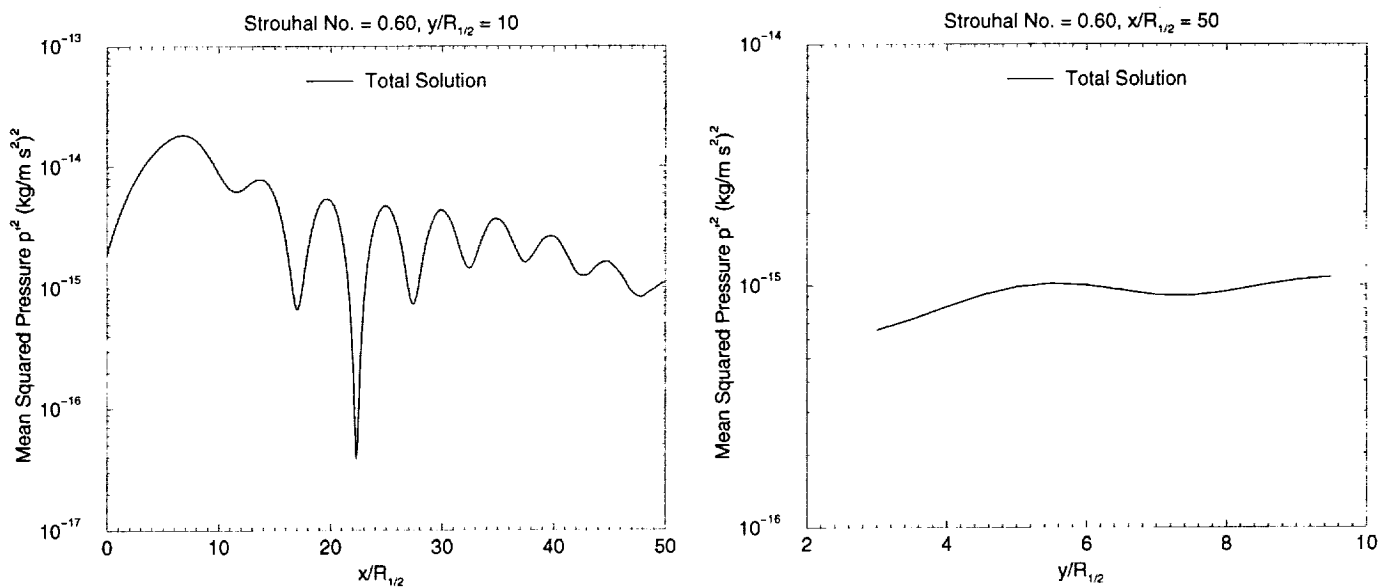
Figure 4: Mean square disturbance pressure outside of the jet at $St = 0.60$, acoustic source only.

Experimental Results

CATEGORY 6
AUTOMOBILE NOISE INVOLVING FEEDBACK -
SOUND GENERATION BY LOW SPEED CAVITY FLOWS

BRENDA HENDERSON
Kettering University
Mechanical Engineering Department
Flint, MI

Abstract

The category 6 problem involves the calculation of interior sound pressure levels produced by the flow of low speed air over a deep cavity. The cavity geometry is similar to the one occurring in vehicle door gaps. The velocity of the approach flow ranges between 26.8 m/s and 50.9 m/s. In this study, experimental data is obtained for comparison with numerical results. Multiple discrete frequencies occur for a range of approach flow velocities and for both "thick" and "thin" boundary layers. These tones appear to be associated with both fluid dynamic and fluid resonant oscillations.

Introduction

The discrete frequency sound produced by the flow of air over cavities is part of a feedback loop. The oscillating shear layer crosses the cavity mouth, impinges on the trailing edge of the cavity, and causes an oscillating mass flow rate in the region of the cavity mouth. Sound is produced by the interaction of the shear layer with the trailing edge wall or by the oscillating mass flow rate in the cavity mouth region. The sound feeds back to the cavity entrance and excites the oscillations of the shear layer, thus closing the feedback loop.

The oscillations occurring in cavity flows can be categorized as fluid-dynamic, fluid-resonant, or fluid-elastic[1]. Fluid-dynamic oscillations arise from the instability of the shear layer in the cavity mouth. Fluid-resonant oscillations are the result of, or are enhanced by, resonant waves within the cavity. Depending on the cavity geometry, either longitudinal waves (waves traveling between the leading edge and trailing edge walls) or transverse waves (waves traveling between the cavity floor and mouth) can be excited[1]. Fluid elastic resonance occurs when fluid resonance is enhanced by oscillations of the cavity surfaces.

The type of fluid resonant behavior displayed by cavity flows depends on the cavity geometry (see Fig. 1). Shallow cavities, cavities with depth to length ratios less than one (D/L < 1), can produce longitudinal waves. These cavities often produce flow that separates from the leading edge, and reattaches at the base of the cavity[2,3,4]. Deep cavities, cavities with a depth to length ratio greater than one (D/L > 1), can produce transverse waves[3]. For the case of steady flow in deep cavities, the separated flow no longer reattaches to the cavity floor and a general vortex system exists in the cavity[2].

A number of models exist for predicting the frequency of discrete tones in cavity flows[1,4,5,6]. The agreement between experimental data and predictions based on these equations depends on the speed of the approach flow. Some experiments also indicate that the frequency of tones can be somewhat dependent on boundary layer thickness[7].

The benchmark problem for category 6 is the numerical simulation of flow for a deep cavity with an overhang at the cavity entrance. The numerical results are to be compared to experimental results obtained in this study.

Problem Statement

The geometry used for the category 6 problem is shown in Fig. 2. The boundary layer is turbulent with a boundary thickness of 1.6 cm at an approach velocity of 26.8 m/s, and 2.2 cm at an approach velocity of 50.9 m/s. A one-seventh power-law velocity profile may be used for simplicity. Compare numerical results for sound pressure level values at the center of the left wall with experimental values for approach flow velocities between 26.5 and 50.9 m/s.

Experiment

The cavity studies were conducted in a recirculating wind tunnel with an 18"x18"x48" test section. The tunnel is equipped with silencers before and after the fan to reduce sound pressure levels in the flow.

For the experiments in this investigation, the top surface of the wind tunnel test section was replaced with a cavity assembly containing the cavity shown in Fig. 2. The width of the cavity was 25 cm. Two 1/4" type TMS140BP and TMS140BF G.R.A.S. condenser microphones were mounted flush with the left wall. The signals from the microphones were analyzed on an HP 35670A dynamic signal analyzer. A flat top window was used for the FFT analysis.

Prior to acquiring the sound-pressure level data, a boundary layer study was conducted with a hot-wire anemometer. Based on the results obtained, two streamwise locations in the test section were chosen for the cavity experiments to determine the effect of boundary thickness on the onset of instability. The boundary layer thickness at the first location was 2mm at 30 m/s, and 1.2 cm at 50 m/s. For the second location, the boundary-layer thickness was 2 mm at 30 m/s, and 1.2 cm at 50 m/s. The boundary layer values at the second location were close to those given in the problem statement. It was not possible to obtain the exact boundary layer thickness prescribed in the problem statement without artificially increasing the roughness of the tunnel surfaces. These two studies are referred to as "thick" and "thin" boundary layer studies in the following sections.

Results

The sound pressure levels associated with the thin and thick boundary layer studies are shown in Figs. 3 and 4. As often occurs for cavities with entrance overhangs[8,9], multiple discrete tones are observed in the spectra. The number of discrete tones produced by the cavity flow depends on the flow speed and the boundary layer thickness. One tone is often associated with fluid-dynamic oscillations while other tones are likely the result of resonance within the cavity. In addition to the expected transverse waves in the cavity, an additional type of tone occurs that does not appear to be related to fluid-dynamic oscillations, expected frequencies for transverse waves, or expected frequencies for longitudinal waves[8]. These tones may be the result of longitudinal wave motion restricted to the cavity mouth region or other cavity modes that are unique to this type of cavity geometry.

The discrete frequencies for the spectra of Figs. 3 and 4 are shown in Tables 1 and 2. The tones have been categorized by resonance mode. Fluid-dynamic tones and transverse wave frequencies have been identified by comparison with other published data and analytical results. Correlation studies were not performed in this investigation.

For the tones associated with fluid-dynamic resonance, the convection speed of the disturbances in the cavity mouth were determined using a simple hydrodynamic model resulting in[5]

$$f_n b = c\left(n - \frac{1}{4} - \frac{\phi}{2\pi}\right),$$

where f is the measured frequency of sound, n is the mode number, b is the length of the cavity mouth, ϕ is a phase angle which accounts for the possibility of a phase shift between the interaction of the disturbance with the edge and the response of the shear layer to the encounter, and c is the convection speed of the

disturbances in the cavity mouth. For low speed flows, good agreement between this equation and experimental values is obtained when $\phi = 0$. The values for c in Table 1 and 2 range from approximately 43% to 50% of the mean stream velocity. The theoretical value for the convection speed of the disturbances is 50% of the mean stream velocity but experimental values are usually slightly lower. This is an indication that these tones are likely the result of fluid-dynamic oscillations. The slightly higher value for c associated with the thick boundary layer and an approach flow velocity of 40 m/s is probably due to breadth of the peak around 1760 Hz. For the thin boundary layer at the same speed, a double peak occurred in the spectrum with frequencies that were quite close together. The broad peak for the thick boundary layer may have masked the double peak and resulted in slightly higher calculated convection speed.

The peaks associated with transverse waves have been identified by comparison with published data[3]. The critical dimensionless numbers for this type of tone are $\dfrac{f_{wave}D}{a}$ and $\dfrac{D}{L}$, where f_{wave} is the frequency of the discrete tone, D is the cavity depth, and L is the cavity length. Good agreement between these experiments and other published data is obtained when the cavity mouth opening is used for L.

One additional consideration should be made when directly comparing numerical results to experimental results. When multiple tones occur in the spectrum, the preferred or dominant mode often changes randomly. This can result in a change of 3 dB or more in the peak sound pressure levels.

It is possible to determine some of the effects of boundary layer thickness on the production of discrete tones by comparing Figs. 3 and 4 as well as Tables 1 and 2. For the thin boundary layer study, well defined discrete frequencies occur consistently for approach flow velocities greater than or equal to 30 m/s. For the thick boundary layer study, well defined discrete frequencies do not appear consistently until the approach flow velocity reaches 35 m/s. The magnitude of the discrete peaks and the shape of the spectra are also somewhat affected by the thickness of the boundary layer.

Conclusions

Multiple discrete frequency tones often occur for cavities with overhangs at the mouth entrance. The tones can be associated with fluid-dynamic resonance and transverse modes within the cavity. An additional discrete frequency tone has been identified and may be the result of other cavity modes unique to this cavity geometry.

The thickness of the boundary layer at the cavity entrance influences the onset of instability. Thinner boundary layers produce resonance at lower approach flow velocities than thick boundary layers. The peak sound pressure level and the shape of the spectra are also somewhat affected by boundary layer thickness.

References

1. Rockwell, D., and Naudasher, E.: Review – Self-sustaining Oscillations of Flow Past cavities, Transactions of ASME, 1978, pp. 152 – 165.
2. Roshko, A.: Some measurements of the Flow in a Rectangular Cutout, NACA NAW-6296, 1954.
3. Morse, P., and Shieh, C.: Parallel Numerical Simulation of Subsonic Cavity Noise, AIAA paper 99-1891, 1999.
4. Rossiter, J.E.: Wind Tunnel Experiments on the Flow Over Rectangular Cavities at Subsonic and Transonic Speeds, Aeronautical Research Council Reports and Memorandum No. 3438, 1966.
5. Blake, W.: *Mechanics of Flow Induced Sound and Vibration*, Vol.1., Academic Press, New York, 1986, pp. 138 – 141.
6. Block, P.: Noise Response of Cavities of Varying Dimensions at Subsonic Speeds, NASA TN D-8351, 1976.

7. DeMetz, F.C., and Farabee, T.M.: Laminar and Turbulent Shear Flow Induced Cavity Resonances, AIAA paper 771293, 1977.

8. Henderson, B., and Navaz, H.: A numerical and Experimental Investigation into the Effects of Cavity Geometry on the Production of Cavity Tones," Joint Meeting for the 137th Meeting of the Acoustical Society of America and the 2nd European Acoustics Association, 1999.

9. Mongaue, L., Bezemek, J., and Danforth, R.: "Pressure Fluctuations in a Flow-excited Door Gap Cavity Model," SAE paper 971923, 1997.
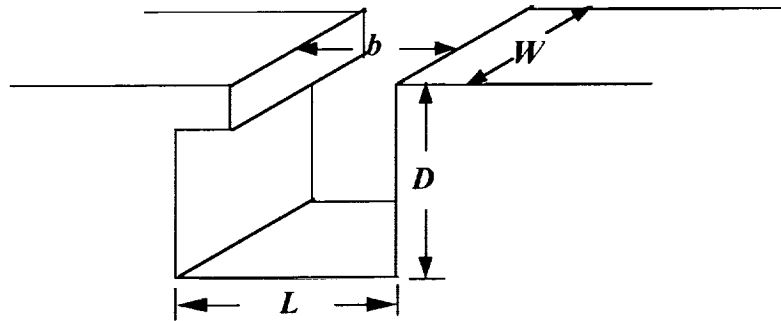
Figure 1. General cavity dimensions.
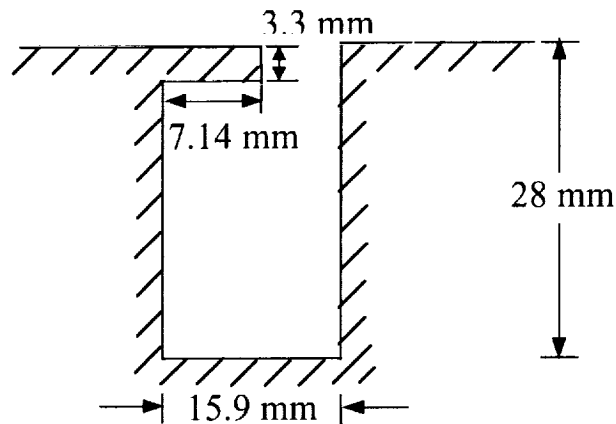
Figure 2. Cavity geometry used for the category 6 problem.
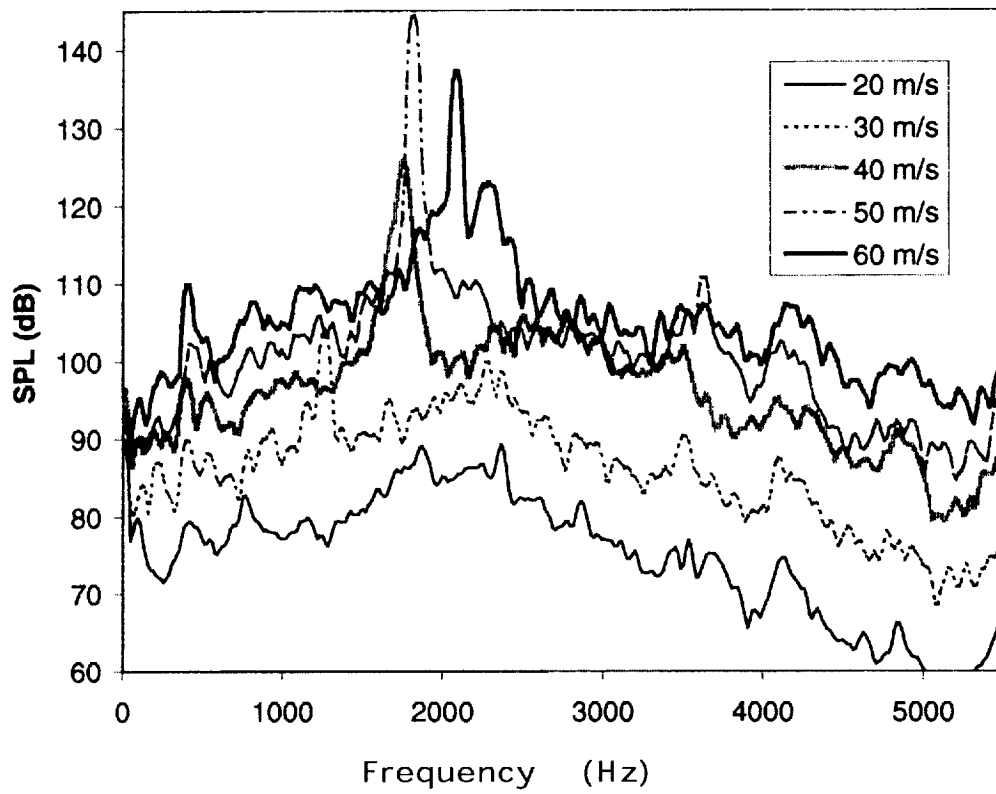
Figure 3. Sound pressure level data for the thin boundary layer study.
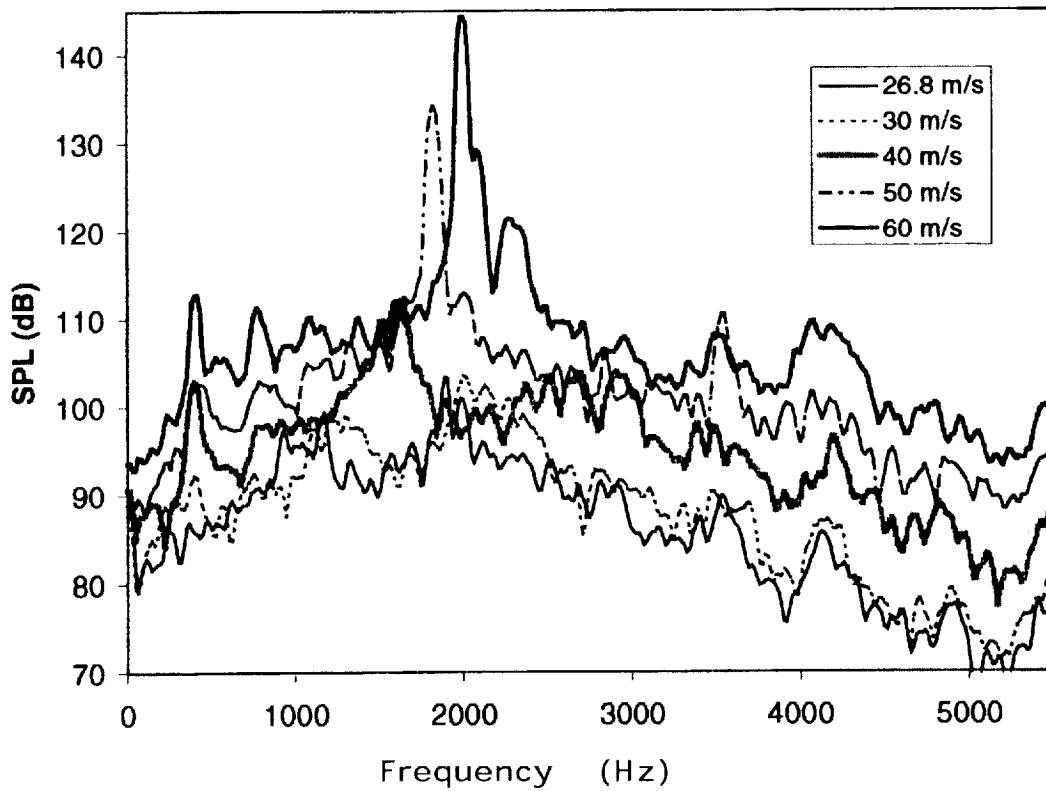
Figure 4. Sound pressure level data for the thick boundary layer study.

Table 1. Peak sound-pressure levels measured for the thin boundary-layer studies. Bold numbers are associated with fluid-dynamic resonance and italic numbers are associated with transverse cavity waves. The origin of the other tones is unknown.

Approach Velocity (U_o) (m/s)	Frequency (Hz)	Amplitude (dB)	Convection Speed (u) $\left(u/U_o\right)$
60	*2096*	*137*	
	2288	**123**	**0.45 U_o**
50	**1824**	**144**	**0.43 U_o**
	3648	**111**	
40	**1760**	**126**	**0.52U_o**
30	**1264**	**105**	**0.49 U_o**
	1664	95	
	3520	90	
20	**768**	**83**	**0.45 U_o**
	1872	89	
	2368	89	
	2864	82	

Table 2. Peak sound-pressure levels measured for the thick boundary-layer studies. Bold numbers are associated with fluid-dynamic resonance and italic numbers are associated with transverse cavity waves. The origin of the other tones is unknown.

Approach Velocity (U_o) (m/s)	Frequency (Hz)	Amplitude (dB)	Convection Speed (u) $\left(u/U_o\right)$
60	*2000*	*144*	
	2288	**121**	**0.45 U_o**
50	**1824**	**134**	**0.43 U_o**
	2016	*113*	
	2848	106	
	3552	111	
40	**1520**	**110**	**0.44 U_o**
	1632	**112**	**or 0.48 U_o**
	400	103	
30	No well defined peaks		
26.8	928	97	
	1168	**99**	**0.51 U_o**
	1890	103	
	1984	*101*	

Contributions of
Workshop Participants

DISCONTINUOUS SPECTRAL ELEMENT SOLUTION OF AEROACOUSTIC PROBLEMS

Patrick Rasetarinera, DAVID A. KOPRIVA[1] and M.Y. Hussaini[1]

Program in Computational Science and Engineering
The Florida State University, Tallahassee, FL 32306

1 Introduction

In this paper, we present solutions to the Problem 1, Category 1 and Problem 1, Category 3 benchmark problems. Both problems are characterized by multiple length scales. The first describes the propagation of acoustic waves in a nearly choked quasi-one-dimensional, converging-diverging nozzle. In the throat portion of the nozzle the acoustic wavelengths are an order of magnitude smaller than elsewhere. The second problem models the acoustic response of an airfoil to a gust where the scales include the airfoil cord length, the incident gust wavelength and the extent of the mean flow.

We solve these multiple scale problems with a discontinuous spectral element method (DSEM). Spectral element methods in general are high order, flexible extensions of the spectral collocation method [2]. Like finite volume or finite element methods, complex geometries are subdivided into multiple elements. Within each element, the solution is approximated by an orthogonal polynomial expansion. Local resolution of the solution can be increased either by decreasing the size of the elements or by increasing the order of the polynomials. The particular method used here is a high order spectral element version of the discontinuous Galerkin method.

For the benchmark problems, discontinuous spectral element methods have practical advantages over high order finite difference methods. They are designed to handle complex geometries, and can use unstructured element grids generated by commercial mesh generation codes [4]. Though block structured finite difference methods permit solutions in complex geometries, DSEM's are not restricted to meshes with smooth metrics. Also, DSEM's approximate boundary surfaces to the same high order as the solution. Cartesian mesh finite difference methods, for instance, do not.

Unlike high order finite difference methods, spectral element methods are compact. Their stencil resides within an element, independent of the approximation order. This means that there are no ghost point issues to complicate the approximation and implementation of boundary conditions. Also, elements can be sized according to the needs of the solution without regard to the size of neighboring elements.

---

[1]Also Department of Mathematics and SCRI.

This gives complete flexibility for changing element sizes, unlike high order finite difference methods for which changes in mesh sizes by factors of two are most convenient.

Spectral element methods are robust. Unlike centered finite difference methods, they do not require the addition of specially tuned artificial dissipation. Also, the discontinuous spectral element method described here does not require special treatment of corner points. This means that special programming is not needed for complex grid topologies or for sharp edges.

Finally, spectral element methods have spectrally small phase and dissipation errors. Waves can propagate over a large number of wavelengths with a minimal number of points per wavelength while keeping the flexibility described above. Examples can be found in the first and second CAA workshop papers [5],[1]. An analysis of the phase and dissipation errors of the discontinuous Galerkin method has also been performed recently in [3],[8]. In the first paper it was shown that for polynomial orders of six to eight, only five to six points per wavelength are needed. If one uses polynomial orders between 8 and 16, only four to five points per wavelength are needed.

2 The Solution Approach

2.1 The Equations

To solve the benchmark problems, we approximate the nonlinear compressible Euler equations of gasdynamics in conservative form. For the Category 3 problem, the equations solved are

$$Q_t + \nabla \cdot \mathbf{F} = Q_t + F_x + G_y = S \tag{1}$$

Explicitly, we have

$$Q = \begin{bmatrix} \rho \\ \rho u \\ \rho v \\ \rho e \end{bmatrix} \quad F = \begin{bmatrix} \rho u \\ p + \rho u^2 \\ \rho u v \\ u(\rho e + p) \end{bmatrix} \quad G = \begin{bmatrix} \rho v \\ \rho u v \\ p + \rho v^2 \\ v(\rho e + p) \end{bmatrix}$$

We assume an ideal gas with $\rho e = p/(\gamma - 1) + (u^2 + v^2)/2$ and $\gamma = 1.4$. The quantity S right hand side of (1) represents a source term.

In the one space dimension Category 1 problem, eq. (1) reduces to

$$Q_t + F_x = S \tag{2}$$

where

$$Q = \begin{bmatrix} \rho A \\ \rho u A \\ \rho e A \end{bmatrix} \quad F = \begin{bmatrix} \rho u A \\ (\rho u^2 + p) A \\ u(\rho e + p) A \end{bmatrix} \quad S = \begin{bmatrix} 0 \\ -p A_x \\ 0 \end{bmatrix}$$

2.2 The Discontinuous Galerkin Spectral Element Method

In two space dimensions, the region under consideration is divided into non-overlapping elements. The elements can have a general quadrilateral shape to permit the accurate resolution of curved boundaries with a minimum number of elements. Each element is mapped individually onto the unit square by an isoparametric transformation. (See, e.g. [6].)

On each element, the mapping transforms eq. (1) to

$$\tilde{Q}_t + \nabla_\xi \cdot \tilde{\mathbf{F}} = \tilde{Q}_t + \tilde{F}_\xi + \tilde{G}_\eta = \tilde{S} \tag{3}$$

The new variables are $\tilde{Q} = JQ$, $\tilde{S} = JS$ and

$$\tilde{F} = y_\eta F - x_\eta G \quad \tilde{G} = -y_\xi F + x_\xi G$$

$$J(X,Y) = x_\xi y_\eta - x_\eta y_\xi \tag{4}$$

The discontinuous Galerkin version of the spectral element method approximates the solution and the fluxes by the Nth order polynomials

$$\tilde{\mathbf{Q}}\left(\xi, \eta\right) = \sum_{\mu,\nu=0}^{N} \tilde{\mathbf{Q}}_{\mu,\nu} \phi_{\mu,\nu}, \quad \tilde{\mathbf{F}}\left(\xi, \eta\right) = \sum_{\mu,\nu=0}^{N} \tilde{\mathbf{F}}_{\mu,\nu} \phi_{\mu,\nu} \tag{5}$$

where $\phi_{\mu,\nu} = \ell_\mu\left(\xi\right)\ell_\nu\left(\eta\right)$. The Lagrange interpolating polynomials, ℓ_i, are defined at the Legendre Gauss quadrature points. The nodal values of the flux are computed from the nodal values of the solution, i.e. $\tilde{\mathbf{F}}_{i,j} = \tilde{\mathbf{F}}\left(\tilde{\mathbf{Q}}_{i,j}\right)$. No assumptions are made about the continuity of the solution, $\tilde{\mathbf{Q}}$, across element boundaries.

In this approximation, the residual is required to be orthogonal to the approximation space within an element, so

$$\left(\tilde{\mathbf{Q}}_t, \phi_{i,j}\right) + \left(\nabla_\xi \cdot \tilde{\mathbf{F}}, \phi_{i,j}\right) = \left(\tilde{\mathbf{S}}, \phi_{i,j}\right) \quad i, j = 0, 1, \ldots, N \tag{6}$$

where $(\cdot, \cdot)$ represents the usual L^2 inner product.

Integration of (6) by parts gives

$$\left(\tilde{\mathbf{Q}}_t, \phi_{i,j}\right) + \int_{\partial E} \phi_{i,j}\tilde{\mathbf{F}} \cdot \hat{N}dS - \left(\tilde{\mathbf{F}}, \nabla_\xi \phi_{i,j}\right) = \left(\tilde{\mathbf{S}}, \phi_{i,j}\right) \quad i, j = 0, 1, \ldots, N \tag{7}$$

where ∂E represents the boundary of the element.

To obtain equations for the nodal values of the solution, $\tilde{\mathbf{Q}}_{i,j}$, the integrals in (7) are replaced by Legendre-Gauss quadratures, which have the property that

$$\int_{-1}^{1} v\left(\xi, \eta\right)d\xi d\eta = \sum_{i,j=0}^{N} v\left(\xi_i, \eta_j\right) w_i w_j \quad \forall v \in P_{2N+1,2N+1} \tag{8}$$

The replacement is exact provided that the element sides are straight. If the sides are curved, however, an additional quadrature error is incurred, just as in the C^0 spectral element method [7]. The advantage gained by using quadrature is that the mass matrix remains diagonal and trivially invertable. This makes the use of high order elements practical and efficient for wave-propagation problems.

After some manipulation, the final approximation in two space dimensions is

$$\frac{d\tilde{Q}_{i,j}}{dt} + \left[\tilde{F}(1,\eta_j)\frac{\ell_i(1)}{w_i} - \tilde{F}(0,\eta_j)\frac{\ell_i(0)}{w_i} - \sum_\mu \tilde{F}_{\mu,j}\frac{(\ell_i',\ell_\mu)_N}{w_i}\right] + $$
$$\left[\tilde{G}(\xi_i,1)\frac{\ell_j(1)}{w_j} - \tilde{G}(\xi_i,0)\frac{\ell_j(0)}{w_j} - \sum_\mu \tilde{G}_{\mu,j}\frac{(\ell_j',\ell_\mu)_N}{w_j}\right] = \tilde{S}_{i,j} \tag{9}$$

where the discrete inner product is the Gauss quadrature

$$(u,v)_N = \sum_{i=0}^{N} u_i v_i w_i. \tag{10}$$

Note that if the approximating polynomial order is zero, (9) reduces to a first-order finite-volume method.

The flux quantities $F(1,\eta_j)$, $F(1,\eta_j)$, $G(\xi_i,1)$, $G(\xi_i,0)$, in (9) represent the element boundary fluxes. As in a finite volume approximation, the solutions are discontinuous at element faces. A Riemann solver is used to compute a continuous flux at the element faces from the discontinuous solution values. For the computations presented here, we have used Roe's approximate Riemann solver [9].

The semi-discrete approximation, (9), is integrated in time by a low storage Runge-Kutta method. Both third and fourth order methods are used.(Cf. [6])

2.3 Steady-State computation

For both the Category 1 and Category 3 problems, the steady solution is computed first. Once the steady solution is found, the incident waves are imposed as boundary conditions. The splitting permits the use of convergence acceleration techniques to get the steady-state. Here we use local time-stepping [4]. We estimate that on the Category 3 problem, the computation of the steady-state is accelerated by a factor of 30 using local time stepping.

2.4 Boundary Conditions

The use of the Riemann solver at element faces makes the imposition of boundary conditions simple. Boundary conditions are implemented by specifying the external state as the input for the Riemann solver [6].

In the two-dimensional problems, it is also necessary to implement radiation boundary conditions. In this paper, we treat the outgoing pressure waves through a damping-layer procedure, which is easy to

apply and inexpensive. The damping-layer approach sets the source term on the right of eq. (1) so that sound waves are damped in time as they propagate toward the outer boundaries. Only the radiating sound waves are damped, so the damping term is written as

$$S = \frac{\sigma}{\gamma - 1} \begin{bmatrix} 0 \\ 0 \\ 0 \\ p - p_{ss} \end{bmatrix} \tag{11}$$

where p_{ss} is the steady-state pressure. The quantity σ is a ramp function that grows smoothly from zero as the outer boundary is approached. We use two such ramp functions. The first increases the damping radially as

$$\sigma(r) = \beta \left(\frac{r - r_0}{r_{\max} - r_0} \right)^{\nu} \tag{12}$$

where r is the radial direction, measured from the center of the airfoil. The rate at which the ramp function increases, ν was chosen to be either one or two. The second ramp function replaced the radial direction with the boundary-normal direction within an element along the outer boundary. Using two different ramp functions and varying r_0 and R_{max} permitted us to assess any contamination of the solution by spurious reflected sound waves.

3   Solutions of the Workshop Problems

3.1   Category 1, Problem 1

Fig. 1 shows the distribution of the maximum acoustic pressure inside the nozzle. The solution was computed with two meshes. The coarse mesh used 16 elements at eighth order in each for a total of 144 collocation points. A fine mesh solution with 300 points is used for comparison. The inlet portion shows that there is only the transmitted wave, and that the wave amplitude is 5.47×10^{-6}. In the throat section, we find a peak amplitude of 1.03×10^{-4}. Finally, the exit section of the nozzle shows reflected and incident waves. The mean value of the coarse grid solution in the exit portion of the nozzle, which should be the incident wave amplitude, is within 0.4% of the exact.

At the top of Fig. 1 we show the distribution of the elements. The ability to adjust the element size according to the resolution needs of the problem is an important feature of the method. It permits the use of a minimum number of degrees of freedom to solve the problem accurately.

3.2   Category 3, Problem 1

For Category 3, Problem 1, we compute the unsteady aerodynamic and aeroacoustic response of a single airfoil to a two-dimensional, periodic vortical gust. In this problem, the incident gust propagates from infinity with the mean flow to the airfoil. At the airfoil surface, sound and vorticity are generated.
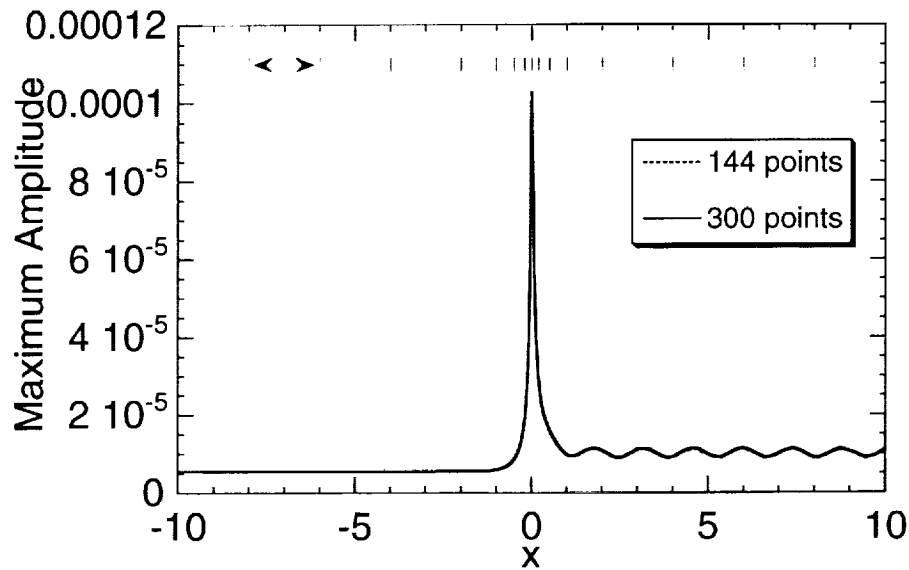
Figure 1: Maximum acoustic pressure amplitude for Category 1, Problem 1. Plotted are coarse and fine grid solutions. The element boundaries are marked at the top of the figure by vertical bars.

The sound propagates outward in all directions from the airfoil, while the vorticity propagates as a vortex street off the trailing edge of the airfoil. We solve this problem in the total-field formulation: We impose the gust as an external boundary condition and compute the time dependent flow as a periodic steady-state of the full nonlinear Euler equations.

Two important computational issues for this problem are the choice of mesh topology and the size of the mesh. First, the mean flow must be well-resolved in the neighborhood of the airfoil. Unlike a pure CFD calculation, however, it is also necessary to have uniform resolution in the far field with which to represent the incoming gust, the expanding sound wave and the vorticity advected downstream from the airfoil. These needs indicate that a grid formed by a conformal mapping would not be efficient, since the conformal grid will produce large elements in the far field. For this reason, we use unstructured grids. Figs. 2 and 3 show representative examples of meshes used about the airfoils.

The distance of the external boundaries from the airfoil also affects the solution. As in a CFD calculation, the outer boundary must be far enough away so that the surface pressure is not affected. An additional constraint is that the velocity in the external regions must be close enough to the uniform free-stream value so that the assumption of setting the gust at the outer boundary as a plane wave is accurate. For instance, we find that the mean flow velocity is within 2.5 % of the free-stream velocity at about 7.5 chord lengths from the non-lifting airfoil. For the lifting case, on the other hand, it is necessary to extend the mesh to 22.5 chord lengths in each direction to get a solution independent of the outer mesh distance.

Two independently written DSEM codes were used to compute the solutions presented here. Code 1 uses elements with straight sides except on the airfoil surface. It parameterizes the airfoil by polar angle θ, which gives better resolution in the neighborhood of the trailing edge. The damping layer in Code 1 has a ramping function that grows in the element normal direction. Code 2 has the ability to
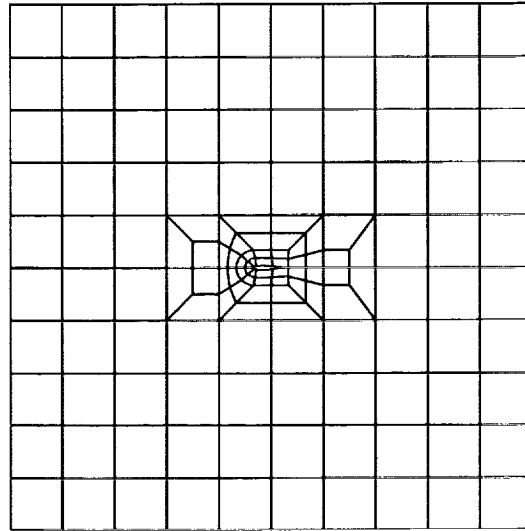
Figure 2: Mesh topology for the non-lifting airfoil
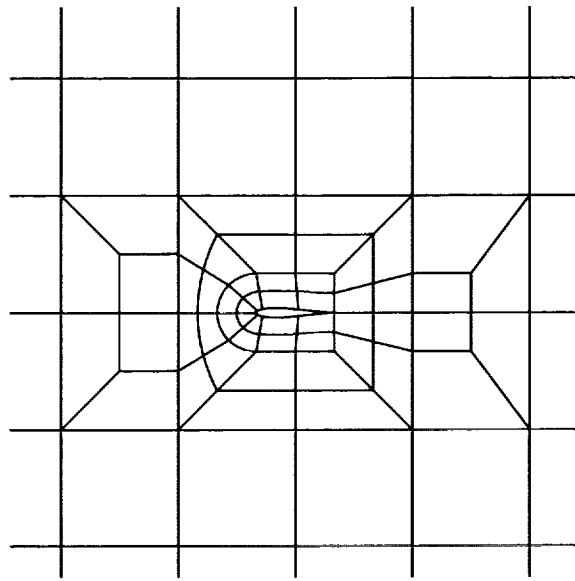
Figure 3: Closeup of a mesh in the neighborhood of the airfoil.

use curved element boundaries on all elements, as shown in Fig.3. It parameterizes the airfoil surfaces by arc length except near the leading edge, where polar angle θ is used. The damping layer in Code 2 is circular, as described in eq. (12). Both codes permit the use of variable order meshes so that the order of the approximating polynomials can be adjusted locally to provide the desired resolution. The use of the two codes permitted the assessment of the effects of the radiation boundary conditions, resolution along the airfoil surface and element shape.
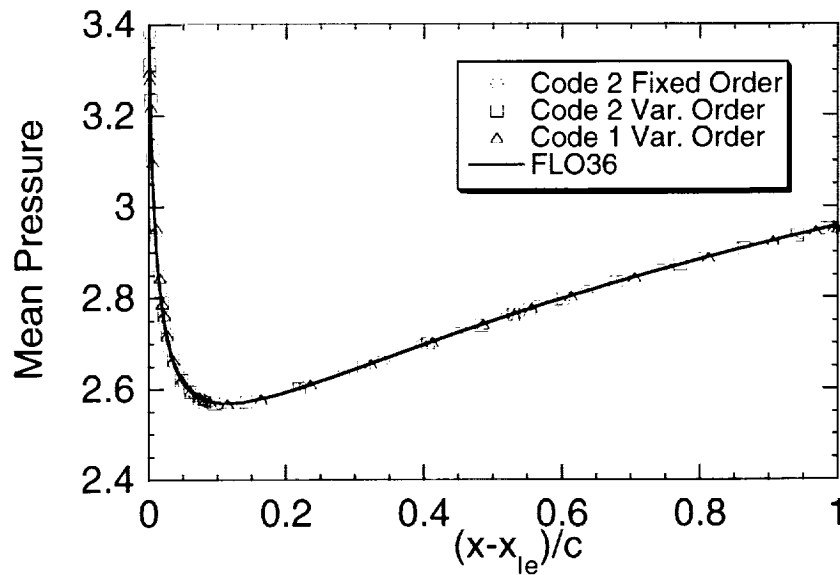
Figure 4: Steady surface pressure for the symmetric airfoil as a function of distance along the horizontal, scaled to the chord length.

3.2.1 Nonlifting Airfoil Solutions

The steady pressure on the surface of the symmetric airfoil is shown in Fig. 4. The grid used for these calculations extended 7.5 cord lengths from the airfoil. The fixed order computation used 11th order polynomials in all elements. The variable order computations used polynomials between six and 11, arranged to approximate a uniform eight points per wavelength of the incident gust. The fixed order calculation put 95 points along the airfoil surface. For the variable order cases, the Code 1 solution used 59 points and the Code 2 solution put 55 points along the surface. The computed solutions are compared to the FLO36 solution used in the workshop overview comparisons. Note particularly that the DSEM's have no problem approximating the solution near the sharp trailing edge of the airfoil.

We first show solutions to the nonlifting airfoil for wavenumber $k = 3$. The acoustic response along the surface is shown in Fig. 5. We find that the three solutions are consistent with each other except near the leading edge. There, the peak pressure is sensitive to the resolution. In particular, the three curves show that the lower the resolution, the lower the peak amplitude.

The computed acoustic intensity is shown in Fig. 6. Shown are the solutions corresponding to the three solutions in Figs. 4 and 5 plus an additional solution computed on a mesh that extended 11.5 chord lengths in each direction. The damping layer in the larger calculation extended three wavelengths beyond the others. The directivity patterns indicate that the radiation boundary conditions are not significantly affecting the solutions. The small difference in the peak values, with variation of 7 % or less, can be attributed to the difference in the peak values at the leading edge of the airfoil.

The Figures 4-6 show that the solutions, computed with different codes and different meshes give consistent results. It is interesting to note, however, the different computational costs between using the variable order and the fixed order meshes. For instance, Code 2 required 6.4 hours on an SGI
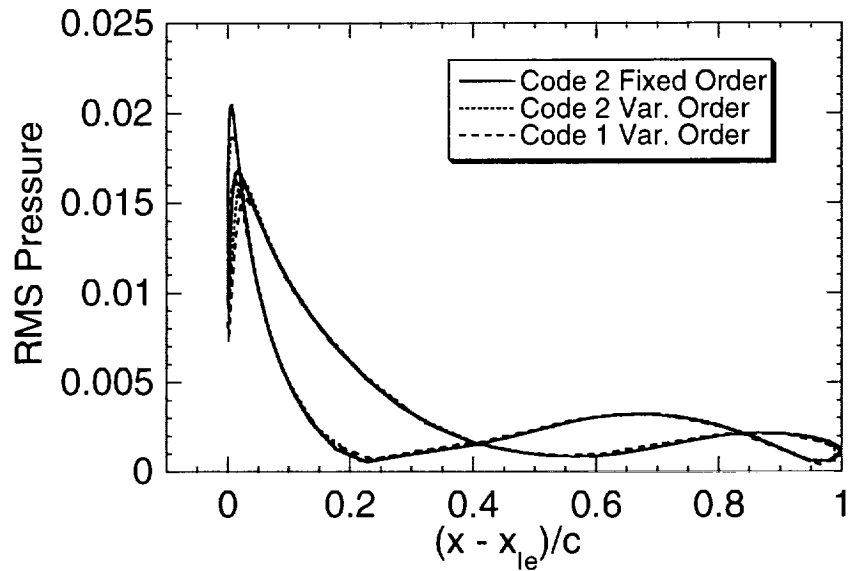
Figure 5: RMS surface pressure for the symmetric airfoil and gust wavenumber $k = 3$.
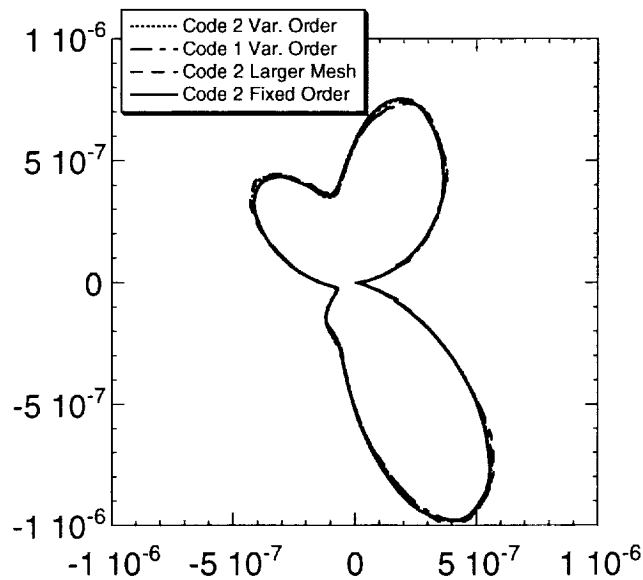
Figure 6: Acoustic intensity at radius eight for the symmetric airfoil and for gust wavenumber $k = 3$.

Origin 200 to compute both the steady and time dependent parts of the solution using the variable order mesh. The fixed order solution required 19 hours. The factor of three difference between the two can be attributed to the factor of three larger time step that could be used by the variable order approximation. The variable order approximation used lower order approximations in the smaller elements found in the neighborhood of the airfoil, thus permitting a larger timestep.

Finally, we present results for the $k = 1$ case. The RMS surface pressure is shown in Fig. 7. The acoustic intensity at four chord lengths is shown in Fig. 8. In both figures, we show solutions computed using the requested gust amplitude of $\epsilon = 0.02$ and an amplitude of $\epsilon = 0.002$ scaled to the amplitude
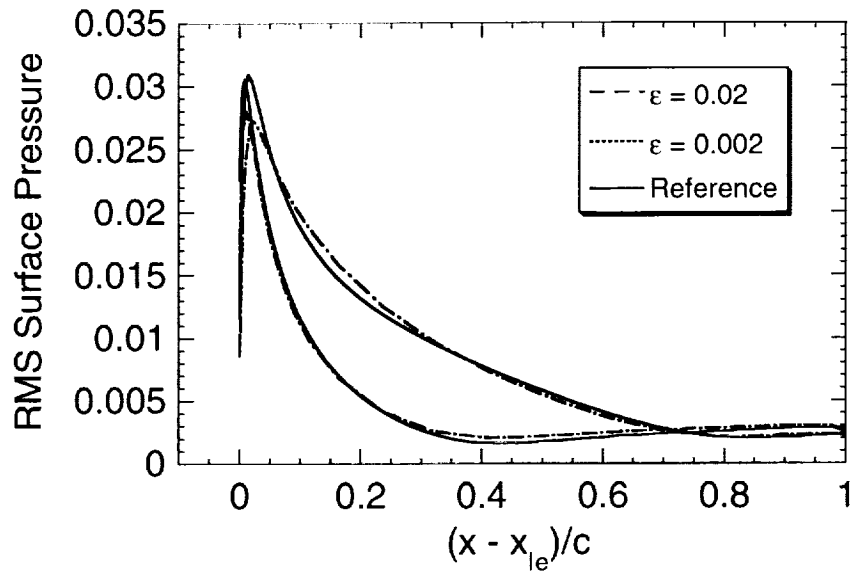
Figure 7: RMS surface pressure for the symmetric airfoil with gust wavenumber $k = 1$. Solutions shown for the requested gust amplitude and one tenth the requested amplitude scaled by ten. The reference solution is shown for comparison.
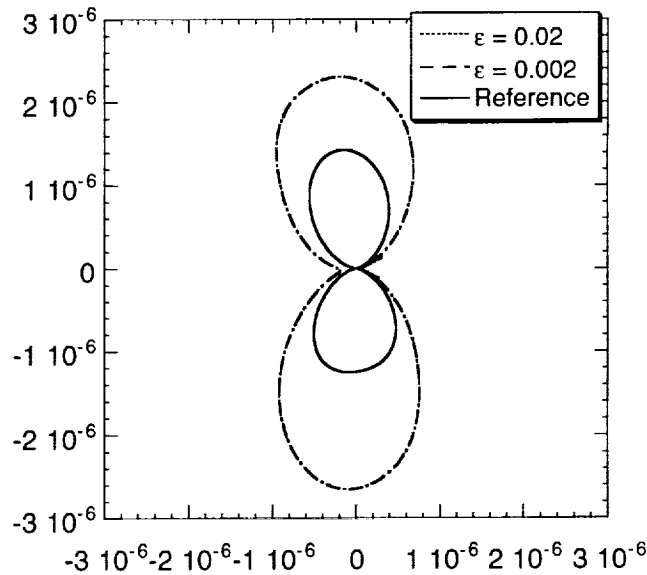
Figure 8: Acoustic intensity at radius eight for the symmetric airfoil with gust wavenumber $k = 1$. Solutions shown for the requested gust amplitude and one tenth the requested amplitude scaled by 100. The reference solution is shown for comparison.
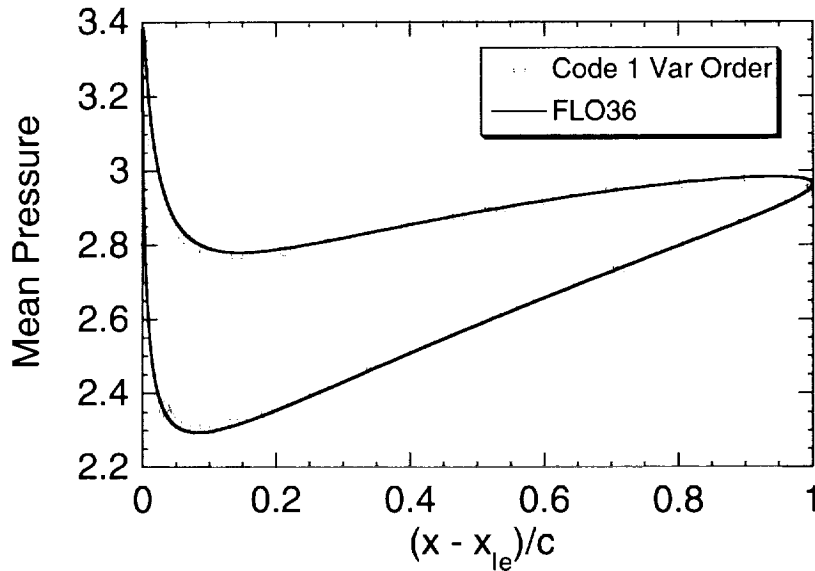
Figure 9: Steady surface pressure for the lifting airfoil as a function of distance along the horizontal, scaled to the chord length.

of the requested solution. Also included on each figure is the reference solution used in the workshop overview. There is a significant difference between the reference solution and the solutions computed here. The fact that the nonlinear computations at the two gust amplitudes match exactly indicates that the differences are not due to nonlinear effects.

3.2.2 Lifting Airfoil Solutions

Finally, we present solutions to the lifting airfoil case for wavenumber $k = 1$. Figs. 9-11 show the results compared to the reference solution. As above, the mean and RMS pressures along the airfoil surface are in good agreement with the reference solutions. Again, as before, there are significant differences in the acoustic intensity at a radius of four chord lengths.

4 Conclusions

In this paper, we have used two discontinuous spectral element codes to compute two of the acoustic workshop benchmark problems. Practical features of the method used are the ability to vary the mesh size and approximation order to resolve local solution features. The method is compact and robust, and does not need the addition of artificial damping in the presence of sharp edges.

For Category 1, Problem 1, solutions were obtained by using small elements in the neighborhood of the throat and larger ones away from the throat. This flexibility permitted an accurate solution with only 144 collocation points, when compared to a reference solution with 300 points.
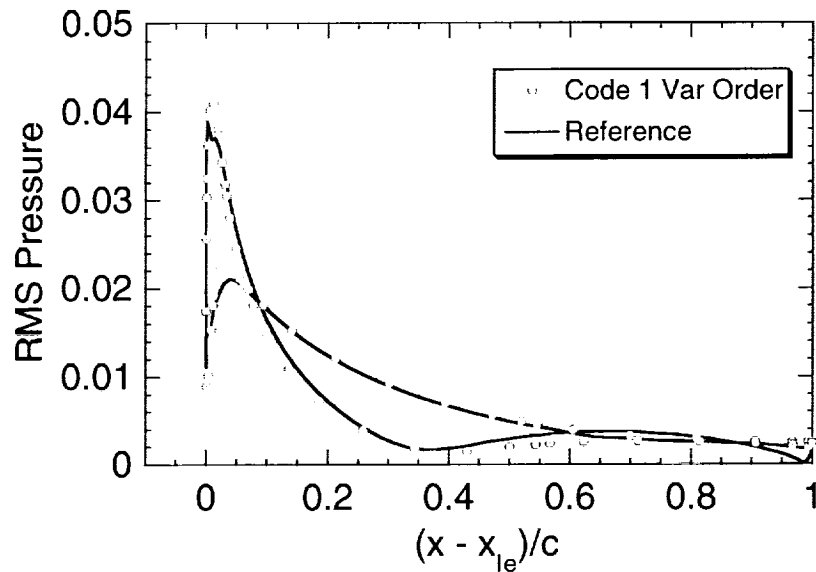
Figure 10: RMS surface pressure for the lifting airfoil with gust wavenumber $k = 1$.
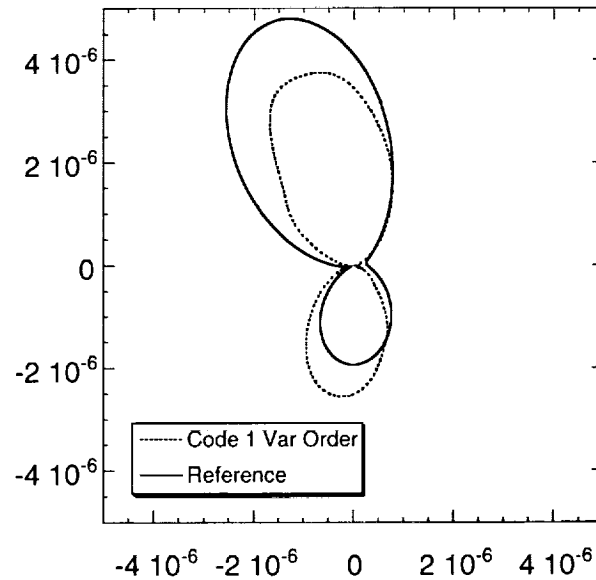
Figure 11: Acoustic intensity at radius eight for the lifting airfoil with gust wavenumber $k = 1$.

Category 3, Problem 1 solutions were computed for $k = 3$ and $k = 1$ for the non-lifting airfoil, and for $k = 1$ for the lifting case. Solutions using different meshes and damping layers were consistent with each other, as shown in the $k = 3$ non-lifting case. Surface quantities were in good agreement with the reference solutions for both airfoils at $k = 1$. The intensities at four chord lengths, however, differ significantly from the reference solution. This difference cannot be accounted for by nonlinear effects.

Acknowledgement

References

[1] P.J. Bismuti and D.A. Kopriva. Solution of acoustic scattering problems by a staggered-grid spectral domain decomposition method. In *Second Computational Aeroacoustics (CAA) Workshop on Benchmark Problems*, pages 69–78, 1997. NASA CP 3352.

[2] C. Canuto, M.Y. Hussaini, A. Quarteroni, and T.A. Zang. *Spectral Methods in Fluid Dynamics*. Springer-Verlag, New York, 1987.

[3] Fang Q. Hu, M.Y. Hussaini, and Patrick Rasetarinera. An analysis of the discontinuous Galerkin method for wave propagation problems. *J. Comp. Phys.*, 151:921–946, 1999.

[4] D.A. Kopriva. Euler computations on unstructured quadrilateral grids by a staggered-grid Chebyshev method. 1998. AIAA Paper 98-0132.

[5] David A. Kopriva and John H. Kolias. Solution of acoustic workshop problems by a spectral multi-domain method. In *ICASE/LARC Workshop on Benchmark Problems in Computational Aeroacoustics (CAA)*, pages 117–124, 1995. NASA CP 3300.

[6] David A. Kopriva and John H. Kolias. A conservative staggered-grid Chebyshev multidomain method for compressible flows. *J. Comp. Phys.*, 125:244–261, 1996.

[7] A.T. Patera. A spectral element method for fluid dynamics. *J. Comp. Phys.*, 54:468–488, 1984.

[8] Patrick Rasetarinera, M.Y. Hussaini, and Fang Q. Hu. Some remarks on the accuracy of the Discontinuous Galerkin Method. In B Cockburn, G. Karniadalkis, and C.-W. Shu, editors, *Proceedings of the International Symposium on Discontinuous Galerkin Methods*, New York, May 1999. Springer-Verlag.

[9] P.L. Roe. Approximate riemann solvers, parameter vectors, and difference schemes. *J. Comp. Phys.*, 43:357–372, 1981.

Validation of a High-Order Prefactored Compact Scheme on Nonlinear Flows With Complex Geometries

RAY HIXON and Reda R. Mankbadi
CAA Group, ICOMP
NASA Glenn Research Center
Cleveland, OH 44135

Abstract

Three benchmark problems are solved using a sixth-order prefactored compact scheme (ref. 1) employing an explicit 10th-order filter (ref. 2) with optimized fourth-order Runge-Kutta time stepping (ref. 3) . The problems solved are Category 1, Problems 1 and 2; and Category 3, Problem 1.

In the Category 1 problems, the spatial accuracy of the scheme is tested on a stretched grid, and the effectiveness of boundary conditions is shown. The solution stability and accuracy near a shock discontinuity is shown as well. Also, 1-D nonlinear characteristic boundary conditions will be evaluated. This work will follow the work in ref. 4.

In the Category 3 problem, a nonlinear Euler solver will be used that solves the equations in generalized curvilinear coordinates using the chain rule transformation. This work, continuing earlier work on flat-plate cascades (ref. 5) and Joukowski airfoils (ref. 6), will focus mainly on the effect of the grid and boundary conditions on the accuracy of the solution. The grids were generated using a commercially available grid generator, GridPro/az3000 (ref. 7).

1) Category 1 Problems

In Category 1, the problems are solved using the quasi-1-D Euler equations, given in the conserved variables as:

$$\left\{ \begin{array}{c} \rho \\ \rho u \\ E \end{array} \right\}_t + \left\{ \begin{array}{c} \rho u \\ \rho u^2 + p \\ u(E + p) \end{array} \right\}_x + \frac{1}{A}\frac{dA}{dx} \left\{ \begin{array}{c} \rho u \\ \rho u^2 \\ u(E + p) \end{array} \right\} = 0 \qquad (1)$$

The nozzle is the same for both problems, extending from -10<x<10 with the distribution:

$$A(x) = \begin{cases} 0.536572 - 0.198086 e^{-(\ln 2)(x/0.6)^2} & x > 0 \\ 1.0 - 0.661514 e^{-(\ln 2)(x/0.6)^2} & x < 0 \end{cases} \qquad (2)$$

Boundary conditions are set using characteristics at the inflow and outflow:

$$
\left\{ \begin{array}{c} L_1 \\ L_2 \\ L_3 \end{array} \right\} = \left\{ \begin{array}{c} \dfrac{\partial \rho}{\partial x} - (1/c^2)\dfrac{\partial p}{\partial x} \\[2mm] \dfrac{\partial p}{\partial x} - \rho c \dfrac{\partial u}{\partial x} \\[2mm] \dfrac{\partial p}{\partial x} + \rho c \dfrac{\partial u}{\partial x} \end{array} \right\}
\tag{3}
$$

which propagate at the speeds:

$$
speed \left\{ \begin{array}{c} L_1 \\ L_2 \\ L_3 \end{array} \right\} = \left\{ \begin{array}{c} u \\ u - c \\ u + c \end{array} \right\}
\tag{4}
$$

Note that in this formulation, the characteristics are not linearized about the mean flow.

1.1) Category 1, Problem 1

The problem to be solved is the upstream propagation of an acoustic wave through a transonic, nearly choked nozzle flow. The mean flow is set as:

$$
\left\{ \begin{array}{c} \bar{\rho} \\ \bar{u} \\ \bar{p} \end{array} \right\}_{outflow} = \left\{ \begin{array}{c} 1 \\ 0.4 \\ 1/\gamma \end{array} \right\}
\tag{5}
$$

The acoustic wave is set at the downstream boundary as:

$$
\left\{ \begin{array}{c} \rho' \\ u' \\ p' \end{array} \right\}_{outflow} = \varepsilon \left\{ \begin{array}{c} 1 \\ -1 \\ 1 \end{array} \right\} \cos\left(\omega\left[\frac{x_{outflow}}{1 - M_{outflow}} + t\right]\right)
\tag{6}
$$

or

$$(L_2)_{outflow} = -2\varepsilon\left(\frac{\omega}{1 - M_{outflow}}\right)\sin\left(\omega\left[\frac{10}{1 - M_{outflow}} + t\right]\right) \qquad (7)$$

In this problem, the initial condition is set as the exact solution for isentropic flow at each grid point, with the perturbation starting from the boundary at time = 0. The solution is run through 40 cycles of the perturbation, when the data is taken.

Initially, the problem was run with a uniformly-spaced grid until grid convergence was obtained in order to determine the necessary spacing at x=0 (the nozzle throat). This was obtained at 3201 equally-spaced points, or a Δx of 0.00625. The minimum spacing was then set, and the grids were stretched algebraically to a maximum Δx of 0.1 and were uniform to the boundary. The stretched-grid solutions were then compared with the 3201-point solution for accuracy.

Figure 1 compares the solution obtained on the 251 point stretched grid with that of the exact solution, while Figure 2 shows the grid spacing distribution as a function of x for the various grids. The solution on this relatively coarse grid agrees very well with the exact solution.
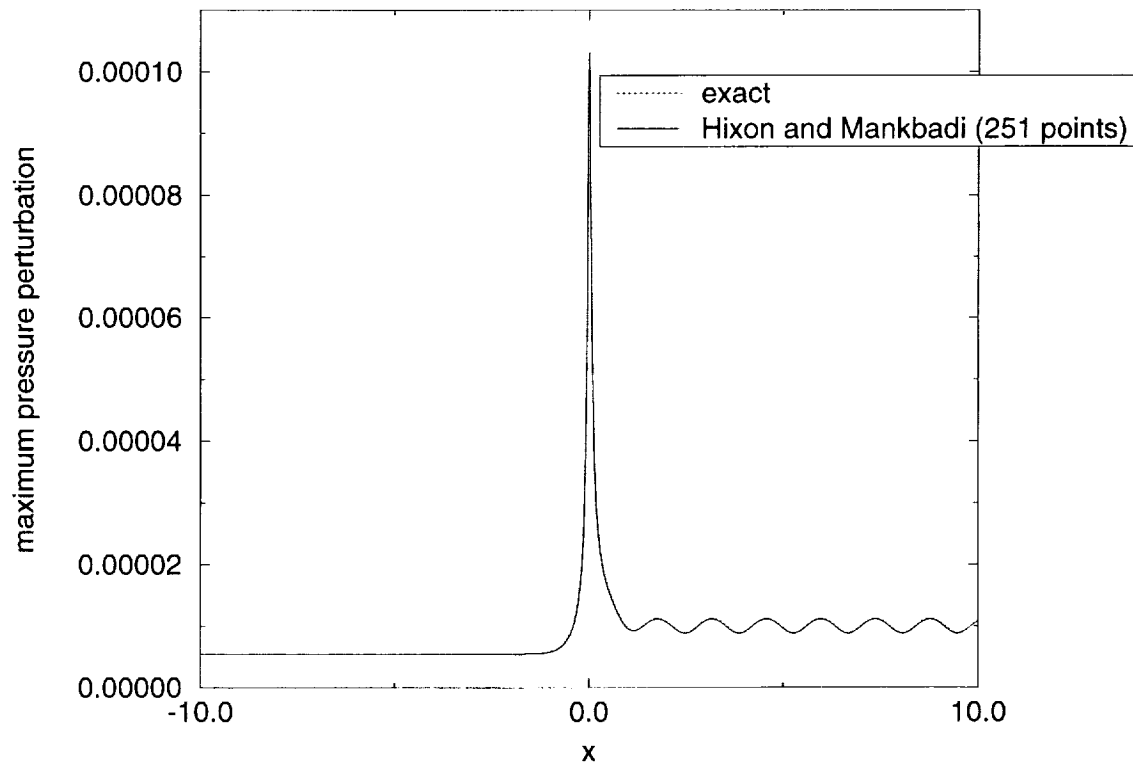
Figure 1: Comparison of Maximum Pressure Distribution for 251 point Stretched Grid with Exact Solution

1.2) Category 1, Problem 2

The problem to be solved is the upstream propagation of an acoustic wave through a shock wave in a convergent-divergent nozzle. The mean flow is set as:

$$\left\{\begin{array}{c} \bar{\rho} \\ \bar{u} \\ \bar{p} \end{array}\right\}_{inflow} = \left\{\begin{array}{c} 1 \\ 0.2006533 \\ 1/\gamma \end{array}\right\} \tag{8}$$

and

$$p_{outflow} = 0.6071752 \tag{9}$$

The acoustic wave is set at the upstream boundary as:
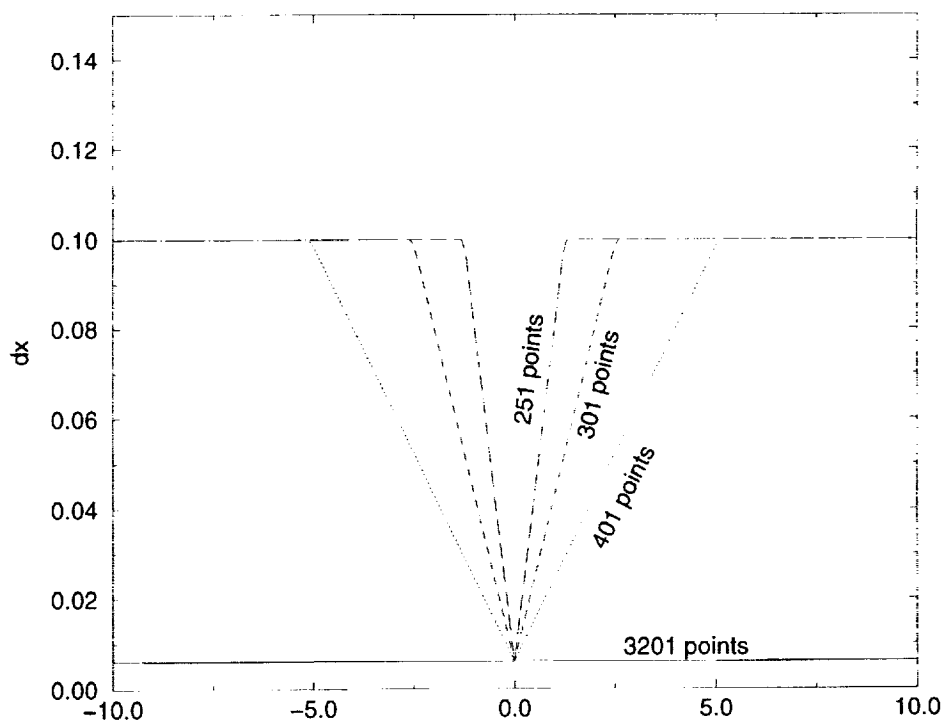
Figure 2: Grid Spacing Distribution for Various Numbers of Grid Points

$$\left\{ \begin{array}{c} \rho' \\ u' \\ p' \end{array} \right\}_{inflow} = \varepsilon \left\{ \begin{array}{c} 1 \\ 1 \\ 1 \end{array} \right\} \sin\left(\omega\left[\frac{x_{inflow}}{(1 + M_{inflow})} + t\right]\right) \tag{10}$$

or

$$(L_3)_{inflow} = 2\varepsilon\left(\frac{\omega}{1 + M_{inflow}}\right)\cos\left(\omega\left[\frac{-10}{(1 + M_{inflow})} + t\right]\right) \tag{11}$$

In this problem, the initial condition is set as the exact solution for isentropic flow at each grid point, with the perturbation starting from the boundary at time = 0. The solution is run through 40 cycles of the perturbation, when the data is taken.

As before, a uniform grid solution of 3201 points was run as a reference solution. The solution that is presented has 201 points in the grid. Figure 4 compares the mean pressure with the exact solution. Figure 5 compares the pressure perturbations between the stretched 201 point grid and the exact solution. Figure 6 compares the outflow pressure history with the exact solutions. Note
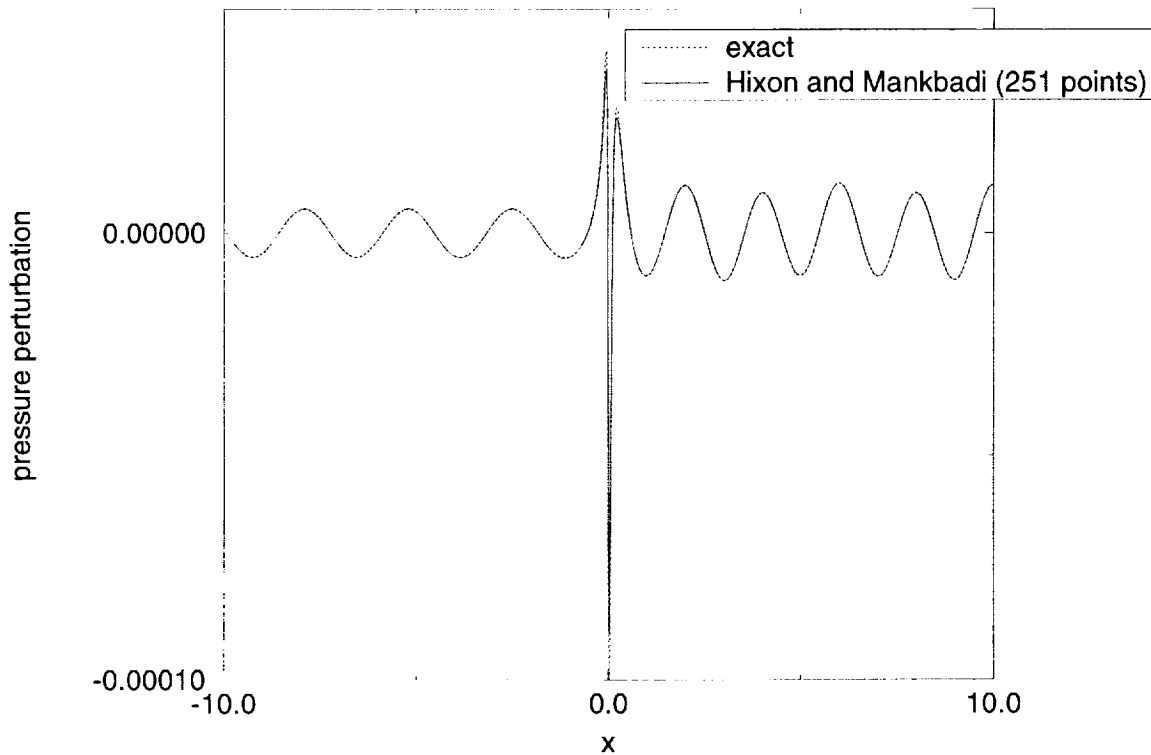
Figure 3: Comparison of Instantaneous Pressure Perturbation for Category 1 Problem 1
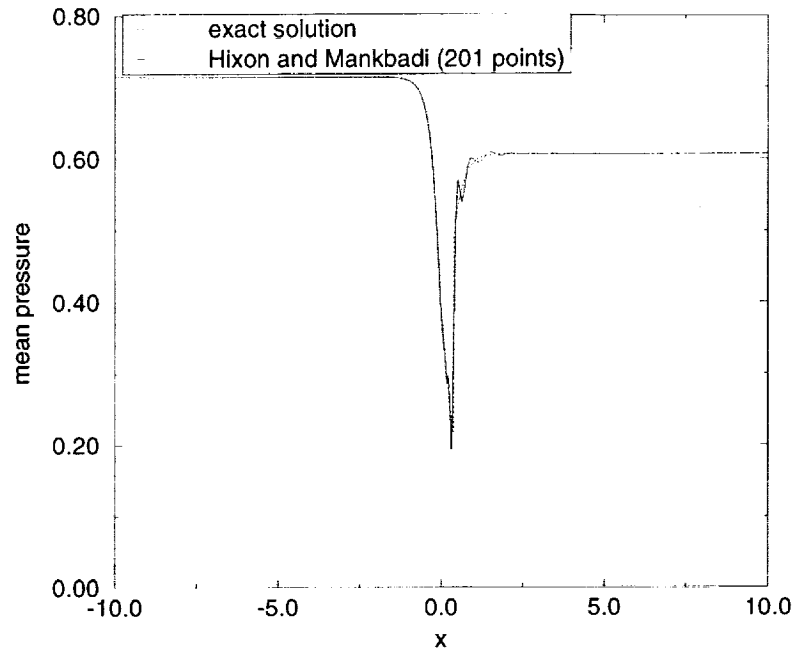
Figure 4: Comparison of Mean Pressure Distribution for Category 1 Problem 2
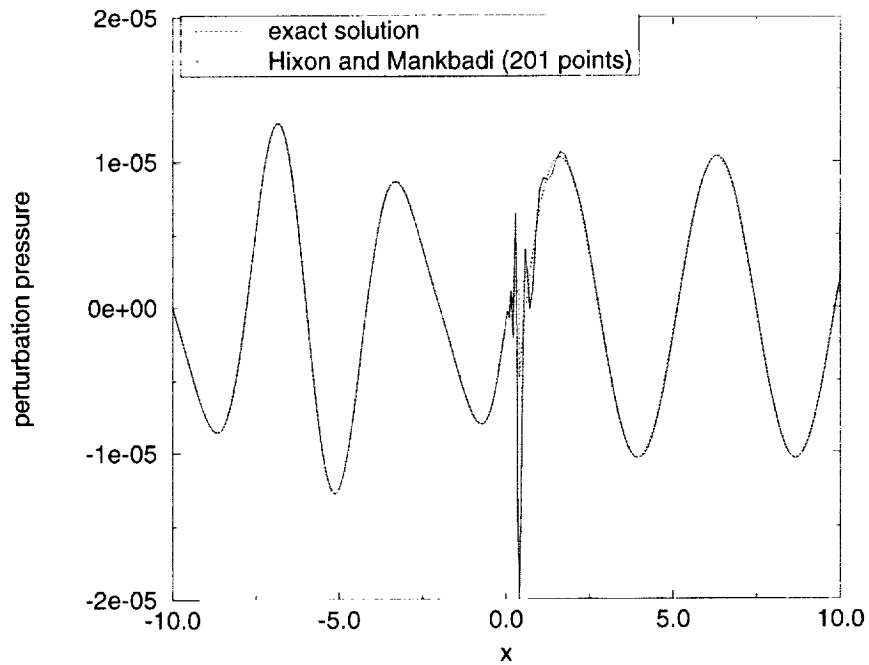
Figure 5: Comparison of Pressure Perturbation for Category 1 Problem 2

122
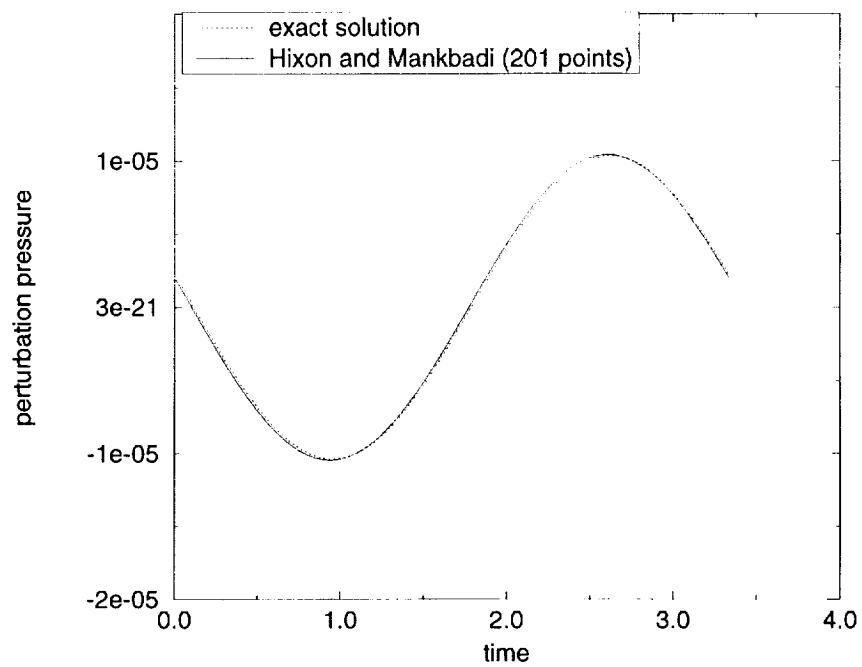
Figure 6: Comparison of Outflow Pressure Perturbation Time History for Category 1 Problem 2
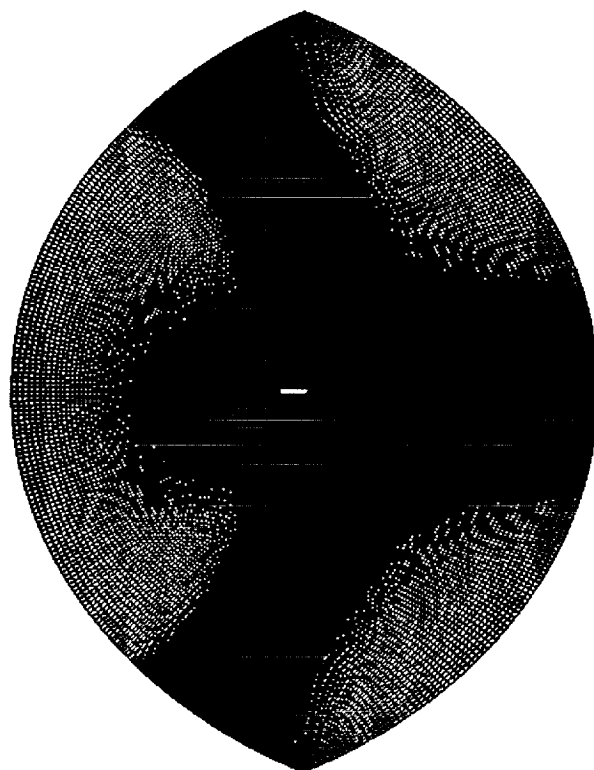
Figure 7: C-Grid used for Joukowski Airfoil (433 x 125)

that, while there are oscillations around the shock, the filtering keeps this from contaminating the solution downstream.

2) Category 3 Problem 1

2.1) Problem Description

In this set of problems, a two-dimensional simple-harmonic vortical gust convects past a 12% thick Joukowski airfoil. The gust has the distribution:

$$u_{gust} = -\varepsilon M\left(\frac{\sqrt{2}}{2}\right)\cos(2k(x+y-Mt)) \tag{12}$$

$$v_{gust} = \varepsilon M\left(\frac{\sqrt{2}}{2}\right)\cos(2k(x+y-Mt)) \tag{13}$$

Here, e = 0.02 and k = 0.1.
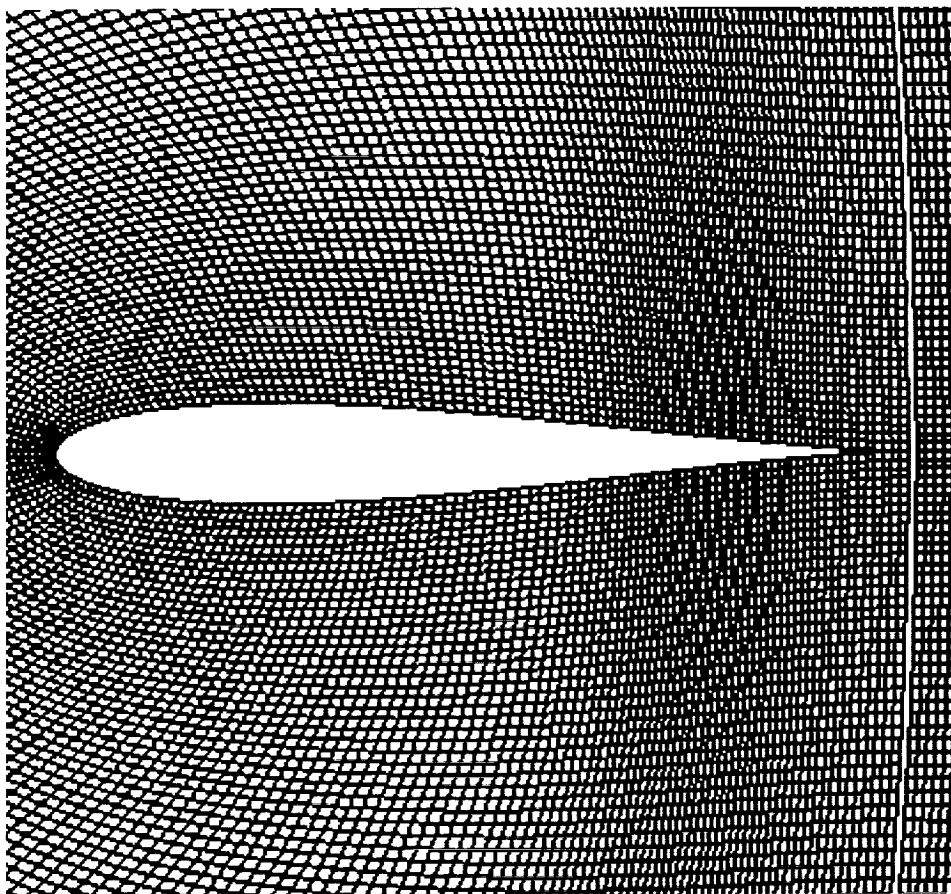
Figure 8: Closeup of Cambered Airfoil Grid

The mean flow at infinity is defined as:

$$\bar{\rho} = 1$$
$$\bar{u} = M$$
$$\bar{v} = 0 \tag{14}$$
$$\bar{p} = \frac{1}{\gamma}(\bar{\rho}^{\gamma})$$

where M = 0.5 and γ = 1.4.

In the first test, a symmetric airfoil is used at a zero degree angle of attack. The second test used a cambered airfoil (camber ratio = 0.02) at a two-degree angle of attack.

2.2) Mathematical and Numerical Formulation

In this work, the nonlinear Euler equations are solved. In Cartesian coordinates these equations are written as:

$$\frac{\partial Q}{\partial t} + \frac{\partial E}{\partial x} + \frac{\partial F}{\partial y} = 0 \tag{15}$$
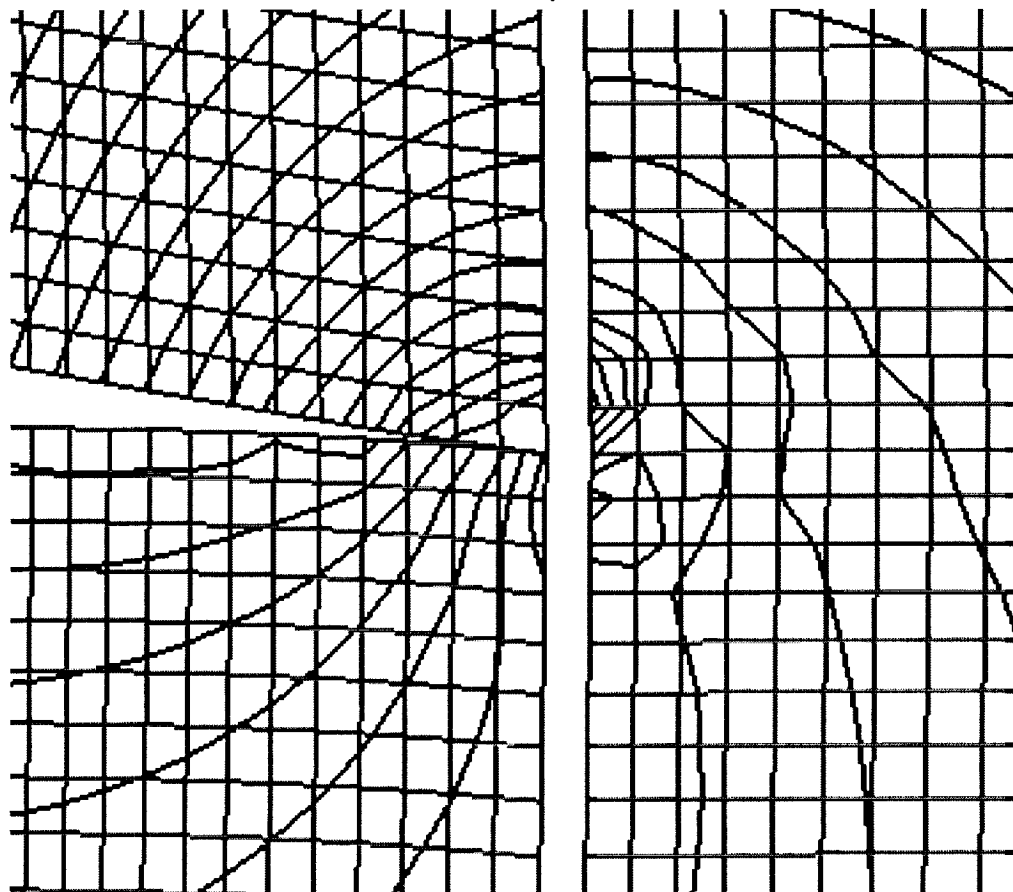
Figure 9: Effect of Trailing Edge Singularity on Instantaneous Pressure Contours (Cambered Airfoil).
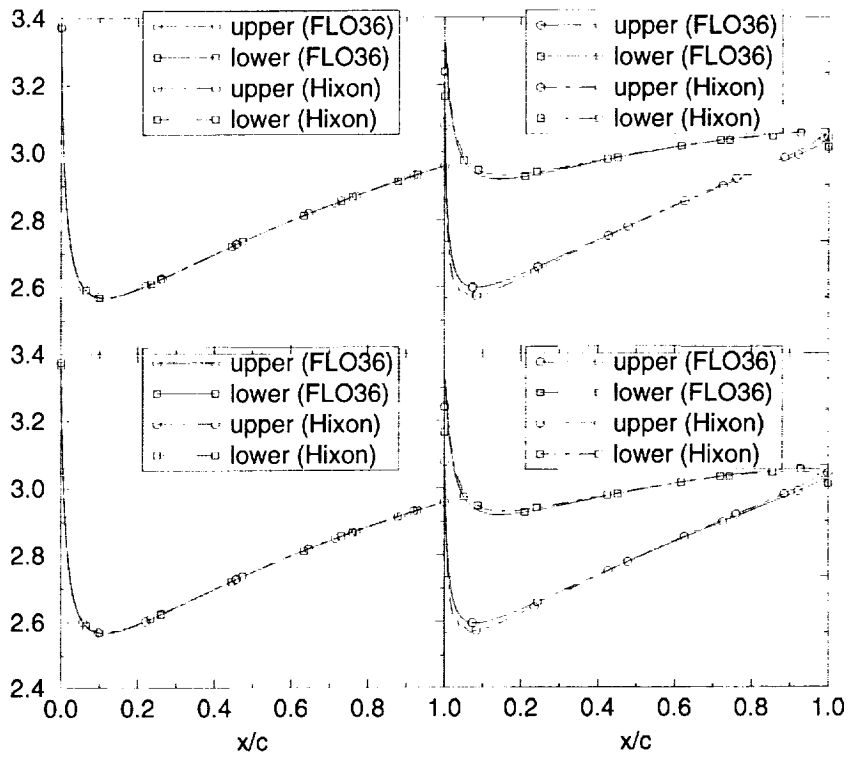
Figure 10: Mean Pressure Distribution on the Airfoil Surface
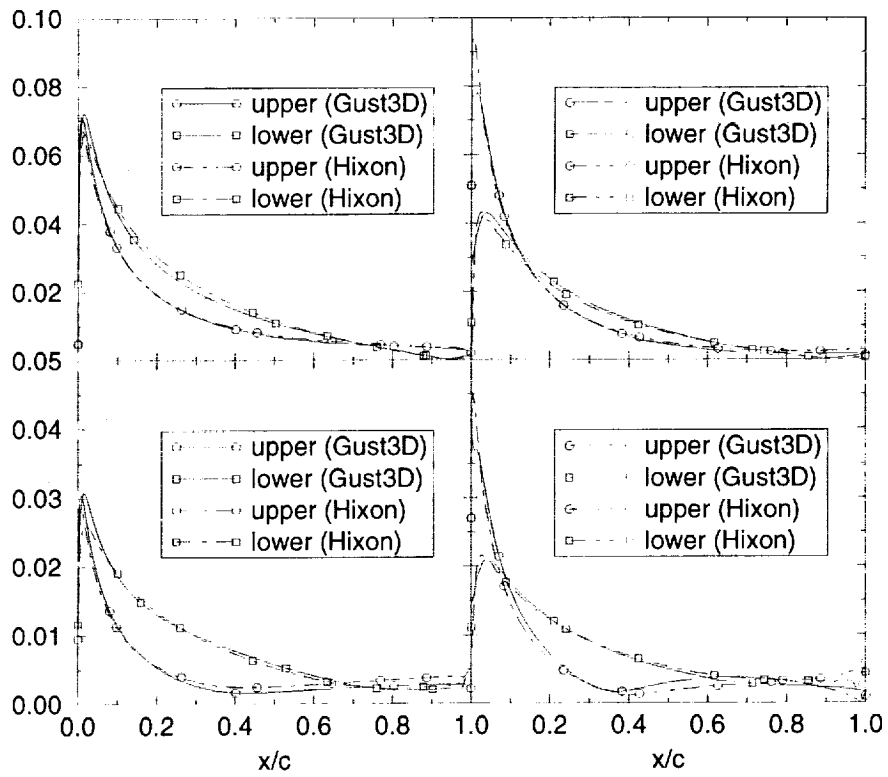
Figure 11: RMS Pressure Disturbance Distribution on the Airfoil Surface

where

$$Q = \begin{bmatrix} \rho \\ \rho u \\ \rho v \\ E \end{bmatrix} \tag{16}$$

$$E = \begin{bmatrix} \rho u \\ \rho u^2 + p \\ \rho uv \\ u(E + p) \end{bmatrix} \tag{17}$$

$$F = \begin{bmatrix} \rho v \\ \rho uv \\ \rho v^2 + p \\ v(E + p) \end{bmatrix} \tag{18}$$

where

$$p = (\gamma - 1)\left(E - \frac{1}{2}\rho(u^2 + v^2)\right) \tag{19}$$

Since the Joukowski airfoil has a complex geometry that does not lend itself to Cartesian grids, the equations were recast in generalized curvilinear coordinates. From previous numerical tests (ref. 8), the chain-rule formulation was chosen as the most accurate form of the equations in three dimensions. The chain-rule curvilinear Euler equations are written as:

$$\frac{\partial Q}{\partial \tau} + \frac{\partial \xi}{\partial x}\frac{\partial E}{\partial \xi} + \frac{\partial \eta}{\partial x}\frac{\partial E}{\partial \eta} + \frac{\partial \xi}{\partial y}\frac{\partial F}{\partial \xi} + \frac{\partial \eta}{\partial y}\frac{\partial F}{\partial \eta} = 0 \tag{20}$$

The time stepping method used was the low storage fourth-order nonlinear extension of Hu's 5-6 Low Dispersion and Dissipation Runge-Kutta scheme (ref. 9) by Stanescu and Habashi (ref. 3). A time step of CFL = 1.5 was used for all calculations, giving 911 time steps per cycle of vorticity for the medium-frequency case and 9110 time steps per cycle of vorticity for the low-frequency case.

The spatial derivatives are calculated using the prefactored sixth-order compact scheme and explicit boundary stencils of Hixon (ref. 1). At block boundaries, an 11-point explicit stencil was used. A 10th order explicit filter (ref. 2) was used at every stage of the Runge-Kutta solver to provide dissipation.
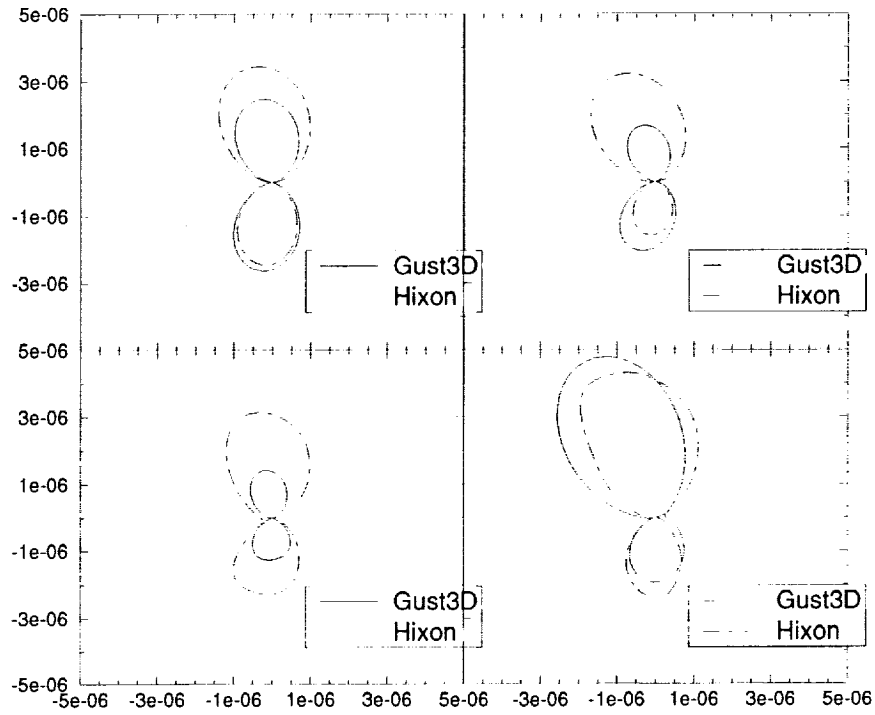
Figure 12: $|p'^2|$ Distribution at R = 4
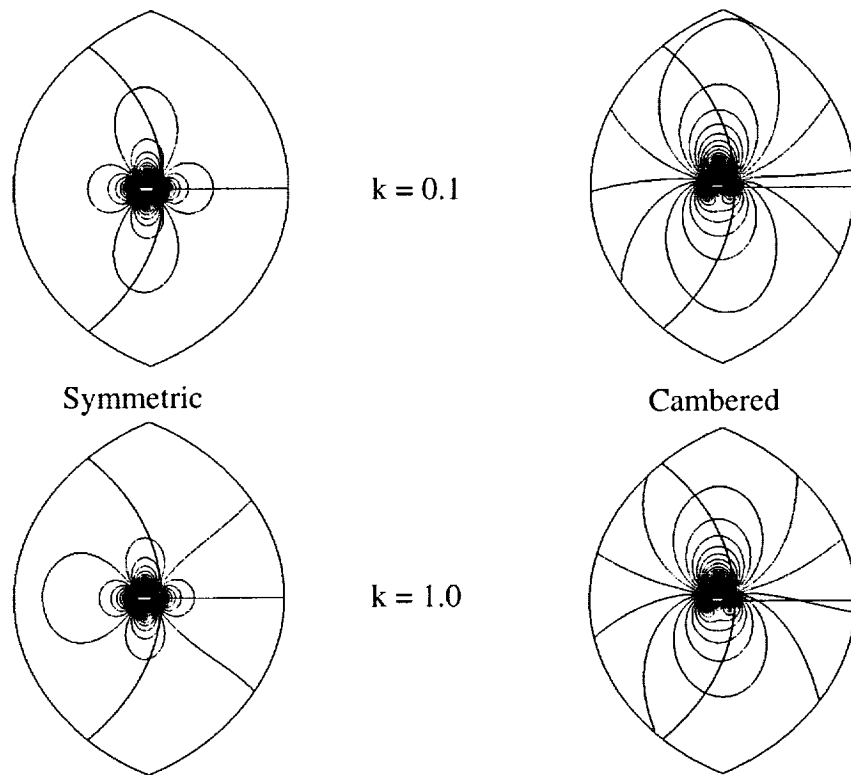
Figure 13: Mean Pressure Contours

The grid used was a C-grid topology (Figure 7), extending at least five chord lengths away in each direction. The grid had 221 points on the airfoil and 106 points along the wake cut. In the normal direction, 125 points were used. The grid was generated using the commercial package GridPro[7].

For the calculation, the grid was split into three blocks: an airfoil block and upper and lower wake blocks. The grid was clustered algebraically in the normal direction ($\Delta n = .01$) and near the trailing edge point ($\Delta x = .01$), as shown in Fig. 8. A stretching ratio of 1.05 was used to a far-field spacing of $\Delta x = \Delta y = 0.106$.

2.3) Initial and Boundary Conditions

For both cases the flow was initialized to the mean flow with the vortical gust superposed:

$$\rho(x, y, 0) = \bar{\rho}$$
$$u(x, y, 0) = \bar{u} + u_{gust}(x, y, 0)$$
$$v(x, y, 0) = v_{gust}(x, y, 0) \tag{21}$$
$$p(x, y, 0) = \bar{p}$$

At the wall, Hixon's inviscid curvilinear wall boundary condition (ref. 10) was used, modified to set the normal momentum to zero at the wall at each Runge-Kutta stage.

k = 0.1

Symmetric   Cambered

k = 1.0
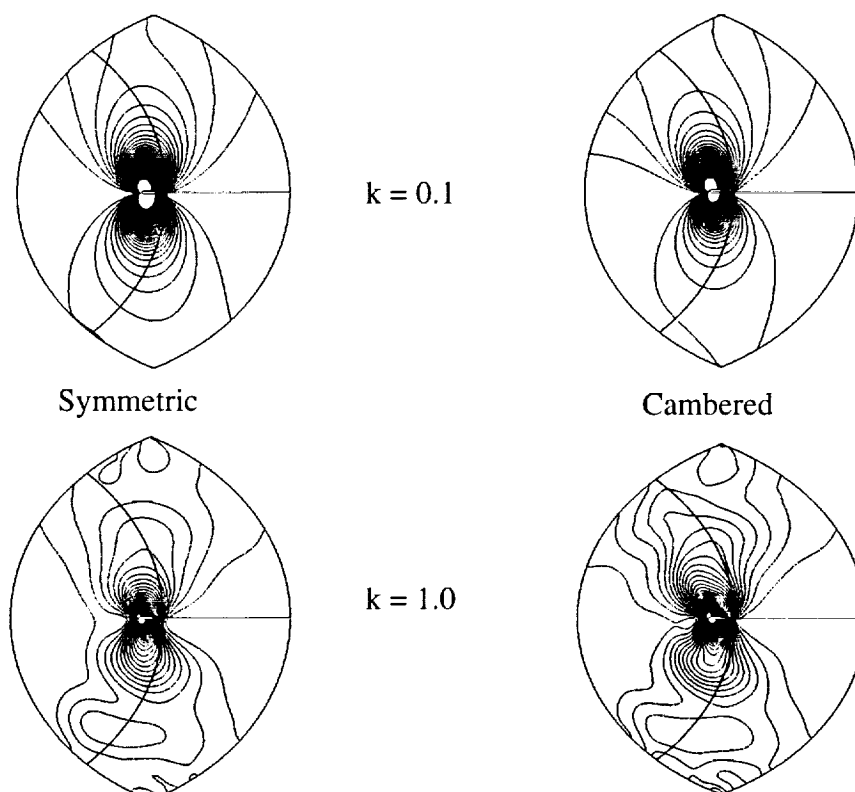
Figure 14: RMS Pressure Disturbance Contours

At the inflow boundary, the acoustic radiation condition of Tam and Webb (ref. 11) was used on the outgoing perturbations. For example, the outgoing u-velocity perturbation was defined as:

$$u_{outgoing} = u_{BC} - \bar{u} - u_{gust} \tag{22}$$

At the outflow boundary, Tam and Webb's radiation outflow condition (ref. 11) was used with no correction for the outgoing vortical gust.

At the trailing edge point on the airfoil, the C-grid topology defines the airfoil geometry incorrectly, causing numerical inaccuracy. While an O-grid geometry would define the trailing edge geometry properly, the C-grid was chosen due to the excessive number of grid points that the O-grid would require to accurately resolve the sharp trailing edge.

At the trailing edge, an upper and lower wall condition is calculated, and averaged to make the trailing edge point single-valued. This averaging, and the discontinuity in the boundary condition on the surface line as it enters the wake, causes a loss of accuracy near the trailing edge. To reduce the effect on the global solution, points were clustered near the trailing edge as shown in Fig. 8. Figure 9 shows the effect of the averaging on the pressure contours near the trailing edge of the cambered airfoil. The effect was much stronger on the cambered lifting airfoil than on the symmetric nonlifting airfoil.

2.4) Results

The compact code was run until the lift coefficient settled to a simple harmonic state, corresponding to a nondimensional time of 210, requiring 72 hours on a 2-processor SGI Octane. As expected, the nonlifting airfoil case converged faster; the lifting airfoil case results are still changing very slightly.

The mean pressures on the airfoil are shown in Figure 10. The effect of the trailing edge condition is apparent in both figures; however, the effect is localized near the trailing edge. In both figures, some oscillations are seen near the peak of the pressure curve; this is due to marginal resolution of the high gradients in both the flow properties and the change in grid spacing in the tangential direction. However, the effect on the mean solution is minimal. It is seen that the lifting airfoil peak pressures are consistently overpredicted; this is attributed to the relatively small computational domain.

Figure 11 shows the RMS pressure disturbance distribution on the airfoil. Again, some oscillations due to marginal resolution can be seen near the peaks of the pressure disturbance, and the trailing edge condition has some effect on the solution on the airfoil. However, the code is predicting the changing pressure distributions due to the two geometries and different frequencies very well.

Figure 12 shows the amplitude of the RMS pressure perturbation at a distance of four chord lengths away from the centerpoint of the airfoil. Here the comparison is not as good as on the airfoil surface; however, the results compare well qualitatively and the magnitudes are in the correct range.

Figure 13 shows the distribution of the mean pressure throughout the computational domain. Note the lack of reflections at the boundaries. Figure 14 shows the RMS pressure perturbation distribution. In this case, it is seen that the boundary conditions work well for the low-frequency case, but there are reflections for the high-frequency case. It is not certain whether the degradation in dispersion performance near the boundaries due to the one-sided boundary stencils is contributing to these reflections.

3) Conclusions

Four benchmark problems of the Third CAA Workshop were solved using a prefactored sixth-order compact scheme with 10th order filtering. These problems tested the accuracy of the code on stretched, curvilinear grids with nonlinear flows. In all cases, the code was robust and converged well. In the one-dimensional problems, the code proved very accurate even in the presence of unresolved shock waves. In the more realistic Category 3 problem, the solution shows the correct trends for the different airfoil geometries and vortical frequencies.

Acknowledgment

References

1) Hixon, R., 'A New Class of Compact Schemes', AIAA Paper 98-0367, Reno, NV, Jan. 1998.

2) Kennedy, C. A. and Carpenter, M. H., 'Several New Numerical Methods for Compressible Shear-Layer Simulations', *Appl. Num. Math.*, Vol. 14, 1994, pp. 397-433.

3) Stanescu, D. and Habashi, W. G., '2N-Storage Low Dissipation and Dispersion Runge-Kutta Schemes for Computational Acoustics', *J. Comp. Phys.*, Vol. 143, No. 2, 1998, p. 674-681.

4) Bui, T. T. and Mankbadi, R. R., 'Numerical Simulation of Acoustic Waves Interacting with a Shock Wave in a Quasi-1D Convergent-Divergent Nozzle Using an Unstructured Finite Volume Algorithm', *IJCFD*, Vol. 10, 1998, pp. 281-289.

5) Hixon, R., Shih, S.-H., and Mankbadi, R. R., 'Evaluation of Boundary Conditions for the Gust-Cascade Problem', *Journal of Propulsion and Power*, Vol. 14, No. 4, 1999.

6) Hixon, R., Shih, S.-H., Mankbadi, R. R., and Scott, J. R., 'Time Domain Solution of the Airfoil Gust Problem Using a High-Order Compact Scheme', AIAA Paper 98-3241, Cleveland, OH, July 1998.

7) GridPro^{TM}/az3000, Program Development Corporation, White Plains, NY, 1996.

8) Hixon, R., Shih, S.-H., Dong, T., and Mankbadi, R. R., 'Evaluation of Generalized Curvilinear Coordinate Transformations Applied to High-Accuracy Finite-Difference Schemes', AIAA Paper 98-0370, Jan. 1998.

9) Hu, F.Q., Hussaini, M. Y., and Manthey, J., 'Low-Dissipation and -Dispersion Runge-Kutta Schemes for Computational Acoustics', ICASE Report 94-102, Dec. 1994.

10) Hixon, R., 'Curvilinear Wall Boundary Conditions for Computational Aeroacoustics', AIAA Paper 99-2395, Los Angeles, CA, June 1999.

11) Tam, C. K. W. and Webb, J. C., 'Dispersion-Relation-Preserving Finite Difference Schemes for Computational Acoustics', *J. Comp. Physics*, Vol. 107, 1993, p. 262-281.

APPLICATIONS OF THE SPACE-TIME CONSERVATION ELEMENT AND SOLUTION ELEMENT (CE/SE) METHOD TO COMPUTATIONAL AEROACOUSTIC BENCHMARK PROBLEMS

XIAO-YEN WANG*,   Ananda Himansu

Taitech Inc., NASA Glenn Research Center, Cleveland, OH 44135

*email: wangxy@turbot.grc.nasa.gov

Sin-Chung Chang   and   Philip C.E. Jorgenson

NASA Glenn Research Center, Cleveland, OH 44135

Abstract

The problems 1 and 2 in Category 1 (Internal Propagation), problem 3 in Category 3 (Fan Noise), and problems 2 and 3 in Category 3 (Turbomachinery Noise in the Second CAA Workshop) are solved using the space-time conservation element and solution element (CE/SE) method. The problems in Category 1 address the propagation of sound waves through a nozzle. Both the nonlinear and linear quasi 1D Euler equations are solved. Numerical solutions are presented and compared with the analytical solution. Problem 3 in Category 3 concerns the effect of the sweep angle on the acoustic field generated by the interaction of a convected gust with a cascade of 3D flat plates. A parallel version of the 3D CE/SE Euler solver is developed and employed to obtain numerical solutions for a family of swept flat plates. Numerical solutions for sweep angles of 0°, 5°, 10°, and 15° are presented. Problems 2 and 3 in Category 3 from the Second CAA Workshop describe the interaction of a 2D vortical gust with a cascade of flat-plate airfoils with/without a downstream moving grid. The 2D nonlinear Euler Equations are solved and the converged numerical solutions are presented and compared with the corresponding analytical solution. All the comparisons demonstrate that the CE/SE method is capable of solving aeroacoustic problems with/without shock waves in a simple and efficient manner. Furthermore, the simple non-reflecting boundary condition used in the CE/SE method which is not based on the characteristic theory works very well in 1D, 2D and 3D problems.

1. Introduction

The method of space-time conservation element and solution element (abbreviated as the CE/SE method) is an innovative numerical method for solving conservation laws. It is designed to be a numerical method in the field of computational fluid dynamics (CFD). Computational aeroacoustics (CAA) is one of its applications.

The space-time CE/SE method is distinguished from other methods by its very conceptual basis — flux conservation in space and time. Simplicity, generality and accuracy are weighted in the development of this method. Its salient properties are summarized briefly as follows. First, both local and global flux conservations are enforced in space and time instead of in space only. Second, all the dependent variables and their spatial derivatives are considered as individual unknowns to be solved for simultaneously at each grid point. Third, every CE/SE scheme starts from a non-dissipative scheme and numerical dissipation is fully controllable, which result in very low numerical dissipation. Fourth, the flux-

based specification of the CE/SE schemes give rise in a natural fashion to extremely simple yet highly effective non-reflecting boundary condition which is an important issue in CAA. This can be contrasted to the complexity of nonreflecting boundary conditions necessary for traditional numerical methods. A detailed description of this method and the accompanied analysis can be found in [1-4].

A variety of numerical tests have been performed previously to illustrate the accuracy of this method. For the CE/SE Euler solver, highly accurate numerical solutions have been obtained for various flow problems involving discontinuities such as shock waves, contact surfaces, and even their interactions[2]. Moreover, applications of the same Euler solver to computational aeroacoustics (CAA) problems reveal that the accuracy of the results is comparable to that of a 4th-order compact difference scheme even though the current solver is only 2nd-order accurate, and the nonreflecting boundary condition can be implemented in a simple way without involving characteristic variables. Results show that the present solver can handle both continuous and discontinuous flows very well[5-13].

In this paper, a quasi 1-D CE/SE Euler solver is used to solve the benchmark problem in Category 1 (Internal Propagation). Among the two proposed problems, one addresses the propagation of sound waves through a transonic nozzle and another concerns shock-sound interaction in a supersonic nozzle. For problem 1, both uniform meshes with constant numerical dissipation models and nonuniform meshes with variable numerical dissipation models are used. Numerical results are presented and compared with the analytical solution. A good agreement is achieved by using 401 stretched mesh points. For problem 2, 101 and 201 point uniform meshes are used and excellent agreements with the analytical solution are obtained. Further, the numerical solutions obtained by solving the linearized equations are compared with those obtained by solving the nonlinear equations for both problems.

A parallel version of the 3D CE/SE Euler solver for the nonlinear equations is developed and employed to obtain numerical solutions of problem 3 in Category 3. The acoustic field generated by the interaction of a gust with a 3D cascade of swept flat plates is simulated at different sweep angles for the cascade. Numerical solutions for sweep angles of $0°, 5°, 10°,$ and $15°$ are presented.

The vectorized 2D CE/SE Euler solver for the nonlinear equations is employed to solve problems 2 and 3 in Category 3 in the Second CAA Workshop. The acoustic field generated by the interaction of a vortical gust with a cascade of flat-plate airfoils is simulated. For problem 2, numerical solutions at both low and high frequency cases are presented. For problem 3 which has a sliding grid downstream of the cascade, only the low frequency case is solved.

The CE/SE Euler solvers are explicit time-marching schemes. They are second-order accurate in both space and time. The scheme has a 3-point stencil for 1D, 4-point stencil for 2D, and a 5-point stencil for 3D. The 1D and multiple dimensional solvers share identical features. In the Euler solver, three parameters α, β, and ϵ are used to specify the numerical dissipation. When $\alpha = \beta = \epsilon = 0$, the Euler solver has no numerical dissipation.

2. Category 1: Problems 1 and 2

For the two problems in Category 1, the CE/SE quasi 1D Euler solver described in [13] for the nonlinear equations is used to compute the steady-state solution of the nozzle flowfield. For the simulation of acoustic wave propagation, both the linear and nonlinear quasi 1D Euler solvers are used under the

same computational conditions. The two solvers are constructed for the linear and nonlinear quasi 1D Euler equations in conservative form. They have the identical formulation except the time-marching variables are different. Both the linear and nonlinear numerical solutions are presented. Numerical solutions of the acoustic wave plotted in all figures are non-dimensionalized by its amplitude ε. In the computations using a uniform mesh, the constant numerical dissipation model with $\epsilon = 0.2, \alpha = 0$, and $\beta = 1$ is used for both problems.

Prob. 1: Propagation of Sound Waves through a Transonic Nozzle

The first problem addresses the propagation of sound waves in a transonic nozzle, in which the local Mach number of the flow near the throat may be close to sonic. The computation of sound propagating through such regions presents a challenging problem. The area of the nozzle is

$$
A(x) = \begin{cases} 0.536572 - 0.198086 \exp\left(-(\ln 2)(\frac{x}{0.6})^2\right), & x > 0 \\ 1.0 - 0.661514 \exp\left(-(\ln 2)(\frac{x}{0.6})^2\right), & x < 0. \end{cases} \tag{1}
$$

In the uniform region downstream of the throat, the diameter of the nozzle is D and the main flow is uniform with Mach number, M_∞, of 0.4, speed of sound, a_∞, and static density, ρ_∞. Flow variables are non-dimensionalized by using a_∞ as the velocity scale, D as the length scale, D/a_∞ as the time scale, ρ_∞ as the density scale, and $\rho_\infty a_\infty^2$ as the pressure scale. Thus the mean flow in the uniform region downstream of the throat is

$$
\rho = 1, \quad v = 0.4, \quad p = 1/1.4. \tag{2}
$$

The acoustic wave, with angular frequency $\omega = 0.6\pi$, is described as

$$
\rho' = p' = \varepsilon \cos\left[\omega(\frac{x}{1 - M_\infty} + t)\right], \quad v' = -\varepsilon \cos\left[\omega(\frac{x}{1 - M_\infty} + t)\right] \tag{3}
$$

where $\varepsilon = 10^{-4}$. It is generated downstream and propagates upstream through the narrow passage of the nozzle throat. The computational domain is $-10 \le x \le 10$. It is recommended that computations use no more than 400 mesh intervals.

First, the steady-state solution of the nozzle flow is computed. The initial conditions are specified using flow properties in the uniform downstream region. The back pressure ($p_{back} = 1/1.4$) is specified at the outlet, and the total pressure and total density are specified at the inlet. The other needed information at both the inlet and outlet are obtained using extrapolation from their neighboring mesh points. The steady-state solution obtained using a 401 point uniform mesh with $CFL = 0.847$ is shown in Fig. 1 and compared with the exact solution represented by solid lines. It can be seen that flow properties are uniform in most region of the nozzle, but change dramatically near the nozzle throat.

After the steady-state nozzle flowfield is computed, the acoustic wave propagation can be simulated using the same nonlinear Euler solver. The initial conditions are specified using the steady-state solution of nozzle flowfield. The exit boundary condition is different from that used for computing the steady-state solution. At the outlet, the time-marching variables are specified as

$$
(u_1)_j^n = \rho + \rho', \quad (u_2)_j^n = (\rho + \rho')(v + v') \tag{4}
$$

$$(u_3)_j^n = \frac{p + p'}{\gamma - 1} + \frac{1}{2}(\rho + \rho')(v + v')^2. \tag{5}$$

At the inlet, the non-reflecting boundary condition is enforced by setting

$$(u_m)_j^{n+1/2} = (u_m)_{j+1/2}^n, \quad (u_{mx})_j^{n+1/2} = 0, \quad m = 1, 2, 3. \tag{6}$$

A detailed analysis of this nonreflecting boundary condition for 1D case is given in [6]. It is based on flux extrapolation.

Different mesh sizes are tested in the current computation. First, uniform meshes with $\Delta x = 0.05$ and 0.025 in the computational domain of $-10 \leq x \leq 10$ are used. Numerical solutions of the acoustic pressure at $t = 20T$ are shown in Figs. 2 and 3, respectively and compared with the analytical solution. It can be seen that the peak values near the throat and the wave pattern upstream of the throat can not be captured correctly using 401 uniform grid points, while a greatly improved result is produced using an 801 point uniform mesh. The amplitude of the acoustic wave upstream of the throat however is lower than that given by the analytical solution. Further, the corresponding solutions obtained with $\Delta x = 0.0125$ in the computational domain of $-5 \leq x \leq 5$ are shown in Fig. 4. Although the peak values are still not the same as the analytical solution, the profiles of the p' both upstream and downstream of the throat agree very well with the analytical solution.

In order to reduce the number of grid points, a 401 point nonuniform mesh that clusters near the throat is used. The ratio of the largest to smallest mesh interval is around 10 with $\Delta x_{min} = 0.0047$. The variable ϵ_j^n and β_j^n described in Eq. (52) in [13], and constant $\alpha = 0$ are used in the computation. The acoustic pressure obtained at $t = 20T$ with $CFL = 0.9084$ is shown in Fig. 5 which is nearly similar to that obtained using an 801 point uniform mesh in the domain of $-10 \leq x \leq 10$. Further improvement can be made in the future by reducing the numerical dissipation or using a more stretched mesh. Its convergence to the time-periodic solution is shown in Fig. 6. Under the same computational conditions and mesh, the corresponding solution obtained using $\varepsilon = 10^{-3}$ is plotted in Fig. 7 showing skewness upstream of the throat. It can be concluded that the amplitude of the acoustic wave should be small enough to avoid the nonlinearity when a nonlinear scheme is used to obtain a solution in the linear regime. In the present computation using the nonlinear solver, the steady-state solution is converged to 10^{-7}, and $\varepsilon = 10^{-4}$ is used.

For the linear solver, the amplitude of the acoustic wave is set to 1, and the steady-state solution obtained by the nonlinear solver is used in the computation. The same three uniform meshes used for the nonlinear solver described above are tested with the linear solver. The linear solutions are very similar to the nonlinear solutions. The solution obtained using an 801 point uniform mesh in the domain of $-10 \leq x \leq 10$ is shown in Fig. 8 as an example. The nonlinear solution is slightly better than the linear solution under the same computational conditions.

Prob. 2: Shock-Sound Interaction

In this problem, the same nozzle geometry from the previous problem is used, but here there is a supersonic shock downstream of the throat. All quantities are non-dimensionalized using the upstream values. The Mach number at the inlet, M_∞, is 0.2006533 and the back pressure, p_{back}, is 0.6071752. Following the same steps described in the first problem, the steady-state nozzle flowfield is computed

and used as the initial condition for the sound-shock interaction simulation. The acoustic wave is described as

$$\rho' = p' = v' = \varepsilon \sin\left[\omega\left(\frac{x}{1 + M_\infty} + t\right)\right] \tag{7}$$

where ε and ω have the same values as that in the first problem. At the inlet, the time-marching variables are specified using Eqs. (4) and (5), while at the outlet, for $m = 1, 2, 3$,

$$\left(u_m\right)_j^{n+1/2} = \left(u_m\right)_{j-1/2}^n, \quad \left(u_{mx}\right)_j^{n+1/2} = 0 \tag{8}$$

are used as the non-reflecting boundary conditions.

Uniform meshes with 101 and 201 grid points are used for this problem. The steady-state solution obtained using a 101 point uniform mesh is shown in Fig. 9 and compared with the analytical solution represented by solid lines. Numerical solutions of the acoustic wave obtained using 101 and 201 point uniform meshes are shown in Fig. 10 in which only the analytical solution of p' is plotted for a comparison. The analytical solutions of the density and velocity are not available. It can be seen that the solution obtained on a 101 point uniform mesh is very close to the analytical solution and that obtained on a 201 point uniform mesh appears to graphically match the analytical solution. A very solid convergence to the time-periodic solution is demonstrated in Fig. 11 for the coarse mesh. Further, the acoustic pressure at the outlet in one time period is plotted in Fig. 12 along with the analytical solution showing an excellent agreement. The linear solution is almost identical to the nonlinear solution which is shown in Fig. 13 for a 101 point uniform mesh.

3. Category 3: Problem 3

This problem concerns the effect of the sweep angle of the flat plate on the acoustic field generated by the interaction of a convected gust with a 3D cascade of flat plates. Consider a rectilinear cascade of swept flat plates. The mean flow is assumed to be uniform and aligned with the x-axis. The mean flow variables are inflow velocity, U_∞, static density, ρ_∞, and static pressure, p_∞. The inflow Mach number, M_∞, is 0.5. The chord length of each plate is c, and the gap-to-chord ratio, s/c, is 1.0. Flow variables are non-dimensionalized by using a_∞ (the speed of sound) as the velocity scale, c as the length scale, c/a_∞ as the time scale, ρ_∞ as the density scale, and $\rho_\infty a_\infty^2$ as the pressure scale. Thus the mean flow is described in dimensionless variables as

$$\rho = 1, \quad u = 0.5, \quad v = 0, \quad w = 0, \quad p = 1.0/1.4. \tag{9}$$

The incident gust carried by the mean flow has x, y, and z velocity components given by

$$u' = -(v_G k_y/k_x)\cos(k_x x + k_y y + k_z z - \omega t) \tag{10}$$

and

$$v' = v_G \cos(k_x x + k_y y + k_z z - \omega t), \quad w' = 0 \tag{11}$$

respectively, where $v_G = 10^{-4}$ and $k_x = 5.5, k_y = \pi, k_z = 0$, and $\omega = 0.5 k_x$, respectively. The corresponding period of the gust wave is $T = 2\pi/\omega$. It is assumed that $\rho' = p' = 0$ which enable the gust to satisfy the linearized Euler equations. The gust is propagating from the inlet along the

mean flow and will interact with the swept flat plates to generate acoustic waves. The whole flow field including the acoustics, gust wave, and mean flow is simulated by solving the nonlinear Euler equations. At $t = 0$, the time-marching variables, $(u_m)_j^n$, in the whole domain are defined using the mean flow variables, and $(u_{mx})_j^n = (u_{my})_j^n = 0$ everywhere.

3.1. Boundary Conditions

With the gust superposed on the mean flow, the time-marching variables at the inlet($x = -6$) are described as:

$$(u_1)_j^n = \rho, \quad (u_2)_j^n = \rho(u + u'), \quad (u_3)_j^n = \rho(v + v'), \quad (u_4)_j^n = \rho(v + w'), \tag{12}$$

$$(u_5)_j^n = \frac{p}{\gamma - 1} + \frac{\rho}{2}[(u + u')^2 + (v + v')^2 + (w + w')^2]. \tag{13}$$

The inlet values of $(u_{mx})_j^n$, $(u_{my})_j^n$, and $(u_{mz})_j^n$ are obtained by taking derivatives of $(u_m)_j^n$. At the outlet($x = 4$), the non-reflecting boundary condition is enforced by setting

$$(u_m)_j^{n+1} = (u_m)_j^{n+1/2}, \quad (u_{mx})_j^{n+1} = (u_{my})_j^{n+1} = (u_{mz})_j^{n+1} = 0, \quad m = 1, 2, 3, 4, 5. \tag{14}$$

The periodic boundary condition is imposed on planes $y = -0.5$ and $y = 1.5$, and the reflecting boundary conditions are used on the flat plate surfaces and the top and bottom walls in the z-coordinate direction. No grid points are located at the flat plate leading and trailing edges to avoid a singular point.

3.2 Numerical Results

The flat-plate cascade sweep angle is varied to determine its effect on the acoustic field generated by the interaction of a convected gust with the flat plates. Four sweep angles are studied here. A structured 200x20x26 hexahedral grid is used in the computational domain $-6 \le x \le 4$, $-0.5 \le y \le 1.5$, and $0 \le z \le 2.6$. The parallel version of the 3D Euler solver is used with $\alpha = 0, \epsilon = 0.5$, and $\beta = 1$. A detailed description of the 3D Euler solver is given in [4]. The parallelization of the code will be reported in another paper.

The numerical solution of the acoustic pressure non-dimensionalized by the amplitude of the gust wave is plotted in all figures. The pressure distribution at some constant lines and pressure contours on x-y, x-z and y-z planes are shown for sweep angles of $0°$, $5°$, $10°$, and $15°$ in Figs. 14–17, respectively. It can be seen that the acoustic field does not vary along the z- direction for $0°$ sweep angle. As the sweep angle increases, the acoustic field yields more obvious variations along the z- coordinate direction. The profile of the acoustic pressure at both the inlet and outlet planes changes gradually for various sweep angles. The RMS pressure at the point $(-5, 0, 1.3)$ near the inlet is plotted in Fig. 18 for different sweep angles showing a decreasing trend with the increased sweep angle in the range of $[0°, 15°]$.

For the current parallelized code using an Origin2000 with 31 CPUs, it takes around 2 hours wall clock time(56 hours CPU time) to run until $t = 20T$ for 624000 cells with a required memory of 763MB.

4. Category 3: Problems 2 and 3(the Second CAA Workshop)

Problem 2 in Category 3 from the Second CAA Workshop concerns the acoustic field generated by the interaction of a 2D gust with a cascade of flat plates. The convection of a gust and acoustic wave are simulated simultaneously. Problem 3 is the same as problem 2 except a sliding grid is added downstream of the plates. This tests the ability of a numerical scheme to model the acoustic wave and the gust across a sliding interface typical of those used in rotor stator interaction problems.

Consider the cascade of flat-plate airfoils shown in Fig. 19. The mean axial flow is uniform with prescribed inflow velocity, U_∞, and static density, ρ_∞. The inflow Mach number, M_∞, is 0.5. The length of each plate is c, and the gap-to-chord ratio, g/c, is 1.0. Flow variables are non-dimensionalized by using U_∞ as the velocity scale, c as the length scale, c/U_∞ as the time scale, ρ_∞ as the density scale, and $\rho_\infty U_\infty^2$ as the pressure scale. Thus the mean flow is described in dimensionless variables as

$$\rho = 1, \quad u = 1, \quad v = 0, \quad p = 4.0/1.4. \tag{15}$$

The vortical gust carried by the mean flow has x and y velocity components given by

$$u' = -(v_G k_y/k_x)\cos(k_x x + k_y y - \omega t) \tag{16}$$

and

$$v' = v_G \cos(k_x x + k_y y - \omega t) \tag{17}$$

respectively, where $k_x = k_y = \omega = 5\pi/2$ and $13\pi/2$ respectively for the two cases studied here. The corresponding periods, $T = 2\pi/\omega$, of the gust wave are 4/5 and 4/13. It is assumed that $\rho' = p' = 0$ which enables the gust to satisfy the linearized Euler equations. The gust is propagating from the inlet along the mean flow direction and will interact with airfoils to generate acoustic waves. The entire flow field is simulated using the full Euler equations. To avoid the nonlinear effect, $v_G = 10^{-5}$ is used in the current computation.

4.1. Boundary and Initial Conditions

With the gust superposed on the mean flow, the time-marching variables at the inlet are described as:

$$(u_1)_{j,k}^n = \rho, \quad (u_2)_{j,k}^n = \rho(u + u'), \quad (u_3)_{j,k}^n = \rho(v + v'), \tag{18}$$

$$(u_4)_{j,k}^n = \frac{p}{\gamma - 1} + \frac{\rho}{2}[(u + u')^2 + (v + v')^2]. \tag{19}$$

The inlet values of $(u_{mx})_{j,k}^n$ and $(u_{my})_{j,k}^n$ are obtained by taking derivatives of $(u_m)_{j,k}^n$. The non-reflecting boundary condition is enforced by setting

$$(u_m)_{j,k}^{n+1} = (u_m)_{j,k}^{n+1/2}, \quad (u_{mx})_{j,k}^{n+1} = 0, \quad (u_{my})_{j,k}^{n+1} = (u_{my})_{j,k}^{n+1/2}, \quad m = 1, 2, 3, 4 \tag{20}$$

at the outlet. This non-reflecting boundary condition allows the flux to "stream" out of the spatial domain smoothly. However, the numerical solutions so obtained at the inlet and outlet are not the correct physical solutions. To accurately compute the required sound intensity, $\overline{p^2} = \frac{1}{T}\int_{t_0}^{t_0+T} p'^2 dt$, at

the inlet $(x = -2)$ and the outlet $(x = 3)$, a larger domain is used. The actual computational domain is $-2 - x_b \leq x \leq 3 + x_b$, where $x_b = 4/5$ and $3/14$, respectively for the two cases.

Periodic boundary conditions are imposed on the upper and lower boundaries, and the reflecting boundary conditions described in [2] are used on the airfoil surfaces. The computational mesh shown in Fig. 19 is laid out in such a way that grid points are purposely not located at the airfoil trailing edges to avoid a singular point. In Fig. 19, there are two sets of grid points, presented as solid circles and open circles. They are used to show the difference in spatial location of grid points a half time step apart.

At $t = 0$, the time-marching variables $(u_m)_{j,k}^n$, $(u_{mx})_{j,k}^n$, and $(u_{my})_{j,k}^n$ in the entire domain are defined in the same way as that for imposing the non-reflecting BCs at the inlet.

4.2. Numerical Results and Discussions

In the following discussion, the number of grid points mentioned pertains to the region $-2 \leq x \leq 3$. In all plots shown here, p' is non-dimensionalized by dividing it by v_G. The details of the 2D Euler solver can be found in [2].

Numerical computations were performed using 301x121 uniform grid points for the low frequency case. This results in a grid size of $\Delta x = 1/60$, $\Delta y = 1/30$ with 24 grid points per wavelength in the x-direction for the shortest wave. In the following numerical tests, $\epsilon = 0.2, \beta = 1$, and $\alpha = 0$ are used.

To show the performance of the non-reflecting BCs at the inlet and outlet, the time history of the acoustic pressure at point $(-2, \Delta y/2)$ obtained using two different computational domains with the same CFL $(= 0.8)$ number is shown in Fig. 20. The corresponding data at point $(3, \Delta y/2)$ are plotted in Fig. 21. Figures. 20 and 21 reveal that the profiles of the converged solutions obtained using different computational domains are very similar at both points. The size of the computational domain has a small effect on the numerical solution. The pressure difference on the flat plate is plotted in Fig. 22(a) and compared with the exact solution showing good agreement. The sound intensity, $\overline{p^2}$, at the inlet and outlet are plotted with the analytical solution in Fig. 22(b). Some discrepancies are observed. Several other numerical results obtained using high-order accurate DRP schemes have a similar or bigger discrepancy with the analytical solution[14]. Contours of the scattered pressure at $t = 200T$ are plotted in Fig. 23.

For the high frequency case, the CE/SE solutions of the pressure difference on the airfoil surface obtained using 651x261 uniform grid points are plotted along with the analytical solutions in Fig. 24(a). The radiated sound intensity at the inlet and outlet are compared with the analytical solutions and shown in Fig. 24(b). Contours of the scattered pressure at $t = 47T$ are plotted in Fig. 24(c).

In Fig. 25, the corresponding data are plotted for the low frequency case with a downstream sliding grid. The grid speed is 5, and the moving distance is one Δy per Δt. No interpolation is needed at the sliding interface, since the grid points are aligned at every time step. The computations use $\epsilon = 0.3$, $\beta = 1$, and $\alpha = 0$ with CFL= 0.8 and a 401x241 uniform grid in the domain of $-2.8 \leq x \leq 3.8$. The computed pressure distribution at $y = 0.5, 1.5, 2.5, 3.5$ and pressure difference across the four flat plates at $t = 38T$ are shown in Fig. 26 and compared with those obtained with a stationary downstream grid under the same computational conditions. It can be seen that the two solutions are identical.

The present vectorized 2D Euler code was run on a Cray C90. For the low frequency case with a 301x121 uniform grid and CFL= 0.8, the CPU time was 28 seconds for one period, and a converged solution at $t = 50T$ took 23 minutes and 39 seconds of CPU time and 2MW memory.

5. Conclusions

In Category 1, a satisfactory numerical solution is obtained using a nonuniform mesh with 401 grid points for problem 1. An excellent agreement between the numerical results and the analytical solution was obtained on a 101 point uniform mesh for problem 2. The non-reflecting boundary condition works extremely well for 1D problems. In Category 3, it is demonstrated that the CE/SE method is capable of solving 3D aeroacoustic problems in an efficient way. The results show a decreased RMS pressure with the increasing sweep angle in the range of $[0°, 15°]$. The Category 3 from the Second CAA Workshop compares well with the analytical solution and the accuracy is comparable to those of several high-order DRP schemes. The simple non-reflecting boundary condition works well for multi-dimensional problems. In summary, it is demonstrated that the CE/SE method is capable of solving aeroacoustic problems with/without shock waves in a simple and efficient way. No special techniques are used for shock waves, and acoustics waves and shock waves can be captured concurrently within the computational domain.

Acknowledgments

References

[1] S.C. Chang, "The Method of Space-Time Conservation Element and Solution Element – A New Approach for Solving the Navier-Stokes and Euler Equations", *J. Comput. Phys.*, **119,** pp. 295-324, (1995).

[2] S.C. Chang, X.Y. Wang, and C.Y. Chow, "The Space-Time Conservation Element and Solution Element Method – A New High-Resolution and Genuinely Multidimensional Paradigm for Solving Conservation Laws", *J. Comput. Phys.*, **156,** pp. 89-136, (1999).

[3] X.Y. Wang and S.C. Chang, "A 2D Non-splitting Unstructured-Triangular-Mesh Euler Solver based on the Method of Space-Time Conservation Element and Solution Element", Vol. 8, No. 2, pp. 326-340, 1999, *Computational Fluid Dynamics JOURNAL.*

[4] X.Y. Wang and S.C. Chang, "A 3D Non-splitting Structured/Unstructured Euler Solver based on the Method of Space-Time Conservation Element and Solution Element", AIAA Paper 98-3278, Norfolk, June 28–July 1, 1999.

[5] S.C. Chang, C.Y. Loh and S.T. Yu, "Computational Aeroacoustics via a New Global Conservation Scheme", *Proceedings of the 15th International Conference on Numerical Methods in Fluid Dynamics*, P. Kutler, J. Flores and J.-J. Chattot, eds., June 24-28, 1996, Monterey, CA.

[6] S.C. Chang, A. Himansu, C.Y. Loh, X.Y. Wang, S.T. Yu and P.C.E. Jorgenson, "Robust and Simple Non-Reflecting Boundary Conditions for the Space-Time Conservation Element and Solution Element Method", AIAA Paper 97-2077, June 29-July 2, 1997, Snowmass, CO.

[7] C.Y. Loh, S.C. Chang, J.R. Scott and S.T. Yu, "Application of the Method of Space-Time Conservation Element and Solution Element to Aeroacoustics Problems", *A Collection of Technical Papers, Volume II*, pp. 713-718, 6th International Symposium on Computational Fluid Dynamics, September 4-8, 1995, Lake Tahoe, NV.

[8] C.Y. Loh, S.C. Chang, J.R. Scott and S.T. Yu, "The Space-Time Conservation Element Method – A New Numerical Scheme for Computational Aeroacoustics", AIAA Paper 96-0276, January 15-18, 1996, Reno, NV.

[9] C.Y. Loh, S.C. Chang and J.R. Scott, "Computational Aeroacoustics via the Space-Time Conservation Element / Solution Element Method", AIAA Paper 96-1687, May 6-8, 1996, State College, PA.

[10] C.Y. Loh, L.S. Hultgren and S.C. Chang, "Computing Waves in Compressible Flow Using the Space-Time Conservation Element and Solution Element method," AIAA Paper 98-0369, January 12-15, 1998, Reno, NV.

[11] X.Y. Wang, C.Y. Chow and S.C. Chang, "Numerical Simulation of Gust Generated Aeroacoustics in a Cascade Using the Space-Time Conservation Element and Solution Element Method," AIAA Paper 98-0178, January 12-15, 1998, Reno, NV.

[12] X.Y. Wang, C.Y. Chow and S.C. Chang, "Non-reflecting Boundary Conditions Based on the Space-Time CE/SE Method for Free Shear Flows," AIAA Paper 98-3020, Albuquerque, New Mexico, June 15-18, 1998.

[13] X.Y. Wang, S.C. Chang and P. Jorgenson, "Prediction of Sound Waves Propagating through a Nozzle without/with a Shock Wave Using the Space-Time CE/SE Method," AIAA Paper 2000-0222, Reno, January 10-13, 2000.

[14] "The Proceedings of the Second Computational Aeroacoustics(CAA) Workshop on Benchmark Problems," C.K.W. Tam and J.C. Hardin, NASA Conference Publication 3352, June, 1997.
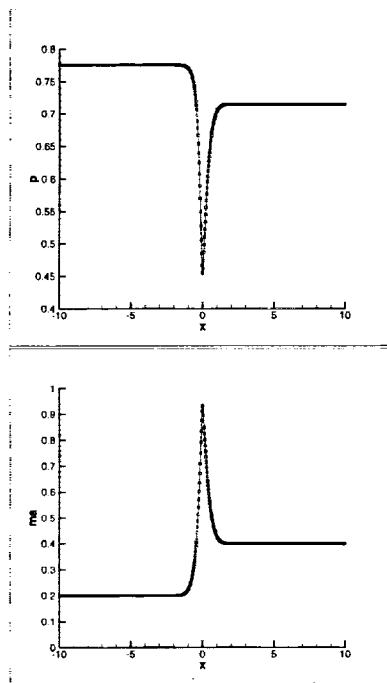
Figure 1: The steady-state solution(401 point uniform mesh) of the nozzle flowfield compared with the exact solution represented by solid lines.
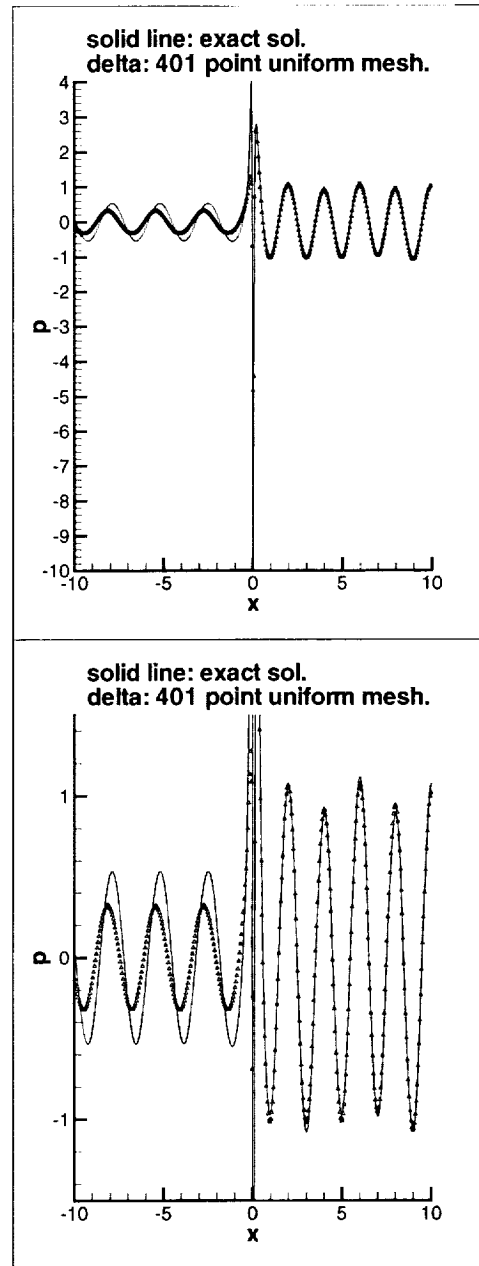
Figure 2: Comparisons between the exact solution and CE/SE solutions obtained using a 401 point uniform mesh in $-10 \leq x \leq 10$.
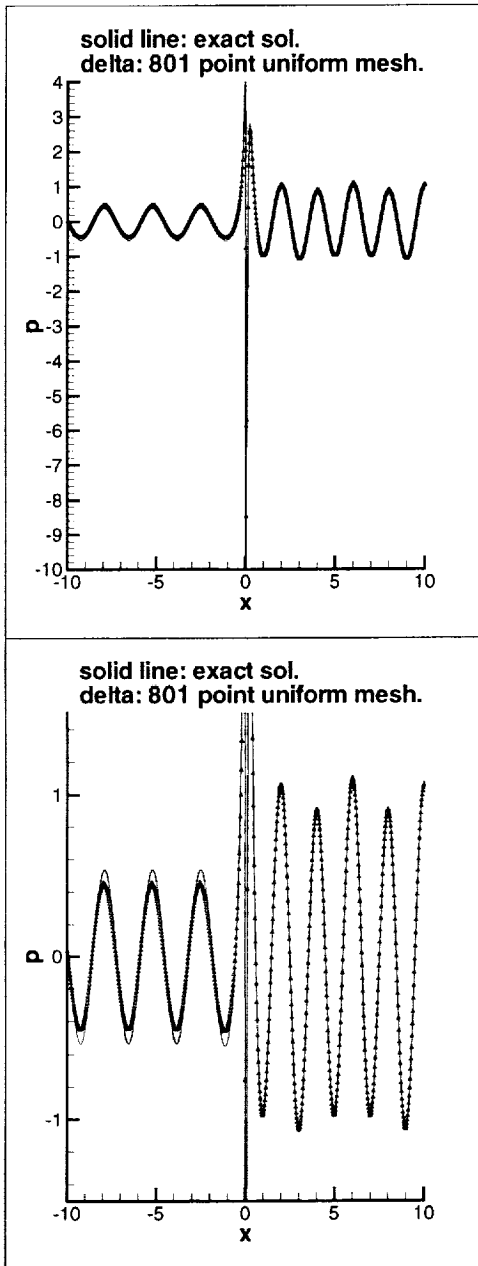
Figure 3: Comparisons between the exact solution and CE/SE solutions obtained using an 801 point uniform mesh in $-10 \leq x \leq 10$.
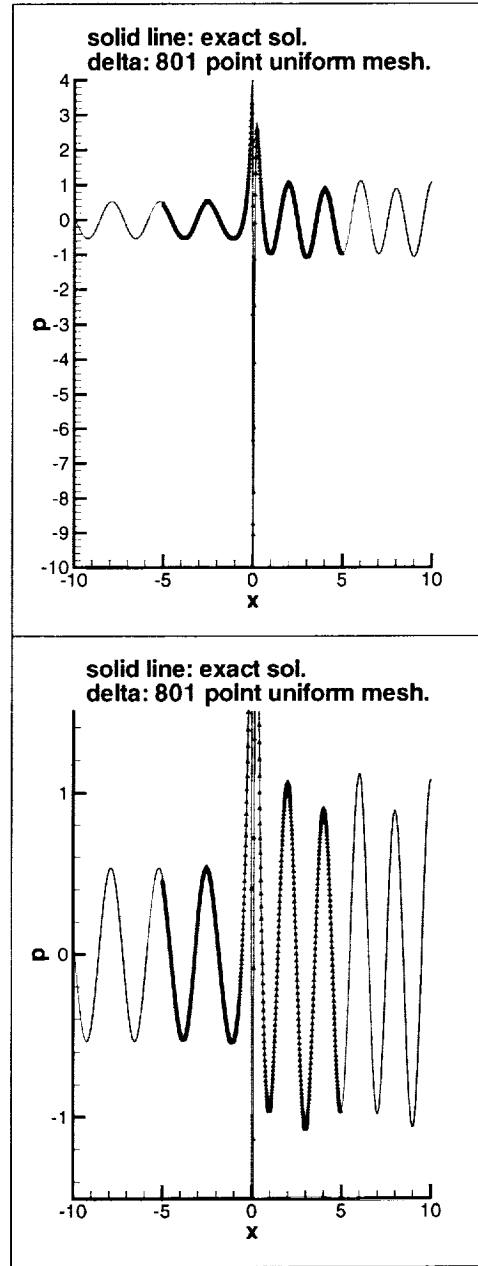
Figure 4: Comparisons between the exact solution and CE/SE solutions obtained using an 801 point uniform mesh in $-5 \leq x \leq 5$.
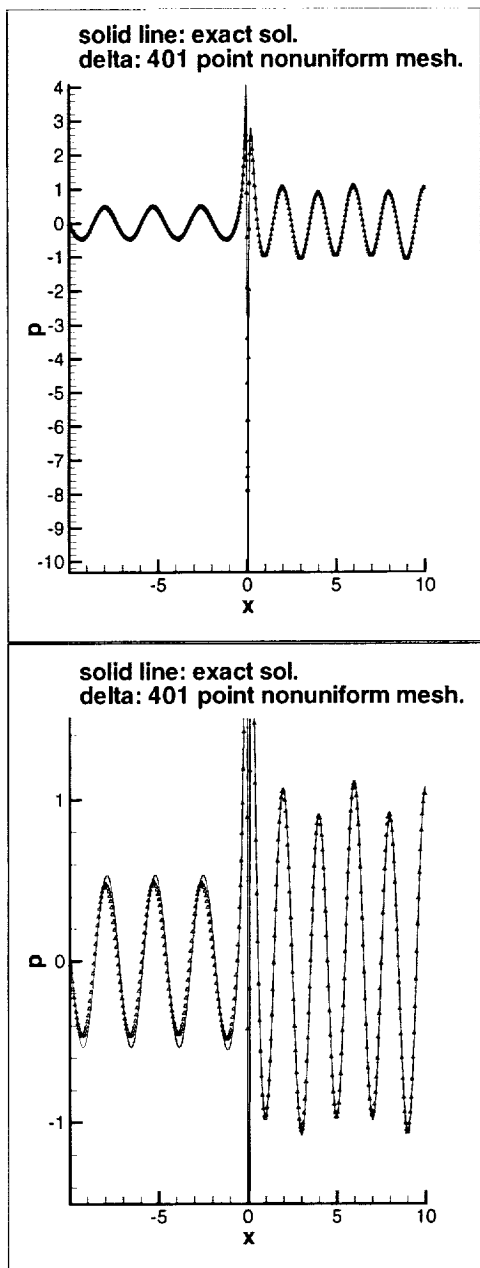
Figure 5: The CE/SE solutions of the acoustic wave p'/ε at $t = 20T$ using a 401 point nonuniform mesh with variable ϵ_j^n and $\beta_j^n (\varepsilon = 10^{-4})$.
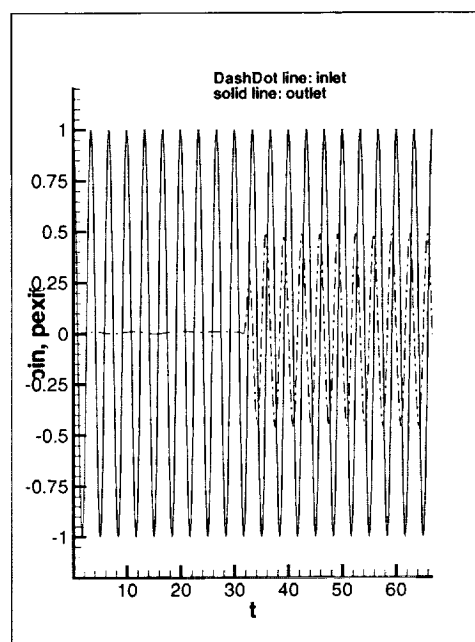
Figure 6: Time history of the acoustic pressure at the inlet and outlet for a stretched 401 point mesh in $-10 \leq x \leq 10$.
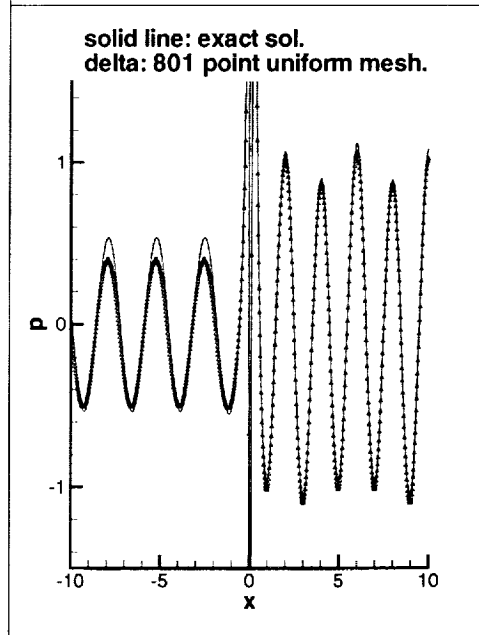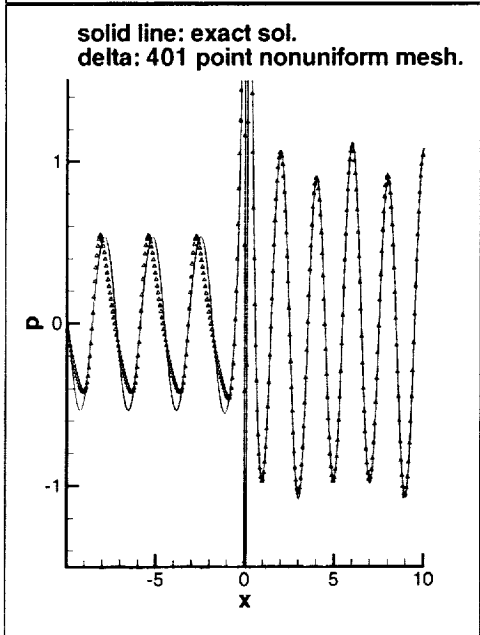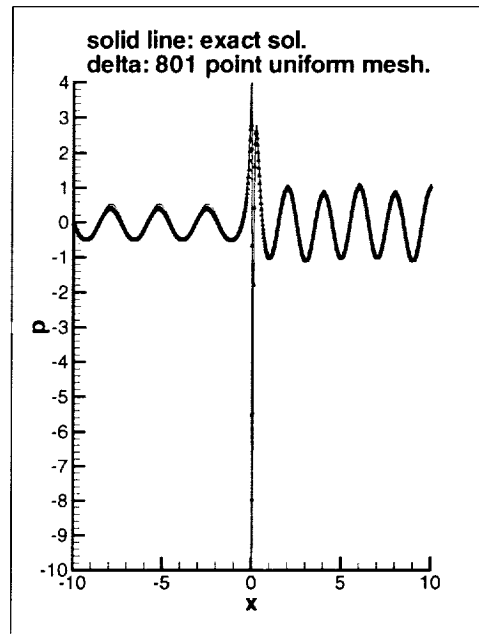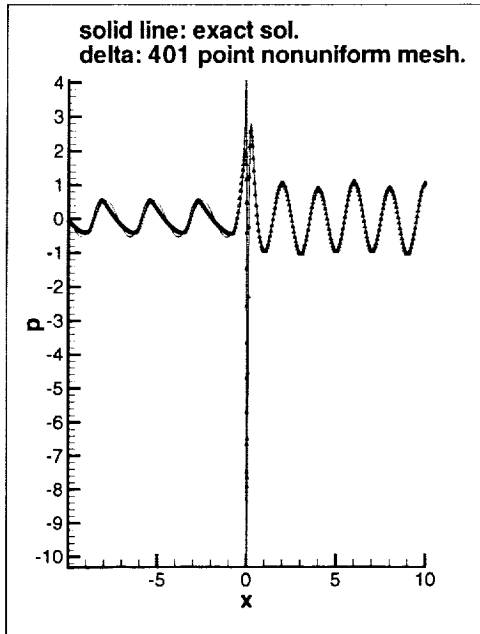
Figure 7: The CE/SE solutions of the acoustic wave p'/ε at $t = 20T$ using a 401 point nonuniform mesh with variable ϵ_j^n and $\beta_j^n (\varepsilon = 10^{-3})$.

Figure 8: Comparisons between the exact solution and CE/SE linear solutions obtained using an 801 point uniform mesh in $-10 \leq x \leq 10$.
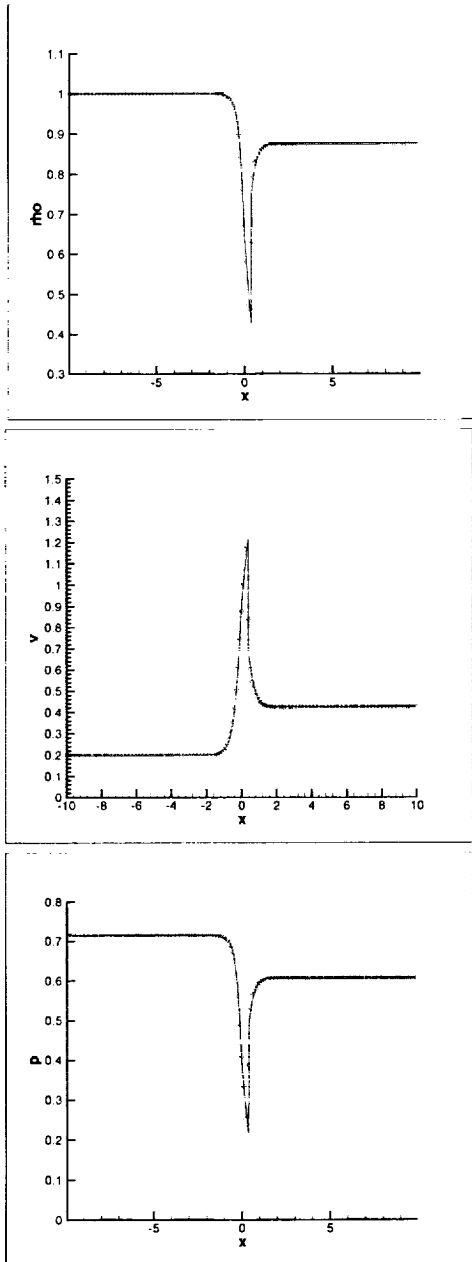
Figure 9: The steady-state CE/SE solution(101 point uniform mesh) of the supersonic nozzle flowfield compared with the exact solution represented by solid lines.
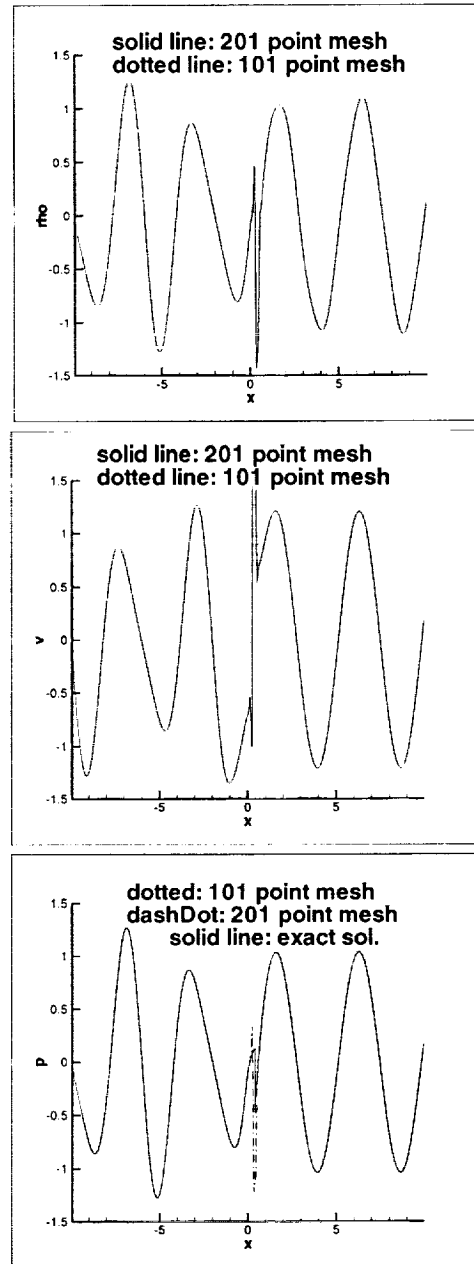
Figure 10: The CE/SE nonlinear solutions of the acoustic wave at $t = 40T$ using 101 and 201 point uniform meshes.
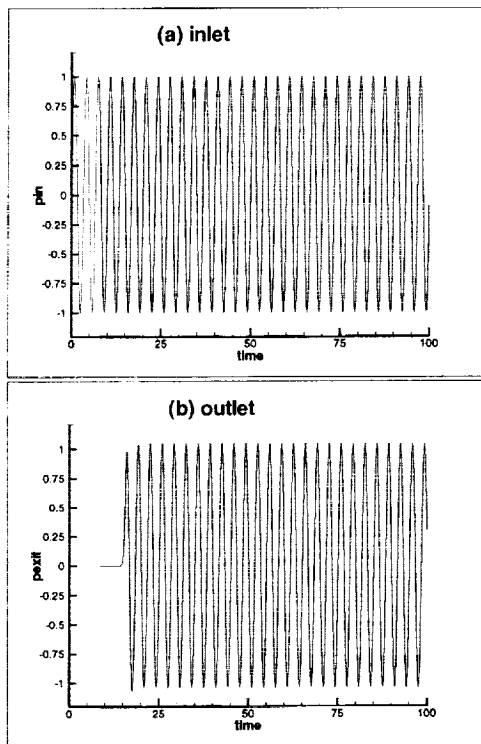
Figure 11: Time history of the acoustic pressure at the inlet and outlet for a 101 point uniform mesh.
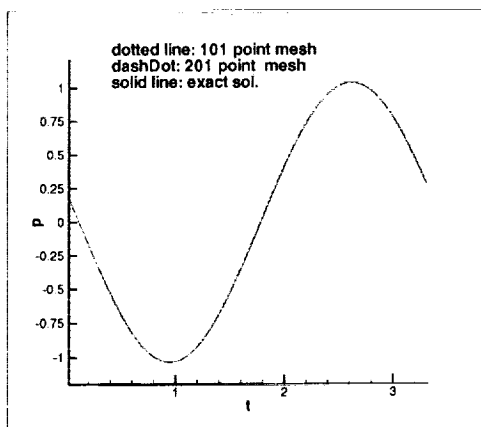
Figure 12: The CE/SE nonlinear solutions of the acoustic wave pressure p' at the outlet in one time period for 101 and 201 point uniform meshes.
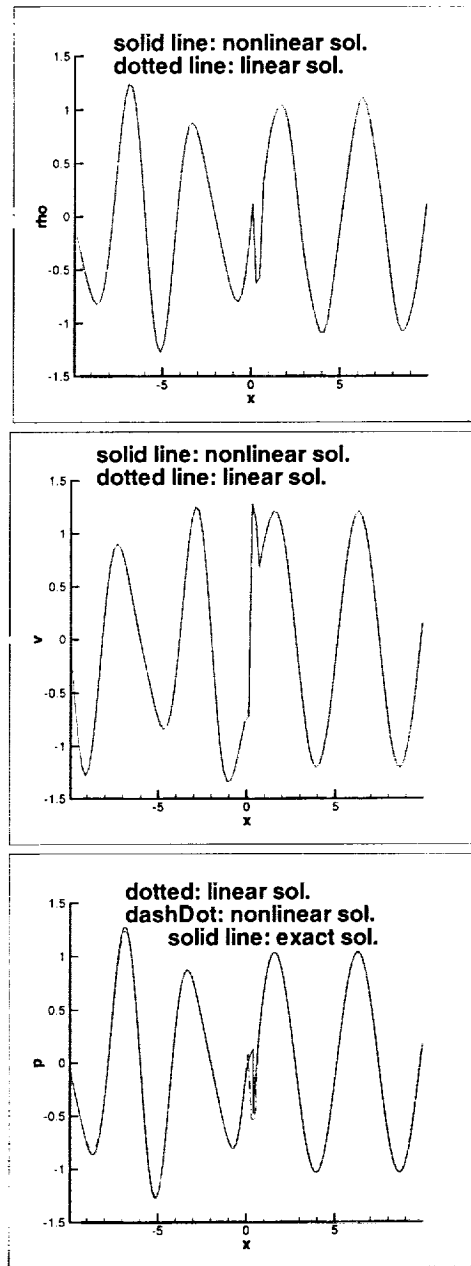
Figure 13: The CE/SE linear solutions of the acoustic wave at $t = 40T$ using a 101 point uniform mesh compared with the corresponding nonlinear solution.
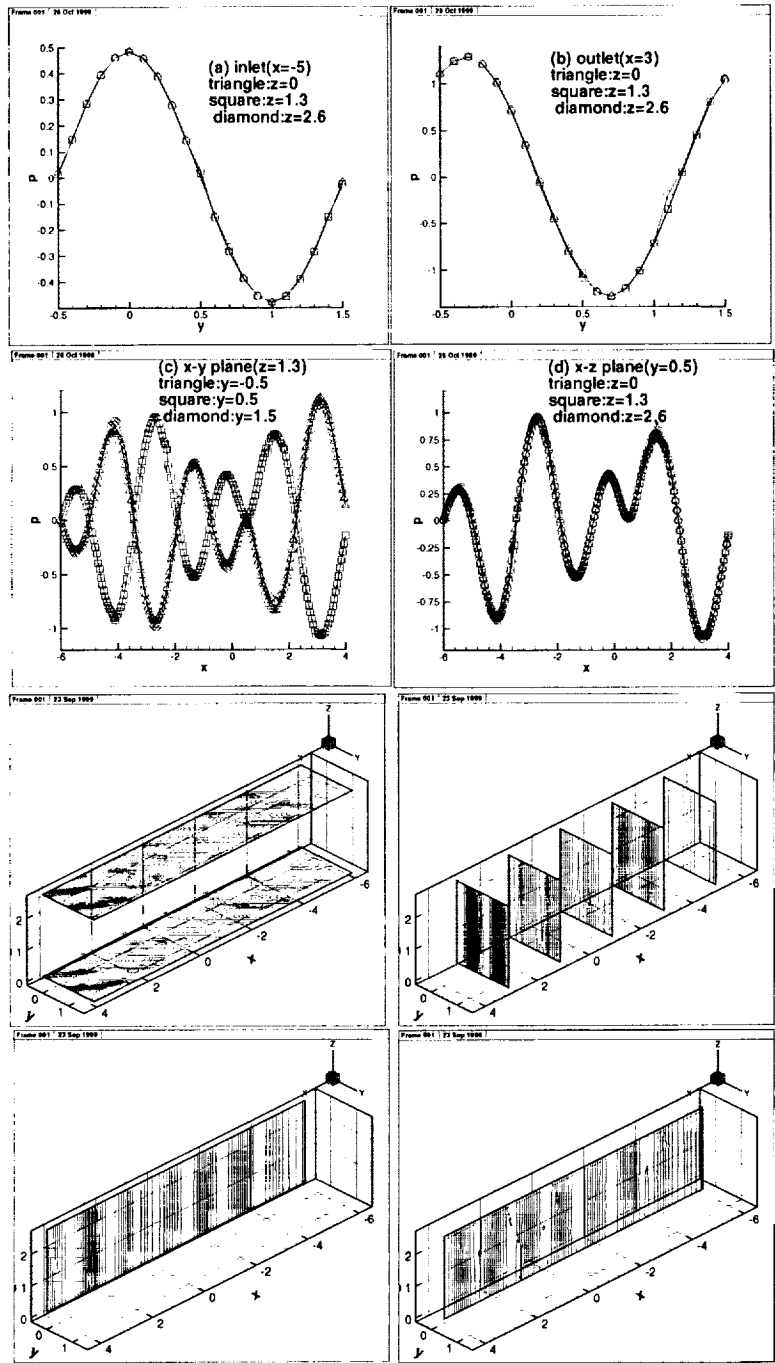
Figure 14: Acoustic pressure contours and distribution on x-y, x-z and y-z planes at $t = 82T$ for $0°$ sweep angle.
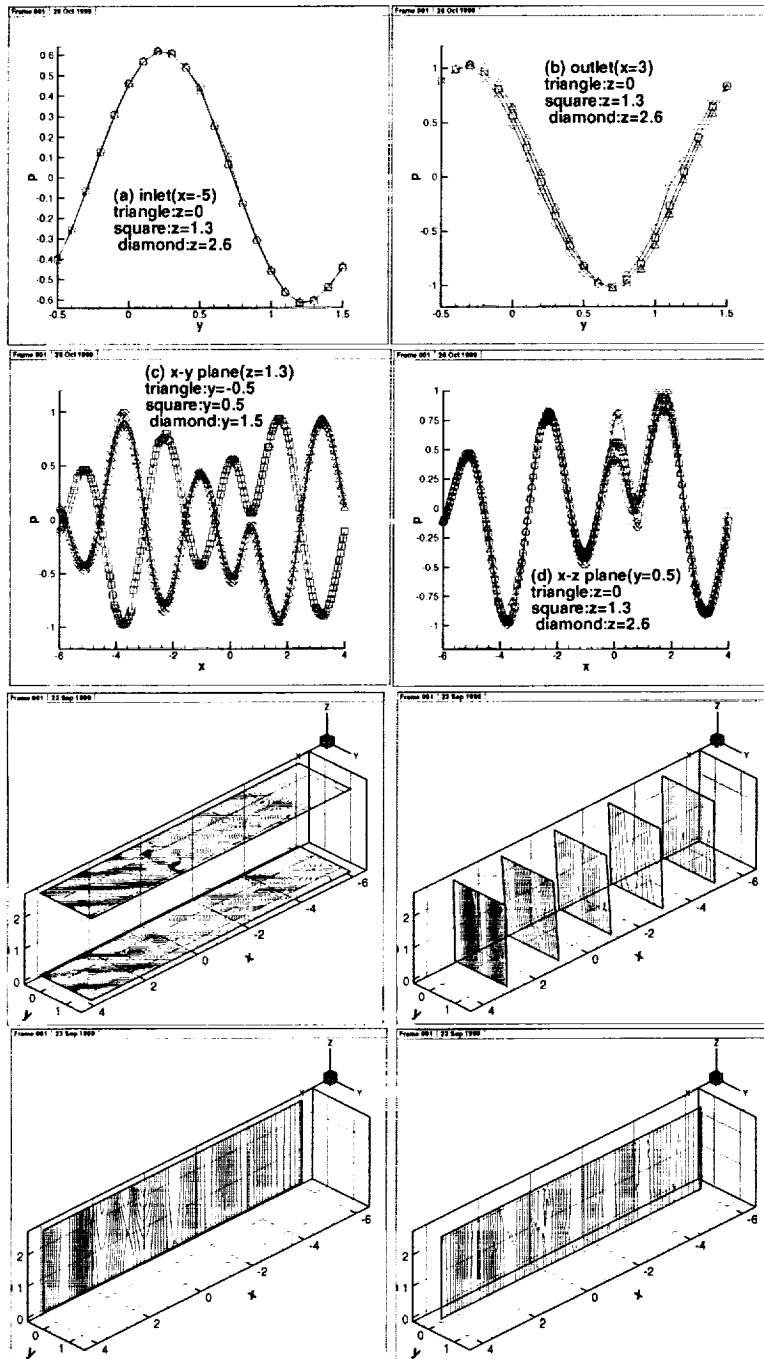
Figure 15: Acoustic pressure contours and distribution on x-y, x-z and y-z planes at $t = 82T$ for 5° sweep angle.
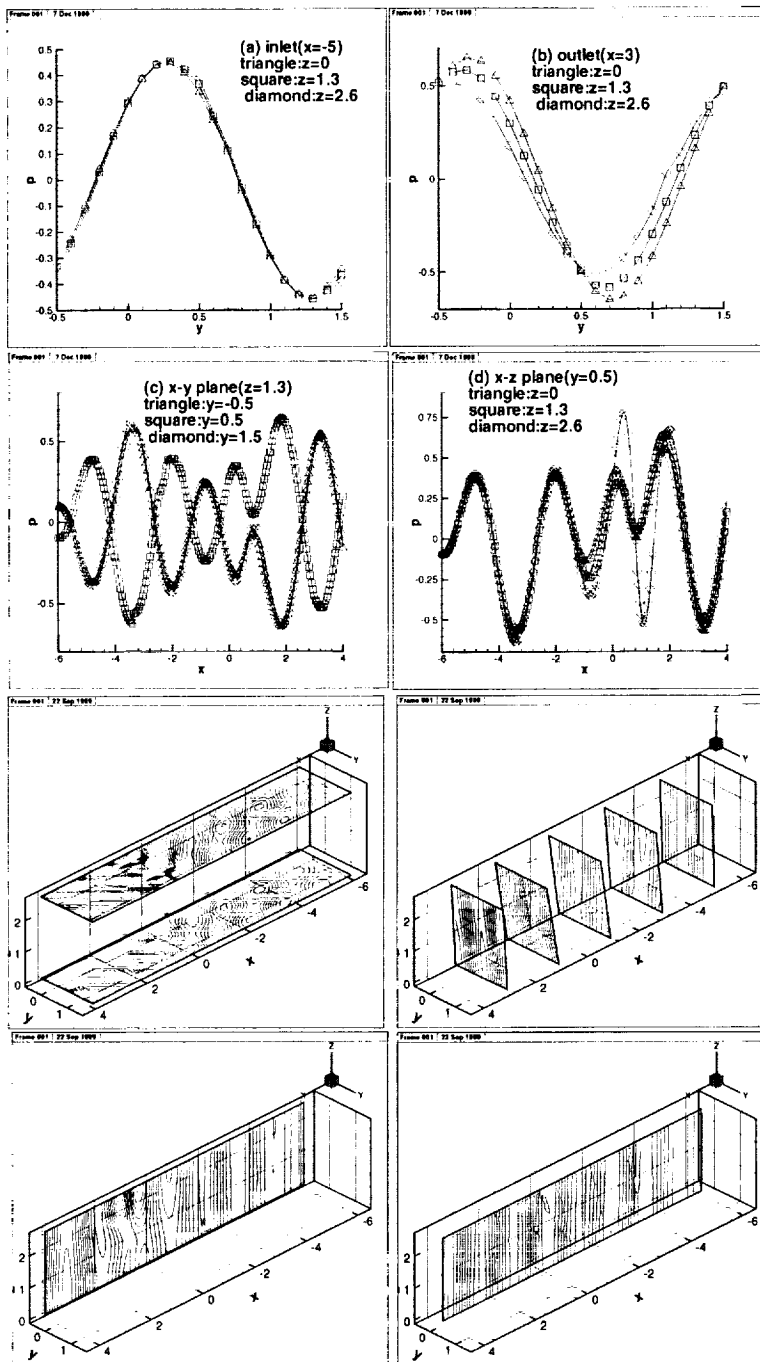
Figure 16: Acoustic pressure contours and distribution on x-y, x-z and y-z planes at $t = 82T$ for $10°$ sweep angle.
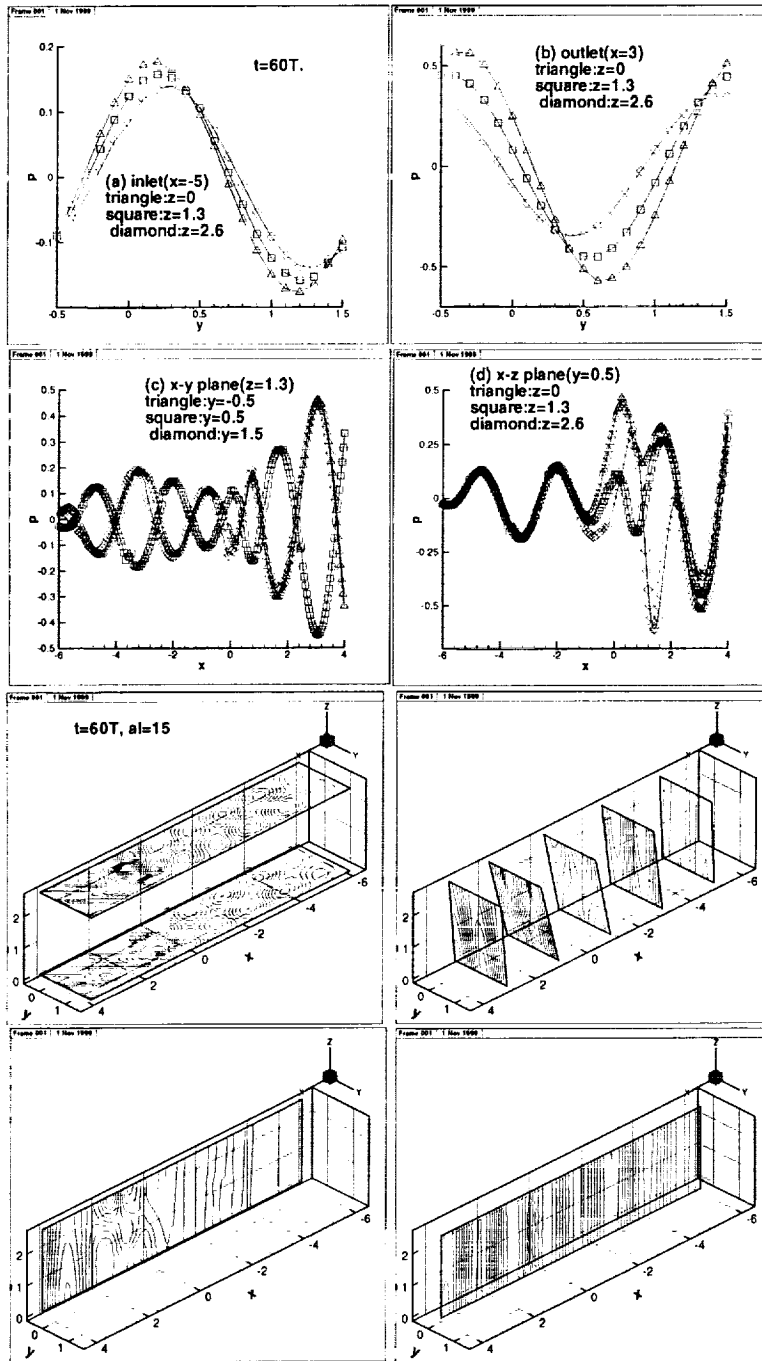
Figure 17: Acoustic pressure contours and distribution on x-y, x-z and y-z planes at $t = 60T$ for 15° sweep angle.
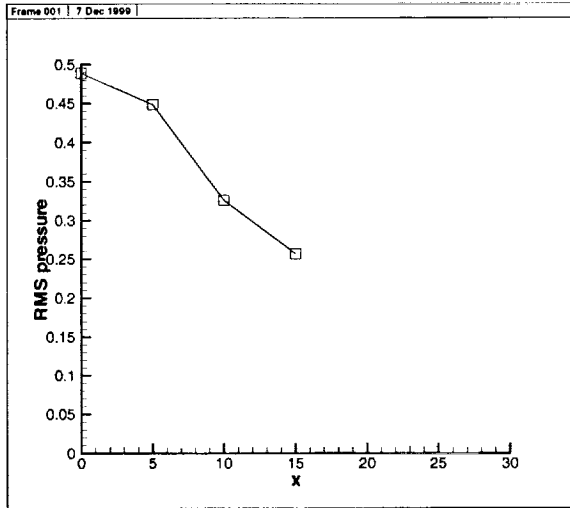
Figure 18: The RMS pressure versus the sweep angle in the range of $[0°, 15°]$.
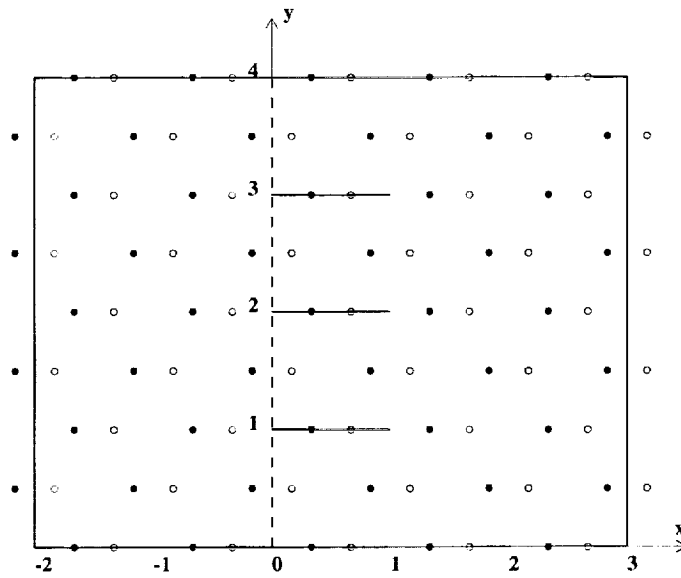
Figure 19: Schematic of computational domain and mesh used in the CE/SE method.

dashed line: x=[-2.8,3.8]; solid line: x=[-3.6,4.6]
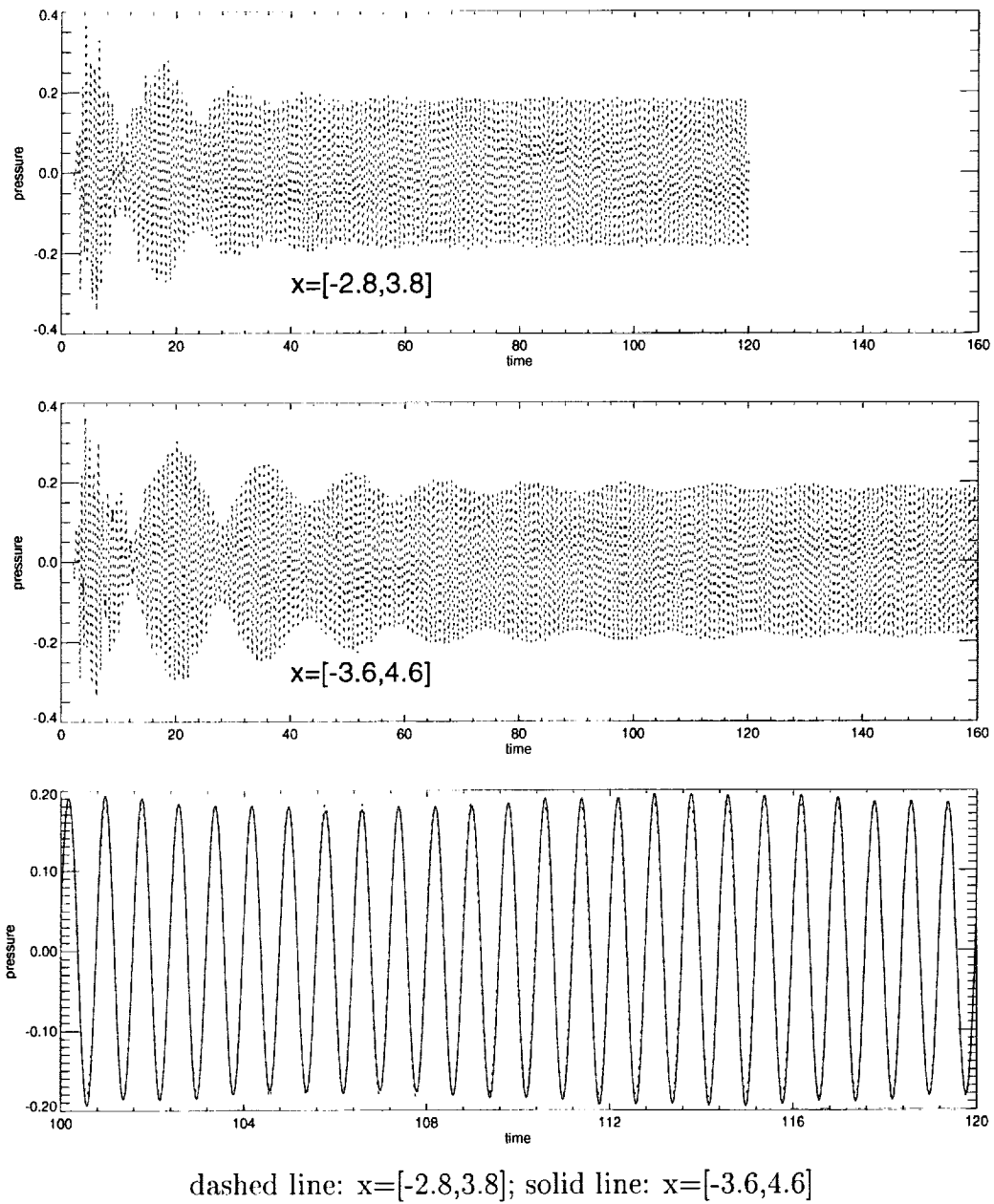
Figure 20: The time history of the acoustic pressure at an inlet point $(-2, \Delta y/2)$ using different computational domains(CFL=0.8).

dashed line: x=[-2.8,3.8]; solid line: x=[-3.6,4.6]
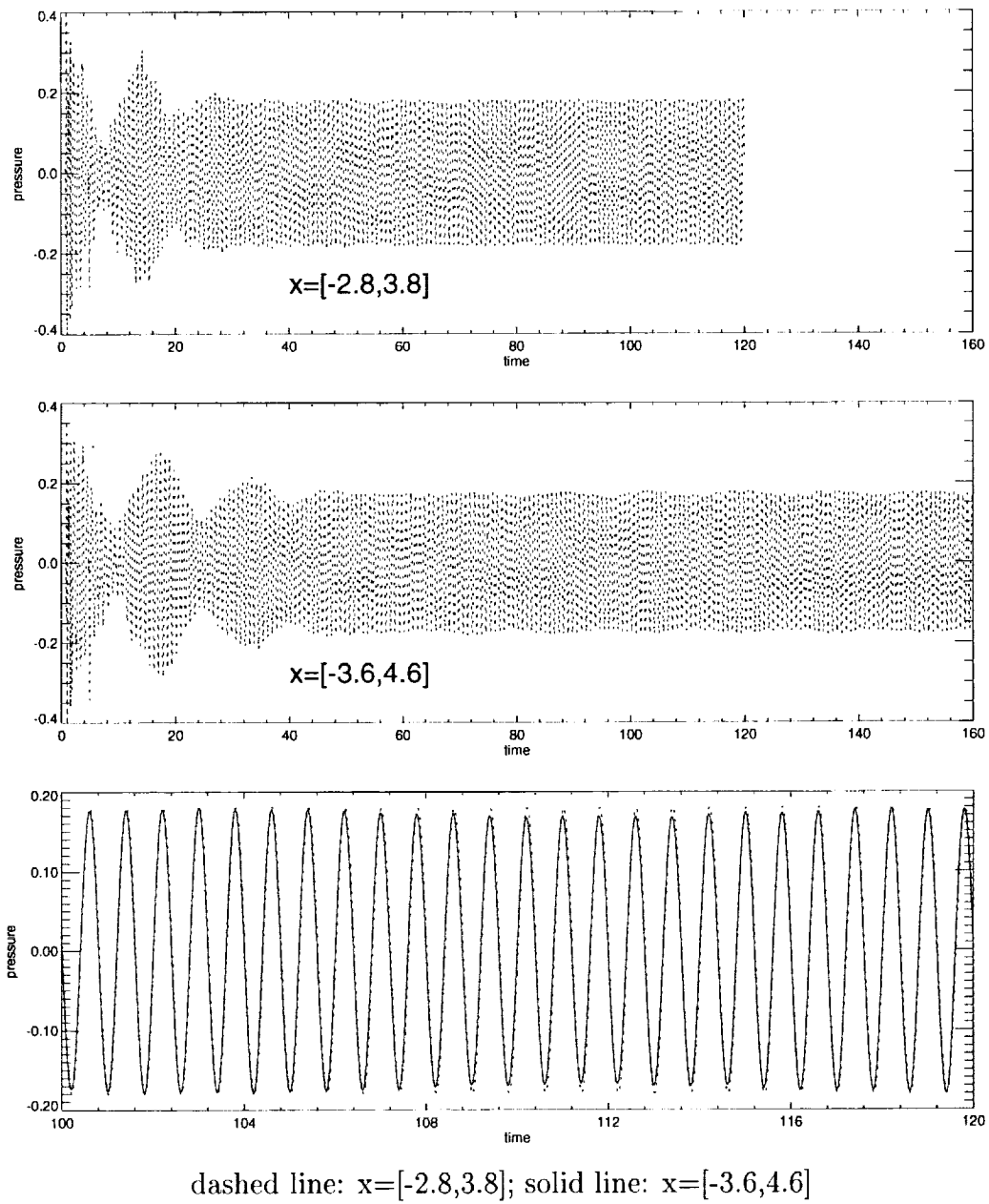
Figure 21: The time history of the acoustic pressure at an outlet point $(3, \Delta y/2)$ using different computational domains(CFL=0.8).

(a) Pressure difference on the airfoil surface

(a) x=-2   (b) x=3
(b) $\overline{p^2}$ at $x = -2$ and $x = 3$
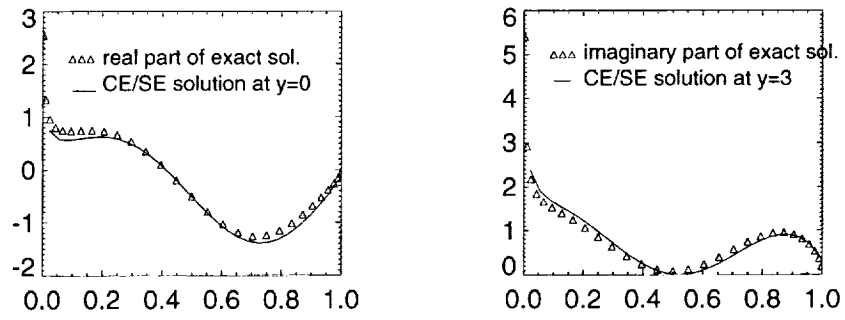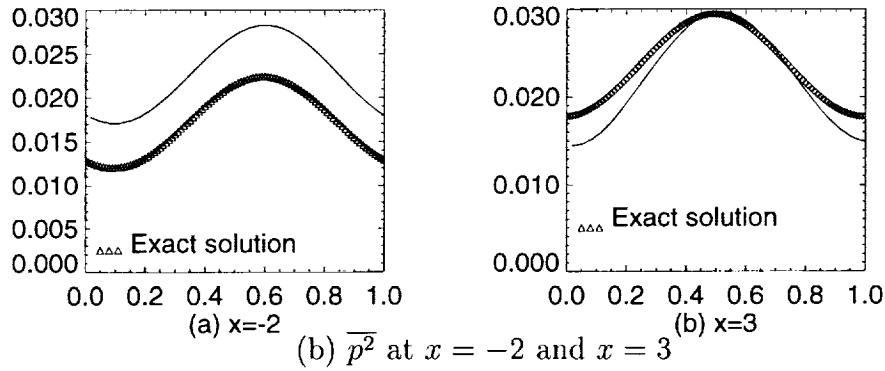
Figure 22: CE/SE solution at $t = 200T$ ($\epsilon = 0.2, \alpha = 0$, x=[-3.6,4.6]).
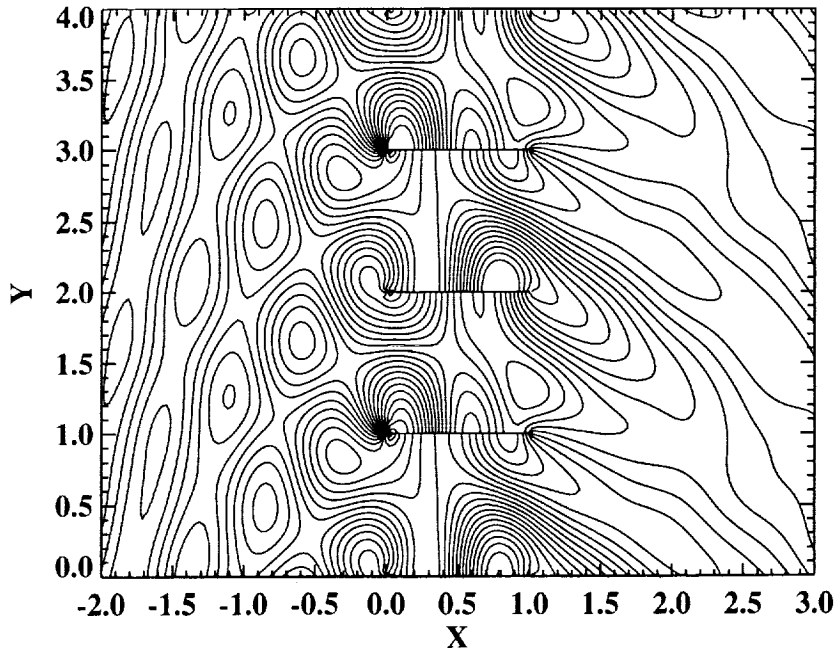
Figure 23: Computed pressure contour for the low frequency case (301x121, $\epsilon = 0.2, \alpha = 0$,x=[-2.8,3.8]).
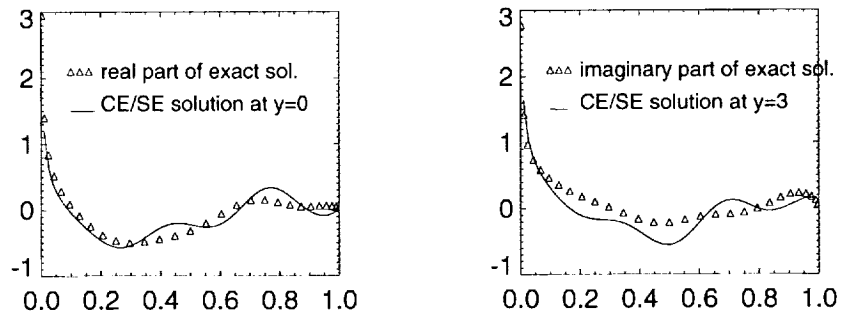
(a) Pressure difference on the airfoil surface
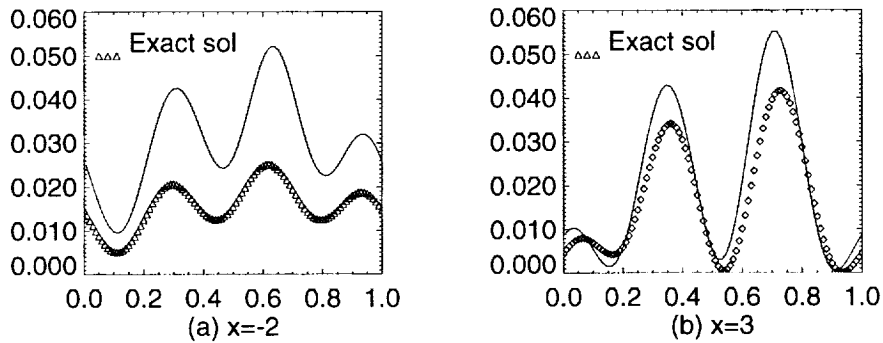
(b) $\overline{p^2}$ at $x = -2$ and $x = 3$
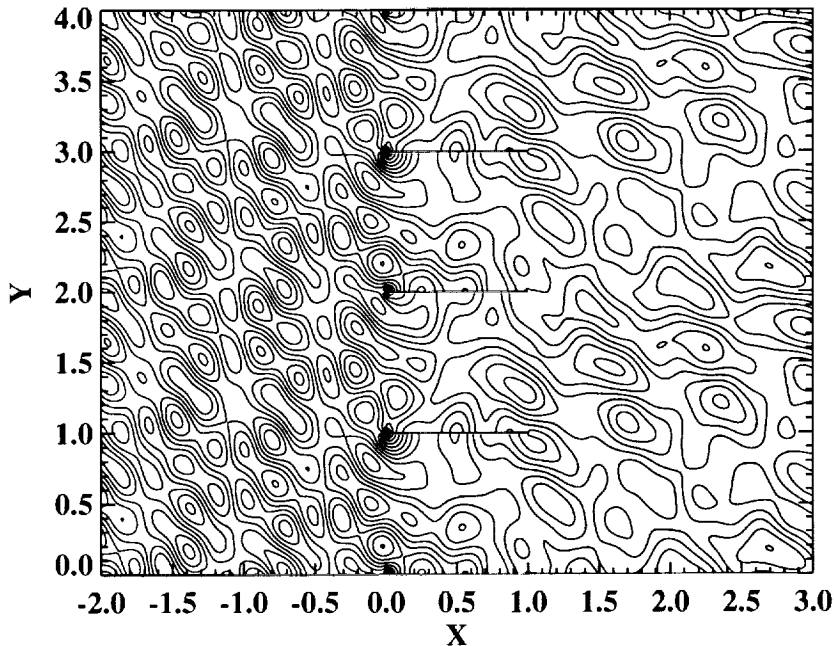
(c) Computed pressure contours at $t = 47T$

Figure 24: CE/SE solution for the high frequency case based on a 651x261 grid $(\epsilon = 0.2, \alpha = 0)$.
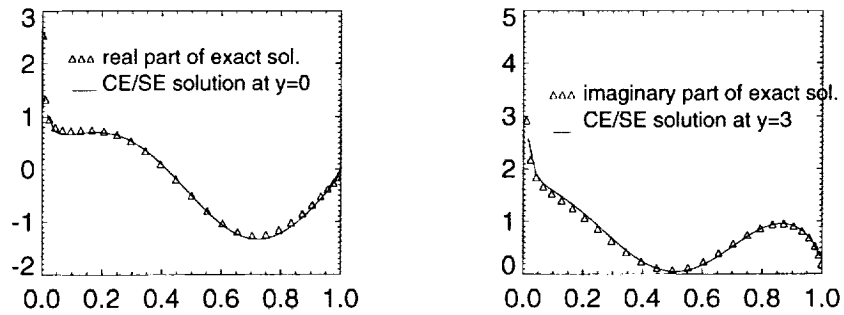
(a) Pressure difference on the airfoil surface

Scattered pressure contours with the moving aft part
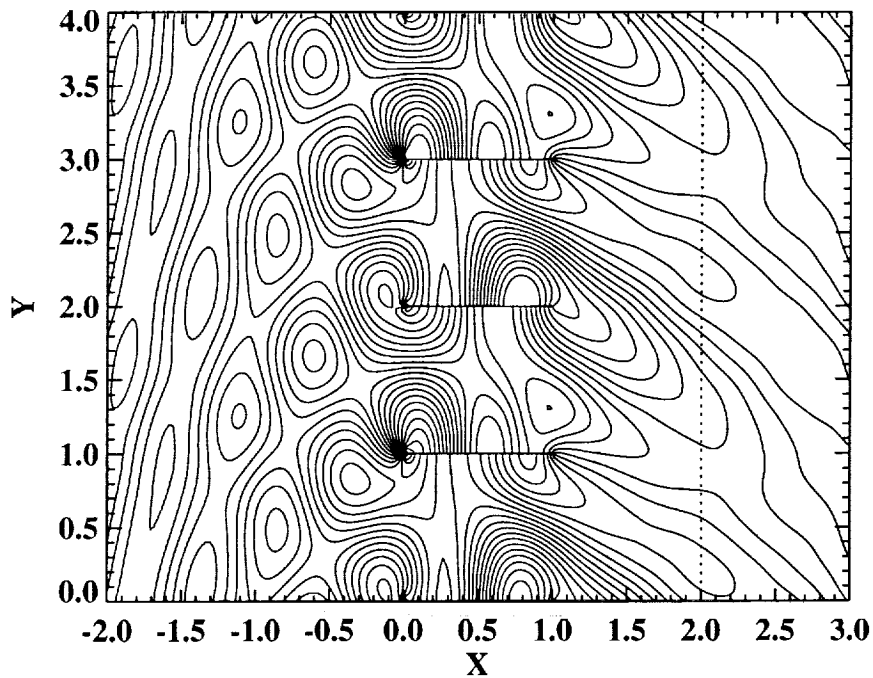
(b) Computed pressure contours at $t = 38T$

Figure 25: CE/SE solution for the low frequency case with a downstream moving grid based on a 401x241 grid ($\epsilon = 0.3, \alpha = 0$).

Pressure distribution at t=38T at y=0.5,1.5,2.5,3.5
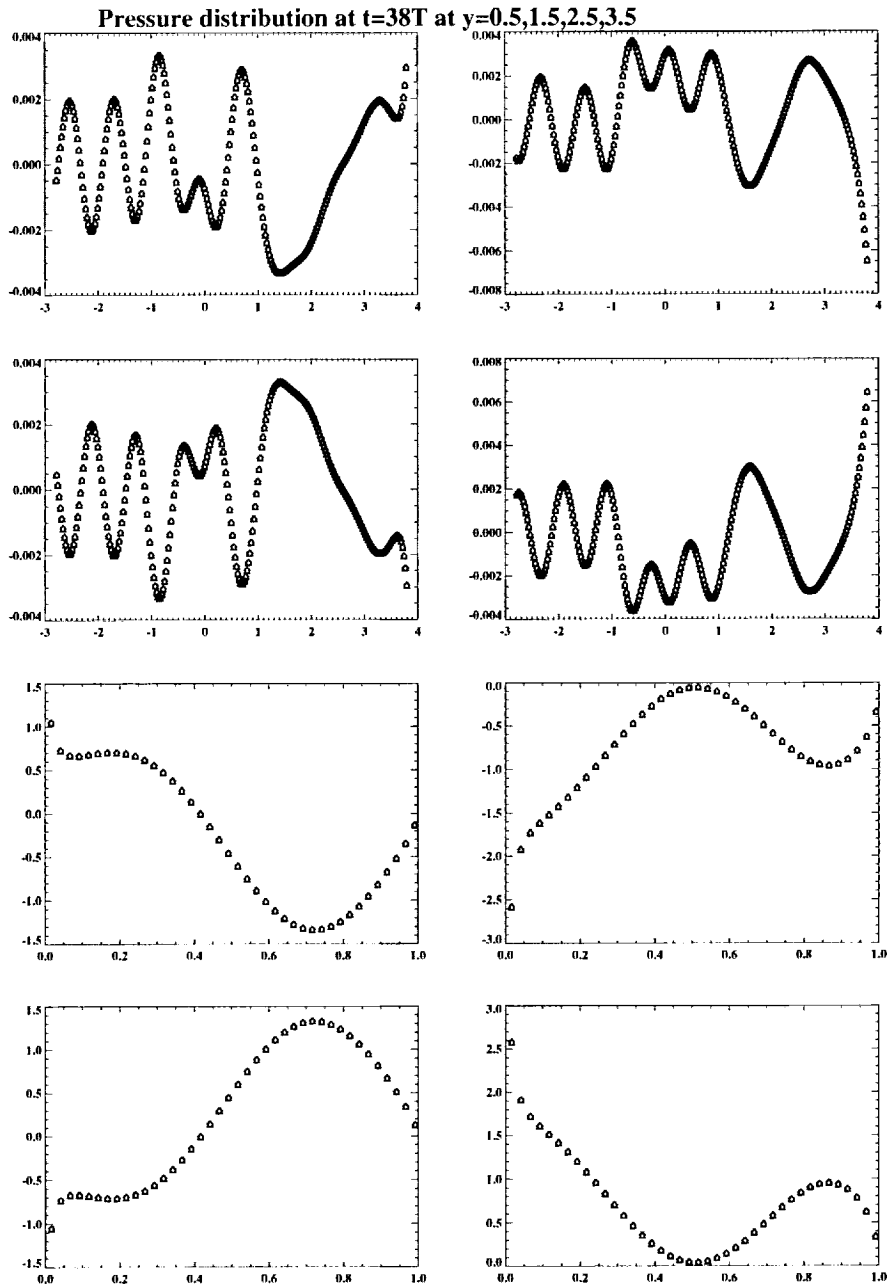
Figure 26: Comparison of the numerical solutions of problem 3 which has a downstream moving grid with those of problem 2(the lower four plots are the pressure difference across the flat plates).

ROTOR NOISE RADIATION
USING A FINITE ELEMENT METHOD

PATRICE MALBÉQUI, CHRISTOPHE PEYRET AND GEORGES ÉLIAS
ONERA, CFD AND AEROACOUSTICS DEPARTEMENT
BP 72, 92320 CHÂTILLON, FRANCE

INTRODUCTION

In Computational Aeroacoustics (CAA), most of the numerical techniques solve the Euler equations using an eulerian representation of the aerodynamic field. In addition, the efficient Dispersion-Relation-Preserving (DRP) finite difference scheme proposed by Tam [1] is usually applied for spatial discretization and the Runge-Kutta method is used for the time integration of the linearized Euler equation. In this paper, an alternative numerical technique is proposed. The fluid variables (i.e., pressure, velocity and density) are first expressed with a mixed eulerian-lagrangian representation, using the displacement vector. Such a representation leads to a second order propagation equation proposed by Galbrun [2]. This wave equation is established without any restriction on the flow, so that it can handle rotational flows. Moreover, it derives from a Lagrangian that provides exact flux energy as well as a straightforward finite element implementation. A finite element method (FEM) is under development at ONERA to solve the Galbrun equation. This paper presents the application of the FEM to the Benchmark Problem-Category 2 on ducted rotor noise, proposed in the third CAA Workshop[1]. The theoretical background of the Galbrun equation including the lagrangian formulation, acoustical energy and preliminary results of duct propagation are summarized in the first section. The modelization of the FEM for the Benchmark Problem on ducted rotor is described in the second Section. The third Section illustrates the results.

1. THEORETICAL BACKGROUND

This section briefly presents the theoretical formulation of the Galbrun equation. It first recalls the definition of the displacement vector and then gives the expression of the Galbrun equation, its lagrangian density and the acoustical intensity (energy flux density) expressed with the displacement. This section is to outline the formulation, but does not aim at providing demonstrations of the algebraic formula. More details can be found in [2-6].

1.1. **Acoustic displacement.** Consider an infinitesimal fluid element inside a flow: between dates t_0 and t_1, the element follows the path $x(t)$ resulting from the flow (solid line in Fig. 1). Now, reconsider the fluid element, inside the flow at same dates and suppose the presence of a disturbance: the element follows the path $y(t)$ resulting from the flow and the displacement caused by the disturbance (dashed line in Fig. 1). The displacement vector is defined as:

$$\xi(x, t) = y(t) - x(t).$$
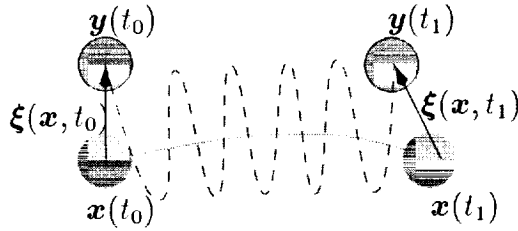
FIGURE 1. Displacement vector, $\boldsymbol{x}(t)$ is solid line and $\boldsymbol{y}(t)$ is dashed line.

The so-called mixed representation of acoustics, developed by Poirée [3] in 1985, uses the displacement vector to separate the acoustic perturbation inside the aerodynamic airflow.

1.2. Galbrun equation. Usually, the flow $(p_0, \rho_0, \boldsymbol{v}_0)$ and the perturbation $(p, \rho, \boldsymbol{v})$ are described with Euler variables. In the case of a small adiabatic perturbation ($p \ll p_0$, $\rho \ll \rho_0$ and $v \ll a_0$). Poirée shows that the usual eulerian variables, namely the acoustic pressure, density and velocity are related to the displacement:

(1)
$$\begin{cases} p = -\rho_0 a_0^2 \, \nabla . \, \boldsymbol{\xi} - \boldsymbol{\xi} . \, \nabla \, p_0 \\ \rho = -\rho_0 \, \nabla . \, \boldsymbol{\xi} - \boldsymbol{\xi} . \, \nabla \, \rho_0 \\ \boldsymbol{v} = \frac{d\boldsymbol{\xi}}{dt} - \boldsymbol{\xi} . \, \nabla \, \boldsymbol{v}_0 \end{cases} ,$$

where $d/dt = \partial/\partial t + \boldsymbol{v}_0 \, . \, \nabla$ is the total time derivative referred to the unperturbed flow. In practice, these relations show that when computing the displacement field with a FEM, it is possible to return to the standard eulerian pressure, velocity or density. Starting from the linearized Euler equations, using the lagrangian displacement and assuming acoustic propagation is isentropic (i.e $ds = 0$ in lagrangian system), the formulation of mass, momentum and energy continuity leads to the Galbrun equation:

(2)
$$G(\boldsymbol{\xi}) = \rho_0 \, \frac{d^2 \boldsymbol{\xi}}{dt^2} - \nabla \left(\rho_0 a_0^2 \, \nabla . \, \boldsymbol{\xi} \right) - \nabla \left(\boldsymbol{\xi} . \, \nabla \, p_0 \right) + \left(\boldsymbol{\xi} . \, \nabla \right) \nabla \, p_0 = 0 \, .$$

The Galbrun equation is a wave equation, based on the single displacement variable, established without any restriction on the flow. As mentioned by Poirée [7], using both the relations (1) and the Galbrun equation (2), few works attempted [8,9] to establish a wave equation based on single variable $(p, \rho, \boldsymbol{v})$, but the authors failed because algebraic expressions are too complex. Obviously, assuming an homogeneous medium, the Helmholtz equation for harmonic solution is directly retrieved.

1.3. Lagrangian formulation. Recently, a lagrangian density of the Galbrun equation was found by Élias [5]. Instead of expressing the lagrangian perturbation of the total energy of the flow (kinetic plus potential energy), an heuristic approach is proposed to formulate the lagrangian density. The lagrangian expression reads:

(3)
$$L(\boldsymbol{\xi}) = \frac{1}{2} \, \rho_0 \left(\frac{d\boldsymbol{\xi}}{dt} \right)^2 - \frac{1}{2} \, \rho_0 a_0^2 \left(\nabla . \, \boldsymbol{\xi} \right)^2 - \left(\boldsymbol{\xi} . \, \nabla \, p_0 \right) \nabla . \, \boldsymbol{\xi} - \frac{1}{2} \, {}^t\boldsymbol{\xi} \left[\nabla \nabla \, p_0 \right] \boldsymbol{\xi} \, .$$

Lagrangians satisfy the least action principle [10]. It states the integration in time and on the finite volume V_0 (whose envelope is S_0) of $L(\boldsymbol{\xi})$ is extremum:

(4)
$$\delta_\xi \int_{-\infty}^{\infty} \left(\iiint_{V_0} L(\boldsymbol{\xi}) \, dV \right) dt = 0 \, .$$

For the Lagrangian expression (3), it turns to:

$$(5) \qquad \int_{-\infty}^{\infty} \left(\iiint_{V_0} G(\boldsymbol{\xi}) . \delta\boldsymbol{\xi} \, dV + \iint_{S_0} b(\boldsymbol{\xi}) . \delta\boldsymbol{\xi} \, dS \right) dt = 0 \,,$$

where:

$$(6) \qquad b(\boldsymbol{\xi}) = p \, \boldsymbol{n} + \rho_0 \, (\boldsymbol{v}_0 . \boldsymbol{n}) \, \frac{d\boldsymbol{\xi}}{dt} \,.$$

In pratice (5) associated with (6) is solved using a Finite Element Method (FEM). As a standard numerical technique, the FEM implementation is not described in this paper. The FEM leads to a large complex sparse linear system to solve the displacement at the mesh nodes.

1.4. **Acoustic power and intensity.** Conservative expressions of acoustic power and intensity were also derived by Élias [5] from the Lagrangian density (3) using properties of Lagrangians [10]. These expressions read:

$$(7) \qquad w = \frac{\rho_0}{2} \frac{d\boldsymbol{\xi}}{dt} . \frac{d\boldsymbol{\xi}}{dt} - \rho_0 \frac{d\boldsymbol{\xi}}{dt} . (\boldsymbol{v}_0 . \nabla \boldsymbol{\xi}) + \frac{1}{2\rho_0 a_0^2} \left[p^2 - (\boldsymbol{\xi} . \nabla p_0)^2 \right] \,,$$

$$(8) \qquad \boldsymbol{i} = \rho_0 \left(\frac{\partial\boldsymbol{\xi}}{\partial t} . \frac{d\boldsymbol{\xi}}{dt} \right) \boldsymbol{v}_0 + p \, \frac{\partial\boldsymbol{\xi}}{\partial t} \,.$$

with:

$$(9) \qquad \frac{\partial w}{\partial t} + \nabla . \boldsymbol{i} = 0 \,.$$

The same expressions were also established by Godin [4] using the reciprocity principle in non uniform flow. In contrast with usual formulations based on eulerian variables, these expressions satisfy the energy conservation law (9) without any additional source terms. Although the intensity in equation (8) can not be expressed with the acoustic velocity, its accuracy has been proved for basic duct problems including high subsonic shear flows (Mach number up to 0.9), in the low frequency range.

1.5. **Preliminary Results.** In the case of acoustic propagation in a circular lined duct in the presence of a shear flow, the Galbrun solution is computed with the FEM and compared to the exact solution obtained by the resolution of the Lilley equation. Both real parts of the pressure field solutions are plotted in figure 2 and are found in good agreement. The in-duct flow is similar to the one used by Eversman for duct acoustics studies [11]. This result illustrates the capability of the Galbrun equation to handle rotational flows. More details about the validation can be found in [12].

2. FEM MODELIZATION OF THE BENCHMARK PROBLEM ON DUCTED ROTOR

The Benchmark problem is detailed in the Proceedings of the third CAA workshop, so only the main variables are presented. The governing equations are the linearized Euler equations. The duct geometry is axisymetric with a constant radius b and rigid walls. The duct length from the rotor plane to the duct exit is $8b$. The distribution of rotating body force on the rotor plane is described with the mth-order Bessel function $J_m(\lambda_{m,N} r)$, where $\lambda_{m,N}$ is the Nth root of J'_m and N the radial mode number. A harmonic time dependence $\exp(-jm\Omega t)$ is assumed, where Ω is the rotational speed. No mean flow is considered in the fluid.
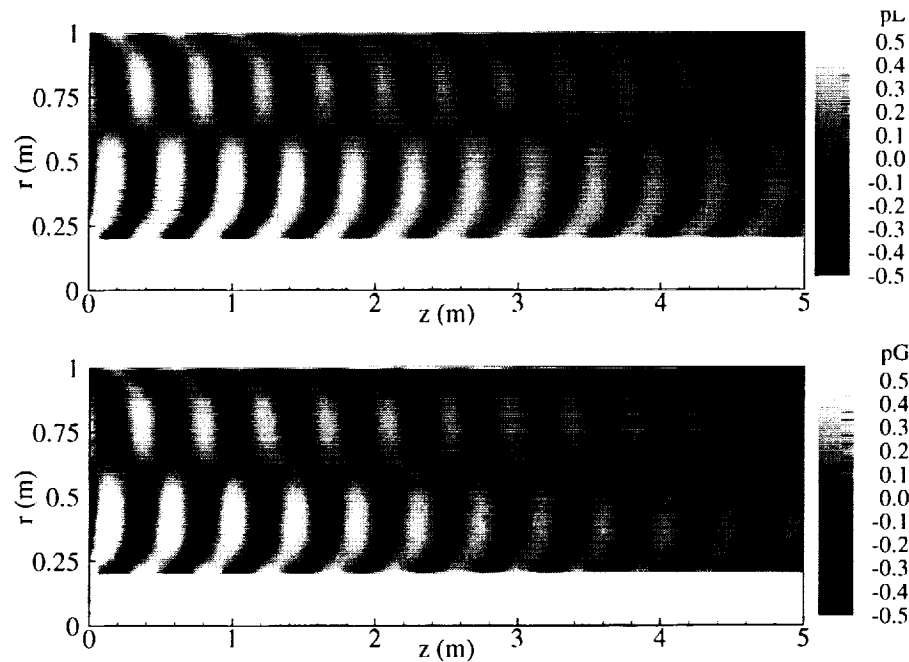
FIGURE 2. $\mathrm{Re}\,(p_{2,2}(r,z))$ at frequency 1350 Hz computed with Lilley equation on the upper plot and Galbrun equation on the lower plot. $M_0 = +0.5$, boundary layer thickness of the flow: 0.15 m, reduced impedance of the liner: $1 - j$.

2.1. Mesh.

For this FEM application, the formulation (5) is transformed into the frequency domain. The cylindrical coordinates (r, θ, z), with a $\exp(-jm\theta)$ dependence of the variables are also used to reduce the three-dimensional problem to a two-dimensional problem. Figure 3 shows the mesh of the fluid used for the computations. The fluid is meshed with non-structured linear elements. To obtain an accurate solution, the size of the elements is of the order of $\lambda/6$. In practice, for the frequencies to be considered, about 23 145 elements are required. Both the in-duct fluid and the fluid in free-field are meshed with conventional finite elements. The coupling between the FEM, with conventional elements in the duct and close to the exit, and the wave envelope technique [13] in the far-field is under development. The duct surface and the rotor plane are also meshed with linear elements (i.e., line segments for the two-dimensional modelization).

2.2. Boundary conditions.

At the duct entrance, $z = 0$, the acoustic pressure described by the mth order Bessel function is considered as the acoustical source. The corresponding values of the displacement is obtained using equations (1) in the absence of mean flow and the linearized Euler equations for the mass conservation:

$$\boldsymbol{\xi} = \begin{bmatrix} \xi_r \\ \xi_\theta \\ \xi_z \end{bmatrix} = \frac{1}{\rho_0 a_0^2 k^2} \begin{bmatrix} (\partial p/\partial r) \\ -j\frac{m}{r}p \\ -jk_z p \end{bmatrix},$$

where k_z is the axial wave number. On the rigid walls of the duct, the normal displacement is fixed to zero. Finally, on the boundary of the exterior domain, a non-reflective condition is needed to properly simulate the Sommerfeld radiation condition (i.e., to avoid numerical reflections). Using the Euler representation, an anechoic termination based on the wave impedance (the pressure over the normal acoustic velocity) can be used for this purpose. A similar condition is applied with the displacement
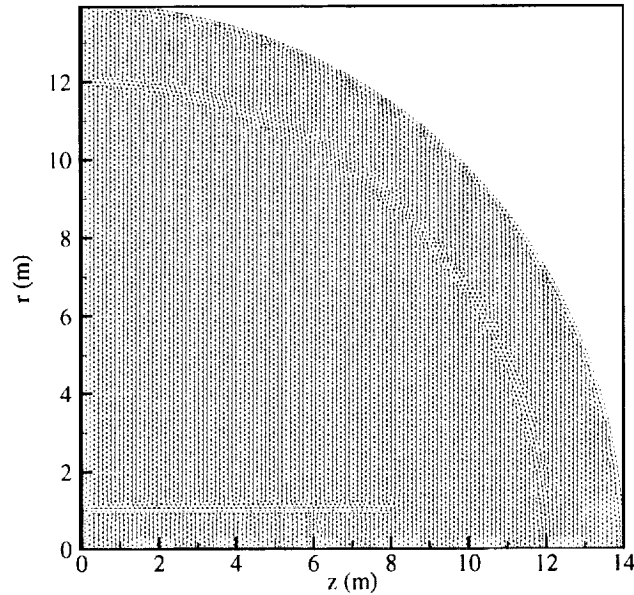
FIGURE 3. Meshing of the geometry

variable using equations (1) together with the linearized Euler equations:

$$b = j\rho_0\, m\Omega \underbrace{\begin{bmatrix} v_0 & & \\ & v_0 & \\ & & \Omega/k_z \end{bmatrix}}_{Z} \boldsymbol{\xi} \, .$$

3. RESULTS

The two rotational speeds $\Omega = 0.85$ (subsonic tip speed) and $\Omega = 1.15$ (supersonic tip speed) are proposed in the Benchmark Problem, with an 8-blade rotor ($m = 8$). Note that Ω is a nondimensional variable with respect to the ambient sound speed and the duct radius. Using the standard modal analysis of the duct acoustics, the in-duct pressure is:

$$p(r, \theta, z, t) = \mathrm{J}_m(\lambda_{m,N} r) \exp[-j(m\Omega t - m\theta + k_z z)] \, ,$$

and the dispersion relation is:

$$k^2 = k_T^2 + k_z^2 \, ,$$

where k is the total wave number ($k = m\Omega$), k_T is the transverse wave number and k_z is the axial wave number. In case of rigid walls, the transverse wave number is equal to $\lambda_{m,N}$. For the two rotational speed $\Omega = 0.85$ and 1.15, k_z is purely imaginary and equals $j6.84$ and $j2.9$, respectively. The mode ($m = 8$, $N = 1$) at these frequencies is evanescent. The attenuation, in decibels, of the sound pressure level along the duct is $20/\log_{10} \mathrm{Im}(k_z)$. At the speed $\Omega = 0.85$ and 1.15, the attenuation is 60 dB and 25 dB per radius, respectively. Many computations have been performed using several meshes to propagate the induct pressure field. However, at present time, the FEM does not provide suitable results for these configurations, including strongly cut-off frequencies. Keeping the same duct geometry and the same mode number ($m = 8$, $N = 1$), additional FEM computations have been performed for a cut-on frequency, $\Omega = 1.7$, corresponding to $k_z = 9.87$. The real part of the pressure field and its amplitude are plotted in 4. As expected, for a propagating spinning mode, at a fixed radius, the amplitude is

constant in the duct. Moreover, the radiated field is characterized by a main lobe around the angular location $\phi = 45$ degrees. This result is in agreement with the Taylor and Sofrin prediction [14], where the angular location is given by $\sin \phi = k_T/k$.
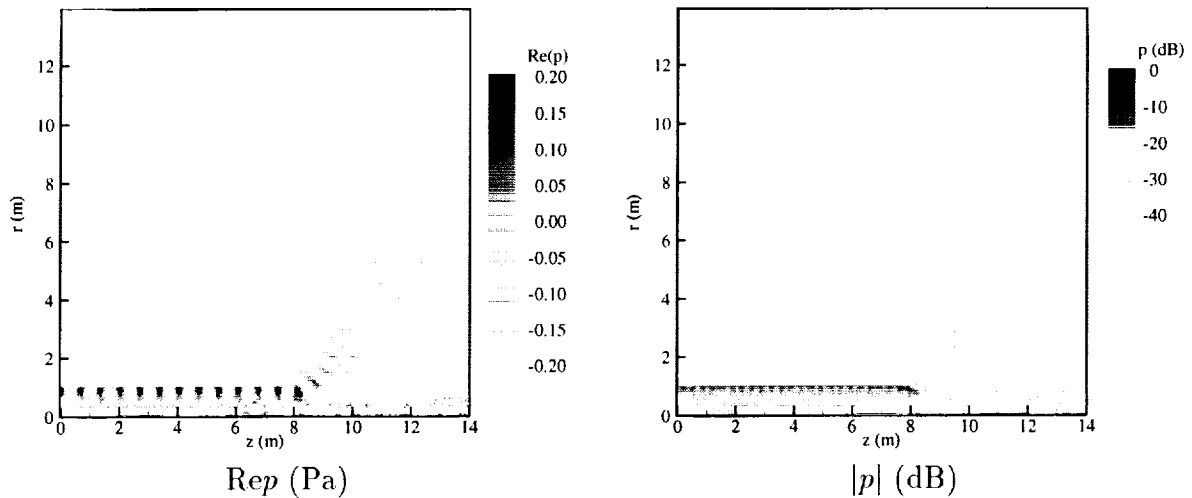
FIGURE 4. Supersonic tip speed $\Omega = 1.70$, ducted rotor

4. CONCLUSION

The FEM based on the Galbrun equation is an attractive technique to solve the linearized Euler equations. In contrast with other wave propagation equations, this equation is established without any restriction on the flow. This is of interest to solve many CAA problems. In this paper, the FEM has been applied to the ducted rotor noise configuration, proposed in the Third Computational Aeroacaoustics Workshop on Benchmark Problems. At present time, the FEM fails to predict the far-field pressure for the strongly cut-off frequencies. On the other hand, keeping the mode number and the duct geometry, the FEM provides results in good agreement with the modal approach, for cut-on frequencies.

REFERENCES

[1] C.W. Tam and J.C. Webb. Dispersion-relation-preserving finite difference schemes for computational acoustics. *J. Computaional Phys.*, 107:262–281, 1993.

[2] H. Galbrun. *Propagation d'une onde sonore dans l'atmosphère et théorie des zones de silence.* Gauthier-Villars, Paris, 1931.

[3] B. Poirée. Les équations de l'acoustique linéaire et non linéaire dans un écoulement de fluide parfait. *Acustica*, 57:5–25, 1985.

[4] O. A. Godin. Reciprocity relations and energy conservation for waves in the system: Inhomogeneous fluid flow-anisotropic solid body. *Acoustical Physics*, 43(6):688–693, 1996.

[5] G. Elias. Acoustic energy and intensity in a non uniform flow. *Acta Acustica*, Submitted.

[6] C. J. Peyret. Acoustic propagation in presence of an arbitrary flow. *Journal of the acoustical Society of America*, 103(5):2840, May 1998.

[7] B. Poirée. Représentation lagrangienne et eulérienne de l'acoustique linéaire et non linéaire. *Journal de Physique*, 40(11), 1979.

[8] J. L. Kerrebrock. Waves and wakes in turbomachine annuli with swirl. *AIAA Paper*, (74-87), 1974.

[9] J. L. Kerrebrock. Small disturbances in turbomachine annuli with swirl. *AIAA Journal*, 15(794-803), 1977.

[10] P. M. Morse and H. Feshbach. *Methods of theorical physics.* McGraw-Hill Publishing Company, New York, 1953.

[11] W. Eversman and R. J. Beckemeyer. The transmission of sound in ducts with thin shear layers – convergence to the uniform flow case. *Journal of Acoustical Society of America*, 52:216–220, 1972.

[12] C.J. Peyret, P. Malbéqui, and G. Elias. A finite element method based on the displacement for duct acoustics analysis. *Journal of the Acoustical Society of America*, Submitted.

[13] I. Danda Roy and W. Eversman. Improved finite element modeling of the turbofan engine inlet radiation problem. *Journal of Vibration and Acoustics*, 117:109–115, 1995.

[14] J.M. Tyler and T.G. Sofrin. Axial flow compressor noise studies. *Society of automotive Engineers Transactions*, 70:306–332, 1962.

Results of Benchmark Problems
for the Third Computational Aeroacoustics Workshop

Fang Q. Hu
Department of Mathematics and Statistics
Old Dominion University, Norfolk, VA 23529
E-mail: fang@math.odu.edu

Introduction

Numerical results for problems in Category 1, 2 and 5 are presented. Due to high resolution requirements of these problems, high-order finite difference schemes are used. Both the spatial and temporal discretizations have been optimized for obtaining low dissipation and low dispersion errors in computation. In addition, Perfectly Matched Layers (PML) are used at all non-reflecting boundaries encountered in Categories 2 and 3. The schemes used in the present work are modified from those for the benchmark problems in the previous two CAA workshops [1,2]. Further details of the algorithms are referred to [1] and [2].

Propagation of sound waves through transonic nozzle

In this problem, an acoustic wave is introduced at the nozzle exit region and the sound wave that travels upstream through the transonic nozzle is to be calculated. The amplitude of the incoming sound wave is 10^{-5}, which is very small compared to the mean values of the flow. The nozzle flow is modeled by the one-dimensional Euler equations with variable nozzle area. In the present work, the acoustic wave will be computed directly by solving the non-linear governing equations, rather than solving the linearized equations. This makes it harder to compute the acoustic waves. The challenge is whether the small amplitude wave can still be captured in the computation.

The governing equations are

$$\frac{\partial \rho}{\partial t} + u\frac{\partial \rho}{\partial x} + \rho\frac{\partial u}{\partial x} + \frac{\rho u}{A}\frac{\partial A}{\partial x} = 0 \tag{1}$$

$$\frac{\partial u}{\partial t} + u\frac{\partial u}{\partial x} + \frac{1}{\rho}\frac{\partial p}{\partial x} = 0 \tag{2}$$

$$\frac{\partial p}{\partial t} + u\frac{\partial p}{\partial x} + \gamma p\frac{\partial u}{\partial x} + \frac{\gamma p u}{A}\frac{\partial A}{\partial x} = 0 \tag{3}$$

where ρ is the density, u is the velocity and p is the pressure. A in (1)-(3) is the nozzle area and is a function of x given by

$$A(x) = \begin{cases} 0.536572 - 0.19808e^{-(\ln 2)\left(\frac{x}{0.6}\right)^2}, & x > 0 \\ 1.0 - 0.661514e^{-(\ln 2)\left(\frac{x}{0.6}\right)^2}, & x < 0 \end{cases}$$

The computational domain is $-10 \leq x \leq 10$. An upstream propagating wave with very small amplitude is introduced at the nozzle exit region in the form of

$$
\begin{bmatrix} \rho \\ u \\ p \end{bmatrix}_{acoustic} = 10^{-5} \begin{bmatrix} 1 \\ -1 \\ 1 \end{bmatrix} \cos \left[\omega \left(\frac{x}{1-M} + t \right) \right] \tag{4}
$$

When propagating upstream, part of the wave will be reflected at the nozzle throat and the other part is transmitted which travels to the left and leaves the inlet region of the nozzle. The mean values at the exit region are given,

$$
\bar{\rho}_{exit} = 1.0, \quad \bar{u}_{exit} = 0.4, \quad \bar{p}_{exit} = 1/\gamma
$$

To solve (1)-(3), boundary conditions are needed at the nozzle inlet and exit. At the inlet, there is a only left traveling wave and at the exit, there are left traveling incoming wave (given in (4)) and its reflection by the nozzle throat, a right traveling wave. The necessary numerical boundary conditions can be obtained in several ways. One approach is to rewrite the non-linear equations (1)-(3) in characteristics form and add the incoming wave as source terms [3, 4, 5]. In the present work, we derived the boundary equations based on the characteristics of the linearized equations of (1)-(3) since the wave amplitude is very small. We note that the linearization is only applied at the exit and inlet regions where the nozzle area is constant.

let

$$
\rho = \bar{\rho} + \rho'
$$

$$
u = \bar{u} + u'
$$

$$
p = \bar{p} + p'
$$

where an overbar indicates the time-independent mean value. Since now $A = constant$, we linearize equations (1)-(3) and write in the matrix form,

$$
\frac{\partial}{\partial t} \begin{pmatrix} \rho' \\ u' \\ p' \end{pmatrix} + \begin{pmatrix} \bar{u} & \bar{\rho} & 0 \\ 0 & \bar{u} & \frac{1}{\bar{\rho}} \\ 0 & \gamma\bar{p} & \bar{u} \end{pmatrix} \frac{\partial}{\partial x} \begin{pmatrix} \rho' \\ u' \\ p' \end{pmatrix} = 0 \tag{5}
$$

The coefficient matrix can be easily diagonalized,

$$
\frac{\partial}{\partial t} \begin{pmatrix} \rho' \\ u' \\ p' \end{pmatrix} + \begin{pmatrix} 1 & \frac{\bar{\rho}}{\gamma\bar{p}} & \frac{\bar{\rho}}{\gamma\bar{p}} \\ 0 & \frac{\bar{\rho}}{\bar{\rho}\bar{a}} & -\frac{1}{\bar{\rho}\bar{a}} \\ 0 & 1 & 1 \end{pmatrix} \begin{pmatrix} \bar{u} & 0 & 0 \\ 0 & \bar{u}+\bar{a} & 0 \\ 0 & 0 & \bar{u}-\bar{a} \end{pmatrix} \begin{pmatrix} 1 & 0 & -\frac{\bar{\rho}}{\gamma\bar{p}} \\ 0 & \frac{\bar{\rho}\bar{a}}{2} & \frac{1}{2} \\ 0 & -\frac{\bar{\rho}\bar{p}}{2} & \frac{1}{2} \end{pmatrix} \frac{\partial}{\partial x} \begin{pmatrix} \rho' \\ u' \\ p' \end{pmatrix} = 0 \tag{6}
$$

where $\bar{a} = \sqrt{\frac{\gamma\bar{p}}{\bar{\rho}}}$ is the speed of sound and $\bar{u}, \bar{u}+\bar{a}, \bar{u}-\bar{a}$ are the eigenvalues.

Boundary conditions can now be formulated using (6). At the inlet, let

$$
\rho = \bar{\rho}_{inlet} + \rho'
$$

$$
u = \bar{u}_{inlet} + u'
$$

$$
p = \bar{p}_{inlet} + p'
$$

where ρ', u', p' are the out-going (traveling to the left) waves. The equations for ρ', u', p' are found by keeping only the negative eigenvalue in the characteristics form (6), namely $\bar{u} - \bar{a}$. It follows that

$$\frac{\partial \rho'}{\partial t} - \frac{(\bar{u}_{inlet} - \bar{a}_{inlet})\bar{\rho}_{inlet}}{2\bar{a}_{inlet}}\frac{\partial u'}{\partial x} + \frac{\bar{u}_{inlet} - \bar{a}_{inlet}}{2\bar{a}_{inlet}^2}\frac{\partial p'}{\partial x} = 0 \tag{7}$$

$$\frac{\partial u'}{\partial t} + \frac{\bar{u}_{inlet} - \bar{a}_{inlet}}{2}\frac{\partial u'}{\partial x} - \frac{\bar{u}_{inlet} - \bar{a}_{inlet}}{2\bar{\rho}_{inlet}\bar{a}_{inlet}}\frac{\partial p'}{\partial x} = 0 \tag{8}$$

$$\frac{\partial \rho'}{\partial t} - \frac{(\bar{u}_{inlet} - \bar{a}_{inlet})\bar{\rho}_{inlet}\bar{a}_{inlet}}{2}\frac{\partial u'}{\partial x} + \frac{\bar{u}_{inlet} - \bar{a}_{inlet}}{2}\frac{\partial p'}{\partial x} = 0 \tag{9}$$

Similarly, at the outlet, we decompose the variables as

$$\rho = \bar{\rho}_{exit} + \rho_a + \rho'$$

$$u = \bar{u}_{exit} + u_a + u'$$

$$p = \bar{p}_{exit} + p_a + p'$$

where ρ_a, u_a and p_a are the incoming wave as specified in (4) and ρ', u' and p' represent the right traveling out-going wave (reflection by the nozzle throat). By only keeping positive eigenvalues in the characteristics equations (6), namely $\bar{u}$ and $\bar{u} + \bar{a}$, we get following equations,

$$\frac{\partial \rho'}{\partial t} + \bar{u}_{exit}\frac{\partial \rho'}{\partial x} + \frac{(\bar{u}_{exit} + \bar{a}_{exit})\bar{\rho}_{exit}}{2\bar{a}_{exit}}\frac{\partial u}{\partial x} - \frac{\bar{u}_{exit} - \bar{a}_{exit}}{2\bar{a}_{exit}^2}\frac{\partial p'}{\partial x} = 0 \tag{10}$$

$$\frac{\partial u'}{\partial t} + \frac{\bar{u}_{exit} + \bar{a}_{exit}}{2}\frac{\partial u'}{\partial x} + \frac{\bar{u}_{exit} + \bar{a}_{exit}}{2\bar{\rho}_{exit}\bar{a}_{exit}}\frac{\partial p'}{\partial x} = 0 \tag{11}$$

$$\frac{\partial p'}{\partial t} + \frac{(\bar{u}_{exit} + \bar{a}_{exit})\bar{\rho}_{exit}\bar{a}_{exit}}{2}\frac{\partial u'}{\partial x} + \frac{\bar{u}_{exit} + \bar{a}_{exit}}{2}\frac{\partial p'}{\partial x} = 0 \tag{12}$$

In the present calculation, Euler equations (1)-(3) are applied in $-8 < x < 8$. The inlet and exit boundary conditions, (7)-(9) and (10)-(12), are applied in $-10 \leq x \leq -8$ and $8 \leq x \leq 10$ respectively, as shown in Figure 1. The partitioning for these domains is somewhat arbitrary, so long as the nozzle areas are constant inside the boundary zones.

The spatial discretizations is carries out using a non-uniform grid with $\Delta x_{min} = 0.0125$ and $\Delta x_{max} = 0.1$ and a total of 381 grid points. The central differencing scheme used is the same as that of [6]. The time integration is carried out by the Low Dissipation and Low-Dispersion Runge-Kutta scheme (LDDRK56 [7]) with a time step $\Delta t = 0.0076$.

The initial values of the density, velocity and pressure are formed by a simple linear distribution, as shown in Figure 2 in dashed lines. As time increases, the solution adjusts itself for the given nozzle shape and mean values at the inlet and exit. The solid line in Figure 2 show the the density, velocity and pressure distribution at $t = 200$. Figure 3 shows a time sequence of the pressure distribution.This is to demonstrate that the transient responses propagate out of the computational domain very effectively. Figure 4 shows the pressure as a

function of time at x=-8, 0 and 8 respectively. Clearly, time periodic solution is reached after about $t = 100$. In the present calculation, the acoustic wave is computed directly from the non-linear equations (1)-(3) and together with the mean flow. It shows that despite the small amplitude of the wave, the scheme can still capture the wave. After subtracting the mean value, the acoustic wave is found and the wave envelope is shown in Figure 5.

Shock-Sound Interaction

In this problem, the pressure at the exit is specified such that a shock is formed inside the nozzle. The mean velocity at the inlet is now given as $\bar{u}_{inlet} = 0.2006533$ and the pressure at the exit is ,

$$\bar{p}_{exit} = 0.6071752$$

The governing equations are the same as that in the previous section, namely (1)-(3). An incoming wave is given in the inlet in the form of

$$\begin{bmatrix} \rho \\ u \\ p \end{bmatrix}_{acoustic} = 10^{-5} \begin{bmatrix} 1 \\ 1 \\ 1 \end{bmatrix} \sin\left[\omega\left(\frac{x}{1+M} - t\right)\right]$$

Numerically, this problem is solved in a similar manner as in the previous one. At the inlet region, we let

$$\begin{bmatrix} \rho \\ u \\ p \end{bmatrix} = \begin{bmatrix} \bar{\rho}_{inlet} \\ \bar{u}_{inlet} \\ \bar{p}_{inlet} \end{bmatrix} + \begin{bmatrix} \rho_a \\ u_a \\ p_a \end{bmatrix} + \begin{bmatrix} \rho' \\ u' \\ p' \end{bmatrix}$$

and ρ', u' and p' are solved using (7)-(9). At the exit region, we let

$$\begin{bmatrix} \rho \\ u \\ p \end{bmatrix} = \begin{bmatrix} \bar{\rho}_{exit} \\ \bar{u}_{exit} \\ \bar{p}_{exit} \end{bmatrix} + \begin{bmatrix} \rho' \\ u' \\ p' \end{bmatrix}$$

and ρ', u' and p' are solved using (10)-(12).

Time history of pressure variation in x is shown in Figure 6 which exhibits in detail the formation of the shock. The final profiles of density, velocity and pressure are given Figure 7. Clearly, there are oscillations near the shock. Since a central difference scheme is used in the present calculation, the oscillations near the shock are not unexpected. Artificial dissipation terms have been introduced in the discretized equations. The magnitude of the artificial viscosity used at each grid point is set to be proportional to the maximum variation of the solution near the point. Again, non-uniform grids are used with $\Delta x_{min} = 0.003125$ and $\Delta x_{max} = 0.1$ with a total of 617 points. As a results, the oscillations near the shock are limited to a very narrow region as shown in Figure 7.

The emphasis of the current calculation is to see whether the small acoustic disturbance can still be accurately computed despite the inaccuracy near the shock. The results are satisfactory. Time periodic solutions are obtained after around $t = 80$ as shown in Figure 8 where pressure as a function of time at $x = -8$, 0

and 8 are given. The small acoustic wave is again captured directly from the non-linear equations (1)-(3). By subtracting the numerical solution by its mean value, wave envelop is found and shown in Figure 9. We see that despite the high spike of the wave near the shock, the transmitted and reflected sound waves are quite accurate.

Rotor Noise

In this problem, sound generated by an 8-blade rotor is simulated. Two cases are considered. The first is an open rotor and the second is a ducted rotor. The rotor is modeled by introducing forcing terms to the governing equations as specified in the problem,

$$
\begin{aligned}
\frac{\partial u}{\partial t} + \frac{\partial p}{\partial x} &= F_x \\
\frac{\partial v}{\partial t} + \frac{\partial p}{\partial r} &= F_r \\
\frac{\partial w}{\partial t} + \frac{1}{r}\frac{\partial p}{\partial \phi} &= F_\phi \\
\frac{\partial p}{\partial t} + \frac{\partial u}{\partial x} + \frac{\partial v}{\partial r} + \frac{v}{r} + \frac{1}{r}\frac{\partial w}{\partial \phi} &= 0
\end{aligned}
\tag{13}
$$

where the forcing terms are given as follows,

$$
\begin{pmatrix} F_x \\ F_r \\ F_\phi \end{pmatrix} = \mathbf{Re} \left\{ \begin{pmatrix} \mathbf{J_m}(\lambda_\mathbf{m}\mathbf{r})e^{-(\ln 2)(10x)^2} \\ 0 \\ \mathbf{J_m}(\lambda_\mathbf{m}\mathbf{r})re^{-(\ln 2)(10x)^2} \end{pmatrix} e^{im(\phi-\Omega t)} \right\}
$$

Here, m represents the number of blades. Equation (13) is further reduced to a 2-D problem by factoring out the ϕ dependency of the solution,

$$
\begin{bmatrix} u \\ v \\ w \\ p \end{bmatrix} = Re \left\{ \begin{bmatrix} \tilde{u} \\ \tilde{v} \\ \tilde{w} \\ \tilde{p} \end{bmatrix} e^{im\phi} \right\}
$$

and we get, in complex variables,

$$
\begin{aligned}
\frac{\partial \tilde{u}}{\partial t} + \frac{\partial \tilde{p}}{\partial x} &= S(r)e^{-(\ln 2)(10x)^2}e^{-im\Omega t} \\
\frac{\partial \tilde{v}}{\partial t} + \frac{\partial \tilde{p}}{\partial r} &= 0 \\
\frac{\partial \tilde{w}}{\partial t} + \frac{im\tilde{p}}{r} &= rS(r)e^{-(\ln 2)(10x)^2}e^{-im\Omega t} \\
\frac{\partial \tilde{p}}{\partial t} + \frac{\partial \tilde{u}}{\partial x} + \frac{\partial \tilde{v}}{\partial r} + \frac{\tilde{v}}{r} + \frac{im\tilde{w}}{r} &= 0
\end{aligned}
\tag{14}
$$

where

$$
S(r) = \begin{cases} \mathbf{J_m}(\lambda_\mathbf{mN}r), & r \leq 1 \\ 0, & r > 1 \end{cases}
$$

in which $\mathbf{J_m}$ is the Bessel function of order m and $\lambda_\mathbf{mN}$ is the Nth root of $\mathbf{J'_m}$. For the problem specified, m = 8 and N = 1 and $\lambda_{8,1} = 9.64742$.

Open Rotor

For the open rotor case, the computational domain of $[-9, 9] \times [0, 9]$ is shown in Figure 10. Spatial derivatives in (14) are discretized by a 7-point optimized central difference scheme (as in the DRP scheme [5]) using a uniform grid of $\Delta x = \Delta y = 0.05$. The time integration is carried out by the Low-Dissipation and Low-Dispersion Runge-Kutta scheme (LDDRK56 [7]) with a time step $\Delta t = 0.025$. In addition, a tenth-order explicit filter is applied throughout the computational domain [2,9].

Perfectly Matched Layer (PML) equations are used at non-reflecting boundaries of the problem shown in Figure 10. The width of the PML domain is 1. Inside the PML domain, the pressure $\tilde{p}$ is split into two parts and the following equations are solved:

$$\tilde{p} = \tilde{p}_1 + \tilde{p}_2$$

$$\frac{\partial \tilde{p}_1}{\partial t} + \sigma_x \tilde{p}_1 + \frac{\partial \tilde{u}}{\partial x} = 0$$

$$\frac{\partial \tilde{p}_2}{\partial t} + \sigma_r \tilde{p}_2 + \frac{\partial \tilde{v}}{\partial r} + \frac{\tilde{v}}{r} + \frac{im\tilde{w}}{r} = 0$$

in which σ_x and σ_r are the absorption coefficients introduced for absorbing the waves that enter the PML domain. The choice of the absorption coefficients follows a "matched" manner [8, 9]. At the right and the left PML domains in Figure 9, $\sigma_r = 0$ and at the top PML domain, $\sigma_x = 0$. At the corner regions, both coefficients are not zero. Specifically, the magnitudes of the absorption coefficients vary smoothly inside the PML domain as follows,

$$\sigma_x = \sigma_{max} \left(\frac{x - x_0}{D} \right)^2$$

$$\sigma_r = \sigma_{max} \left(\frac{r - r_0}{D} \right)^2$$

where x_0 and r_0 are the location of the initial positions of the PML domain and D is the width of the PML domain. In all calculations, $\sigma_{max} \Delta x = 2$.

At the centerline $r = 0$,

$$\tilde{v} = \tilde{w} = \tilde{p} = 0$$

and singular terms in equation (14) are replaced by partial derivative terms using L'Hospital's Rule, namely,

$$\frac{\tilde{v}}{r} = \frac{\partial \tilde{v}}{\partial r}, \quad \frac{\tilde{w}}{r} = \frac{\partial \tilde{w}}{\partial r}, \quad \frac{\tilde{p}}{r} = \frac{\partial \tilde{p}}{\partial r}$$

at $r = 0$.

Pressure contours are shown in Figure 11 (a) and (b) for $\Omega = 0.85$ and 1.15 respectively. To show that a time periodic state has been reached, the pressure as function of time at point $(0, 8.5)$ is shown in Figure 12. We note that although the pressure contours show similar patterns of sound radiation for both cases, the

intensities are quite different. The second frequency, $\Omega = 1.15$, has supersonic tip speed and radiation is stronger.

Ducted Rotor

For the ducted rotor, the computational domain is shown in Figure 13. The discretization process is identical to the previous case except now an infinitely thin duct wall is placed at $r = 1$ for $-4 \leq x \leq 8$.

When the rotor is placed inside the duct, very little sound will be radiated because both frequencies are cut-off. Figure 14 shows the pressure contours at $t = 10, 20, 45, 100$. It shows that the intensity of sound radiation decreases dramatically after the initial transient state. Pressure history is shown in Figure 15 and no time periodic solution is found.

Generation and Radiation of Acoustic Waves from a 2-D Shear Layer

In this problem, a point source is placed inside a 2-D jet and acoustic radiation is to be computed. The governing equations are the linearized Euler equations,

$$
\begin{aligned}
\frac{\partial \rho'}{\partial t} &+ \bar{u}(y)\frac{\partial \rho'}{\partial x} + \bar{\rho}(y)\frac{\partial u'}{\partial x} + \bar{\rho}(y)\frac{\partial v'}{\partial y} + \frac{d\bar{\rho}}{dy}v' = 0 \\
\frac{\partial u'}{\partial t} &+ \bar{u}(y)\frac{\partial u'}{\partial x} + \frac{1}{\bar{\rho}(y)}\frac{\partial p'}{\partial x} + \frac{d\bar{u}}{dy}v' = 0 \\
\frac{\partial v'}{\partial t} &+ \bar{u}(y)\frac{\partial v'}{\partial x} + \frac{1}{\bar{\rho}(y)}\frac{\partial p'}{\partial y} = 0 \\
\frac{\partial p'}{\partial t} &+ \bar{u}(y)\frac{\partial p'}{\partial x} + \frac{\partial u'}{\partial x} + \frac{\partial v'}{\partial y} = Ae^{-B(\ln 2)(x^2+y^2)}\cos(\Omega t)
\end{aligned}
\tag{15}
$$

In the present calculation, the variables are non-dimensionalized by the mean values at the jet centerline, namely, the speed of sound a_j for the velocity, ρ_j for density and $\rho_j a_j^2$ for the pressure. The parallel mean velocity profile is,

$$
\bar{u}(y) = \begin{cases} M_j e^{-(\ln 2)\left(\frac{|y|-h}{b}\right)^2}, & |y| \geq h \\ M_j, & |y| \leq 0 \end{cases}
\tag{16}
$$

and the mean density is obtained by the Crocco's relation. Mach number of the jet $M_j = 2$. The other parameters are $A = 1$, $B = 8$, $h = 0.6$ and $b = 0.4$.

The computational domain of $[-8, 54] \times [0, 12]$ is shown in Figure 16. Due to symmetry in the mean flow and the source term, only the solution in the upper half plane is computed. Symmetry condition is applied for ρ', u' and p' and antisymmetry condition is applied for v'.

As indicated in Figure 16, supersonic and subsonic non-reflecting boundary conditions are treated differently. By (16), mean flow is supersonic for $|y| < 1$. At supersonic inflow, all variables are set to be zero and at supersonic outflow, backward difference is used for all the spatial derivatives in (15). At subsonic non-reflecting boundaries, the following PML equations are used [9],

$$\frac{\partial \rho_1'}{\partial t} + \sigma_x \rho_1' + \bar{u}(y)\frac{\partial \rho'}{\partial x} + \bar{\rho}(y)\frac{\partial u'}{\partial x} = 0$$

$$\frac{\partial \rho_2'}{\partial t} + \sigma_y \rho_1' + \bar{\rho}(y)\frac{\partial v'}{\partial y} + \frac{d\bar{\rho}}{dy}v' = 0$$

$$\frac{\partial u_1'}{\partial t} + \sigma_x u_1' + \bar{u}(y)\frac{\partial u'}{\partial x} + \frac{1}{\bar{\rho}}\frac{\partial p'}{\partial x} = 0$$

$$\frac{\partial u_2'}{\partial t} + \sigma_y u_2' + \frac{d\bar{u}}{dy}v' = 0$$

$$\frac{\partial v_1'}{\partial t} + \sigma_x v_1' + \bar{u}(y)\frac{\partial v'}{\partial x} = 0 \qquad (17)$$

$$\frac{\partial v_2'}{\partial t} + \sigma_y v_2' + \frac{1}{\bar{\rho}}\frac{\partial p'}{\partial y} = 0$$

$$\frac{\partial p_1'}{\partial t} + \sigma_x p_1' + \frac{\partial u'}{\partial x} = 0$$

$$\frac{\partial p_2'}{\partial t} + \sigma_y p_2' + \frac{\partial v'}{\partial y} = 0$$

where σ_x and σ_y are the absorption coefficients. A more detailed and general formulation for non-uniform mean flow is given in [9]. The width of the PML domain is 2 at the top and left radiation boundaries and 4 at the right outflow boundary for better absorption of the growing instability waves.

A uniform grid is used in x with $\Delta x = 0.1$ while a non-uniform grid is used in y for an increased resolution inside the shear layer. The grid size in y is such that $\Delta y = 0.025$ for $0 < y < 2$, $\Delta y = 0.05$ for $2 < y < 3$ and $\Delta y = 0.1$ for $3 < y < 12$. Again, the spatial derivatives are approximated by the optimized 7-point central difference scheme (DRP in [6]), time integration by LDDRK56 [7] and a tenth-order explicit filter is applied throughout the computational domain for the elimination of short waves that are not resolved in the discretization [9].

Instantaneous pressure contours are shown in Figure 17 for the two frequencies specified in the problem, $\Omega = 0.28\pi$ (St=$\frac{2fR_{1/2}}{u_j} = 0.14$) and $\Omega = 1.2\pi$ (St=0.6), respectively. Since the shear layer is unstable in the low frequency case, the excitation of the instability wave results in stronger sound radiation. This is also seen in the instantaneous pressure profile along $y = 1$ (the center of the shear layer), shown in Figure 18, and $\bar{p}^2$ along $y = 10$, shown in Figure 19. Indeed, in an earlier calculation where the values of h and b were inadvertently interchanged, which results in a larger shear layer thickness, the growth of instability wave was much smaller and the sound radiation weaker.

REFERENCES

[1] F. Q. Hu, M. Y. Hussaini and J. L. Manthey, "Application of low dissipation and dispersion Runge-Kutta schemes to benchmark problems in computational aeroacoustics", *Benchmark Problems In Computational Aeroacoustics*, NASA CP 3300, 73-98, 1995.

[2] F. Q. Hu and J. L. Manthey, "Application of PML absorbing boundary conditions to the Benchmark Problems of Computational Aeroacoustics", *Second Computational Aeroacoustics (CAA) Workshop on Benchmark Problems*, NASA CP 3352, 119-151, 1997.

[3] K. W. Thompson, "Time dependent boundary conditions for hyperbolic systems", Journal of Computational Physics, Vol. 68, 1-24, 1987.

[4] T. Z. Dong and R. R. Mankbadi, "Numerical simulations of small amplitude acoustic wave propagation in a converging-diverging nozzle, *Benchmark Problems In Computational Aeroacoustics*, NASA CP 3300, 285-290, 1995.

[5] C. K. W. Tam, "Computational Aeroacoustics: Issues and methods", AIAA Journal, Vol. 33, 1788-1796, 1995.

[6] C. K. W. Tam, T. Z. Dong and K. A. Kurbatskii, "Multi-size-mesh, multi-time-step computational algorithm", AIAA paper 99-1850, 1999.

[7] F. Q. Hu, M. Y. Hussaini, J. L. Manthey, "Low-dissipation and -dispersion Runge-Kutta schemes for computational acoustics", Journal of Computational Physics, Vol. 124, 177-191, 1996.

[8] F. Q. Hu, "On absorbing boundary conditions for linearized Euler equations by a perfectly matched layer", Journal of Computational Physics, Vol. 129, 201-219, 1996.

[9] F. Q. Hu, "On Perfectly Matched Layer as an absorbing boundary condition", AIAA paper 96-1664, 1996.

FIGURES
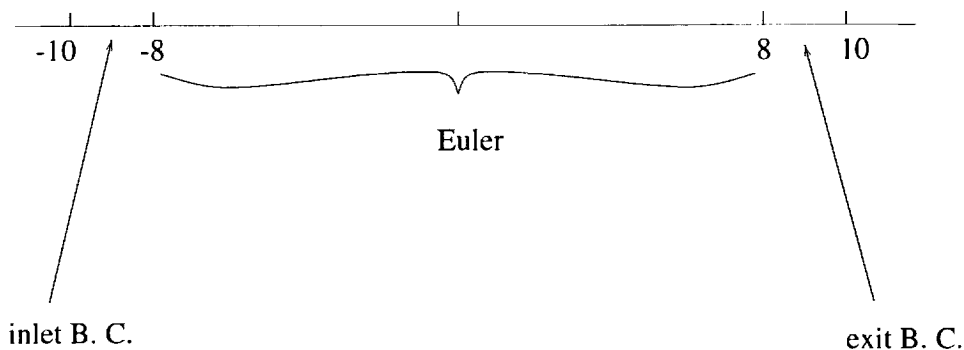
Figure 1. Schematic of computational domain partitions.
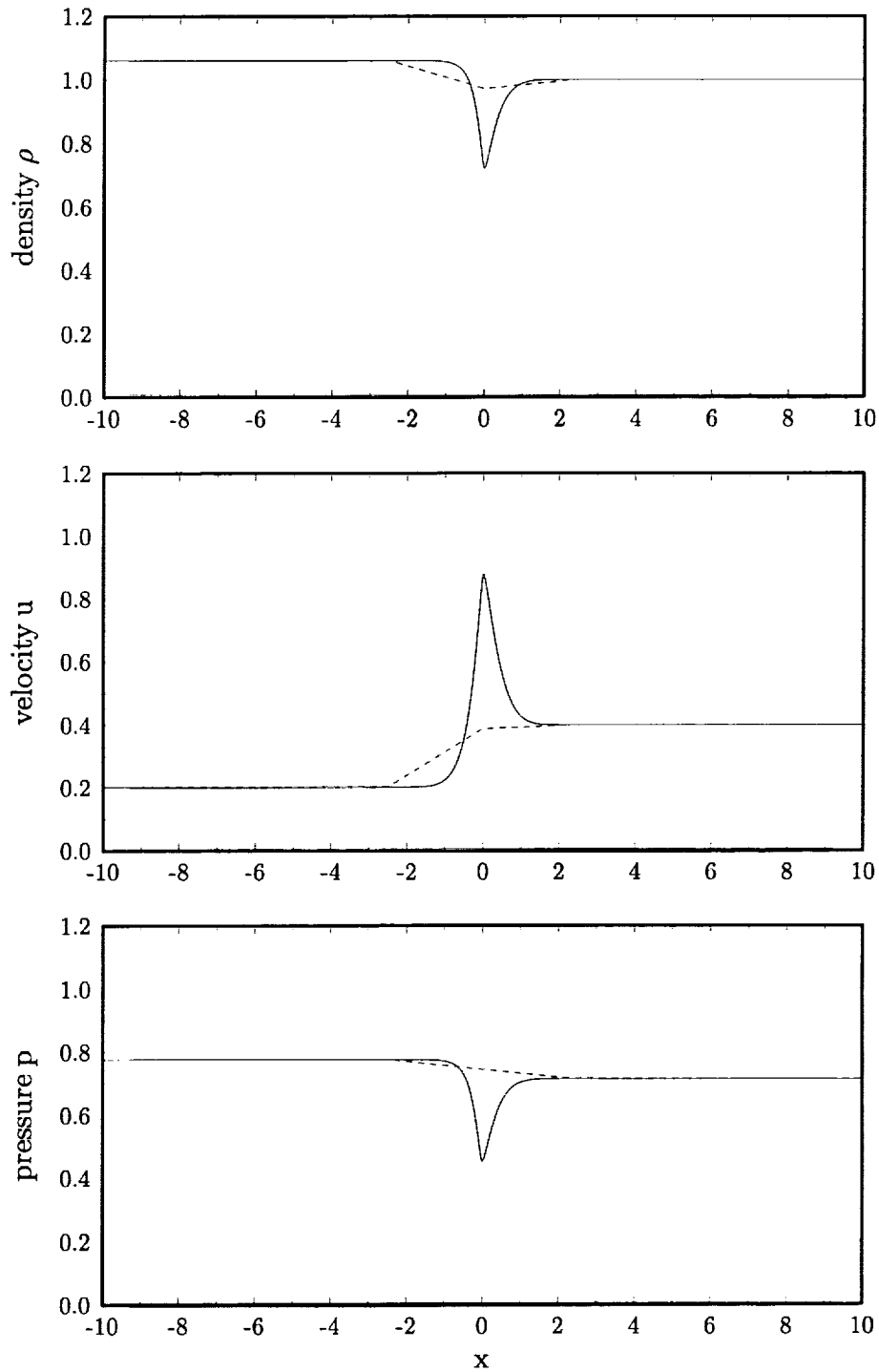
Figure 2. Spatial distribution of density, velocity and pressure at the initial (dashed) and final (solid) stages.

178
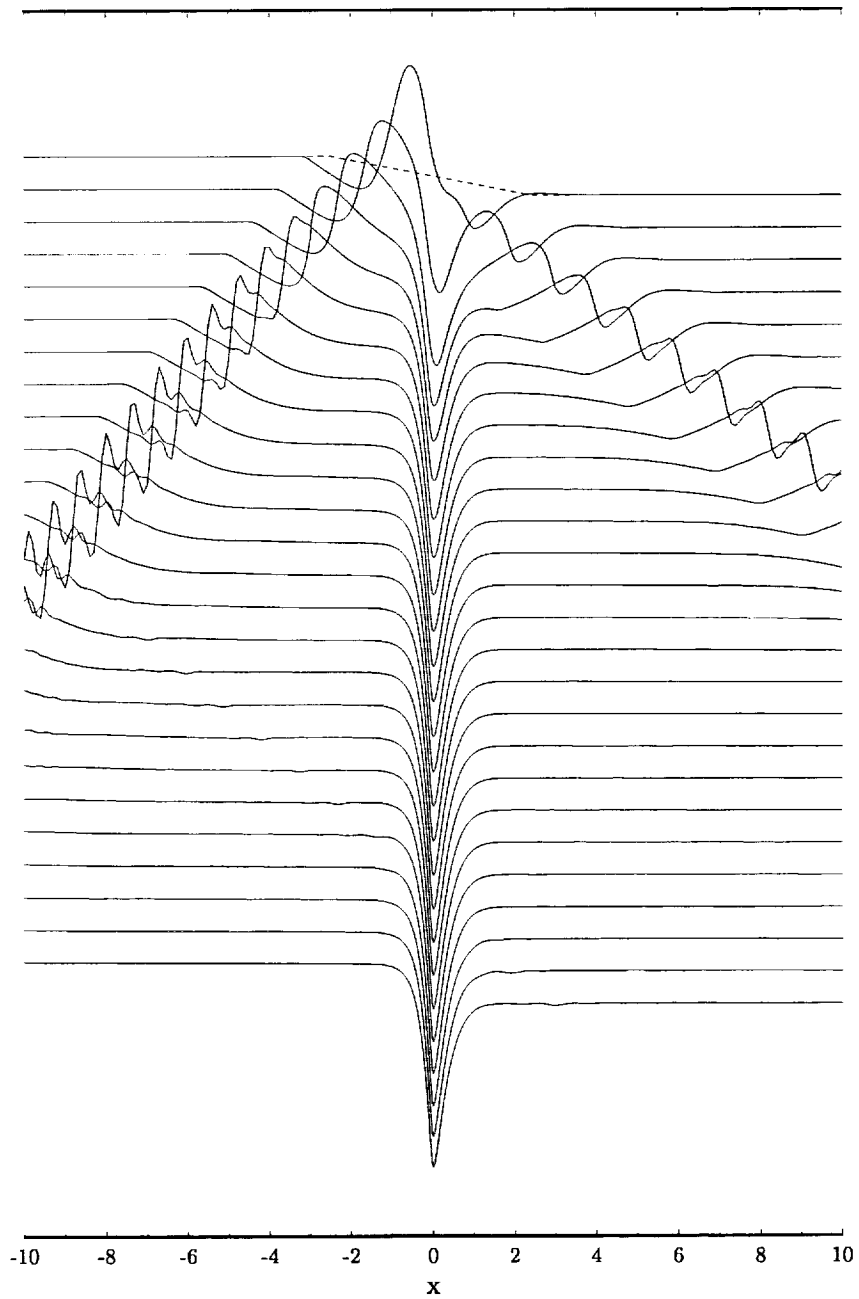
Figure 3. Time history of the pressure distribution showing the propagation of the initial transient variations.
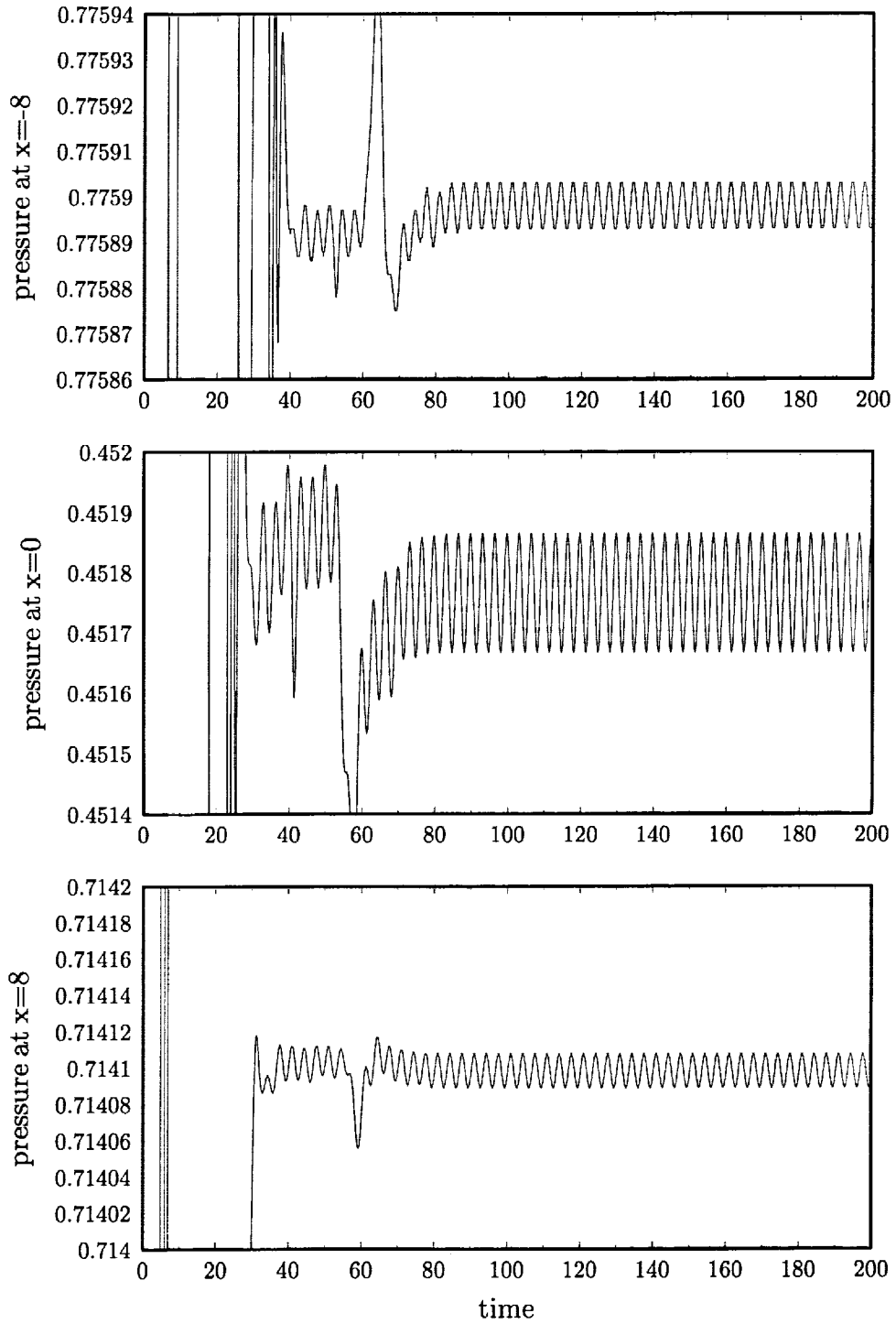
Figure 4. Pressure as a function of time at $x = -8$, 0 and 8 respectively.
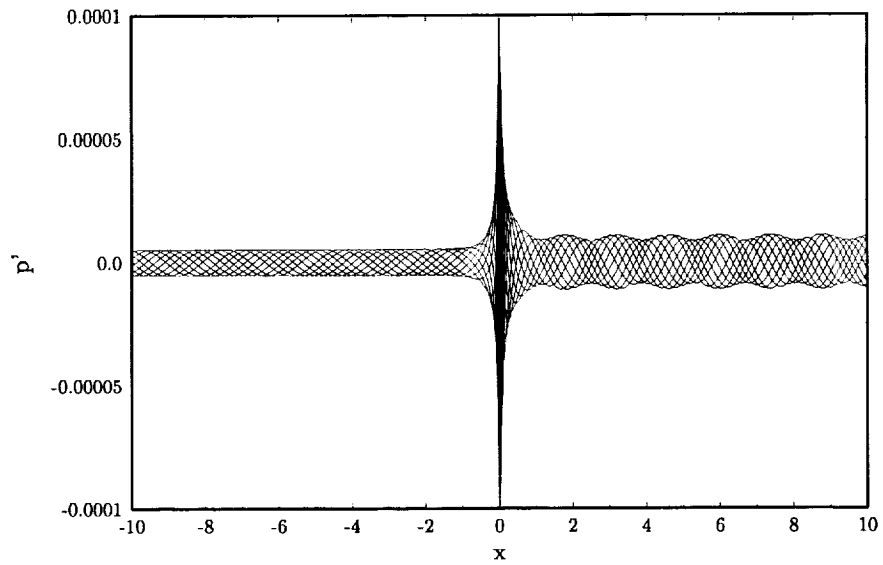
Figure 5. Pressure as a function of x spanning a period, showing the wave envelope.
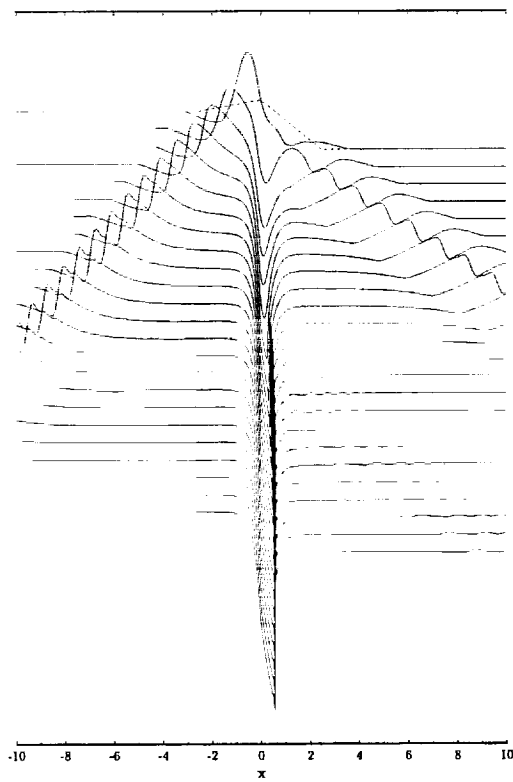
Figure 6. Time history of pressure as a function of x, showing the formation of shock from the initial profile (dashed).
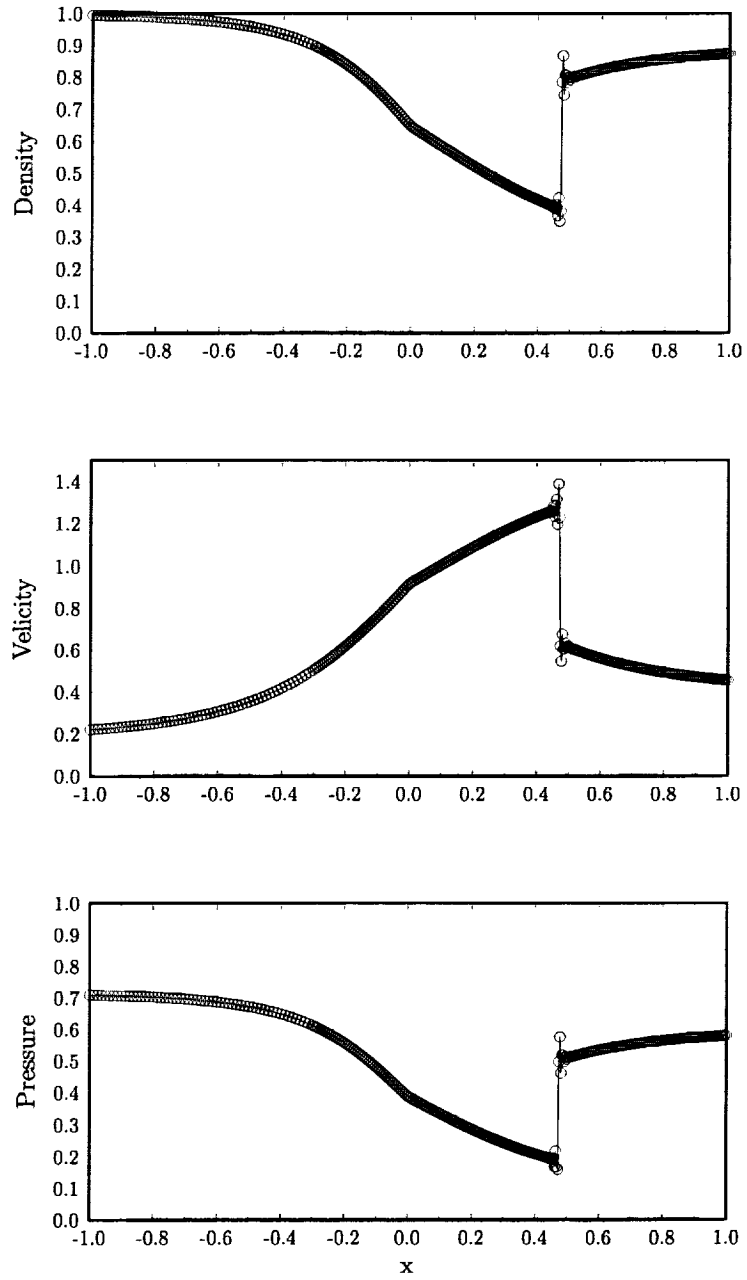
Figure 7. Final stage of density, velocity and pressure.

182
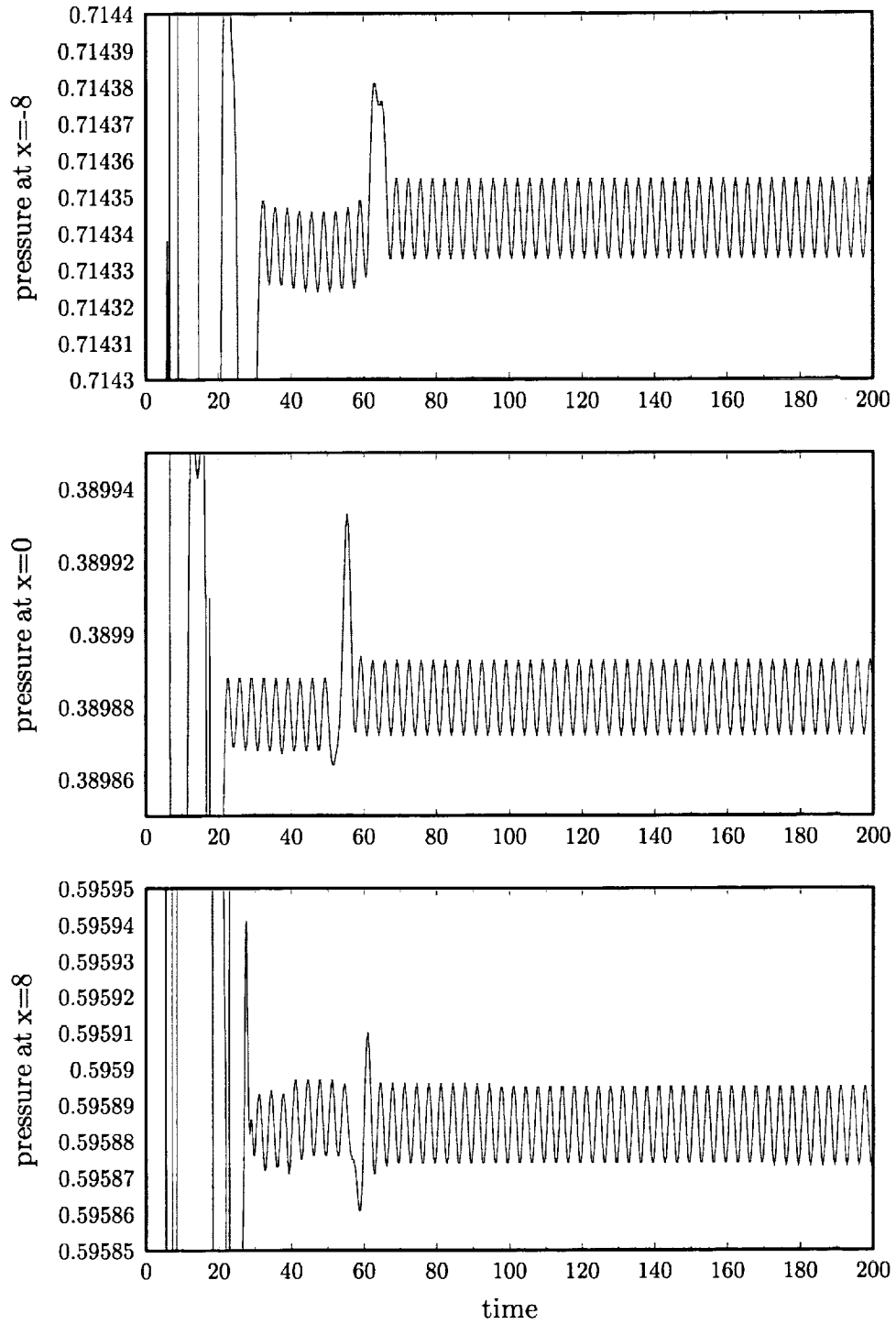
Figure 8. Pressure as a function of time at $x = -8$, 0 and 8.
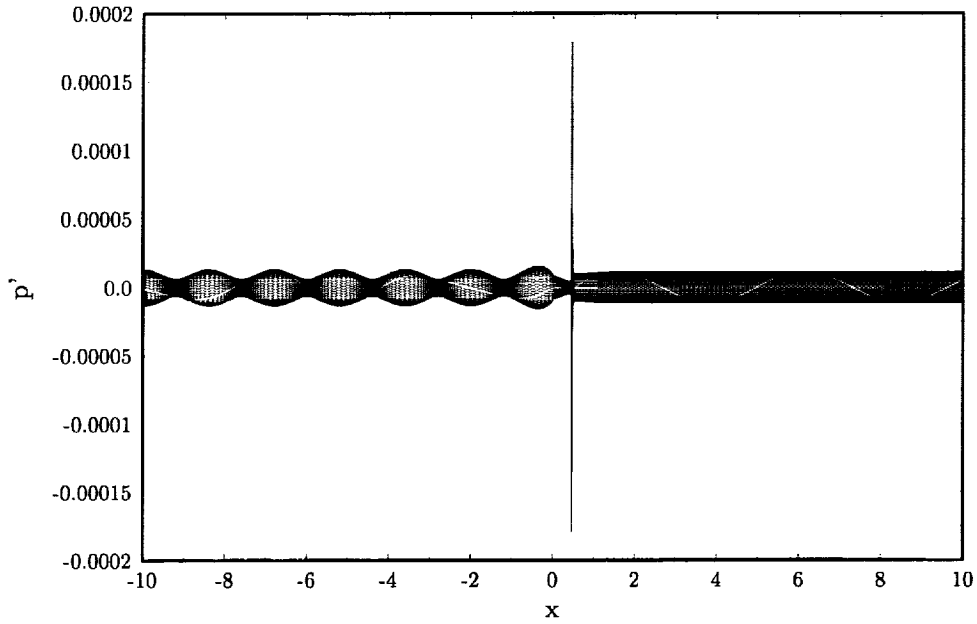
Figure 9. Pressure as a function of x at selected time steps spanning a period, showing the wave envelope.
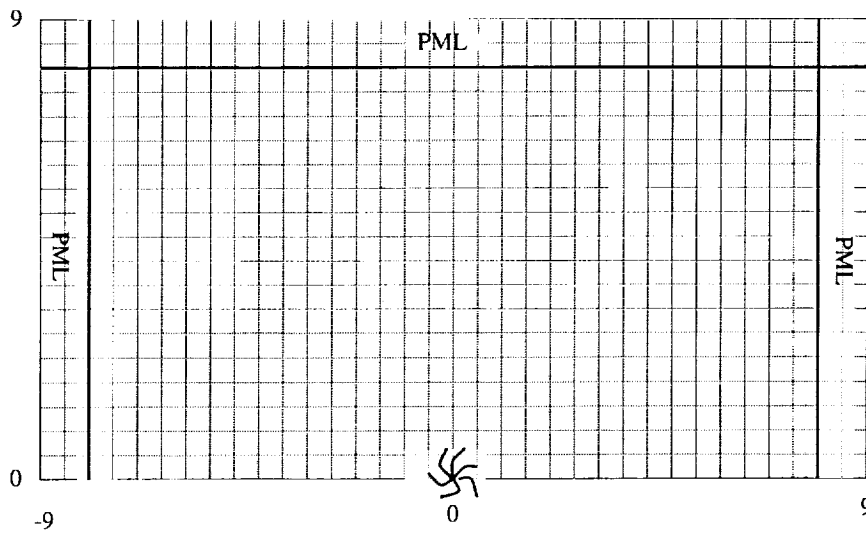
Figure 10. Computational domain for open rotor, showing the PML domains at non-reflecting boundaries.
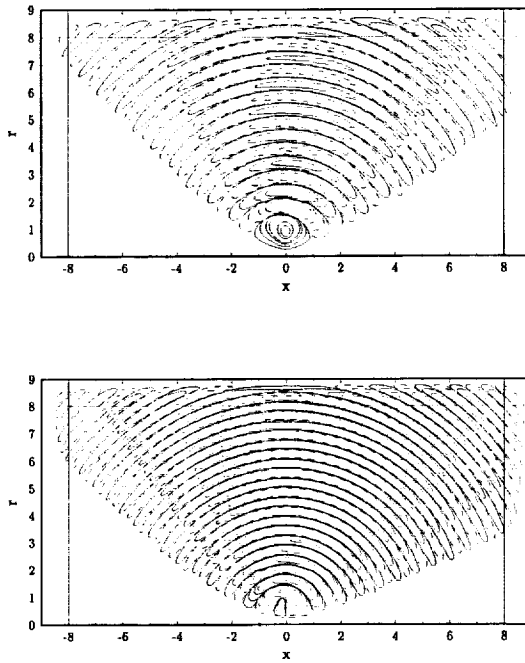
Figure 11. Pressure contours for (a) $\Omega = 0.85$, (b) $\Omega = 1.15$.
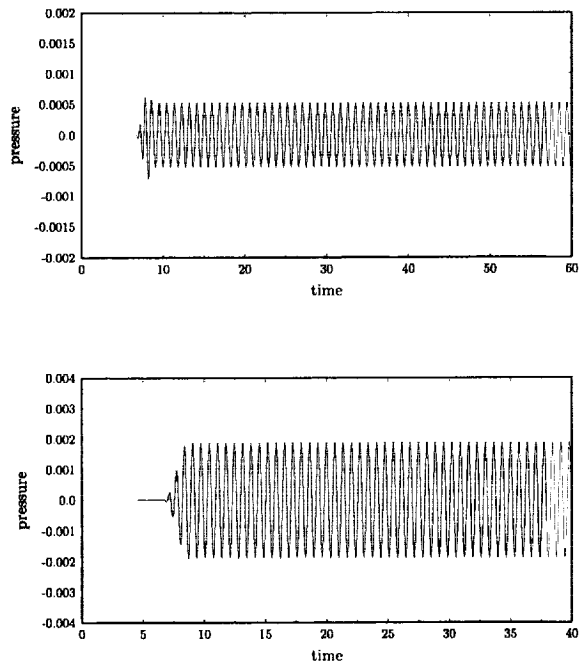
Figure 12. Pressure as a function of time at $(0, 8.5)$, (a) $\Omega = 0.85$, (b) $\Omega = 1.15$.
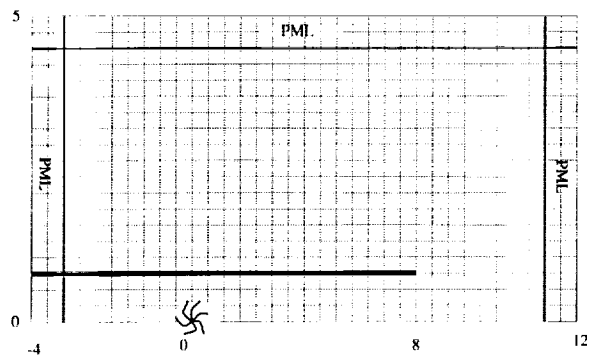
Figure 13. Computational domain for ducted rotor.
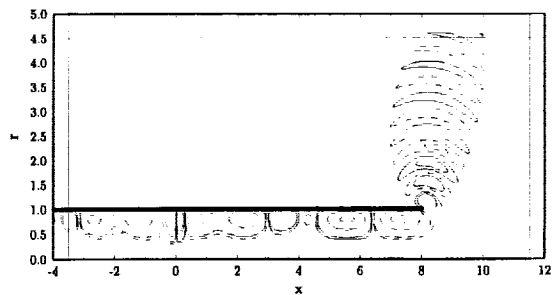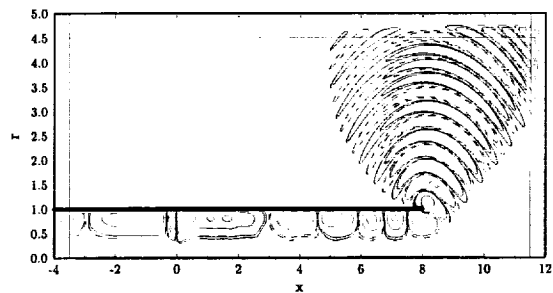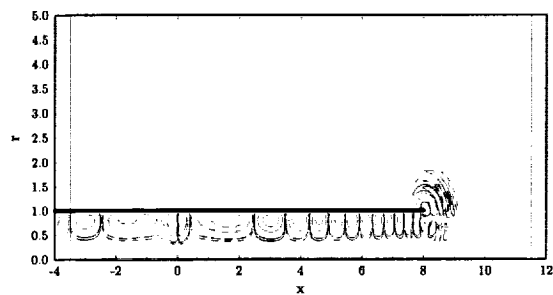
(continued next page)
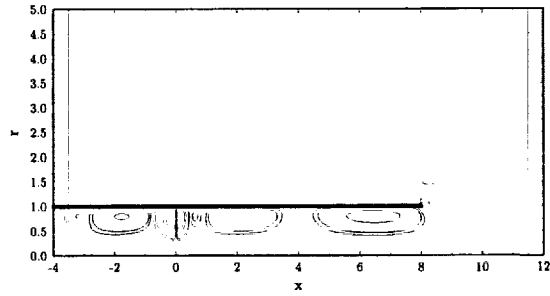
Figure 14. Pressure contours at $t = 10, 20, 35, 100$.
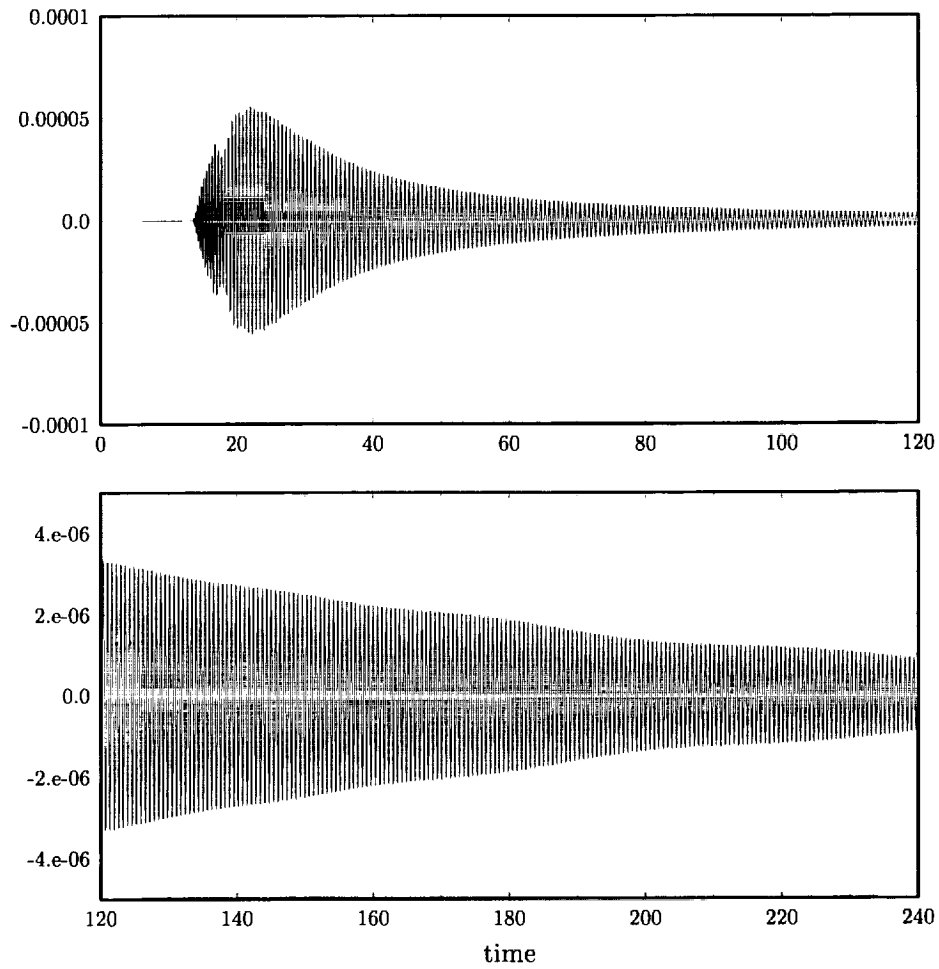
Figure 15. Pressure as a function of time at $(0, 8.5)$. $\Omega = 0.85$. No time periodic solution is found.
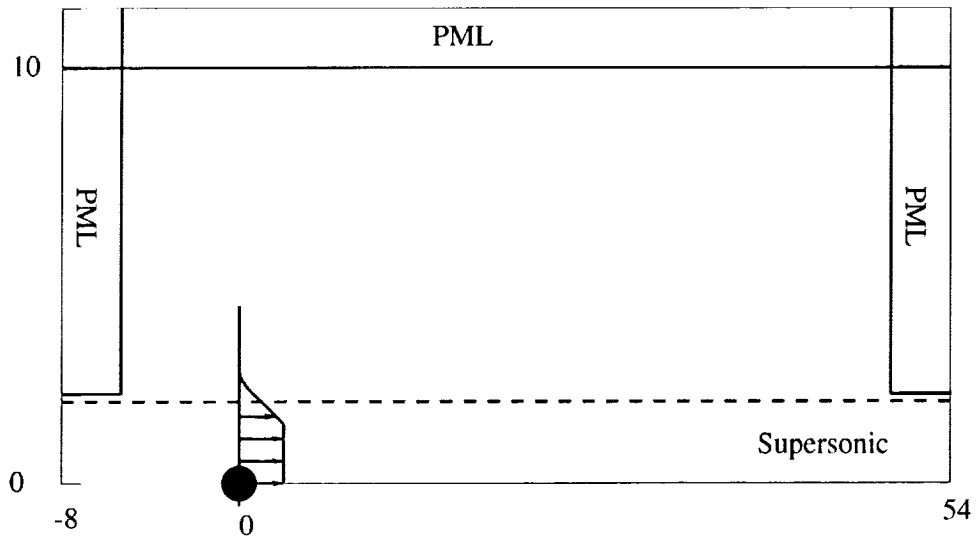
Figure 16. A schematic of computational domain showing the use of PML domains at all the subsonic non-reflecting boundaries.
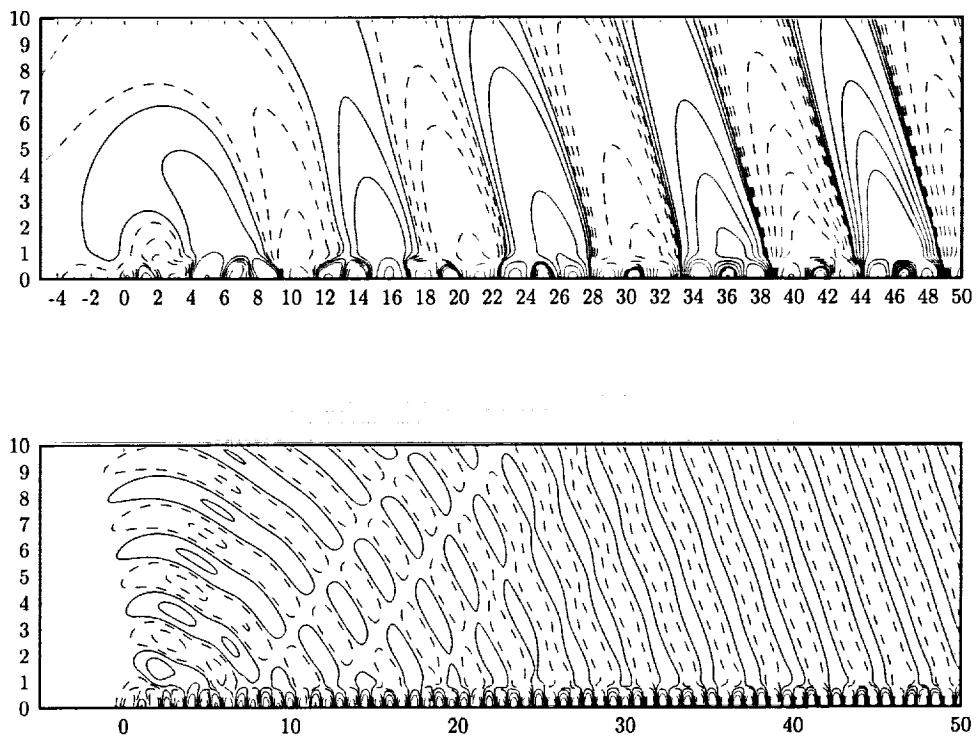
Figure 17. Instantaneous pressure contours for $\Omega = 0.28\pi$(top) and $\Omega = 1.2\pi$(bottom).
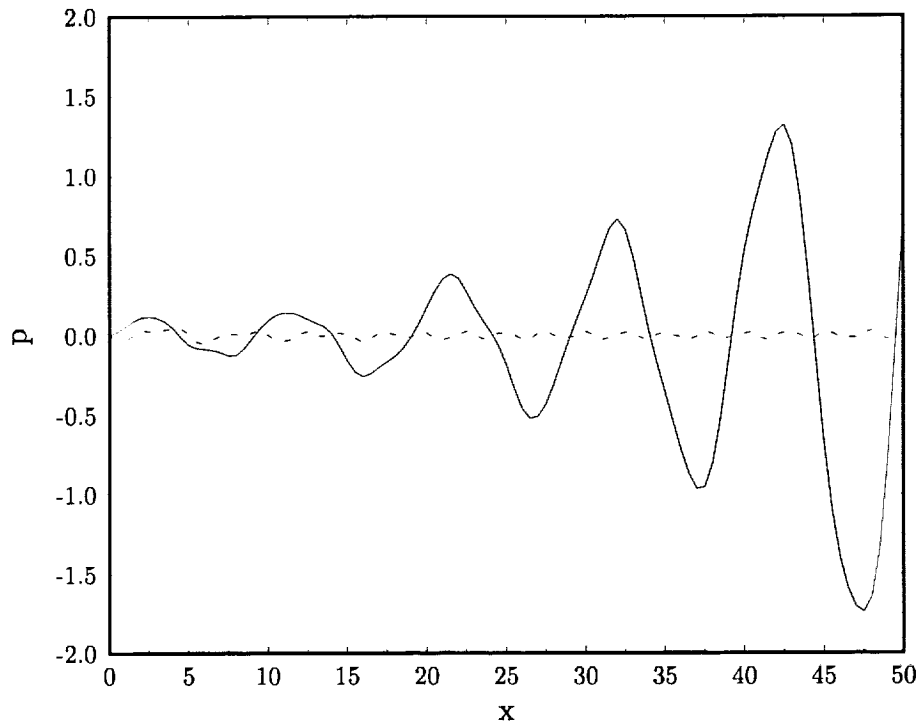
Figure 18. Pressure profile along $y = 1$ for $\Omega = 0.28\pi$ (solid) and $\Omega = 1.2\pi$ (dashed).
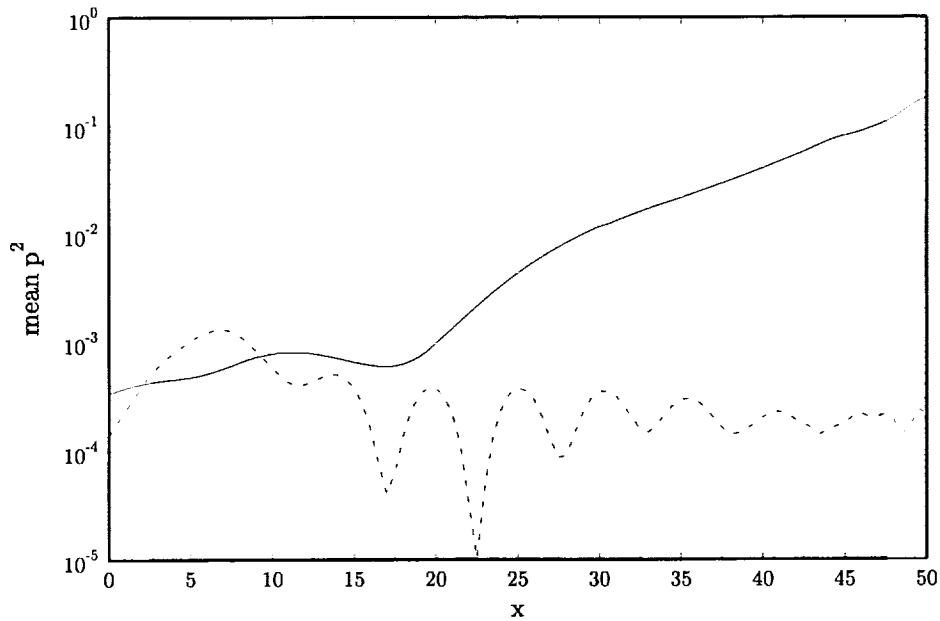
Figure 19. Mean p^2 along $y = 10$ for $\Omega = 0.28\pi$ (solid) and $\Omega = 1.2\pi$ (dashed).
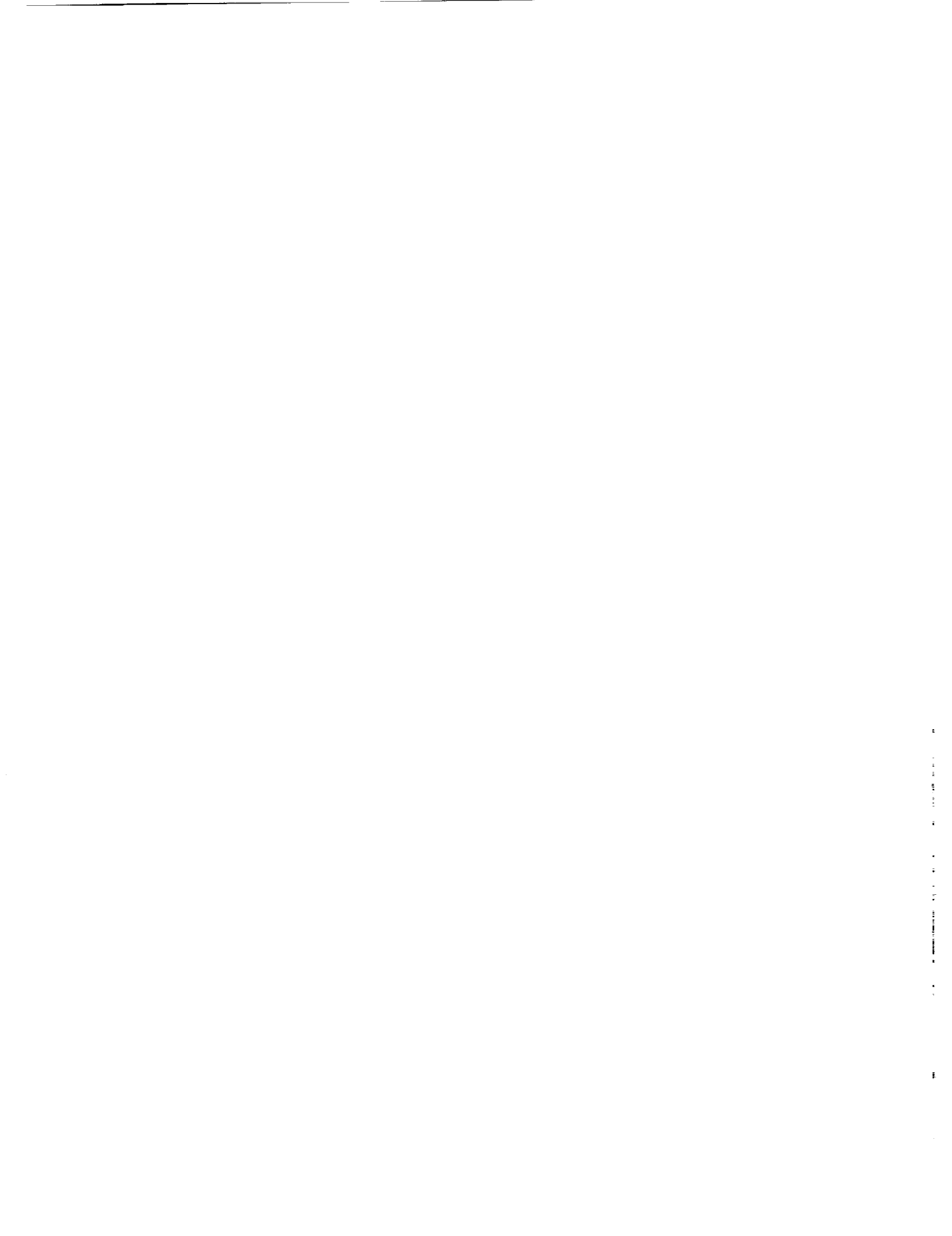
COMPUTATION OF TRANSONIC NOZZLE SOUND TRANSMISSION AND ROTOR PROBLEMS BY THE DISPERSION-RELATION-PRESERVING SCHEME

CHRISTOPHER K.W. TAM
Department of Mathematics
Florida State University
Tallahassee, FL 32306-4510
Email: tam@math.fsu.edu

and

Alexei Aganin
Department of Mathematics
Florida State University
Tallahassee, FL 32306-4510

Abstract

The transonic nozzle transmission problem and the open rotor noise radiation problem are solved computationally. Both are multiple length scales problems. For efficient and accurate numerical simulation, the multiple-size-mesh multiple-time-step Dispersion-Relation-Preserving scheme is used to calculate the time periodic solution To ensure an accurate solution, high quality numerical boundary conditions are also needed. For the nozzle problem, a set of nonhomogeneous outflow boundary conditions are required. The nonhomogeneous boundary conditions not only generate the incoming sound waves but also, at the same time, allow the reflected acoustic waves and entropy waves, if present, to exit the computation domain without reflection. For the open rotor problem, there is an apparent singularity at the axis of rotation. An analytic extension approach is developed to provide a high quality axis boundary treatment.

1. Introduction

Category 1, Problem 1 and Category 2 problems are solved by the Dispersion-Relation-Preserving (DRP) scheme (Tam and Webb, Ref. [1]). Both problems are characterized by multiple length scales. This is typical of most aeroacoustics problems. For this type of problems, the spatial resolu-

tion requirements varies significantly from region to region in the computation domain. To provide adequate computation accuracy locally, a multiple-size-mesh is used. The computation domain is divided into a number of subdomains in each of which the mesh size is uniform. In each of the subdomains the solution is computed by the DRP time marching scheme. At the mesh size change boundaries special stencils are used. To advance in time, the scheme uses the local time step that satisfies the local stability requirement dictated by the local mesh size. In other words, different size time steps are used in different subdomains. This is possible because the DRP scheme is a multi-level time matching algorithm. We will refer to the computing scheme as the multiple-size-mesh multiple-time-step Dispersion-Relation-Preserving scheme. Recently such a scheme has been used successfully to simulate the generation of screech tones from imperfectly expanded supersonic jets (Ref. [2]) and the micro-vortex shedding phenomenon associated with an acoustic liner in a high acoustic intensity environment (Ref. [3]). Presently, there are very few time marching computation algorithms that permit the use of multiple time steps. This feature makes the DRP scheme ideal for solving aeroacoustics problems.

2. Category 1, Problem 1

Since the amplitude of the incoming sound wave is very small, it is sufficient to look for a linear solution of the problem. The mean flow solution of the nozzle flow is,

$$\bar{\rho}\,\bar{u}\,A = \rho_r u_r A_r$$

$$\frac{\bar{p}}{\bar{\rho}^\gamma} = \frac{p_r}{\rho_r^\gamma} \tag{2.1}$$

$$\frac{\bar{u}^2}{2} + \frac{\gamma}{\gamma-1}\frac{p_r}{\rho_r^\gamma}\bar{\rho}^{\gamma-1} = \frac{u_r^2}{2} + \frac{\gamma}{\gamma-1}\frac{p_r}{\rho_r}$$

where subscript r denotes the reference station. We will use the uniform flow region at Mach 0.4 as the reference station so that $\rho_r = 1$, $u_r = 0.4$, $p_r = \frac{1}{\gamma}$ and $A_r = 0.536572$. It is easy to find that the Mach number at the nozzle throat is equal to 0.94. The governing equations for small amplitude disturbances are,

$$\frac{\partial \rho}{\partial t} + \frac{\bar{\rho}\,\bar{u}}{A}\frac{dA}{dx} + \bar{\rho}\,\frac{\partial u}{\partial x} + u\frac{d\bar{\rho}}{dx} + \rho\frac{\bar{u}}{A}\frac{dA}{dx} + \rho\frac{d\bar{u}}{dx} + \bar{u}\frac{\partial \rho}{\partial x} = 0$$

$$\bar{\rho}\,\frac{\partial u}{\partial t} + \bar{\rho}\,\bar{u}\frac{\partial u}{\partial x} + \rho\,\bar{u}\frac{d\bar{u}}{dx} + \bar{\rho}\,u\frac{d\bar{u}}{dx} + \frac{\partial p}{\partial x} = 0 \tag{2.2}$$

$$\frac{\partial p}{\partial t} + \bar{u}\frac{\partial p}{\partial x} + u\frac{d\bar{p}}{dx} + \frac{\gamma}{A}(\bar{p}\,u + p\,\bar{u})\frac{dA}{dx} + \gamma\bar{p}\frac{\partial u}{\partial x} + \gamma p\frac{d\bar{u}}{dx} = 0.$$

In the uniform flow regions upstream and downstream of the nozzle throat, (2.2) reduces to

$$\frac{\partial \rho}{\partial t} + \bar{\rho}\frac{\partial u}{\partial x} + \bar{u}\frac{\partial \rho}{\partial x} = 0$$

$$\frac{\partial u}{\partial t} + \bar{u}\frac{\partial u}{\partial x} + \frac{1}{\bar{\rho}}\frac{\partial p}{\partial x} = 0 \qquad (2.3)$$

$$\frac{\partial p}{\partial t} + \bar{u}\frac{\partial p}{\partial x} + \gamma\bar{p}\frac{\partial u}{\partial x} = 0$$

(2.3) supports three independent wave solutions. They are the upstream propagating acoustic waves, which may be written in the form,

$$\begin{bmatrix} \rho \\ u \\ p \end{bmatrix} = \begin{bmatrix} \frac{1}{\bar{a}^2} \\ -\frac{1}{(\bar{\rho}\bar{a})} \\ 1 \end{bmatrix} F\left(\frac{x}{\bar{a}-\bar{u}}+t\right), \qquad (2.4)$$

the downstream propagating acoustic waves,

$$\begin{bmatrix} \rho \\ u \\ p \end{bmatrix} = \begin{bmatrix} \frac{1}{\bar{a}^2} \\ \frac{1}{(\bar{\rho}\bar{a})} \\ 1 \end{bmatrix} G\left(\frac{x}{\bar{a}+\bar{u}}-t\right), \qquad (2.5)$$

and the entropy wave,

$$\begin{bmatrix} \rho \\ u \\ p \end{bmatrix} = \begin{bmatrix} 1 \\ 0 \\ 0 \end{bmatrix} H\left(x-\bar{u}t\right), \qquad (2.6)$$

where F, G and H are arbitrary functions. $\bar{a} = \left(\frac{\gamma\bar{p}}{\bar{\rho}}\right)^{\frac{1}{2}}$ is the local speed of sound.

2.1. Mesh Design

For an upstream propagating time harmonic acoustic wave of angular frequency ω, (2.4) becomes

$$p = \text{Re}\left[Ae^{-i\omega\left(\frac{x}{\bar{a}-\bar{u}}+t\right)}\right]. \qquad (2.7)$$

Thus the acoustic wave length λ is given by,

$$\lambda = \frac{2\pi\bar{a}(1-M)}{\omega} \qquad (2.8)$$

where $M = \frac{\overline{u}}{\overline{a}}$ is the local Mach number of the mean flow. Formula (2.8) indicates that at the nozzle throat with $M = 0.94$ the acoustic wave length is nearly ten times shorter than that in the Mach 0.4 uniform region of the nozzle. We will use the Dispersion-Relation-Preserving (DRP) scheme for our computation. With a 7-point stencil, the scheme can calculate waves of wave length equal to or longer than 7 mesh spacings with good accuracy. Based on these estimates and $\omega = 0.6\pi$, a computational mesh as shown in figure 1 is used for the calculation. In this figure, only the mesh distribution from $x = 0$ to $x = 10$ is shown. Four mesh sizes are used. The mesh sizes are related by $\Delta x_n = 2^n \Delta x_0$ ($n = 1, 2, 3$). The finest mesh is at the nozzle throat region with $\Delta x_0 = 0.0125$. There are altogether 359 mesh points, which is less than the maximum 400 mesh points stipulated by the benchmark problem.
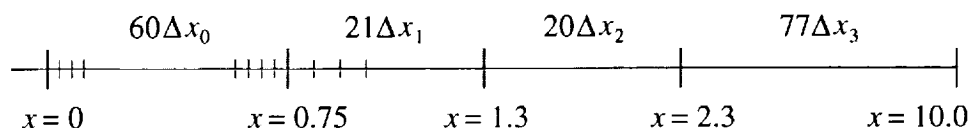
Figure 1. Mesh distribution from $x = 0$ to $x = 10$

2.2. Numerical Boundary Conditions

In the inflow region of the nozzle, there are only upstream propagating acoustic waves. The form of the solution is given by (2.4). It is straightforward to show by differentiation that regardless of what the function F is, the waves satisfy the following relationship.

$$\frac{\partial}{\partial t} \begin{bmatrix} \rho \\ u \\ p \end{bmatrix} - (\overline{a} - \overline{u}) \frac{\partial}{\partial x} \begin{bmatrix} \rho \\ u \\ p \end{bmatrix} = 0. \tag{2.9}$$

(2.9) is the inflow boundary condition. It is used to advance the solution in time at the last 3 mesh points on the left of the computation domain.

In the outflow region, there could be three types of waves. They are the incoming acoustic waves, the reflected acoustic waves and the entropy waves. We may, therefore, write

$$\begin{bmatrix} \rho \\ u \\ p \end{bmatrix} = \begin{bmatrix} \rho_{\text{out}} \\ u_{\text{out}} \\ p_{\text{out}} \end{bmatrix} + \varepsilon \begin{bmatrix} 1 \\ -1 \\ 1 \end{bmatrix} \cos \left(\omega \left(\frac{x}{1 - M} + t \right) \right). \tag{2.10}$$

The second term on the right of (2.10) is the incoming acoustic wave given by the benchmark problem. The first term represents disturbances that would exit the computation domain through the right boundary. These disturbances are composed of the reflected acoustic waves and possible entropy

waves (convected downstream by the mean flow). Thus by (2.5) and (2.6) we have,

$$
\begin{bmatrix} \rho_{\text{out}} \\ u_{\text{out}} \\ p_{\text{out}} \end{bmatrix} = \begin{bmatrix} \frac{1}{\bar{a}^2} \\ \frac{1}{(\bar{\rho}\,\bar{a})} \\ 1 \end{bmatrix} G\left(\frac{x}{\bar{a} + \bar{u}} - t \right) + \begin{bmatrix} 1 \\ 0 \\ 0 \end{bmatrix} H\left(x - \bar{u}\,t \right).
\tag{2.11}
$$

By simple differentiation, it is straightforward to find, on eliminating the unknown functions G and H of (2.11), the following outflow boundary conditions,

$$
\frac{\partial p_{\text{out}}}{\partial t} = -\left(1 + M\right) \frac{\partial p_{\text{out}}}{\partial x}
$$

$$
\frac{\partial u_{\text{out}}}{\partial t} = -\left(1 + M\right) \frac{\partial u_{\text{out}}}{\partial x}
\tag{2.12}
$$

$$
\frac{\partial \rho_{\text{out}}}{\partial t} = -M \frac{\partial \rho_{\text{out}}}{\partial x} - \frac{\partial p_{\text{out}}}{\partial x}.
$$

(2.12) is used to advance the values of (ρ_{out}, u_{out}, p_{out}) at the last three mesh points (the outflow region) at the right end of the computation domain. Once these quantities are known, the values of (ρ, u, p) are found by (2.10). Since a 7-point stencil is used, the stencils used to compute (2.12) would extend beyond the first 3 mesh points into the interior region. In the interior region, the values of (ρ, u, p) are advanced in time. To calculate the values of ($\rho_{\text{out}}, u_{\text{out}}, p_{\text{out}}$) to support the time advancement of the unknowns in the boundary region, (2.10) is again used. This arrangement automatically generates the incoming wave in the outflow region and, at the same time, permits any outgoing disturbances to leave the computation domain smoothly.

2.3. Numerical Results and Comparisons with the Exact Solution

To find the solution of the sound transmission problem, (2.2) is first discretized according to the DRP scheme using the mesh as given in figure 1. At the mesh size change interface, special 7-point stencils are used. These stencils are provided in the Appendix of Ref. [3]. Because of space limitation, they will not be repeated here. The DRP scheme is a central difference algorithm. As such, there is no intrinsic numerical damping. To assure that short spurious waves are eliminated so as not to pollute the numerical solution, artificial selective damping is included as discussed in Ref. [4]. [5]. The inverse mesh Reynolds number, R_Δ^{-1}, is taken to be 0.05 in the computation.

The DRP scheme is a time marching scheme. To start the calculation, the zero initial condition is used; i.e., $t = 0$, $\rho = u = p = 0$ for all mesh points except the last three mesh points on the right

boundary. This is the outflow boundary region. In this region, we set $\rho_{out} = u_{out} = p_{out} = 0$ at $t = 0$. The incoming wave is, however, not equal to zero. Since a time periodic state is to be found, such a solution is attained after a long period of computation. In the present calculation, the incoming wave is turned on slowly. Thus, in the outflow boundary region, instead of (2.10) we use

$$
\begin{bmatrix} \rho \\ u \\ p \end{bmatrix} = \begin{bmatrix} \rho_{out} \\ u_{out} \\ p_{out} \end{bmatrix} + \varepsilon \begin{bmatrix} 1 \\ -1 \\ 1 \end{bmatrix} \left(1 - e^{-\frac{t}{\tau}} \right) \cos \left[\omega \left(\frac{x}{1 - M} + t \right) + \phi \right].
\tag{2.13}
$$

where τ is taken to be $\frac{10\pi}{\omega}$ or five oscillation periods. The phase ϕ is to be adjusted such that the cosine term is zero at the third mesh point from the right at $t = 0$. This ensures that the initial condition is continuous at the interface between the interior region and the outflow region.

On starting with initial condition (2.13) in the outflow boundary region and the zero condition in the rest of the computation domain, (2.2) is solved by the multiple-size-mesh multiple-time-step DRP scheme on the mesh as shown in figure 1. The maximum pressure envelope is measured after a time periodic state has been achieved. It is shown in figures 2 and 3. Plotting in these figures also is the exact solution. As can be seen, there is good agreement between the numerical and the exact solutions. The amplitude of the computed transmitted wave is slightly lower. This is due to the artificial selective damping. The agreement between the numerical and the exact solution can be improved by increasing the mesh Reynolds number or by reducing the mesh size.
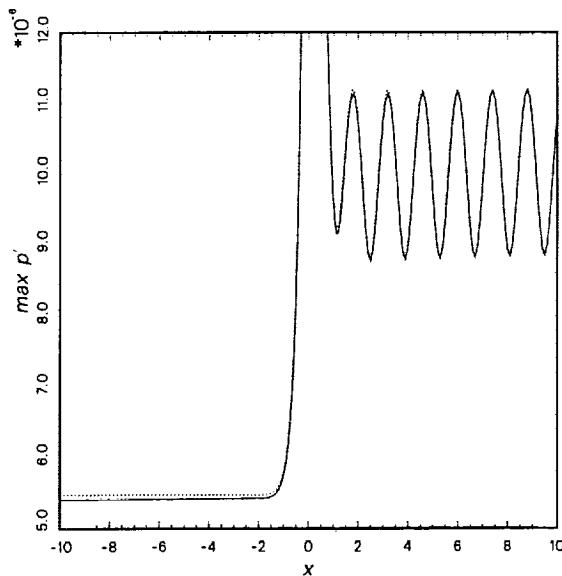
Figure 2. Comparison between numerical solution and exact solution,
———— numerical, · · · · · · · exact
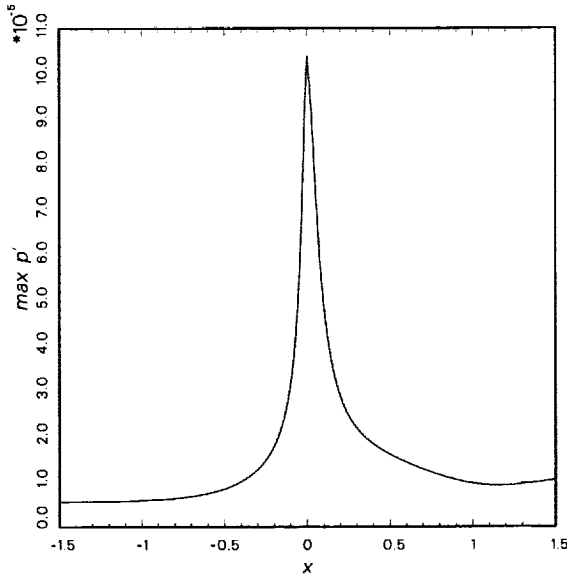
Figure 3. Comparison between numerical solution and exact solution near the nozzle throat, ——— numerical, ······· exact

3. Category 2 Problems

It is easy to show, for the given rotor problem, the rotational frequency of the ducted rotor is below the cut-on frequency. In other words, all the acoustic disturbances are cut-off or nonpropagating. Thus, there is no sound radiation out of the open end of the duct. For this reason, only the open rotor problem is computed.

The governing equations are,

$$
\frac{\partial \tilde{v}}{\partial t} = -\frac{\partial \tilde{p}}{\partial r}
$$

$$
\frac{\partial \tilde{w}}{\partial t} = -\frac{im}{r} \tilde{p} + \tilde{F}_\phi e^{-im\Omega t}
$$

$$
\frac{\partial \tilde{u}}{\partial t} = -\frac{\partial \tilde{p}}{\partial x} + \tilde{F}_x e^{-im\Omega t}
$$

$$
\frac{\partial \tilde{p}}{\partial t} + \frac{1}{r}\frac{\partial (\tilde{v} r)}{\partial r} + \frac{im \tilde{w}}{r} + \frac{\partial \tilde{u}}{\partial x} = 0
$$

(3.1)

The forcing functions are

$$
\tilde{F}_\phi = \begin{cases} F(x) r J_m(\lambda_{mN} r), & r \le 1 \\ 0, & r > 1 \end{cases}
$$

(2.5)

$$
\tilde{F}_x = \begin{cases} F(x) J_m(\lambda_{mN} r), & r \le 1 \\ 0, & r > 1 \end{cases}
$$

(3.3)

$$F(x) = \exp\left[-(\ln 2)(10x)^2\right].$$

To ensure that the computed solution is accurate, one must make provisions to take into account two important characteristics of this problem. First is that the noise source is discontinuous at the blade tip. This could be a source of short spurious waves. Second is that the blades are slender. That is, the loading is concentrated over a narrow width. Computationally, this requires a finer spatial resolution in the source region than in the acoustic radiation field.

3.1. Grid Design

The half-width of the forcing function (2.5) and (3.3) is 0.2. To resolve this width a minimum of 10 mesh points is necessary. In other words, the maximum mesh size in the source region is 0.02. This high resolution is not needed as one moves away into the acoustic field. We will use the multiple-size-mesh multiple-time-step DRP algorithm for computation. This allows us to use coarser and coarser mesh starting from the source region. Figure 4 shows our computation domain. The domain is divided into three regions. The mesh size as well as the time step double themselves each time one crosses into an outer region. It is possible to use more regions with larger savings in computing time. But this will require slightly more programming effort.
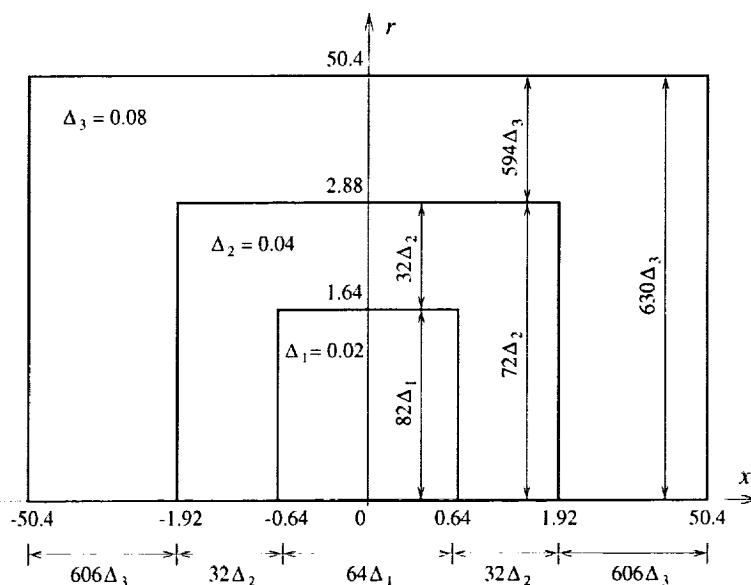
Figure 4. The computation domain and mesh size distribution

3.2. Numerical Boundary Conditions

Two types of numerical boundary conditions are needed. Along the outer boundary of the computation domain, radiation boundary conditions are required. Along the axis of the cylindrical coordinates; i.e., $r = 0$, a special set of axis boundary condition is needed. In this work, the following radiation boundary conditions (see Ref. [1]) are used.

$$\left(\frac{\partial}{\partial t} + \frac{\partial}{\partial R} + \frac{1}{R} \right) \begin{bmatrix} \widetilde{u} \\ \widetilde{v} \\ \widetilde{w} \\ \widetilde{p} \end{bmatrix} = 0 \tag{3.4}$$

where $R = (r^2 + x^2)^{\frac{1}{2}}$.

As $r \to 0$ (3.1) has a numerical singularity and cannot be used as it is. We note, however, that near the axis, if we consider the Fourier-Laplace transform of (3.1) in x and t, the local solution has the form

$$\widetilde{u} \sim J_m(\beta r)$$

$$\widetilde{v} \sim \frac{dJ_m(\beta r)}{dr}$$

$$\widetilde{w} \sim \frac{J_m(\beta r)}{r} \tag{3.5}$$

$$\widetilde{p} \sim J_m(\beta r)$$

where β is a parameter involving the transformed variables and $J_m(\ )$ is the mth-order Bessel function. It is well established (see Ref. [6]), that Bessel functions of integer order can be analytically extended into the region of negative argument as,

$$J_m(-\beta r) = (-1)^m J_m(\beta r). \tag{3.6}$$

By means of (3.6), the solution may be extended to the negative r part of the $x - r$-plane as follows,

$$\widetilde{u}(-r, x) = (-1)^m \, \widetilde{u}(r, x)$$

$$\widetilde{v}(-r, x) = (-1)^{m-1} \, \widetilde{v}(r, x)$$

$$\widetilde{w}(-r, x) = (-1)^{m-1} \, \widetilde{w}(r, x) \tag{3.7}$$

$$\widetilde{p}(-r, x) = (-1)^m \, \widetilde{p}(r, x).$$

Formula (3.7) allows us to extend the computed solution into the lower half of the $x - r$-plane as indicated in figure 5. In this way, points near the axis, but not on the axis such as point A in figure 5, the 7-point stencil can be extended into the negative r half-plane as shown. For the points on the axis, such as point B in figure 5, they will not be calculated by the time marching DRP scheme. They are to be found, after the values at all the other points have been updated to a new time level, by symmetric interpolation. Such a 7-point interpolation stencil for point B is shown in figure 5.
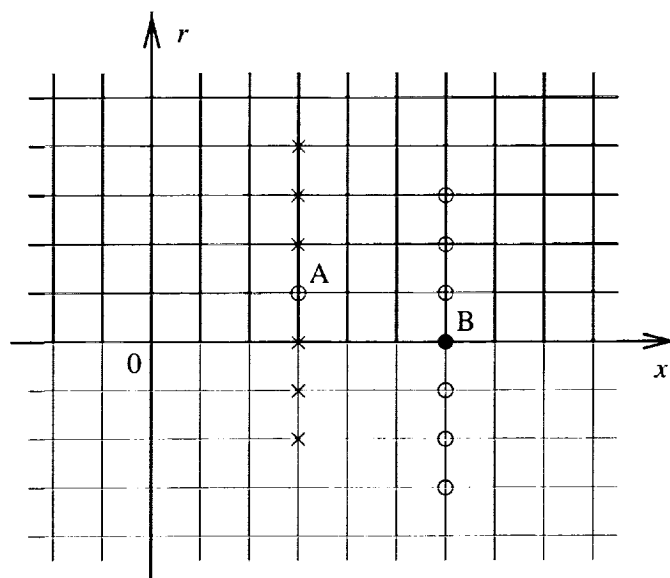
Figure 5. Extension of the computational domain in the upper half
$x - r$ plane to the nonphysical lower half plane

3.3. Artificial Selective Damping

Artificial selective damping is incorporated into the DRP computation algorithm for two purposes. First, it is used to provide background damping to eliminate short spurious waves to prevent them from propagating across the computation domain. Generally speaking, small amplitude short spurious waves are just low level pollutants of the numerical solution. But if these waves are allowed to impinge on an internal or external boundary of the computation domain, they could lead to the reflection of large amplitude long waves. These spurious long waves are sometimes not distinguishable from the physical solution and is, therefore, extremely undesirable. The second reason to add artificial selective damping is to stabilize the numerical solution at a discontinuity. The damping prevents the build-up of spurious short waves, which are generated by the discontinuity, and this promotes stability.

In the present problem, the forcing functions are discontinuous at the blade tip. Thus, in addition to the general background damping with an inverse mesh Reynolds number 0.05, extra damping is added around the blade tip region. The mesh size change interface as well as the external boundary of the computation domain are also a form of discontinuity. Extra damping is added around these boundaries as well. For extra damping, a distribution of inverse mesh Reynolds number in the form of a Gaussian function with a half-width of 4 mesh spacings normal to the boundary is used. The maximum of the Gaussian is on the discontinuity with an assigned value of 0.05. At the tip of the blade, where the forcing function is discontinuous, more damping is required. A maximum value of 0.75 is used instead.

3.4. Numerical Results

Equations (3.1) are discretized according to the multiple-size-mesh multiple-time-step DRP scheme and marched in time to a time periodic state. To start the computation, the zero initial condition is used. Figure 6 shows a comparison of the directivity at $R = 50$ obtained computationally and the exact solution for $\Omega = 0.85$, the subsonic tip speed case. As expected, most of the acoustic radiation is concentrated in the plane of rotation. There is good agreement between the numerical results and the exact solution. Figure 7 shows the directivity at supersonic tip speed with $\Omega = 1.15$. There is again good agreement. At the higher frequency, the acoustic wave length is shorter. Thus, figure 7 is a more stringent test of the accuracy of the entire computation algorithm.
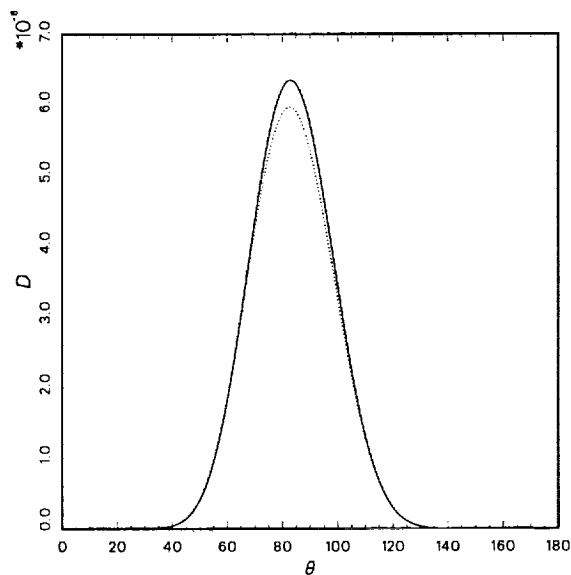
Figure 6. Directivity of sound radiation at $R = 50$, $\Omega = 0.85$,
——— numerical, $\cdots\cdots\cdots$ asymptotic
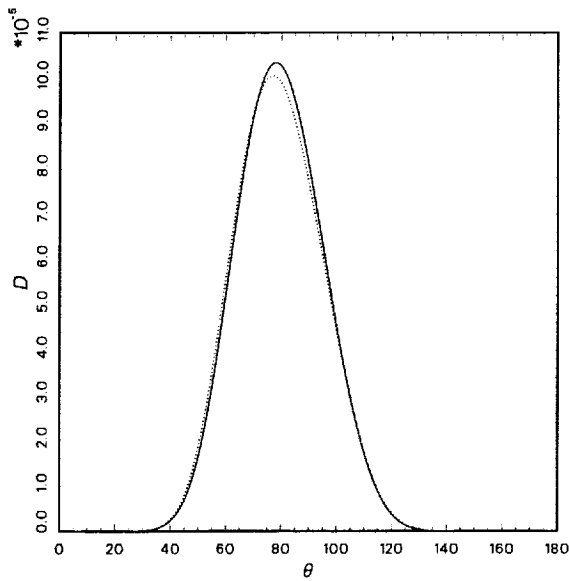
Figure 7. Directivity of sound radiation at $R = 50$, $\Omega = 1.15$,
———— numerical, $\cdots\cdots\cdots$ asymptotic

Acknowledgments

References

1. Tam, C.K.W. and Webb, J.C.: Dispersion-Relation-Preserving Finite Difference Schemes for Computational Acoustics. *J. Computational Physics*, vol. 107, Aug. 1993, pp. 262–281.

2. Shen, H. and Tam, C.K.W.: Numerical Simulation of the Generation of Axisymmetric Mode Jet Screech Tones. *AIAA J*, vol. 36, Oct. 1998, pp. 1801–1807.

3. Tam, C.K.W. and Kurbatskii, K.A.: Microfluid Dynamics and Acoustics of Resonant Liners. AIAA Paper 99-1850, May 1999; to appear in the *AIAA J*.

4. Tam, C.K.W. Webb, J.C. and Dong, Z.: A Study of the Short Wave Components in Computational Acoustics. *J. Comput. Acoustics*, vol. 1, Mar. 1993, pp. 1–30.

5. Tam, C.K.W.: Computation Aeroacoustics: Issues and Methods. AIAA J., vol. 33, Oct. 1995, pp. 1788–1796.

6. Magnus, W. and Oberhettinger, F.: *Formulas and Theorems for the Functions of Mathematical Physics*. Chelsea Publishing Company, New York, 1949.

ON COMPUTATIONS OF THIRD CAA WORKSHOP BENCHMARK PROBLEMS

Jianping Yin and Jan Delfs

DLR, Institute of Design Aerodynamics, Technical Acoustics
Lilienthalplatz 7
38108 Braunschweig, Germany

Abstract

The high order Dispersion-Relation-Preserving (DRP) scheme is used to solve the first two category 1 problems of the third CAA Benchmark workshop. The perturbation equations about the mean flow are used as governing equations in solving two problems. Special non-homogeneous inflow and outflow boundary conditions are derived to generate incoming or outgoing disturbances. In order to create accurate results and keep a minimum number of grid points, a non-uniform grid system in which neighboring mesh sizes differ by a factor of 2 are used. In the area of grid interface, a combination of Tam & Webb DRP and Lele's cell-centered high order differencing scheme are implemented, not requiring any interpolation. Large oscillations typically produced by high order spatial schemes when the stencil extends across a discontinuity such as a shock are avoided by introducing three methods, namely shock perturbation relation method (SPRM), averaged mean flow discontinuity method (AMFDM) and limiter method (LM).The mean flow solutions are obtained analytically by using one dimensional isentropic flow as well as the shock relations.

1. Introduction

The focus of computational aeroacoustics (CAA) is concentrated on obtaining long term time accurate numerical solutions to unsteady flow and acoustic problems. There are several different concepts of how to simulate acoustic problems numerically(refs.1). The main three of which are (1) employing an acoustic wave-equation approach in combination with a predetermined dedicated acoustic source term, (2) the direct numerical simulation (DNS) of all vortical scales, or the large eddy simulation (LES) of all essential scales including the sound generation, and (3) the perturbation approach, in which an averaged (quasi-) steady flow is pre-computed and any perturbations to it are simulated, using Euler's equations. In this paper, only method 3 is used to solve the third benchmark problem.

The numerical study of aeroacoustic problems places stringent demands on the choice of a computational algorithm. For long it has been recognized that numerical schemes with minimal dispersion and dissipation error are needed, since the acoustic waves are non-dispersive and non-dissipative in their propagations. Therefore, all the benchmark problems considered here are solved by using Tam & Webb's 7 points DRP scheme (ref. 2) which is generally only used for uniform grids. In case of non-uniform grid systems in which the neighboring mesh sizes differ by a factor of 2, a combination of DRP scheme and Lele's cell-centered high order scheme (ref. 3) are implemented to describe the derivative. The time advancing schemes used here are classical 4 stage Runge-Kutta schemes.

2. Category 1, Problem 1: Propagation of sound wave through a transonic nozzle

To reduce the complexity of the problem, but maintaining the basic physics, this problem has been modeled by a one-dimensional acoustic wave transmission problem through a nearly choked nozzle.

The governing equations, which are non-dimensionized with respect to the characteristic values in the uniform region downstream of the throat, read as follows,

$$\frac{\partial \rho}{\partial t} + \frac{1}{A}\frac{\partial}{\partial x}(\rho u A) = 0 \qquad (1)$$

$$\frac{\partial u}{\partial t} + u\frac{\partial u}{\partial x} + \frac{1}{\rho}\frac{\partial p}{\partial x} = 0$$

$$\frac{\partial p}{\partial t} + \frac{1}{A}\frac{\partial}{\partial x}(p u A) + \frac{\gamma-1}{A}p\frac{\partial}{\partial x}(u A) = 0, \ (\gamma = 1.4)$$

where A describes the cross section along the nozzle with following area distributions

$$A(x) = \begin{cases} 0.536572 - 0.198086e^{-(\ln 2)\left(\frac{x}{0.6}\right)^2}, x > 0 \\ \\ 1.000000 - 0.661514e^{-(\ln 2)\left(\frac{x}{0.6}\right)^2}, x < 0 \end{cases} \qquad (2)$$

The computation domain extends from x=-10 to x=10 with the nozzle throat located at x=0, as shown in Fig.(1)
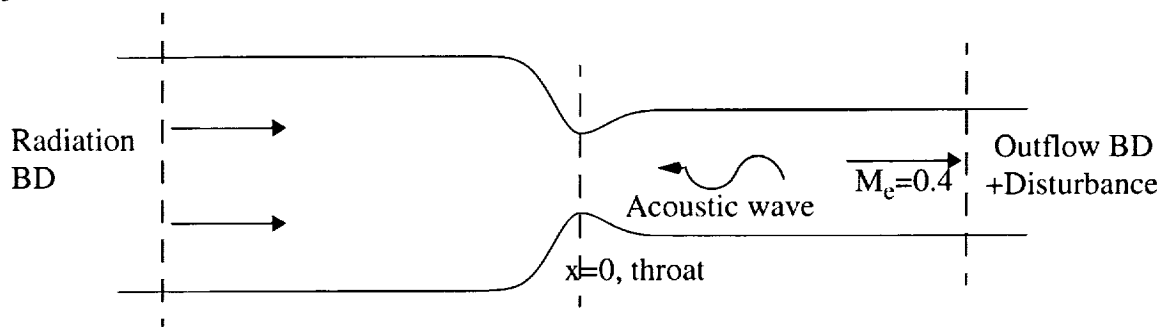
Fig. 1   Schematic diagram of the computation domain for the propagation of sound through a transonic throat of a subsonic nozzle

The perturbation formulation can be obtained by splitting the flow variables into the mean and perturbations, the given mean flow field $(\bar{\rho}, \bar{u}, \bar{p})$, which is steady density, velocity and pressure, respectively. The perturbation equations about the mean flow then have the following forms,

$$\frac{\partial}{\partial t}\rho' + \frac{1}{A}\frac{\partial}{\partial x}(\bar{\rho}u' + \rho'\bar{u} + \rho'u')A = 0 \qquad (3)$$

$$\frac{\partial}{\partial t}u' + (\bar{u} + u')\frac{\partial}{\partial x}u' + \left(u' + \frac{\rho'\bar{u}}{\bar{\rho} + \rho'}\right)\frac{\partial}{\partial x}\bar{u} + \frac{1}{\bar{\rho} + \rho'}\frac{\partial}{\partial x}p' = 0$$

$$\frac{\partial}{\partial t}p' + \frac{1}{A}\frac{\partial}{\partial x}(\bar{p}u'A) + \frac{1}{A}\frac{\partial}{\partial x}(p'\bar{u}A) + \frac{1}{A}\frac{\partial}{\partial x}(p'u'A) + \frac{\gamma-1}{A}p'\frac{\partial}{\partial x}(\bar{u}A) +$$

$$\frac{\gamma-1}{A}(\bar{p} + p')\frac{\partial}{\partial x}(u'A) = 0$$

In this problem, a single frequency $(\omega = 0.6\pi)$ sound wave with very small amplitude $(\varepsilon = 10^{-5})$ is

generated way downstream of the nozzle throat, and it propagates upstream through the nozzle, as shown in Fig. (1). The upstream propagating wave far downstream of the nozzle throat is given as

$$F = \begin{bmatrix} \rho' \\ u' \\ p' \end{bmatrix} = \varepsilon \begin{bmatrix} 1 \\ -1 \\ 1 \end{bmatrix} \cos\left[\omega\left(\frac{x}{1-M}+t\right)\right] \tag{4}$$

Firstly, the steady solution is determined and secondly the perturbation solution is solved.

2.1 Steady flow solution

The physical quantities of the mean flow in the nozzle are connected by the isentropic flow relations as well as the continuity equation. With area ratio A/A_e and M_e known, $\bar\rho$ is first found by solving the following non-linear equation:

$$\bar\rho^{\gamma-1}\frac{1}{\gamma-1} + \frac{M_e^2}{2}\left(\frac{A}{A_e}\right)^{-2}\bar\rho^{-2} - \left(\frac{M_e^2}{2}+\frac{1}{\gamma-1}\right) = 0 \tag{5}$$

where A_e and M_e are area and Mach number at the uniform region downstream of the nozzle throat and $A(x)$ is the area at any given position x in the nozzle.

The other flow variable, pressure $\bar p$, local sound speed a, Mach number M and velocity $\bar u$ can easily be found by

$$\bar p = \frac{1}{\gamma}\bar\rho^\gamma,\ a = \sqrt{\bar\rho^{\gamma-1}},\ M = \frac{M_e}{\bar\rho a}\left(\frac{A}{A_e}\right)^{-1},\ \bar u = Ma \tag{6}$$

For $M_e = 0.4$, the steady solutions are shown in Fig.(2). It can be seen that the local Mach number at the nozzle throat is about 0.94 which is close to sonic. With the known mean solution, the perturbation equation (3) can now be solved by using high order schemes.

2.2 Radiation and outflow boundary condition

From a physical point of view, the upstream propagating sound wave will partly be reflected from the area of the transonic nozzle throat and partly transmitted to the upstream of the nozzle throat. In the nozzle throat, the sound wave amplitude will be amplified. Therefore, to ensure that the computed solutions are of high quality on the limited computation domain, the farfield boundary condition (BD) has to be imposed on both sides of the computation domain as shown in Fig.(1).

At the left boundary of the computation domain, radiation boundary conditions which permit the transmitted acoustic waves to leave the computation domain are to be imposed. These boundary conditions are developed by using asymptotic solutions of the governing equations,

$$\left[\frac{\partial}{\partial t} - (1-M)\frac{\partial}{\partial x}\right]\begin{bmatrix} \rho' \\ u' \\ p' \end{bmatrix} = \begin{bmatrix} 0 \\ 0 \\ 0 \end{bmatrix} \tag{7}$$
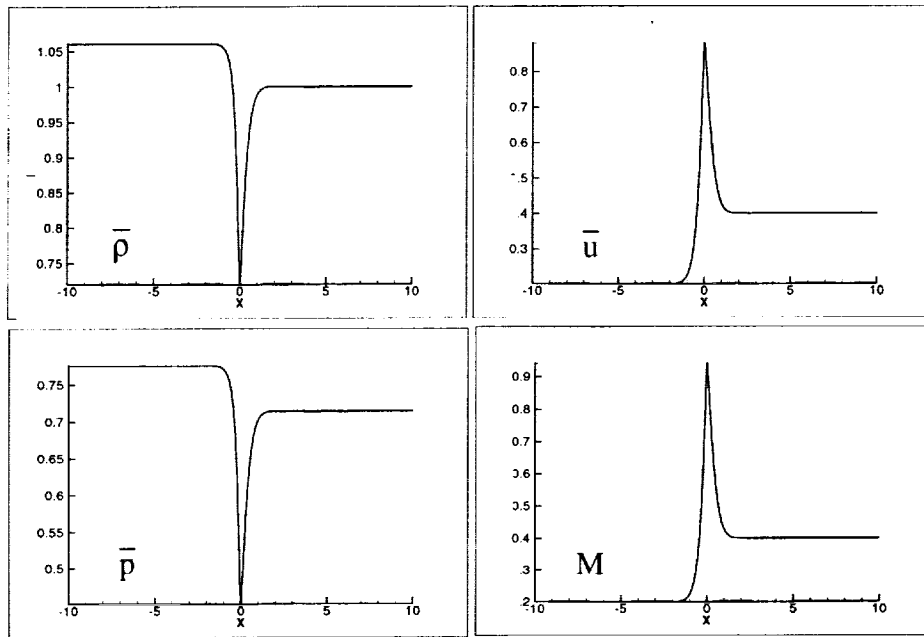
Fig. 2   Mean flow ($\bar{\rho}$, $\bar{u}$, $\bar{p}$, M) distribution along the nozzle for problem 1

At the right boundary of the computation domain, outflow boundary conditions are applied which allow incoming sound waves to propagate upstream into computation domain and at the same time permit entropy waves and reflected acoustic waves to leave the computation domain. Thus by means of the asymptotic solution, in general the density, velocity, and pressure fluctuation can be written in the form of

$$\begin{bmatrix} \rho' \\ u' \\ p' \end{bmatrix} = \begin{bmatrix} 1 \\ 1 \\ 1 \end{bmatrix} F\left(\frac{x}{1-M} + t\right) + \begin{bmatrix} 1 \\ 0 \\ 0 \end{bmatrix} G\left(\frac{x}{M} - t\right) + \begin{bmatrix} 1 \\ 1 \\ 1 \end{bmatrix} H\left(\frac{x}{1+M} - t\right) \tag{8}$$

Where G and H are unknown entropy waves and unknown reflected acoustic waves, respectively, and F is given as Eq.(4). By differentiating Eq.(8) with respect to t and x and eliminating H and G, the following non-homogeneous outflow flow BD can be obtained,

$$\frac{\partial}{\partial t}\rho' + M\frac{\partial}{\partial x}\rho' + \frac{\partial}{\partial x}p' = -\frac{2\omega\varepsilon}{1-M}\sin\left[\omega\left(\frac{x}{1-M} + t\right)\right]F\left(\frac{t}{\tau}\right) \tag{9}$$

$$\frac{\partial}{\partial t}u' + (1+M)\frac{\partial}{\partial x}u' = \frac{2\omega\varepsilon}{1-M}\sin\left[\omega\left(\frac{x}{1-M} + t\right)\right]F\left(\frac{t}{\tau}\right)$$

$$\frac{\partial}{\partial t}p' + (1+M)\frac{\partial}{\partial x}p' = -\frac{2\omega\varepsilon}{1-M}\sin\left[\omega\left(\frac{x}{1-M} + t\right)\right]F\left(\frac{t}{\tau}\right)$$

where $F\left(\dfrac{t}{\tau}\right) = 1 - e^{-\frac{t}{\tau}}$ is a "turning-on" function which has been added to the right side of Eq (9) in order

to turn on the disturbance gradually. The larger τ, the smaller is the DC component in the time history of the solution. Equations (7) and (9) of inflow and outflow BD are used to update the solution at the left and right boundary points of the computation domain.

2.3 Grid systems

In order to keep adequate approximation to the partial derivative, a minimum of 6 to 8 mesh points per wave length is required by the DRP scheme. The mean flow in the nozzle is so strongly non-uniform, especially close to the nozzle throat, that the wavelength of the propagated acoustic waves are strongly varying too. In general the non-dimensional wavelength can be estimated as $\lambda \cong 2\pi(1 - M)/\omega$. Since the maximum M in the nozzle throat is 0.94, the sound wave has a minimum wave length of $\lambda \cong \lambda_0 \bullet 0.06$ in that area, where λ_0 corresponds to non-dimensional wavelength under zero mean flow and $\lambda_0 = 3.33$ in the present case. Due to the problem description, it is required that no more that 400 mesh points be used. A uniformly spaced grid mesh with 400 grid points in the computation domain could only render 4 mesh points per wave length, which is much less than that required by the DRP scheme. Therefore, a non-uniform grid system in which the neighboring mesh size differs by a factor of 2 is used, as shown in Fig.(3)
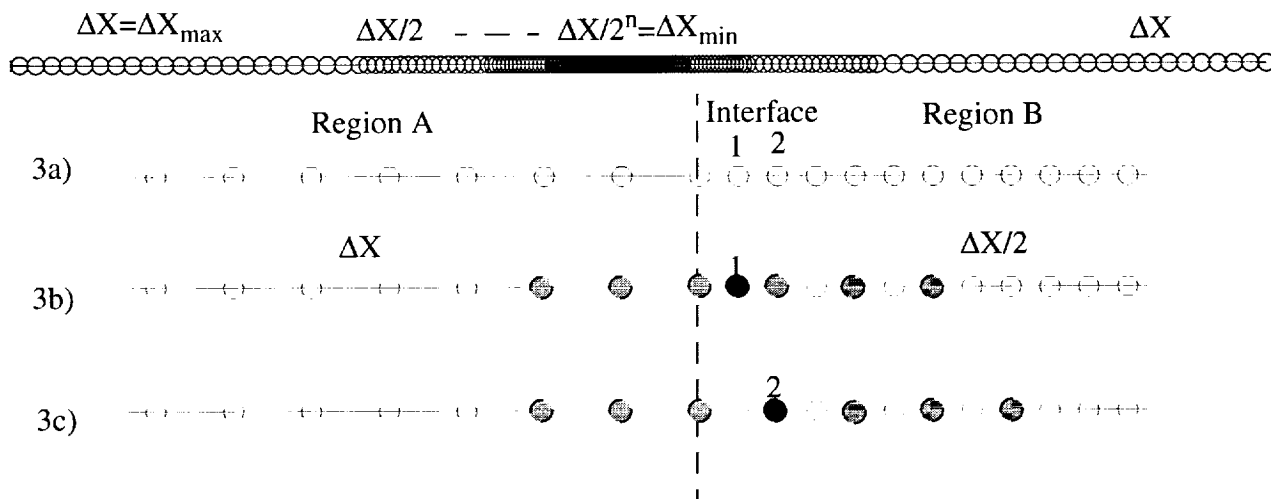
Fig. 3   A non-uniform grid system. The neighboring mesh size differs by a factor of 2.

Since the grid size in adjacent areas differs by a factor of 2 as shown in Fig.(3a), it is not difficult to form a 7 points DRP stencil at every point in region A with a mesh size of Δx and every point in region B using a mesh size of $\Delta x/2$ except for the first two points from the interface.

For the second point shown in Fig.(3c), a DRP stencil with a grid size of Δx can be implemented. For the first point, a Lele cell-centered symmetric stencil (CC), as shown in Fig.(3b), is used. A 6th-order explicit scheme based on this stencil can be obtained from an approximation of the form

$$f'_i = \frac{c}{5h}\left(f_{i+\frac{5}{2}} - f_{i-\frac{5}{2}}\right) + \frac{b}{3h}\left(f_{i+\frac{3}{2}} - f_{i-\frac{3}{2}}\right) + \frac{a}{h}\left(f_{i+\frac{1}{2}} - f_{i-\frac{1}{2}}\right) \qquad (10)$$

where $h = \Delta x$ and $a = 1.171875, b = -0.1953125, c = 0.0234375$. It should be noted that this concept can be directly transferred to 2D and 3D, by applying the mid-point differencing of Lele along the grid diagonals in 2D and 3D.

The spectrum characteristics of Eq.(10) and its comparison with the DRP scheme as well as the exact solution are given in Fig.(4), where $\bar{\alpha}$ and α are the wave number representation of the finite difference scheme and of the partial derivative respectively.

It can be seen that with $\alpha\Delta x$ up to 1.2 the curve for the CC scheme is nearly the same as the DRP scheme. After that, the CC scheme shows better resolution characteristics than that of the DRP scheme which drops down very quickly for high wavenumbers.
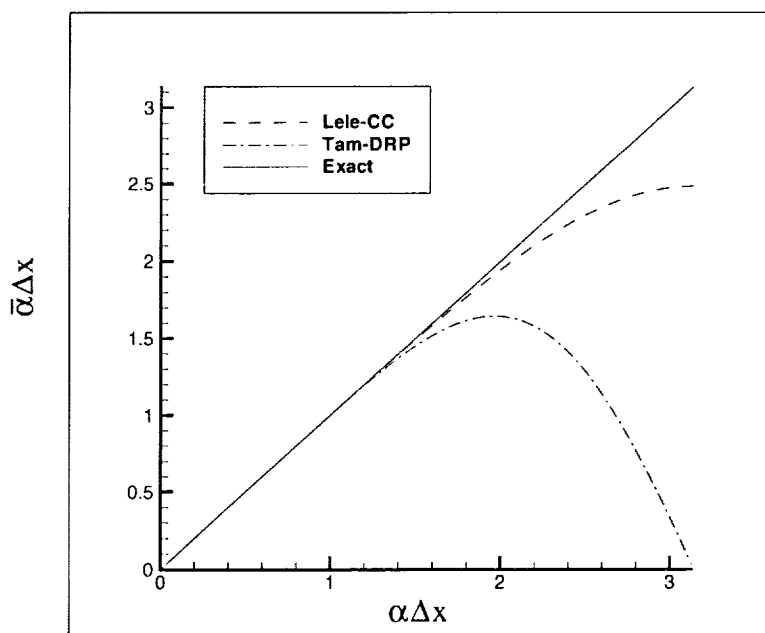
Fig. 4   Plot of modified wavenumber vs. wavenumber for DRP and CC-schemes

To test the numerical dispersion and dissipation properties due to the non-uniform grid, a one dimension nozzle with a uniform area distribution of A=1.0 and uniform mean flow $\left(M = 0.5, \bar{\rho} = 1, \bar{p} = \frac{1}{\gamma}\right)$ is used and a Gaussian distributed acoustic pressure pulse is seeded into the computation domain at x=0.0 at time t=0.0. This initial value problem is solved by the 7 points DRP scheme for the uniform grid and by the combination of DRP and CC schemes for the non-uniform grid. The half width b of the pressure pulse is $3 \bullet 0.25$, which means that the half width of the pulse is resolved with more than 15 points for the uniform grid. In order to eliminate the short wavelength spurious numerical waves generated due to the changing of the grid size and different schemes used in the interface area, Tam's artificial selective damping (ref. 4) is additionally introduced. A background damping coefficient of 2 is used in the numerical computation. In the calculations of the propagation of sound wave through the transonic nozzle, extra damping coefficients are also added to

the background damping in the area close to the nozzle throat where strong flow gradients occur. With inclusion of the artificial selective damping terms, spurious waves are effectively eliminated in the numerical solutions.

The governing equation has the form of Eq.(3). Computations are based on two different grids, one uniform grid with 400 grid points and grid size $\Delta x = 0.05$ and one non-uniform grid with only 209 grid points and the grid size decreasing from $\Delta x_{max} = 0.25$ to $\Delta x_{min} = 0.015625$.

Initial value problem,t=0

$$p = \rho =$$

$$\exp\left[-(\ln 2)\frac{(x^2 + y^2)}{(3 \bullet 0.25)^2}\right]$$

M=0.5

uniform grid:
DRP scheme +
Atificial selective damping
Non-uniform grid:
DRP scheme +
CC scheme +
Atificial selective damping
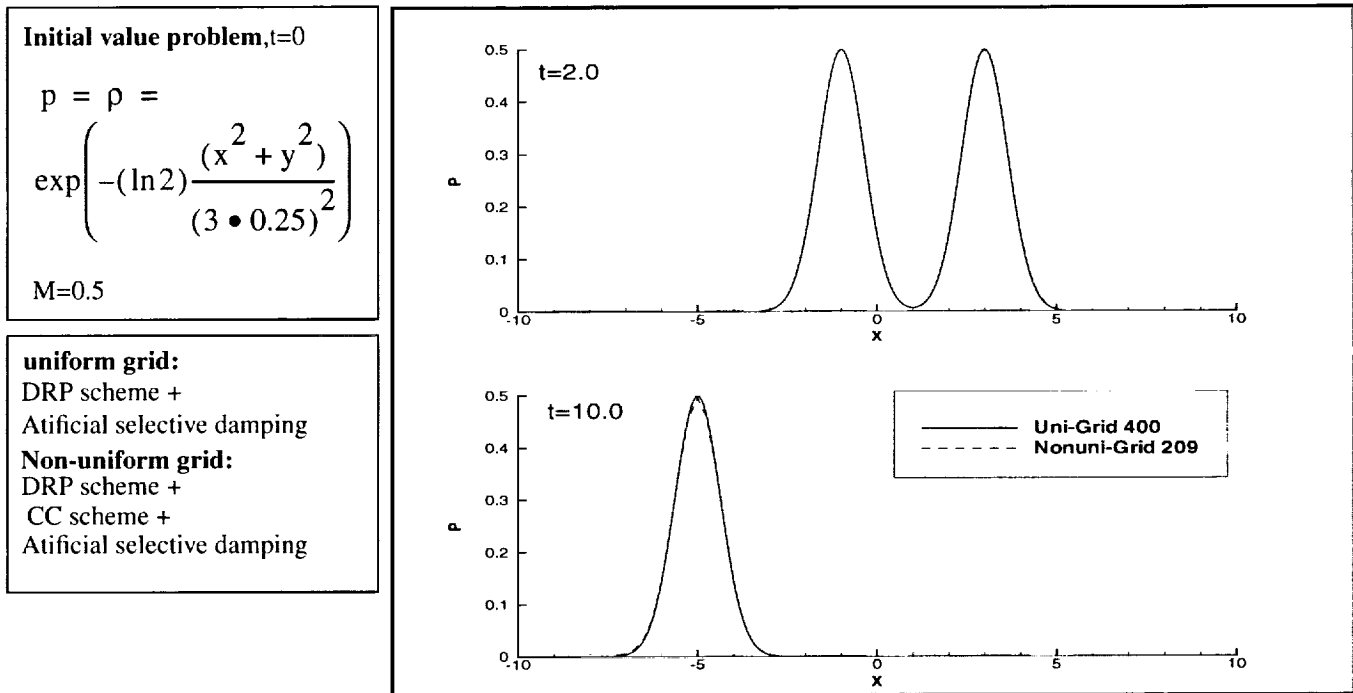
Fig. 5   Acoustic pressure distribution along nozzle axis (uniform cross section)

The calculated waveform at two different time instants t=2.0 and t=10.0 are shown in Fig.(5). When released at time t=0.0 an acoustic pressure pulse is generated and then split into two, the one propagating in the upstream direction and the other in the downstream direction. At time t=10.0, the downstream propagated signal has already left the computation domain. The results for both grids show very small dispersion error. Both the peak value and shape of the waveform on the two grid systems match very well except at t=10.0. At t=10.0, the magnitude of the peak is almost identical. The difference on the shape of the waveform close to the peak is purely due to the graphical representation on the large grid spacing used in the non-uniform grid system.

2.4 Numerical solution for propagation of sound wave through a transonic nozzle

The computation is performed by solving Eq.(3) with the above mentioned hybrid high order schemes and farfield boundary condition. Three different types of grid arrangements, one for uniform grids with 400 grid points and the other two for the non-uniform grids with 209 and 321 grid points, are used. The grid point distribution is so arranged for the non-uniform grid that the finest grid size is always located around the nozzle throat to give the best wave resolution. The numerical computations continue for each grid until a time-periodic state is achieved.

The effects of the different τ on the asymptotic DC component are studied. The non-uniform grid with 209 points is used to carry out a numerical simulation. Fig.(6) shows the time history of the pressure disturbance at the nozzle throat at $\tau = 30$ and the effect of different τ on the DC-component. With increasing τ, the transient DC component drops very sharply from positive to one negative value and then gradually asymptotes to the zero-axis. Although with large τ the DC can be reduced, long running time is needed until the solution attains an asymptotic periodic state. This zero-frequency component will remain in the solution since there is no natural decay of it in a one-dimensional problem. Finally $\tau = 30$ is selected in the following computations.
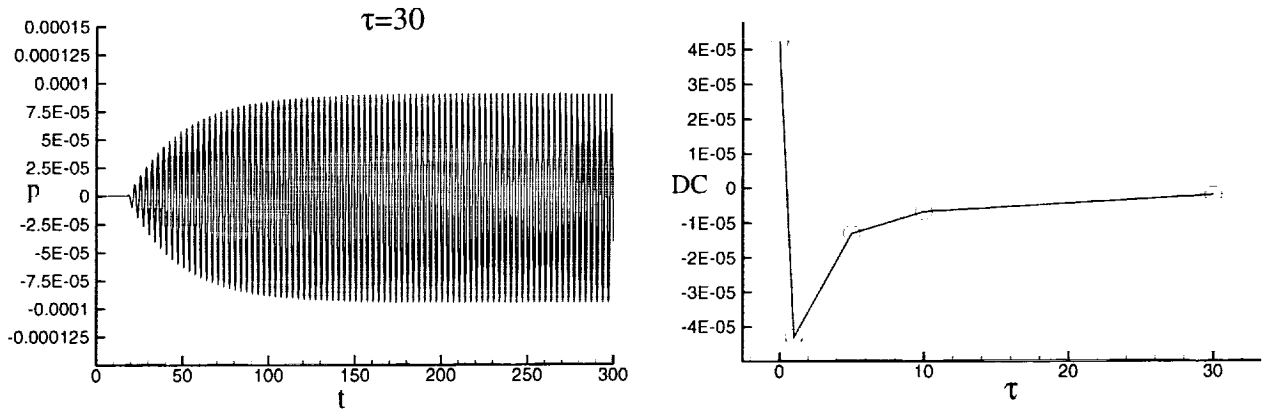
Fig. 6   Time history of pressure disturbance at x=0 and effect of different τ on the DC-component

Turning back to the non-constant nozzle area case, the pressure distribution for the non-uniform grid with 321 grid points in which Δx_{max} and Δx_{min} are 0.125 and 0.0078125 respectively is given in Fig.(7) at time t=320. It shows that the transmitted waves travel upstream from the nozzle throat and leave the domain through the left BD smoothly. Moreover, sound wave interference between upstream propagated wave from outflow BD and reflected waves from nozzle throat is very obvious. In the nozzle throat, the sound signal has been accumulated and amplified.

Fig.(8) shows the distribution of the maximum acoustic pressure over a cycle and the strong gradients zoomed close to the peak area. The comparisons between non-uniform and uniform grid display the effectiveness of the grid refinements. Even with 209 points on the non-uniform grid, almost half of 400 uniform-grid, one can still obtain much better results. The grid refinement is necessary close to the transonic nozzle to capture the physical behavior and this has a pronounced effect on transmitted waves.

3. Category 1,Problem 2: Shock-sound interaction

In this problem, a shock occurs downstream of the nozzle throat in the mean flow solution.The same governing equations as Eq.(1) are used, with which the problem is simplified as a sound wave passing through a shock in a quasi-1D supersonic nozzle. All physical quantities used in the governing equations are non-dimensionalized using the upstream value. The same geometry is used as in problem 1.

Due to the formation of a shock in the nozzle, the change of the perturbation signal is attributed to the induced motion of the shock wave and its interaction with the disturbances in the flow. These disturbances may be large so that the mean flow and shock position will change or they are small such as in the case of acoustic wave or vorticity wave. Since the sound wave used in the present problem has the magnitude of 10^{-5}, the

problem is solved again by using perturbation formulation. In doing so, there is no feed-back loop between the mean flow and the perturbation is assumed and the motion of shock is neglected, which is believed to be very small due to the small disturbance.
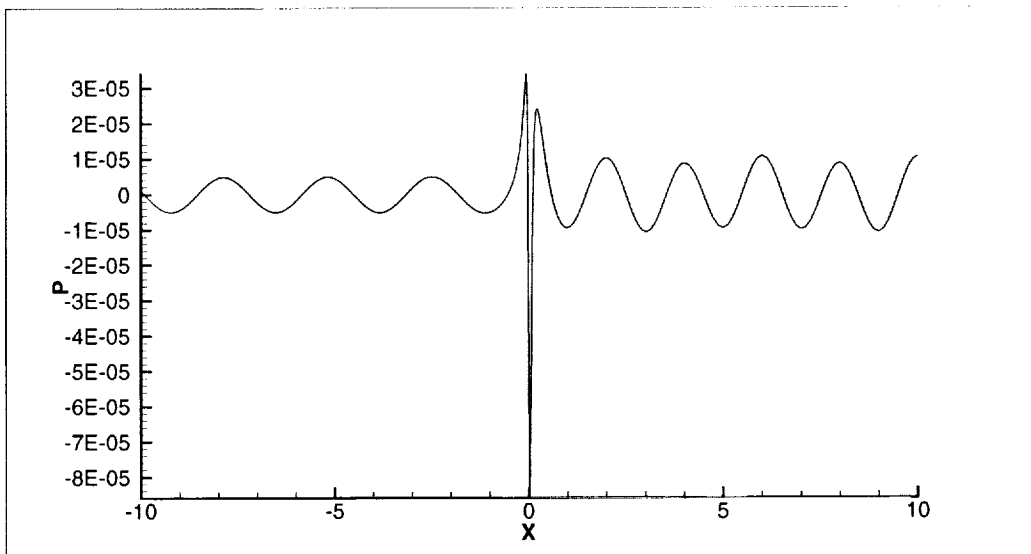
Fig. 7   Pressure distribution for non-uniform grid with 321 grid points at t=320
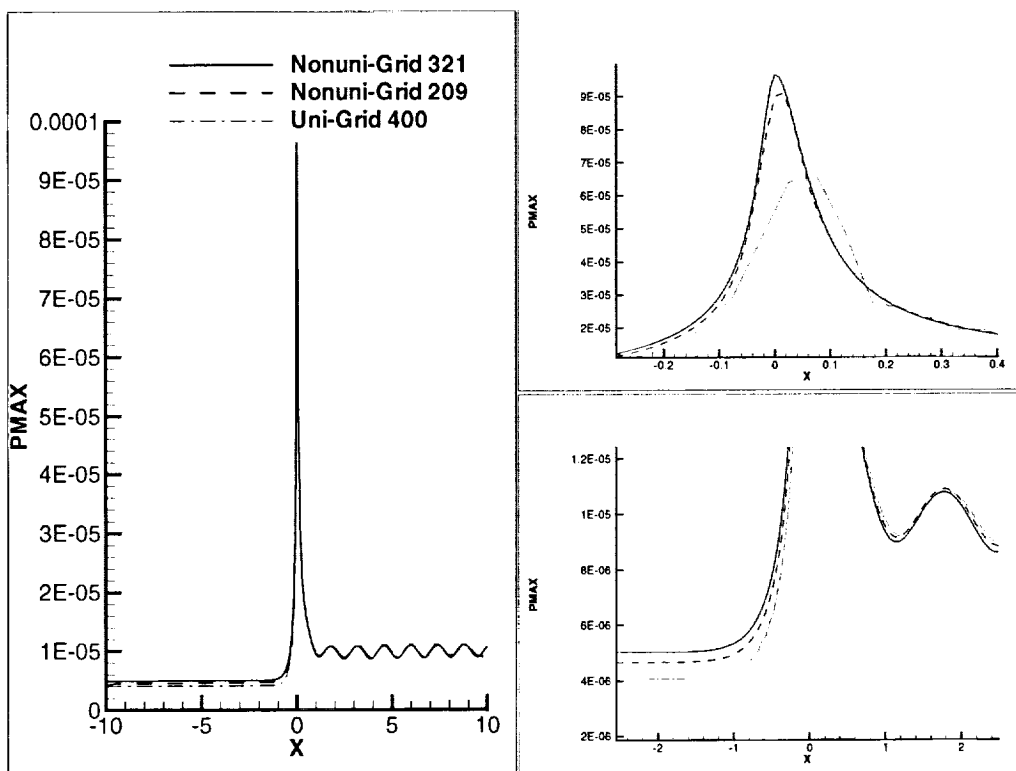
Fig. 8   The distribution of the maximum acoustic pressure over a cycle

In order to propagate reliable information to the area downstream of the shock, the interaction between the shock and the disturbance must be accurately predicted. Numerical difficulties in the form of large oscillations occur using high order spatial schemes such as DRP or CC schemes when the stencil spans a discontinuity

such as a shock. Three methods, which are named shock perturbation relation method (SPRM), averaging mean flow discontinuity method (AMFDM) and limiter method (LM) are developed to avoid these problems.

The steady shock flow is solved by using isentropic flow and shock relations. The similar non-uniform grid system as in problem 1 with the finest grid size in the area of the shock is used in the numerical simulation.

3.1 Steady shock flow solution

Two separated isentropic flow relations, one for the domain extending from inflow face to the pre-shock position and the other for the flow behind the shock are used and are connected by shock relations. Using isentropic flow relations and shock relations and assuming total temperature keeping constant across the shock, one can figure out the equation for the pre-shock mach number M_1,

$$\left(\frac{\bar{p}_{02}}{\bar{p}_{01}}\right)^{\gamma-1}\left(1 + \frac{2\gamma}{\gamma+1}(M_1^2 - 1)\right)\left((\gamma-1)M_1^2 + 2\right)^{\gamma} - \left((\gamma+1)M_1^2\right)^{\gamma} = 0 \tag{11}$$

Where $\bar{p}_{01}$ and $\bar{p}_{02}$ are total pressure of pre- and after shock respectively.

$$\bar{p}_{02} = \bar{p}_e\left(\frac{(\gamma-1)}{2}M_e^2 + 1\right)^{\frac{\gamma}{\gamma-1}}, \bar{p}_{01} = \bar{p}_t\left(\frac{(\gamma-1)}{2}M_t^2 + 1\right)^{\frac{\gamma}{\gamma-1}}, M_t = 1.0 \tag{12}$$

$$M_e^2\left(\frac{(\gamma-1)}{2}M_e^2 + 1\right) = \left(\frac{\bar{p}_t}{\bar{p}_e}\right)^2\left(\frac{A_t}{A_e}\right)^2\left(1 + \frac{\gamma-1}{2}\right)$$

The subscript t and e here represent taking the value at nozzle throat and uniform region downstream of the shock. $\bar{p}_t$ can be solved by replacing M_e and A_e with M_t and A_t in the Eq.(5) and (6). $\bar{p}_e$ is given as 0.6071752. Then the shock position x_1 can be found by solving the following equation,

$$\frac{A(x_1)}{A_t} = \frac{1}{M_1}\sqrt{\left(\frac{(\gamma-1)}{2}M_1^2 + 1\right)\left(\frac{\left(\frac{(\gamma-1)}{2}M_1^2 + 1\right)}{\left(1 + \frac{\gamma-1}{2}\right)}\right)^{\frac{1}{\gamma-1}}}{\left(1 + \frac{\gamma-1}{2}\right)} \tag{13}$$

The steady solutions are shown in Fig.(9). The shock position is around $x_1 = 0.4$.

3.2 Inflow and outflow boundary condition

The same computation domain is chosen as for problem 1 except small sound waves are introduced at the inflow BD. Therefore, the inflow BD of Eq.(7) has to be modified to include this disturbance,

$$\left[\frac{\partial}{\partial t} - (1 - M)\frac{\partial}{\partial x}\right]\begin{bmatrix} \rho' \\ u' \\ p' \end{bmatrix} = -\begin{bmatrix} 1 \\ 1 \\ 1 \end{bmatrix}\frac{2\omega\varepsilon}{1 + M}\cos\left[\omega\left(\frac{x}{1 + M} - t\right)\right]F\left(\frac{t}{\tau}\right) \tag{14}$$

Where ω and ϵ are the same as problem 1. The outflow BD can be obtained by setting F=0 in Eq.(9).
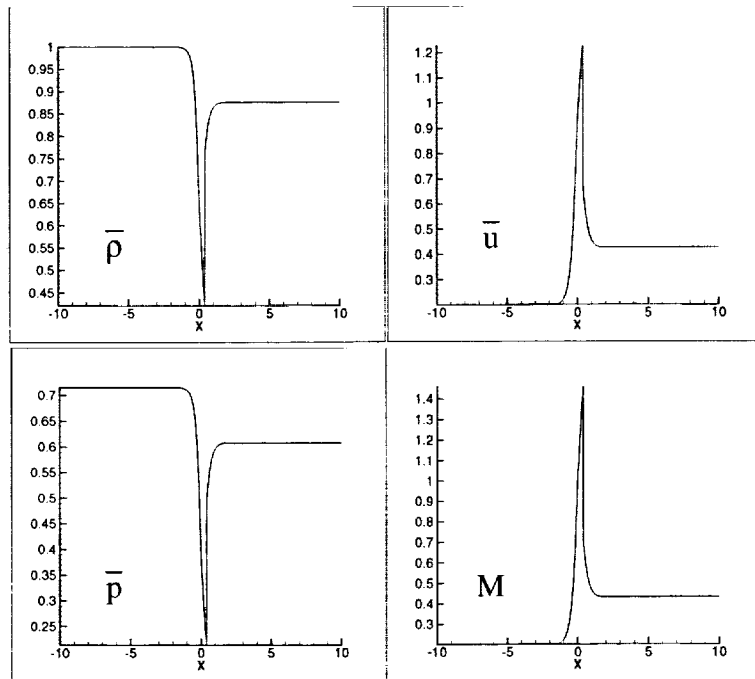
Fig. 9   Mean flow ($\bar{\rho}$, $\bar{u}$, $\bar{p}$, M) distribution along the nozzle

3.3 Numerical solution on sound-shock interaction

In order to reduce or avoid large oscillation when using high order schemes, three methods are introduced.

(1). Averaging mean flow discontinuity method (AMFDM)

In this method whenever DRP (or other high-order scheme) stencils come across the shock located between $x=s_1$ and s_2 as shown in Fig.(10), the function values at s_1 and s_2 are averaged. As an example of a DRP-stencil centered at a pre-shock position, the following approximation for the finite difference scheme at x will be used,

$$\frac{\partial}{\partial x}\bar{f}(x) \cong \frac{1}{(\Delta x)}\left(\sum_{j=-3}^{0} a_j\bar{f}(x+j\Delta x) + a_1 f(x_1) + \frac{a_2}{2}(\bar{f}(x_2)+\bar{f}(x_3)) + \frac{a_3}{2}(\bar{f}(x_2)+\bar{f}(x_3)) \right) \tag{15}$$
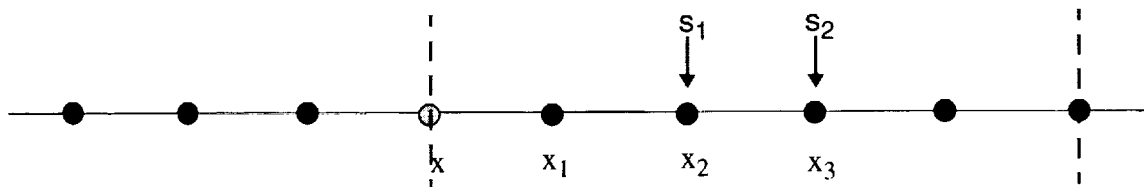
Fig. 10   Stencil used for AMFDM method

(2). Limiter method (LM) - set a limiter on finite difference of mean flow

Two procedures have to be executed for this method. DRP differentiation at x is considered. Firstly, for domain bounded by the vertical dashed line, see Fig.(11), two extra-points are linearly interpolated between two adjacent grid points using the function value on these two grid points. Secondly, the generated extra-points are used in the DRP stencil and a limiter is set on it as given in Eq.(16)
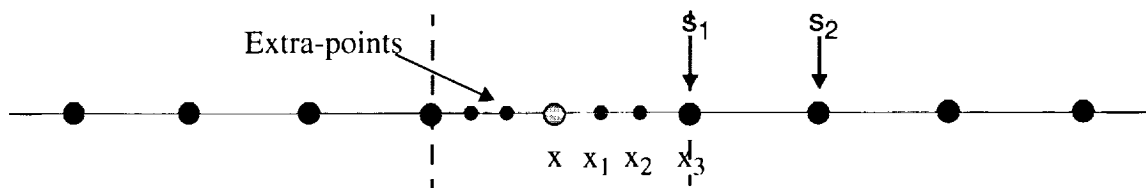
Fig. 11 Stencil used for LM method

$$\frac{\partial}{\partial x}\bar{f}(x) \cong \frac{\kappa}{((\Delta x)/3)}\left(\sum_{j=-3}^{0} a_j \bar{f}\left(x + j\frac{\Delta x}{3}\right) + a_1 f(x_1) + a_2 \bar{f}(x_2) + a_3 \bar{f}(x_3) \right), \kappa = 0.6 \tag{16}$$

(3). Shock perturbation relation method (SPRM)

By perturbing the shock relation about the mean flow, an explicit linearized relation between the pre-and post-shock perturbations may be obtained:

$$
\begin{bmatrix} \rho'_2 \\ u'_2 \\ p'_2 \end{bmatrix} =
\begin{bmatrix} \bar{u}_2 & \bar{\rho}_2 & 0 \\ \bar{u}_2^2 & 2\bar{u}_2\bar{\rho}_2 & 1 \\ \dfrac{-\gamma}{\gamma-1}\dfrac{\bar{p}_2}{\bar{\rho}_2^2} & \bar{u}_2 & \dfrac{\gamma}{\gamma-1}\dfrac{1}{\bar{\rho}_2} \end{bmatrix}^{-1}
\begin{bmatrix} \bar{u}_1 & \bar{\rho}_1 & 0 \\ \bar{u}_1^2 & 2\bar{u}_1\bar{\rho}_1 & 1 \\ \dfrac{-\gamma}{\gamma-1}\dfrac{\bar{p}_1}{\bar{\rho}_1^2} & \bar{u}_1 & \dfrac{\gamma}{\gamma-1}\dfrac{1}{\bar{\rho}_1} \end{bmatrix}
\begin{bmatrix} \rho'_1 \\ u'_1 \\ p'_1 \end{bmatrix} \tag{17}
$$

Where indices 1, 2 denote pre- and post-shock state respectively. To implement this method, following scheme arrangements are used. For the three pre-shock grid points the DRP-backward stencils are used as shown in Fig.(12). For the two post-shock points downstream of s_2 the DRP forward stencils including point s_2 are used. To update the value at s_2, Eq.(17) is used. This method avoids the DRP stencils across the shock.
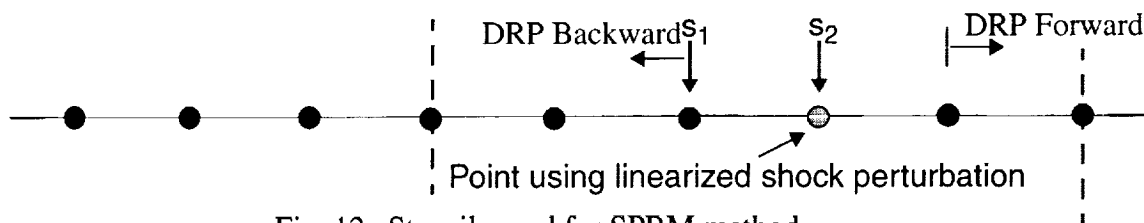
Fig. 12 Stencils used for SPRM method

In order to implement AMFDM and LM methods, Eq.(3) has been modified, in that the differentials for the mean flow variables and the perturbation variables are separated, as given in Eq.(18). Eq.(3) is used for the implementation of the SPRM method. A non-uniform grid with 393 grid points is used. Fig.(13) shows the time-asymptotic distribution of the pressure perturbation at start of a period for above three methods in comparison with the exact solution. Comparisons show that the effects of different shock treatments on the results upstream of the nozzle throat are very small since no information will be fed back upstream due to the supersonic flow.

$$\frac{\partial}{\partial t}\rho' + \frac{u'}{A}\frac{\partial}{\partial x}\bar{\rho}A + \frac{\rho'}{A}\frac{\partial}{\partial x}\bar{u}A + \bar{\rho}\frac{\partial}{\partial x}u' + \bar{u}\frac{\partial}{\partial x}\rho' + \frac{1}{A}\frac{\partial}{\partial x}\rho'u'A = 0 \tag{18}$$

$$\frac{\partial}{\partial t}u' + (\bar{u} + u')\frac{\partial}{\partial x}u' + \left(u' + \frac{\rho'\bar{u}}{\bar{\rho} + \rho'}\right)\frac{\partial}{\partial x}\bar{u} + \frac{1}{\bar{\rho} + \rho'}\frac{\partial}{\partial x}p' = 0$$

$$\frac{\partial}{\partial t}p' + \frac{u'}{A}\frac{\partial}{\partial x}(\bar{p}A) + \left(\frac{1}{A} + \frac{\gamma - 1}{A}\right)p'\frac{\partial}{\partial x}(\bar{u}A) + \bar{p}\frac{\partial}{\partial x}u' + \bar{u}\frac{\partial}{\partial x}p' +$$

$$\frac{1}{A}\frac{\partial}{\partial x}(p'u'A) + \frac{\gamma - 1}{A}(\bar{p} + p')\frac{\partial}{\partial x}(u'A) = 0$$

The pressure distributions, shown as well in zoom scale near shock show the SPRM method gives the best representation of the sound wave in general, while LM and AMFDM have some dispersion error. The sound waves downstream of the shock and in the shock area are very much dependent on the different shock treatments. The LM method renders a fairly good representation of the amplitude downstream of the shock, but there is a small phase difference to exact solution. AMFDM method in general underestimates the signal downstream of the shock.
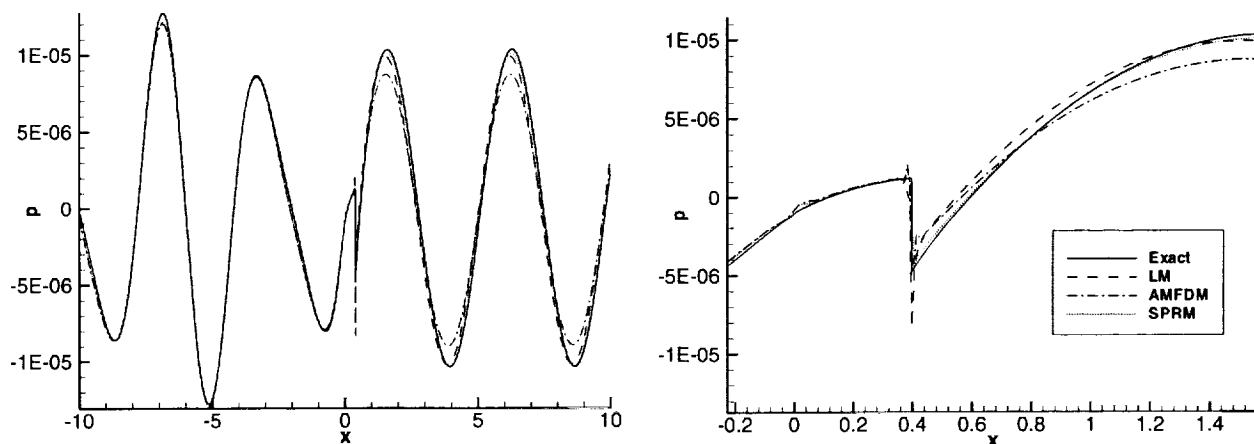
Fig. 13 Distribution of the pressure perturbation at the start of a period

The instantaneous pressure field at the exit plane through one period as given in Fig.(14) again shows the same tendency.
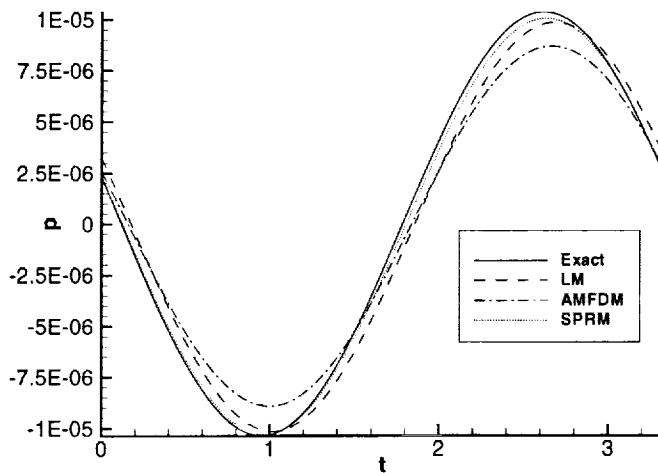
Fig. 14   Instantaneous pressure field at the exit plane through one period.

Conclusions

(1) In order to produce accurate results and keep a limited number of grid points, a non-uniform grid system is used to solve problems 1 and 2. The results show the grid refinements to be effective when a combination of the DRP and cell-centered high order schemes as well as artificial selective damping are used at the grid interface.

(2) The DRP scheme and proper treatments in the area close to the shock can generate convergent results.

(3) The effects of different treatments on the results are seen in the area downstream of the shock; but little effects on the results are observed in the area upstream of the shock.

(4) The SPRM method gives the best representation of the sound wave in general.

References

1.Delfs, J., Yin, J. and Li, X. :Leading Edge Noise Studies using CAA, AIAA 99-1897,1999.
2.Tam, C.K.W. and Webb, J.C. : Dispersion Relation Preserving Finite Difference Schemes for Computational Acoustics, J. Comp. Phys.,107,262-281,1993.
3.Lele, S.K. :Compact Finite Difference Schemes with Spectral-like Resolution, J. Comp. Phys., 103,16-42,1992.
4.Tam, C.K.W. and Dong, Z.: Wall Boundary Conditions for High-order Finite Difference Schemes in Computational Aeroacoustics, Theoretical and Computational Fluid Dynamics,6,303-322,1994.

SOLUTION OF THIRD COMPUTATIONAL WORKSHOP INTERNAL PROPAGATION PROBLEMS USING LOW ORDER SCHEMES

JEFFREY HILTON MILES

National Aeronautics and Space Administration

Glenn Research Center at Lewis Field

Cleveland, OH 44135

Abstract

The problems solved are Category 1 Problems 1 and 2. Problem 1 is solved using a MacCormack scheme. Problem 2 is solved by perturbation of a conservative Euler equation solution to the steady state. The problems are solved on evenly spaced grids. While solutions were found, the methods selected and not using stretched grids lead to solutions which do not compare well with those found using more accurate schemes. However, the perturbation of the mean flow scheme used to solve problem 2 shows promise.

1 Introduction

The claim is often made that the computation of aeroacoustic problems requires numerical schemes of high accuracy, low dispersion, and almost non-dissipation [1, 2]. This paper shows some of the complications that arise in obtaining a solution for the propagation of sound waves through a transonic nozzle for cases where the flow is nearly sonic and for cases where the flow has shocks if one ignores these requirements and uses lower order schemes.

The problems solved are Category 1 Problems 1 and 2. Problem 1 is solved using a MacCormack scheme. Problem 2 is solved by perturbation of a conservative Euler equation solution to the steady state. The problems are solved on evenly spaced grids. While solutions were found, the methods selected and not using stretched grids lead to solutions which do not compare well with those found using more accurate schemes.

2 Governing Equations and Numerical Formulation

2.1 Problem 1

The solution scheme used to solve the propagation of sound waves through a transonic nozzle problem uses the conservative nonlinear acoustic formulation Hariharan and Lester [3, 4] and a low order MacCormack computation scheme. The mean flow was found using analytical gas dynamic equations.

The MacCormack differencing scheme used to generate numerical solutions has two steps applied at $\Delta t/2$ intervals. The first step involves a backward predictor, $L^+ = \frac{\partial f}{\partial x} = (f_i - f_{i-1})/h$ and a forward corrector, $L^- = \frac{\partial f}{\partial x} = (f_{i+1} - f_i)/h$. The second step uses a forward predictor with a backward corrector.

In addition, no grid stretching was used since use of constant spacing maximized the time step size. A total of 381 grid points are used. The largest CFL number that could be used for a convergent solution was $CFL = 4.10^{-3}$. Consequently, for each cycle about 9925 steps were used.

2.2 Problem 2

The solution scheme presented for the Shock-Sound Interaction Problem is based on perturbation of a conservative Euler equation solution. The Euler equation solution is solved using the Steger and Warming (1981) [5] flux vector wave speed splitting technique. Note that while the Steger and Warming (1981) [5] paper discusses using MacCormack schemes to obtain solutions for the flow field, the steady state flow field discussed herein was obtained using procedures described in Chapter 10 Section 3 of Ref. [6] which require a block-tridiagonal solver. The block-tridiagonal solver used is described in Ref. [7].

In addition, again no grid stretching was used since use of constant spacing maximized the time step size. A total of 701 grid points are used. The CFL number used in these calculations was unity.

2.3 Shocks

Due to the limited number of points in the nozzle region the steady state solution did not work well with supersonic flow. To make the code more robust in the nozzle region the following scheme was used when the code has a problem obtaining a solution due to a shock. The code was prompted to use analytical solutions as follows:

$$c_{j-1} = \sqrt{\gamma p_{j-1} c_{ref}^2 / \rho_{j-1}}$$

$$M_{j-1} = u_{j-1} c_{ref} / c_{j-1}$$

$$M_j^2 = \frac{M_{j-1}^2 + \frac{2}{\gamma-1}}{\frac{2\gamma}{\gamma-1} M_{j-1}^2 - 1.}$$

When $M_j^2 > 0$ then

$$T_{j-1} = \frac{MW p_{j-1} c_{ref}^2}{\rho_{j-1} R_{gas}}$$

$$T_j = T_{j-1} \frac{1 + \frac{\gamma-1}{2} M_{j-1}^2}{1 + \frac{\gamma-1}{2} M_j^2}$$

$$p_j = p_{j-1} \frac{1 + \gamma M_{j-1}^2}{1 + \gamma M_j^2}$$

$$\rho_j = \rho_{j-1} \frac{(\gamma+1) M_{j-1}^2}{(\gamma-1) M_{j-1}^2 + 2}$$

$$c_j = \sqrt{\frac{\gamma p_j c_{ref}^2}{\rho_j}}$$

$$u_j = c_j M_j / c_{ref}$$

When $M_j^2 \leq 0$ use

$$
\begin{aligned}
u_j &= u_{j-1} \text{ if } j = 2 \\
u_j &= 0.5(u_{j-1} + u_{j-2}) \text{ if } j > 2 \\
p_j &= 0.2\rho_\infty c_\infty^2 / \rho_{ref} c_{ref}^2 \\
\rho_j &= \gamma p_{j-1} / u_j^2
\end{aligned}
$$

2.4 Formulation of Perturbation Scheme

After making sure one can use the mean flow program and obtain a mean flow solution for $\bar{\rho}$, $\bar{u}$, and $\bar{p}$, one must modify the steady state program to solve the perturbation problem.

The first step in creating the perturbation scheme is to note that one can create the average of density, velocity and pressure using a recursive method. Y(n) the average of x(n) over n time steps can be calculated from

$$
\begin{aligned}
y(n) &= \frac{1}{n+1} \sum_{k=0}^{n} x(k) \\
(n+1)y(n) &= \sum_{k=0}^{n-1} x(k) + x(n) = ny(n-1) + x(n) \\
y(n) &= \frac{n}{n+1} y(n-1) + \frac{x(n)}{n+1}
\end{aligned}
$$

The second step is to define the start of a period of a wave with frequency f_0 which is advanced in a time step Δt from t to $t + \Delta t$.

Let

$$
\begin{aligned}
\theta_0 &= 2\pi f_0 (\Delta t - 1.10^{-6}) \\
\theta &= 2\pi t
\end{aligned}
$$

Then the start of a cycle is defined as the time at which $\cos(\theta) > \cos(\theta_0)$, $\sin(\theta) > 0$, and $\sin(\theta) < \sin(\theta_0)$. Using this scheme the average over a period for the Nth period of the density, $< \rho >$, velocity, $< u >$, and pressure, $< p >$ can be calculated. Then the acoustic perturbation quantities are defined as follows

$$
\begin{aligned}
(\rho')^n &= \rho^n - <\rho>(N) \\
(u')^n &= u^n - <u>(N) \\
(p')^n &= p^n - <p>(N)
\end{aligned}
$$

For the first period one can use the mean flow values

$$< \rho > (1) = \bar{\rho}$$
$$< u > (1) = \bar{u}$$
$$< p > (1) = \bar{p}$$
$$(\rho')^n = \rho^n - \bar{\rho}$$
$$(u')^n = u^n - \bar{u}$$
$$(p')^n = p^n - \bar{p}$$

3 Boundary Conditions

For Problem 2 the boundary conditions for the case studied have two parts. One part is for the steady flow and the second is for the unsteady flow. The boundary conditions used for both parts are based on the acoustic characteristic equations for flow in a constant area tube. The governing isentropic differential equations are

$$\frac{\partial \rho}{\partial t} + \frac{\partial \rho u}{\partial x} = 0$$
$$\rho \left(\frac{\partial \rho}{\partial t} + u \frac{\partial u}{\partial x} \right) + \frac{\partial p}{\partial x} = 0$$
$$\frac{\partial p}{\partial t} + \frac{\partial p u}{\partial x} + (\gamma - 1) p \frac{\partial u}{\partial x} = 0 \tag{1}$$

The acoustic system equations are derived by decomposing the fluid variables into a steady flow component and an acoustic perturbation component.

$$\{\phi\} = \{\phi\}_0 + \{\phi'\}$$

$$\{\phi\} = \begin{bmatrix} \rho \\ u \\ p \end{bmatrix}, \qquad \{\phi\}_0 = \begin{bmatrix} \rho_0 \\ u_0 \\ p_0 \end{bmatrix} \qquad \{\phi'\} = \begin{bmatrix} \rho' \\ u' \\ p' \end{bmatrix}$$

Using this assumption Eq. 1 can be written as

$$\frac{\partial \{\phi'\}}{\partial t} + [M] \frac{\partial \{\phi'\}}{\partial x} = 0$$

where

$$[M] = \begin{bmatrix} u_0 & \rho_0 & 0 \\ 0 & u_0 & \frac{1}{\rho_0} \\ 0 & \gamma p_0 & u_0 \end{bmatrix}$$

Note that $\gamma p_0 = \rho_0 c_0^2$.

The matrix differential equation is diagonalized by a similarity transformation using the matrix $[T]$ such that

$$[\lambda_T] = [\mathbf{T}]^{-1}[\mathbf{M}][\mathbf{T}]$$

where

$$[\lambda_T] = \begin{bmatrix} u_0 & 0 & 0 \\ 0 & u_0 - c_0 & 0 \\ 0 & 0 & u_0 + c_0 \end{bmatrix}$$

$$[\mathbf{T}] = \begin{bmatrix} 1 & 1/c_0^2 & 1/c_0^2 \\ 0 & -1/\rho_0\,c_0 & 1/\rho_0\,c_0 \\ 0 & 1 & 1 \end{bmatrix}$$

$$[\mathbf{T}]^{-1} = \begin{bmatrix} 1 & 0 & -1/c_0^2 \\ 0 & -\rho_0 c_0/2 & 1/2 \\ 0 & \rho_0 c_0/2 & 1/2 \end{bmatrix}$$

Then

$$\frac{\partial\,\{\mathbf{W}\}}{\partial t} + [\lambda_T]\frac{\partial\{\mathbf{W}\}}{\partial x} = 0$$

where

$$\{\mathbf{W}\} = \{w_1, w_2, w_3\}^T = [\mathbf{T}]^{-1}\{\phi'\}$$

$$= \begin{bmatrix} \rho' - p'/c_0^2 \\ (p' - \rho_0\,c_0 u')/2 \\ (p' + \rho_0\,c_0 u')/2 \end{bmatrix}$$

For subsonic flow the entropy wave associated with w_1 moves with the flow at velocity u_0, an acoustic wave associated with w_3 move with the flow at velocity $u_0 + c_0$, and another acoustic wave associated with w_2 moves against the flow with velocity $u_0 - c_0$. Consequently, at the inlet where two characteristics enter the duct for the steady state case two boundary conditions can be set and the third can be extrapolated from interior values.

3.1 Problem 1

The inlet is assumed not to produce reflections. Consequently, the gradients of the upstream moving characteristic waves are zero. The downstream moving characteristic wave is assumed to be the same at points 1 and 2. The inlet boundary condition for the steady state and perturbed flow is then derived from

$$(p_3 - p_2) - \bar{\rho}_2\bar{c}_2(u_3 - u_2) = T_a$$
$$(\rho_2 - \rho_1) - (p_2 - p_1)/\bar{c}_1^2 = 0$$
$$(p_2 - p_1) + \bar{\rho}_1\bar{c}_1(u_2 - u_1) = 0$$

The solution for ρ_1, u_1 and p_1 is

$$\rho_1 = \rho_2 - T_a/2\bar{c}_1^2$$
$$u_1 = u_2 + T_a/2\bar{\rho}_1\bar{c}_1$$
$$p_1 = p_2 - T_a/2$$

At the exit

$$\theta = \omega\left(x_{exit}/(1 - M_{exit}) + t\right)$$
$$\rho_{exit} = \varepsilon \cos(\theta)$$
$$u_{exit} = -\varepsilon \cos(\theta)$$
$$p_{exit} = \varepsilon \cos(\theta)$$

3.2 Problem 2

For subsonic flow the entropy wave associated with w_1 moves with the flow at velocity u_0, an acoustic wave associated with w_3 move with the flow at velocity $u_0 + c_0$, and another acoustic wave associated with w_2 moves against the flow with velocity $u_0 - c_0$. Consequently, at the inlet where two characteristics enter the duct for the steady state case two boundary conditions can be set and the third can be extrapolated from interior values. The inlet boundary condition for the steady state and perturbed flow is then

$$\rho_1^{n+1} = 1 + \varepsilon \sin\theta$$
$$u_1^{n+1} = 2u_2^n - u_3^n + \varepsilon \sin\theta$$
$$p_1^{n+1} = 1/\gamma + \varepsilon \sin\theta$$
$$\theta = \omega\left(\frac{x_1}{1 + M_1} - t\right)$$

At the exit since two characteristics leave the duct and one enters, one can specify only one boundary condition. The other two boundary conditions are found by extrapolation from the interior.
Thus for this case where the exit pressure, p_{exit}, is constant we have

$$\rho_{jbc}^{n+1} = 2\rho_{jmax}^n - \rho_{jmax-1}^n + (\rho')_{jbc}^{n+1}$$
$$u_{jbc}^{n+1} = 2u_{jmax}^n - u_{jmax-1}^n + (u')_{jbc}^{n+1}$$
$$p_{jbc}^{n+1} = p_{exit} + (p')_{jbc}^{n+1}$$

Additional comments on boundary conditions for one dimensional flow are presented in section 10.4 of Ref. [6] and in section 16.4.2 thru 16.4.4 in Ref. [8].
The unsteady part is also based on acoustic characteristic equations.
For density and velocity perturbations we use

$$(\rho')_{jbc}^{n+1} = 2(\rho')_{jmax}^n - (\rho')_{jmax-1}^n$$
$$(u')_{jbc}^{n+1} = 2(u')_{jmax}^n - (u')_{jmax-1}^n$$

At the exit a non-reflecting boundary condition is used. Consequently, the wave components propagating in the negative x direction are zero and we have $\frac{\partial w_2}{\partial x} = 0$.
Consequently,

$$\frac{\partial p'}{\partial x} - \rho_0 c_0 \frac{\partial u'}{\partial x} = 0$$
$$(p')_{jbc}^{n+1} = (p')_{jmax}^{n+1} + \rho_0 c_0 \left[(u')_{jbc}^n - (u')_{jmax}^n \right]$$

Note that these boundary conditions are used in the solution in flux vector form

$$Q_1 = \rho$$
$$Q_2 = \rho u$$
$$Q_3 = \rho e_t = \rho(e + u^2/2) = p/(\gamma - 1) + \rho u^2/2$$

In addition, the quantity solved for in the tridiagonal matrix equation is $\Delta Q = Q^{n+1} - Q^n$.

4   Results

4.1   Problem 1

The steady mean normalized density, $\bar{\rho}/\rho_{exit}$, velocity, $\bar{u}/c_{exit}$, and pressure, $\bar{p}/p_{exit}$ are shown in Figs. 1-3 for Category 1 Problem 1. The distribution of maximum acoustic pressure during cycle 2 is shown in Figs. 4 and 5. The ripple found between the nozzle throat and the nozzle exit in solutions by other participants did not appear.

4.2   Problem 2

The steady mean pressure distribution is shown in Fig. 6 and a close up view of the nozzle region is shown in Fig. 7. The steady mean Mach number distribution is shown in Fig. 8 and a close up view of the nozzle region is shown in Fig. 9. While the overall plots of pressure and Mach number shown in Figs. 6 and 8 appear fine, the plots in the nozzle region (Figs 7 and 9) only roughly resembles a good steady state solution.
Calculations were done using a CFL number of 1. For the shock sound interaction problem the pressure perturbation distribution at the start of cycle 500 is shown in Fig. 5. Comparison with solutions using other methods show that the solution after the shock is much better than the solution before the shock.
The pressure perturbation at the exit over one cycle starting at the start of cycle 500 is shown in Fig. 6. The solution for the pressure time history at the exit shows a phase lag of about 320 degrees.
The error at the end of a period for the pressure perturbation distribution at the start of each cycle is shown in Fig. 7. A stable solution is obtained after cycle 400.

5 Conclusions

The problems solved are Category 1 Problems 1 and 2. Problem 1 is solved using a MacCormack scheme. Problem 2 is solved by perturbation of a conservative Euler equation solution to the steady state. The problems are solved on evenly spaced grids. While solutions were found, the methods selected and not using stretched grids lead to solutions which do not compare well with those found using more accurate schemes and stretched grids. The perturbation of the mean flow scheme used to solve problem 2 shows promise. Investigations should be undertaken on how to improve accuracy by use of grid stretching and use of more sophisticated methods of solving the mean flow.

References

[1] C. K. W. Tam. Computaional aeroacoustics: Issues and methods. *AIAA Journal*, **33** No. 10:1788–1796, Oct. 1995.

[2] D. P. Lockard, K. S. Brentner, and H.L. Atkins. High-accuracy algorithms for computaional aeroacoustics. *AIAA Journal*, **33** No. 2:246–251, Feb. 1995.

[3] S.I. Hariharan and Harold C. Lester. A finite difference solution for the propagation of sound in near sonic flows. *J. Acoust. Soc. Am*, **74** No. 4:1052–1061, April 1984.

[4] S.I. Hariharan and Harold C. Lester. Acoustic shocks in a variable area duct containing near sonic flows. *Journal of Computational Physics*, **58** :134–145, 1985.

[5] Joseph L. Steger and R. F. Warming. Flux vector splitting of the inviscid gasdynamic equations with applications to finite-difference methods. *Journal of Computational Physics*, **40** :263–293, 1981.

[6] Klaus A. Hoffmann. *Computational Fluid Dynamics for Engineers*. Engineering Education System, Austin TX, 1989.

[7] Dale A. Anderson, John C. Tannehill, and Richard H. Pletcher. *Computational fluid mechanics and heat transfer*. Hemisphere publishing Company, 1984.

[8] Charles Hirsch. *Numerical Computation of Internal and External Flows. Volume II: Computational Methods for Inviscid and Viscous Flows*. John Wiley & Sons, New York, 1988.
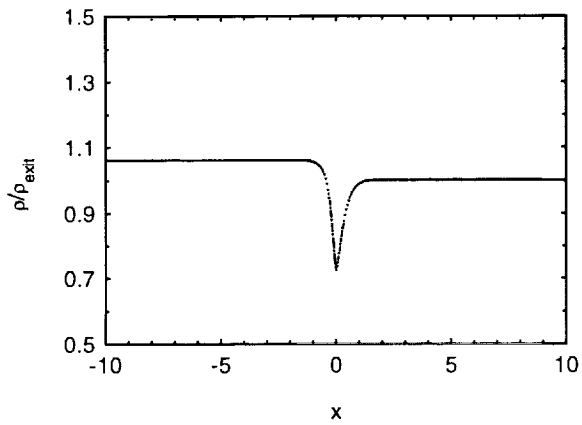
Figure 1.—Distribution of density, ρ/ρ_{exit}, for Category 1 Problem 1.
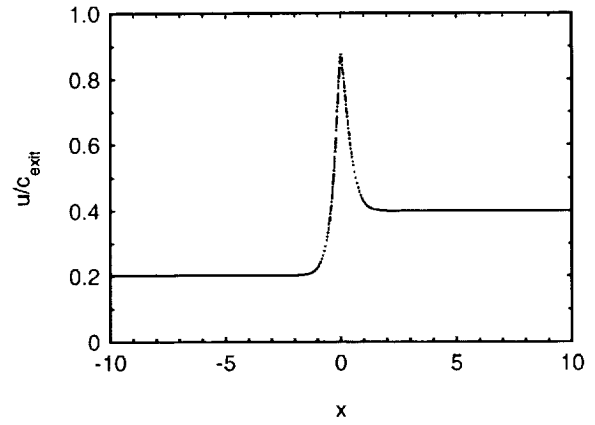
Figure 2.—Distribution of velocity, u/c_{exit}, for Category 1 Problem 1.
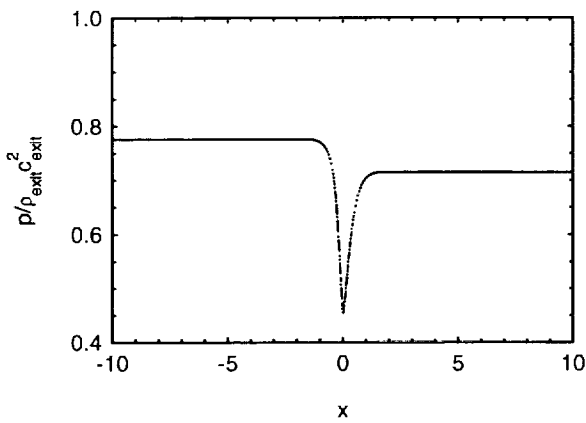
Figure 3.—Distribution of pressure, $\rho/\rho\, c^2_{exit}$, for Category 1 Problem 1.
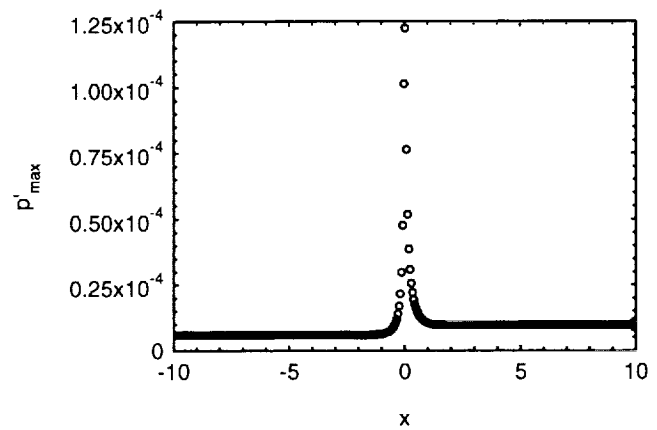
Figure 4.—Distribution of maximum acoustic pressure during cycle 2 for Category 1 Problem 1 ($-10 < x < 10$).
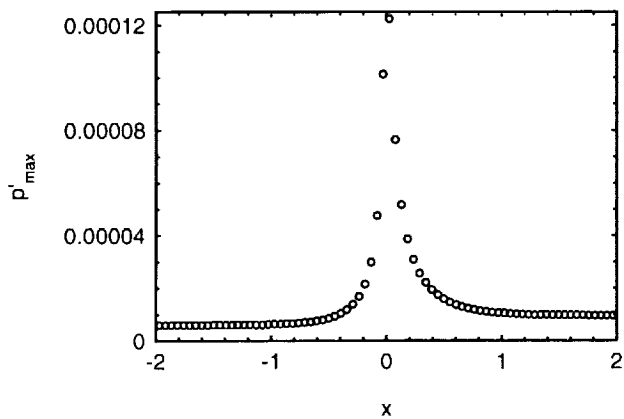
Figure 5.—Distribution of maximum acoustic pressure during cycle 2 for Category 1 Problem 1 ($-2 < x < 2$).
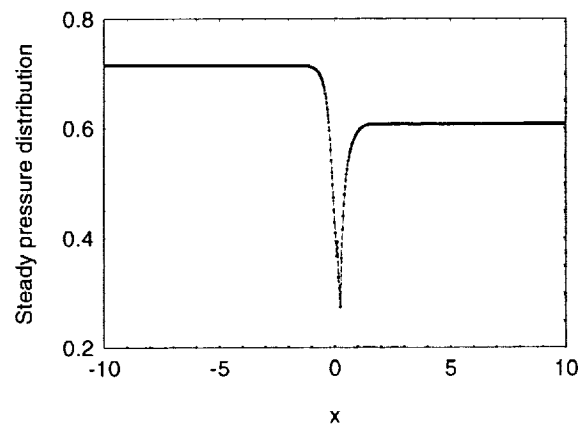
Figure 6.—Steady mean pressure distribution for Category 1 Problem 2 ($-10 < x < 10$).
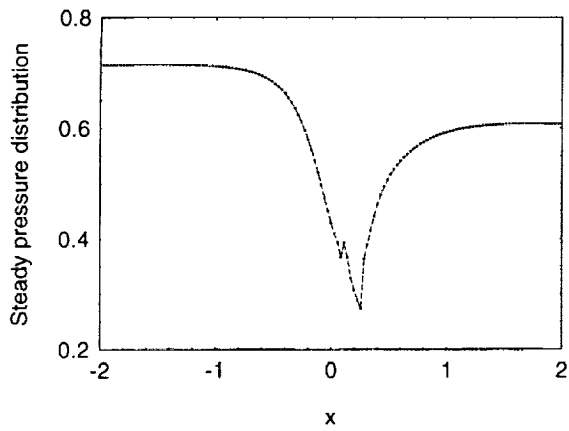
Figure 7.—Steady mean pressure distribution for Category 1 Problem 2 (–2 < x < 2).
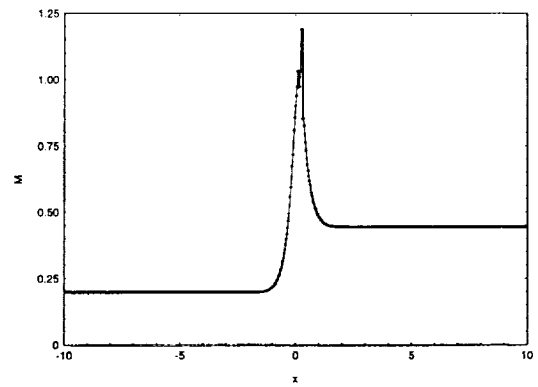
Figure 8.—Steady mean Mach number distribution for Category 1 Problem 2 (–10 < x < 10).
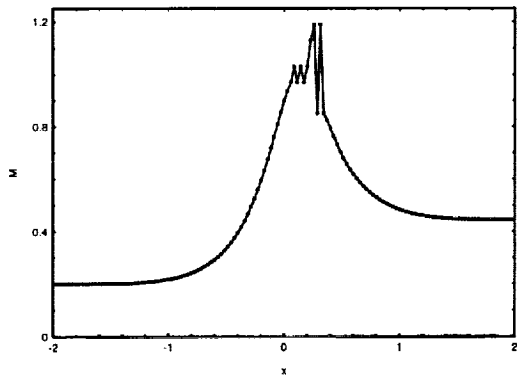
Figure 9.—Steady mean Mach number distribution for Category 1 Problem 2 (–2 < x < 2).
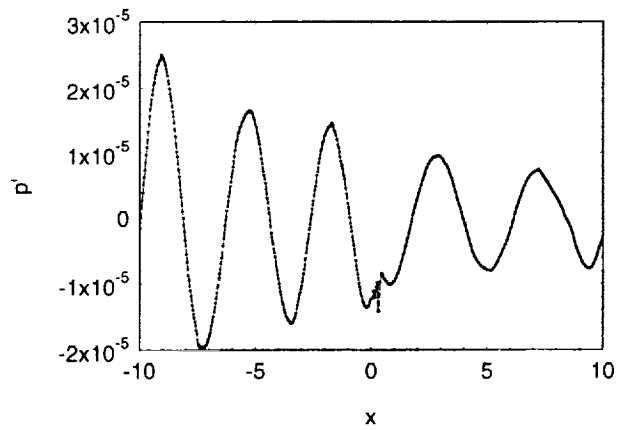
Figure 10.—Pressure perturbation distribution at start of cycle 500, $p'_i = p_i - < p_i >$ for Category 1 Problem 2
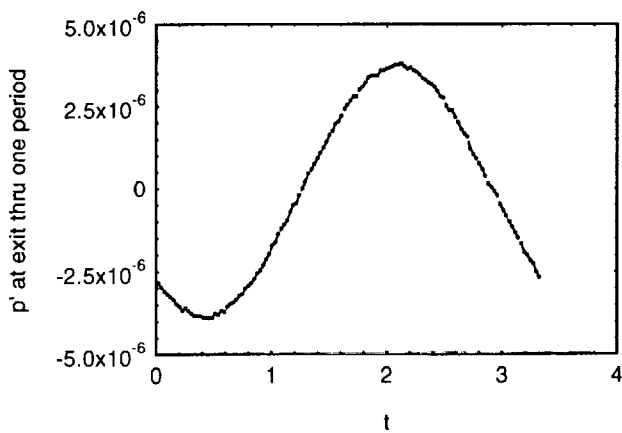
Figure 11.—Pressure perturbation at the exit over one cycle, $p'_{exit} = p_{exit} - < p_{exit} >$ for Category 1 Problem 2
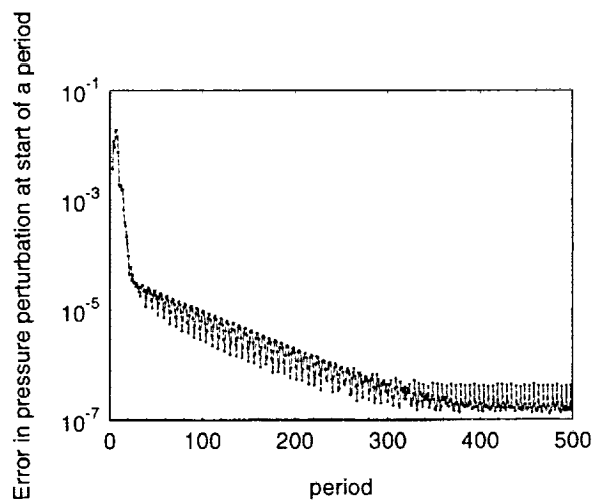
Figure 12.—Error at end of period verses period for Category 1 Problem 2.

OPTIMIZED WEIGHTED ESSENTIALLY NON-OSCILLATORY FINITE DIFFERENCE SCHEMES FOR COMPUTATIONAL AEROACOUSTICS

R. F. Chen and ZHI JIAN WANG

CFD Research Corp., 215 Wynn Drive, Huntsville, AL 35805

Abstract

Optimized weighted essentially non-oscillatory (WENO) finite difference schemes have been developed to take advantage of the optimized schemes of resolving broadband noise with less grid points per wavenumber (PPW) and the WENO scheme of highly accurate resolution for discontinuities. Optimized schemes for all stencils used in essentially non-oscillatory (ENO) are constructed based on a given order of accuracy and by minimizing truncation error for a given range of wavenumbers. Then these optimized schemes are combined following the idea of the WENO scheme through weights. The weights, however, are not constructed purely to achieve higher order of accuracy in smooth regions as in the WENO scheme. They are constructed also to minimize the truncation error in the wavenumber space. The smoothness indicators are built in the weights as in the WENO scheme so that the weights of the stencil containing a discontinuity can be essentially 0 to emulate the ENO idea. A seven point stencil, third order accurate optimized weighted essentially non-oscillatory finite difference scheme is constructed. The scheme has been tested for the scalar model wave equation and compared to the seventh order accurate WENO scheme using the same stencils. The test shows the developed scheme gives much better results in resolving a wave with 6 ppw than the WENO scheme, and it performs as well as the WENO scheme near discontinuities. The scheme together with a third order TVD Runge-Kutta method is then applied to the linearized Euler equations to solve the two benchmark problems in Category 1. Analytical mean flow solutions are used in the linearized Euler equations for both problems. For the first problem, the weights without smoothness indicators are used because the mean flow is smooth. For the second problem, the smoothness indicators are built in the weights to damp the spurious oscillations near the shock wave.

Introduction

The recent past has seen impressive progresses made in Computational Aeroacoustics (CAA). As pointed out by Tam[1], aeroacoustic problems differ significantly from the aerodynamic problems in the nature, characteristics, and objectives. They are intrinsically unsteady, and the dominating frequencies are usually high. Therefore the development of CAA algorithms needs independent thinking. As a result of this independent thinking, many powerful numerical algorithms have been developed to address the particular problems in CAA. One landmark development in CAA algorithms is the Dispersion-Relation-Preserving (DRP) finite difference schemes developed by Tam and Webb[2]. Many other CAA researchers have applied high order schemes to CAA[3-9]. In the DRP schemes, central differences are employed to approximate the first derivative. They are, therefore, non-dissipative in nature. Although non-dissipative schemes are ideal for aeroacoustic problems, numerical dissipations are required to damp any non-physical waves generated by boundary and/or initial conditions. In practice, high-order dissipation terms are added to the DRP schemes to damp spurious oscillations. The amount of artificial dissipations required is, however, problem dependent. One may need to fine tune the artificial damping to obtain the best results for a particular problem at hand. To remedy this problem, optimized upwind DRP schemes have been developed more recently by Zhuang and Chen[10]. Instead of using the central difference stencil, an upwind-biased stencil was selected based on the local wave propagating direction. Then the upwind schemes are optimized in the wave-number space following the same idea of DRP schemes. The upwind DRP schemes are by design dissipative. Therefore they are capable of damping spurious waves without any extra artificial damping, relieving the user from fine tuning the amount of numerical dissipations. Another advantage of the upwind DRP schemes is that

acceptable results can be obtained even if the mean flow contains discontinuities. With both the DRP and upwind DRP schemes, it is nearly impossible to obtain oscillation-free numerical solutions if the mean flow is discontinuous. For non-linear shock-acoustic wave interaction problems, numerical oscillations may contaminate the resultant solutions.

The pursuit of non-oscillatory numerical schemes for hyperbolic conservation laws has resulted in many significant developments in CFD during the last two decades. Notable examples include the MUSCL scheme by van Leer, TVD schemes by Harten, and other high-resolution schemes. The MUSCL and TVD schemes are designed for shock-capturing, and is usually first-order near smooth extrema. In order to achieve uniformly high-order accuracy throughout the computational domain, the Essentially Non-Oscillatory (ENO) schemes were developed[12]. More recently, weighted ENO (WENO) schemes were developed to further increase the order of accuracy, while resolving discontinuities with essentially no numerical oscillations[13]. Both ENO and WENO were designed to achieve high-order accuracy in smooth flow region while minimizing oscillations near discontinuities by avoiding the discontinuity-containing stencils. Like the ENO scheme, the WENO scheme is designed for problems with piecewise smooth solutions containing discontinuities often encountered in aerodynamic flows. Their high accuracy is referred to the truncation error for smooth solutions and can be achieved for relatively long waves. For short waves, the scheme quickly becomes less accurate[14]. Unfortunately, acoustic problems always contain sound waves with broadband wavenumbers. Therefore, the direct application of ENO or WENO schemes to CAA would not be optimum.

In this study, we attempt to unite the advantages of both the DRP schemes and WENO schemes in the development of Optimized WENO (OWENO) schemes. The idea is to optimize the WENO schemes in the wave number space following the practice of the DRP schemes to achieve high-resolution for high-frequency waves, i.e., to resolve a wave with about 6 points-per-wavelength (PPW). At the same time, OWENO scheme will retain the advantages of WENO schemes in that discontinuities are capturing with essentially no oscillations, and without any extra numerical damping. Therefore, the OWENO scheme will perform as well as the WENO scheme near discontinuities while having the advantage of the optimized schemes of resolving broadband noise with minimum PPW.

Optimized WENO (OWENO) Schemes

Optimized schemes preserve the wave propagation characteristics for a relatively large range of wavenumbers and require less PPW. They are usually constructed by optimizing the finite difference approximations of the spatial and temporal derivatives in the wave and frequency domains[1,2]. We start with a one-dimensional model wave equation on a uniform grid and use conservative approximation to the spatial derivative following common approaches for finite difference method in CFD[15]. The constructed scheme for the model equation can then be easily extended to the Euler equation in conservative form in multi-dimensions. Consider the scalar wave equation with constant wave speed a:

$$\frac{\partial u}{\partial t} + a\frac{\partial u}{\partial x} = 0 \tag{1}$$

Given the point values of the solution $u(x)$: $u_i = u(x_i, t)$, and a stencil $\{x_{i-r}, ..., x_{i+s}\}$ with $r+s+1 = k$, k is a predefined stencil size, one can construct polynomials of degree at most k-1 to approximate $u(x)$ in the interval $[x_{i-1/2}, x_{i+1/2}]$. The polynomial approximations on the two boundary points of the interval can be written as the linear combination of the values of $u(x)$ at the given stencil points as

$$\tilde{u}_{i+1/2}^{r,-} = \sum_{j=0}^{k-1} c_{rj} u_{i-r+j} \qquad \tilde{u}_{i-1/2}^{r,+} = \sum_{j=0}^{k-1} \tilde{c}_{rj} u_{i-r+j} \tag{2}$$

The superscript r means that there are r points to the left of grid point x_i. We note that the difference between

the values with superscripts at the same location $x_{i+1/2}$ is due to the one stencil point shift. Therefore it is clear $\tilde{c}_{rj} = c_{r-1,j}$ Without loss of generality we consider the case of $a > 0$ only and drop the superscript $\pm$ for convenience. Consider the finite difference approximation to the spatial derivative in equation (1) to the p_1-th order of accuracy:

$$\frac{1}{\Delta x}(\tilde{u}^r_{i+1/2} - \tilde{u}^r_{i-1/2}) = \left(\frac{\partial u}{\partial x}\right)_i + O(\Delta x^{p_1}) \tag{3}$$

where $\Delta x = x_{i+1/2} - x_{i-1/2}$ and $p_1 \leq k$. Assuming a solution in the form $u(x,t) = U(t)\exp(i\alpha x)$ and substituting it into equation (3) we have:

$$\bar{\alpha}^r \equiv \frac{-\sqrt{-1}}{\Delta x} \sum_{j=-r}^{s} c_{r,j+r} \exp(\sqrt{-1}j\alpha\Delta x)[1-\exp(-\sqrt{-1}\alpha\Delta x)] = \alpha + O(\alpha\Delta x)^{p_1} \tag{4}$$

The left hand side of the above equation is known as the numerical wavenumber. From Taylor expansions, it is seen that equation (4) gives p_1 equations for k unknown coefficients, $j=-r,..., s$. If $p_1 < k$, this leaves $k-p_1$ coefficients as free parameters. These parameters can then be determined by minimizing the following L_2 norm of the approximation error of the numerical wavenumber to the actual wave number for a range of waves. To be more specific, we seek c_{rj} so that they satisfy equation (4) and minimize the following integral

$$E = \int_{-\alpha_0\Delta x}^{\alpha_0\Delta x} \{\lambda[\mathrm{Re}(\bar{\alpha}^r\Delta x) - \alpha\Delta x]^2 + (1-\lambda)[\mathrm{Im}(\bar{\alpha}^r\Delta x)]^2\} d\alpha\Delta x \tag{5}$$

where α_0 is a predetermined wave number which gives the optimized range of wavenumbers. Parameter λ is chosen to be between 0 and 1 balancing the error in real part and in imaginary part. The imaginary part of error affects the magnitude of computed wave, while the real part contributes to the phase error.

It is seen that there are k candidate stencils $\{x_{i-r}..., x_{i+s}\}$ for $r = 0, 1,..., k-1$. In both ENO and WENO approaches, c_{rj} are solely determined by equation (3) with $p_1=k$, i.e. no optimized procedure is used. ENO picks a preferred stencil by comparing divided differences of the solution $u(x)$ to achieve the idea of "adaptive stencil", while WENO convexly combines all of them through weights[15]. In the OWENO approach, optimized procedure is used for all the candidate stencils which are then combined through weights following the idea of the WENO. The weights, however, are not constructed purely to achieve higher order of accuracy in smooth regions as in the WENO scheme. They are constructed also to minimize the truncation error in the wavenumber space. Smoothness indicators are built in the weights as in the WENO scheme so that the weights of the stencil containing a discontinuity can be essentially 0 to emulate the ENO idea. More specifically, we first seek constants d_r in the combination $\tilde{u}_{i+1/2} = \sum_{r=0}^{k-1} d_r \tilde{u}^r_{i+1/2}$ so that if the solutions is smooth over all the candidate stencil, we have

$$\frac{1}{\Delta x}(\tilde{u}_{i+1/2} - \tilde{u}_{i-1/2}) = \left(\frac{\partial u}{\partial x}\right)_i + O(\Delta x^{p_1+p_2}) \tag{6}$$

with $\sum_{r=0}^{k-1} d_r = 1$ and $p_2 \leq k-1$. This can be done by Taylor expansions which leaves $k-1-p_2$ weights as free parameters. These parameters can then be determined by minimizing integral in equation (5) with $\bar{\alpha}^r$ replaced by $\bar{\alpha} = \sum_{r=0}^{k-1} d_r \bar{\alpha}^r$. Since d_r is determined based on the assumption of smooth solution, it is not suitable when solution has a discontinuity in one or more of the candidate stencils. In this case we expect weights to be essentially 0 in the stencils containing discontinuities to emulate the ENO idea. We would use

nonlinear weights w_r to replace d_r with a built in smoothness indicator so that $w_r = d_r + O(\Delta x^{p_2-1})$ for smooth solution, and it is automatically set to a small value close to 0 for the stencils containing a discontinuity. Following the approach in [15], we choose the following weights

$$w_r = \frac{\alpha_r}{\sum_{r=0}^{k-1}\alpha_r}, \ \alpha_r = \frac{d_r}{(\varepsilon + \beta_r)^2}, \ \beta_r = \sum_{l=0}^{k-1}\int_{x_{i-1/2}}^{x_{i+1/2}}\Delta x^{2l-1}\left(\frac{\partial^l p_r(x)}{\partial^l x}\right)^2 dx, \ r = 0, \dots, k-1 \qquad (7)$$

where $p_r(x)$ is the polynomial of $(k$-1)th order over the interval $[x_{i-1/2}, x_{i+1/2}]$ determined by the given values on stencil $\{x_{i-r}, \dots, x_{i+s}\}$.

In this paper we constructed a third order accurate OWENO scheme with $k = 4$, $p_1 = 2$, $p_2 = 1$, $\lambda = 0.5$ and $\alpha_0\Delta x = 0.35\pi$. Figure 1 shows numerical wavenumber comparison between the third order accurate OWENO scheme and the 7th $(2k$-1) order accurate WENO scheme with same stencils. It is seen for the same accuracy the OWENO can resolve wave with $\alpha\Delta x$ up to 1.05 while WENO with $\alpha\Delta x$ up to 0.7. In another word the OWENO requires only 6 ppw while WENO requires 9 ppw.
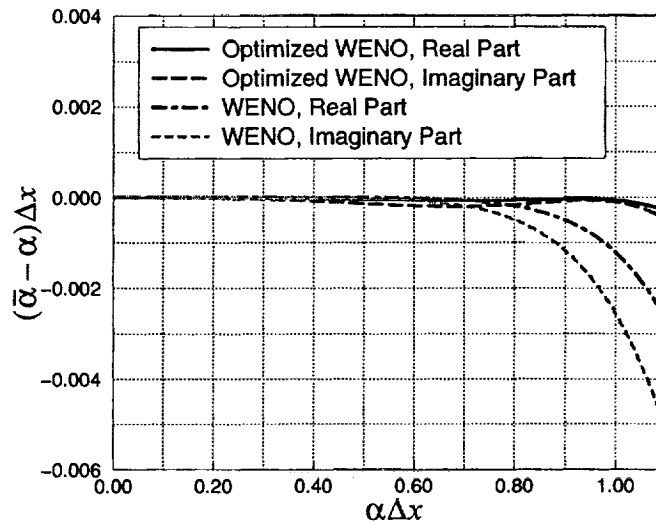
Figure 1. Comparison of numerical wavenumbers of the OWENO and the WENO schemes

Validation

To validate the designed advantages of OWENO over WENO, two cases for the model wave equation (1) with a=1 are chosen for the comparison of OWENO and WENO schemes. A third order accurate TVD Runge-Kutta method is used for time integration for both schemes[15]. In the first case a sinuousoidal wave $u_0(x) = \sin(\pi/3x)$ is released initially. Weights without smoothness indicators are used, i.e. $w_r = d_r$. Figure 2a shows the comparison of computational errors for the two schemes at t=60, with spatial size $\Delta x = 1$ or ppw=6. It is seen the numerical error by OWENO is significantly less than that by WENO. In the second case a periodic step wave is released initially. Figure 2b shows the numerical results compared with exact solution at $t = 100$ with $\Delta x = 0.5$. It indicates that the OWENO behaves as well as the WENO near discontinuities. In both cases time step Δt is set to 0.1 which is small enough so that the error due to time integration is negligible.
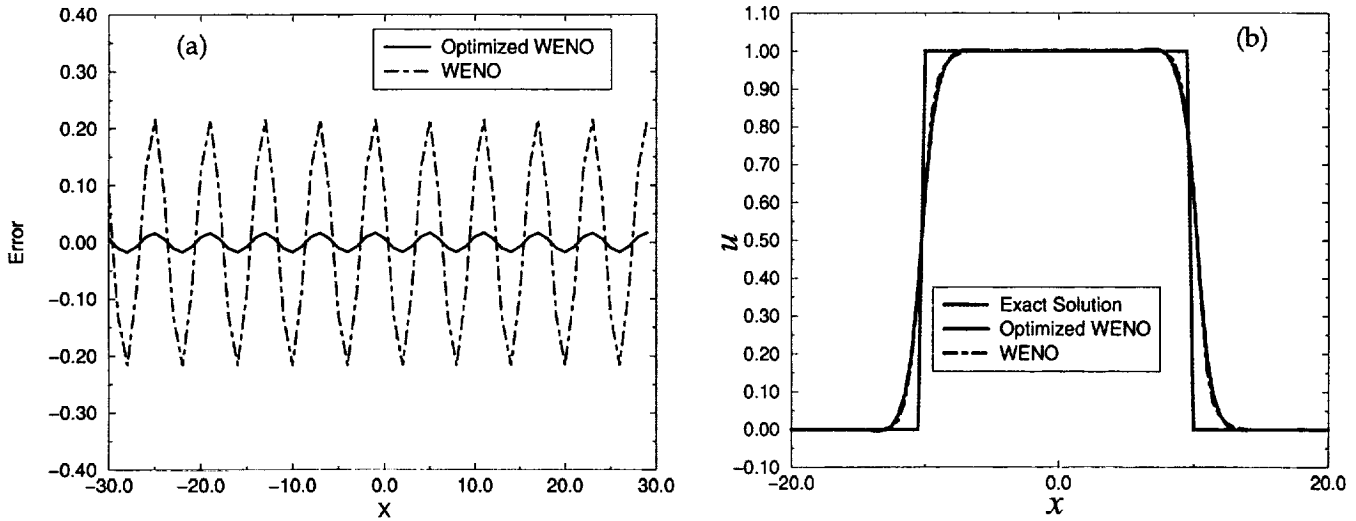
Figure 2. (a) Computational errors for sinuousoidal wave; (b) Comparison of numerical results with the exact solution for the step wave

Application to Benchmark Problems

In this section we extend the OWENO scheme to the linearized Euler equations and apply the scheme to the two benchmark problems in Category 1. For both problems the third order accurate TVD Runge-Kutta method used in the validation cases is applied for time integration. Near boundary, waves are decomposed into incoming and outgoing components. One-side biased 3rd order optimized schemes are constructed and applied to the decomposed wave components.

Propagation of sound waves through a transonic nozzle

In this problem, non-conservative linearized Euler equations in curvilinear coordinate $x = x(\xi)$ are used. The equations can be written as:

$$\frac{\partial \vec{q}}{\partial t} + \left(A_0 \frac{\partial \vec{q}}{\partial \xi} \right) \frac{d\xi}{dx} = \vec{S} \tag{8}$$

where A_0 is the Jacobian matrix with respect to the mean flow. $\vec{S}$ contains mean flow variables, and mean flow variable derivatives and nozzle area derivatives. Mean flow and mean flow derivatives are obtained analytically. We extend the OWENO scheme to equation (8) as the following:

$$\frac{\partial \vec{q}_i}{\partial t} + \frac{1}{\Delta \xi} [A_0^+ (\tilde{q}_{i+1/2}^- - \tilde{q}_{i-1/2}^-) + A_0^- (\tilde{q}_{i+1/2}^+ - \tilde{q}_{i-1/2}^+)] \left(\frac{d\xi}{dx} \right)_i = \vec{S}_i \tag{9}$$

with $\tilde{q}_{i+1/2}^-$ and $\tilde{q}_{i+1/2}^+$ obtained by the procedure described in above section. The Jacobian matrix is decomposed into two parts, $A_0 = A_0^+ + A_0^-$, with A_0^+ containing only non-negative eigenvalues and A_0^- only non-positive eigenvalues. A non-uniform grid with 301 points on domain [-10, 10] is used with hyperbolic sine transformation. No smoothness indicators are used in the weights because of smoothness of the mean flow. Figure 3 displays the maximum pressure envelope on three intervals for better comparison with the exact solution. It is seen that about 6 ppw is used for the wave near the outlet. Excellent agreement between the numerical result and the exact solution is shown.
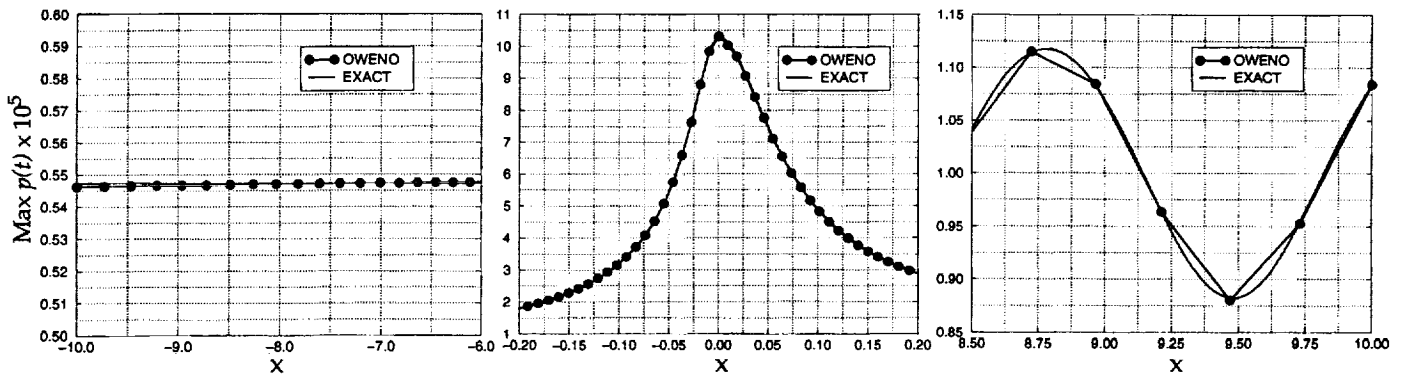
Figure 3 Comparison of numerical maximum pressure distributions with the exact solution

Shock-Sound Interaction

Since there is a shock wave in the mean flow, we use conservative linearized equations written as

$$\frac{\partial \vec{Q}}{\partial t} + \frac{\partial}{\partial x}(B_0 \vec{Q}) = \vec{H} \tag{10}$$

where $\vec{Q}$ is conserved perturbation variables, B_0 is the Jacobian matrix of conserved fluxes with respective to the mean flow conserved variable. Now source term does not contain the derivatives of mean flow variables. The mean flow is obtained analytically. Define left and right propagating flux vectors as

$$F^- = 0.5[B_0 - \max|\lambda'(\vec{Q}_0)|]\vec{Q} \qquad F^+ = 0.5[B_0 + \max|\lambda'(\vec{Q}_0)|]\vec{Q} \tag{11}$$

where λ', $l=1,2,3$ are three eigenvalues of matrix B_0. We then extend the OWENO to equation (10) as the following:

$$\frac{\partial \vec{Q}_i}{\partial t} + \frac{1}{\Delta x}(\tilde{F}_{i+1/2} - \tilde{F}_{i-1/2}) = \vec{H}_i \qquad \tilde{F}_{i+1/2} = \tilde{F}^-_{i+1/2} + \tilde{F}^+_{i+1/2} \tag{12}$$

A uniform grid with 201 points on domain [-10, 10] is used. Figure 4 shows the comparison of numerical results with the exact solutions. Results obtained with OWENO using conservative linearized equations agree very well with the exact solutions except for a little overshooting near the shock wave. This may be caused by the extension of scalar scheme to the split flux vectors of equation (11). Characteristics based extension may give better prediction near the shock wave. Furthermore the smoothness indicator given in equation (7) may not be most suitable for the optimized schemes. Future work will investigate effects of different extension and smoothness indicators. We note that non-conservative equation under predicts the pressure in the exit plane, because the solution is not continuous.

Conclusions

OWENO schemes have been developed to combine the advantages of both the DRP and WENO schemes. By design, OWENO schemes have high-resolutions for broadband waves with wave-lengths longer than 5-6 grid points per wave. Meanwhile, the OWENO schemes retain the essentially non-oscillatory nature of WENO schemes in the presence of discontinuities, such as shocks and contact discontinuities. Numerical tests with model wave equations confirm the expected advantages of OWENO schemes. The OWENO schemes have been applied to solve the first two problems in the Third Computational Aeroacoustics (CAA) Workshop on Benchmark Problems. Numerical results for both smooth and shocked mean flows agree well with analytical results. The OWENO schemes are ideally suited to solve the non-linear Euler equations for shock-acoustic

wave, and shock-vortex interaction problems. The implementation of the OWENO schemes for the Euler equations is now under way.
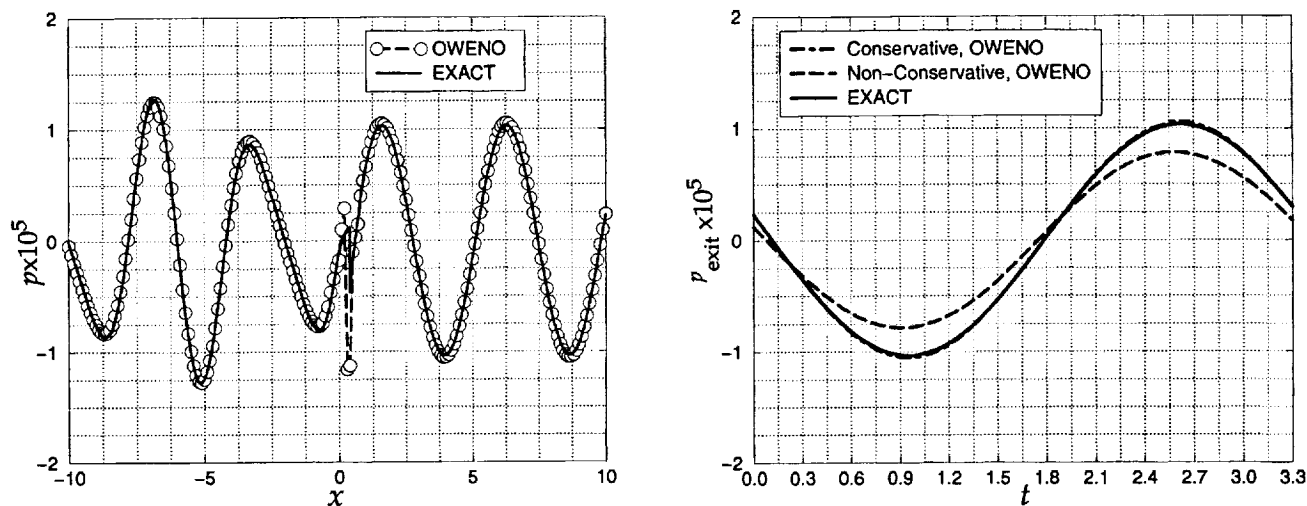
Figure 4. Left: Comparison of computed pressure with the exact solution; Right: Comparison of pressure at exit plane computed with conservative and non-conservative linearized equations with the exit solution

References

1 Tam, C.K.W., "Computational Aeroacoustics: Issues and Methods," AIAA Journal, Vol. 33, No. 10, 1995.
2 Tam, C.K.W., and Webb, J.C., "Dispersion-Relation-Preserving Finite difference Schemes for Computational Acoustics," J. Comput. Phys., Vol. 107, No. 2, 1993.
3 Hardin, J.C., Ristorcelli, J.R., and Tam, C.K.W., ICASE/LaRC workshop on Benchmark Problems in Computational Aeroacoustics. NASA CP 3300, May 1995.
4 Hixon, R., "Evaluation of a High-Accuracy MacCormack-Type Scheme Using Benchmark Problems," NASA Contractor Report 202324, ICOMP-97-03.
5 Lockard, D.P., Brentner, K.S., and Atkins, H.L., "High-Accuracy Algorithms for Computational Aeroacoustics," AIAA Journal, Vol. 33, No. 2, 1995.
6 Lin, S.Y., and Chin, Y. S., "Comparison of Higher Resolution Euler Schemes for Aeroacoustics Computations," AIAA Journal, Vol. 33, No. 2, 1995.
7 Lele, S.K., "Compact Finite Difference Schemes with Spectral-Like Resolution," J. Comput. Phys., Vol. 103, 1992.
8 Zigg, D.W., "A Review of High-Order and Optimized Finite-Difference Methods for Simulating Linear Wave Phenomena," AIAA Paper 97-2088.
9 Kim, C., Roe, P.L. and Thomas, J.P., "Accurate Schemes for Advection and Aeroacoustics," AIAA Paper 97-2091.
10 Zhuang, M. and Chen, R.F., "Optimized Upwind Dispersion-Relation-Preserving Finite Difference Schemes for Computational Aeroacoustics." AIAA Journal, Vol. 36, No. 11, 1998.
11 Zhuang, M., and Chen, R.F., "Applications of the Optimized Upwind Dispersion Relation Preserving Schemes for Multi-Dimensional Acoustic Problems." AIAA 98-2367.
12 Harten, A., Engquist, B., Osher, S. and Charkravarthy, S., "Uniformly High Order Essentially Non-Oscillatory Schemes III," J. Comput. Phys., Vol. 71, 1987.
13 Jiang, G. and Shu, C.-W., "Efficient Implementation of Weighted ENO Schemes," J. Comput. Phys., Vol. 126, 1996.
14 Liu, Y., "Fourier Analysis of Numerical Algorithms for the Maxwell Equations," J. Comput. Phys., Vol. 124, 1996.
15 Shu, C.-W., "Essentially Non-Oscillatory and Weighted Essentially Non-Oscillatory Schemes for Hyperbolic Conservation Laws," ICASE Report 97-65, 1997.
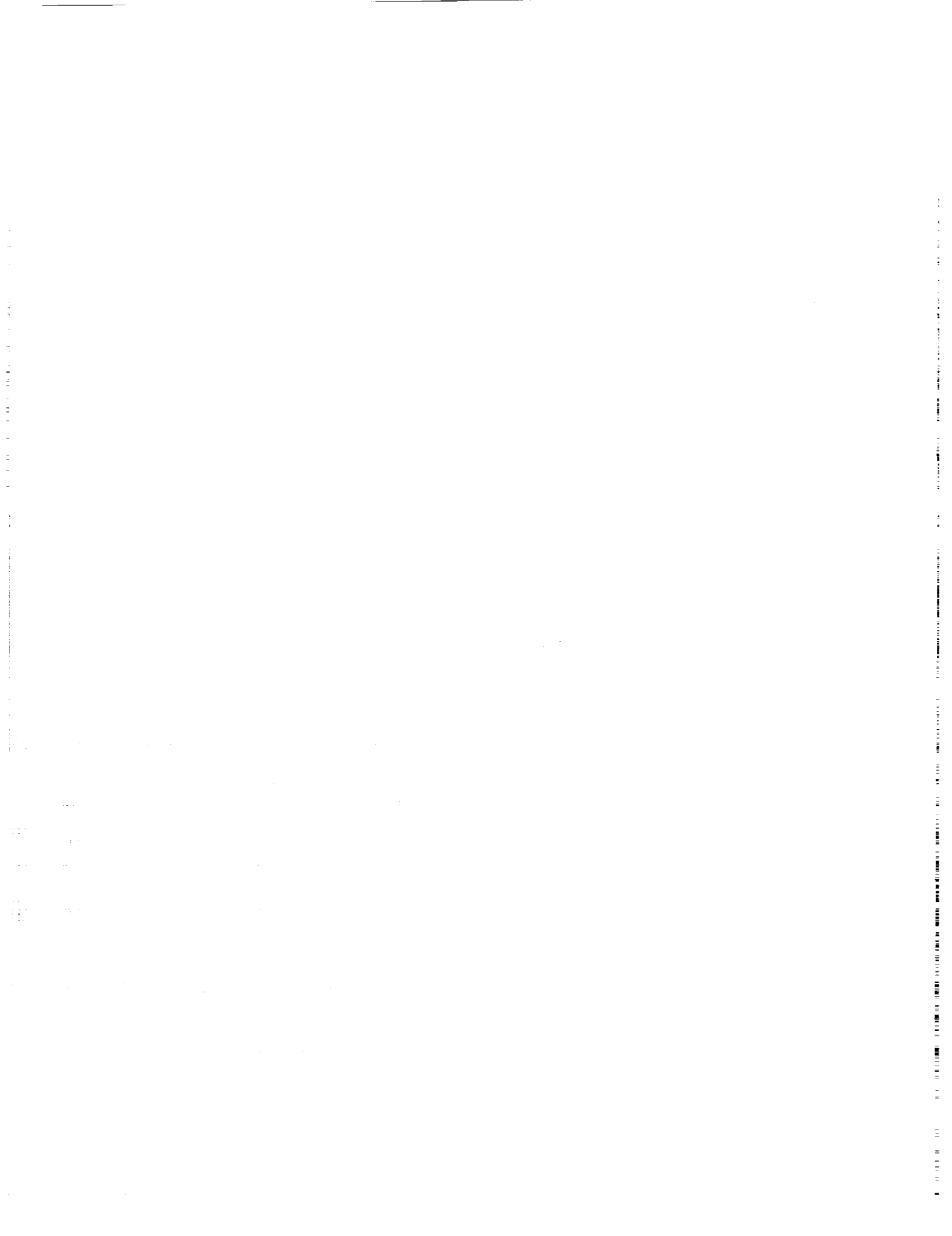
ADAPTIVE NONLINEAR ARTIFICIAL DISSIPATION MODEL FOR CAA

JAE WOOK KIM and Duck Joo Lee
Korea Advanced Institute of Science and Technology
Taejon, Korea

1. Introduction

Several kinds of artificial dissipation models were developed so far for the purpose of obtaining numerical stability and efficient convergence features of numerical schemes based on the central differences [1-7]. These present good resolution characteristics near discontinuity of nonlinear waves but have a tendency to damp out the amplitude of linear waves seriously, because these were originally designed to suppress the low wavenumber components of a wave profile. Therefore these are not suited for the time-accurate numerical solutions of aeroacoustic problems that contain linear waves of very small amplitudes in the far field. Jameson [1], Pulliam [2] and others [3-5] applied the nonlinear artificial dissipation model to the steady Euler computations, which was a blend of the second-order and fourth-order derivative term with the nonlinear switching coefficients. It has excellent shock-capturing properties and helps fast convergence to the steady state, but it leads to the unnecessary damping of the linear waves because it cannot distinguish the small-amplitude linear waves from the spurious numerical oscillations. The artificial selective damping model was introduced by Tam et al. [6, 7] to solve the nonlinear acoustic problems using the dispersion-relation-preserving scheme [8] which is a high-order and high-resolution solver based on the central differences. The artificial selective damping model has been used for time-dependent CAA solutions and not for the convergence to a steady-state solution. It was designed to damp out the spurious wave components effectively in the high wavenumber range unresolved by the finite difference scheme, while at the same time keeping the wave components in a wide band of the low wavenumber range unaffected. It is good for linear waves without unnecessary damping, however it lacks the shock-capturing properties to resolve the nonlinear discontinuity and is not able to remove the spurious oscillations completely around the nonlinear waves.

In this paper, an improved formulation of artificial dissipation model is derived for CAA, which removes the spurious numerical oscillations produced by the nonlinear waves sufficiently but does not have an effect on the linear waves. The artificial selective damping model and the nonlinear artificial dissipation model are combined for the numerical stability and temporal accuracy of CAA performed by the high-order and high-resolution central difference schemes. The artificial selective damping model is reformulated into a conservative form to maintain the correct phase speeds of nonlinear waves. The second-order derivative term in the nonlinear artificial dissipation model is combined with the artificial selective damping model to improve the shock-capturing property progressively. Quasi-one-dimensional formalism is presented in the generalized coordinates for Problem 1 and 2 in Category 1 of the Third CAA Workshop on Benchmark Problems. An adaptive constant is devised to control the local magnitude of the dissipation level automatically and need not be readjusted for a variety of problems. The compressible Euler equations in the conservative form are solved for the present computations. The optimized fourth-order compact schemes based on the central differences [9, 10] are used for evaluation of the spatial derivatives and the classical fourth-order Runge-Kutta method is used for temporal integration of the flow variables. The feasibility and performance of the adaptive nonlinear artificial dissipation model are investigated for CAA in the present paper.

2. Governing Equations

The entire conservation forms of quasi-one-dimensional Euler equations are used for the governing equations of Problems 1 and 2 in Category 1. The equations are fully nonlinear ones, which are somewhat different from the equations of non-conservation form provided by the Workshop Committee. The words 'conservation form' mean all the spatial variables including transformation metrics and Jacobian are contained in the differential operator. The equations are expressed in Cartesian coordinate as

$$\frac{\partial (A\mathbf{Q})}{\partial t} + \frac{\partial (A\mathbf{E})}{\partial x} - \mathbf{H} = 0 \tag{2-1}$$

where $\mathbf{Q}$ is the vector of conservative variables, $\mathbf{E}$ is the vector of inviscid fluxes and $\mathbf{H}$ is the source vector. $A = A(x)$ is the cross-sectional area. The vectors and their components of the conservative variables and the inviscid fluxes are expressed as

$$\mathbf{Q} = [\rho , \rho u , \rho e_t]^T , \quad \mathbf{E} = [\rho u , \rho u^2 + p , (\rho e_t + p)u]^T$$

where the total internal energy e_t is defined as

$$e_t = \frac{1}{\gamma - 1} \frac{p}{\rho} + \frac{1}{2} u^2 .$$

Actually, the equation (2-1) should be transformed to those in the generalized coordinate for obtaining efficient solutions on variable grid meshes. The equations in the generalized coordinate are expressed as

$$\frac{\partial (A\hat{\mathbf{Q}})}{\partial t} + \frac{\partial (A\hat{\mathbf{E}})}{\partial \xi} - \hat{\mathbf{H}} = 0 . \tag{2-2}$$

The superscript '∧' denotes the functions in the generalized coordinates system. These vectors are given as

$$\hat{\mathbf{Q}} = \frac{\mathbf{Q}}{J} , \quad \hat{\mathbf{E}} = \frac{\xi_x \mathbf{E}}{J} , \quad \hat{\mathbf{H}} = \frac{\xi_x}{J} \frac{dA}{d\xi} [0 , p , 0]^T$$

where J is the transformation Jacobian and ξ_x is the transformation metric from the Cartesian to the generalized coordinates. In the one-dimensional case, J is identical with ξ_x .

3. High-Order and High-Resolution Schemes and Boundary Conditions

Recently, the need of accurate and efficient numerical algorithms with high truncation order and high resolution has been increased for CAA in that these are able to simulate the generation and propagation of high-wavenumber (or high-frequency) and small-amplitude wave components directly. These are almost non-dissipative and less dispersive than the standard low-order ones that have been used widely so far. For the present work, the optimized fourth-order compact schemes are used for the evaluation of spatial derivatives and the classical fourth-order Runge-Kutta scheme is used for the integration in time. To be

compatible with the high-order and high-resolution schemes, the characteristic boundary conditions are implemented as physically correct and time-dependent numerical boundary conditions for CAA.

Optimized Compact Finite Difference Scheme at Interior Nodes

The main scheme presented here is the pentadiagonal type of central compact scheme to be used on interior nodes and it is the generalization of the Padé scheme of the seven-point stencil as shown below:

$$\beta f'_{i-2} + \alpha f'_{i-1} + f'_i + \alpha f'_{i+1} + \beta f'_{i+2} = a\frac{f_{i+1} - f_{i-1}}{2\Delta\xi} + b\frac{f_{i+2} - f_{i-2}}{4\Delta\xi} + c\frac{f_{i+3} - f_{i-3}}{6\Delta\xi} \tag{3-1}$$

where f_i is a objective function, f'_i is its spatial derivative at node i and a, b, c, α and β are the coefficients of compact discretization with an order of truncation. This is the central difference formation for the evaluation of the first derivatives on the interior nodes. The relations to determine the truncation order of this scheme are derived by using Taylor's series expansion of Eq. (3-1). Only the tenth-order scheme has unique values of the coefficients, and these are of the highest order obtainable with Eq. (3-1). The other lower order schemes should have free coefficients that are not determined completely until more constraints are imposed, and these can be used to improve the resolution characteristics. Analytic and systematic constraints for the determination of the free coefficients are considered. The nature of these constraints is minimization of the dispersive (phase) errors in the wavenumber domain by the Fourier analysis. Using these constraints, the authors succeeded in optimizing the central compact schemes and showed that the optimized fourth-order pentadiagonal scheme is the most accurate among the standard central schemes and non-optimized compact schemes [9, 10]. The coefficients were obtained as follows:

$$a = 1.279672797796143, \quad b = 1.051191982414920, \quad c = 0.04475268855213291,$$
$$\alpha = 0.5900108167074074, \quad \beta = 0.09779791767419070.$$

Optimized Compact Finite Difference Scheme near and at Boundary Nodes

Equation (3-1) can be solved by inversion of pentadiagonal matrix and the matrix should be closed at the boundaries. Therefore some different formulations were considered near and at the boundaries. The non-central or one-sided compact schemes to be used on near-boundary and boundary nodes are expressed as

- $i = 0$: $f'_0 + \alpha_{0,1} f'_1 + \beta_{0,2} f'_2 = \dfrac{1}{\Delta\xi}\displaystyle\sum_{j=0}^{3} a_{0,j} f_j$, $\tag{3-2}$

- $i = 1$: $\alpha_{1,0} f'_0 + f'_1 + \alpha_{1,2} f'_2 + \beta_{1,3} f'_3 = \dfrac{1}{\Delta\xi}\displaystyle\sum_{j=0}^{4} a_{1,j} f_j$, $\tag{3-3}$

- $i = 2$: $\beta_{2,0} f'_0 + \alpha_{2,1} f'_1 + f'_2 + \alpha_{2,3} f'_3 + \beta_{2,4} f'_4 = \dfrac{1}{\Delta\xi}\displaystyle\sum_{j=0}^{5} a_{2,j} f_j$. $\tag{3-4}$

Equations (3-2)-(3-4) were derived to close the pentadiagonal matrix at the boundaries and the optimum coefficients were so determined that the schemes became the fourth-order ones except on the boundary nodes ($i = 0$) for numerical stability. These formulations are, of necessity, non-central or one-sided differences and their error characteristics are both dispersive and dissipative. The two kinds of errors can be analyzed simultaneously in the wavenumber domain by the Fourier analysis and the authors minimized these errors with the analytic optimization method too [9, 10]. The relations to determine the

truncation orders of these schemes are derived by using Taylor's series expansion of Eq. (3-2)-(3-4). The optimum coefficients were obtained as follows:

- $i = 0$: Second Order :
  $a_{0,0} = -2.95516745786296,$ $a_{0,1} = -1.63175038219495,$ $a_{0,2} = 4.28093227034817,$ $a_{0,3} = 0.305985569709741,$
  $\alpha_{0,1} = 4.57321732196853,$ $\beta_{0,2} = 2.27485354566209.$

- $i = 1$: Fourth Order :
  $a_{1,0} = -0.643755519081585,$ $a_{1,1} = -0.215562412498565,$ $a_{1,2} = 1.39308006947385,$ $a_{1,3} = -0.47778109295963,$
  $a_{1,4} = -0.055981044934069,$
  $\alpha_{1,0} = 0.204356208611126,$ $\alpha_{1,2} = 0.046406522760991,$ $\beta_{1,3} = -0.337432463538152.$

- $i = 2$: Fourth Order :
  $a_{2,0} = -0.147618978190642,$ $a_{2,1} = -0.659846174346428,$ $a_{2,2} = -0.182251818640843,$ $a_{2,3} = 0.686060397630997,$
  $a_{2,4} = 0.29761855559004,$ $a_{2,5} = 0.00603801795687542,$
  $\beta_{2,0} = 0.0402516485629226,$ $\alpha_{2,1} = 0.449236223001478,$ $\alpha_{2,3} = 0.659998776315685,$ $\beta_{2,4} = 0.10500904552933.$

The optimum coefficients provide high accuracy and maximum resolutions for the central, non-central and one-sided compact schemes, and these schemes were proposed as the optimized high-order compact (OHOC) schemes. And these are used to evaluate the spatial derivatives accurately in the whole computational domain for the present work.

Characteristic Boundary Conditions

The boundary conditions to be used for CAA in this paper are based on the local one-dimensional characteristics. The characteristic variables are analyzed by transforming the governing equations to the characteristic wave convection equations. The local one-dimensional relations between the characteristic convection terms and the primitive variables are generated from the wave convection equations. The physical boundary conditions are imposed to the characteristic convection terms using the local one-dimensional relations. No extrapolations are needed in the implementation of the present boundary conditions. Full nonlinear Euler equations in their entire conservation forms are directly solved at the boundary without linearization or simplifications. The non-reflecting inflow/outflow conditions are used for the steady mean solutions, and the transparent source conditions are employed to simulate the acoustic disturbances at the inlet or outlet boundaries.

4. Adaptive Nonlinear Artificial Dissipation Model

The classical artificial dissipation consists of the second-order and fourth-order derivative term in conservative form. The former is for a shock-capturing feature and the latter is for a background smoothing effect. But the effect of the background smoothing term is so excessive that it may damp out the linear acoustic waves seriously and it is not proper for CAA. On the other hand, the artificial selective damping model lacks a stability to capture a high discontinuity generated from a strong nonlinear wave and still produces numerical oscillations near the discontinuity. It was proposed in a non-conservative form so it may have some error in reproducing the phase speeds of nonlinear waves if it is used in the original form. In this paper, a revised formulation of the artificial selective damping term in conservative form is presented. Then, it is desirable to combine the shock-capturing term and the artificial selective damping

term as the background smoothing term. In this paper, this combination is proposed as an adaptive nonlinear artificial dissipation (ANAD) model.

Quasi-one-dimensional formalism of an ANAD model is suggested in the generalized coordinates. Consider the dissipation term added on the right hand side of the quasi-one-dimensional Euler equations in the flux vector form at the i-th grid point as:

$$\frac{\partial(A\hat{Q})}{\partial t}\bigg|_{i} + \frac{\partial(A\hat{E})}{\partial\xi}\bigg|_{i} - \hat{H}_{i} = \hat{D}_{i}$$

(4-1)

where the vectors of the conservative variables, the inviscid fluxes and the source term are represented in section 2. The dissipation term $\hat{D}_{i}$ is given by the flux differences of the midpoint values as

$$\hat{D}_{i} = \frac{A_{i+\frac{1}{2}}\hat{d}_{i+\frac{1}{2}} - A_{i-\frac{1}{2}}\hat{d}_{i-\frac{1}{2}}}{\Delta\xi}.$$

(4-2)

Then the numerical dissipation flux vector in the generalized coordinates is given in this paper as

$$\hat{d}_{i+\frac{1}{2}} = \frac{|\lambda|_{i+\frac{1}{2}}^{\text{stencil}}}{J_{i+\frac{1}{2}}}\left[\varepsilon_{i+\frac{1}{2}}^{(2)}(Q_{i+1} - Q_{i}) - \varepsilon_{i+\frac{1}{2}}^{(4)}\sum_{m=-2}^{3}b_{m}Q_{i+m}\right]$$

$$= \frac{|\lambda|_{i+\frac{1}{2}}^{\text{stencil}}}{J_{i+\frac{1}{2}}}\left\{\varepsilon_{i+\frac{1}{2}}^{(2)}(Q_{i+1} - Q_{i}) - \varepsilon_{i+\frac{1}{2}}^{(4)}\left[b_{1}(Q_{i+1} - Q_{i}) + b_{2}(Q_{i+2} - Q_{i-1}) + b_{3}(Q_{i+3} - Q_{i-2})\right]\right\}$$

(4-3)

where the differencing coefficients of the background smoothing term are obtained by constructing the conservative form of the artificial selective damping term, which is also the flux differencing form of the midpoint values. The resulting coefficients are as follows:

$b_1 = -b_0 = -0.1624382574577463$, $\quad b_2 = -b_{-1} = 0.07309131357825455$, $\quad b_3 = -b_{-2} = -0.01447042896399915$.

The cross-section area on the midpoint in Eq. (4-2) and the transformation Jacobian on the midpoint in Eq. (4-3) are evaluated just by the arithmetic averages of their values on the adjacent two grid points as

$$A_{i+\frac{1}{2}} = \frac{A_{i+1} + A_{i}}{2}, \quad J_{i+\frac{1}{2}} = \frac{J_{i+1} + J_{i}}{2}.$$

The stencil eigenvalue and the absolute eigenvalue are defined as

$$|\lambda|_{i+\frac{1}{2}}^{\text{stencil}} = \max_{m=-2}^{3}(|\lambda|_{i+m}) - \min_{m=-2}^{3}(|\lambda|_{i+m}), \quad |\lambda|_{i} = (|u| + c)_{i}|\xi_{x}|_{i}.$$

The nonlinear dissipation functions in Eq. (4-3) determine magnitudes of the second-order dissipation and the fourth-order dissipation according to the change of pressure gradient. In regions of strong discontinuity, the second-order dissipation, i.e. the shock-capturing term dominates and the fourth-order

one is turned off. Out of the region, the second-order one becomes a very small value and the fourth-order one, i.e. the background smoothing term, governs the dissipation. The nonlinear dissipation functions are suggested in this thesis as

$$\varepsilon_{i+\frac{1}{2}}^{(2)} = \kappa^{(2)} \max_{m=-2}^{3}(v_{i+m}), \quad \varepsilon_{i+\frac{1}{2}}^{(4)} = \max\left[0, \left(\kappa^{(4)} - \varepsilon_{i+\frac{1}{2}}^{(2)}\right)\right],$$

where the shock detector, v_i is given as

$$v_i = \frac{|p_{i-1} - 2p_i + p_{i+1}|}{p_{i-1} + 2p_i + p_{i+1}}.$$

The adaptive control constants in the generalized coordinates are devised in this paper as

$$\kappa^{(2)} = \kappa^{(4)} = \frac{1}{\sigma^R}\left[1 + (\sigma - 1)\tanh\left(\frac{\alpha}{\beta} - 1\right)\right]\left(\sqrt{\hat{\alpha}\hat{\beta}}\right)^{1+\tanh(\sigma-1)},$$

$$\sigma = \frac{p^{max}}{p^{min}}, \quad \alpha = \frac{|\lambda|^{max}}{|\lambda|^{min}}, \quad \beta = \frac{(|\lambda|/|\xi_x|)^{max}}{(|\lambda|/|\xi_x|)^{min}}, \quad R = \frac{\alpha + \beta}{2\alpha\beta},$$

$$\hat{\alpha} = \frac{\alpha + 1}{\alpha - 1}\tanh(\alpha - 1), \quad \hat{\beta} = \frac{\beta + 1}{\beta - 1}\tanh(\beta - 1).$$

(4-4)

where the meanings of the superscripts, 'max' and 'min' are explained by the following relations:

$$f^{max} = \max_{i=0}^{imax} f_i, \quad f^{min} = \min_{i=0}^{imax} f_i.$$

The adaptive control constants expressed in Eq. (4-4) are newly suggested in this paper for effective applications of the artificial dissipation model to various CAA problems in the one-dimensional generalized coordinates, which can be used for the linear and nonlinear waves at once. At each time step, the optimal values of the control constants are calculated automatically by the flow properties. One need not readjust the constants according to case-by-case nor waste additional computation time to find an optimal value of them.

5. Application to Benchmark Problems

In this section, the numerical algorithms and ANAD (adaptive nonlinear artificial dissipation) model presented in this thesis are applied to actual computations of Problems 1 and 2 of Category 1 in the Third CAA Workshop on Benchmark Problems, and their accuracy and performance are investigated. It is shown that the ANAD model enables the central difference schemes to simulate the propagation of sound waves and shock-sound interactions in the transonic nozzle successfully.

Problem 1 of Category 1

The numbers of grid points used are 301 and the grids are clustered near the nozzle throat. The time step used is determined by CFL condition with a Courant number of 0.9. The convergence criterion for the steady state is that the maximum value of the residual defined as $|\rho^{(n+1)}-\rho^{(n)}|/\rho^{(n)}$ is below 1×10^{-15} which is the order of machine error. The computation time to obtain the steady mean solutions is 92.6 second in 25,000 operations using an IBM PC with an Intel Celeron Processor of 400 MHz. After the steady state is reached, the acoustic perturbation starts at the exit plane, and the periodic oscillatory state with constant magnitudes is achieved after 25 wavelets are produced. The error residual history for steady mean solutions is represented in Fig. 1.

The steady mean solutions are represented in Fig. 2, where it is shown that the numerical solutions are in good agreement with the analytic solutions. The perturbation distributions ($\rho(x)-\bar{\rho}(x)$, $p(x)-\bar{p}(x)$, $u(x)-\bar{u}(x)$) at an instant are expressed in Fig. 3, where the interference between incident and reflected waves at the upstream region, the shock-sound interaction at the throat, and the transmitted waves at the downstream region are shown well. The distribution of maximum pressure perturbation in one period is represented in Fig. 4.
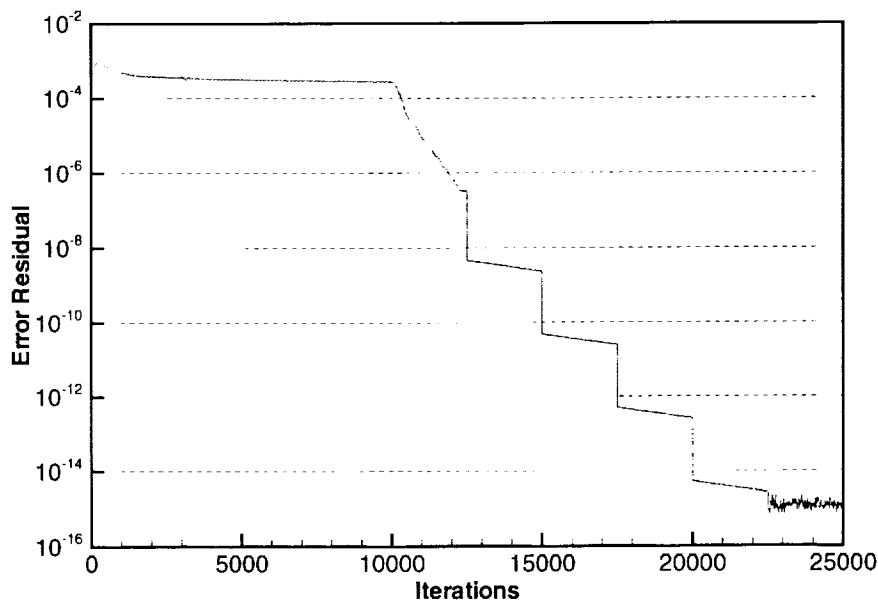
Fig. 1. Error residual history for steady mean solutions: Problem 1 of Category 1.
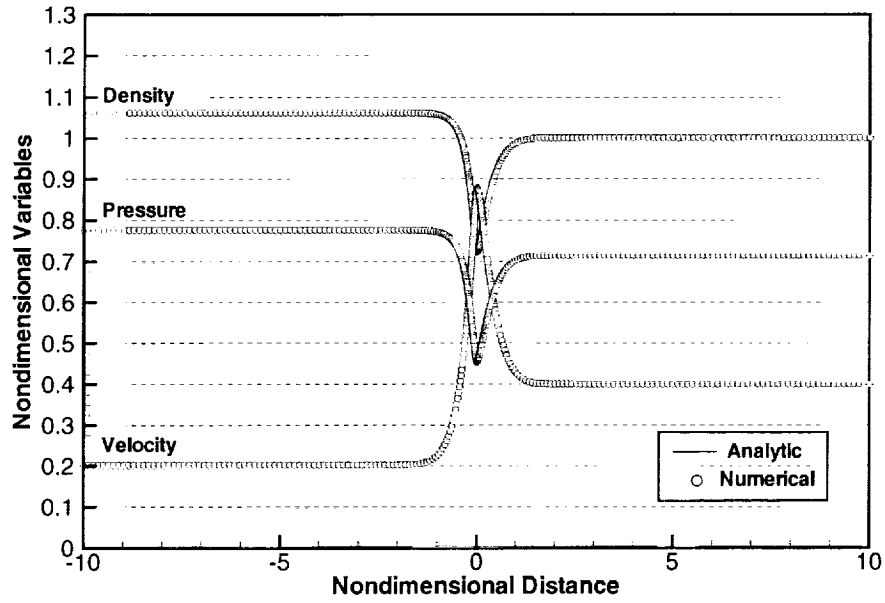
Fig. 2. Steady mean solutions compared with analytic solutions: Problem 1 of Category 1.
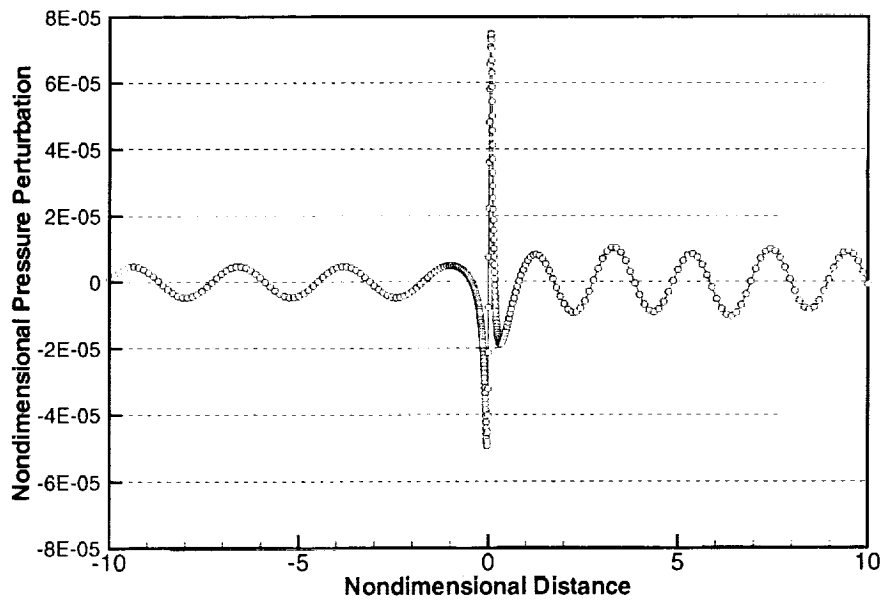
Fig. 3. Distribution of pressure perturbations at the start of a period: Problem 1 of Category 1.
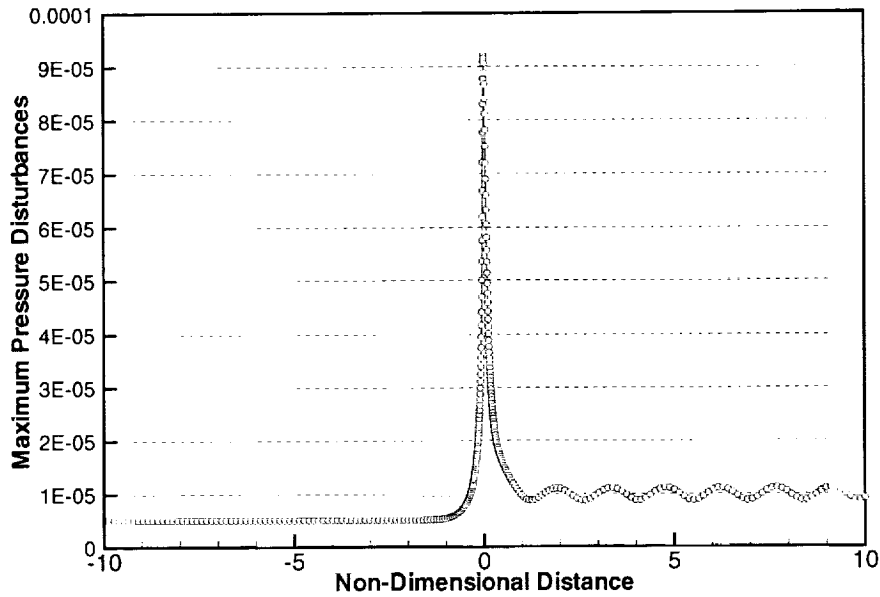
Fig. 4. Distribution of maximum pressure perturbation in one period: Problem 1 of Category 1.

Problem 2 of Category 1

The number of grid points used is 251 and the grids are clustered near the nozzle throat. The CFL condition for time step and the convergence criterion for the steady state are the same as for Problem 1. The computation time to obtain the steady mean solutions is 46.1 second in 16,000 operations using an IBM PC with an Intel Celeron Processor of 400 MHz. After the steady state is reached, the acoustic perturbation starts at the inlet plane, and the periodic oscillatory state with constant magnitudes is achieved after 25 wavelets are produced. The error residual history for steady mean solutions is represented in Fig. 5.
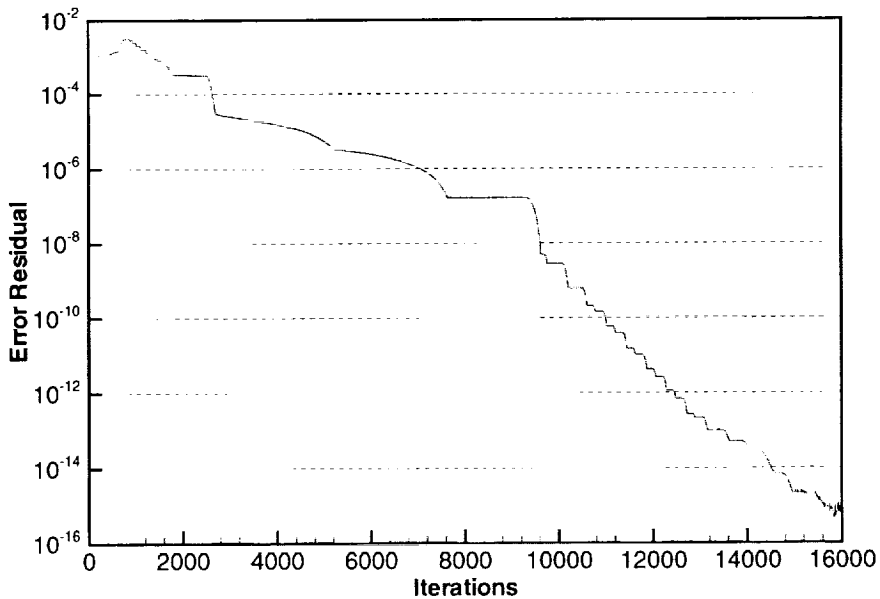
Fig. 5. Error residual history for steady mean solutions: Problem 2 of Category 1.

The steady mean solutions are represented in Fig. 6, where it is shown that the numerical solutions are in good agreement with the analytic solutions. The perturbation distributions ($\rho(x) - \bar{\rho}(x)$, $p(x) - \bar{p}(x)$, $u(x) - \bar{u}(x)$) at an instant are expressed in Fig. 7, where the interference between incident and reflected waves at the upstream region, the shock-sound interaction at the throat, and the transmitted waves at the downstream region are shown well. The exit pressure signal through one period is represented in Fig. 8. The results in Fig. 7 and 8 are also in good agreement with the analytic solutions that are provided by the committee of the Third CAA Workshop on Benchmark Problems.
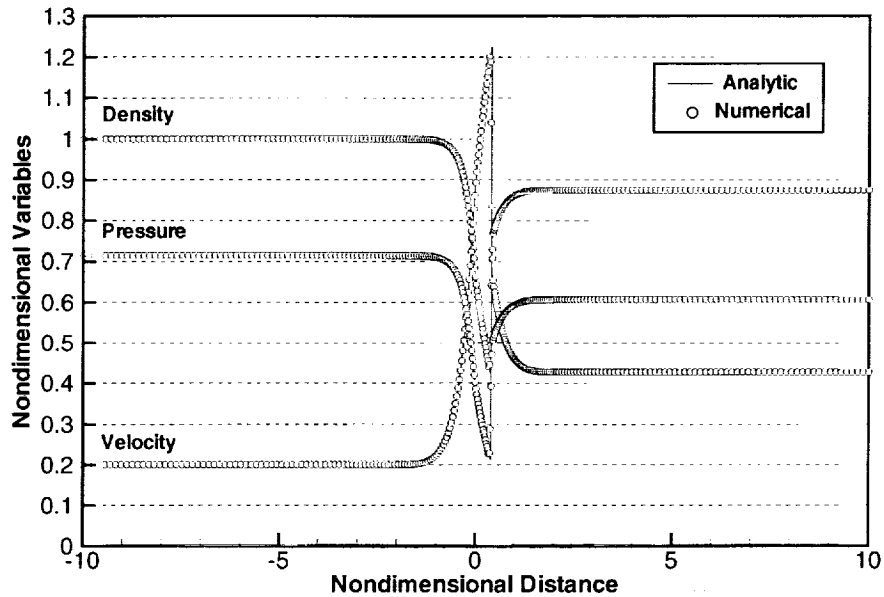
Fig. 6. Steady mean solutions compared with analytic solutions: Problem 2 of Category 1.
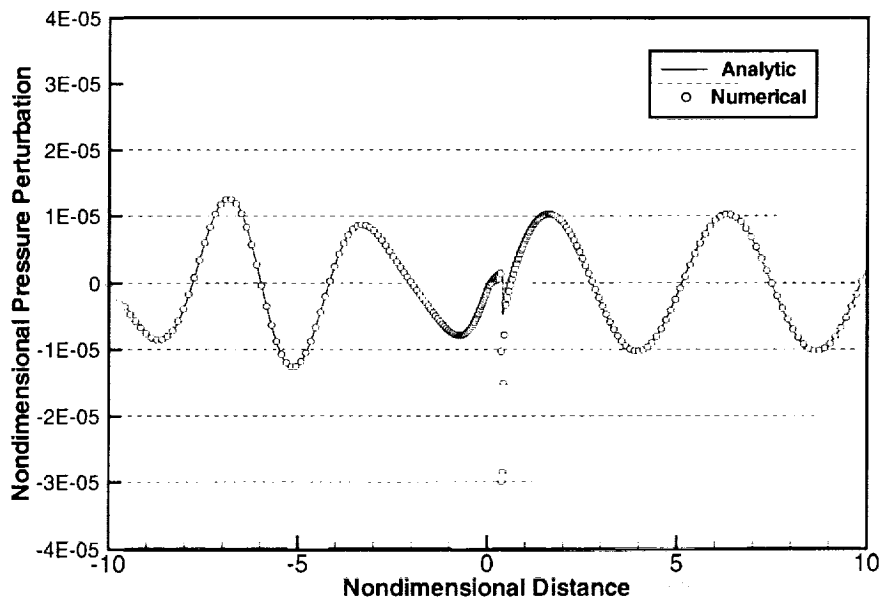
Fig. 7. Distribution of pressure perturbations at the start of a period: Problem 2 of Category 1.
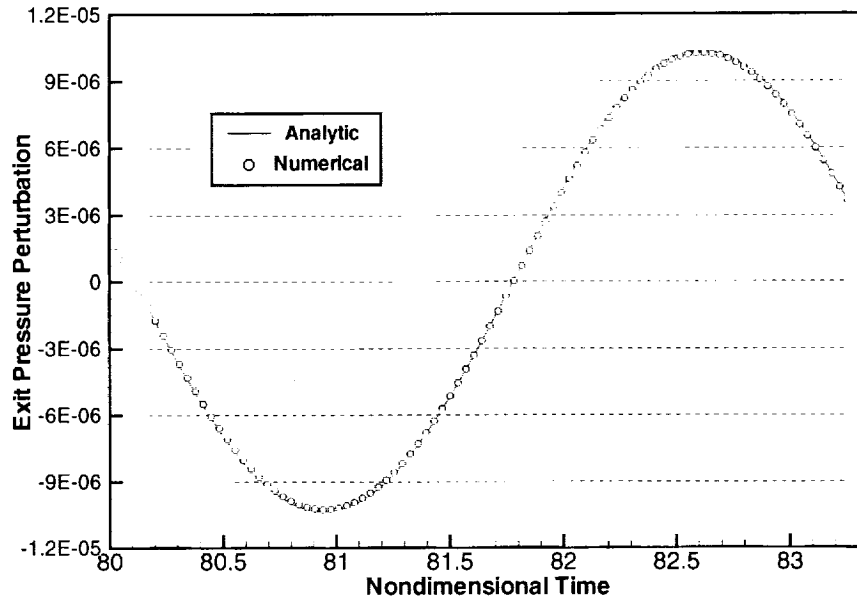
Fig. 8. Exit pressure perturbation signal through one period: Problem 2 of Category 1.

References

1. Jameson, A., "Transonic Aerofoil Calculations Using the Euler Equations," *Numerical Methods in Aeronautical Fluid Dynamics*, New York, Academic Press, 1982.
2. Pulliam, T. H., "Artificial Dissipation Models for the Euler Equations," AIAA Paper 85-0438.
3. Jameson, A., Schmidt, W., and Turkel, E., "Numerical Simulation of the Euler equations by Finite Volume Methods Using Runge-Kutta Time Stepping Schemes," AIAA Paper 81-1259.
4. Pulliam, T. H., and Steger, J. L., "Recent Improvements in Efficiency, Accuracy and Convergence for Implicit Approximate Factorization Algorithms" AIAA Paper 85-0360.
5. Swanson, R. C., and Turkel, E., "Artificial Dissipation and Central Difference Schemes for the Euler and Navier-Stokes Equations," AIAA Paper 87-1107.
6. Tam, C. K. W., Webb, J. C., and Dong, Z., "A Study of the Short Wave Components in Computational Acoustics," *Journal of Computational Acoustics*, Vol. 1, 1993, pp. 1-30.
7. Tam, C. K. W., and Shen, H., "Direct Computation of Nonlinear Acoustic Pulses Using High-Order Finite Difference Schemes," AIAA Paper 93-4325.
8. Tam, C. K. W., and Webb, J. C., "Dispersion-Relation-Preserving Finite Difference Schemes for Computational Acoustics," *Journal of Computational Physics*, Vol. 107, 1993, pp. 262-281.
9. Kim, J. W., and Lee, D. J., "Optimized Compact Finite Difference Schemes with Maximum Resolution," *AIAA Journal*, Vol. 34, No. 5, 1996, pp. 887-893.
10. Kim, J. W., and Lee, D. J., "Implementation of Boundary Conditions for Optimized High-Order Compact Schemes," *Journal of Computational Acoustics*, Vol. 5, No. 2, 1997, pp. 177-191.
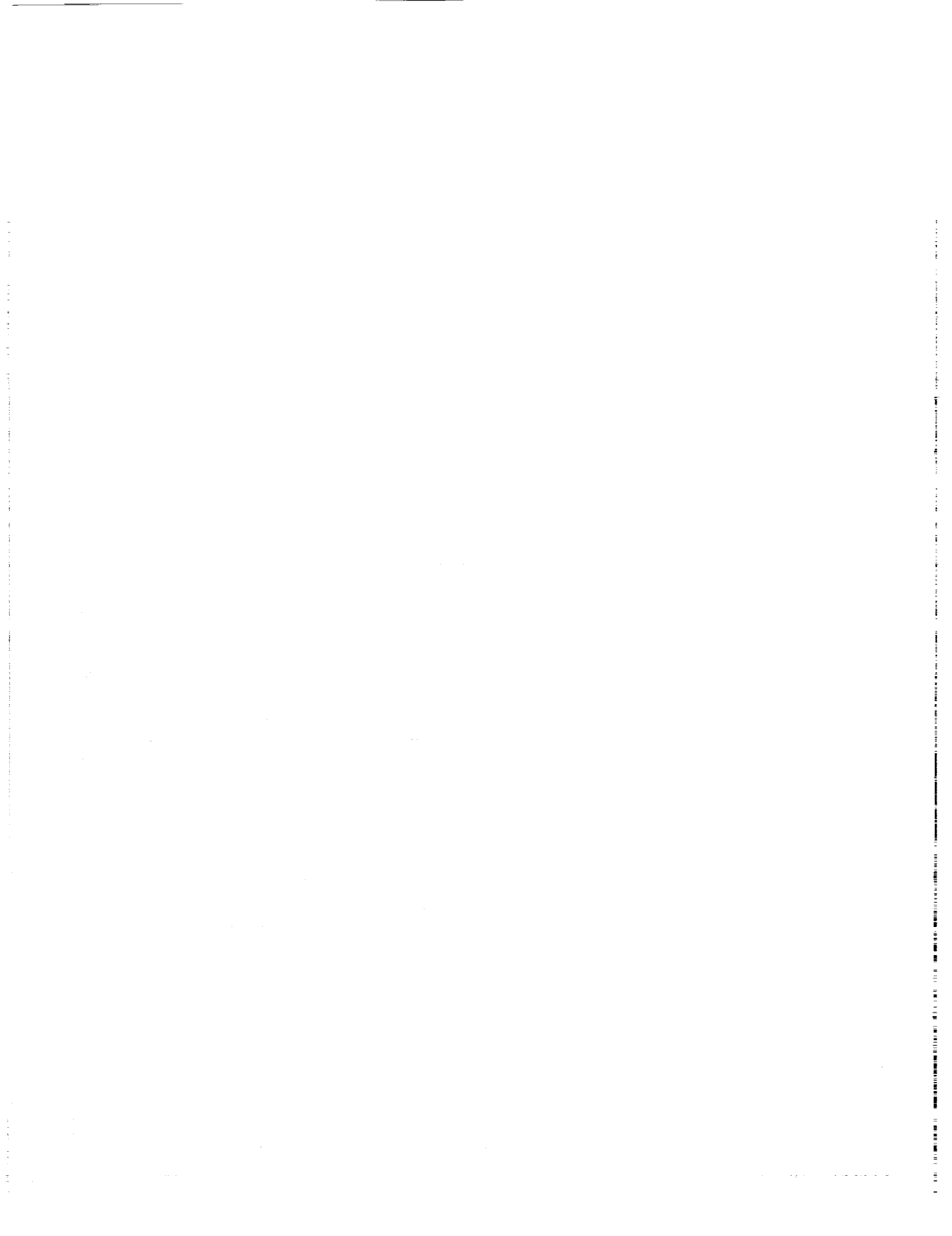
SOLUTIONS OF SOUND WAVE PROPAGATION AND SHOCK-SOUND INTERACTION USING THE OPTIMIZED UPWIND DRP SCHEME AND THE CE/SE METHOD

MEI ZHUANG
SHI ZHENG

Department of Mechanical Engineering
Michigan State University
East Lansing, Michigan 48824

Abstract

The optimized upwind DRP scheme (refs. 1 and 2) and the method of space-time CE/SE (ref. 3) are used to solve two of the workshop benchmark problems, problems 1 and 2 of category 1. For problem 1 of category 1, both uniform and non-uniform grids are considered. A nearly converged solution is achieved with 400 uniform grid points for the upwind DRP scheme and with 1600 uniform grid points for the CE/SE method. The use of the non-uniform grid points significantly reduces the number of grid points needed for obtaining accurate numerical solutions. The pressure fluctuation increases drastically around the throat of the nozzle. The fluctuation is accurately predicted by the upwind DRP scheme. For problem 2 of category 1, a converged solution is achieved with 200 uniform grid points for both numerical methods. The steady flow variables for both problems are calculated using the CE/SE method. The calculated steady flow solutions agree with the analytical solutions very well.

Introduction

Aeroacoustic problems are governed by the same equations as those in aerodynamics, namely the Navier-Stokes equations. Aeroacoustic problems, however, have their own nature, characteristics and objectives, which are distinctly different from those commonly encountered in aerodynamics (ref. 4). During the past years, many numerical schemes have been developed and applied for computational aeroacoustics. For the current investigation, two of the numerical schemes, the optimized upwind DRP scheme (refs. 1 and 2) and the CE/SE method (ref. 3), are used to solve problems 1 and 2 of category 1 for the 3rd CAA benchmark problems.

The optimized upwind DRP scheme was developed for computational aeroacoustics. The scheme is high order accurate, uses fewer grid points per wavelength compared with that of standard high order accurate schemes from the Taylor series expansion, and automatically damps out spurious short waves. The upwind DRP scheme used here is the 7-stencil DRP upwind difference approximation with optimized coefficients. The scheme is a fourth-order scheme. For instance, the first order derivative $\frac{\partial u}{\partial x}$ at the lth node of a grid with spacing Δx is approximated by,

$$\left(\frac{\partial u}{\partial x}\right)_l = \frac{1}{\Delta x}\sum_{j=-2}^{4} a_j u_{l+j} \quad \text{or} \quad \left(\frac{\partial u}{\partial x}\right)_l = \frac{1}{\Delta x}\sum_{j=-4}^{2} a_j u_{l+j}$$

where the coefficients a_j (ref. 1) are:

$$a_{-2}^{24} = 0.041382855555706463$$

$$a_{-1}^{24} = -0.44077420643183318$$

$$a_{0}^{24} = -0.50020513450976445$$

$$a_{1}^{24} = 0.12475721579099250$$

and

$$a_{2}^{24} = -0.45448643568845881$$

$$a_{3}^{24} = 0.12265083451112346$$

$$a_{4}^{24} = -0.016140071346698814$$

$$a_{-4}^{42} = 0.016140071346698814$$

$$a_{-3}^{42} = -0.12265083451112346$$

$$a_{-2}^{42} = 0.4544863568845881$$

$$a_{-1}^{42} = -0.12475721579099250$$

$$a_{0}^{42} = 0.50020513450976445$$

$$a_{1}^{42} = 0.44077420643183318$$

$$a_{2}^{42} = -0.041382855555706463$$

The coefficients above are used for calculations in the interior computational domain. For the boundaries, the coefficients (ref. 5) are:

$$a_{-5}^{51} = -0.0283927780285557$$

$$a_{-4}^{51} = 0.192107686530459$$

$$a_{-3}^{51} = -0.617980095557289$$

$$a_{-2}^{51} = 1.28536574416235$$

and

$$a_{-1}^{51} = -2.14340185401956$$

$$a_{0}^{51} = 1.11244509330028$$

$$a_{1}^{51} = 0.199856203612323$$

$$a_{-6}^{60} = 1/6$$

$$a_{-5}^{60} = -6/5$$

$$a_{-4}^{60} = 15/4$$

$$a_{-3}^{60} = -20/3$$

$$a_{-2}^{60} = 15/2$$

$$a_{-1}^{60} = -6$$

$$a_{0}^{60} = 49/20$$

It is noted that a_j^{60} represents standard six order accurate one-side scheme and was obtained solely from the Taylor series expansion. The reason for choosing a_j^{60} from the Taylor series expansion is that optimization did not make visible improvement for this case. In addition, it is worthwhile to mention that $a_j^{15} = -a_{-j}^{51}$ and $a_j^{06} = -a_{-j}^{60}$. The temporal discretization used in the scheme is from Tam and Webb (ref. 6).

The CE/SE method was developed for solving general fluid dynamics problems (ref. 3). The conservation equations are solved in integral forms with flux conservation in space and time. Space and time are unified and treated on the same footing. The CE/SE method used in the current study is a second-order scheme.

The objectives of the current investigations are to evaluate the accuracy of the two schemes for the benchmark problems and to compare the solutions from the two numerical schemes.

Mathematical Formulations

It is known that the computation of sound wave propagation through a transonic nozzle and the simulation of the shock-sound interactions are challenging problems for computational aeroacoustics (CAA). In order to study the reliability and the accuracy of the current numerical methods for the CAA, simplified model problems are formulated and solved using the upwind DRP and the CE/SE methods. The first problem is a

one-dimensional acoustic wave transmission problem through a nearly choked nozzle; and the second problem is described as a sound wave passing through a shock in a quasi-one-dimensional supersonic nozzle. For both problems, the area of the nozzle is given by:

$$A(x) = \begin{cases} 0.536572 - 0.198086\,e^{-\ln 2\left(\frac{x}{0.6}\right)^2}, & x > 0 \\ 1.0 - 0.661514\,e^{-\ln 2\left(\frac{x}{0.6}\right)^2}, & x < 0 \end{cases} \tag{1}$$

The governing equations for both problems are the quasi-one-dimensional Euler equations. The dimensionless form of the equations is given as follows:

$$\frac{\partial}{\partial t}(\rho A) + \frac{\partial}{\partial x}(\rho u A) = 0 \tag{2}$$

$$\rho\left(\frac{\partial u}{\partial t} + u\frac{\partial u}{\partial x}\right) + \frac{\partial p}{\partial x} = 0 \tag{3}$$

$$\frac{\partial}{\partial t}(p A) + \frac{\partial}{\partial x}(p u A) + (\gamma - 1)p\frac{\partial}{\partial x}(u A) = 0 \tag{4}$$

For problem 1, the inlet and outlet boundary conditions used in the computations are radiation boundary conditions. At the inflow boundary,

$$\frac{1}{1-M}\frac{\partial}{\partial t}\begin{pmatrix} \rho' \\ u' \\ p' \end{pmatrix} - \frac{\partial}{\partial x}\begin{pmatrix} \rho' \\ u' \\ p' \end{pmatrix} = 0 \tag{5}$$

At the outflow boundary,

$$\frac{\partial}{\partial t}\begin{pmatrix} p' \\ u' \\ \rho' \end{pmatrix} + (1+M)\frac{\partial}{\partial x}\begin{pmatrix} p' \\ u' \\ \rho' \end{pmatrix} = \begin{pmatrix} -1 \\ 1 \\ -1 \end{pmatrix}\frac{2\varepsilon\omega}{1-M}\sin\left[\omega\left(\frac{x}{1-M}+t\right)\right] \tag{6}$$

where $\varepsilon = 10^{-5}$, $\omega = 0.6\pi$ and $M = 0.4$. For problem 2, the radiation boundary condition and the outflow boundary condition are used for the inlet and the outlet, respectively. At the inlet,

$$\left(\frac{1}{1-M}\frac{\partial}{\partial t} - \frac{\partial}{\partial x}\right)\begin{pmatrix} \rho' \\ u' \\ p' \end{pmatrix} = -\begin{pmatrix} 1 \\ 1 \\ 1 \end{pmatrix}\frac{2\omega\varepsilon}{1-M^2}\cos\left[\omega\left(\frac{x}{1+M}-t\right)\right] \tag{7}$$

At the outlet,

$$\frac{1}{1+M}\frac{\partial p'}{\partial t}+\frac{\partial p'}{\partial x}=0 \tag{8}$$

$$\frac{\partial u'}{\partial t}+\bar{u}\frac{\partial u'}{\partial x}+\frac{1}{\bar{\rho}}\frac{\partial p'}{\partial x}=0 \tag{9}$$

$$\frac{\partial \rho'}{\partial t}+\bar{u}\frac{\partial \rho'}{\partial x}=\frac{\bar{\rho}}{\gamma \bar{p}}\left(\frac{\partial p'}{\partial t}+\bar{u}\frac{\partial p'}{\partial x}\right) \tag{10}$$

where $\varepsilon=10^{-5}$, $\omega=0.6\pi$ and $M=0.2006533$. The computational domain is considered as $-10 \leq x \leq 10$.

Results and Discussions

The solutions of the two problems of category 1 are presented. In the first problem, both uniform grid and non-uniform grid are considered. All the variables are non-dimensionalized with the characteristic values in the uniform region downstream of the nozzle throat. In the second problem, only uniform grid is considered. All the variables are non-dimensionalized using the upstream values such as the inlet nozzle height, the inlet gas density, and the inlet speed of sound, etc. The steady state solutions for both problems are solved using the CE/SE method.

Category 1 Problem 1

The acoustic waves, with angular frequency $\omega=0.6\pi$, are generated downstream of the nozzle and propagate upstream through the narrow passage of the nozzle throat. Figure 1 shows the pressure perturbation along the nozzle at time $t=40$ using the upwind DRP scheme with uniform grid. The numbers of the grid points used in Figure 1 are 200, 400 and 800, respectively. We can see that a converged solution is achieved with 400 uniform grid points. The maximum acoustic pressure distribution is shown in Figure 2 for the same numbers of the uniform grid points. However, after enlarging the region around the peak pressure fluctuation of Figure 2, it is shown in Figure 3 that a non-uniform grid is needed to achieve a more accurate solution if no more than 400 mesh points are allowed. The non-uniform grid points used in Figure 3 were obtained from the following transformation

$$x = \frac{A}{\beta}\ln\left(\frac{1+\xi\ \tanh(\beta)}{1-\xi\ \tanh(\beta)}\right) \tag{11}$$

where $A=5$, $\beta=1.6$ and $-1\leq\xi\leq1$. The pressure perturbation along the nozzle at time $t=40$ is shown in Figure 4 for the CE/SE method with 200, 400 and 800 uniform grid points. It is shown in Figure 4 that a converged solution is not achieved yet. As the number of the uniform grid points increases to 1600, a nearly converged solution, shown in Figure 5, is obtained by the CE/SE method. Again if non-uniform grid points are used, a converged solution can be obtained by fewer than 400 grid points. The steady flow solutions are

calculated by the CE/SE method. Figure 6 shows the numerical solutions agree with the analytical solutions very well.

<u>Category 1 Problem 2</u>

The small amplitude acoustic waves, with angular frequency $\omega = 0.6\pi$, are generated upstream at the nozzle inlet and propagate downstream through a shock in a quasi-one-dimensional supersonic nozzle. The pressure perturbations along the nozzle are shown in Figures 7 and 8 for the upwind DRP and the CE/SE schemes, respectively. It is seen that a converged solution is obtained for both schemes with 400 uniform grid points. The comparisons of the solutions from the two schemes are given in Figures 9, 10 and 11 for pressure, density, and velocity perturbations. We can see that there are some discrepancies between the results from the two schemes, particularly after the shock. Since the same density and pressure perturbations are expected, the wiggles in the density perturbations from the upwind DRP scheme, shown in Figure 10, are the result of numerical errors. The pressure, density, and velocity perturbations from the upwind DRP scheme are shown in Figure 12. It is seen that the pressure and density perturbations are identical before the shock but different after the shock. However, there are no wiggles in the density perturbations from the CE/SE method (Figure 13). One possible reason for this is that the CE/SE method is based on the conservative formulation whereas the upwind DRP is not. If the conservative formulation were used for the upwind DRP scheme, the wiggles in the density perturbation would disappear. Pressure perturbations at the exit through a period of time are given in Figure 14 for both the numerical schemes with 400 uniform grid points. The numerical steady flow solutions are compared with the analytical solutions in Figure 15. The agreement between the numerical solutions and the analytical solutions is excellent.

Results of the two benchmark problems suggest that for the first problem the fourth-order upwind DRP scheme needs fewer grid points than the second-order CE/SE method if uniform grid points are used. This result is expected since the upwind DRP scheme used has a higher order of accuracy. However, for the problem involving a shock-sound interaction (the second problem), the CE/SE method gives more accurate results due to the conservative formulation.

Conclusions

In the paper, the two problems of category 1 have been solved using two numerical schemes, the upwind DRP scheme and the CE/SE method. The results show that both methods give accurate numerical solutions for both benchmark problems. For the first problem if the same grid point distribution is used the advantage of the higher order scheme is that it requires fewer grid points for achieving an accurate solution. However when there is a shock wave in the flow field, the conservative formulation becomes crucial for the accuracy of numerical solutions.

Acknowledgments

References

1. Zhuang, M. and Chen, R. [1998] "An Optimized Upwind Dispersion-Relation-Preserving Finite Difference Scheme for Computational Aeroacoustics," *AIAA J.* 36(11), 2146-2148.
2. Zhuang, M. and Chen, R. [1998] "Applications of the Optimized Upwind Dispersion-Relation-Preserving Schemes for Multi-Dimensional Acoustic Problems," *the 4th AIAA/CEAS Aeroacoustics Conference,* Toulouse, France, 2-4 June, 1998, AIAA Paper No. 98-2367.
3. Chang, S. [1995] "The Method of Space-Time Conservation Element and Solution Element – A New Approach for Solving the Navier-Stokes and Euler Equations," *Journal of Computational Physics* 119, 295-324.
4. Tam, C. K. W. [1995] "Computational Aeroacoustics: Issues and Methods," *AIAA J.* 33(10), 1788-1796.
5. Chen, R. F. [1998] "Study on Optimized Upwind Schemes for Computational Aeroacoustics and Extension of a Fully Conservative Chimera to Finite Difference Schemes," Ph.D thesis, Department of Mechanical Engineering, Michigan State University.
6. Tam, C. K. W., and Webb, J. C., [1993] "Dispersion-Relation-Preserving Finite Difference Schemes for Computational Acoustics", *J. Comp. Phys.* 107(2), 262-281.
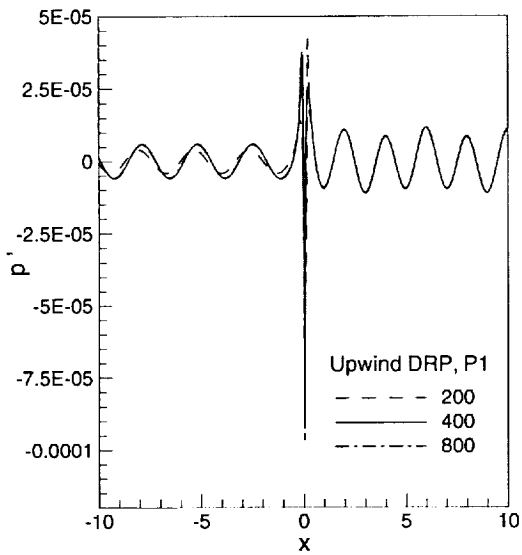
Figure 1. Pressure perturbation at t=40
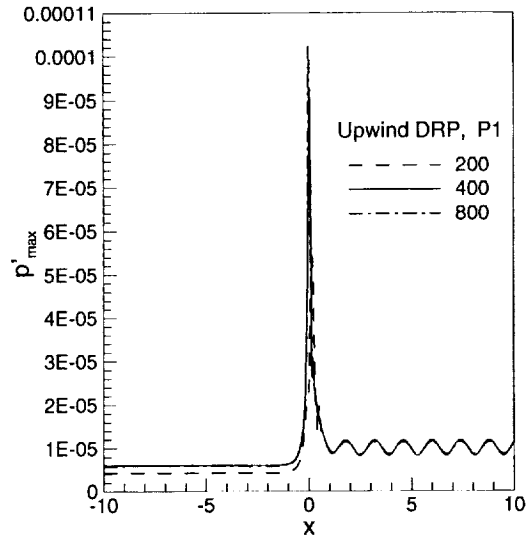
Figure 2. Maximum pressure perturbation
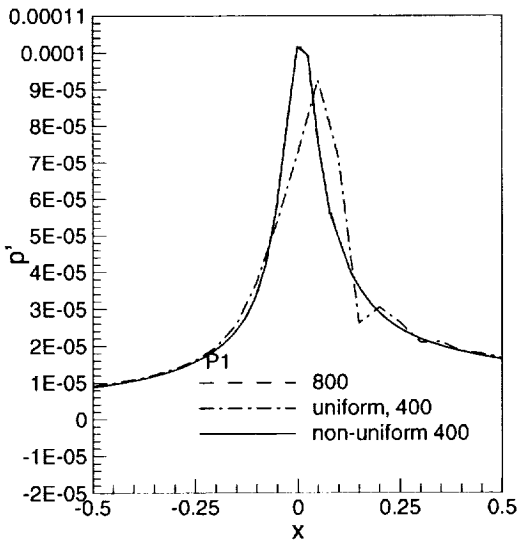
Figure 3. Enlarged plot of Figure 2 in
the region of -0.5<x<0.5
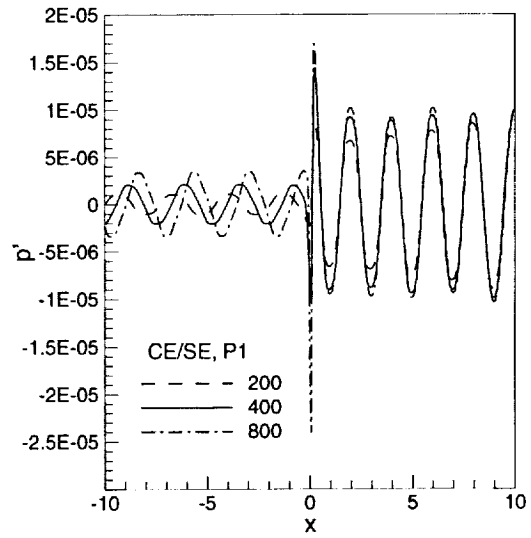
Figure 4. Pressure perturbation at t=40
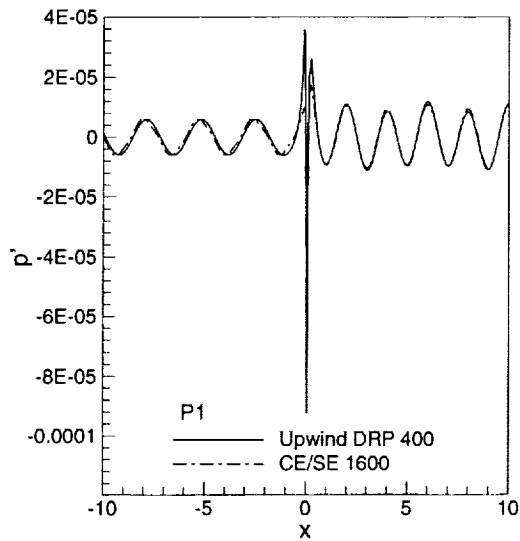
Figure 5. Pressure perturbation at t=40
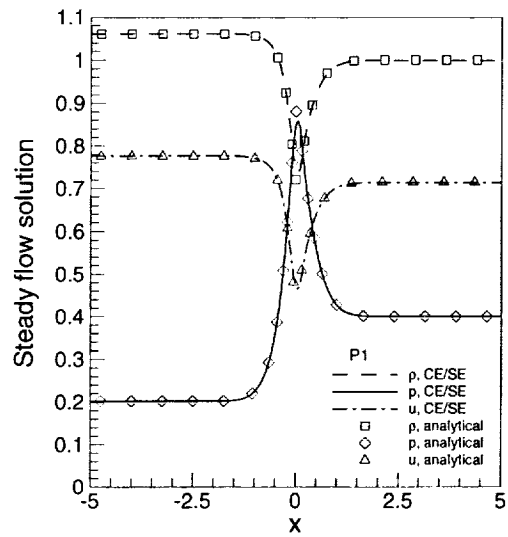
Figure 6. Comparisons of numerical meanflow
solutions with the analytical solutions
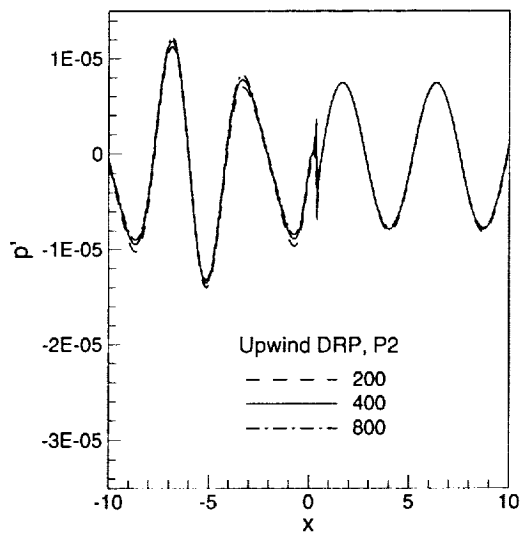
Figure 7. Pressure perturbation at t=40
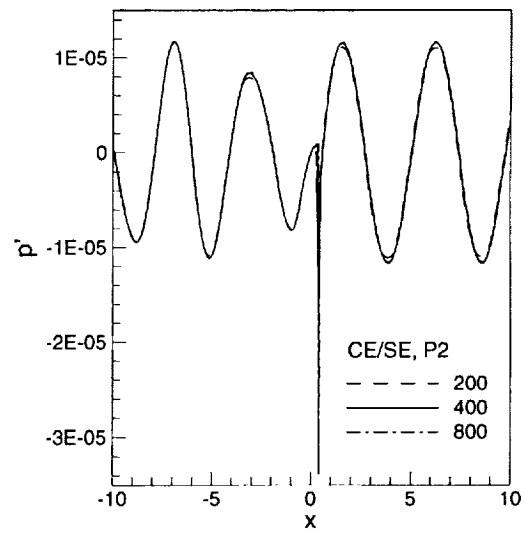
Figure 8. Pressure perturbation at t=40
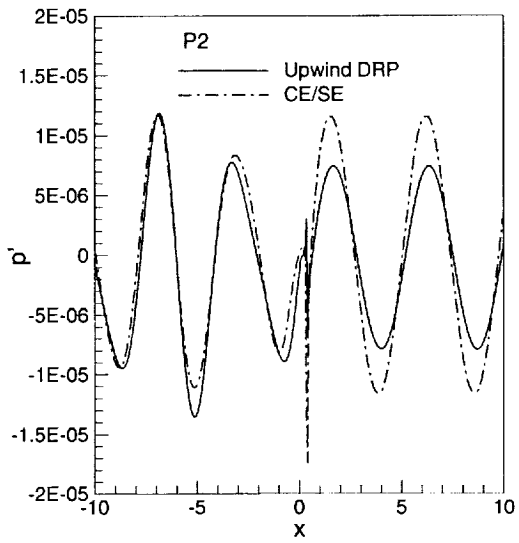
Figure 9. Pressure perturbation at t=40
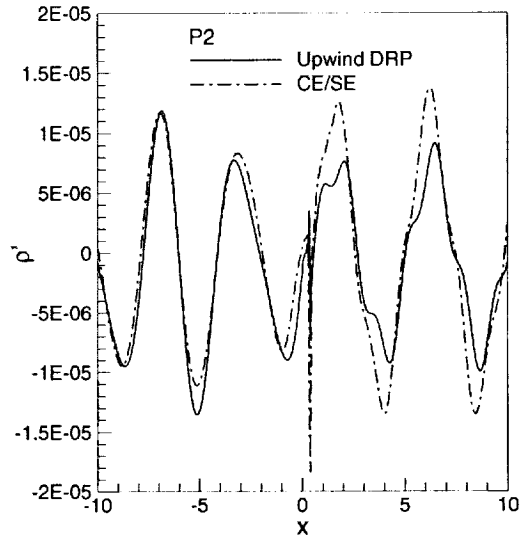
Figure 10. Density perturbation at t=40
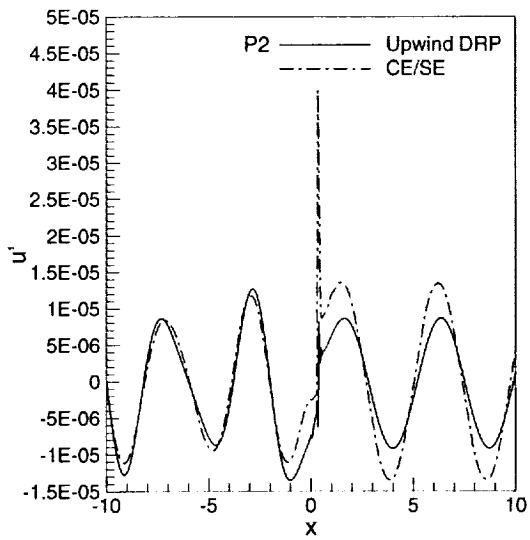
Figure 11. Velocity perturbation at t=40
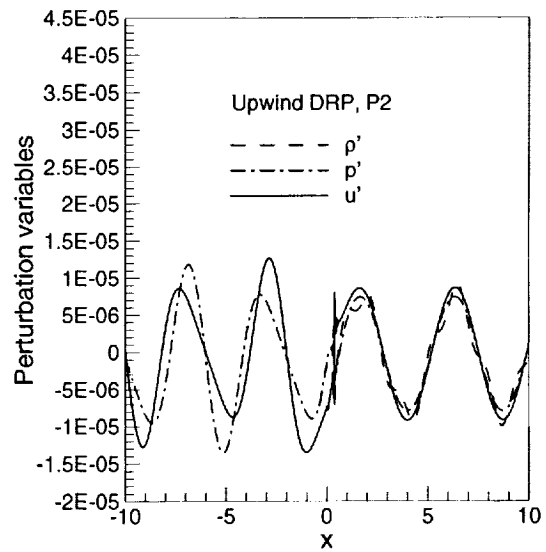
Figure 12. Density, pressure and
velocity perturbations
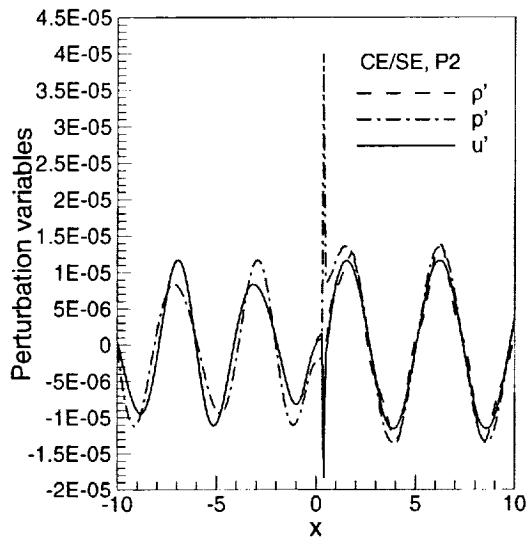
Figure 13. Density, pressure and velocity perturbations
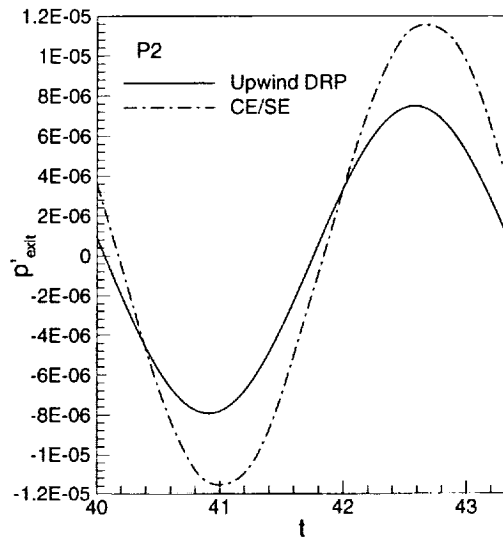
Figure 14. Pressure perturbation at the exit
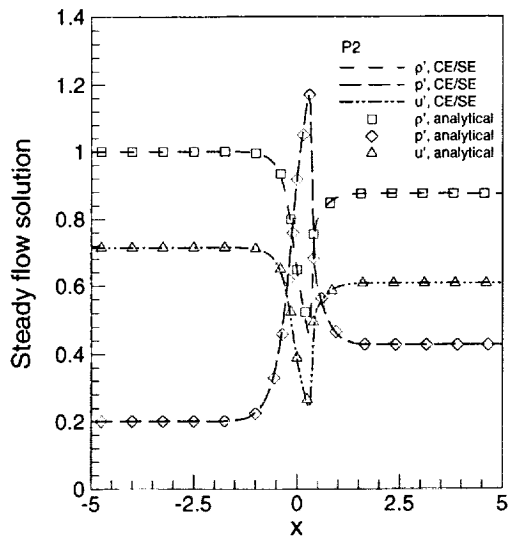
Figure 15. Comprisons of the numerical meanflow solutions with the analytical solutions

ESSENTIALLY NON-OSCILLATORY METHODS FOR SHOCK-SOUND INTERACTION

Yong Seok Kim* and Duck Joo Lee**
Department of Aerospace Engineering
Korea Advanced Institute of Science and Technology
Taejon, Korea

SUMMARY

High-order modified flux type Essentially Non-Oscillatory (ENO) schemes are used to solve the Shock-Sound interaction problem of Category 1. The shock-capturing capability inherent to the ENO scheme eliminates the oscillations near shock effectively. The peculiar characteristic of the ENO scheme is the adaptive stenciling, however, this free adaptation of stencils is not necessary in regions where the solution is smooth. This drawback is remedied by biasing stencils toward those that are linearly stable. Nonreflecting numerical boundary conditions are employed at the inflow and outflow for both the steady-state solution and time-dependent solution.

INTRODUCTION

As the computer is developed rapidly, the fluid and the acoustic fields can be solved directly by using CAA (computational Aeroacoustics) technique. A class of uniformly high-order accurate, essentially nonoscillatory (ENO) schemes have been developed by Harten and Oshcer [1], Harten et al. [2]. An attempt to apply the ENO schemes to aeroacoustic problems was made by Meadow, Caughy, and Casper [3], who discussed spurious entropy waves in calculations of unsteady shock in the flow field. J.Y. Yang [4] implemented the Lagrangian ENO interpolation of the third-order accuracy. Ko and Lee [5] improved the fourth-order modified flux approach ENO scheme of high-resolution and high-order. The ENO schemes used in this paper not only produce sharp shock profiles but also resolve the small amplitude waves.

At the radiation fields, Thomson's [6-7] non-reflecting characteristic-based boundary condition was used as the physical boundary conditions so that no propagating waves reflect back inward contaminating the acoustic field. Thompson decomposed hyperbolic equations into wave modes of definite velocity and then specified characteristic boundary conditions for incoming waves.

The starting point of his analysis was nonlinear Euler equations. The idea of his approach was that one-dimensional characteristic analysis could be performed by consideration of the transverse terms as constant source term. The amplitudes of outward propagating waves are defined entirely from the variables inside computational domain, while those of inward propagating waves are specified as the characteristic boundary conditions.

---

* Graduate Student
** Professor

NUMERICAL METHOD

The ENO scheme used in this work is briefly described as follows [8]. Consider the one-dimensional Euler equations of inviscid gas dynamics in conservation law form:

$$\partial_t Q + \partial_x F = 0 \tag{1}$$

where

$$Q = [\rho, \quad \rho u, \quad \rho e_t]^T$$

$$F = [\rho u, \quad \rho u^2 + p, \quad (\rho e_t + p)u]^T$$

$$p = (\gamma - 1)[\rho e_t - 0.5\rho u^2] \tag{2}$$

$$h = e_t + p/\rho$$

$$\gamma = 1.4$$

Eq. (1) can be expressed in quasilinear form as:

$$\partial_t Q + A(Q)\partial_x Q = 0 \tag{3}$$

where A is the Jacobian matrix $\partial F/\partial Q$ and has real eigenvalues:

$$(a_1, \quad a_2, \quad a_3) \quad = \quad (u, \quad u+c, \quad u-c) \tag{4}$$

where $c = \sqrt{\gamma p/\rho}$ is the sound speed. One can transform Eq. (3) to a diagonal form using the $\Lambda = RAR^{-1}$ and $W = R^{-1}Q$ relations:

$$\partial_t W + \Lambda \partial_x W = 0 \tag{5}$$

Eq. (1), based on Roe's approximate method, can be written as

$$Q_j^{n+1} = Q_j^n - \lambda [\tilde{F}_{j+1/2}^n - \tilde{F}_{j-1/2}^n] \tag{6}$$

where $\tilde{F}_{j+1/2}^n$ is the numerical flux and defined by

$$\tilde{F}_{j+1/2}^n = \frac{1}{2}[F_j^n + F_{j+1}^n + R_{j+1/2}^n \cdot \Phi_{j+1/2}^n] \tag{7}$$

In light of the Godunov-type method this reflects different ways of resolving the Riemann problem at the cell interface and Roe's approach is an ingenious way of extending the linear wave decomposition, which is the exact linear solution to Riemann's problem, to nonlinear equations. Here for the first order upwind scheme, the components of the column vector $\Phi_{j+1/2}^n$ are given by:

$$\phi_{j+1/2}^l = -|\Lambda_{j+1/2}^l|R_{j+1/2}^{-1}(Q_{j+1}^n - Q_j^n)$$

$$= -|\Lambda_{j+1/2}^l|\delta w_{j+1/2}^l \tag{8}$$

where $R_{j+1/2}$ is the right eigenvector matrix and $\delta w_{j+1/2}^l$ is the element of the characteristic vector as defined by:

$$\delta W = [\delta w^1, \delta w^2, \delta w^3] = \left[\delta\rho - \frac{\delta p}{c^2}, \frac{\delta p}{\rho c} + \delta u, \frac{\delta p}{\rho c} - \delta u \right] \tag{9}$$

The cell interface values are obtained by Roe's average. A higher-order ENO scheme for Eq. (1) can be expressed in the form of Eq. (7) in terms of the numerical flux:

$$\tilde{F}_{j+1/2}^n = \frac{1}{2}[F_j^n + F_{j+1}^n + R_{j+1/2}^n \cdot \Phi_{j+1/2}^n] \tag{10}$$

258

The components of $\Phi^n_{j+1/2}$ are defined as:

$$\phi^l_{j+1/2} = g^l_{j+1}(a^l_{j+1/2}) + g^l_j(a^l_{j+1/2}) - |a^l_{j+1/2}|\{a^l_{j+1/2}\Delta_+ w^l_j + g^l_{j+1}(a^l_{j+1/2}) - g^l_j(a^l_{j+1/2})\} \qquad (11)$$

where the characteristic speed, $a^l_{j+1/2}$, are the elements of the diagonal matrix $A^l_{j+1/2}$ and the first difference of a characteristic value, $\Delta_\pm w^l_j$, is the lth element of the characteristic vector, $\Delta_\pm W^n_j = R^{-1}_{j+1/2}\Delta_\pm Q^n_j$. g^l are similar in the constant-coefficient case except three characteristic waves exist. For the third-order accuracy these are given by:

$$g^l_j(a^l_{j+1/2}) = \sigma(a^l_{j+1/2})\beta^l_j + \tilde{\sigma}(a^l_{j+1/2})\tilde{\beta}^l_j + \hat{\sigma}(a^l_{j+1/2})\hat{\beta}^l_j \qquad (12)$$

where the $\sigma, \tilde{\sigma}, \hat{\sigma}$ functions and the values of divided differences are expressed as below in case of third-order:

$$\sigma(a) = |a|(1 - \lambda|a|)/2$$

$$\tilde{\sigma}(a) = a^+(2 - 3|\lambda a| + |\lambda a|^2)/6 + a^-(1 - |\lambda a|^2)/6 \qquad (13)$$

$$\hat{\sigma}(a) = a^+(1 - |\lambda a|^2)/6 + a^-(2 - 3|\lambda a| + |\lambda a|^2)/6$$

$$\beta^l_j = m(\Delta_- w^l_j, \Delta_+ w^l_j)$$

$$\tilde{\beta}^l_j = m(\Delta_-\Delta_- w^l_j, \Delta_-\Delta_+ w^l_j), \quad \hat{\beta}^l_j = 0 \qquad if\,(\Delta_- w^l_j \le \Delta_+ w^l_j) \qquad (14)$$

$$\hat{\beta}^l_j = m(\Delta_-\Delta_+ w^l_j, \Delta_+\Delta_+ w^l_j), \quad \tilde{\beta}^l_j = 0 \qquad otherwise$$

ENO schemes are uniformly high-order accurate right up to the shock. However, they also have certain drawbacks. One problem is with the freely adaptive stencil. This free adaptation of stencils is not necessary in regions where the solution is smooth. For the present work, this drawback is remedied by biasing stencils toward those that are linearly stable. Casper and Meadows [9] have suggested a nonlinear biasing algorithm that retain the linearly stable stencils in smooth region, yet allow more freedom near a discontinuity.

RESULTS AND DISCUSSIONS

The high-order ENO schemes discussed above are now applied to the solution of the shock-sound interaction problem in a quasi-one-dimensional converging-diverging nozzle. The conservative forms of the quasi-one-dimensional Euler equations are represented as follows:

$$\frac{\partial}{\partial t}(AQ) + \frac{\partial}{\partial x}(AF) = H \qquad (15)$$

where

$$Q = \begin{bmatrix} \rho \\ \rho u \\ \rho e_t \end{bmatrix}, \qquad F = \begin{bmatrix} \rho u \\ \rho u^2 + p \\ (\rho e_t + p)u \end{bmatrix}, \qquad H = \begin{bmatrix} 0 \\ p\dfrac{dA}{dx} \\ 0 \end{bmatrix} \qquad (16)$$

The variables $\rho, u, p, e,$ and A are the density, velocity, pressure, total energy, and nozzle area, respectively. And p is related to other variables by $p = (\gamma - 1)[\rho e_t - \rho(u^2 + v^2)/2]$ where γ is the ratio of specific heats.

The area of the nozzle and its derivative are illustrated in Fig. 1. A steady-state solution (Fig. 2) is obtained from a third-order ENO scheme with a biased stencil algorithm when the residuals are driven to 10^{-11} order. It should be noted that this numerically converged initial condition cannot be obtained with a freely adaptive stencil algorithm. Fig. 3 illustrates the residual of the steady-state solution. A suitably converged solution demonstrates that the biased stencil algorithm is well applied.

After steady state is achieved, an acoustic disturbance is introduced at the inlet, x=-10: At the inlet boundary, the conditions are:

$$\begin{bmatrix} \rho \\ u \\ p \end{bmatrix} = \begin{bmatrix} 1 \\ M \\ 1/\gamma \end{bmatrix} + \begin{bmatrix} 1 \\ 1 \\ 1 \end{bmatrix} \varepsilon \cdot \sin\left(\omega \left(\frac{x}{1+M} - t \right) \right) \qquad (17)$$

where $\varepsilon = 1.0 \times 10^{-5}$, $\omega = 0.6\pi$, $M_{inlet} = 0.2006533$. The pressure will be set at the outflow boundary to create a shock $(p)_{exit} = 0.6071752$. The calculation is performed on 251 cells clustered near the nozzle throat. The time step used is determined by a CFL condition with a Courant number of 0.9. The inflow is perturbed for $0 < t/T_\lambda \leq 50$, where $T_\lambda = 2\pi/\omega$ is one period of the incoming acoustic wave. Fig. 4 shows the perturbation at the start of a period $(x, \rho(x) - \bar{\rho}(x), u(x) - \bar{u}(x), p(x) - \bar{p}(x))$ over the period of the perturbation. The acoustic wave propagates to the shock and where a reflected wave and a transmitted wave are formed. It is observed that a large amplitude is generated at the shock position due to the interaction between the acoustic wave and the shock wave. The pressure perturbation at the exit plane over one period $(t, p(t) - \bar{p}(t))$ is shown in Fig. 5.

REFERENCES

1. Harten, A. and Osher, S.: Uniformly High-Order Accurate Nonoscillatory Schemes I, *SIAM Journal on Numerical Analysis*, Vol. 24, No. 2, 1987, pp. 279-309.

2. Harten, A., Engquist, B., Osher, S., and Chakravarthy, S. R.: Uniformly High-Order Accurate Essentially Non-Oscillatory Schemes III, Journal of Computational Physics, Vol. 71, No. 2. 1987, pp. 231-303.

3. Meadows, K. R., Caughey, D. A., and Casper, J.: Computing Unsteady Shock Waves for Aeroacoustic Applications, AIAA paper 93-4329, 1993.

4. Yang, J. Y.: High-Resolution, Nonoscillatory Schemes for Unsteady Compressible Flows, *AIAA Journal*, Vol. 30, No. 6, 1992, pp. 1570-1575.

5. Ko, D. K. and Lee, D. J.: Development of an Efficient Fourth-Order Non-oscillatory Scheme for Compressible Flows, *Computational Fluid Dynamics Journal* Vol. 6, 1998, pp. 519-526.

6. Thompson, K. W.: Time Dependent Boundary Conditions for Hyperbolic Systems, *Journal of Computational Physics*, Vol. 68, 1987, pp. 1-24.

7. Thompson, K. W.: Time Dependent Boundary Conditions for Hyperbolic Systems II, *Journal of Computational Physics*, Vol. 89, 1990, pp. 439-461.

8. Kim, Y. S. and Lee, D. J.: Numerical Prediction of I.C. Engine Intake Noise with a Moving Piston and a Valve, AIAA/CEAS Paper 99-1833, 1999.

9. Casper, J. and Meadows, K.: Using High-Order Accurate Essentially Nonoscillatory Schemes for Aeroacoustic Applications, *AIAA Journal*, Vol. 34, No. 2, 1996, pp. 244-250.
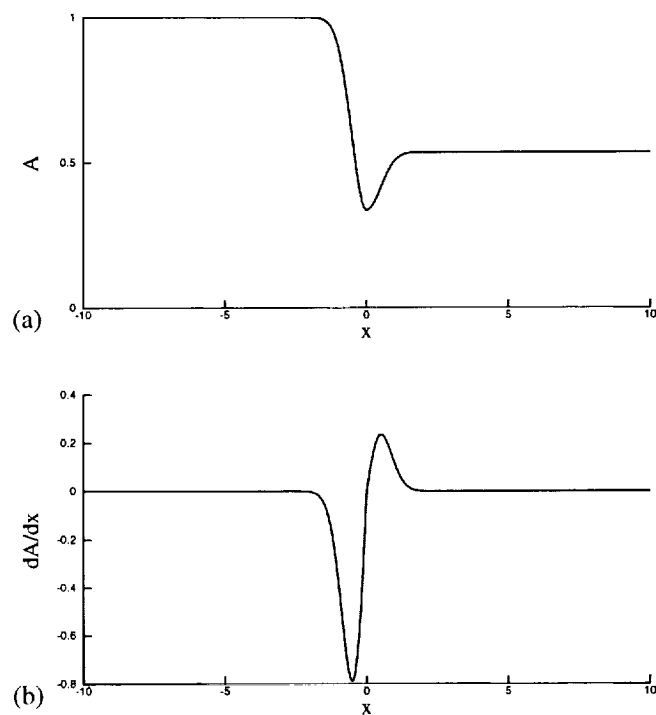
Figure 1. (a) Nozzle area A(x), and (b) area derivative dA/dx
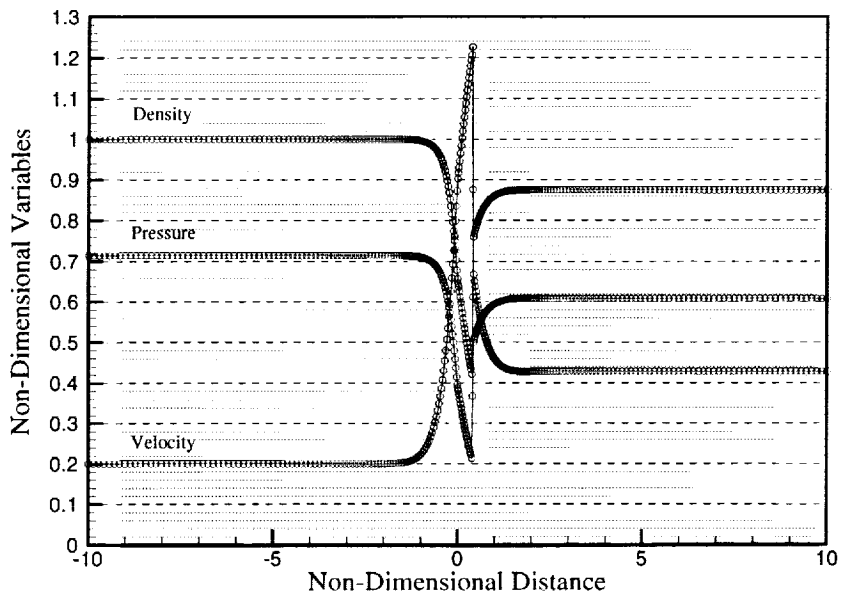
Figure 2. Initial steady-state solution
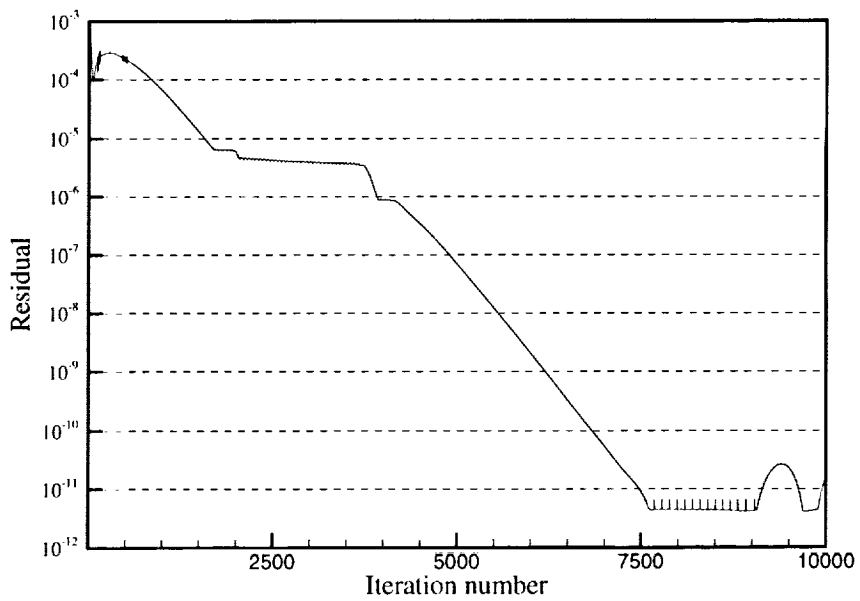
Figure 3. Residual of the steady state solution
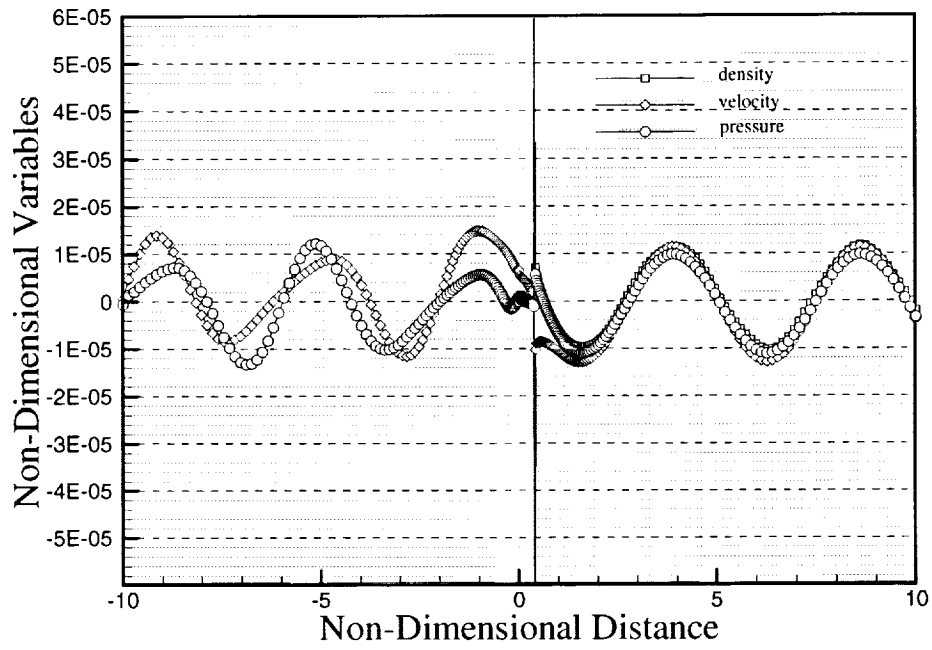
Figure 4. Spatial distribution of perturbed solution
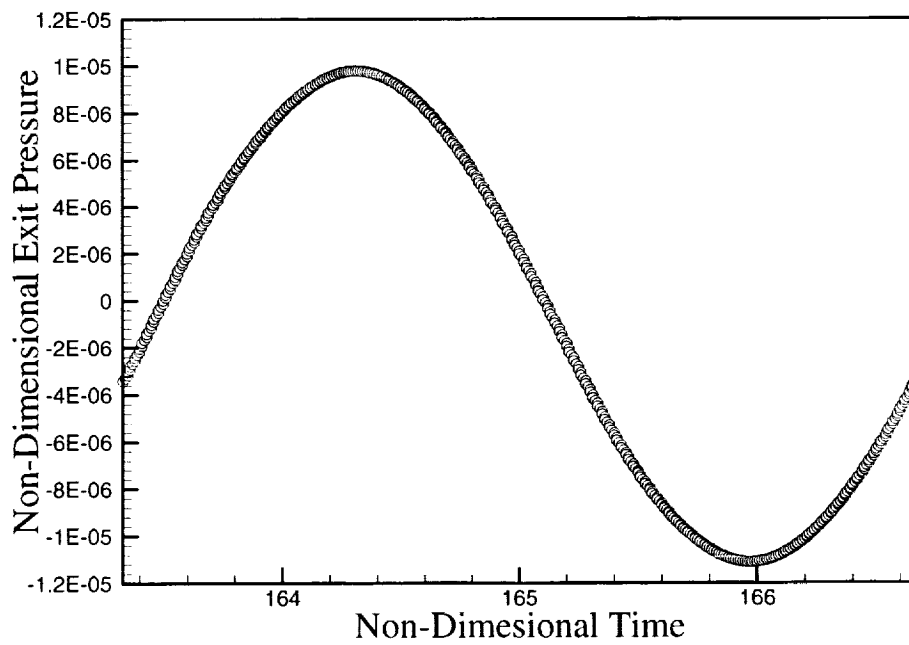
Figure 5. Pressure perturbation at the exit plane through one period
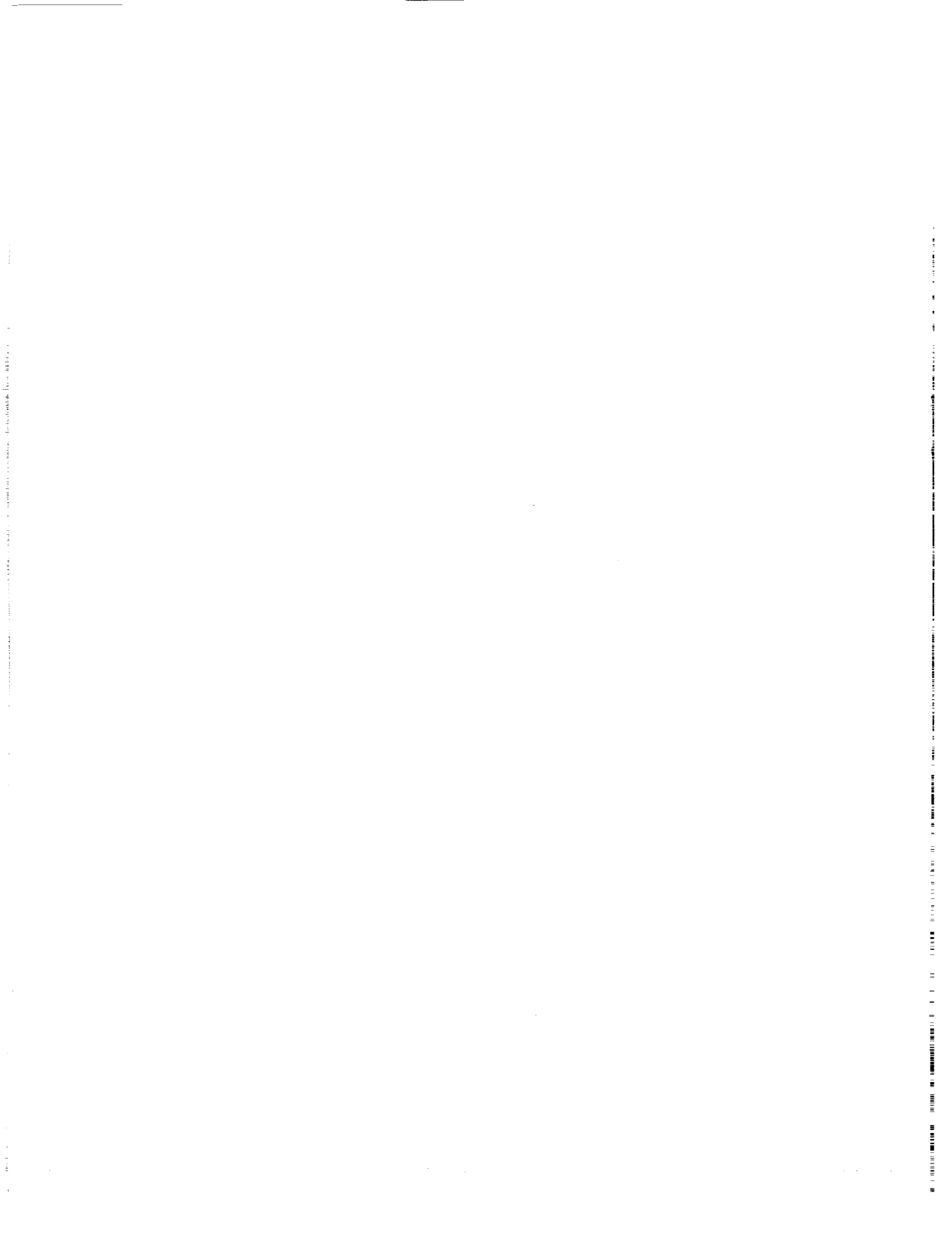
A Low Order and a High Order Solution
For A Converging-Diverging Nozzle Problem

John W. Goodrich
NASA Glenn Research Center
Cleveland, OH 44135

1 Introduction

The Computational Aeroacoustics Workshops on Benchmark problems are conducted in order to generate solutions with a variety of methods for problems that are chosen both to be representative of significant and relevant acoustic phenomena. It is generally recognized that CAA applications require the resolution in time and in space of solution details over a significantly broader range of scales than typical CFD applications. These requirements are forcing the development of new methodologies for CAA applications. This paper presents numerical results from a third and a seventh order algorithm for the propagation of an acoustic signal through a converging-diverging nozzle. These two algorithms are members of a new family of high accuracy methods that have the same order acuracuy in both space and time, and are an extension of previous work for linearized Euler equations [3, 4, 5, 7] to fully nonlinear time dependent problems. The simulations are all with the fully nonlinear quasi one dimensional Euler equations for the total solution, which includes both the fluid dynamics and the acoustics. The acoustic solution is obtained from the time dependent nonlinear solution by subtracting the steady solution.

2 The Governing Equations

The Euler equations for a quasi one dimensional problem with an ideal polytropic gas are:

$$\frac{\partial \rho}{\partial t} + \frac{1}{A}\frac{\partial A\rho v}{\partial x} = 0, \tag{1}$$

$$\frac{\partial v}{\partial t} + v\frac{\partial v}{\partial x} + \rho\frac{\partial p}{\partial x} = 0, \tag{2}$$

$$\frac{\partial p}{\partial t} + v\frac{\partial p}{\partial x} + \gamma p\frac{\partial v}{\partial x} + \gamma p v\frac{1}{A}\frac{dA}{dx} = 0, \tag{3}$$

where p is pressure, ρ is density, and v is velocity, and where $A(x)$ is the cross sectional area of a converging-diverging nozzle. We will take $\gamma = 1.4$ for air at standard conditions. The cross sectional area of the converging-diverging nozzle $A(x)$ is given as

$$\begin{aligned} A(x) &= 0.536572 - 0.198086\exp(-\tfrac{\ln(2)}{0.36}x^2), \quad -10 \leq x < 0, \\ &= 1.000000 - 0.661514\exp(-\tfrac{\ln(2)}{0.36}x^2), \quad 0 \leq x \leq +10. \end{aligned} \tag{4}$$

Note that the first derivatives of A are continuous at $x = 0$, but that the second and higher are not. This implies that there will be jump conditions at the throat for the second and higher derivatives

of the solution. The benchmark problem is scaled such that the conditions for the steady base flow at the nozzle exit are: $M_\infty = 0.4$; $v_\infty = 0.4$; $\rho_\infty = 1$; $c_\infty = \sqrt{\gamma \frac{p_\infty}{\rho_\infty}} = 1$; and consequently, $p_\infty = \frac{1}{\gamma}$. An $O[10^{-5}]$ acoustic disturbance is imposed on the $O[1]$ steady flow at the nozzle exit, and the goal is to find the time dependent pressure disturbance, and the maximum acoustic pressure distribution.

For an ideal gas with constant specific heats, the entropy is $S(x,t) = c_v \log(\frac{p}{\rho^\gamma})$, where

$$\frac{\partial S}{\partial t} + v \frac{\partial S}{\partial x} = 0, \tag{5}$$

so that entropy is convected with v. The stated problem has $v > 0$ throughout the nozzle, and we may assume that the solution is isentropic. For the isentropic case with the scaling for this problem,

$$p = \frac{1}{\gamma} \rho^\gamma, \tag{6}$$

the pressure equation reduces to the continuity equation, and p can be eliminated. The speed of sound $c = \sqrt{\rho^{\gamma-1}}$, or $\rho = c^{\frac{2}{\gamma-1}}$. The momentum equation can be written as

$$\frac{\partial v}{\partial t} + v \frac{\partial v}{\partial x} + \frac{2}{\gamma-1} c \frac{\partial c}{\partial x} = 0, \tag{7}$$

and the continuity equation can be written as

$$\frac{\partial c}{\partial t} + v \frac{\partial c}{\partial x} + \frac{\gamma-1}{2} c \frac{\partial v}{\partial x} + \frac{\gamma-1}{2} cv \frac{d \log(A)}{dx} = 0. \tag{8}$$

Our general solution approach is to take S constant in the nozzle, with the value from the specified steady solution at the nozzle exit, and to solve for c and v with the momentum and continuity equations. Note that the equations for c and v have the Riemann invariants

$$R_\pm = \frac{2}{\gamma-1} c \pm v, \tag{9}$$

and that for subsonic flow, R_+ goes right and R_- goes left. A steady solution for the converging-diverging nozzle is readily obtained as in Anderson [1]. The definition of entropy and the problem reformulation in terms of c and v is from Whitham [8].

3 Numerical Methods

The computational results reported in this paper are from fully nonlinear simulations. The time accurate algorithms are used to compute converged steady solutions for the flow in the nozzle, and then to propagate the acoustic disturbance by oscillating the outflow boundary data about the steady solution values. The results presented in this paper are from two algorithms that are nonlinear realizations of a method for developing algorithms that can be applied to a variety of time evolution problems [3, 4, 5, 7]. Both of the algorithms for the nozzle problem must provide accurate nonlinear propagation of the solution, stable inflow and outflow boundary conditions, and jump conditions for second and higher order derivatives at the throat. Because of space limitations, only a summary of the algorithms can be given here, but further details will be presented in [6]. A comprehensive presentation of our method for developing algorithms is also being prepared.

The algorithms that we are using in this paper are for nonlinear propagation of c and v, for the total unsteady flow solution which includes the acoustic perturbation. The two nonlinear

third order derivatives at each grid point, and are third and seventh order accurate in space and time, respectively. Higher order methods are possible. We use a staggered grid with a two point stencil, and data at each grid point for both c and v, and their spatial derivatives up to the specified order for each particular algorithm. We use a local Hermite spatial interpolation with data at one time level, and then obtain time derivatives by a realization of the Cauchy-Kowaleskya method [2]. This approach yields a local approximation of the system solution, and not an approximation of derivative terms in an equation, so that the dynamics of the governing system are built into the algorithms. The solution variables c and v, and their spatial derivatives up to the order specified for each algorithm, are all propagated in time. The linear stability constraint is $V \frac{\Delta t}{\Delta x} < 1$, where V is the velocity maximum in the scale of the problem. These algorithms are not in conservation law form.

At the inflow boundary, R_+ is specified as a function of time, and R_- is propagated from the interior. At the outflow boundary, for the computation of the steady solution, R_- is specified as a function of time, and R_+ is propagated from the interior, while for the propagation of the unsteady acoustic disturbance, c is specified as a function of time, and R_+ is propagated from the interior. The data for the acoustic disturbance is taken from the specified data for $p(x, t)$ at the right boundary. Spatial derivatives for the imposed boundary data can be obtained from the time history of the boundary data.

There is a discontinuity in the second derivative of A at the throat, and consequently, in the second and higher derivatives of the solution as well. Second or higher order interpolation across the throat will introduce errors, and a special treatment at the throat is desirable. At the throat, we compute R_+ and its required spatial derivatives by propagation from the left, and R_- and its required derivatives from the right. The interpolation stencils for each method are taken on the appropriate side of the throat. In the case of the third order c2o1jd1 algorithm, only c, v, $\partial_x c$ and $\partial_x v$ are required at the throat, and since they are continuous across the throat, this data can be obtained directly from the data for the Riemann invariants. In the case of the seventh order c2o3jd3 algorithm, the second and third derivatives are different on either side of the throat, and these values must be obtained from the second and third derivatives of $R_\pm$ with their jump conditions. The jump conditions are obtained from the evolution equations for the Riemann invariants.

4   Numerical Results

Numerical results will be presented from the third order c2o1jd1 algorithm with $\Delta x = \frac{1}{256}$, and from the seventh order c2o3jd3 algorithm with $\Delta x = \frac{1}{20}$. Both algorithms use a uniform grid and take $\frac{\Delta t}{\Delta x} = \frac{1}{4}$. Note that the third order method uses approximately twelve times the number of grid points as the seventh order method. With both algorithms, a steady solution is computed, then time is reset to 0 and the disturbance oscillation is imposed. The acoustic disturbance at the boundary is run for at least $0 \leq t \leq 100$ in order to let transients pass out of the nozzle. The numerical results that we show have been computed on an IBM RS6000/397 workstation. On this machine, the computation of the solution for three periods (say $90 \leq t \leq 100$) takes approximately 674 seconds for the c2o1jd1 algorithm, and approximately 67 seconds for the c2o3jd3 algorithm.

Figures 1 and 2 present the total pressure at the throat for $90 \leq t \leq 100$ from the third and seventh order algorithms, respectively. The mean pressure level is slightly higher for the results from the seventh order algorithm, but if the mean pressure levels are aligned, then the two time traces are indistinguishable. The pressure disturbance is obtained by subtracting the mean pressure from the total pressure. Figures 3 and 4 present the instantaneous acoustic pressure distributation at $t = 100$ for the third and seventh order methods, respectively. These profiles are virtually identical. Note

that the wavelength and amplitude differ in the entrance and exit ducts, since the mean convection velocity is higher in the exit duct than in the entrance duct. The maximum acoustic pressure can also be obtained at each point by subtracting the minimum total pressure from the maximum total pressure, and then dividing by 2. The maximum acoustic pressure occurs at the throat, and is 9.500×10^{-5} for the third order method, and 9.572×10^{-5} for the seventh order method. The maximum acoustic pressure distribution for the third order algorithm is presented in Figure 5 for $-10 \leq x \leq 10$ and $100 \leq t \leq 110$. We have included a magnified plot of the instantaneous pressure at $t = 100$ for the seventh order algorithm in Figure 6, for $-1 \leq x \leq 1$, or just across the throat of the nozzle. This figure includes symbols for the grid points, and vividly shows the very few grid points that are used by this seventh order algorithm to resolve the transmission of the acoustic signal through the throat.

5 Conclusions

- It is possible to simultaneously compute the fluid dynamics and the acoustics for relevant problems with a single algorithm and computation.

- High order acuracy is possible in both space and in time, even for nonlinear problems.

- Accurate algorithms with high order and high resolution can produce valid results with considerably less total computational effort than less accurate methods, even for nonlinear problems.

References

[1] J.D. Anderson, *Modern Compressible Flow*, (McGraw-Hill, Boston, 1990).

[2] P.R. Garabedian, *Partial Differential Equations*, (John Wiley, New York, 1964).

[3] J. W. Goodrich, "An Approach to the Development of Numerical Algorithms for first Order Linear Hyperbolic Systems in Multiple Space Dimensions: The Constant Coefficient Case," NASA TM 106928, (1995).

[4] J. W. Goodrich, "Accurate Finite Difference Algorithms," *Barriers and Challenges in Computational Fluid Dynamics*, edited by V. Venkatakrishnan, M.D. Salas, S.R. Chakravarthy, (Kluwer Academic Publishers, Dordrecht, 1998), and as NASA TM 107377, (1996).

[5] J. W. Goodrich, "High Accuracy Finite Difference Algorithms for Computational Aeroacoustics," AIAA 97-1584, *The 3rd AIAA/CEAS Aeroacoustics Conference*, Atlanta, GA, May, 1997.

[6] J. W. Goodrich, "High Order and High Resolution Algorithms for Nonlinear Propagation of an Acoustic Signal in a Converging-Diverging Nozzle," in preparation.

[7] J. W. Goodrich and J. Hardin, "Accurate Finite Difference Algorithms for Computational Aeroacoustics," *Computational Fluid Dynamics Review 1998*, edited by M.M. Hafez and K. Oshima, (World Scientific, Singapore,1998).

[8] G.B. Whitham, *Linear and Nonlinear Waves*, (John Wiley, New York, 1974).

CAA WS 1a: Throat Pressure with Downstream Forcing.

c2o1jd1 for c and v: dx=1/256, dt/dx=1/4.
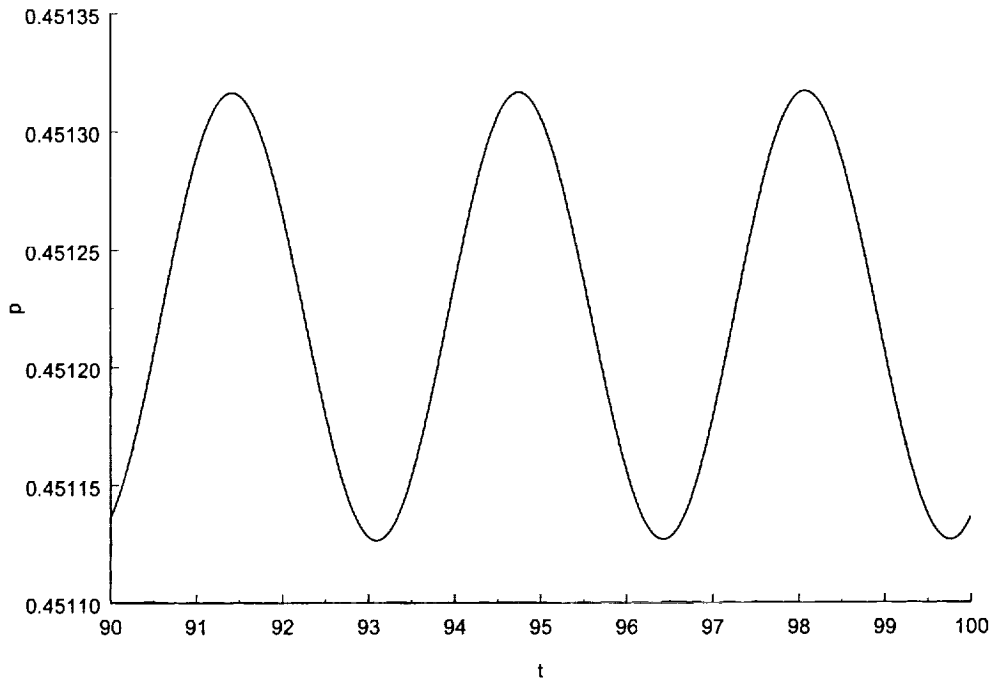
Figure 1: Throat Pressure History from the Third Order Algorithm

CAA WS 1a: Throat Pressure with Downstream Forcing.

c2o3jd3 for c and v: dx=1/20, dt/dx=1/4.
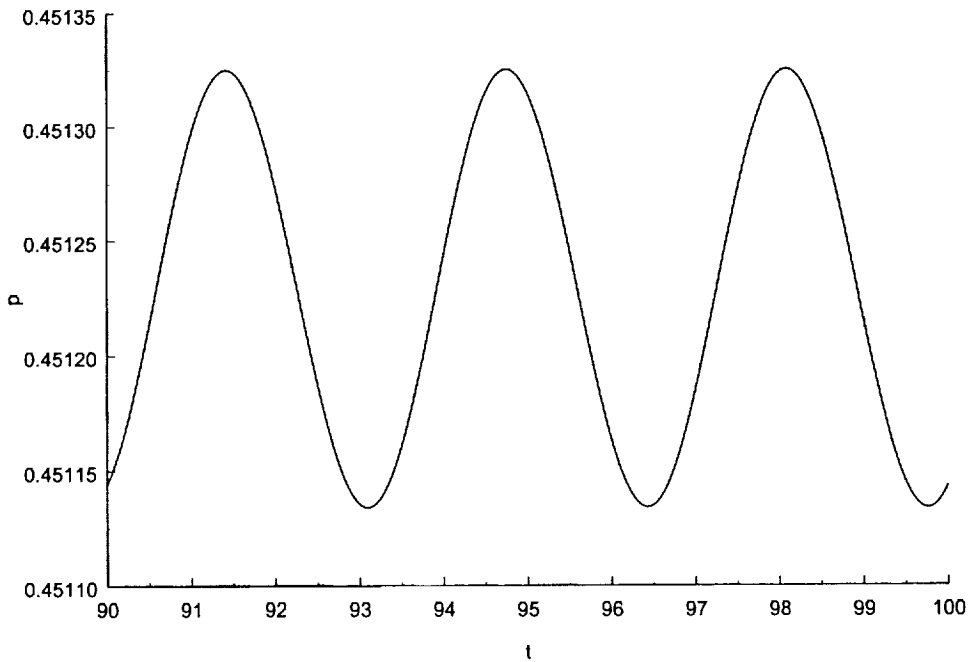
Figure 2: Throat Pressure History from the Seventh Order Algorithm

CAA WS 1a: Instantaneous Pressure Disturbance.

c2o1jd1: dx=1/256, dt/dx=1/4, t=100.
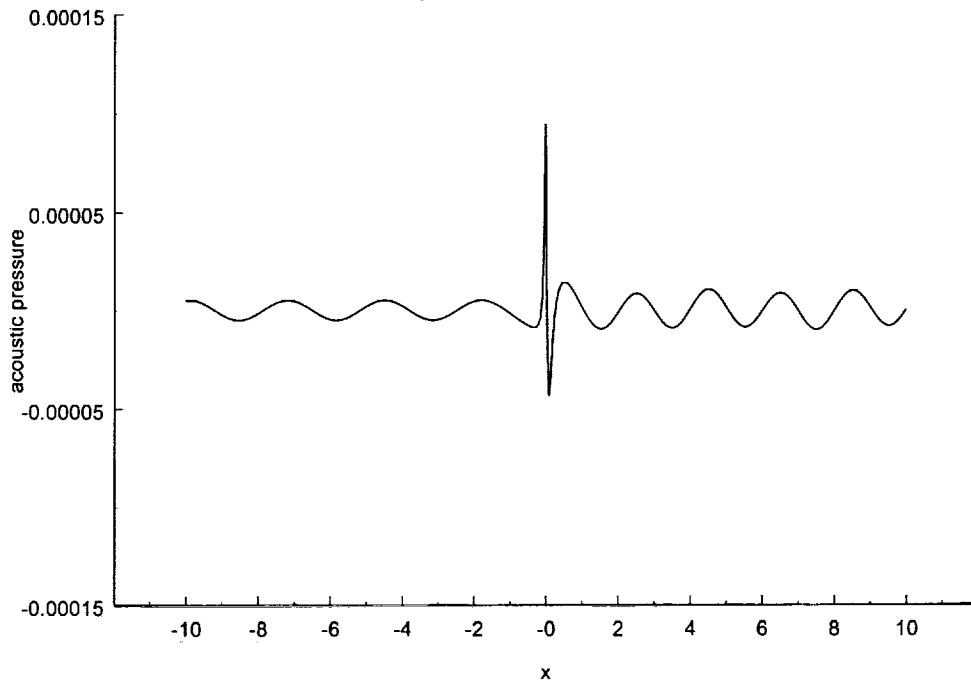
Figure 3: Instantaneous Pressure Disturbance for the Third Order Algorithm

CAA WS 1a: Instantaneous Pressure Disturbance.

c2o3jd3: dx=1/20, dt/dx=1/4, t=100.
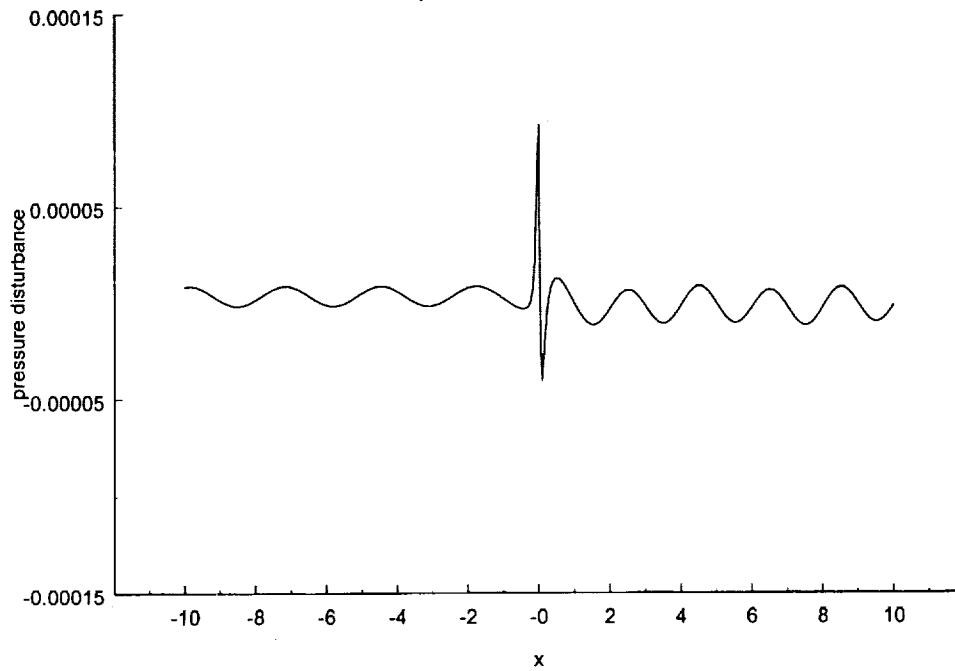
Figure 4: Instantaneous Pressure Disturbance for the Seventh Order Algorithm

CAA WS 1a: Maximum Acoustic Pressure Distribution.

c2o1jd1 for c and v: dx=1/256, dt/dx=1/4, 100<=t<=110.
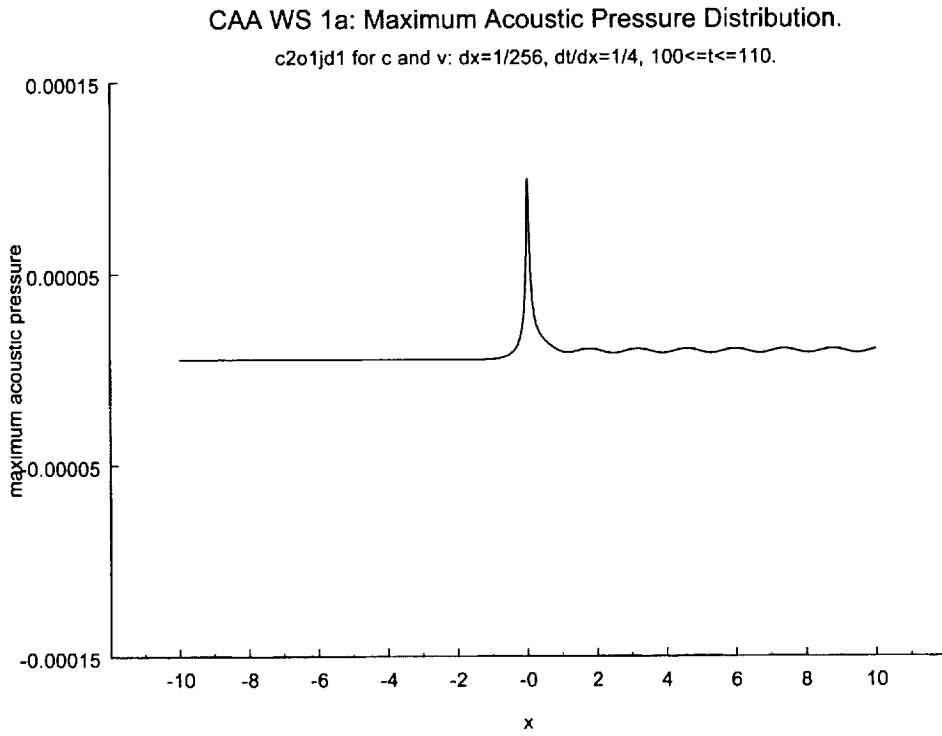
Figure 5: Maximum Acoustic Pressure Distribution for the Third Order Algorithm

CAA WS 1a: Instantaneous Pressure Disturbance.

c2o3jd3: dx=1/20, dt/dx=1/4, t=100.
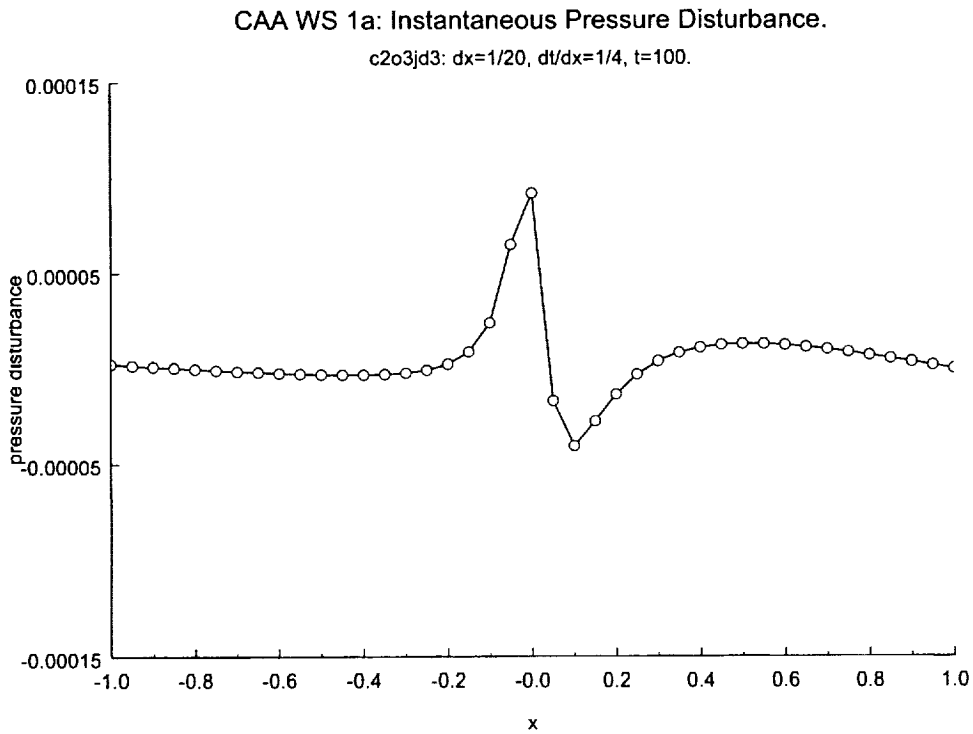
Figure 6: Pressure Distribution Detail for the Seventh Order Algorithm
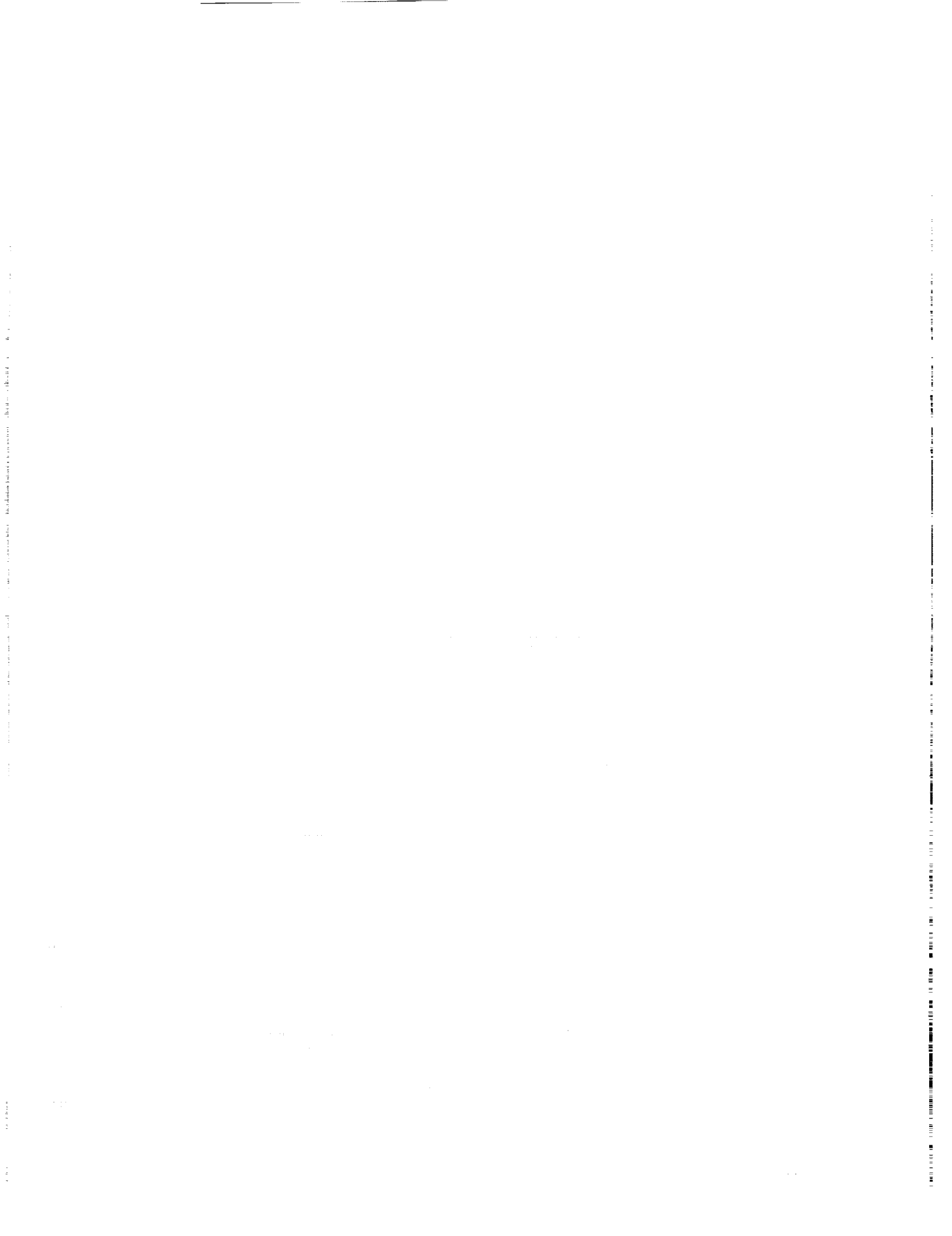
SPECTRAL METHODS FOR COMPUTATIONAL AEROACOUSTICS

DAN STANESCU

CFD Laboratory, Concordia University, Montreal, Canada

D. Ait-Ali-Yahia

Analytical Systems, Pratt and Whitney Canada

and

W. G. Habashi

CFD Laboratory, Concordia University, Montreal, Canada

Introduction

This paper presents an application of spectral methods to computational aeroacoustics problems. The physics of sound propagation is modeled by the system of partial differential equations that describe conservation of mass, momentum and energy in inviscid flows. The equations are solved numerically in the time domain as an initial and boundary value problem to obtain the time-dependent acoustic pressure in the flow field, from which sound pressure levels are obtained by integration.

Both global spectral methods and multidomain spectral methods are used to discretize the space terms that appear in the governing equations. While global spectral methods have some advantages, such as ease of coding, use of fast Fourier transforms for computing derivatives and high accuracy, the multidomain methods offer a viable alternative for domains with nontrivial geometric shapes. They are handled by the use of unstructured grids of non-overlapping hexahedra that may have curved boundaries. An isoparametric mapping is used to transform each hexahedron on the master element, on which an efficient collocation spectral approximation can be defined by the use of tensor products. Continuity of the solution in space is enforced as part of the solution process by the use of a set of staggered grids that do not involve the element corners.

For time advancement, a set of Runge-Kutta methods optimized for wave propagation and with minimal storage requirements are used for integration in time. Very simple yet effective radiation boundary conditions are constructed by adding directional damping terms to the governing equations in regions near far-field boundaries, but without splitting the equations. As such, the cost at which these boundary conditions can be implemented is very small. Furthermore, a method for numerically capturing discontinuities is introduced, that allowed us not only to compute spectral solutions for flows with shock waves, but also to simulate sound wave propagation through such discontinuities.

Category 1, Problem 1

For the category 1 problems, the nonlinear Euler equations are solved in the form

$$\frac{\partial Q}{\partial t} + \frac{\partial F}{\partial x} = H \tag{1}$$

with the state vector Q, the flux vector F and the source term H given by

$$Q = \begin{bmatrix} \rho \\ \rho u \\ \rho E \end{bmatrix}, \quad F = \begin{bmatrix} \rho u \\ \rho u^2 + p \\ (\rho E + p)u \end{bmatrix}, \quad H = \begin{bmatrix} -\dfrac{\rho u}{A}\dfrac{\partial A}{\partial x} \\ -\dfrac{\rho u^2}{A}\dfrac{\partial A}{\partial x} \\ -\dfrac{(\rho E + p)u}{A}\dfrac{\partial A}{\partial x} \end{bmatrix} \tag{2}$$

For a usual spectral collocation method based on Chebyshev polynomials, the state vector as well as the flux derivatives and the source terms are computed at the Gauss-Lobatto points $\xi_i = -\cos\left(\dfrac{\pi i}{N}\right)$, with N the number of modes retained in the approximation. This would cluster the points quadratically towards the ends of the interval and would only allow a time step $\Delta t \sim \dfrac{1}{N^2}$. To alleviate this restriction on the time step, we used the Kosloff-Tal-Ezer [1] mapping,

$$\chi = \frac{\arcsin(\varpi \xi)}{\arcsin(\varpi)} \tag{3}$$

such that the position of the corresponding images χ_i depends on the parameter ϖ, with the two limit cases being $\varpi = 1$, which corresponds to equi-distant nodes as for Fourier methods, and $\varpi = 0$, in which case χ_i will be the same Lobatto points. Differentiation using the Chebyshev polynomials in ξ will correspond to the use of a non-polynomial basis in χ. The mapping introduces an error, which can be made of the order of machine accuracy ε by setting

$$\varpi = \frac{2}{\varepsilon^{1/N} + \varepsilon^{-1/N}} \tag{4}$$

which is the value that we actually used for these computations, and still results in a useful mapping for sufficiently high values of N. To further cluster points in the central region of interest, the collocation points in the x coordinate are obtained through a mapping of the form

$$\frac{x(\chi)}{10} = q\chi \pm (1 - q)\left(1 - \frac{\tanh[r(1 \pm \chi)]}{\tanh r}\right) \tag{5}$$

where the parameter q controls the slope of the mapping, and r its departure from nonlinearity ($q=0.01$ and $r = 3$ have been used for the results). With these mappings computed, derivatives are computed in ξ-space using a Fast Cosine Transform method to evaluate the Chebyshev coefficients [2], and the derivatives in x are afterwards evaluated using the chain rule for differentiation.

The Euler equations become after discretization of the flux derivative a system of ordinary differential equations of the form

$$\frac{dQ}{dt} = \mathbf{F}(t, Q(t)); \quad Q(t^n) = Q^n \tag{6}$$

and is advanced in time with a low-storage, nonlinear, low dissipation and dispersion Runge-Kutta method [3] of the form

$$w_i = \alpha_i w_{i-1} + \Delta t \mathbf{F}(t_{i-1}, Q_{i-1}) \\ Q_i = Q_{i-1} + \beta_i w_i \Bigg\} \, , \qquad i = 1, \ldots, s \qquad (7)$$

with $\alpha_1 = 0$ for the algorithm to be self-starting. Here we denote $Q_0 = Q^n$, $Q^{n+1} = Q_s$ and $t_i = t^n + c_i \Delta t$. It is found out that this discretization is however unstable due to nonlinear effects, for which reason we had to use an exponential filter of the form

$$\sigma_k = \begin{cases} 1, & k < C \\ e^{-\omega \left(\frac{k-C}{N-C} \right)^o}, & k \geq C \end{cases} \qquad (8)$$

with o the order of the filter, $C \sim N$ a cut-off frequency, and $\omega = -\ln(\varepsilon)$ in order to preserve accuracy. This filter is applied directly to the Chebyshev coefficients $\hat{Q}_k$ of the state vector only at the end of a time step. We must note here that the filtered state vector $\sum_k \sigma_k \hat{Q}_k T_k(.)$ does not any more satisfy the discrete equations, i.e. its residual is not of the order of ε; however, the discrete residual change after the application of the filter is very small (of the order of 10^{-8} for N=128, and diminishing with N) such that we did not experience any problem in computing the propagation of the acoustic signal.

For boundary conditions at the inflow and outflow boundaries, we used a simple Riemann solution between the state as computed from the interior discretization and an external state, which is defined by the problem specification. For computation of the mean flow this external state is constant in time; after saving the steady-state solution, it is allowed to vary in time such as to specify the incoming acoustic wave. Since the Riemann solver properly accounts for the correct propagation of waves in unidimensional flows, no other special treatment is required. Figure 1(a) shows the solution obtained for the maximum acoustic pressure along the nozzle using N=256 modes.

The main disadvantages of a global spectral method, in particular its lack of geometrical flexibility, can be overcome by the use of multidomain spectral discretizations, in which the spectral expansion is accomplished individually on each subdomain Ω_i in a non-overlapping decomposition of the computational domain $\Omega = \bigcup_i \Omega_i$. The subdomains are then patched together to ensure continuity of the solution across their interfaces. For the present work, we chose the multidomain method first introduced by Kopriva and Kolias [4], extended to aeroacoustic problems in [5]. Since the method is extensively described in these references, we only note here that we used a number of 9 subdomains, with N=25 on each subdomain, giving a total of 225 discretization points. No filtering of the solution is necessary in this case; the steady state solution was converged to machine accuracy. The subdomains have been clustered in the region of area variation for a better resolution of the amplitude of the acoustic signal, as can be seen in figure 1(b).

Category 1, Problem 2

Shock capturing has long been considered a difficult problem for spectral methods, in particular because of the lack of complete understanding of the Gibbs phenomenon. Lately however, a large amount of work has been directed towards this problem, and it has been proved that one can use

the spectral expansion of a discontinuous function to find the position and the strength of the discontinuities and to build a spectrally accurate approximation [6], [7]. For the purpose of this work, we took a different approach and implemented the so-called spectral viscosity method, first introduced by Tadmor [9] and used for Chebyshev discretizations in [8].

In this case, the governing equations are modified by the addition of a numerical viscosity taking the form:

$$\frac{\partial Q}{\partial t} + \frac{\partial F}{\partial x} = \frac{\epsilon(N)}{w^{c_1}(x)}\frac{\partial}{\partial x}\left(R * \frac{\partial Q/\partial x}{w^{c_2}(x)}\right) \tag{9}$$

where the coefficient $\epsilon(N) \sim 1/N$, $w(x) = 1/\sqrt{1-x^2}$ is the Chebyshev weight function, and the exponents c_1 and c_2 are two parameters (taken as $c_1 = 3$ and $c_2 = 0$ in our computations). The viscosity term involves the convolution of the viscosity kernel R with the first derivative of Q; for convenience, the convolution is actually evaluated in spectral space. The particularity of the viscosity kernel is that it acts only on the high frequencies of the spectrum of Q, so that it does not affect regions where the variables are smooth. Explicitly, the computation of the right-hand side means evaluating

$$R * \frac{\partial Q/\partial x}{w^{c_2}(x)} = \sum_k \hat{R}_k \hat{q}_k T_k(.) \tag{10}$$

where $\hat{q}_k$ are the Chebyshev coefficients of $\dfrac{\partial Q/\partial x}{w^{c_2}(x)}$. We used a scalar model for the viscosity, based on the actual time-dependent variable in each of the three equations, and chose for the kernel the form:

$$R_k = \begin{cases} 0, & k < C \\ 1 - \left(\dfrac{C}{k}\right)^2, & k \geq C \end{cases} \tag{11}$$

with $C(N)$ the lowest mode at which the viscosity begins to operate. In figures 2, 3, 4, we present results for a mesh made of 16 subdomains with $N = 18$ Gauss points each (hence a total of 288 discretization points), the mesh being somewhat clustered in the shock region as can be seen from the data points in the figures (the smallest subdomain has a length $\Delta x = 0.1$).

Category 5 Problems

For this problem, the acoustic solver presented in reference [5] has been used. We solve the full nonlinear Euler equations, and account for the known mean flow by subtracting the mean-flow fluxes from the full instantaneous fluxes, such that the actual time-dependent variable is the perturbation itself. For the discretization to be consistent with the staggered-grid multidomain spectral method, however, the mean-flow fluxes must be computed and stored direction by direction; complete details are given in [10]. The main issues for this computation are a good resolution of the shear layer, and the free field boundary conditions. As the Riemann solver we use is unidimensional, it does not correctly represent the vorticity waves generated in the shear region, so that we found it necessary to use the damping layer technique described in [5], based on adding a temporal damping term to each equation of the form

$$\frac{\partial Q}{\partial t} + \frac{\partial F_i}{\partial x_i} = -\sigma(\vec{x})(Q - \bar{Q}) \tag{12}$$

where we take advantage of the fact that the mean flow is known beforehand. The damping varies according to a power law in the damping layer,

$$\sigma(\vec{x}) = \sigma_M \sum_i \left(\frac{x_i - x_i^{int}}{x_i^{ext} - x_i^{int}} \right)^\beta \tag{13}$$

with x_i^{int} and x_i^{ext} the coordinates of the interior and exterior limits of the layer. We emphasize that, because the equations are not split, the extra cost introduced by the evaluation of the damping terms is minimal.

For the computations, we used a grid made of 672 subdomains, covering the region $(x, y) \in [-8, 56] \times [0, 15]$, with 11 layers of elements between $y = 0$ and $y = 1.9$ for a better resolution of the shear layer. The number of Gauss points in each element was varied between $N = 5$ and $N = 9$, which leads to a total number of discretization points approximately between 16,000 and 54,000. Since, due to the nature of the discretization, the points are not equidistant, data along the respective line segments were extracted using the computational field postprocessor (hence linear interpolation). The perturbation has been introduced by adding the corresponding source term to the energy equation. A non-dimensional amplitude of 0.001 has been used for the source, which might introduce some nonlinearity into the solution, but we did not have the time to repeat the experiment for a smaller source amplitude. Based on the maximum CFL number the time step size was $\Delta t = 0.06$ on the coarsest grid, and the solution has been advanced at least up to $t = 300$. Computational times for the problem on different grids varied from approximately three hours on one CPU to about five hours on four CPU's for an Origin2000 machine with 195MHz R10000 processors. However, the results did not vary significantly over the stated range of grid sizes.

As a final comment, we remark that we expect the damping layer (its limits are set at the outflow from $x = 52$ to $x = 56$ and at the upper boundary from $y = 11.5$ to $y = 15$) to perform much better for the higher frequency case, since the sound will travel more wavelengths in this case within this region. The computational results actually confirm this expectation. Recent work [11] indicates that this kind of damping layer is best used in conjunction with grid stretching and low-pass filtering, but we did not explore this issue here. Results obtained for the two cases, $St = 0.14$ and $St = 0.6$, in this category, are given in figures 5- 8. Insufficient resolution in the shear layer may be the cause for the unexpected variation of the pressure perturbation at higher frequency $(St = 0.6)$ at $y = 1$ displayed in figure 8.

References

[1] Kosloff, D., and Tal-Ezer, H., "A Modified Chebyshev Pseudospectral Method with an $O(N^{-1})$ Time Step Restriction", *J. Comp. Physics*, Vol. 104, 1993, pp. 457.

[2] Canuto, C., Hussaini, M.Y., Quarteroni, A., and Zang, T.A., *Spectral Methods in Fluid Mechanics*, Springer-Verlag, 1987.

[3] Stanescu, D. and Habashi, W.G., "2N-Storage Low Dissipation and Dispersion Runge-Kutta Schemes for Computational Acoustics", *J. Comp. Physics*, Vol. 143, 1998, pp. 674.

[4] D. A. Kopriva and J. H. Kolias, "A Conservative Staggered-Grid Chebyshev Multidomain Method for Compressible Flows", *J. Comp. Physics* Vol. 125, 1996, pp. 244.

[5] Stanescu, D., Ait-Ali-Yahia, D., Habashi, W.G., and Robichaud, M., "Multidomain Spectral Computations of Sound Radiation from Ducted Fans", *AIAA Journal* Vol. 37, 1999, pp. 296.

[6] Eckhoff, K.S., "Accurate and efficient reconstruction of discontinuous functions from truncated series expansions" *Mathematics of Computation* Vol. 61, 1993, pp. 745.

[7] Geer, J. and Banerjee, N.S., "Exponentially accurate approximations to piece-wise smooth periodic functions", ICASE Report 95.

[8] Andreassen, O., Lie, I., and Wasberg, C.E., "The spectral viscosity method applied to simulation of waves in a stratified atmosphere", *J. Comp. Physics* Vol. 110, 1994, pp. 257.

[9] Tadmor, E., "Convergence of spectral methods for nonlinear conservation laws", *SIAM J. Num. Anal.* Vol. 26, 1989, pp. 30.

[10] Stanescu, D., "A multidomain spectral method for computational aeroacoustics", Ph.D. thesis, Concordia University, Montreal, Canada, 1999.

[11] Yang, B., Gottlieb, D., and Hesthaven, J.S., "Spectral simulation of electromagnetic wave scattering" *J. Comp. Physics* Vol. 134, 1997, pp. 216.
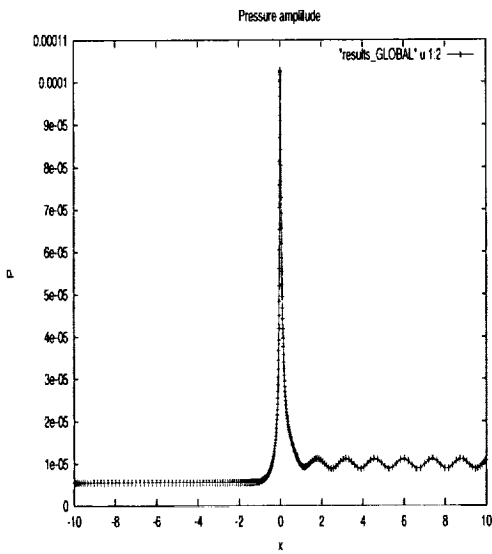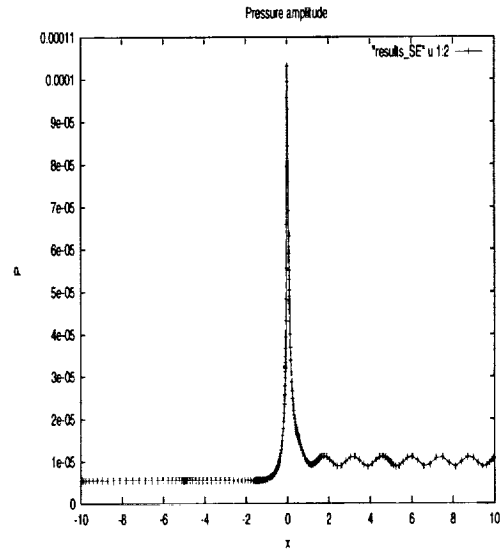
Fig. 1: Acoustic pressure amplitude along the nozzle for problem 1, category 1 (a) global spectral discretization (b) mutidomain spectral.
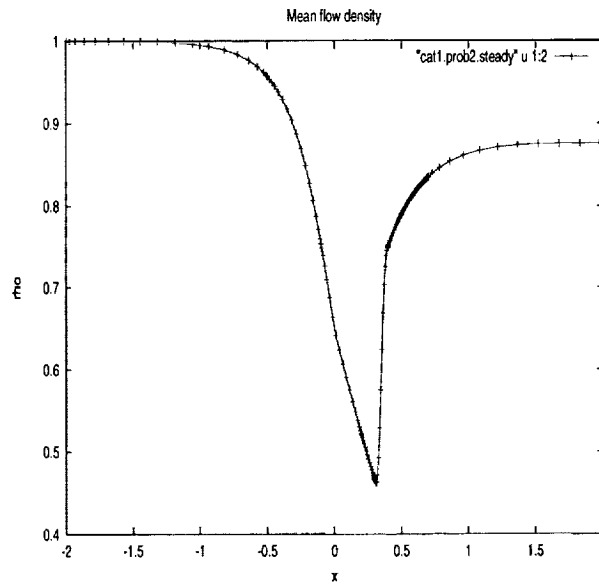
Fig. 2: Mean flow density for problem 2 category 1.
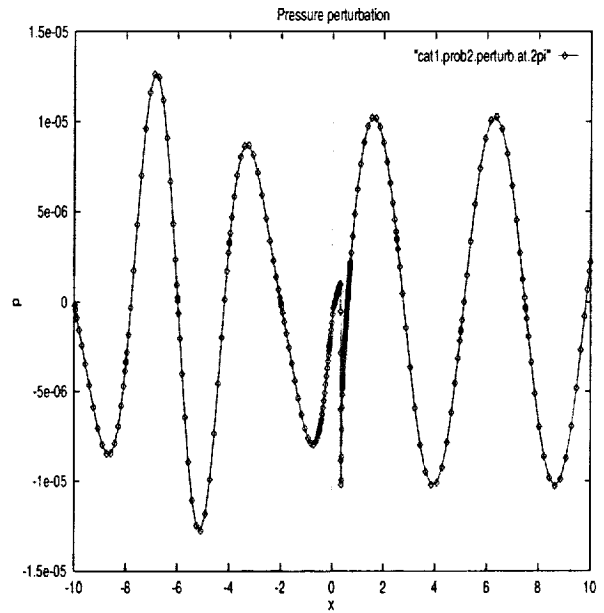
Fig. 3: Pressure perturbation for problem 2 category 1.
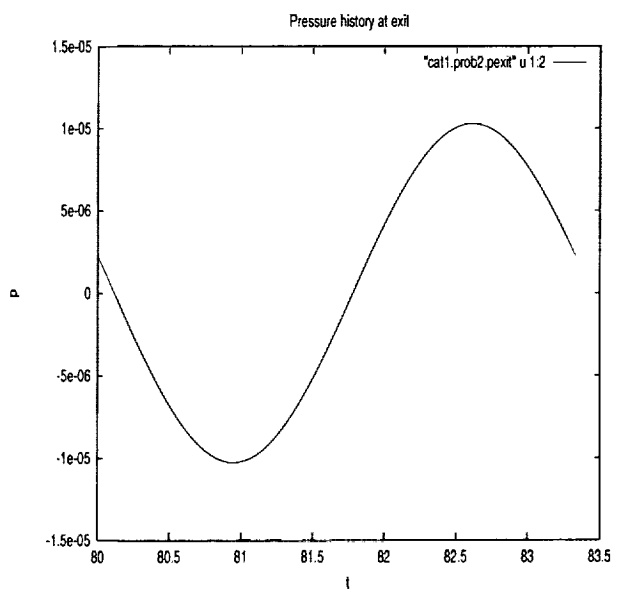
Fig. 4: Pressure history at the exit for problem 2 category 1.
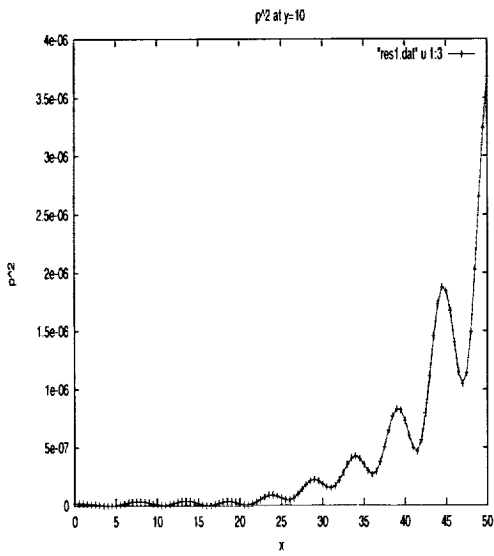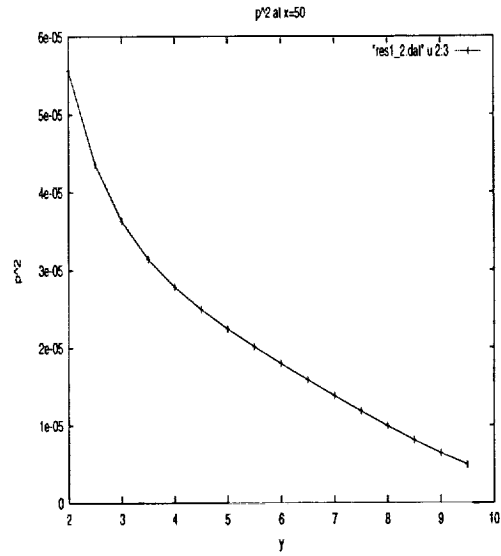
Fig. 5: RMS pressure for $St = 0.14$: (a) on line $y = 10$ (b) on line $x = 50$.
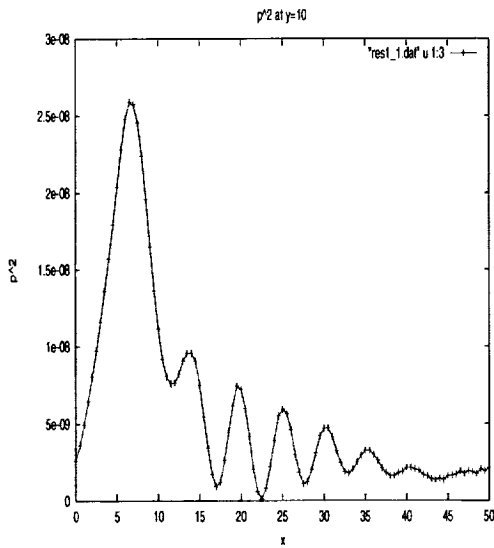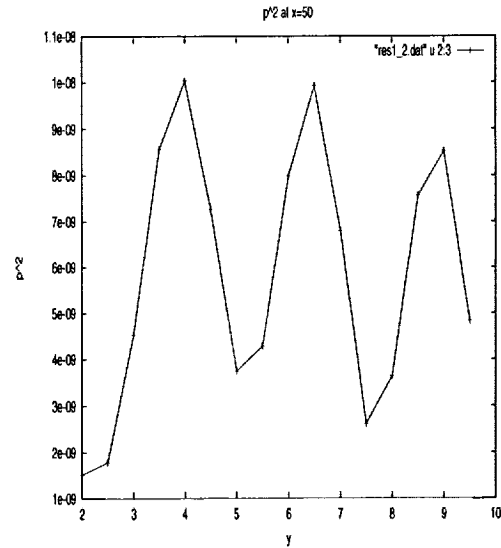
Fig. 6: RMS pressure for $St = 0.60$: (a) on line $y = 10$ (b) on line $x = 50$.
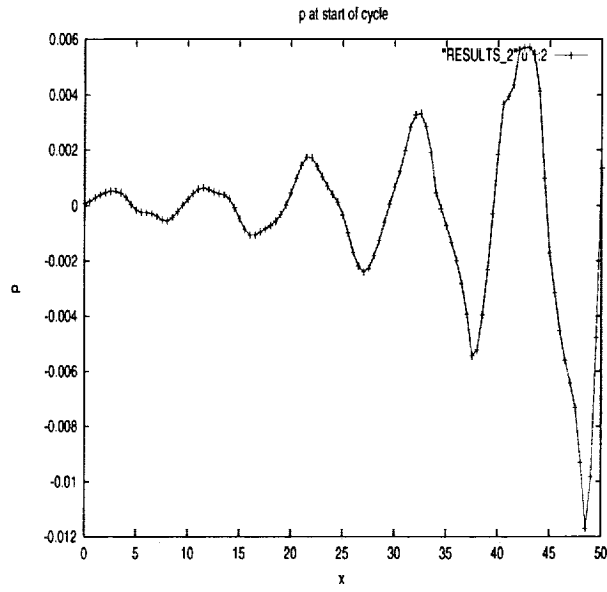
Fig. 7: Acoustic pressure at start of a cycle on the line $y = 1$, St=0.14.
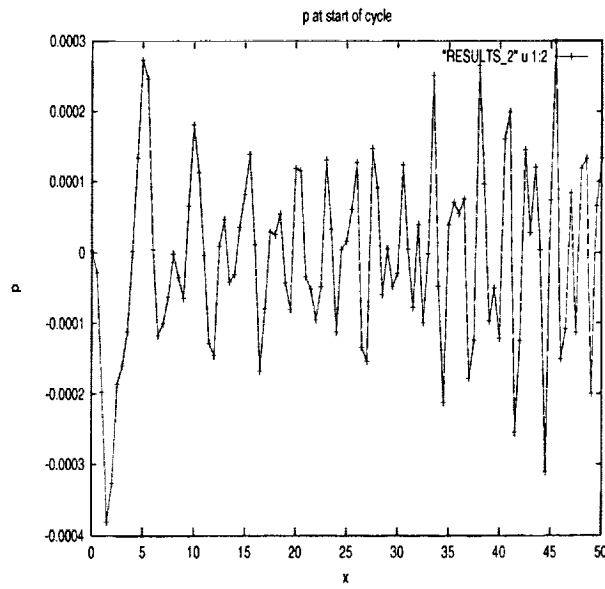
Fig. 8: Acoustic pressure at start of a cycle on the line $y = 1$, St=0.60.

Computation of Generation and Radiation of Acoustic Waves in Supersonic Flows.

Christophe Bailly

Laboratoire de Mécanique des Fluides et d'Acoustique
Ecole Centrale de Lyon & UMR CNRS 5509
BP 163, 69131 Ecully cédex, France.

Abstract

Category 5 and category 1, problem 2 are solved computationally using the fourth-order DRP scheme for spatial discretization, combined with a fourth-order Runge-Kutta algorithm for time integration. In the category 5 problem, an unstable 2-D shear layer is excited by an acoustic source, and instability wave radiation is observed for a range of excitation frequencies. The main difficulty of this problem is to allow growing instability waves to leave the computational domain. The category 1, problem 2 deals with internal sound propagation through a shock in a quasi-one-dimensional nozzle. The numerical solution is obtained in two steps. First the steady-state solution is calculated using Euler's equations. Then an acoustic wave is imposed at the inflow condition to evaluate the transmitted acoustic wave at the nozzle exit.

1 Introduction

Two benchmark problems are solved, category 5 and category 1 problem 2. The category 5 problem deals with instability wave radiation in a 2-D supersonic shear layer. The Linearized Euler Equations (LEE) solver used to compute the acoustic field generated by growing instability waves is the same as the author has used previously to study 2-D and 3-D propagation problems.[1,2] In the category 1 problem 2, the quasi-one-dimensional Euler equations are solved using the fourth-order DRP scheme for space discretization and a fourth-order Runge-Kutta method for time advancement. This kind of numerical algorithm is not optimal for supersonic flows in the presence of discontinuities. However, propagation of a sound wave through a steady-state shocked flow in a converging-diverging nozzle is numerically investigated in spite of errors in the mean-flow solution. The paper is organized as follows: the numerical algorithm used to solve LEE is described in section 2; then numerical results of category 5 and category 1 problem 2 are presented in sections 3 and 4 respectively.

2 LEE solver

2.1 Governing equations

The two-dimensional Linearized Euler Equations (LEE) may be written in cartesian coordinates as:

$$\frac{\partial \mathbf{U}}{\partial t} + \frac{\partial \mathbf{E}}{\partial x} + \frac{\partial \mathbf{F}}{\partial y} + \mathbf{H} = \mathbf{S} \tag{1}$$

where $\mathbf{U} = [\rho', \rho_o u', \rho_o v', p']^t$ is the unknown vector, $\mathbf{E}$ and $\mathbf{F}$ are the 2-D flux vectors. The vector $\mathbf{H}$ contains refraction terms related to the gradients of the mean flow, which are equal to zero when the mean flow is uniform. The vector $\mathbf{S}$ represents acoustic sources in the flow. The density ρ', the velocity $\mathbf{u}' = (u', v')$ and the pressure p' are small perturbations superimposed on a mean flow of density ρ_o, velocity $\mathbf{u}_o = (u_o, v_o)$ and pressure p_o respectively. The three vectors $\mathbf{E}$, $\mathbf{F}$ and $\mathbf{H}$ are written as:

$$\mathbf{E} = \begin{pmatrix} \rho' u_o + \rho_o u' \\ u_o \rho_o u' + p' \\ u_o \rho_o v' \\ u_o p' + \gamma p_o u' \end{pmatrix} \quad \mathbf{F} = \begin{pmatrix} \rho' v_o + \rho_o v' \\ v_o \rho_o u' \\ v_o \rho_o v' + p' \\ v_o p' + \gamma p_o v' \end{pmatrix} \quad \mathbf{H} = \begin{pmatrix} 0 \\ (\rho_o u' + \rho' u_o)\frac{\partial u_o}{\partial x} + (\rho_o v' + \rho' v_o)\frac{\partial u_o}{\partial y} \\ (\rho_o u' + \rho' u_o)\frac{\partial v_o}{\partial x} + (\rho_o v' + \rho' v_o)\frac{\partial v_o}{\partial y} \\ (\gamma - 1)\left(p' \nabla.\mathbf{u}_o - u'\frac{\partial p_o}{\partial x} - v'\frac{\partial p_o}{\partial y}\right) \end{pmatrix}$$

where γ is the ratio of specific heats which is assumed to have a constant value.

2.2 Numerical algorithm

A 2-D and 3-D LEE solver has been built using appropriate Computational AeroAcoustics (CAA) techniques and has been used sucessfully on a wide range of problems,[1-3] including previous CAA benchmark problems.[4,5] An outline of the numerical procedure is given below. The linearized Euler equations (1) are solved in a dimensionless form with length scale L_d, velocity scale u_d, density scale ρ_d, pressure scale $\rho_d u_d^2$ and time scale L_d/u_d. The 7-point stencil, dispersion relation preserving (DRP) scheme of Tam & Webb[6] is used for the spatial flux derivations. For uniform mesh step sizes Δx and Δy, the discretized form of the equation (1) is:

$$\frac{\partial \mathbf{U}_{i,j}}{\partial t} = \mathbf{K}_{i,j} \quad \text{with} \quad \mathbf{K}_{i,j} = -\sum_{l=-3}^{3} a_l \left(\frac{1}{\Delta x}\mathbf{E}_{i+l,j} + \frac{1}{\Delta y}\mathbf{F}_{i,j+l}\right) - \mathbf{H}_{i,j} + \mathbf{S}_{i,j}$$

In some cases it is necessary to remove spurious numerical oscillations due to non linearities or mismatches with the boundary or initial conditions. These short waves can be filtered out by artificial selective damping.[7,8] The damping terms are added to the right-hand side of system (1) to obtain:

$$\frac{\partial \mathbf{U}_{i,j}}{\partial t} = \mathbf{K}_{i,j} + \mathbf{D}_{i,j} \quad \text{with} \quad \mathbf{D}_{i,j} = -\frac{1}{MR_s}\sum_{l=-3}^{3} d_l \left(\frac{1}{\Delta x}\mathbf{U}_{i+l,j} + \frac{1}{\Delta y}\mathbf{U}_{i,j+l}\right) \tag{2}$$

where $M = u_d/c_o$, $c_o = \sqrt{\gamma p_o/\rho_o}$ is the speed of sound and $R_s = c_o \Delta/\nu_a$ is the mesh Reynolds number, Δ being the physical mesh size and ν_a the dimensional artificial viscosity. The value of R_s is usually taken in the interval [5 ; 20]. The time integration is performed by a four step Runge-Kutta algorithm for its high

stability limit and its low storage requirement.[9,10] The solution at time step $n+1$ is obtained by the following algorithm:

$$
\begin{aligned}
\mathbf{U}_{i,j}^1 &= \mathbf{U}_{i,j}^n + \alpha_1 \Delta t \mathbf{K}_{i,j}^n \\
\mathbf{U}_{i,j}^2 &= \mathbf{U}_{i,j}^n + \alpha_2 \Delta t \mathbf{K}_{i,j}^1 \\
\mathbf{U}_{i,j}^3 &= \mathbf{U}_{i,j}^n + \alpha_3 \Delta t \mathbf{K}_{i,j}^2 \\
\mathbf{U}_{i,j}^{n+1} &= \mathbf{U}_{i,j}^n + \alpha_4 \Delta t \left(\mathbf{K}_{i,j}^3 + \mathbf{D}_{i,j}^n \right)
\end{aligned}
\tag{3}
$$

The time step is given by $\Delta t = \text{CFL} \times \min\{\Delta x/(u_o + c_o), \Delta y/(v_o + c_o)\}$ where CFL is the Courant-Friedrichs-Lewy number. The stability limit requires a value of the CFL number smaller than 1.73 and the accuracy limit to reduce dissipation and dispersion errors[10] is CFL < 0.73.

The 2-D and 3-D LEE solver is vectorized up to 520 MFlops on a Cray C98, with a time per iteration and per node of 1.4 and 1.9 μs respectively. The same computation on a Dec α 8200 at 625 MHz is 30 times longer. The program is written in Fortran 90. All the calculations presented in this work are executed in double precision on a single processor Dec α.

2.3 Boundary Conditions

Formulation of the boundary conditions is very important in computational aeroacoustics.[8] Indeed, because of the high quality of the numerical algorithm, any disturbance of small amplitude can propagate in the computational domain contaminating the numerical solution. Several boundary treatments have been considered before choosing the most accurate methods for direct numerical simulation of acoustics.[11] These boundary conditions are given in the form of differential equations which are integrated in time with the same Runge-Kutta algorithm (3) used for the interior points. The spatial derivatives are computed with optimized backward difference stencils[6,8] for the three ghost points surrounding the computational domain.

2.3.1 Radiation boundary condition

The non-reflecting boundary condition of Tam and Webb[6] is implemented. This radiation boundary formulation for outgoing acoustic waves is based on an asymptotic solution of the linearized Euler equations:

$$
\left[\frac{\partial}{\partial t} + v_g \frac{\partial}{\partial r} + \frac{1}{2^{1-m} r} \right] \mathbf{U} = 0 \quad \text{when} \quad r \to \infty,
$$

where $m = 0$ and $m = 1$ for 2-D and 3-D geometry respectively, and r is the distance from acoustic sources. In two-dimensions, and in polar coordinates (r, θ) centered at the source position, the group velocity v_g of acoustic waves used in geometrical acoustics, is defined by $v_g(\theta) = \mathbf{u}_o.\mathbf{e}_r + \sqrt{c_o^2 - (\mathbf{u}_o.\mathbf{e}_\theta)^2}$ where $\mathbf{e}_r$ and $\mathbf{e}_\theta$ are the unit vectors in the radial direction and the azimuthal direction respectively.

2.3.2 Outflow boundary conditions

For an outflow boundary condition, the pressure disturbance is an acoustic fluctuation, which is not the case for the velocity and density disturbances. For these last two variables, linearized Euler's equations are

used. This yields a set of compatible first-order differential equations[6]:

$$\frac{\partial \rho'}{\partial t} + \mathbf{u}_o.\nabla \rho' = \frac{1}{c_o^2}\left\{\frac{\partial p'}{\partial t} + \mathbf{u}_o.\nabla p'\right\}$$

$$\frac{\partial u'}{\partial t} + \mathbf{u}_o.\nabla u' = -\frac{1}{\rho_o}\frac{\partial p'}{\partial x}$$

$$\frac{\partial v'}{\partial t} + \mathbf{u}_o.\nabla v' = -\frac{1}{\rho_o}\frac{\partial p'}{\partial y}$$

$$\frac{\partial p'}{\partial t} + v_g\left\{\cos\theta\frac{\partial p'}{\partial x} + \sin\theta\frac{\partial p'}{\partial y} + \frac{p'}{2r}\right\} = 0$$

2.3.3 Symmetric boundary condition

For a symmetric problem in $y = 0$, the boundary conditions at $y = 0$ are given by $\partial/\partial y\,[\rho', u', p']^t = 0$ and $v' = 0$. Three ghost points are used across the symmetric axis to implement numerically these conditions: $\rho_{i,-j}^n = \rho_{i,j}^n$, $u_{i,-j}^n = u_{i,j}^n$, $p_{i,-j}^n = p_{i,j}^n$ and $v_{i,-j}^n = -v_{i,j}^n$ for $j = 1,...,3$, where $j = 0$ designates the position of the symmetric axis.

3 Generation and radiation of acoustic waves from a 2-D shear flow

The category 5 problem deals with instability wave radiation. The 2-D supersonic mean-flow is parallel to, and symmetric about, the x-axis. According to the boundary layer type approximation the mean static pressure across the jet is taken as constant. The velocity profile is represented by:

$$u_o(y) = \begin{cases} u_\infty + (u_j - u_\infty)\exp\left[-\ln 2\left(\frac{y-h}{b}\right)^2\right], & y \geq h \\ u_j & 0 \leq y < h \end{cases}$$

where $b = 0.4$ m is the half-width of the shear layer and $h = 0.6$ m is the width of the uniform core. All the data concerning the mean flow are given in Table 1. The mean density profile is related to the axial velocity by using the Busemann - Crocco relation, which is valid for parallel flow with a Prandtl number Pr $= 1$ and constant pressure[12]:

$$\frac{1}{\rho_o} = \frac{1}{\rho_j}\frac{u_o - u_\infty}{u_j - u_\infty} + \frac{1}{\rho_\infty}\frac{u_j - u_o}{u_j - u_\infty} - \frac{1}{2}\frac{\gamma - 1}{\gamma p_o}(u_o - u_j)(u_o - u_\infty)$$

An acoustic source excites instability waves in the shear layer. This source term takes the form:

$$\mathbf{S}(x,y,t) = [0,0,0,1]^T A e^{-B \ln 2 (x^2+y^2)}\cos\omega t$$

where $A = 10^{-3}$ kg.m^{-1}.s^{-3}, $B = 8$ m^{-2}, and $\omega = 2\pi T$ is the angular frequency. The velocity is normalized by the jet exit velocity u_j, the density by ρ_j and the pressure by $\rho_j u_j^2$. The length scale is given by the half-velocity distance $R_{1/2} = h + b$ and the appropriate time scale is $R_{1/2}/u_j$. Therefore, the non-dimensional amplitude of the acoustic source is very small, $A = 10^{-3} \times R_{1/2}/(\rho_j u_j^3) \simeq 3.40 \times 10^{-12}$.

LEE (1) are solved for two forcing frequencies St $= 0.14$ and St $= 0.6$ where the Strouhal number is defined by St $= 2fR_{1/2}/u_j$. For these two excitations, the computational grid is built up to correctly discretize all

$T_{jo} = 300$ K	
$M_j = 2$	$M_\infty = 0$
$T_j = T_{jo} / \left[1 + \frac{\gamma-1}{2} M_j^2\right] = 166.67$ K	$T_\infty = 300$ K
$c_j = \sqrt{\gamma r T_j} = 258.73$ m.s^{-1}	$c_\infty = \sqrt{\gamma r T_\infty} = 347.12$ m.s^{-1}
$u_j = M_j c_j = 517.46$ m.s^{-1}	$u_\infty = 0$
$P_j = P = 101330$ Pa	$P_\infty = P = 101330$ Pa
$\rho_j = P/\left(r T_j\right) = 2.12$ kg.m^{-3}	$\rho_\infty = P/\left(r T_\infty\right) = 1.18$ kg.m^{-3}

Table 1: Mean flow data (problem 5). The subscript j denotes the exit value at the centerline of the jet and the subscript ∞ denotes the ambient value. The constant r of the perfect gas equation of state $p = \rho r T$ is taken as $r = 286.8875$, and the ratio of specific heats is taken to be $\gamma = 1.4$.
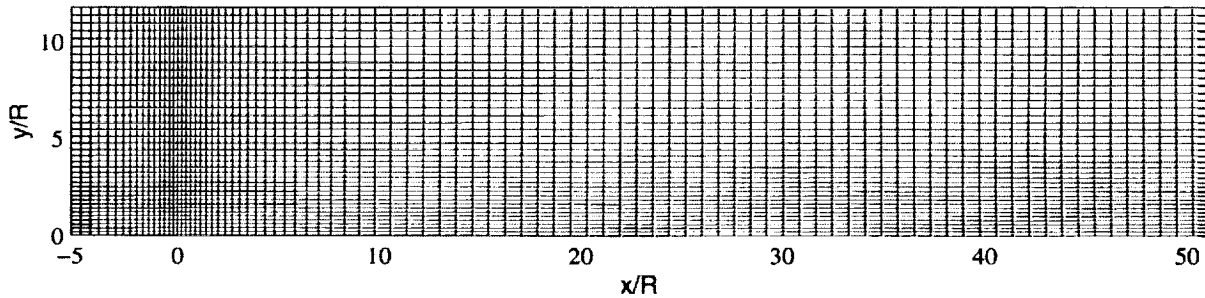
Figure 1: Computational domain: only every fourth line is shown in the two directions.

acoustic waves given in Table 2 as well as the shear-layer. The mesh is stretched in the radial direction with a minimum spacing of $\Delta y_{min} = 0.05$. The location of the radial grid points is given by:

$$y_i = y_{i-1} + \frac{\Delta y_{max} + \Delta y_{min}}{2} + \frac{\Delta y_{max} - \Delta y_{min}}{2} \tanh\left[\frac{y_{i-1} - 4R_{1/2}}{1.8R_{1/2}}\right]$$

with $\Delta y_{max} = 0.1$. In the axial direction, the mesh is smoothly stretched at a rate of 1.5% from the location of the acoustic source where $\Delta x_{min} = 0.05$, to $\Delta x_{max} = 0.2$ and then the grid is uniform again, as shown in Figure 1. The number of grid points is 361×151 points in the x and y directions respectively, giving 54511 points in total, and there is 20 points inside the shear-layer $R_{1/2}$. The stencil Reynolds number R_s is taken to be $R_s = 20$ and the Mach number in equation (2) is $M = u_j/c_\infty = 1.5$. In our case, the best results are obtained with the radiation condition applied to the outflow boundary.

Kelvin-Helmholtz instability waves are expected since the associated convection Mach number given by $M_c = (u_j + c_j)/(c_j + c_\infty) \simeq 1.28$ is supersonic. These instability waves are of the form $\tilde{p}_i(y)e^{i(kx-\omega t)} = \tilde{p}_i(y)e^{-k_i x}e^{ik_r(x-c_\varphi t)}$ where the wave vector $k = k_r + ik_i$ is a function of the frequency ω. For positive growth rates $-k_i$, a strong acoustic radiation is generated in the Mach wave emission angle θ. This angle is obtained in matching the phase velocity of instability waves and acoustic waves, $\cos\theta = c_\infty/c_\varphi = k_r c_\infty/\omega$. Figure 2 displays instantaneous pressure contours for the low frequency case St $= 0.14$. The acoustic intensity reaches

frequency	$\dfrac{\lambda^-}{R_{1/2}} = \dfrac{u_j - c_j}{u_j}\dfrac{2}{St}$	$\dfrac{\lambda}{R_{1/2}} = \dfrac{c_j}{u_j}\dfrac{2}{St}$	$\dfrac{\lambda^+}{R_{1/2}} = \dfrac{u_j + c_j}{u_j}\dfrac{2}{St}$
St = 0.14	7.14	7.14	21.43
St = 0.6	1.67	1.67	5.00

Table 2: Apparent acoustic wave lengths corresponding to the two excitations.
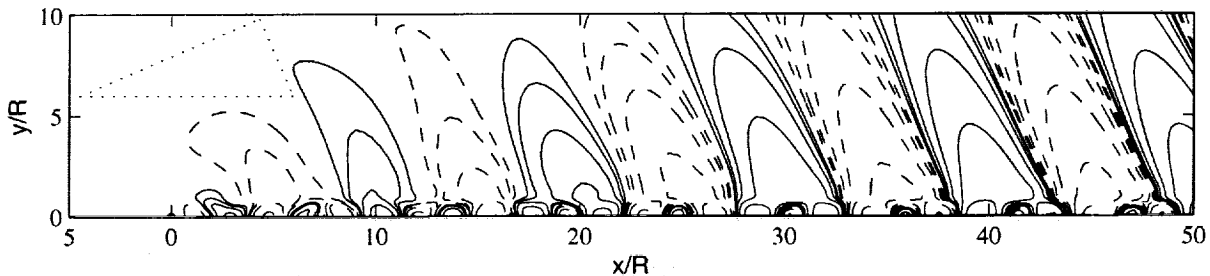
Figure 2: Instantaneous pressure contours for St = 0.14 at $t = 37.8T$. ——— Isolines from 0.25×10^{-12} to 16×10^{-12} with a geometrical progression of 2, ----- dashed lines are negative contours. The dotted triangle indicates the emission angle of instability wave radiation.

a peak for $\theta \simeq 23.5°$, in agreement with the linear instability theory. The radiated field is due to the two contributions of the acoustic source and the instability wave, but this last component is larger. The acoustic perturbation excites a growing instability wave, as shown in Figure 3 where the pressure is plotted along $y = 1$ in the shear layer at the start of a cycle. Figure 4 shows the mean quadratic fluctuations of the pressure $\overline{p'^2}$ along the two lines $y/R_{1/2} = 10$ and $x/R_{1/2} = 50$.

Results obtained for the high frequency St = 0.6 are displayed in Figures 5, 6 and 7 in a similar way. No instability wave radiation is observed for this Strouhal number. For this neutral mode, the pressure fluctuations are convected without amplification in the shear-layer. The radiated field is due only to the acoustic source of small amplitude, located in a shear mean flow.

4 Internal propagation: shock-sound interaction

The second problem of category 1 is solved by using the quasi-one-dimensional Euler equations:

$$\frac{\partial A\mathbf{U}}{\partial t} + \frac{\partial A\mathbf{E}}{\partial x} = \mathbf{H} \tag{4}$$

where $\mathbf{U} = [\rho, \rho u, \rho e_t]^t$ is the unknown vector and $A(x)$ is the smoothly varying cross-section of the nozzle. For a perfect gas, the total specific energy e_t is $\rho e_t = \rho e + \rho u^2/2 = p/(\gamma - 1) + \rho u^2/2$ where the variables ρ, u and p are density, velocity and pressure. The two vectors $\mathbf{E}$ and $\mathbf{H}$ are given by $[\rho u, \rho u^2 + p, u(\rho e_t + p)]^t$ and $[0, p dA/dx, 0]^t$ respectively.
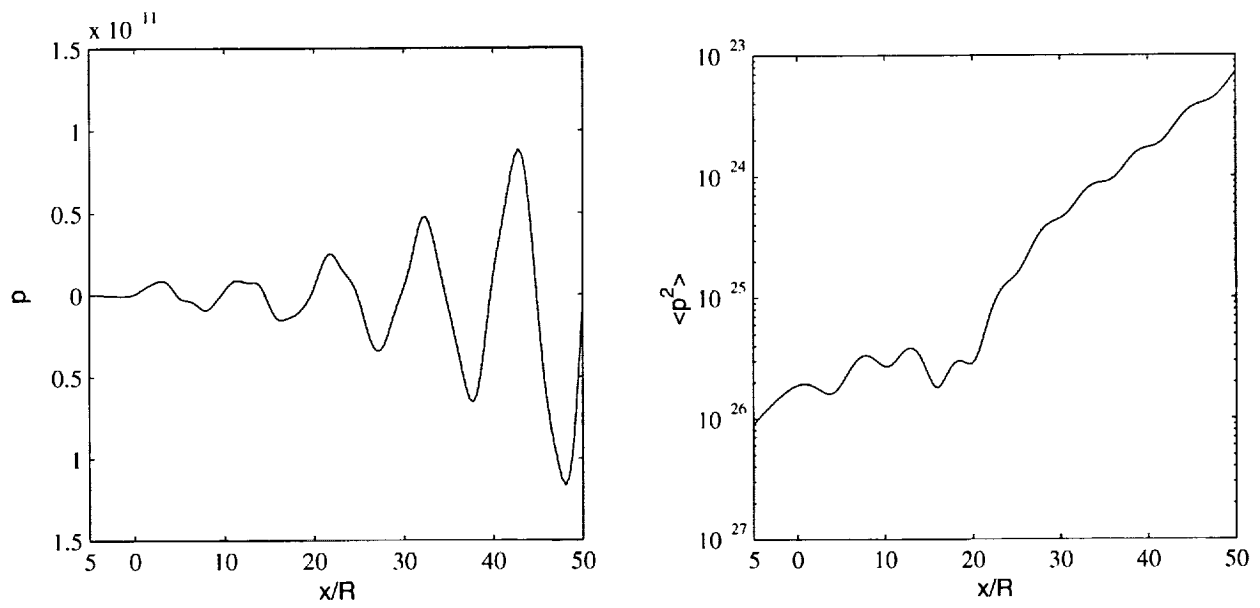
Figure 3: Left: pressure profile along the line $y/R_{1/2} = 1$ at the start of a cycle, $t = 37T$, and for a Strouhal number St=0.14. Right: growth rate of the fluctuating pressure along the line $y/R_{1/2} = 10$.
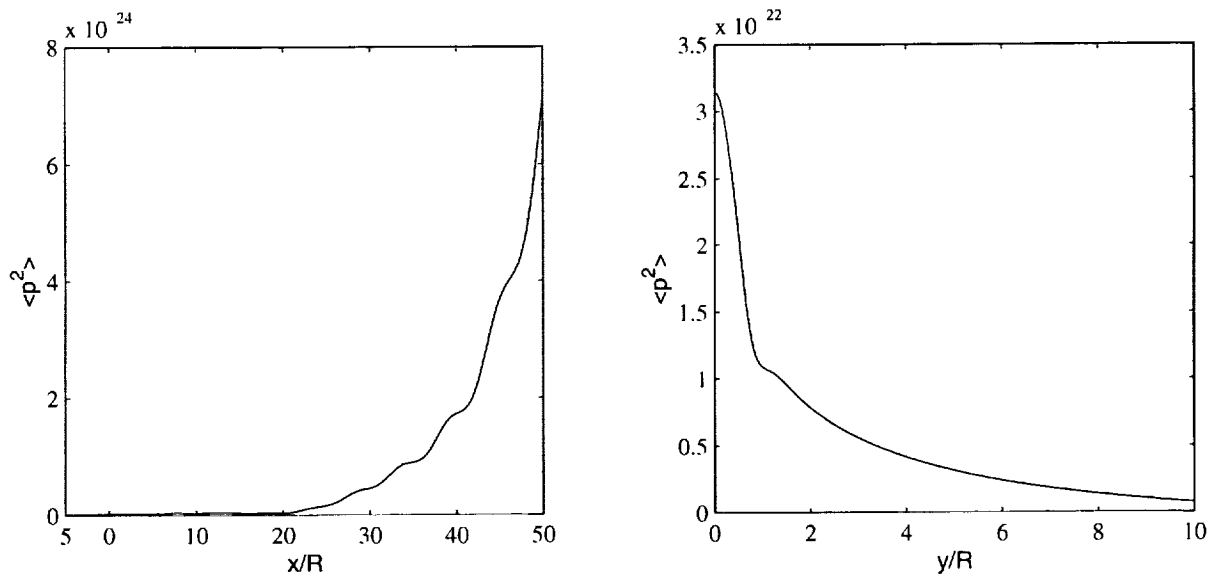
Figure 4: $\overline{p'^2}$ along the line $y/R_{1/2} = 10$ and $x/R_{1/2} = 50$ respectively. Strouhal number St=0.14.
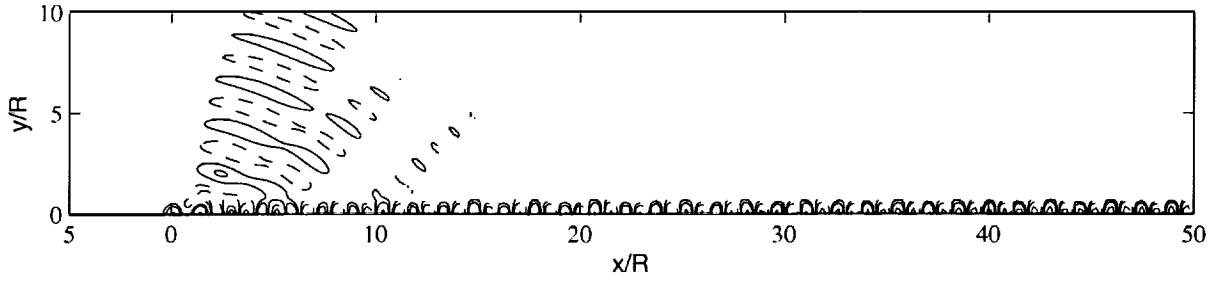
Figure 5: Instantaneous pressure contours for St = 0.6 at $t = 162T$. —— Isolines from 0.25×10^{-12} to 16×10^{-12} with an increment of 2, ----- negative values.
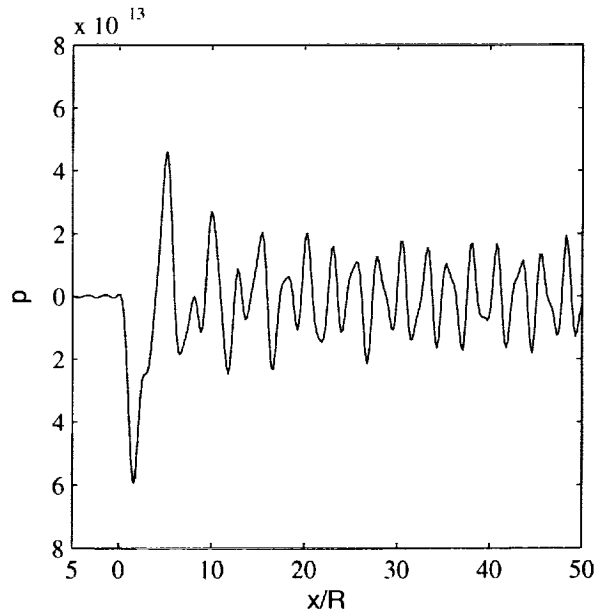
Figure 6: Pressure profile along the line $y/R_{1/2} = 1$ at the start of a cycle at time $t = 162T$ and for a Strouhal number St=0.6.
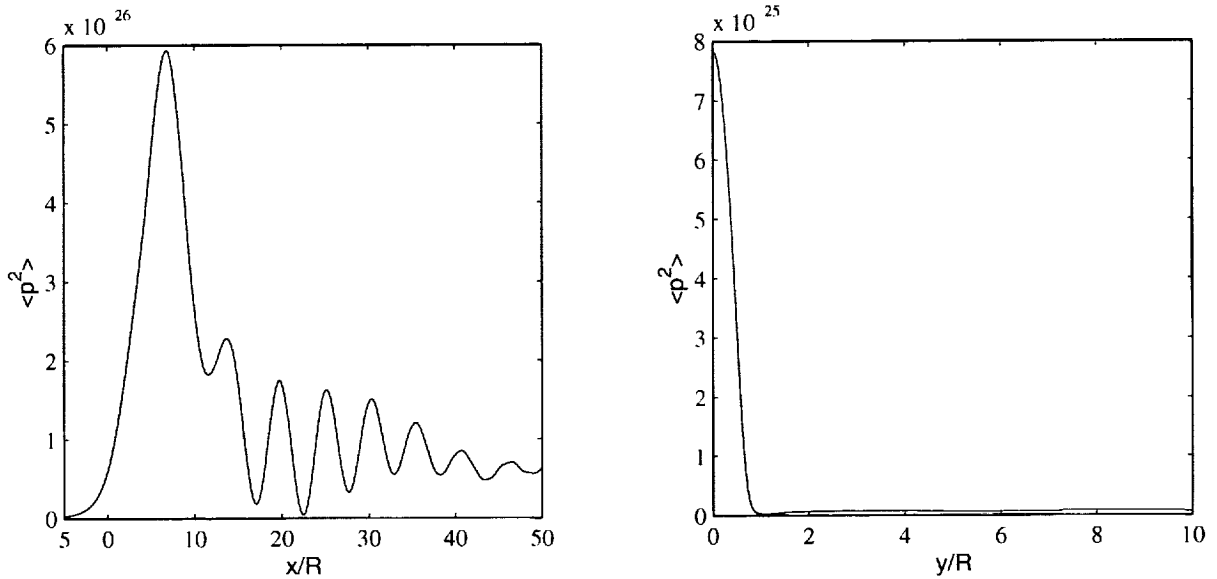
Figure 7: $\overline{p'^2}$ along the line $x/R_{1/2} = 50$ and $y/R_{1/2} = 10$ respectively. Strouhal number St=0.6

The space derivatives are calculated by using the DRP scheme and the time integration is obtained with the Runge-Kutta algorithm (3). Moreover, a variable artificial selective damping[13] based on the difference of velocity u_s in the stencil is implemented:

$$\frac{\partial \mathbf{U}_i}{\partial t} = \underbrace{-\frac{1}{\Delta x} \sum_{j=-3}^{3} a_j \mathbf{E}_{i+j}}_{\mathbf{K}_i} \underbrace{-\frac{1}{R_s}\frac{u_s}{\Delta x} \sum_{j=-3}^{3} d_j \mathbf{U}_{i+j}}_{\mathbf{D}_i} \qquad R_s = \frac{\Delta x \, u_s}{\nu_a} \qquad (5)$$

where $u_s = |u_{max} - u_{min}|$ with $u_{max} = \max\{u_{i+j}\}$ and $u_{min} = \min\{u_{i+j}\}$ for $j = -3, ..., 3$. The variable damping is applied with $R_s = 0.1$. This damping is strong near shocks and very small in other regions. Thus an additional constant artificial damping (2) with $R_s = 5$ is applied to all points of the computational domain. Non-linear characteristics are used at boundary conditions. The compatibility equations of system (4) are given by:

$$\begin{cases} \dfrac{\partial \rho}{\partial t} - \dfrac{1}{c^2}\dfrac{\partial p}{\partial t} + L_1 = 0 \\[2mm] \dfrac{\partial p}{\partial t} + \rho c \dfrac{\partial u}{\partial t} + L_2 + \rho u c^2 \dfrac{1}{A}\dfrac{dA}{dx} = 0 \\[2mm] \dfrac{\partial p}{\partial t} - \rho c \dfrac{\partial u}{\partial t} + L_3 + \rho u c^2 \dfrac{1}{A}\dfrac{dA}{dx} = 0 \end{cases} \quad \text{with} \quad \begin{cases} L_1 = u\left(\dfrac{\partial \rho}{\partial x} - \dfrac{1}{c^2}\dfrac{\partial p}{\partial x}\right) \\[2mm] L_2 = (u+c)\left(\dfrac{\partial p}{\partial x} + \rho c \dfrac{\partial u}{\partial x}\right) \\[2mm] L_3 = (u-c)\left(\dfrac{\partial p}{\partial x} - \rho c \dfrac{\partial u}{\partial x}\right) \end{cases}$$

In order to set the pressure at the outflow boundary condition to create a shock, $p_{exit} \simeq 0.6071752$, a correction term is added to obtain the steady-state solution:

$$\frac{\partial p}{\partial t} + \underbrace{\frac{L_2 + L_3}{2}}_{L_3 = -L_2} + \alpha\left(p - p_{exit}\right) = 0 \quad \text{with} \quad 5 \times 10^{-3} \leq \alpha \leq 10^{-2}$$

The area distribution $A(x)$ is given by:

$$A(x) = \begin{cases} 0.536572 - 0.198086e^{-\ln 2\left(\frac{x}{0.6}\right)^2} & x > 0 \\ 1. - 0.661514e^{-\ln 2\left(\frac{x}{0.6}\right)^2} & x < 0 \end{cases} \qquad -10 \le x \le 10$$

and the location of the grid points is obtained using the following mapping:

$$x_i = \frac{1}{\tau}\tanh^{-1}\left(\xi_i \tanh \tau\right) = \frac{1}{\tau}\frac{1}{2}\ln\left[\frac{1 + \xi_i \tanh \tau}{1 - \xi_i \tanh \tau}\right]$$

where $-1 \le \xi_i = 2i/n_x - 1 \le 1$, $n_x = 401$ and $\tau = 2$. The minimum step size is at the throat with $\Delta x_{min} = 0.0241$ and the larger step size is $\Delta x_{max} \simeq 0.3205$ at $x = \pm 10$. As a preliminary to solve the workshop problem, propagation of an incoming acoustic wave is calculated in the nozzle without flow. The numerical solution is compared with the solution provided by Webster's equation:

$$\frac{\partial^2 \hat{p}}{\partial x^2} + \frac{1}{A}\frac{dA}{dx}\frac{\partial \hat{p}}{\partial x} + k^2 \hat{p} = 0 \qquad k = \frac{\omega}{c_o} \qquad p = \hat{p}e^{i\omega t} \qquad (6)$$

Figure 9 shows the distribution of maximum acoustic pressure along the nozzle. The two solutions are in agreement. Interferences of the reflected and incident waves produce a standing-wave pattern in the left part of the nozzle. The transmitted wave calculated with (5) is slightly damped due to the coarse grid in the downstream direction.

The numerical steady-state solution is displayed in Figure 9. No other special method were used at the discontinuities than filtering with (5). The shock is located at $x \simeq 0.35$ and the pre-shock Mach number is $M_1 \simeq 1.44$. When the residual is reduced to machine zero, a low-amplitude disturbance is imposed at the inflow boundary using characteristic L_2:

$$L_2 = (u + c)(1 + \rho c)\frac{\epsilon\omega}{u + c}\cos\left[\omega\left(\frac{x}{u + c} - t\right)\right]$$

with $\epsilon = 10^{-5}$ and $\omega = 0.6\pi = 2\pi/T$. The amplitude ϵ was turned on gradually using the expression $\epsilon \times [1 - \exp(-t/2T)]$ and the CFL number was taken as CFL $= 0.7$. Figure 10 shows the distribution of pressure, velocity and density at the start of a period. The pressure perturbation at the exit plane through one period is also plotted. The exit pressure amplitude is around 1.04×10^{-5}.

Acknowledgments
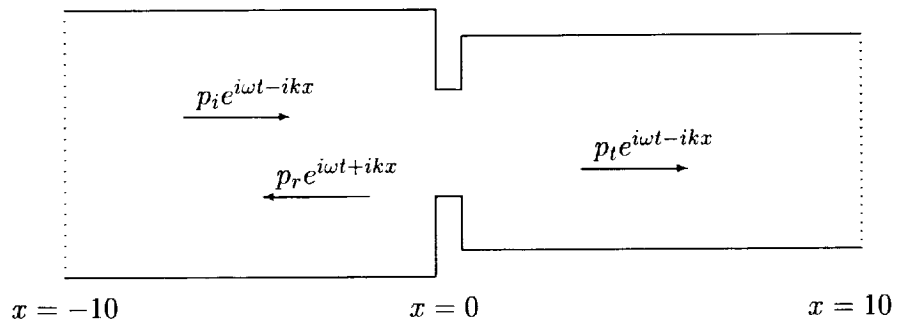
Figure 8: Sketch of the geometry for solving Webster's equation (6).
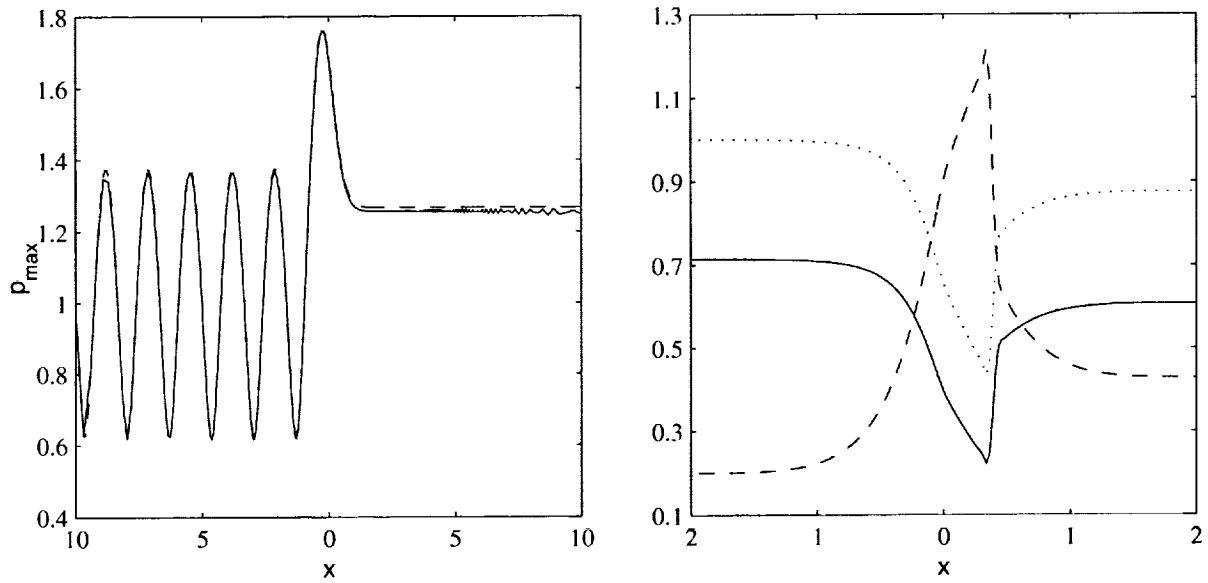
Figure 9: Left: distribution of maximum acoustic pressure, —— Euler's equation, – – – Webster's solution. Right: steady-state solution, —— pressure, – – – velocity and ······ density.
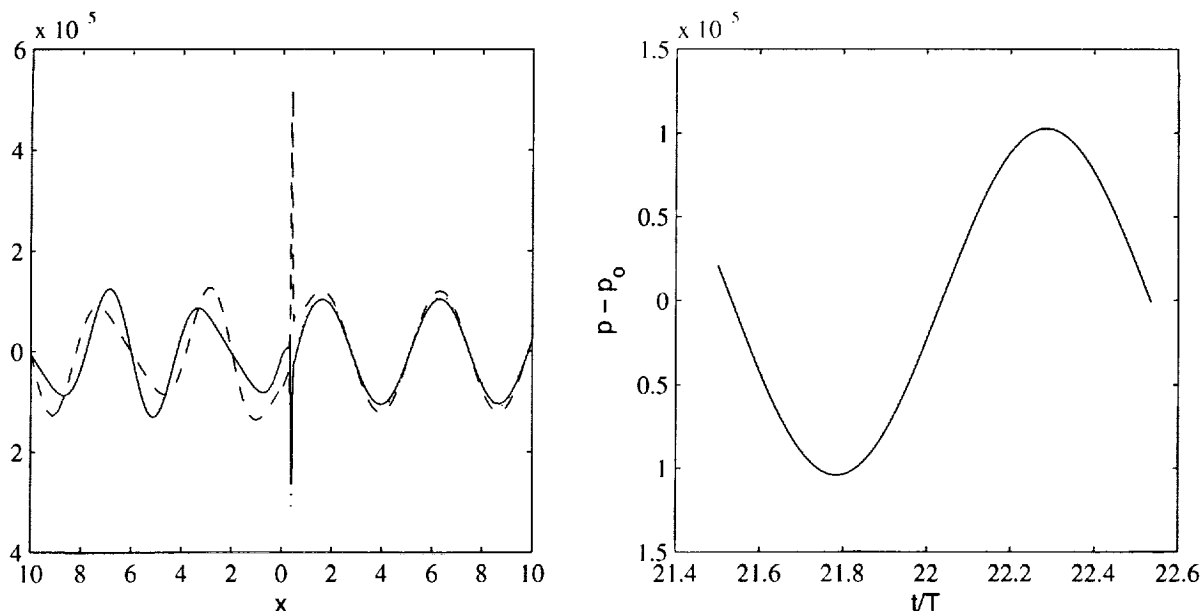
Figure 10: Left: perturbation of pressure ——, velocity – – – and density ······ at the start of a period. Right: pressure perturbation at nozzle exit through one period.

References

[1] BAILLY, C. & JUVÉ, D., 1998, Numerical solution of acoustic propagation problems using linearized Euler's equations, accepted in the *AIAA Journal*, AIAA Paper 98-2267.

[2] BAILLY, C. & JUVÉ, D., 1999, A stochastic approach to compute subsonic noise using linearized Euler's equations, AIAA Paper 99-1872.

[3] BAILLY, C., THÉVENIN, R. & JUVÉ, D., 1997, Numerical simulation of sound source radiation in flows, *Theoretical and Computational Acoustics '97*, World Scientific Publishing Co., 595-608.

[4] NASA, ICASE, 1995, Workshop on benchmark problems in computational aeroacoustics, edited by J.C. Hardin, J.R. Ristorcelli and C.K.W. Tam, NASA CP - 3300.

[5] NASA, ICASE, 1997, Second computational aeroacoustics workshop on benchmark problems, edited by C.K.W. Tam and J.C. Hardin, NASA CP - 3352.

[6] TAM, C.K.W. & WEBB, J.C., 1993, Dispersion-relation-preserving finite difference schemes for computational acoustics, *J. Comput. Phys.*, **107**, 262-281.

[7] TAM, C.K.W., WEBB, J.C. & DONG, Z., 1993, A study of the short wave components in computational acoustics, *Journal of Comput. Acous.*, **1**(1), 1-30.

[8] TAM, C.K.W., 1995, Computational aeroacoustics: issues and methods, *AIAA Journal*, **33**(10), 1788-1796.

[9] WILLIAMSON, J.H., 1980, Low-storage Runge-Kutta schemes, *J. Comput. Phys.*, **35**, 48-56.

[10] HU, F.Q., HUSSAINI, M.Y. & MANTHEY, J.L., 1996, Low-dissipation and low-dispersion Runge-Kutta schemes for computational acoustics, *J. Comput. Phys.*, **124**, 177-191.

[11] BOGEY., C., BAILLY, C. AND JUVÉ, D., 1999, Computation of mixing layer moise using large eddy simulation, AIAA Paper 99-1871.

[12] WHITE, F.M., 1991, Viscous fluid flow, *McGraw-Hill, Inc.*, second edition.

[13] TAM, C.K.W. & SHEN, H., 1993, Direct computation of nonlinear acoustic pulses using high order finite difference schemes, AIAA Paper 93-4325.

NUMERICAL SOLUTIONS TO THE THIRD CAA WORKSHOP
BENCHMARK PROBLEMS

Roy H. Loh and WEN H. LIN
The Boeing Company
Rocketdyne Propulsion & Power
Canoga Park, CA

ABSTRACT

This paper presents numerical solutions to Problems 1 and 2 of Categories 1 and 6 of the 3rd NASA CAA Workshop on benchmark problems. The numerical algorithm is based on a dual time scheme for temporal discretization and a third-order finite volume scheme for spatial discretization. The aims of this study are to apply a dual time stepping scheme to treat aeroacoustic problems of sound propagation and to validate our CAA solver with the benchmark problems for developing a numerical tool for noise analysis and control.

1. INTRODUCTION

Flow-generated sound accompanies the operations of almost every device in our daily life. Accurate determination of sound pressure level is vital for us to understand the physics of noise generation, control, and reduction in relation to designing a quiet device, machinery, or vehicle. Currently, an analytic solution to a problem of flow-generated sound is formidable, if not impossible, because the governing equations, boundary conditions, and initial conditions are so complicated. In most cases, experimental or numerical schemes are used to obtain the desired sound pressure level for a flow-induced noise problem. In this paper we employed a finite-volume method for spacial discretization and a dual-time stepping scheme for temporal discretization to treat acoustic wave propagation in an arbitrary flow field. The aim of this study is to demonstrate the applicability and accuracy of the proposed method in solving an "aeroacoustic" problem in a transient flow environment. The ultimate goal of the study is to develop and validate the proposed numerical tool to compute aeroacoustic signals for engineering analysis.

In the following the mathematical equations and numerical algorithm are briefly discussed. Then the computed results of the mentioned benchmark problems are presented.

2. GOVERNING EQUATIONS

Acoustic wave motion in a flow field is considered a small perturbation to the flow. The total field of the reference flow and acoustic perturbations satisfies the equations of continuity, momentum, energy, and state. For a viscous compressible fluid the two-dimensional governing equations written in a flux vector form with a pre-condition matrix are

$$D_p \frac{\partial Q_p}{\partial \tau} + \frac{\partial Q_c}{\partial t} + \frac{\partial E}{\partial \xi} + \frac{\partial G}{\partial \eta} = 0, \tag{1}$$

where $Q_p = \{p, u, v, h\}$, $Q_c = \{\rho, \rho u, \rho v, \rho e\}$, D_p is a pre-condition matrix, τ and t are respectively pseudo and real time, p, u, v, and h are pressure, velocity components, and enthalpy, ρ and e are density and internal energy, E and G are fluxes.

Consider the total field is a time-stationary process such that every field variable can be written as the sum of a mean part and a purely fluctuating part [1]:

$$F(x_i, t) \equiv \overline{F}(x_i) + F'(x_i, t) \tag{2}$$

$$\overline{F}(x_i) \equiv \frac{1}{2\tau} \int_{-\tau}^{\tau} F(x_i, t)\, dt$$

$$\int_{-\tau}^{\tau} F'(x_i, t)\, dt = 0$$

where $i = 1, 2, 3$, and F is any variable in Q_p and Q_c. Applying this concept to Equation (1), one has the governing equations for the fluctuating variables as

$$D_p \frac{\partial Q_p'}{\partial \tau} + \frac{\partial Q_c'}{\partial t} + \frac{\partial E'}{\partial \xi} + \frac{\partial G'}{\partial \eta} = 0 \tag{3}$$

It is noted that the pre-condition matrix D_p in the above equation is evaluated with the mean-flow state.

At the $(n+1)^{th}$ physical-time and $(s+1)^{th}$ iterative-time levels, we write the above equations in a semi-discrete form with a temporal accuracy parameter θ ($0 \le \theta \le 1$) as

$$D_p \left(\frac{\partial Q_p'}{\partial \tau} \right)^{s+1} + (1+\theta) \left(\frac{\partial Q_c'}{\partial t} \right)^{n+1} - \theta \left(\frac{\partial Q_c'}{\partial t} \right)^{n} + \left(\frac{\partial E'}{\partial \xi} \right)^{n+1} + \left(\frac{\partial G'}{\partial \eta} \right)^{n+1} = 0.$$

Defining $D_c = \left(\dfrac{\partial Q_c'}{\partial Q_p'} \right)^{s}$, we then have

$$D_p \frac{(Q_p')^{s+1} - (Q_p')^{s}}{\Delta \tau} + (1+\theta) D_c \frac{(Q_p')^{s+1} - (Q_p')^{s}}{\Delta t} + \left(\frac{\partial E'}{\partial \xi} \right)^{n+1} + \left(\frac{\partial G'}{\partial \eta} \right)^{n+1}$$

$$= -(1+\theta) \frac{(Q_c')^{s} - (Q_c')^{n}}{\Delta t} + \theta \frac{(Q_c')^{n} - (Q_c')^{n-1}}{\Delta t} \tag{4}$$

Now letting $D \equiv D_p + D_c \dfrac{(1+\theta)\Delta \tau}{\Delta t}$, we have

$$D \frac{(Q_p')^{s+1} - (Q_p')^{s}}{\Delta \tau} + A \frac{\partial Q_p'}{\partial \xi} + B \frac{\partial Q_p'}{\partial \eta}$$

$$= -(1+\theta) \frac{(Q_c')^{s} - (Q_c')^{n}}{\Delta t} + \theta \frac{(Q_c')^{n} - (Q_c')^{n-1}}{\Delta t} - \left(\frac{\partial E'}{\partial \xi} \right)^{s} - \left(\frac{\partial G'}{\partial \eta} \right)^{s} \tag{5}$$

where transformation matrices A and B are defined as

$$A \equiv \left(\frac{\partial E}{\partial Q_p'} \right)^{s} = \left(\frac{\partial E}{\partial Q_c'} \frac{\partial Q_c'}{\partial Q_p'} \right)^{s}, \qquad B \equiv \left(\frac{\partial G}{\partial Q_p'} \right)^{s} = \left(\frac{\partial G}{\partial Q_c'} \frac{\partial Q_c'}{\partial Q_p'} \right)^{s}$$

Equation (5) is the two-dimensional dual time stepping equation used to design the numerical algorithm in modular forms in a Boeing-Rocketdyne CFD solver named TIDAL (Time Iterative Density-based Algorithm) to compute the acoustic quantities. Details of the acoustic algorithm of TIDAL can be found in Reference [2] and therefore omitted in this study.

3. NUMERICAL RESULTS AND DISCUSSION

Using TIDAL, we solved the following four benchmark problems of the third NASA Computational Aeroacoustics (CAA) Workshop: Problems 1 and 2 of Category 1 for sound wave propagating in a one-dimensional nozzle and Problems 1 and 2 of Category 6 for sound radiation due to boundary

layer flows passing a cavity. All these examples were selected to study the functionality, accuracy, and performance of the acoustic solver of TIDAL in solving the problems of sound propagation. Results of the study are briefly presented in the following paragraphs.

3.1 PROBLEM 1 OF CATEGORY 1

Figure 1 shows the distributions of mean flow density, Mach number, and pressure. The computed Mach number is 0.938 at the throat, which is very close to the analytical value of 0.940 [3]. The mean flow is nearly sonic at the throat. These results were obtained using a uniform grid of 1000 points for a domain of size 20 (i. e., $-10 \leq x \leq 10$). If a uniform grid of 400 points is used, the computed Mach number is 0.928 at the throat. In all calculations for Category 1 problems both grids were used. Figure 2 shows the variations of acoustic pressures with respect to the number of grid points. It is noted from this figure that at least 300 grid points are needed to resolve the right magnitude and phase of the sound wave. However, the result obtained by the 1000-point grid has higher values at the throat and in the upstream of throat than that obtained by 400-point grid. This phenomenon is mainly caused by the spatial resolution associated with the third-order finite volume scheme.

Figure 3 shows the variations of acoustic pressures with time. The upstream propagating sound wave has a speed of 0.6 in the constant area downstream of the throat and a varied speed in the convergent-divergent area. At the throat the wave only travels at a speed of .0721738 because the flow speed is 0.9278262 there. Therefore, at t = 10 the wave front only travels six units from downstream and for t greater than 20 it already passes the throat. Since the wave can not travel much upstream of the throat, most of its energy is blocked and accumulated near the throat. A shock-like wave front of maximum pressure is therefore formed just downstream of the throat, and this maximum oscillates continuously with time.

Figures 4a and 4b respectively show the time series and Fourier spectra of the maximum sound pressure. The amplitude of the maximum pressure is 7.76719×10^{-5} obtained by the 1000-point grid and 4.58071×10^{-5} by a 400-point grid. All these values are smaller than the analytical value predicted by Tam [3]. Again, the under-prediction of peak value is caused by the spatial resolution limited by the third-order finite volume scheme. Fourier spectra show that the main frequency is 0.3, which is the same as the frequency of input wave. In figure 4b there is a harmonic of very small amplitude $(6.72744 \times 10^{-6}, 1.05585 \times 10^{-6})$ at the frequency of 0.9, which is three times the fundamental frequency.

This harmonic is due to the nonlinear effect of sound wave propagation in a flowing fluid because the acoustic solver of TIDAL includes nonlinear terms.

Figure 5 shows the envelope of the maximum acoustic pressure distribution inside the nozzle. There are five complete waves downstream of the throat and only 3.75 waves upstream of the throat. The non-dimensional wavenumber of the sound wave is 0.6 in the constant area downstream of the throat, roughly equal to π in the varying area, and equal to $3\pi/4$ in the constant area upstream of the throat. The small amplitude (7.10818×10^{-7}) of the wave, obtained by the 400-point grid, in the upstream of the throat is 7.10818% of the input wave amplitude. Because the mean flow speed at the throat is not exactly sonic, the sound wave still has energy to propagate upstream.

3.2 PROBLEM 2 OF CATEGORY 1

Figure 6 shows the density, velocity, and pressure of the mean flow. As seen from this figure, a normal shock is formed just downstream of the throat. In the constant areas up- and down- stream of the throat the flow properties are all constant.

Figure 7 shows the acoustic density, velocity, and pressure at the start of a period. All acoustic quantities are amplified by the shock; the perturbed density and pressure are all in phase everywhere in the nozzle, while the perturbed velocity is only in phase with the density and pressure after the shock. Before the shock the acoustic velocity lags behind the acoustic density and pressure. The input sound wave propagates from left to right, reflects from, and travels through the shock. The transmitted wave continues traveling downstream of the shock and exits the nozzle; however, the reflected wave interacts with the input wave and causes amplification and cancellation.

Figure 8 shows the envelope of the maximum acoustic pressure distribution in the nozzle for $t = 40$. The maximum pressure amplitude behind the shock is constant and equal to the amplitude of the input wave. However, the maximum pressure before the shock oscillates with respect to the amplitude of the input wave. At the shock the amplitude of the maximum pressure is approximately 3.47999 times that of the input wave. A comparison is shown in Figure 9 of the computed acoustic pressure and the corresponding exact solution [4]. Except for the phase and peak value at the shock, the computed result agrees quite well with the exact solution.

Figure 10 shows the time series of acoustic pressures at the exit plane and at one plane in the constant area upstream of the throat. This figure shows that both sound waves in front of and behind the shock are harmonic with the same frequency as the input sound wave.

3.3 PROBLEM 1 OF CATEGORY 6

Figure 11 shows the time series and Fourier spectra of sound pressures at the center of the left wall at the center of the cavity mouth, and at one point 3D above the opening, where D is the dimension of the intrusive plate at the opening. This figure indicates that pressure fluctuations at these three locations are harmonics and that the pressure fluctuations at the left wall are out of phase with respect to those at the mouth and outside. Most of the pressure fluctuations at the cavity mouth do not radiate into the cavity or outside as sound waves. Carefully examining the figure indicates that there are 12 waves associated with the pressure fluctuations at each location in 0.008 second. Therefore, the dominant frequency of these waves is 1500 Hz.

The most distinct modes are at 125, 750, 1500, 2250, 3000, 3750, and 4500 Hz, and the maximum sound pressure level is at 1500 Hz for all three locations. The sound pressure level at 1500 Hz is 117.33 dB at the left wall center, 123.34 dB at the point 3D above the cavity mouth, and 133.63 dB at the center of the mouth, where the sound pressure level in dB is referenced to 20 μPa. The sound pressure levels of other modes in the frequency range of 100 to 6000 Hz are all above 55 dB.

3.4 PROBLEM 2 OF CATEGORY 6

The differences between this and previous problems are the incoming flow speed and the boundary layer thickness over the cavity. Figure 12 shows the time series and Fourier spectra of sound pressures at the center of the left wall, at the center of the cavity mouth, and at a point 3D above the opening. Again, carefully examining this figure indicates that the pressure fluctuations at the mouth center and the point outside are in phase and those at the left wall are not quite in phase with the former two. There are about 15 waves associated with these pressure fluctuations within .006 second; therefore, the dominant frequency of these waves is 2500 Hz.

The most distinct modes are at 1500, 1800, 2500, 3500, 4350, 5000, 5700, 6350, 6800, and 8000 Hz and the maximum sound pressure level is at 2500 Hz for all three locations. The sound pressure level at 2500 Hz is 116.29 dB at the left wall center, 125.79 dB at the point 3D above the cavity mouth, and 140 dB at the center of mouth. The sound pressure levels of other modes in the frequency range of 0 to 10000 Hz are all above 75 dB. The energy level of the sound wave at the mouth center is much greater in this problem than in the first problem where the incoming velocity was 26.8 m/s. However,

the maximum radiated sound levels at the left wall of the cavity are very close to each other for both U = 26.8 and 50.9 m/s.

ACKNOWLEDGMENTS

REFERENCES

1. Doak, P. E.: Fluctuating Total Enthalpy as the Basic Generated Acoustic Field. *Theoret. and Comput. Fluid Dynamics*, vol. 10 (1-4), 1998, pp. 115-133.
2. Loh, H. T., Smith-Kent, R., Perkins, F., and Chwalowski, P.: Evaluation of Aft Skirt Length Effects on Rocket Motor Base Heat, Using Computational Fluid Dynamics, AIAA Paper 96-2645.
3. Tam, C. K. W.: Problem 1 of Category 1 - Benchmark Problem and Solution. Third Comput. Aeroacoustics (CAA) Workshop on Benchmark Problems, Nov. 8-10, 1999, Cleveland, Ohio.
4. Hixon, R.: Problem 2 of Category 1 - Benchmark Problem and Solution. Third Comput. Aeroacoustics (CAA) Workshop on Benchmark Problems, Nov. 8-10, 1999, Cleveland, Ohio.
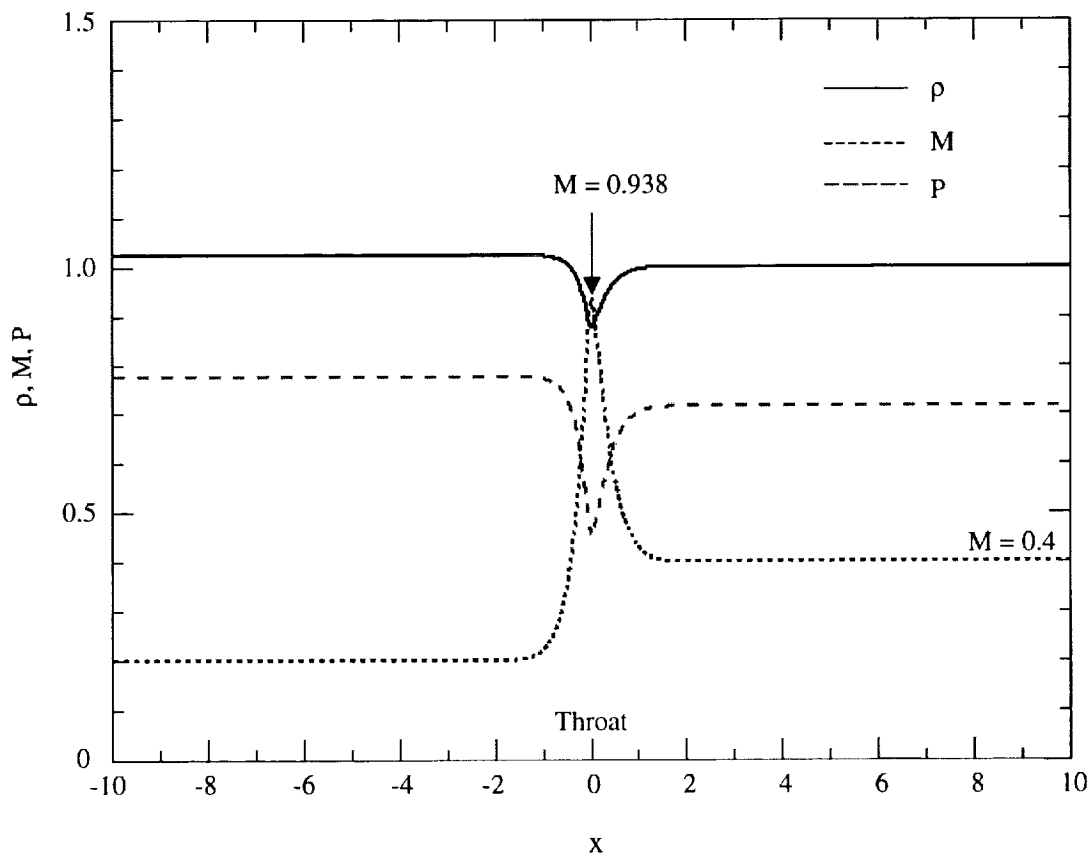
Fig. 1 Distributions of mean flow density, Mach number, and pressure
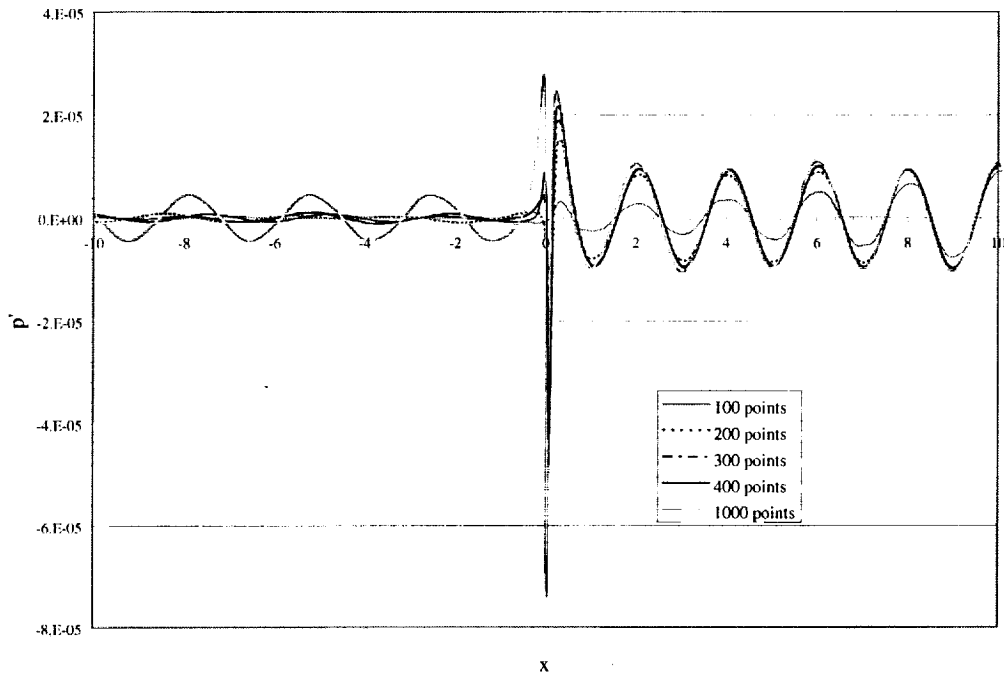
Fig. 2 Variations of acoustic pressures with respect to grid points for t = 40
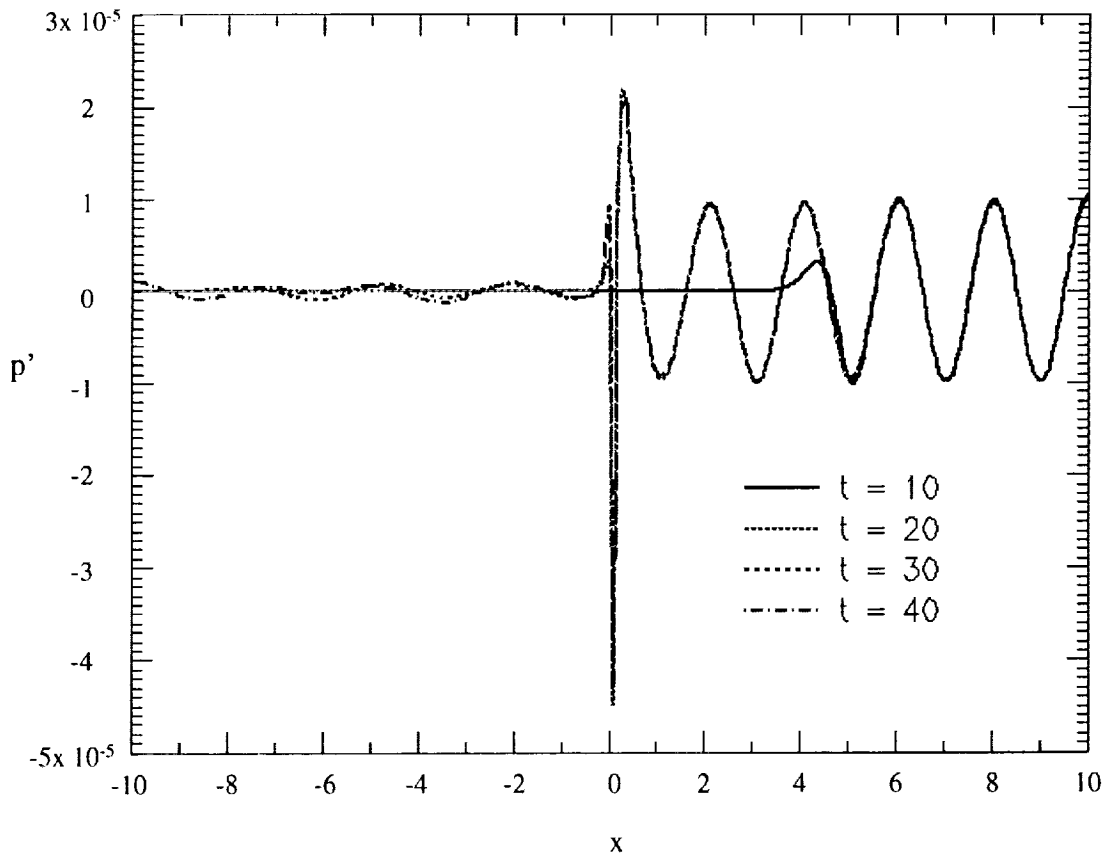
Fig. 3 Variations of acoustic pressures with respect to time for a grid of 400 points
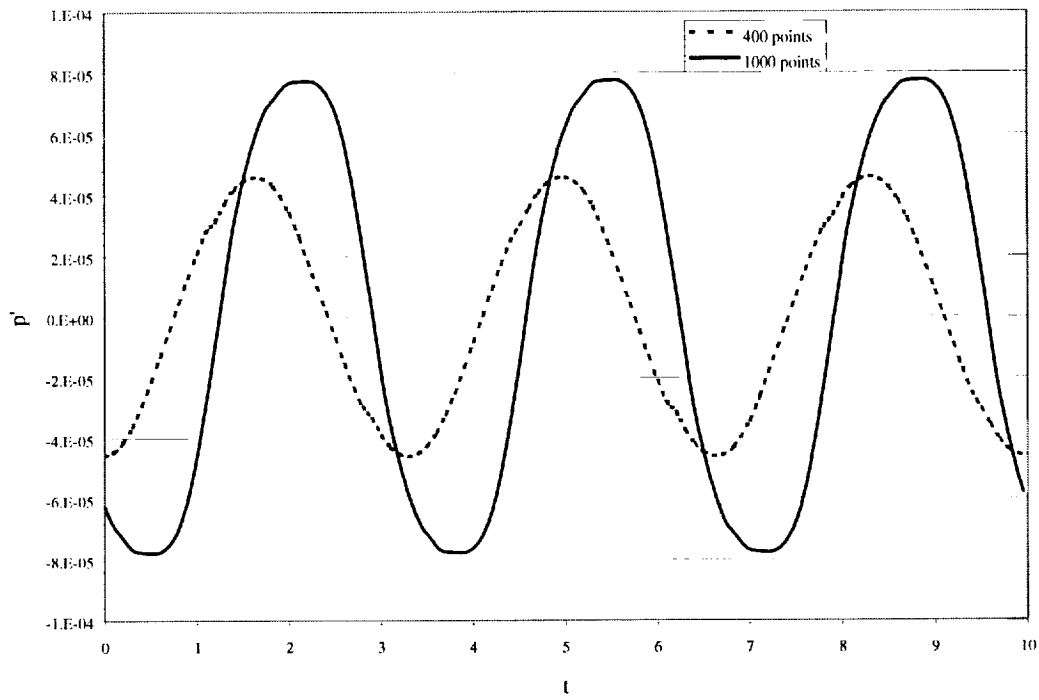
Fig. 4a Time series of maximum acoustic pressures
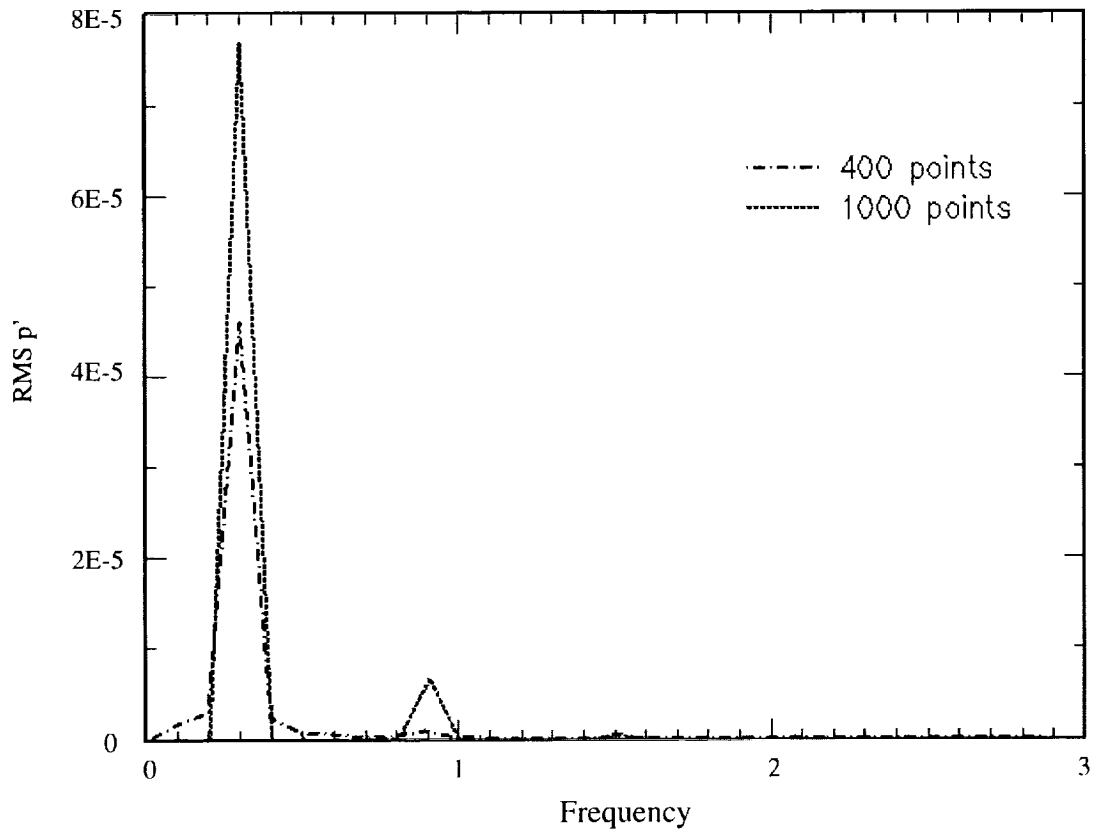
Fig. 4b Fourier spectra of maximum acoustic pressures
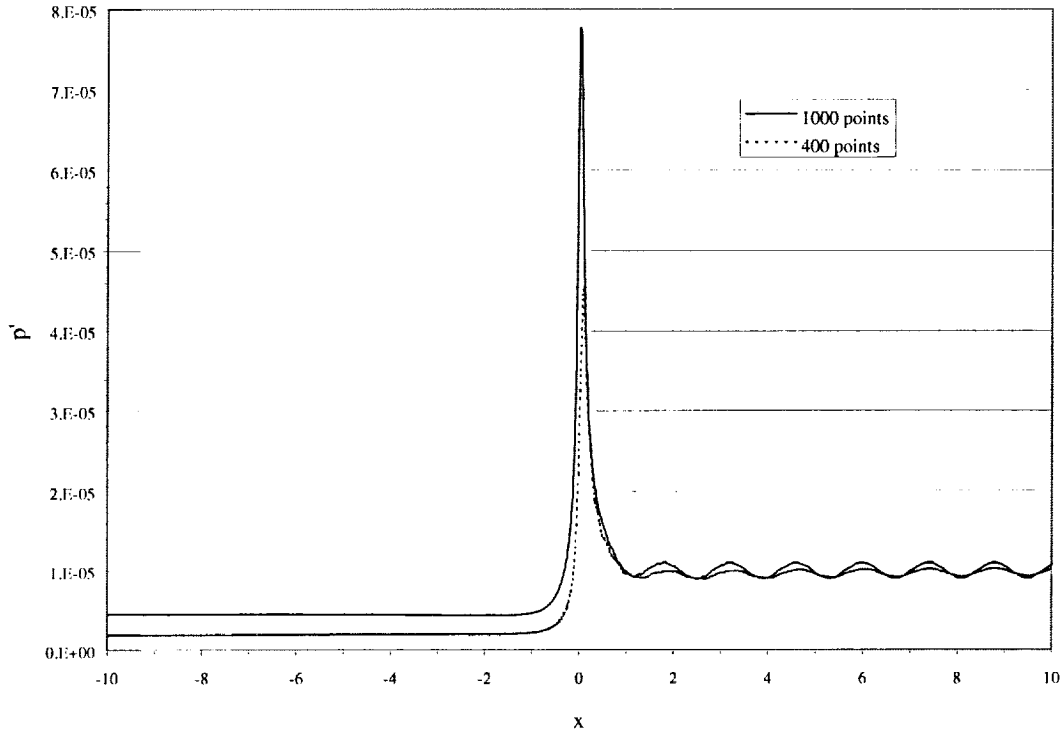
Fig. 5 Envelopes of acoustic pressures for t = 40
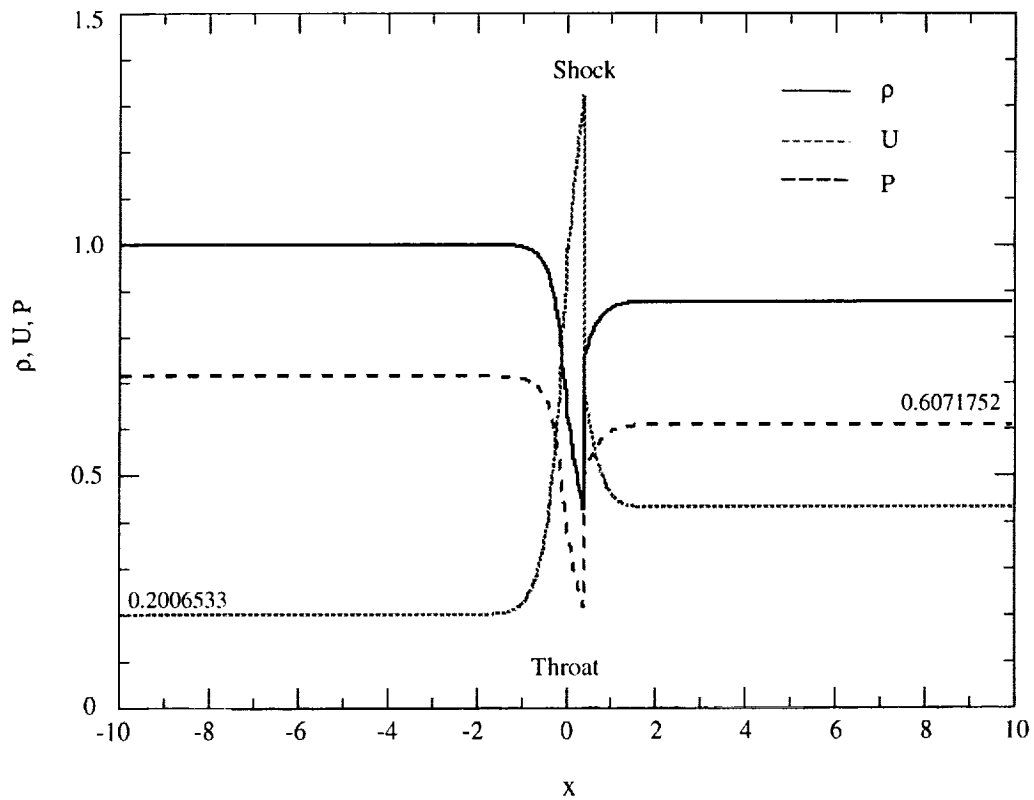
Fig. 6 Density, velocity, and pressure of mean flow
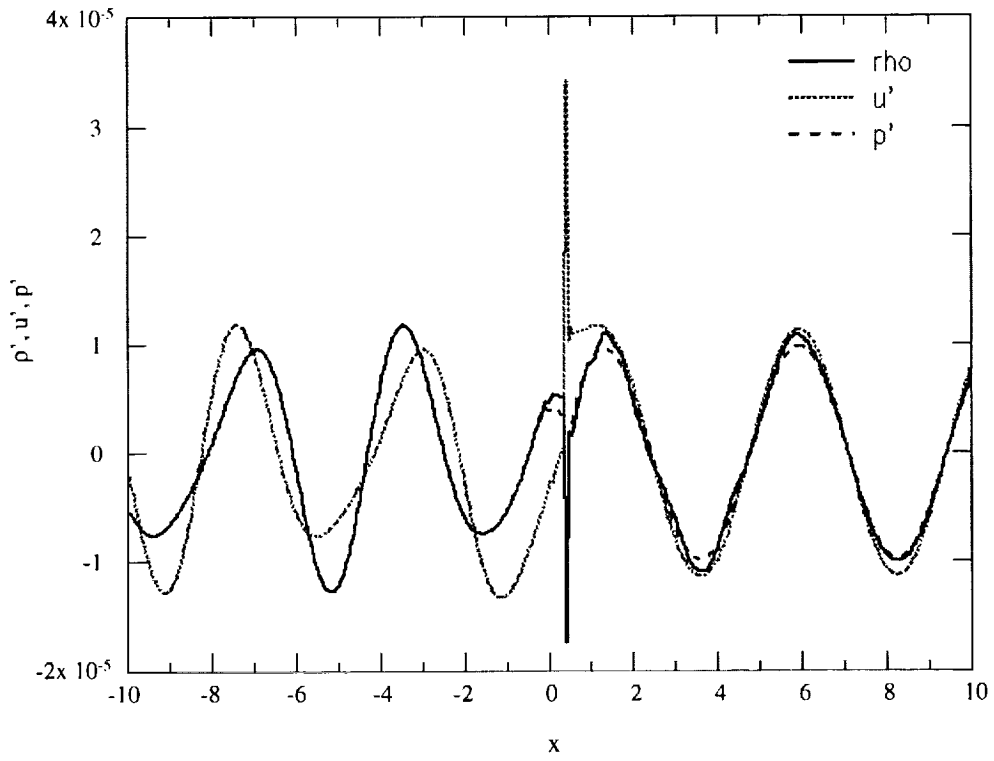
Fig. 7 Acoustic density, velocity, and pressure
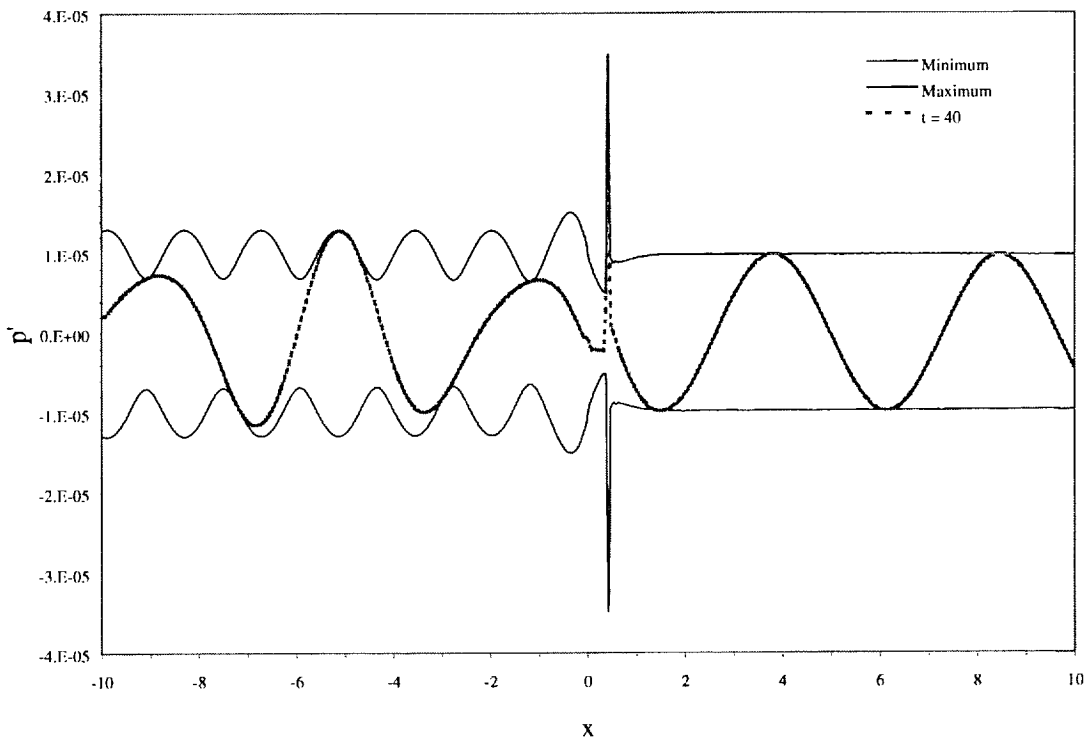
Fig. 8 Envelope and distribution of acoustic pressure at t = 40
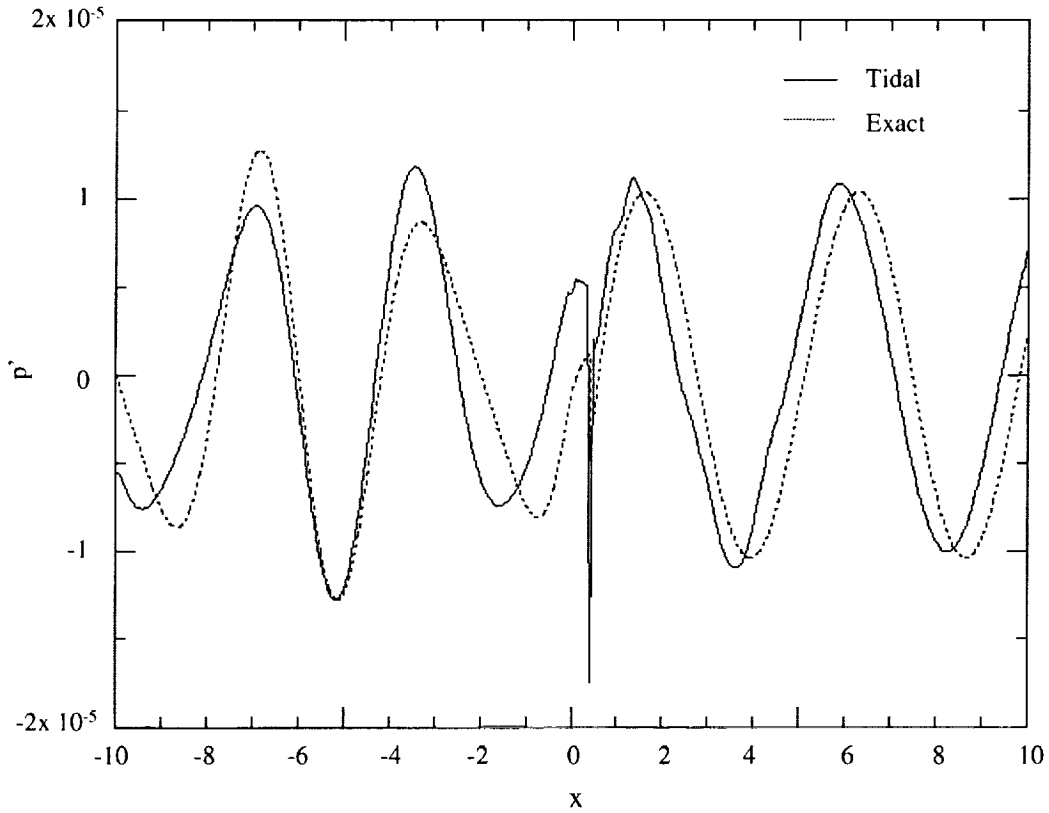
Fig. 9 Comparison of acoustic pressures
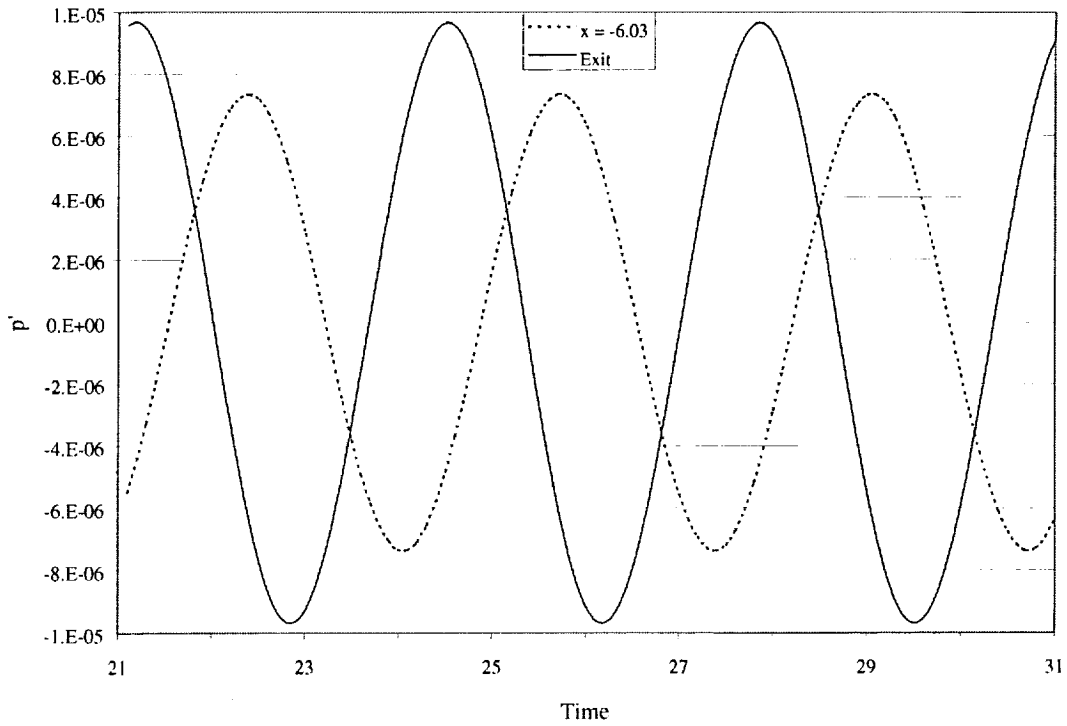
Fig. 10 Time series of acoustic pressures at the exit and at a plane upstream of the throat
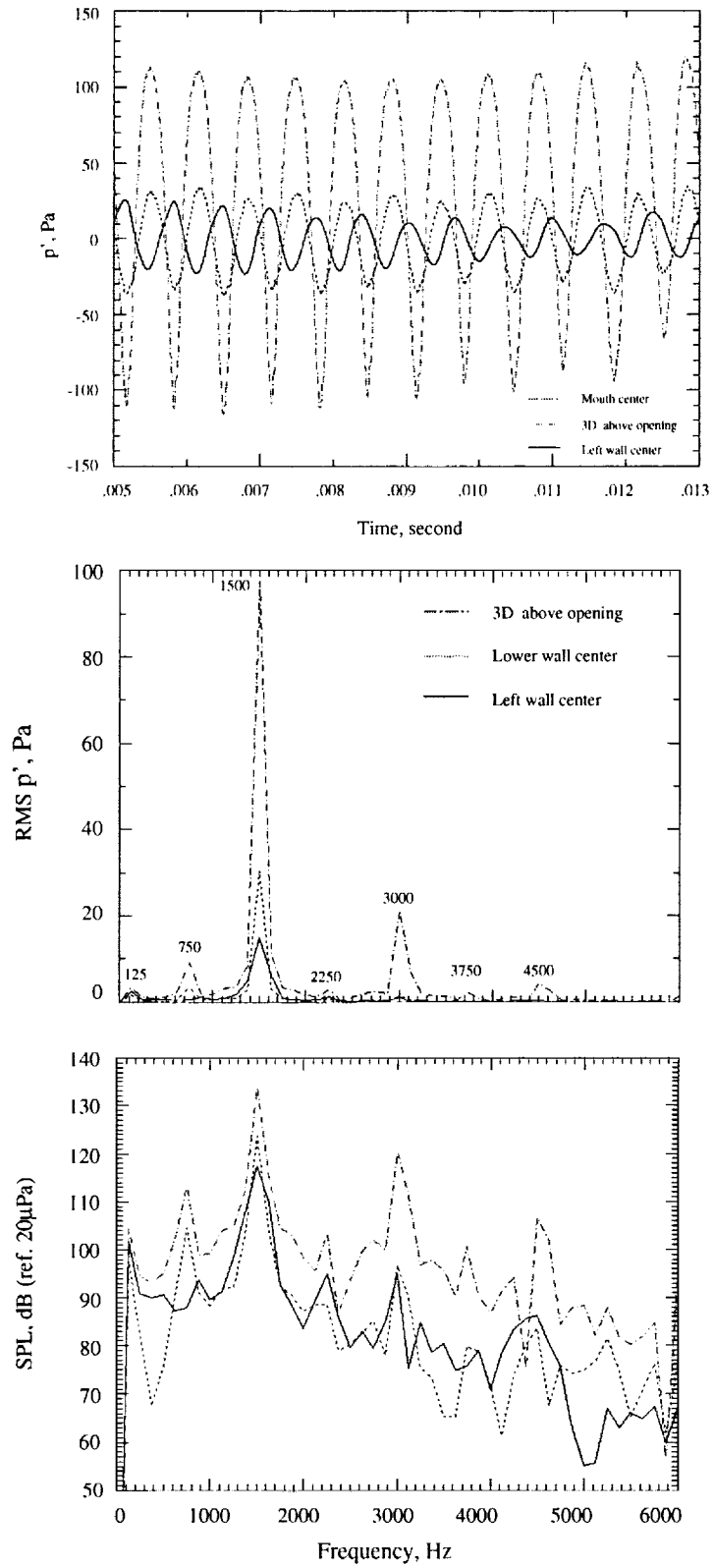
Fig. 11 Time series and Fourier spectra of sound pressures at the left wall, mouth center, and 3D above the mouth, U = 26.8 m/s and δ = 1.6 cm
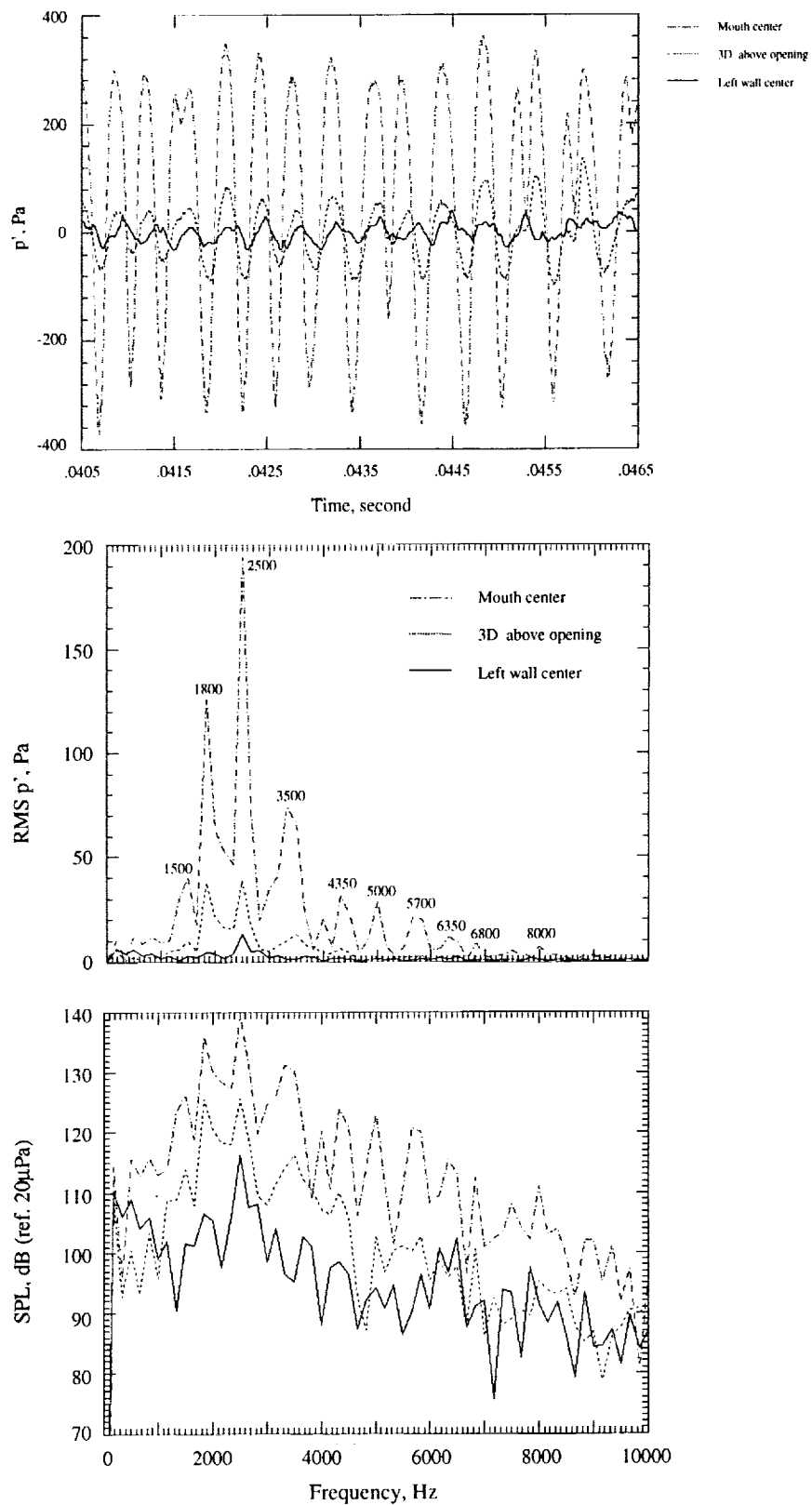
Fig. 12 Time series and Fourier spectra of sound pressures at the left wall, mouth center, and 3D above the mouth, U = 50.9 m/s and δ = 2.2 cm

GENERATION AND RADIATION OF ACOUSTIC WAVES FROM A 2-D SHEAR LAYER *

Anurag Agarwal[†]and PHILIP J. MORRIS[‡]
Department of Aerospace Engineering
The Pennsylvania State University
University Park, PA 16802

Introduction

A parallel numerical simulation of the radiation of sound from an acoustic source inside a 2-D jet is presented in this paper. This basic benchmark problem is used as a test case for scattering problems that are presently being solved by using the Impedance Mismatch Method (IMM) [1, 2, 3]. In this technique, a solid body in the domain is represented by setting the acoustic impedance of each medium, encountered by a wave, to a different value. This impedance discrepancy results in reflected and scattered waves with appropriate amplitudes. The great advantage of the use of this method is that no modifications to a simple Cartesian grid need to be made for complicated geometry bodies. Thus, high order finite difference schemes may be applied simply to all parts of the domain. In the IMM, the total perturbation field is split into incident and scattered fields. The incident pressure is assumed to be known and the equivalent sources for the scattered field are associated with the presence of the scattering body (through the impedance mismatch) and the propagation of the incident field through a non-uniform flow. An earlier version of the technique could only handle uniform flow in the vicinity of the source and at the outflow boundary. Scattering problems in non-uniform mean flow are of great practical importance (for example, scattering from a high lift device in a non-uniform mean flow or the effects of a fuselage boundary layer). The solution to this benchmark problem, which has an acoustic wave propagating through a non-uniform mean flow, serves as a test case for the extensions of the IMM technique.

Governing Equations

The Governing Equations are the linearized Euler equations. These equations are solved using the Impedance Mismatch Method. The linearized Euler equations can be rearranged in the following form

$$\frac{\partial}{\partial t}\begin{bmatrix} \rho' \\ p' \\ u' \\ v' \end{bmatrix} + \frac{\partial}{\partial x}\begin{bmatrix} \rho(y)u' + U(y)\rho' \\ \gamma Pu' + U(y)p' \\ p'/\rho(y) + U(y)u' \\ U(y)\frac{\partial v'}{\partial x} \end{bmatrix} + \frac{\partial}{\partial y}\begin{bmatrix} \rho(y)v' \\ \gamma Pv' \\ 0 \\ 0 \end{bmatrix} = \begin{bmatrix} 0 \\ S \\ -v'\frac{\partial U(y)}{\partial y} \\ -\frac{\partial p'}{\partial y}/\rho(y) \end{bmatrix} \qquad (1)$$

where S is a source term. The mean quantities, U and ρ are functions of y only (in the present problem) and the static pressure P is a constant (except inside a scattering body). It should be noted that, in the IMM, the density inside the scattering body is set to a lower value than the ambient density. The speeds of sound in the two media are assumed to be equal. This non-physical treatment recovers the physical solution in the ambient medium. The details of the methodology, including the rationale for choice of body impedance is given in [1, 2, 3].

The total perturbation flow-field, q, is split into incident and scattered fields.

$$q' = q_i + q_s \qquad (2)$$

Then, equation (1) can be written compactly as

$$\frac{\partial q_l}{\partial t} + \frac{\partial E_l^z}{\partial x} + \frac{\partial F_l^z}{\partial y} = \frac{\partial q_l}{\partial t} - R_l^z = \mathbf{S} \qquad (3)$$

with l being either i for incident or s for scattered, z being either n for non-uniform field or u for uniform field. E and F are flux vectors in the x and y directions. R represents the residual. The incident field is assumed to propagate in a uniform flow. Therefore, the governing equation for the incident field is

$$\frac{\partial q_i}{\partial t} - R_i^u = \mathbf{S} \qquad (4)$$

From equations (3 - 4), the equation for the scattered field becomes

$$\frac{\partial q_s}{\partial t} - R_s^n = -\{R_i^u - R_i^n\} \qquad (5)$$

The right hand side of this equation acts as a source for the scattered field, it is non-zero inside a scattering body and in a region of non-uniform mean flow.

Numerical Algorithm

A fourth-order Dispersion-Relation-Preserving (DRP) scheme with a seven point stencil developed by Tam and Webb [5] is used for spatial discretization and a fourth-order Runge-Kutta scheme is used for time integration. The time integration method is applied to both the incident and the scattered fields. The integration of the incident field is performed after the first and third stages of the scattered field integration. To damp out spurious high frequency waves, a sixth-order artificial dissipation term is used.

The spatial domain and its decomposition for parallel implementation is shown in figure (1). A symmetry boundary condition is applied at the lower boundary for both the incident and scattered fields. Buffer zones [6]
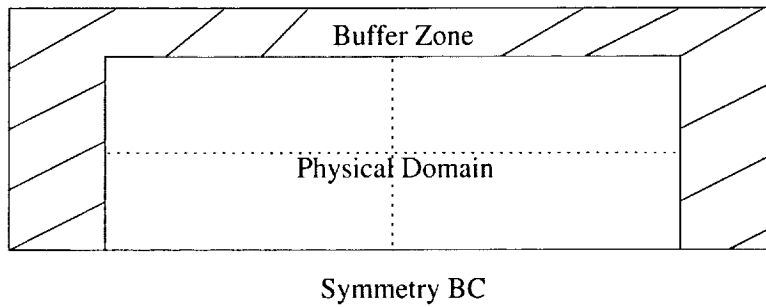
Figure 1: A schematic representation of boundary conditions and domain decomposition

are employed at the other boundaries for the scattered field and Tam and Webb [5] uniform radiation boundary conditions are used for the incident field. In the buffer zone, the perturbation quantities are gradually reduced to zero by directly multiplying them with an appropriate damping function.

The parallel implementation is based on a technique developed by Lockard and Morris [4]. The code is written in Fortran 90 and uses the Message Passing Interface (MPI) for communication between processors. The message passing boundaries are shown by dotted lines in figure (1). Since the spatial stencil for the finite-difference approximations uses seven points, a three-point overlap region is constructed along the interface of each sub-domain.

Numerical Results

The physical domain extends from -5 to 50 in the x direction and from 0 to 10 in the y direction. The actual domain used, including the buffer zones spans from -20 to 65 in the x direction and from 0 to 15 in the y direction. A uniform grid of 401×451 grid points is used. This grid is used for both the incident and the scattered fields.
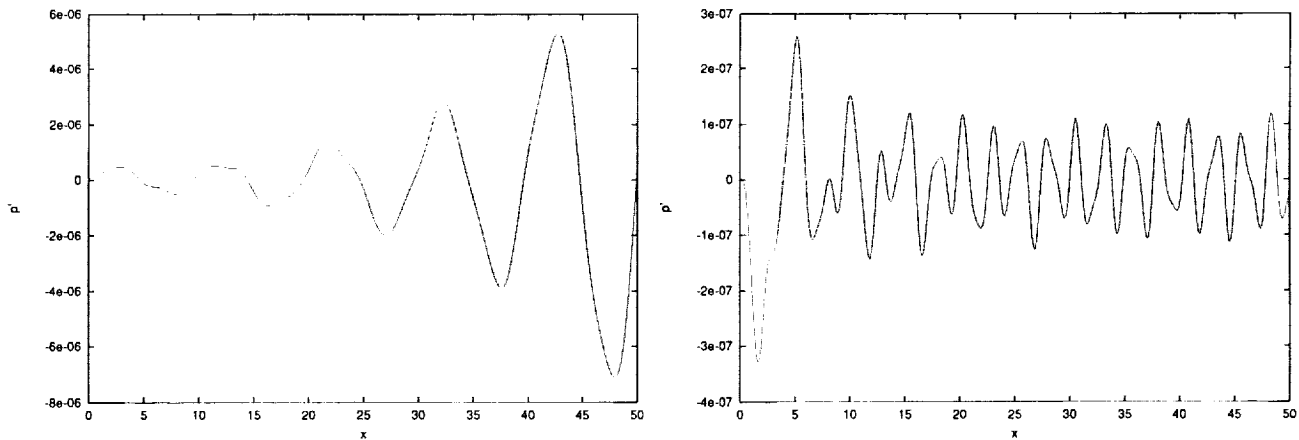
Figure 2: Perturbation pressure, p' along $y = 1$ for $S = 0.14$ and 0.6
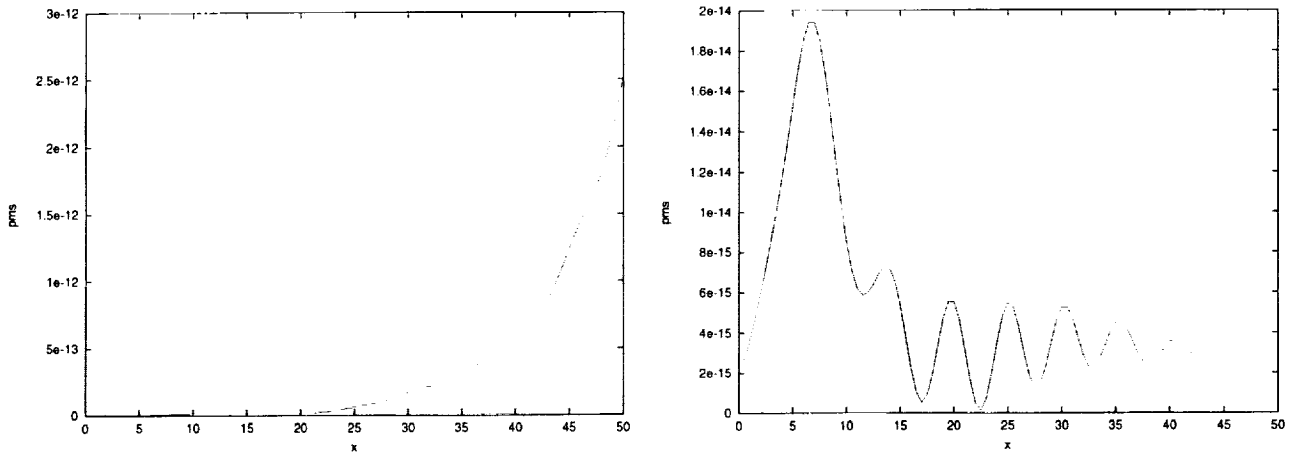
Figure 3: Mean square pressure, $\bar{p}^2$ along $y = 10$ for $S = 0.14$ and 0.6
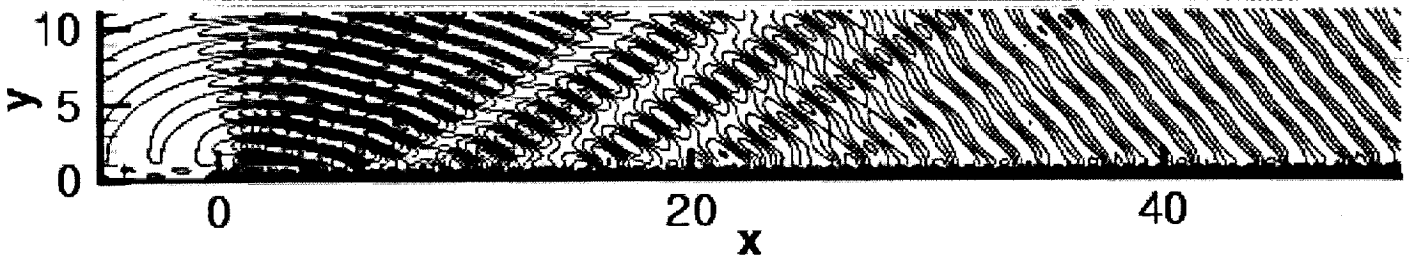
Figure 4: Perturbation pressure contour plot for $S = 0.6$ at the start of a cycle

Figure (2) shows plots of perturbation pressure along $y = 1$ for the two Strouhal numbers. It illustrates that for $S = 0.14$, an instability wave is excited, whereas $S = 0.6$ corresponds to a neutral stability case. Separate analytical computations show that the eigenvalue (wave number k) for the instability wave is $0.6149 - 0.06724i$. This is in exact agreement with the growth rate and wavelength obtained in the numerical computation. In the higher Strouhal number case, the pressure at $y = 1$ shows the interference between the acoustic perturbations and the nearly neutral instability wave.

Figure (3) shows the mean square pressure along the outer boundary at $y = 10$ for the Strouhal number of 0.14 and 0.6 respectively. The average is taken over 10 cycles for the lower Strouhal number and over 40 cycles for the higher Strouhal number. The exponential growth for $S = 0.14$ is as expected. However, since $S = 0.6$ corresponds to a weak neutral stability case, the acoustic waves contaminate the result for the domain of interest. As a result a constant amplitude is not seen (as one might expect for a neutral stability case) for the higher Strouhal number. Figure (4), that shows contours of equal instantaneous pressure perturbation, illustrates this point. In the vicinity of the source the cylindrical wave pattern, distorted by the mean flow convection, dominates the solution. Further downstream the wave field is associated with the Mach waves generated by the instability wave. In the intermediate region, for $10 \le x \le 30$, the interference between the acoustic disturbance and the disturbance generated by the instability wave is evident. In contrast, from figure (5) it can be seen that the strong instability waves dominate the solution at higher x for the lower Strouhal number.
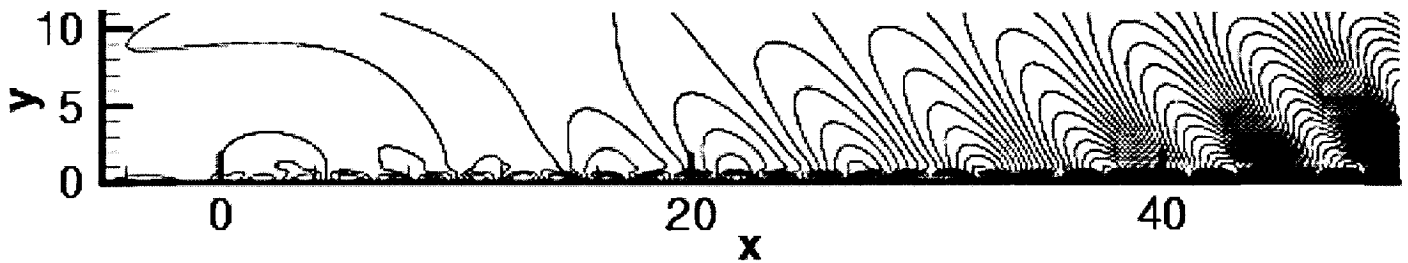
Figure 5: Perturbation pressure contour plot for $S = 0.14$ at the start of a cycle

Simulations with a scattering body

A scattering body, an ellipse with aspect ratio 20 : 3, is placed in the domain. It is centered at $x = 35$, $y = 5$. For these computations, the physical domain is extended to $x = 65$ and $y = 17$. Figure (6) shows the instantaneous pressure contours around the ellipse. A shadow region can be seen above the body. Figure (7) compares instantaneous pressures for a domain containing the scattering body to a domain that does not, for a y location just above the ellipse. It can be seen that there is a drop in pressure amplitude above and downstream of the scattering body due to its presence. However, since the instability continues to be excited and grows further downstream, the amplitude continues to increase beyond the body. In a case, such as a real jet, where the shear layer grows, the instability would decay further downstream and the shielding effect of the ellipse would be more evident. An application for this model problem would be the shielding of jet noise radiation for engines mounted above the wing.
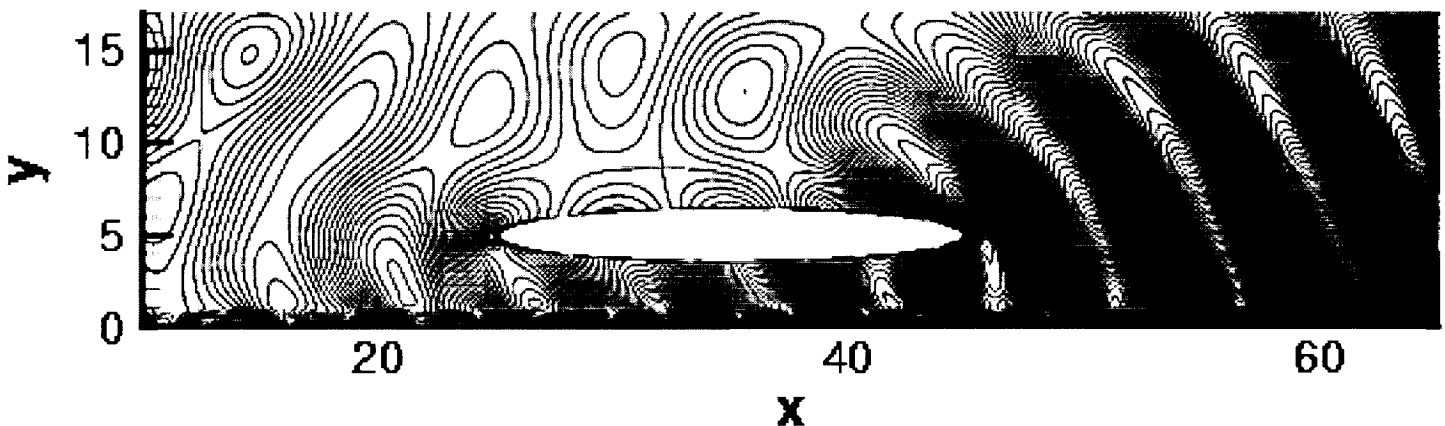
Figure 6: Instantaneous perturbation pressure contour plots around an ellipse outside the shear layer

All computations were performed on 16 processors of a Cray T3E at the University of Texas at Austin. 38200 seconds of total CPU time was used. A time step of .0146 seconds was used for 16800 iterations. The equivalent single CPU/grid point/time step was 201 μs.
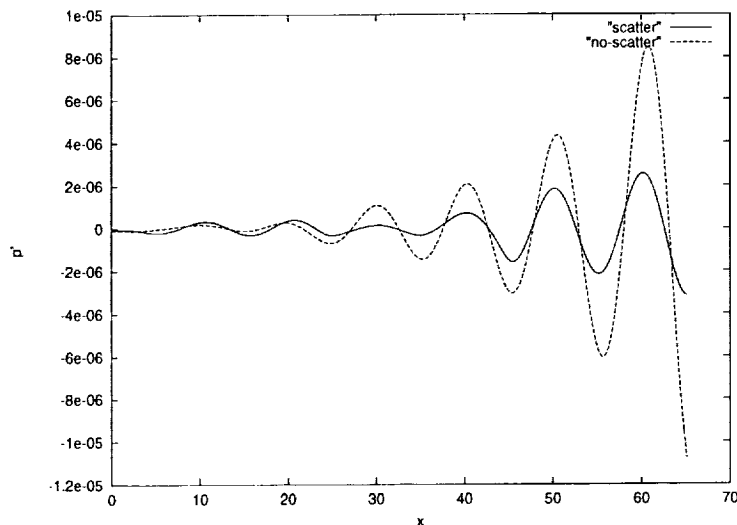
Figure 7: Comparison of perturbation pressures with and without a scattering body. ($S = 0.14, y = 6.6$)

References

[1] C. Chung. *Wave propagation and Scattering in computational aeroacoustics.* PhD thesis, The Pennsylvania State University, Department of Aerospace Engineering, 1995.

[2] C. Chung and P. J. Morris. Acoustic scattering from two- and three-dimensional bodies. *J. Computational Acoustics*, 6(3):357–375, 1998.

[3] O. A. Laik and P. J. Morris. Direct simulation of acoustic scattering from two- and three-dimensional bodies. *Journal of Aircraft*, 37(1), 2000.

[4] D. Lockard and P. J. Morris. A parallel implementation of a computational aeroacoustic algorithm for airfoil noise. *AIAA Journal*, 96-1754, 1996.

[5] C. K. W. Tam and Jay C. Webb. Dispersion-relation-preserving finite difference schemes for computational acoustics. *Journal of Computational Physics*, 107:262–281, 1993.

[6] B. Wasistho, B.J. Geurts, and J.G.M. Kuerten. Simulation techniques for spatially evolving instabilities in compressible flow over a flat plate. *Computers & Fluids*, 26:713–739, 1997.

GENERATION AND RADIATION OF ACOUSTIC WAVES FROM A 2-D SHEAR LAYER

THOMAS E. SCHEIDEGGER* and Philip J. Morris[†]
Department of Aerospace Engineering
The Pennsylvania State University, University Park, PA 16802

Introduction

The two-dimensional excited shear flow provides a good test case to evaluate computational aeroacoustics (CAA) algorithms and boundary conditions. Both the propagation of acoustic waves and the generation of instability waves in the shear layer have to be accurately resolved. Also, due to the exponential growth of the instability wave, the problem is in some respects even more demanding on boundary conditions than a nonlinear flow problem.

An additional motivation for the present work was to compare boundary condition configurations which had previously been applied to fully three-dimensional turbulent jet flows [1], where it had become clear that further improvements were necessary. In practical CAA simulations, it is often necessary to average far-field data over relatively long periods, and the minimization of artificial reflections at computational boundaries plays an important role. Issues considered here are the placement of the different boundary conditions, the location where they join, and the size of the computational domain compared to the physical domain. Also of interest are the effects of grid stretching and refinement in the shear layer.

Numerical Method

The linearized Euler equations are solved using the Dispersion-Relation-Preserving (DRP) scheme [2] on a stretched grid and a RK4 scheme for time integration. Artificial sixth-order dissipation is added for stability. At the inflow at $x = -5$, characteristics based (MOC) boundary conditions [3] are used for $y < 3$ and Tam and Webb (T&W) radiation conditions [2] for $3 < y < 10$. At the far-field boundary, $y = 10$, either T&W radiation conditions are specified or a buffer zone is added which extends to $y = 20$. At the outflow at $x = 50$, either outflow conditions (Tam and Dong (T&D) [4] or MOC) are specified for $y < y_0$ and T&W radiation outside, or again a buffer is added which extends up to $x = 80$.

---

*Post-doctoral research associate
[†]Boeing/A. D. Welliver Professor of Aerospace Engineering

Two different buffer methods are evaluated:(i) a simple technique (Wasistho *et al.* [5]) where all perturbation variables are forced to zero near the computational boundary by applying the buffer function

$$f_{\text{buffer}}(x_b) = (1 - c_1 x_b{}^2)\left(1 - \frac{1 - e^{c_2 x_b{}^2}}{1 - e^{c_2}}\right), \quad 0 < x_b < 1$$

at every stage of the RK4 integration;(ii) a convective buffer (Freund type [6]) where the governing equations are augmented by artificial convection $(u_b(x), v_b(y))$ and damping $\sigma(x,y)$ terms according to

$$\partial_t \rho = \quad \dots \quad + u_b(x)\rho_{,x} + v_b(y)\rho_{,y} + \sigma(x,y)\rho$$
$$\partial_t u = \quad \dots \quad + u_b(x)u_{,x} + v_b(y)u_{,y} + \sigma(x,y)u$$
$$\partial_t v = \quad \dots \quad + u_b(x)v_{,x} + v_b(y)v_{,y} + \sigma(x,y)v$$
$$\partial_t p = \quad \dots \quad + u_b(x)p_{,x} + v_b(y)p_{,y} + \sigma(x,y)p \ .$$

Cosine profiles $(1 + \cos((1 + x_b)\pi))/2$ are chosen for both convection $(u_{bmax}, v_{bmax} = 1.2c_\infty)$ and damping.

Results and Discussion

Excited at the lower frequency, $St = 0.14$, the shear flow is unstable and generates exponentially growing instability waves downstream of the source. The flow is neutrally stable for an excitation at $St = 0.60$ and the main radiation occurs in the vicinity of the excitation. Figure 1 shows the instantaneous pressure in the shear layer for the two Strouhal numbers and different boundary conditions. The different solutions agree very well. However, the instantaneous pressure has not been found to be a good measure to assess the quality of the different boundary conditions used.

Simulations on various grids indicated that the minimum resolution required is determined by the resolution of the shear layer and not the number or grid points per wavelength of the acoustic or instability waves. Sufficient resolution in the y-direction is found for 16 grid points per half-width b of the shear layer. This yields 401 grid points within the physical domain $0 < y < 10$. In order to reduce the total number of grid points, calculations have also been carried out on geometrically stretched grids, where the resolution within $0 < y < 2$ is kept at $b/\Delta y = 16$ and then decreases to match the uniform axial grid spacing at $y = 10$. The axial spacing is chosen to be $\lambda_j/\Delta x = 10, 15, 20,$ and 40, where λ_j is the acoustic wavelength at the excitation frequency. Table 1 shows the grid sizes for both Strouhal numbers. A missing entry indicates that the corresponding resolution is either insufficient or not necessary to obtain acceptable solutions. The mean-square pressure is averaged from $t = 10T$ to $30T$ for $St = 0.14$ and from $t = 40T$ to $130T$ for $St = 0.60$.

Figure 2 shows the effects of grid resolution and stretching on the mean-square pressure at $y = 10$ for both T&D and MOC outflow $(y < 3)$ boundary conditions. The mean-square pressure at the outer edge of the computational domain appears to be very indicative of imperfections in the boundary conditions. Neglecting the acoustic field due to the exciting source, the pressure is expected to rise exponentially for $St = 0.14$. Oscillations are due to reflections at the boundaries. This will become clear below where the results for the buffer zone approach are shown. One notes that the T&D boundary conditions perform considerably better than the characteristics-based MOC boundary conditions. It is also interesting to note that the oscillations become stronger as the resolution decreases, even though the shear layer is equally well resolved in the y-direction in in all cases $(y < 2)$ and the resolution is at least 15 points per wavelength in both directions (whole domain). Differences are also noticeable between the stretched and uniform grid with the highest axial

resolution. This is surprising since the resolution in these two cases is at least 40 points per wavelength in the whole domain.

Figure 3 shows the mean-square pressure p'_{ms} at $y = 10$ for $St = 0.60$. The waves that are convected across the boundaries are much weaker for the higher Strouhal number and the MOC outflow boundary conditions performed equally well (not shown). The main radiation is due to the acoustic source at $x = 0$, and the radiation conditions at $y = 10$ are well suited to let these waves leave the domain. The acoustically dominated flow is sufficiently resolved with 10 points per wavelength and the stretched grid can be used without loss of accuracy.

The influence of the artificial dissipation on the growth of the instability wave is shown in Fig. 4. Its effect is relatively small for the whole range of values used. The simulations became unstable for $\epsilon = 5.0 \times 10^{-5}$, and a value of 2.0×10^{-4} was chosen for all runs.

The advantages of a buffer zone approach over standard outflow boundary conditions are apparent in Fig. 5 for $St = 0.14$. The computational domain is extended to $x_{max} = 80$ and $y_{max} = 20$, i.e. buffers are added at the outflow and outer radiation boundaries. The grid inside the buffer is geometrically stretched by a factor of 5, which increases the total number of grid points by only 33 percent. The stretching is such that acoustic waves at the buffer exit are still resolved by at least 8 points per wavelength. Judging by the smoothness of the mean-square pressure at $y = 10$, the simple Wasistho buffer produces the best results, followed by the Freund approach where the flow is supersonically convected across the boundaries. One also sees that the reflections become considerably larger if the regular boundary conditions (T&W radiation and T&D outflow) are prescribed at the exit of the enlarged domain instead of the physical boundary. This is due to the very high amplitude of the exponentially growing disturbance at the new outflow location. The best T&D result of Fig. 2(a) is shown for comparison (dotted line). It is not *a priori* clear whether these reflections are caused by the radiation or outflow boundary conditions, but one can clearly conclude that due to the nature of the exponentially growing instability wave there is no benefit in moving the boundary conditions further away from the physical domain of interest.

The benefits of a buffer are smaller for $St = 0.60$. Compared in Fig. 6 are the mean-square pressure for the Wasistho buffer ($x_{max}=65$, $y_{max}=20$) with results for T&D outflow conditions applied to both the enlarged and regular domain. Results for the Freund buffer are identical and not shown. No further stretching is used in the buffer region since for $St = 0.60$ the resolution outside the shear layer is only 10 points per wavelength. It is likely that the radiation and outflow conditions perform, compared to the buffer approach, better for the higher Strouhal number since, in that case, the main source location of the radiation is known ($x = 0$). One notices that towards the exit ($x = 50$) the curve for the Wasistho buffer is much smoother than the ones for T&D. A possible explanation for the deterioration in the latter case is the lower (second) order stencil near the boundary. However, one would expect this influence to become negligible in the case where the boundary conditions are applied to the extended domain. By increasing the strength of the acoustic source it has been verified that the irregularities are not due to numerical round-off errors.

Figure 7 indicates that the weak oscillations present in the mean-square pressure for the Freund buffer zone (cf. Fig. 5) cannot be removed by increasing the amplitude of the damping function. Shown is the RMS pressure at $y = 10$ for the whole computational domain, including the buffer zone. Simulations are carried out for $0.1 < \sigma_{max} < 12.5$, without observing any effect on the flow in the physical domain. The exponential growth of the linear instability wave is too strong to be overcome by the artificial damping for the buffer size used. It appears as if the artificial convection velocity in the buffer is the main contributor to the effectiveness of the boundary condition, and that the damping does not play a significant role. Instantaneous pressure contours for the Freund buffer, showing the artificial convection within the buffer zone, are given in Fig. 8.

The effectiveness of the Wasistho buffer is remarkable, and attempts to minimize its size have been made. Figure 9 shows that the buffer size in the x-direction can be reduced to $x_{max} = 65$ without affecting the results significantly. The grid in the shorter buffer is again stretched by a factor of 5 and the grid overhead compared to the physical domain is now reduced to only 18 percent. The buffer size could undoubtedly be shrunk further. Figure 10 shows the damping functions in the x-directions for the two buffer sizes. One notes that the suppression of the outgoing waves occurs over a remarkably few grid points. Instantaneous pressure contours for the larger Wasistho buffer are shown in Figure 11. One attractive feature of the Wasistho buffer not shown is the observation that the grid in the buffer can actually be stretched beyond what would be required to accurately propagate acoustic waves through the same domain.

Conclusions

Several boundary conditions, including buffer zones, have evaluated in terms of their effectiveness in letting acoustic and instability waves leave the physical domain for the case of a two-dimensional shear layer. The simple Wasistho buffer performs remarkably well without requiring a large buffer size and buffer resolution. Tam and Dong outflow boundary conditions produce considerably less reflections than nonreflecting MOC boundary conditions for the shear flow investigated. Due to the nature of the exponentially growing instability wave for $St = 0.14$, there is a clear disadvantage rather than advantage if standard boundary conditions are applied to an enlarged domain. The quality of the boundary conditions is assessed based on the degree of artificial oscillations in the mean-square pressure along the boundaries.

References

[1] P. J. Morris, L. N. Long, and T. Scheidegger. Parallel Computations of High Speed Jet Noise, AIAA Paper 99-1873, 1999.

[2] C. K. W. Tam and J. C. Webb. Dispersion-Relation-Preserving Difference Schemes for Computational Aeroacoustics. *J. Computational Physics*, 107(2):262–281, 1993.

[3] K. W. Thompson. Time-Dependent Boundary Conditions for Hyperbolic Hystems, II. *J. Computational Physics*, 89:439–461, 1990.

[4] C. K. W. Tam and Z. Dong. Radiation and Outflow Boundary Conditions for Direct Computation of Acoustic and Flow Disturbances in a Nonuniform Mean Flow, AIAA Paper 95-007, 1995.

[5] B. Wasistho, B. J. Geurts, and J. G. M. Kuerten. Simulation Techniques for Spatially Evolving Instabilities in Compressible Flow over a Flat Plate. *Computers & Fluids*, 26:713–739, 1997.

[6] J. B. Freund. Proposed Inflow/Outflow Boundary Conditions for Direct Computation of Aerodynamic Sound. *AIAA*, 35(4):740–742, 1997.
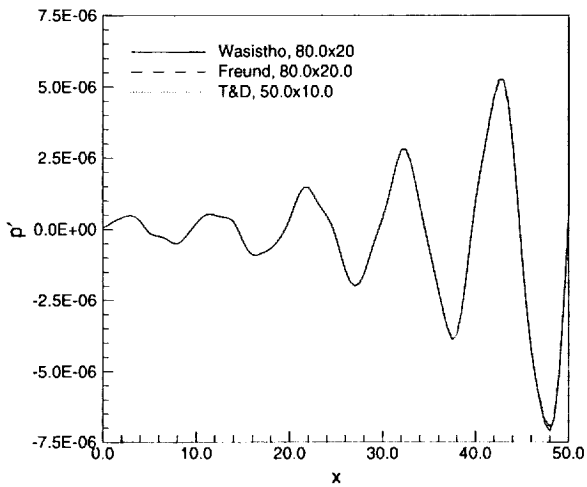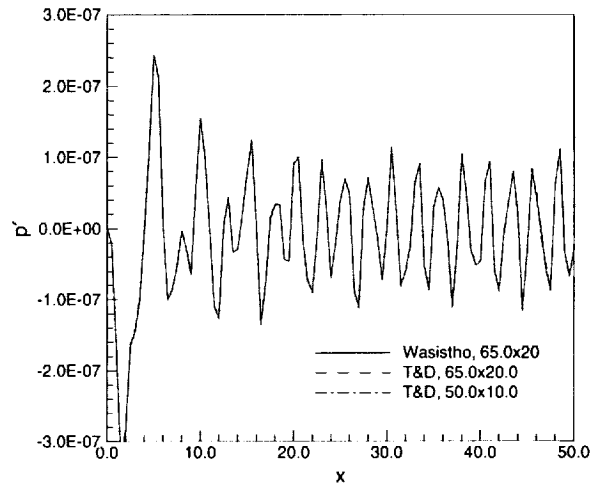
(a) $St = 0.14, t = 30T$ (b) $St = 0.60, t = 130T$

Figure 1: Pressure along shear layer at $y = 1$. 309×401 grid points in physical domain (x_{max}=50, y_{max}=10). Note that the pressure is interpolated onto a coarser mesh than that used in the simulations.
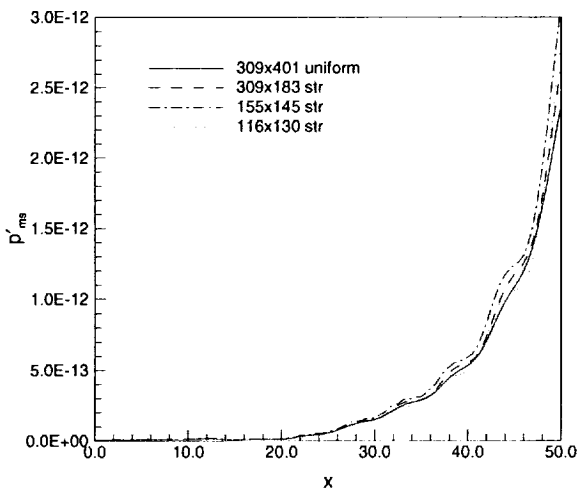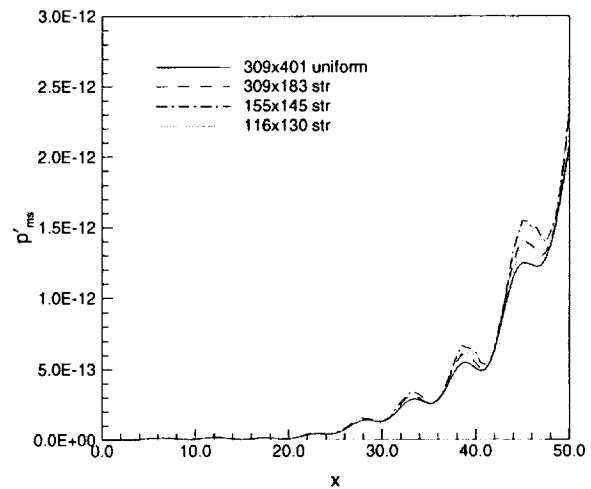
(a) T&D outflow for $y < 3$ (b) MOC for $y < 3$

Figure 2: Effects of grid resolution and stretching on mean-square pressure p'_{ms} at $y = 10$; $St = 0.14$.
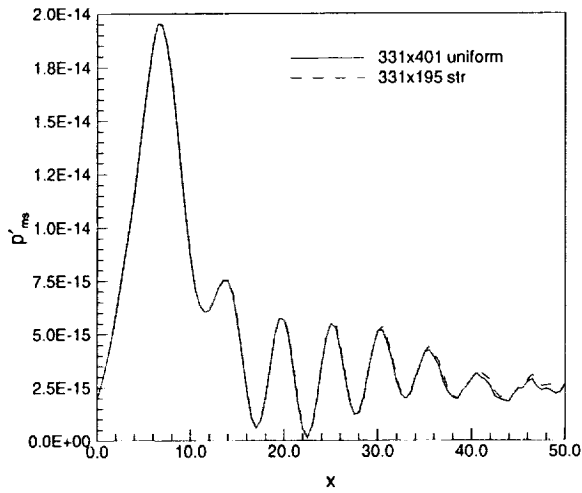
Figure 3: Effects of grid stretching on mean-square pressure p'_{ms} at $y = 10$ for T&D outflow boundary conditions; $St = 0.60$.
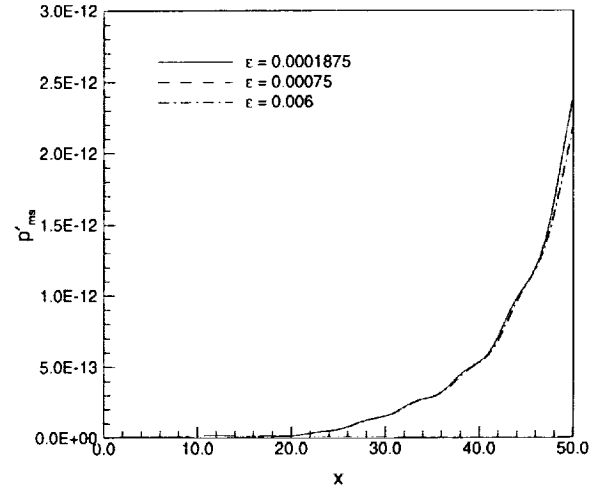
Figure 4: Influence of artificial dissipation on mean-square pressure p'_{ms} at $y = 10$; $St = 0.14$. T&D outflow boundary conditions.
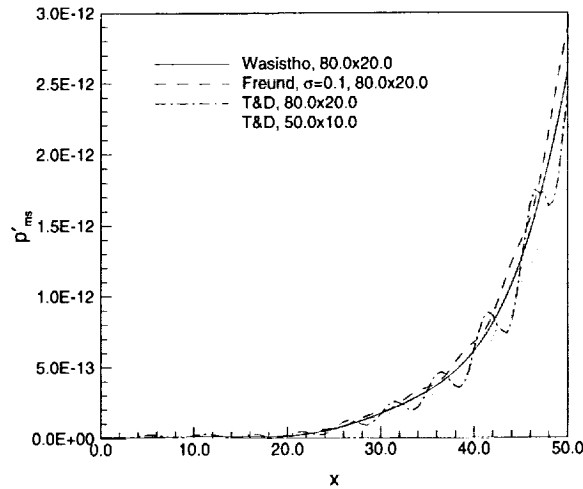
Figure 5: Mean-square pressure p'_{ms} at $y = 10$ for enlarged domain (x_{max}=80, y_{max}=20), $St = 0.14$. Comparison between buffer approach and T&D outflow conditions on enlarged domain. Shown is also T&D on regular domain (y_{max}=50, y_{max}=10).

$\lambda_j/\Delta x$	$St = 0.14$			$St = 0.60$		
	nx	ny		nx	ny	
10	—	—		331	401	uniform
10	—	—		331	195	stretched
15	116	130	stretched	—	—	
20	155	145	stretched	—	—	
40	309	401	uniform	—	—	
40	309	183	stretched	—	—	

Table 1: Grid size within physical domain ($-5 < x < 50, 0 < y < 10$).
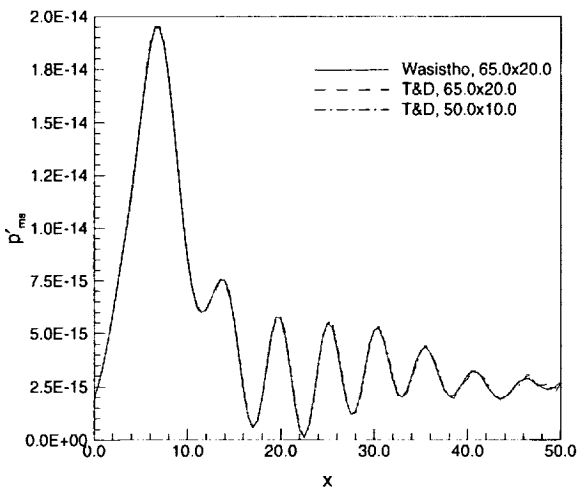
Figure 6: Mean-square pressure p'_{ms} at $y = 10$ for enlarged domain (x_{max}=65, y_{max}=20), $St = 0.60$. Comparison between buffer approach and T&D outflow conditions on enlarged domain. Shown is also T&D on regular domain (x_{max}=50, y_{max}=10).
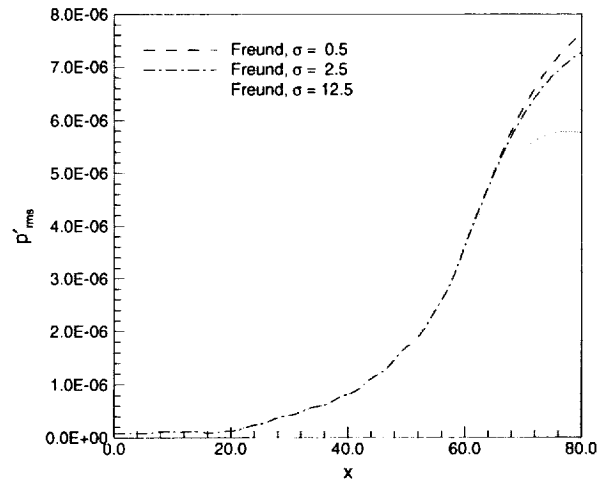
Figure 7: Effects of damping function σ on RMS pressure p'_{rms} at $y = 10$ for Freund type buffer; $St = 0.14$.
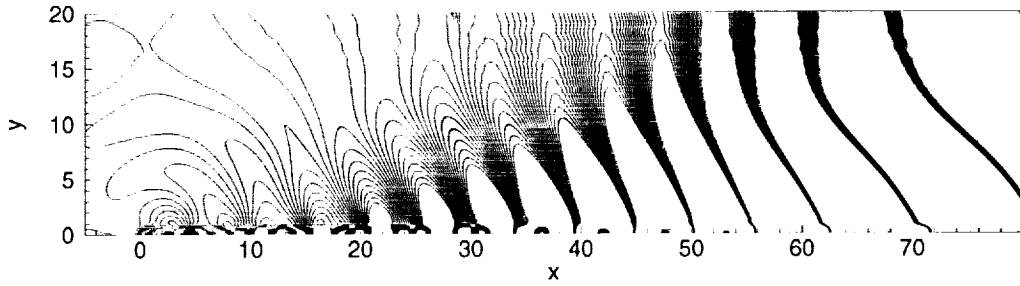
Figure 8: Instantaneous pressure contours $\{-1.0 \times 10^{-6}, 1.0 \times 10^{-6}, \text{step } 1.05 \times 10^{-7}\}$ for $St = 0.14$ at $t = 30T$; Freund buffer, $\sigma_{max} = 0.5$. Shown is the whole computational domain.
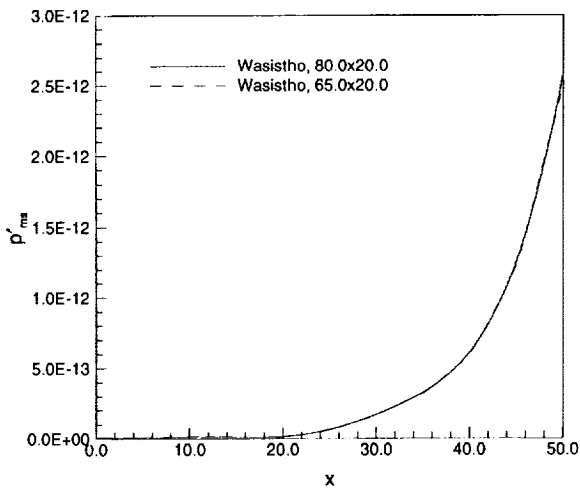
Figure 9: Mean-square pressure p'_{ms} at $y = 10$ for two buffer sizes; $St = 0.14$.
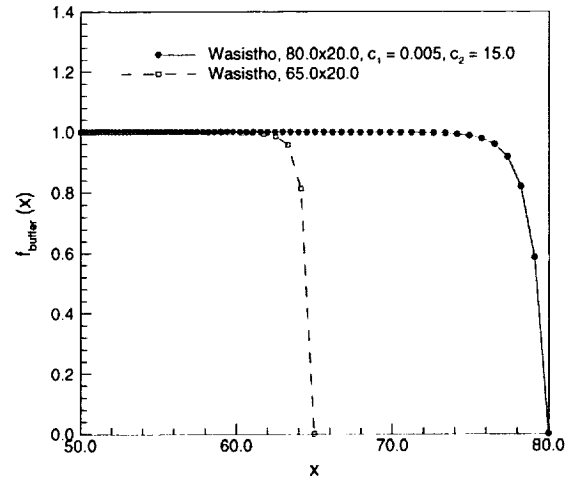
Figure 10: Buffer damping function; $c_1 = 0.005$, $c_2 = 15.0$.
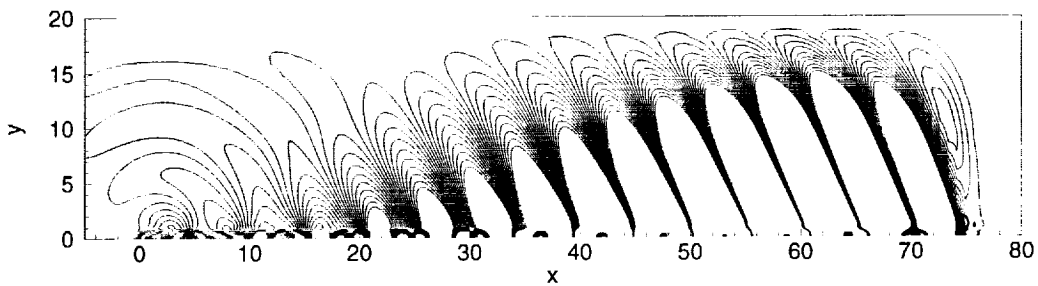
Figure 11: Instantaneous pressure contours $\{-1.0 \times 10^{-6}, 1.0 \times 10^{-6}, \text{step } 1.05 \times 10^{-7}\}$ for $St = 0.14$ at $t = 30T$; Wasistho buffer. Shown is the whole computational domain.

Numerical Computation of the Generation and Radiation of Acoustic Waves from a 2-D Shear Layer

Xiaodong Li
Department of Jet Propulsion
Beijing University of Aeronautics and Astronautics
Beijing, 100083, P.R.China

and

Frank Thiele
Hermann-Föttinger-Institut für Strömungsmechanik
Technische Universität Berlin
Strasse des 17, Juni 135
D-10623, Berlin, Germany

Abstract

The category 5 problem 'Generation and Radiation of Acoustic Waves from a 2-D Shear Layer' is solved based on the 2-D linearized Euler equations. The dispersion-relation-preserving (DRP) finite difference scheme is applied for spatial discretization and the low-dissipation and low-dispersion Runge-Kutta (LDDRK) scheme is utilized for the time integration. Special attention is paid to the implementation of the non-reflecting far-field boundary conditions.

Physical problem

It is well known that an acoustic source inside a jet can excite an instability wave in the shear layer. This will result in sound generation and radiation to the far-field. The category 5 problem is an idealized case of this physical phenomenon. The linearized Euler equations are utilized as the governing equations:

$$\frac{\partial \rho'}{\partial t} + U(y)\frac{\partial \rho'}{\partial x} + \rho(y)\frac{\partial u'}{\partial x} + \rho(y)\frac{\partial v'}{\partial y} + v'\frac{\partial \rho(y)}{\partial y} = 0 \tag{1}$$

$$\frac{\partial u'}{\partial t} + U(y)\frac{\partial u'}{\partial x} + v'\frac{\partial U(y)}{\partial y} = -\frac{1}{\rho(y)}\frac{\partial p'}{\partial x} \tag{2}$$

$$\frac{\partial v'}{\partial t} + U(y)\frac{\partial v'}{\partial x} = -\frac{1}{\rho(y)}\frac{\partial p'}{\partial y} \tag{3}$$

$$\frac{\partial p'}{\partial t} + U(y)\frac{\partial p'}{\partial x} + \gamma P\frac{\partial u'}{\partial x} + \gamma P\frac{\partial v'}{\partial y} = A\exp\left[-B(\ln 2)(x^2 + y^2)\right]\cos(\omega t) \tag{4}$$

and the mean flow variables are given by

$$U(y) = \begin{cases} U_\infty + (U_j - U_\infty) \exp\left[-(\ln 2)(\frac{y}{b} - \frac{h}{b})^2\right], & y \geq h \\ U_j & 0 \leq y < h, \end{cases}$$

$$\frac{1}{\rho(y)} = -\frac{1}{2}\frac{\gamma - 1}{\gamma P}(U(y) - U_j)(U(y) - U_\infty) + \frac{1}{\rho_j}\frac{(U(y) - U_\infty)}{(U_j - U_\infty)} + \frac{1}{\rho_\infty}\frac{(U_j - U(y))}{(U_j - U_\infty)}$$

The jet static pressure is assumed to be constant. The jet flow is parallel and symmetric about the x-axis as shown in Fig.1.

The length scale is given by the half-velocity distance $R_{1/2}$. The velocity is scaled by the jet velocity U_j, the density by ρ_j, the pressure by $\rho_j U_j^2$, and the time and frequency by $R_{1/2}/U_j$. The constants are given as $P = 101330$ (kg/m s^2), $R = 286.8875 (m^2/s^2$ K), $U_j = 517.4569$ (m/s), $T_j = 166.6667$ (K), $U_\infty = 0$, $T_\infty = 300$ (K), $M_j = 2$, $T_{j0}/T_\infty = 1, \gamma = 1.4, R_{1/2} = h + b = 1(m)$, $h = 0.6$ (m), $b = 0.4$ (m), $A = 0.001$ (kg/m s^3), and $B = 8$ (1/m^2).
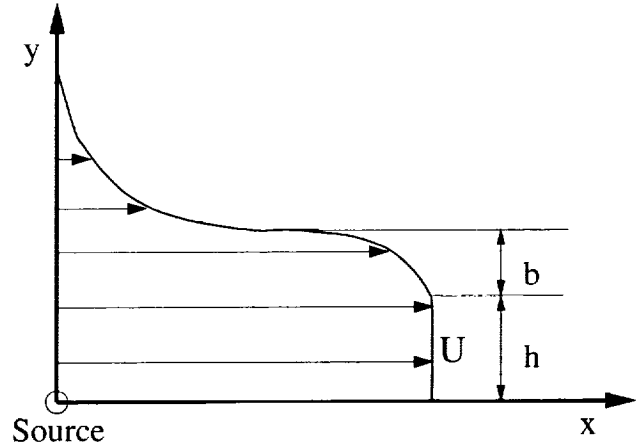
Figure 1: A sketch of the physical problem

Numerical Methods

The discretization scheme and non-reflecting far-field boundary conditions are the key technical issues for accurate CAA simulations.

The present research employs the dispersion-relation-preserving (DRP) scheme Tam and Webb[5]. The 46 low-dissipation and low-dispersion Runge-Kutta (LDDRK) scheme by Hu et al. [2] is explored for time integration. Furthermore, in order to enhance the predictive quality of the solution and to stabilize the numerical procedure, the selective artificial damping method [6] is adopted for eliminating short wavelength spurious waves.

The non-reflecting boundary conditions in the far-field are crucial to the present numerical simulations.

The computational domain is depicted in Fig. 2 with $-5 \leq x/R_{1/2} \leq 50$ and $0 \leq y/R_{1/2} \leq 10$.

The characteristic boundary conditions by Thompson [7] are applied at the inflow boundary region where $Ma \geq 0.001$. Since the inflow is supersonic, all characteristics are incoming and all are set to zero.

At the outer boundary region where the local mean flow Mach number $Ma < 0.001$, the asymptotic radiation boundary conditions by Bayliss & Turkel [1] or Tam & Webb [5] are specified.

At the downsteam boundary region where $Ma \geq 0.001$, the outflow boundary conditions by Tam & Webb [5] are implemented. This boundary condition has an assumption of uniform mean flow which is not true for the present flow cases. However, the numerical results given below are rather good with little reflections.

A symmetric boundary condition is applied at $y/R_{1/2} = 0$.

The developed CAA code has been validated by a series of benchmark problems from the first and second CAA workshops. It has been written into a parallelized version and applied to duct acoustics[3][4].

Simulation Results and Discussions

One of the main difficulties of simulating a shear layer in a large computational domain lies in different resolution requirements in different regions. Usually, the grids must be fine enough to capture the sound generation process across the thin shear layer whereas the grids can be relatively coarse in the propagation region. For simplicity, a uniformly distributed small mesh size has been used in all the simulations with $\Delta x/R_{1/2} = \Delta y/R_{1/2} = 1/32$. This ensures a high resolution across the whole computational domain. However, much more CPU time is required due to a large number of grid points. For accelerating the computations, 24 evenly distributed multi-block grids are generated by a domain decomposition technique [3]. All the computations are performed on a 24 PC cluster (Pentium II 450Mhz). Numerical calculations show that the CPU time is 0.6 second per time step. And the parallel efficiency is 80%.

For $St = 0.14$, the time step size is chosen as $\Delta t = 0.014285714$. The instantaneous pressure contours at $t = 428.57143$ (at the start of cycle 31) are shown in Fig. 3. The radiation pattern shows that the acoustic intensity increases along the downstream direction. This implies that the acoustic source inside the jet has excited an amplified instability wave mode which has generated and radiated amplified sound field along the downstream direction. There are very little reflections at all the outer computational boundaries. Fig. 4 gives the sound pressures along the line $y/R_{1/2} = 1$ for $St = 0.14$ which also shows the amplification tendency along the downstream direction.

For $St = 0.6$, the time step size is chosen as $\Delta t = 0.011111111$. The instantaneous pressure contours are shown in Fig. 5 at $t = 403.333333333$ (at the start of cycle 122) whereas the pressures along the line $y/R_{1/2} = 1$ are shown in Fig. 6. Quite different from the case of $St = 0.14$, the acoustic intensity for $St = 0.6$ approaches a stable level along the downstream direction gradually. This indicates that a neutral instability mode has been excited at $St = 0.6$. Furthermore, the outer boundary conditions have also been shown very effective with little reflections.

Figs. 7 and 8 give the calculated sound intensities $\overline{p'}^2$ along $y/R_{1/2} = 10$ for $St = 0.14$ and $St = 0.6$, respectively. The far field prediction results (along $y/R_{1/2} = 10$) are consistent with the near field prediction results (along $y/R_{1/2} = 1$), (see Figs. 4 and 6). The sound intensities $\overline{p'}^2$ along $x/R_{1/2} = 50$ (downstream boundary) are shown in Figs. 9 and 10 for $St = 0.14$ and $St = 0.6$, respectively. We can see that the sound intensity of case $St = 0.14$ is approximately several thousands larger than that of the case $St = 0.6$.

Table 1 gives a summary of the computer used, the number of grid points, the total CPU time, the time step size and the total number of time steps, etc.

Table 1: A summary of main parameters in the calculations

Main parameters	St=0.14	St=0.60
Computer used	24 PC (Pentium II 450Mhz)	24 PC (Pentium II 450Mhz)
Number of grid points (each block)	25245	25245
Total number of grid points	605880	605880
Time step size	0.014285714	0.011111111
Total time steps	30000	36300
CPU time per time step	0.6s	0.6s
CPU time on each PC (s)	18000	25245
Total CPU time (s)	432000	522720
Parallel efficiency	80%	80%

Radiation BC

Radiation BC

Ma<0.001

Radiation BC

Ma<0.001

Characteristic inflow BC

Asympotic outflow BC

Symmetric BC
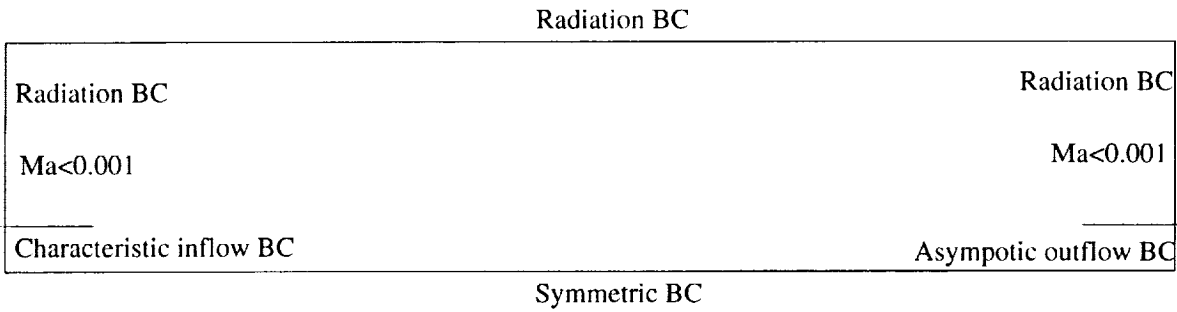
Figure 2: The computational domain and boundary conditions.
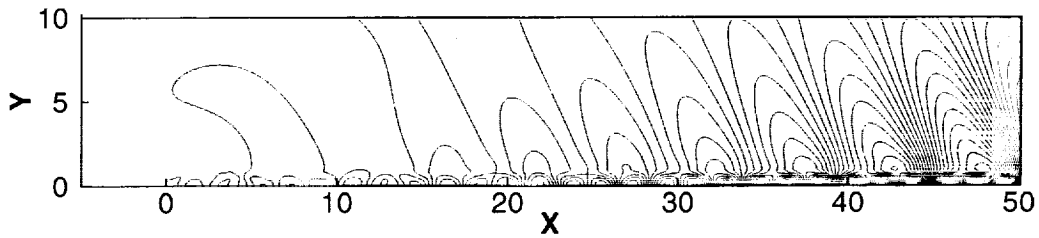
Figure 3: Instantaneous acoustic pressure contours at $t = 428.57143$, $St = 0.14$.
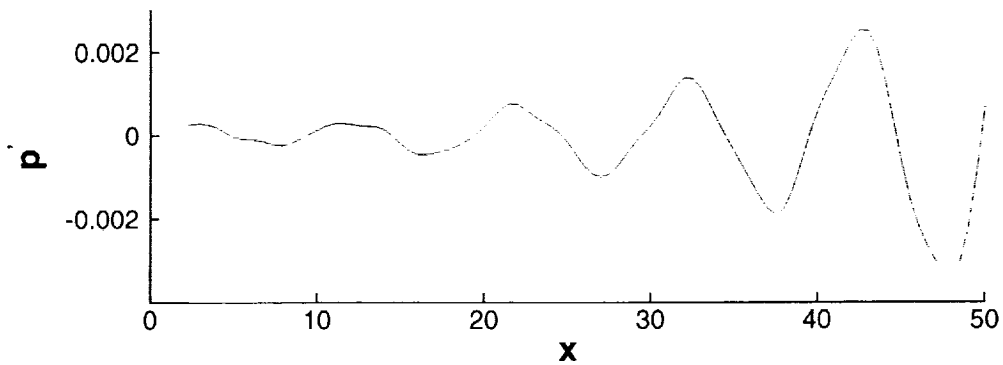
Figure 4: The acoustic pressures along $y/R_{1/2} = 1$ at $t = 428.57143$, $St = 0.14$.
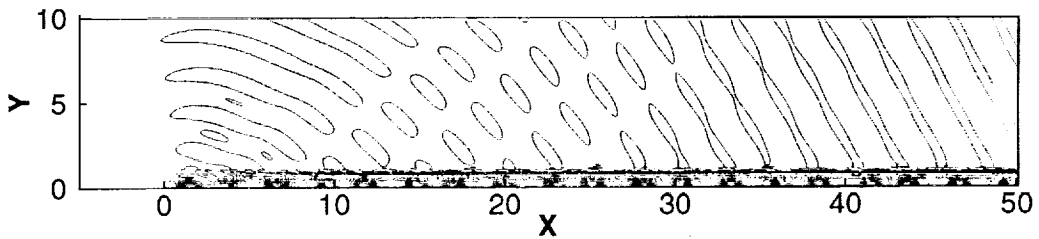
Figure 5: Instantaneous acoustic pressure contours at $t = 403.333333333$, $St = 0.6$.
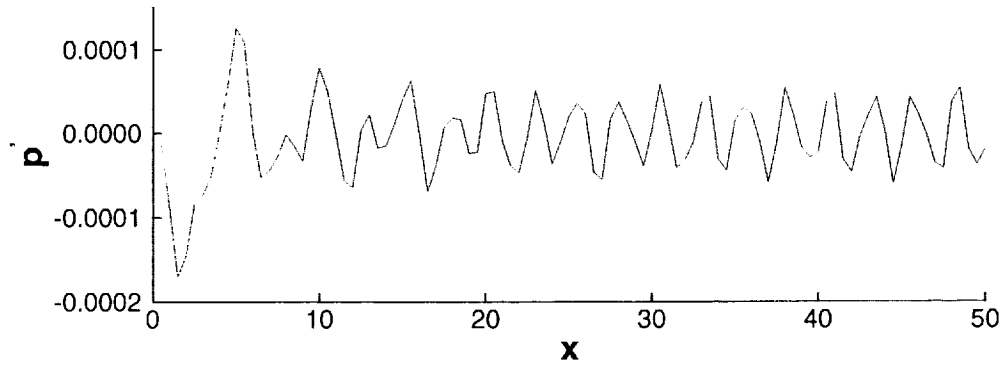
Figure 6: The acoustic pressures along $y/R_{1/2} = 1$ at $t = 403.333333333$, $St = 0.6$.
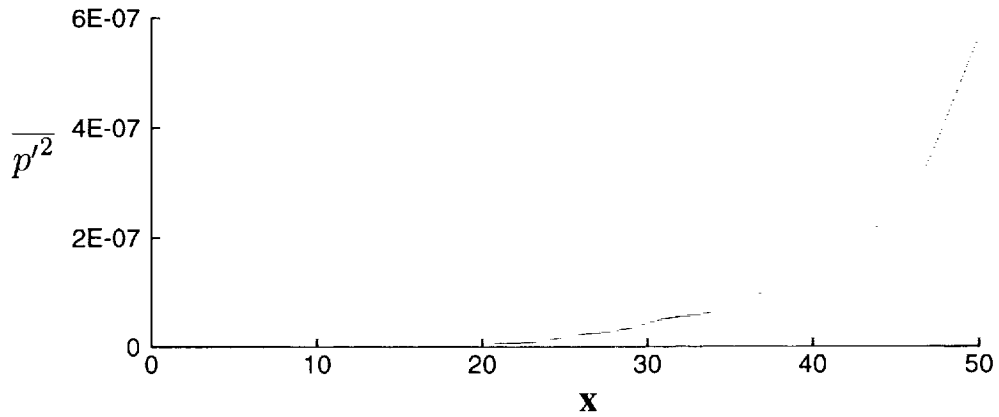
Figure 7: Intensity of radiated sound, $\overline{p'^2}$ along $y/R_{1/2} = 10$, $St = 0.14$.
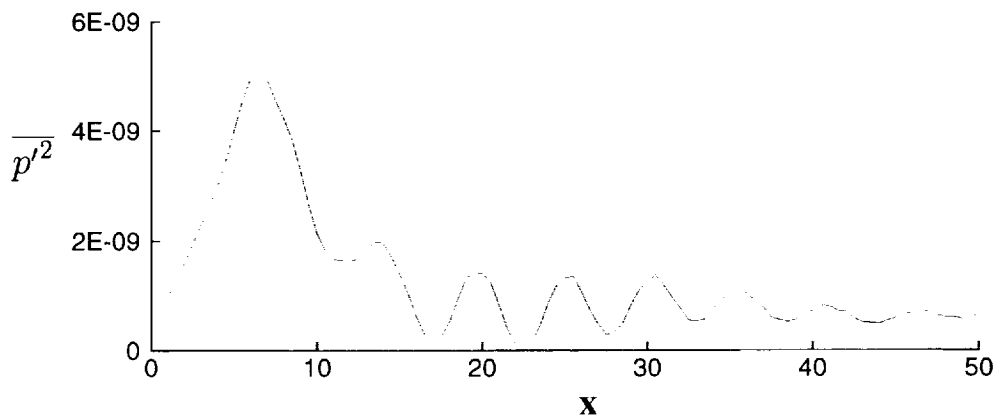
Figure 8: Intensity of radiated sound, $\overline{p'^2}$ along $y/R_{1/2} = 10$, $St = 0.6$.
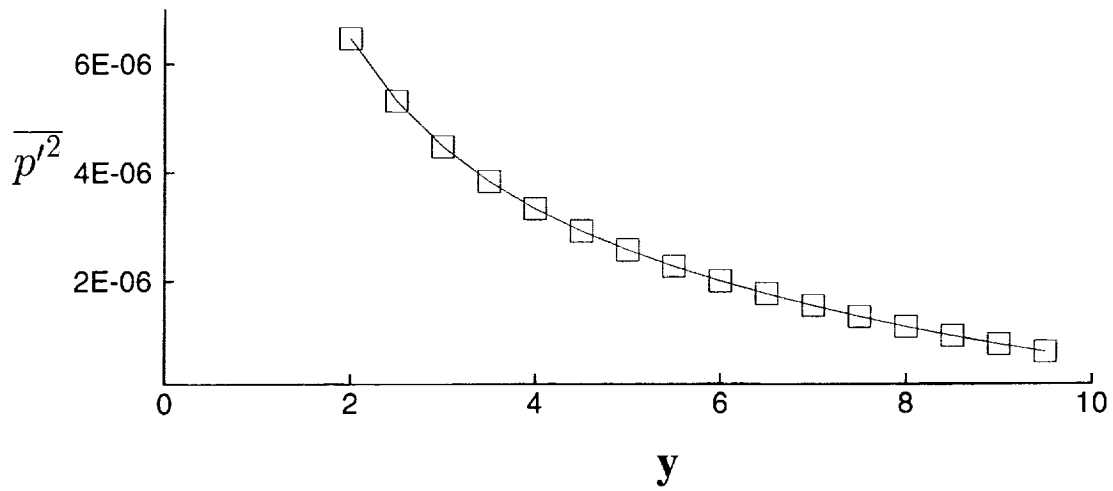
Figure 9: Intensity of radiated sound, $\overline{p'^2}$ along $x/R_{1/2} = 50$, $St = 0.14$.
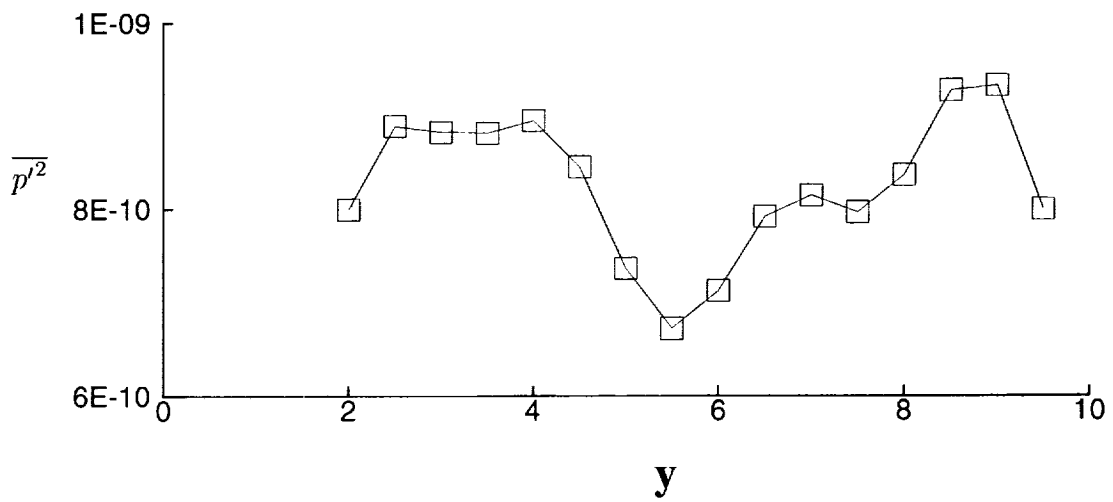
Figure 10: Intensity of radiated sound, $\overline{p'^2}$ along $x/R_{1/2} = 50$, $St = 0.6$.

Conclusions

The generation and radiation of acoustic waves from a 2-D parallel shear layer is calculated based on the linearized Euler equations. The high order DRP scheme and LDDRK scheme are applied for space and time discretizations, respectively. Appropriate non-reflecting boundary conditions have been implemented for different boundary regions. All the computations were performed on a 24-PC cluster efficiently by the parallelized CAA code. Numerical results have shown that $St = 0.14$ and $St = 0.6$ are corresponding to an amplification and a neutral instability mode, respectively. Further work is still required on grid generation and far-field boundary conditions.

Acknowledgements

References

[1] Bayliss, A., and Turkel, E., "Far Field Boundary Conditions for Compressible Flows," *J. Computational Physics*, Vol.48, 1982, pp.182–199.

[2] Hu, F. Q., Hussaini, M. Y., and Manthey, J. L., "Low-Dissipation and Low-Dispersion Runge-Kutta Schemes for Computational Acoustics," *J. Computational Physics*, Vol.124, 1996, pp.177-191.

[3] Li, X.D., Xue, L.P., Yan, J.P., and Thiele, F., "Parallel Computation of Duct Acoustics by Computational Acoustics Approach," AIAA 99-1819, May 1999.

[4] Li, X.D., Yan, J.P., Rung, T., Thiele, F., "Numerical Simulation of Duct Inlet Noise," Presented at the 8th International Symposium of CFD, Bremen, September 1999.

[5] Tam, C.K.W., and Webb, J.C., "Dispersion-Relation-Preserving Finite Difference Schemes for Computational Acoustics," *J. Computational Physics*, V.107, 1993, pp.262-281.

[6] Tam, C.K.W., Webb, J.C., and Dong, T.Z., "A Study of the Short Wave Components in Computational Acoustics," *J. Computational Acoustics*, Vol.1, 1993, pp.1-30.

[7] Thompson, K.W., "Time Dependent Boundary Conditions for Hyperbolic Systems," *J. Computational Physics*, V. 89, 1990, pp.439-461.
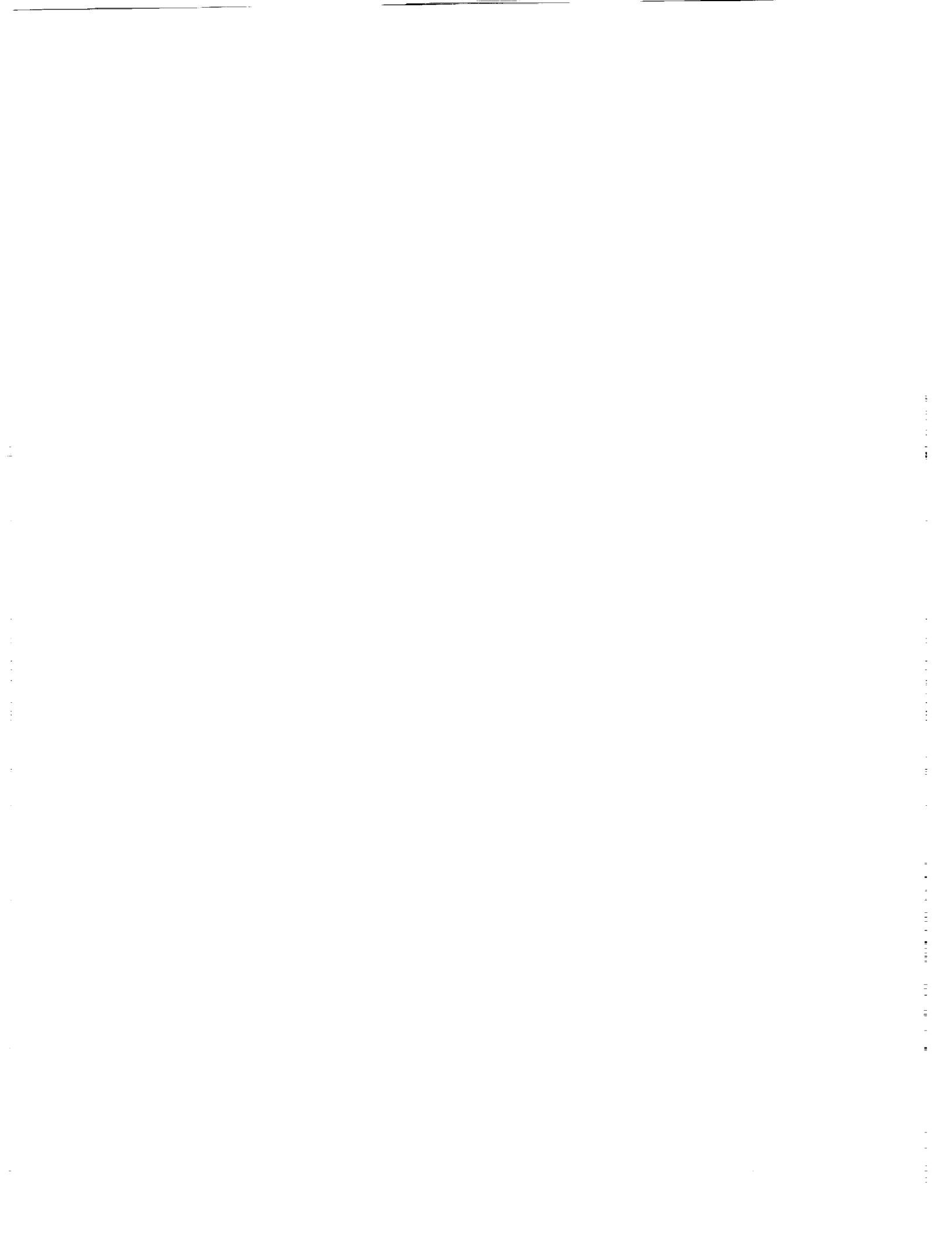
AN APPLICATION OF THE QUADRATURE-FREE DISCONTINUOUS GALERKIN METHOD

DAVID P. LOCKARD[*] AND HAROLD L. ATKINS[†]
NASA Langley Research Center, Hampton, VA 23681-2199, U.S.A

Introduction

The process of generating a block-structured mesh with the smoothness required for high-accuracy schemes is still a time-consuming process often measured in weeks or months. Unstructured grids about complex geometries are more easily generated, and for this reason, methods using unstructured grids have gained favor for aerodynamic analyses. The discontinuous Galerkin (DG) method is a compact finite-element projection method that provides a practical framework for the development of a high-order method using unstructured grids. Higher-order accuracy is obtained by representing the solution as a high-degree polynomial whose time evolution is governed by a local Galerkin projection. The traditional implementation of the discontinuous Galerkin uses quadrature for the evaluation of the integral projections and is prohibitively expensive. Atkins and Shu[1] introduced the quadrature-free formulation in which the integrals are evaluated a-priori and exactly for a similarity element. The approach has been demonstrated to possess the accuracy required for acoustics even in cases where the grid is not smooth. Other issues such as boundary conditions and the treatment of non-linear fluxes have also been studied in earlier work[2,3].

This paper describes the application of the quadrature-free discontinuous Galerkin method to a two-dimensional shear layer problem. First, a brief description of the method is given. Next, the problem is described and the solution is presented. Finally, the resources required to perform the calculations are given.

Numerical Method

The discontinuous Galerkin method is applicable to systems of first-order equations of the form

$$\frac{\partial \mathbf{q}}{\partial t} + \frac{\partial \mathbf{f}_i}{\partial x_i} = \mathbf{s}. \tag{1}$$

A summation convention is used for all repeated indices. Here, i ranges from unity to the number of coordinate directions. The domain of interest is divided into non-overlapping elements each of which is defined on some domain Ω with a boundary $\partial\Omega$. For the two-dimensional linearized Euler equations, $\mathbf{q}$, $\mathbf{f}$, and $\mathbf{s}$ are given by

$$\mathbf{q} = \begin{pmatrix} \rho \\ p \\ u \\ v \end{pmatrix}, \quad \mathbf{f}_1 = \begin{pmatrix} \overline{U} & 0 & \overline{\rho} & 0 \\ 0 & \overline{U} & \gamma\overline{P} & 0 \\ 0 & 1/\overline{\rho} & \overline{U} & 0 \\ 0 & 0 & 0 & \overline{U} \end{pmatrix} \mathbf{q}, \quad \mathbf{f}_2 = \begin{pmatrix} \overline{V} & 0 & 0 & \overline{\rho} \\ 0 & \overline{V} & 0 & \gamma\overline{P} \\ 0 & 0 & \overline{V} & 0 \\ 0 & 1/\overline{\rho} & 0 & \overline{V} \end{pmatrix} \mathbf{q},$$

---

[*] Research Scientist
[†] Senior Research Scientist

$$
\mathbf{s} \;=\; \begin{pmatrix} 0 & 0 & 0 & 0 \\ 0 & (1-\gamma)(\overline{U}_x+\overline{V}_y) & (\gamma-1)\overline{P}_x & (\gamma-1)\overline{P}_y \\ -(\overline{UU}_x+\overline{VU}_y)/\overline{\rho} & (1/\overline{\rho})_x & \overline{V}_y & -\overline{U}_y \\ -(\overline{UV}_x+\overline{VV}_y)/\overline{\rho} & (1/\overline{\rho})_y & -\overline{V}_x & \overline{U}_x \end{pmatrix} \mathbf{q}. \tag{2}
$$

The vector of dependent variables is $\mathbf{q}$. An over-line has been used to denote local temporal-mean quantities, and subscripted values denote differentiation. ρ and p are the perturbation density and pressure, and u and v are the x and y directed velocities, respectively. The ratio of specific heats is γ. The equations have been made dimensionless using the ambient speed of sound c_o as the reference velocity.

The discontinuous Galerkin method is obtained by approximating the solution in each element Ω in terms of an appropriate set of basis functions b_m.

$$
\mathbf{q} \approx \sum_{m=1}^{N} \boldsymbol{q}_m b_m = \boldsymbol{q}_m b_m
$$

where $\{b_m,\; m=1,2,\ldots,N\}$ is a set of basis functions. The coefficients of the approximate solution q_m are the new unknowns, and equations governing these unknowns are obtained by an integral projection of the governing equations onto the basis set. The weak conservation form is obtained by integrating by parts.

$$
\int_{\Omega} b_k \frac{\partial \mathbf{q}}{\partial t} J\, d\Omega \;-\; \int_{\Omega} \frac{\partial b_k}{\partial \xi_i} \mathbf{J}^{-1}\mathbf{f}_i J\, d\Omega + \int_{\partial\Omega} b_k (J\mathbf{J}^{-1}\mathbf{f}_i n_i)^R ds = \int_{\Omega} b_k \mathbf{s} J\, d\Omega \tag{3}
$$

for $k=1,2,\ldots,N$. Because the solution $\mathbf{q}$ is approximated as a local expansion in terms of the basis functions, both $\mathbf{q}$ and $\mathbf{f}_i$ are discontinuous at the boundaries between neighboring elements. The discontinuity in $\mathbf{q}$ between adjacent elements is treated with an approximate Riemann flux, which is denoted by the superscript R. The Jacobian of the transformation from the global coordinates (x,y) to the local coordinates (ξ,η) of the element is $\mathbf{J}$ and $J=|\mathbf{J}|$. The basis set must be complete, but many classes of functions could be used. A common choice is a set of polynomials of the form $\xi^i \eta^j$ that are defined local to the element. The basis set for degree p contains all polynomials of the form $\xi^i \eta^j$ such that the integers $i+j \le p$. A possible basis set in two dimensions and $p=2$ is $\{1,\xi,\eta,\xi^2,\xi\eta,\eta^2\}$.

To implement the quadrature-free approach, the flux $\mathbf{f}_i$ must also be written as an expansion in terms of basis functions:

$$
\mathbf{f}_i(\mathbf{q}) \approx \boldsymbol{f}_{ij}(\mathbf{q}) b_j,
$$

and a similar expansion is made for the approximate Riemann flux and the source $\mathbf{s}$. Because the functional behavior of all of the variables is known, the integrations in equation (3) can be performed analytically. To obtain the values of the integrals for a particular set of coefficients requires the multiplication of a matrix times the vector of the coefficients of the flux polynomial.

The final form of the semi-discrete equation is

$$
\begin{aligned}
\frac{\partial q_m}{\partial t} &= \frac{1}{J}\left[M_{km}^{-1} A_{ikj}(J\mathbf{J}^{-1}\boldsymbol{f}_{ij}) - M_{km}^{-1} B_{lnk}\left(J\mathbf{J}^{-1}\boldsymbol{f}_{ln}\right)^R \right] + \boldsymbol{s}_m \\
&= \frac{1}{J}\left[\tilde{A}_{imj}\boldsymbol{f}_{ij} - \tilde{B}_{lmn}\tilde{\boldsymbol{f}}_{ln}^R \right] + \boldsymbol{s}_m
\end{aligned} \tag{4}
$$

The exact definitions of the A and B matrices can be found in reference 4. The groupings $\check{f}_{ij} = JJ^{-1}f_{ij}$ and $\check{f}_{ln}^R = (JJ^{-1}f_{ln})^R$ have been used because that is what is normally stored in the computer implementation. Because all elements of a given type are mapped into the same similarity element, the coefficients $\tilde{A}_{imj}$ and $\tilde{B}_{lmn}$ can be precomputed once and applied throughout the calculation. Equation (4) is advanced in time by using the five-stage, fourth-order, Runge-Kutta method of Kennedy et $al.$[5] Analysis of the stability of this approach can be found in reference 1.

Problem Definition

The DG method was applied to the category 5 problem of the 1999 CAA Workshop on Benchmark problems. The problem involves an acoustic source within a two-dimensional, supersonic shear layer. The velocity profile is given by

$$\overline{U}(y) = \left\{ \begin{array}{l} U_\infty + (U_j - U_\infty) \exp\left[-(\ln 2)\left(\frac{y}{b} - \frac{h}{b}\right)^2 \right], \ y \geq h \\ U_j, \ 0 \leq y < h \end{array} \right\} \tag{5}$$

and the density is obtained from the mean velocity. The mean pressure is uniform, and the flow in the core is at Mach 2. A source term on the pressure equation of the form

$$A \, \exp\left[-B(\ln 2)(x^2 + y^2) \right] \cos(\omega t) \tag{6}$$

excites the shear layer with an acoustic source. The parameters are set as follows: $P = 101330$ kg/(m s^2), $h = 0.6$ m, $b = 0.4$ m, $A = 0.001$ kg/(m s^3), $B = 8$/m^2, $T_\infty = 300$ K, and $T_{j0}/T_\infty = 1$. The shear layer is forced at frequencies of St$=2fL/U_j = 0.14$ and 0.6. The length scale $L = 1$ m. The solution is required between $x = 0$ m to 50 m and $y = 0$ m to 10 m.

Solution Procedure
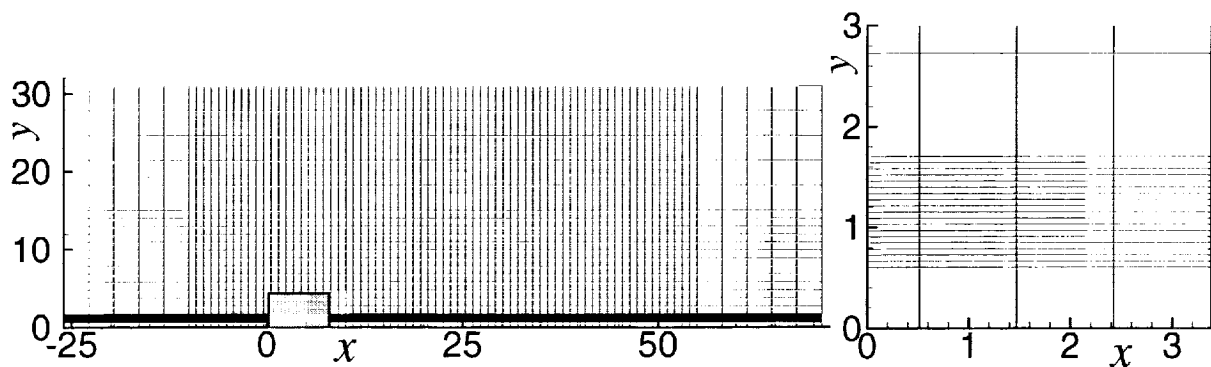
Figure 1: Grid used for the St=0.14 case. Shaded region is enlarged on the right.

A basis set consisting of standard polynomials up to degree four is used which yields a scheme which is fifth-order spatially. The efficient solution procedures discussed in reference 4 about polynomial

(a) St=0.14 (b) St=0.6
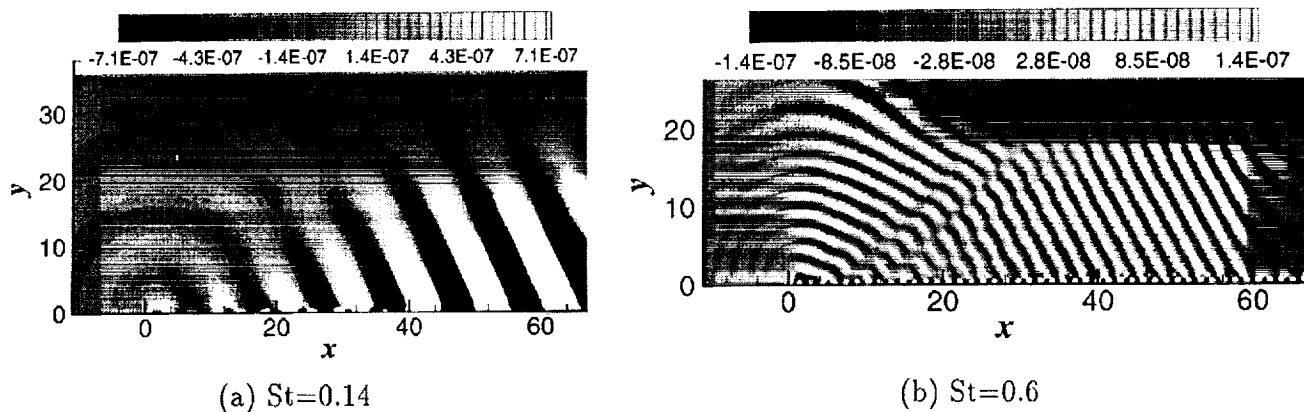
Figure 2: Pressure contours in Pa.

products are used in the current work. A typical grid of rectangular elements is shown in figure 1. The right part of the figure is a magnified view of the grayed out portion of the grid on the left. The enlarged region shows the clustering of elements in the vicinity of the shear layer. Eighteen elements are used between $y = 0.6$ and $y = 1.7$ where $\frac{\partial U}{\partial y}$ is large and the perturbation solution varies significantly. Uniform cells are used in the rest of the specified computational domain from $x=-5$ to 50 and $y=0$ to 10. A simple symmetry boundary condition is applied along the line $y = 0$. Characteristic conditions[3] on the other boundaries produced unacceptable reflections, so a buffer technique is applied. The region outside of the specified domain is considered the buffer region. The grid spacing is unchanged for 5 m outside of the specified domain extent, then it is abruptly coarsened. Because the DG method is insensitive to grid smoothness, the grid spacing was altered abruptly to conserve grid points without degrading the solution. Within the buffer, the equations are modified to include a Newtonian cooling term,[6] and the mean velocities are modified to obtain supersonic outflow at the boundaries[7] using a $1/2(1 + \cos)$ term. Very little optimization of the buffer parameters was performed. Figure 2 shows the pressure contours throughout the entire computational domain for the two frequencies. The pressure is reported in dimensional units of Pa throughout the paper. A growing instability dominates the low frequency solution, whereas the waves have neutral growth at the higher frequency.

Grid Refinement

A grid refinement was used to assess the quality of the solutions. The number of points within the shear layer was increased first until the growth rate of the instability did not change significantly. Next, the overall number of grid points was varied. Figure 3 shows compares the solutions from two different grids for the St=0.14 case. Figure 3(a) shows the $\overline{p^2}$ along $y = 10$, and (b) depicts the pressure along $y = 1$ at fifty uniformly spaced points between $x = 0$ m and $x = 50$ m. The solutions are very similar for this grid resolution, and the grid can be coarsened considerably with only a small degradation in the solution.

A similar grid refinement for the St=0.6 case is presented in figure 4. Again, the solutions are quite similar between the two grids. Because a fixed number of sampling points are used to generate the figures, the solution looks unresolved in figure 4(b). However, the actual solution is quite smooth.
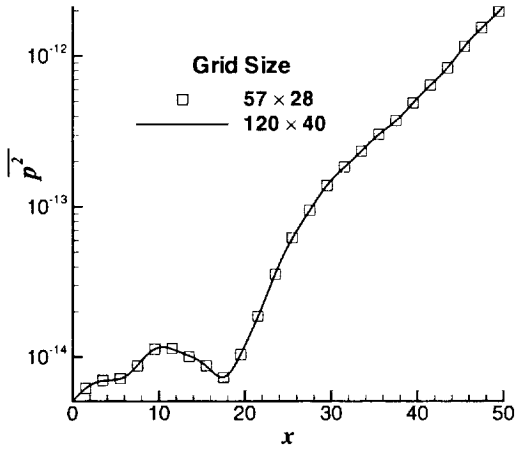
(a) $\overline{p^2}$ along $y = 10$
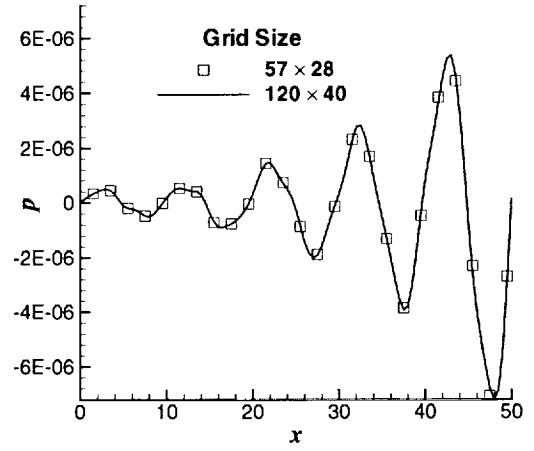
(b) p along $y = 1$

Figure 3: Grid refinement for St=0.14
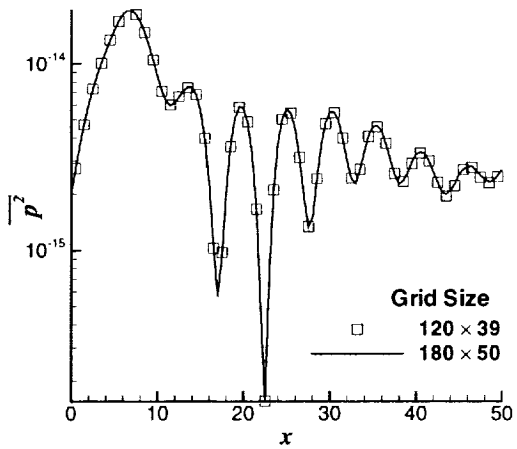
(a) $\overline{p^2}$ along $y = 10$
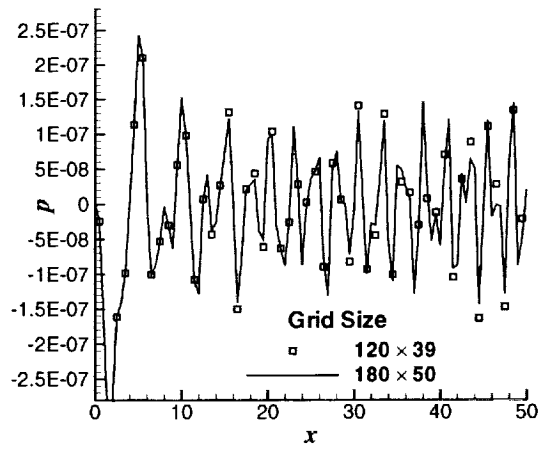
(b) p along $y = 1$

Figure 4: Grid refinement for St=0.6

Buffer Length

Using the coarsest grid that provided a grid independent solution, the length of the buffer was also varied to assess the required length to minimize reflections. Figure 5 reviews the results for the St=0.14 case. The solution along $y = 10$ is more sensitive to the buffer length, but the solutions for the two longest buffer lengths are nearly identical. There is almost no noticeable difference in the solutions along $y = 1$. At the higher frequency, the buffer length was decreased because the wavelength is much shorter. Figure 6 shows that the solutions showed very little variation for the two buffer lengths tested. However, the solution along $x = 50$ m, which is not shown, changed significantly, and a completely grid independent solution was never obtained. The acoustic signal is extremely weak in that region, so even small errors show up in the solution.

(a) $\overline{p^2}$ along $y = 10$ (b) p along $y = 1$
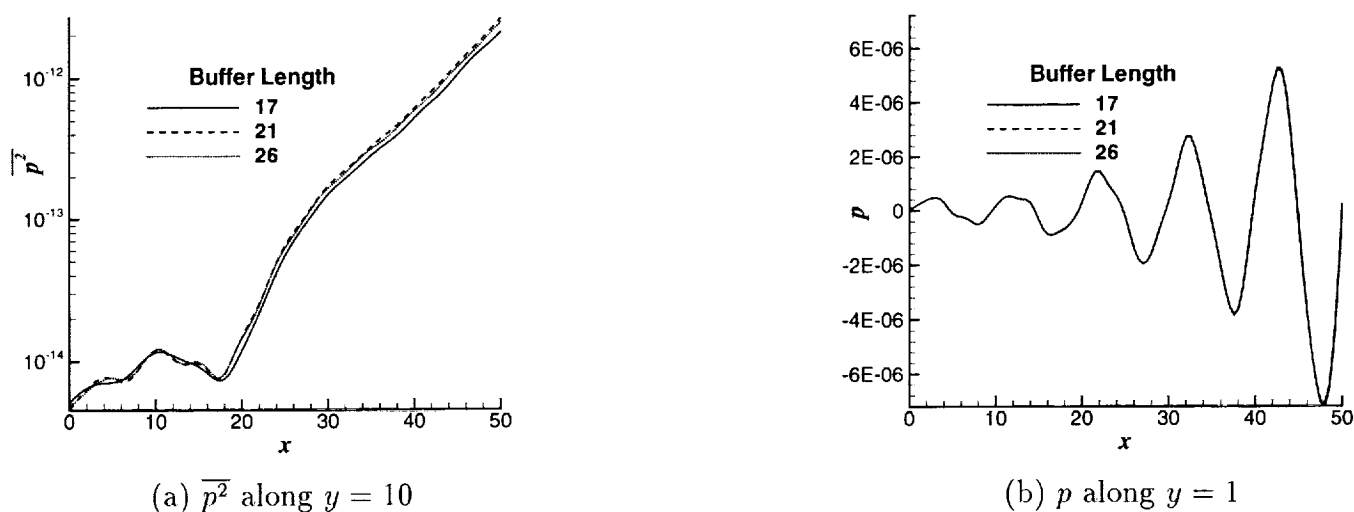
Figure 5: Variation of solution with buffer length for St=0.14

Resources

This section describes the resources used to obtain the solutions submitted to the workshop. All cases were run on a single processor of a 250 MHz, SGI R10k Octane. There were 3784 fifth-order rectangular elements for the $St = 0.14$ case. The grid was partitioned into several uniformly spaced regions and can be seen in figure 1. Eighteen elements were placed between 0.6 and 1.7 to resolve the shear layer, and 10 elements in the rest of the region up to $y = 10$. The grid was uniform in x with 58 elements between $x = -5$ m and 50 m. The buffer extended an additional 21 m at all inflow/outflow boundaries and required 710 elements. The grid was unaltered in the first 5 m of the buffer, and then the spacing was tripled. 15715 steps were required to run to a time of $t = 15T = 0.414$ s where T is the period of the source. The time step was $\Delta t = 9.54 \times 10^{-4}T = 2.635e\text{-}5$ s. The required CPU time was 5.7 hours.

There were 6816 fifth-order rectangular elements for the $St = 0.6$ case. A refined version of the grid used for the lower frequency was used. Again, eighteen elements were placed between 0.6 and 1.7 to resolve the shear layer, but 24 elements in the rest of the region up to $y = 10$. The grid was uniform in
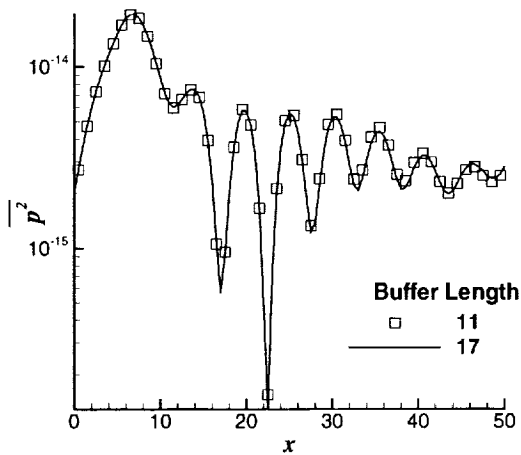
(a) $\overline{p^2}$ along $y = 10$
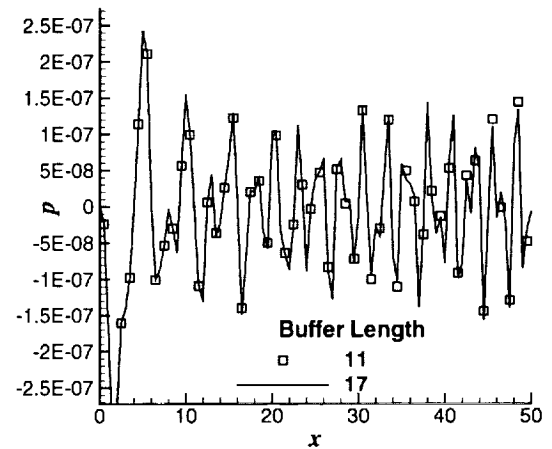
(b) p along $y = 1$

Figure 6: Variation of solution with buffer length for St=0.6

x with 110 elements between $x = -5$ m and 50 m. The buffer extended an additional 15 m at all inflow/outflow boundaries and required 1226 elements. The grid spacing in the buffer was tripled after 5 m. 13833 steps were required to run to a time of $t = 60T = 0.387$ s where T is the period of the source. The time step was $\Delta t = 4.12 \times 10^{-3}T =$ 2.794e-5 s. The required CPU time was 10.2 hours.

References

[1] Atkins, H. L., and Shu, C. W. Quadrature-free implementation of discontinuous Galerkin method for hyperbolic equations. *AIAA Journal*, **36(5)**, pp. 775–782, 1997.

[2] Atkins, H. L. Continued development of the discontinuous Galerkin method for computational aeroacoustic applications. AIAA Paper-97-1581, 1997. Third Joint CEAS/AIAA Aeroacoustics Conference, May 12-14.

[3] Atkins, H. L. Local analysis of shock capturing using discontinuous Galerkin methodology. AIAA Paper 97-2032, 1997. 13th AIAA Computational Fluid Dynamics Conference, Snowmass Village, Colorado, June 29-July 2.

[4] Lockard, D. P., and Atkins, H. L. Efficient implementations of the quadrature-free discontinous galerkin method. AIAA Paper No. 99-3309, July 1999.

[5] Kennedy, C. A., Carpenter, M. H., and Lewis, R. Low-storage explicit Runge-Kutta schemes for the compressible Navier-Stokes equations. to appear in *Applied Numerical Mathematics.*

[6] Israeli, M., and Orszag, S. A. Approximation of radiation boundary conditions. *Journal of Computational Physics*, **35**, pp. 115–135, 1981.

[7] Streett, C. L., and Macaraeg, M. G. Spectral multi-domain for large-scale fluid dynamic simulations. *Applied Numerical Mathematics*, **6**, pp. 123–129, 1989/90.
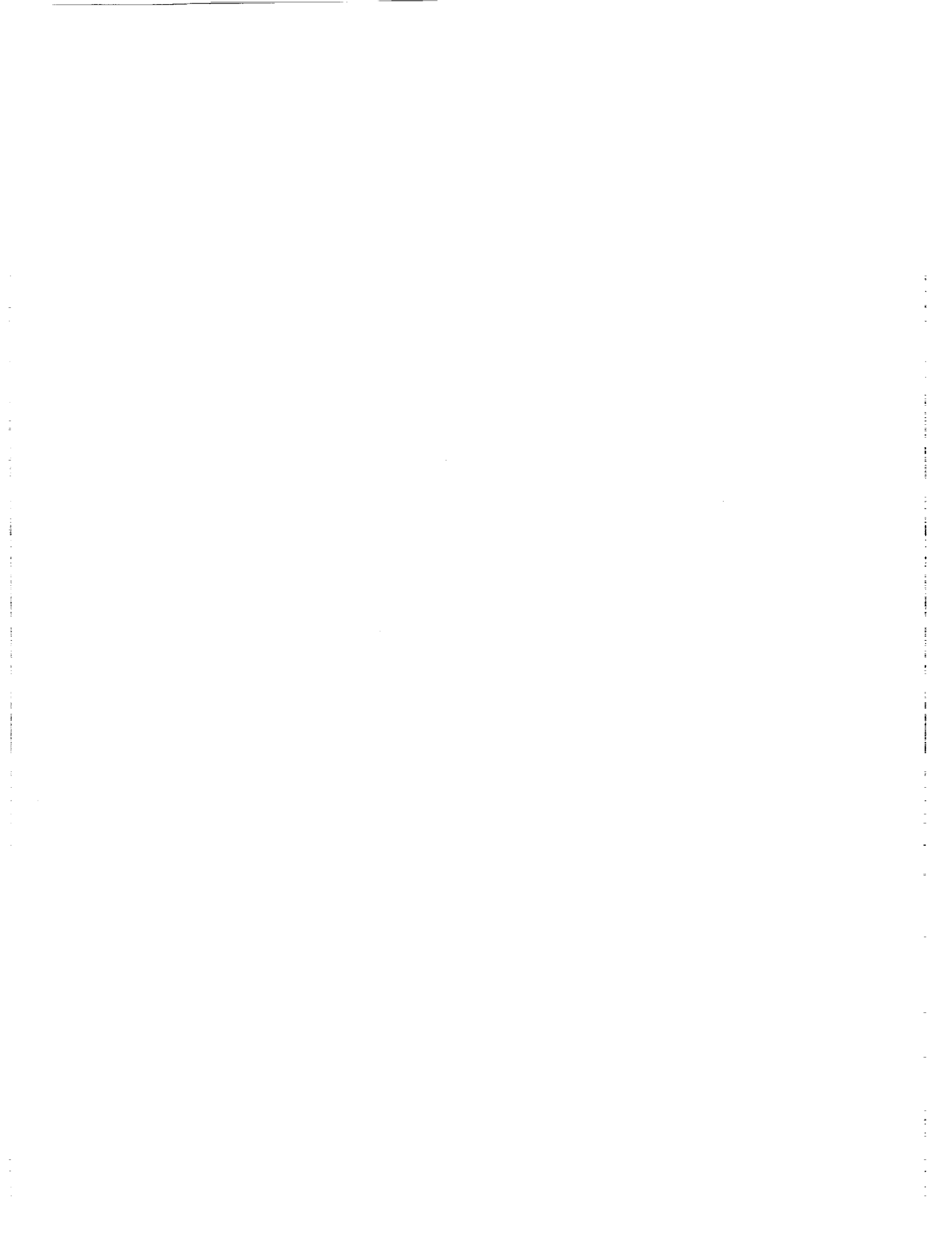
Generation and Radiation of Acoustic Waves from a 2-D Shear Layer Using the CE/SE Method

Ching. Y. Loh,* Xiao Y. Wang,† Sin-Chung Chang, and Philip C. E. Jorgenson
NASA Glenn Research Center, Cleveland, Ohio 44135, USA

In the present work, the Category 5 problem in the 3rd CAA Workshop is considered. An acoustic source inside of a 2-D jet excites an instability wave in the shear layer, resulting in sound Mach radiation.

The numerical solution is obtained by solving the Euler equations using the space time conservation element and solution element (CE/SE) method. Linearization is achieved through choosing a small acoustic source amplitude. The Euler equations are nondimensionalized as instructed in the problem statement. All other conditions are the same except that the Crocco's relation has a slightly different form. In the following, after a brief sketch of the CE/SE method, the numerical results for the Category 5 problem are presented. A detailed description of the 2-D CE/SE approach can be found in [1-2].

1. The 2-D CE/SE Euler Scheme

1.1. *Conservation Form of the 2-D Unsteady Euler Equations*

Consider a dimensionless conservation form of the 2-D unsteady Euler equations of a perfect gas:

$$\mathbf{U}_t + \mathbf{F}_x + \mathbf{G}_y = 0, \tag{1.1}$$

where the conservative flow variable vector $\mathbf{U}$ and the flux vectors, $\mathbf{F}$ and $\mathbf{G}$, are given in the usual way. Note that, in contrast to other schemes, not only $\mathbf{U}$ but also its spatial derivatives $\mathbf{U_x}$ and $\mathbf{U_y}$ are considered as unknowns. Also, the fluxes $\mathbf{F}$ and $\mathbf{G}$ are conveniently written in terms of components of $\mathbf{U}$. The integral form of Eq. (1.1) in the space-time 3-D Euclidean Space, E_3, is to be solved by the CE/SE scheme:

$$\oint_{S(V)} \mathbf{H_m} \cdot d\mathbf{S} = 0, \qquad m = 1, 2, 3, 4, \tag{1.2}$$

where $S(V)$ denotes the surface around a volume, V, in E_3 and $\mathbf{H_m} = (\mathbf{F_m}, \mathbf{G_m}, \mathbf{U_m})$. In the CE/SE scheme, the above flux conservation relation in space-time is the *only* mechanism that transfers information between node points (see filled and open circles in Fig. 1). No extrapolations (interpolations) across a stencil of cells are needed or allowed. The conservation element, CE, is the finite volume to which the integral flux condition (1.2) is to be applied (Fig. 2(a)). Discontinuities are allowed to occur in the interior of a conservation element. A solution element, SE, associated with a grid node is shown as a set of three interface planes in E_3 that pass through this node in Fig. 2(b). The solution vectors $\mathbf{U}$, $\mathbf{U_x}$, and $\mathbf{U_y}$ are calculated at this node. Within a given solution element $SE(j, k, n)$, where (j, k, n) is the node index, the flow variables are not only considered continuous but are also approximated by linear Taylor series expansions.

The grid is staggered in both time and space. For a spatial plane in E_3, the grid nodes, see Fig. 1, are grouped as two staggered sets Ω_1 (open circles) and Ω_2 (filled circles). The solution is alternatively evaluated on grid set Ω_1 or Ω_2 with each half time step. As can be seen in this figure, each 'interior' node then has three

---
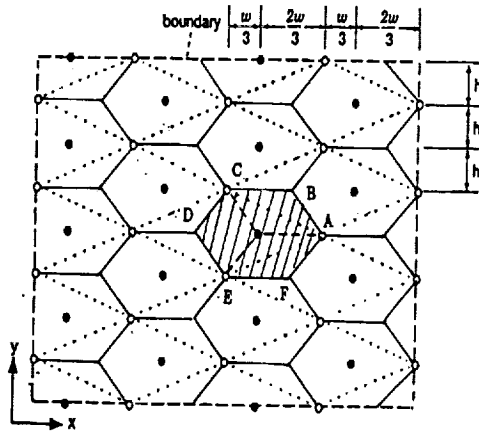
Fig. 1 Spatial node locations of the two grid sets (hollow and solid circles).

CE$_1$ (j, k, n) = box GFABG'F'A'B'
CE$_2$ (j, k, n) = box GBCDG'B'C'D'
CE$_3$ (j, k, n) = box GDEFG'D'E'F'

SE (j, k, n) = the union of four planes A'B'C'D'E'F', GBB''G'', GDD''G'', and GG''F'F and their immediate neighborhoods.
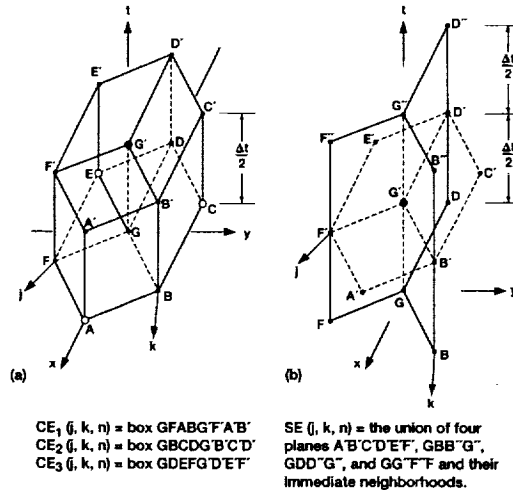
Fig.2 (a) conservation element, (b) solution element.

nearest neighbors at the previous half time step. Thus, there are three CE's associated with each node in this arrangement, consequently there are the same number of relations as there are unknowns. Figure 2 illustrates the three conservation elements associated with the node point G' and its three nearest neighbors A, C, and E at the previous time step.

For full details of the implementation of the 2-D CE/SE Euler method leading to the a, $a - \epsilon$ and weighted $a - \epsilon$ schemes, the reader is referred to [2]. The weighted $a - \epsilon$ scheme is used here. The adjustable parameter ϵ ($0 \leqslant \epsilon \leqslant 1$) controls the numerical dissipation, and the weighted scheme is intended for cases where discontinuities may be present in the inviscid flow field.

1.2. *Non-Reflecting Boundary Conditions*

In the CE/SE scheme, the idea of characteristics stemming from differential equation theory does not apply, since we are solving integral equations instead of differential equations. Rather, the following basic criterion is adopted: *In a CE located at the numerical domain boundary, a non-reflecting boundary condition is equivalent to letting the incoming flux from the interior domain to the boundary CE smoothly exit to the exterior of the domain.* As a matter of fact, the 2-D non-reflecting boundary condition (NRBC) has been proven to be successful even at the near field boundary [3-5]. There are various versions of the NRBC. The following are the typical NRBCs employed in our computations. For a grid node (j, k, n) lying at the domain boundary, the first one labeled type I requires that $(\mathbf{U}_x)^n_{j,k} = (\mathbf{U}_y)^n_{j,k} = 0$; while $\mathbf{U}^n_{j,k}$ is kept fixed at the initially given steady boundary value. Type II, for cases where there is a substantial gradient in the y direction, requires that $(\mathbf{U}_x)^n_{j,k} = 0, \mathbf{U}^n_{j,k} = \mathbf{U}^{n-1/2}_{j',k'}$, and $(\mathbf{U}_y)^n_{j,k} = (\mathbf{U}_y)^{n-1/2}_{j',k'}$. The proposed NRBCs above are all simple, truly multi-dimensional, and effective. Our experiences show that, in general, the reflection amounts to about 1% or even lower. However, when an extremely clean acoustic field is needed, such as in our current computation, a buffer zone of a few cells with increasing size is adopted at the computational domain outflow boundary. In the buffer zone, as in the rest of the computational flow field, the same Euler equations are solved with no special treatment needed.

2. Generation and Radiation of Acoustic Waves From a 2-D Shear Layer

In the CE/SE approach, we choose to solve the original Euler equations in the conservation form. The linearization is achieved by using a source of very small amplitude, A. The source term on the right hand side
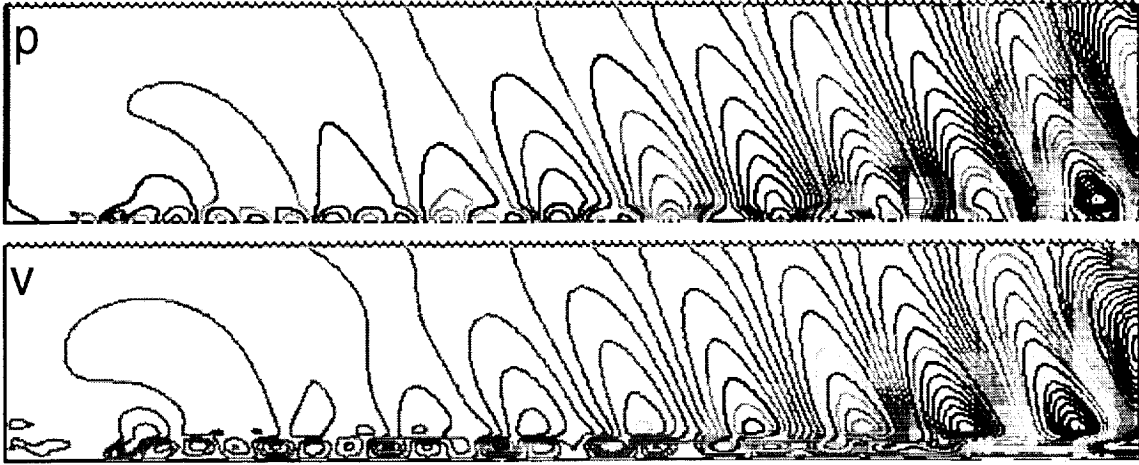
Figure 3: Isobars and v-contours at $t = 100$ (14T); 249×140 grid, $\Delta t = .01$.

of the energy equation has the form: $\frac{A}{\gamma-1} exp[-Bln(x^2 + y^2)]cos(\omega t)$, where the constant $B = 8$ and $A = .001$, or $.00005$ in the actual computations. The angular frequency, $\omega = 2\pi f$, is obtained from the given Strouhal number, St. Our investigation is mostly concentrated on the case with $St = 0.14$.

2.1. Low Strouhal number case: St=0.14

2.1.1. Preliminary computation

For this case, we have conducted several calculations with different grids. In the first calculation, the computational domain is chosen exactly the same as the physical domain, i.e., $-5 \leqslant x \leqslant 50$ and $0 \leqslant y \leqslant 10$. A grid of 249×140 nonuniform cells is adopted. The grid is uniform in x direction but stretched in y direction so that more points can be packed around the shear layer. As stated in the Workshop problem statement, the jet Mach number, M_j, of 2 is used. The acoustic source is located at the origin of the coordinate system with $A = 0.001$. A marching time step size, Δt, of 0.01 is chosen. Initially, the shear layer is already formed according to the given condition. The ambient flow is stationary and the static pressure p_0 is assumed constant over the entire domain.

Figure 3 shows the flow variables p and v at an early stage of (non dimensional) time $t = 100$, or 14 periods (10000 steps). The NRBC as mentioned in the section above is used, and no visible numerical reflection is found. Mach radiation from the supersonic shear layer is clearly displayed from the isobars and v contours. The Mach radiation direction forms about 23.5^o with the x axis and the wave length $\lambda = 9.58$. The angle and wave length agree well with the analytical solution. Since $A = 0.001$ is a relatively strong source, the radiation directly from the source is also visible from the p and v plots; but it is much weaker than the Mach radiation.

2.1.2. Detailed computation

In the second calculation, similar but slightly longer and higher computational domain is chosen to avoid any possible influence from the domain boundaries. A 279×144 grid (Grid A) is used, where 20 cells of increasing size at the outflow boundary are used as buffer zone to guarantee an extremely clean acoustic field. In addition, A is reduced to $.00005$. Figures 4a and 4b present the contours of p and v. Due to a weak A, direct radiation from the source is no longer visible; but the patterns of Mach radiation and their propagating direction remain the same. Let $p' = p - p_0$ be the sound fluctuation pressure, where $p_0 = \frac{1}{\gamma M_j^2} = .1785714$ is the nondimensional static pressure of the flow field and is assumed constant over the entire domain. Figure 5a displays p' along the line $y = 1$ at $t = 400$ (40000 steps) or the end of Period 28 (28T, T stands for period)
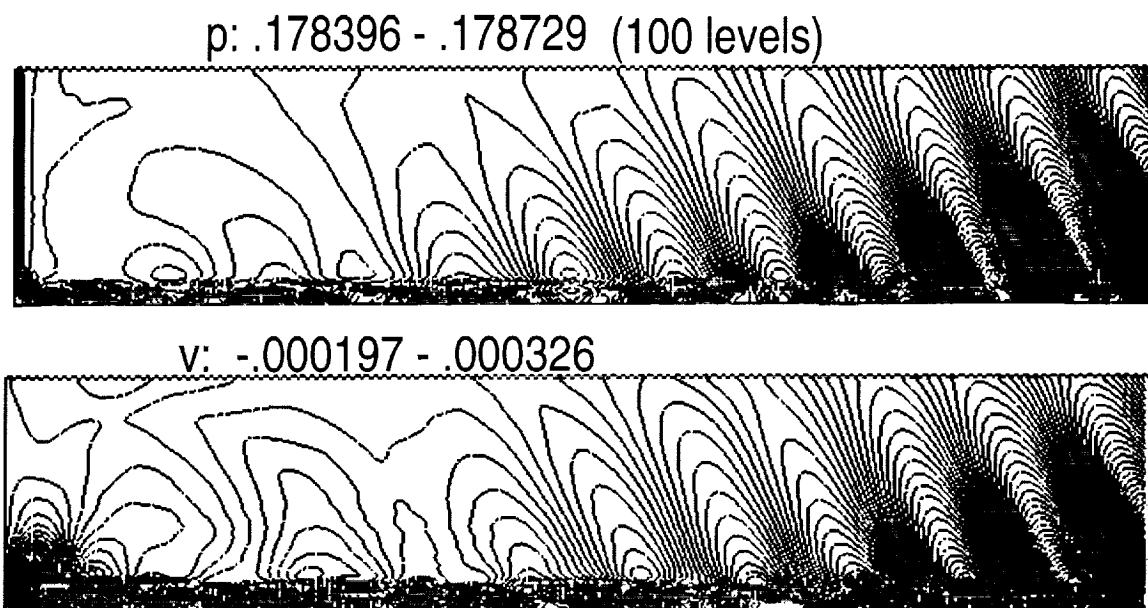
Figure 4: Isobars and v-contours at $t = 400$ (28T); 249×140 grid, $\Delta t = .01$.

and at $t = 600$ (60000 steps) or the end of Period 42 (42T). It shows that periodicity is already achieved at 28T. In the following, all the computations are run to t=28T.

A grid of 319×144 nodes (Grid B) is also tested. The only difference between Grids A and B is that Grid B has 30 more uniform cells in the x direction than Grid A. The purpose of this computation is to check the influence of the outflow NRBC. Figure 5b shows the sound intensity levels (square of RMS p') along the line $y = 10$ at $t = 400$ (40000 time steps or 28T) for Grid A and Grid B (the longer one). It is observed that the maximum difference is about 2×10^{-10}, far below the discretization error, so the outflow NRBC (with the buffer zone) is effective. It is also observed that p'^2 growth rate increases when $x \geqslant 40$.

A grid independence check is shown in Fig. 5c, 5d and 5e. For this purpose, Grid B is used as the coarse grid and a third grid, Grid C, of 619×144 nodes with half grid spacing in x direction but identical grid spacing in y direction is used as the fine grid. In each case, the Richardson extrapolation is applied to obtain a more accurate result. Figure 5c demonstrates the sound intensity level p'^2 (time average over 14T, 10000 time steps) at $y = 10$ with Grid B and Grid C. If the Richardson extrapolation is considered as the more accurate solution, then the solution with the coarse grid (Grid B) has a maximum error of about 1×10^{-9} and the solution with the fine grid has an even lower error of about 2×10^{-10}. Both errors are far below the nominal 2nd order accuracy of the CE/SE scheme.

Figure 5d displays the comparison of p' along $y = 1$ at the end of a cycle (28T). Good agreement between solutions of coarse and fine grids is found, although p' fluctuates at a level still far below the scheme's discretization error.

Figure 5e demonstrates the sound intensity level p'^2 (time average over 14T) at $x = 50$. Good agreement of the solutions with different grids is found for $y \geqslant 2$ but relatively 'larger' deviation ($2 - 4 \times 10^{-8}$) appears in the 2-D jet core area ($y \leqslant 1$). This suggests that the grid may need further refinement at the jet core. Also in this plot, since we are solving the Euler equations and nonlinear effect might take place, deviation from the results via linearized Euler equations is possible.

All the computations are conducted on a DELL Dimension XPS PC with Pentium II 450MHz processor and the Linux operating system. For case using Grid A, CPU time is about 4.5 sec. per time step (single precision). Figure 5a shows that a single precision computation does not introduce excessive error even after tens of thousands of time steps.
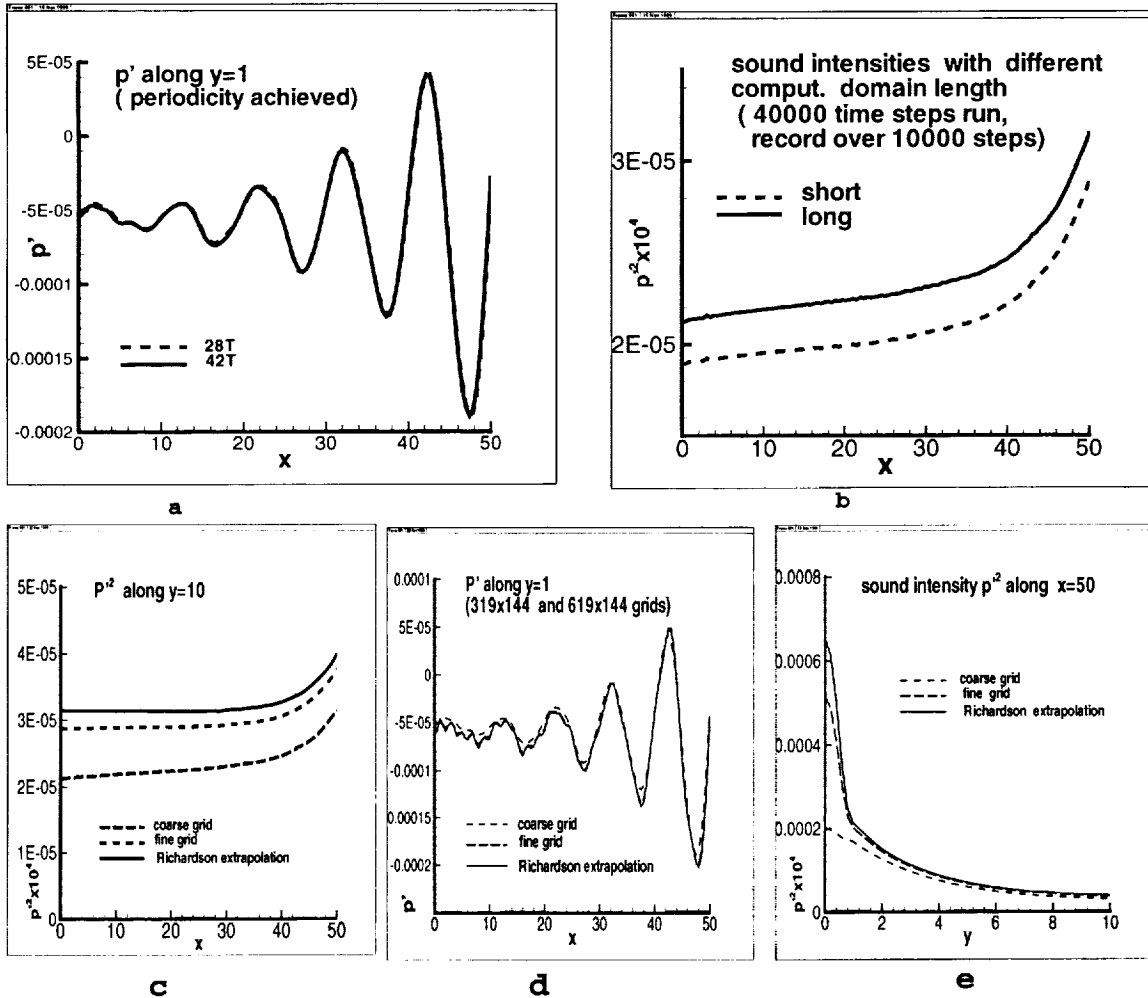
Figure 5: (a) periodicity achieved at 28T; (b) influences from the outflow boundary; (c)sound intensity (time-average over 14T, or 10000 time steps) p'^2 along $y = 10$; (d) p' at the end of 28T along $y = 1$, with different grids; (e) sound intensity along $x = 50$ (time average over 14T).

isobars at t=120T (40000 steps), St=0.6,529x190 grid, A=.00005, dt=0.01

Figure 6: Isobars at $t = 120T$; $St = 0.6$.
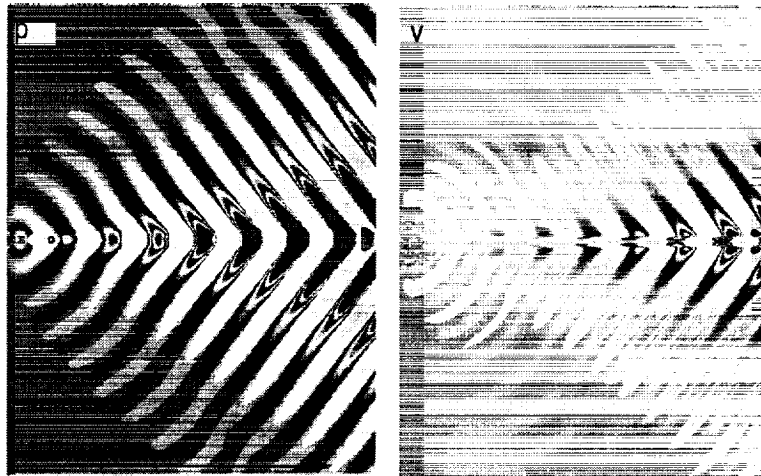
Figure 7: Isobars and v-contours for an axisymmetric jet at $M_j = 2.0$, $A = 0.001$ and $St = .2$.

2.2. High Strouhal number case: St=0.6

For this case, a grid of 529×190 nonuniform cells is adopted. The grid is actually uniform in x direction except the buffer zone at the outflow. Due to the higher frequency, more points are needed. The physical conditions are exactly the same as the case described above except the Strouhal number, St, is set equal to 0.6. The amplitude A remains at 0.00005.

For the acoustic flow field at 40000 time steps or $120T$, the isobars are shown in Fig. 6. It is observed that the Mach radiation is much weaker than the previous case while the direct radiation from the source becomes relatively strong. This result is not a surprise, since the eigen-frequency of Mach radiation is mostly associated with St around 0.2 and $St = 0.6$ is significantly higher.

2.3. Axisymmetric Mach radiation

The current 2-D problem is also extended to an axisymmetric case. The circular jet with $M_j = 2.0$, $A = 0.001$, and $St = 0.2$ is considered. Figure 7 shows good agreement in radiation angle and wavelength with other computations [6].

3. Concluding Remarks

In this workshop paper, the Category 5 problem is solved by the CE/SE scheme. The following features of the CE/SE scheme for CAA computations are demonstrated:

(a) The (2nd order) CE/SE scheme is robust, efficient and yields high resolution, low dispersion results similar to those of higher-order schemes;

(b) The novel NRBC based on flux balance is strikingly simple, genuinely multi-dimensional, and easy to implement. A combination of the NRBC and a small outflow buffer zone results in a low outflow boundary influence far below the discretization error.

References

[1] Chang, S. C., "The Method of Space-Time Conservation Element and Solution Element—A New Approach for Solving the Navier-Stokes and Euler Equations," Journal of Computational Physics. v. 119, 295-324 (1995).

[2] Chang, S.-C., Wang, X.-Y. and Chow, C.-Y., "The Space-Time Conservation Element and Solution Element Method—A New High Resolution and Genuinely Multidimensional Paradigm for Solving Conservation Laws. Part I: The Two-Dimensional Time-Marching Schemes," NASA TM-1998-208843 (1998). Also to appear in J. Comp. Phys. (1999).

[3] Loh, Ching Y., Hultgren, Lennart S. and Sin-Chung Chang, "Computing Waves in Compressible Flow Using the Space-Time Conservation Element Solution Element Method," AIAA Paper 98-0369 (1998).

[4] Loh, C. Y., Hultgren, L. S., Chang, S.-C. and Jorgenson, P. C. E., "Vortex Dynamics Simulation in Aeroacoustics by the Space-Time Conservation Element Solution Element Method," AIAA Paper 99-0359 (1999).

[5] Wang, X.Y., Chow,C.Y. and Sin-Chung Chang, "Numerical Simulation of Gust Generated Aeroacoustics in a Cascade Using the Space-Time Conservation Element Solution Element Method", AIAA Paper 98-0178 (1998)

[6] S.H.Shih, D.R.Hixon and R.R.Mankbadi, 'Zonal Approach for Prediction of Jet Noise', AIAA Journal of Propulsion and Power, Vol. 13, pp745-752.
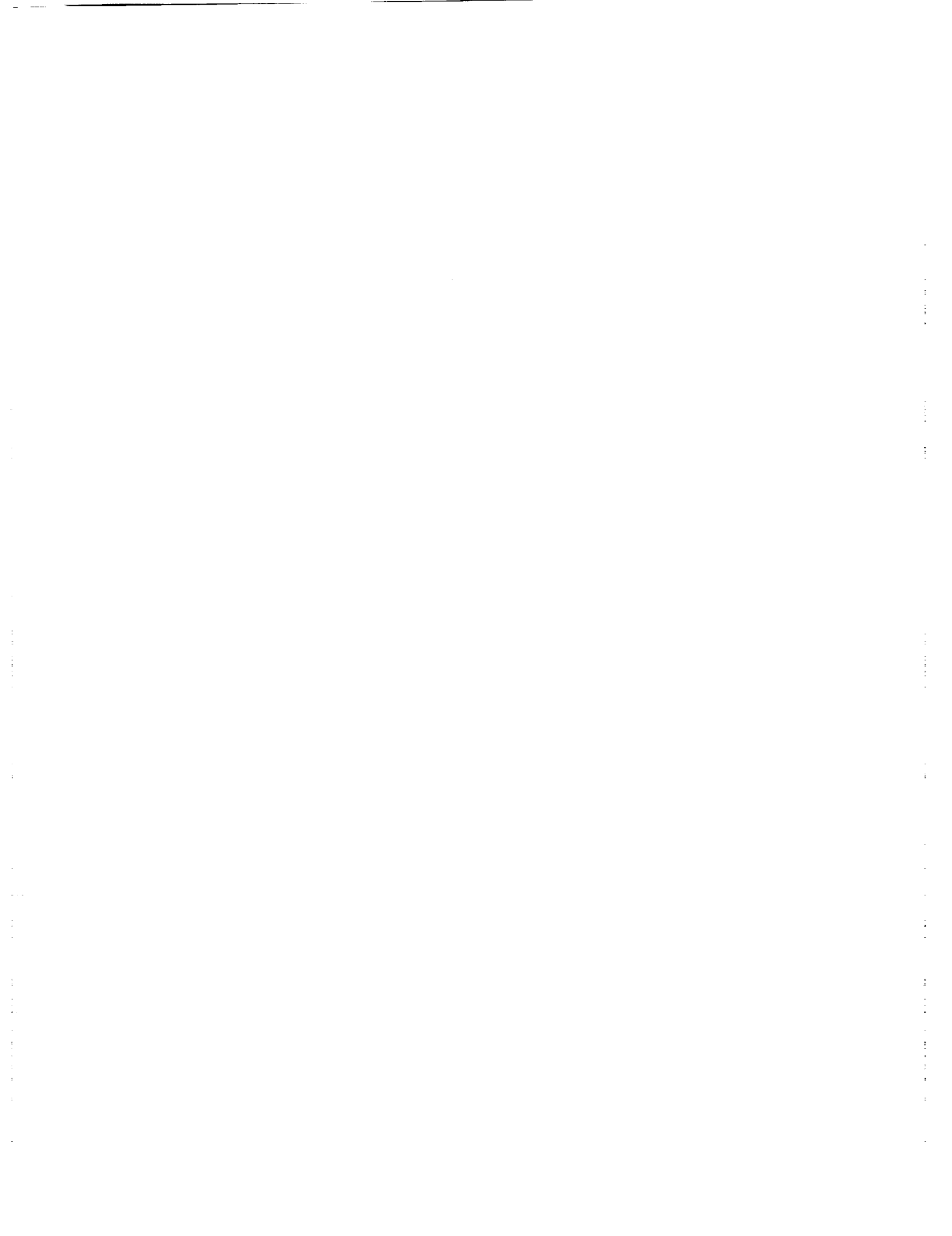
AEROACOUSTIC COMPUTATIONS OF THE UNSTEADY FLOWS
OVER A RECTANGULAR CAVITY WITH A LIP

Young J. Moon,[*] Sung R. Koh, Yong Cho, and Jong M. Chung
Department of Mechanical Engineering
Korea University
Seoul, Korea

Introduction

A problem of automobile noise involving feedback is solved. Figure 1 shows a schematic configuration of a cavity with a lip, which models a gap between the front and back doors of an automobile. A self-sustained free shear layer impingement on the downstream cavity edge generates a tonal noise, and this could be one of the major automobile airframe noise sources. In the experiment (ref. 1), turbulent boundary layer flows with free stream velocities of 26.8 m/s (case 1) and 50.8 m/s (case 2) are tested with the boundary layer thicknesses of 15 mm and 19 mm, respectively.

In the present study, we start with laminar flow calculations to understand basically what the important parameters computationally in simulating this type of flow are and how relevantly these solutions compare with experiment. So we calculate two cases with the same incoming velocities as the experiment, but reduced the boundary layer thickness to 10% of the cavity base length, L. The Reynolds numbers based on a displacement thickness are 850 and 1,620 correspondingly for the cases 1 and 2, and these are within a range between 600 and 3000 for the laminar instability of a free shear layer.

Since the flow speeds of both cases are low enough to be assumed as an incompressible flow (i.e. M_∞ = 0.077 and 0.147), a splitting approach proposed by Hardin and Pope (ref. 2) was taken. The unsteady incompressible Navier-Stokes equations are first solved by an unstructured triangular mesh flow solver, which is based on a cell-centered finite-volume formulation. Then the unsteady flow solutions are coupled with a set of acoustically perturbed equations for the acoustic field computations.

Numerical methods

The unsteady incompressible Navier-Stokes equations are solved by using a projection method based algorithm called SMAC (Simplified Marker and Cell) (ref. 3). First, the momentum equations are split into two steps:

$$\frac{\hat{u} - u^n}{\Delta t} = f\left(u^n, p^n\right) \tag{1}$$

$$\frac{u^{n+1} - \hat{u}}{\Delta t} = f\left(0, p^{n+1} - p^n\right) = f(0, \delta p) = -\nabla \delta p \tag{2}$$

Instead of solving eq. (2), we solved a divergent form of this while enforcing the continuity eq., which is then a Poisson equation of,

$$\nabla^2 \phi = \nabla \cdot \hat{u} \quad (\phi \equiv \delta p \cdot \Delta t) \tag{3}$$

The velocity and pressure fields at n+1 step are then updated from

$$p^{n+1} = p^n + \delta p = p^n + \frac{\phi}{\Delta t}, \quad u^{n+1} = u^n + \Delta t \cdot f(u^n, p^{n+1}) \tag{4}$$

---

[*] On a sabbatical leave at the Department of Mathematics, Florida State University, Tallahassee, FL 32306, U.S.A.

The governing equations (1), (3), and (4) are discretized on unstructured triangular meshes by a cell-centered based finite-volume method. The momentum equations (eq. (1)) are expressed as

$$\Omega_i \Delta Q_i / \Delta t_i = - \sum_{j=k(i)} \left[(F - F_v / Re) / \Delta y - (G - G_v / Re) / \Delta x \right]_{i,j} \tag{5}$$

and solved by a four-stage Runge-Kutta method in time, with the second-order upwind scheme applied to the convective fluxes in the right hand side. The Poisson equation, eq. (3), are also cast

$$\sum_{j=k(i)} \left(\phi_x \Delta y - \phi_y \Delta x \right) = \sum_{j=k(i)} \left(\hat{u} \Delta y - \hat{v} \Delta x \right) \quad \text{with} \quad \phi_x = \frac{1}{\Omega} \oint \phi \, dy \quad \text{and} \quad \phi_y = -\frac{1}{\Omega} \oint \phi \, dx \tag{6}$$

and solved by a point Gauss-Seidel relaxation method. These solution procedures are sub-iterated until satisfying the continuity equation at each time level.

The fluctuating quantities of velocities, pressure, and density from the mean state are defined as

$$u_i = U_i + u'_i, \quad p = P + p', \quad \rho = \rho_0 + \rho' \tag{7}$$

and a set of acoustic field equations [4] are derived by subtracting the incompressible Navier-Stokes equations from the compressible Navier-Stokes equations;

$$\frac{\partial \rho'}{\partial t} + \frac{\partial f_i}{\partial x_i} = 0, \quad \frac{\partial f_i}{\partial t} + \frac{\partial}{\partial x_j} \left[f_i \left(U_j + u'_j \right) + \rho_0 U_j u'_j + p' \delta_{i,j} \right] = 0, \quad \frac{\partial p'}{\partial t} + c^2 \frac{\partial f_i}{\partial x_i} = -\frac{\partial P}{\partial t} \tag{8}$$

where $f_i = \rho u'_i + \rho' U_i$ and $c^2 = \gamma P / \rho$. Equations (8) are solved by a MacCormack's predictor-corrector scheme, coupled with the solution procedure described above for the unsteady flow calculation.

Unsteady incompressible flow and acoustic field computations

A self-sustained periodically oscillating flow over a cavity with a lip is calculated on unstructured triangular meshes. In the present computation, all the length scales are non-dimensionalized by the cavity base length L. Figure 2 shows a global view of computational meshes with a total of 11,240 elements (case 1). One hundred and ten mesh points are used in the streamwise direction for the upstream region, where a laminar boundary layer develops and grows to a thickness close to $0.1*L$. For the downstream region where the vorticity waves propagate, 200 mesh points are used, since the grid resolution on that region might affect the unsteady solution accuracy of the flow in feedback mechanism. One other crucial scale for resolving the free shear layer instability is a normal grid spacing across it. So a minimal normal spacing of 0.001 is used for case 1, and 0.0005 for case 2, with 100 mesh points distributed in y-direction from the wall to the top boundary. The feedback mechanism is generated by disturbances from the downstream cavity edge, which then propagate upstream and enhance the vortex shedding from the lip. Therefore, in order to resolve this flow feature, 40 points are used across the lip, 60 along the lip, and 80 along the cavity opening. For the cavity inside flow, 100 points are also distributed along the left vertical wall. Also one more important factor that affects the solution of this problem is an outflow boundary condition. In this study, a convective boundary condition is imposed at the downstream outflow boundary. For example, a wave equation, $\partial \phi / \partial t + c \partial \phi / \partial x = 0$, is solved at the boundary, where ϕ is either u or v and a local streamwise velocity is used for c representing a local wave speed.

The self-sustained oscillating flows are computed for case 1 and the solutions of the first shear layer mode are presented in Fig. 3 for the two instants in one period. The first one (cavity: expansion) corresponds to a non-dimensional time, tU/L, at 35.9 and the second one (cavity: compression) is $0.41*T$ apart from the first one, where T indicates a period of oscillation close to 1.47. This value also corresponds to a Strouhal number of 0.68 or 1,215 Hz in frequency. This periodic behavior is demonstrated in Fig. 4 by a time history of v-velocity right before the downstream cavity edge. This regularity of unsteadiness in a feedback mechanism is well captured by the present grid (called grid-a), although this computation is quite sensitive

to the grid resolution on many aspects of parameters. We have done some of the grid sensitivity tests: (i) doubling the minimum normal grid spacing (grid-*b*) and (ii) halving the grid points in the streamwise direction for the downstream region where the vorticity waves convect (grid-*c*). The computed results for v-velocity at the downstream cavity edge are shown in Fig. 5. The regularity of this unsteady flow feature starts to break down on grid-*b* and gets even worse on grid-*c*. The computed periodicity of the flow, however, is still somewhat maintained on both grids. Comparing the vorticity waves computed on two different grids, Fig. 6 might indicate a point such that the grid resolution in the downstream region could play an important factor for imposing a different numerical impedance to the vorticity wave propagation, and that might feed back to affect the unsteady flow behavior upstream.

An acoustic field of this oscillating flow is computed on the cartesian grid shown in Fig. 7. Since the flow Mach number is quite low as 0.077 for case 1, the acoustic wave length is approximately close to 19 based on the relation, $\lambda / L = 1 / (St_L \cdot M_\infty)$, and therefore the computational domain is stretched out to ± 60 to include a couple of acoustic wavelengths. The number of grid points is selected such that roughly 25 points are included in one wave length for the use of the MacCormack's scheme in the computations. The computed sound pressure field is presented in Fig. 8, where the dashed line indicates the boundary of PML zones. One can see from the left figure that the PML boundary condition encounters some difficulties handling outgoing acoustic waves. The shaded flooding contours also show well a nearly circular radiation of sound waves generated from the cavity (shown as a very tiny stick-out at (0,0) in the figure). The computed acoustic wave length is close to 18, and the highest intensity of the radiated sound noise is between 135 and 180 degrees, meaning that the passengers sitting in the front seats will hear louder noise. The computed sound noise level outside of the cavity is approximately in the range of 80-90 dB. The sound pressure field near and inside of the cavity is shown in Fig. 9, indicating that the cavity inside experiences a lateral mode of compression and expansion, as a vortex shed from the lip starts to roll upstream of the opening and then impinges off the downstream cavity edge, alternately. Figure 10 shows a time history of the sound pressure at the center of the left vertical wall, and the sound pressure level (SPL) is predicted as 118 dB with a frequency of 1,215 Hz. Even though the computational condition (a relatively thin laminar boundary layer) is different from the experimental one (a thick turbulent boundary layer), quantitative comparisons are within a range. Figure 14 shows experimental results for cases 1 and 2. In case 1, the experiment seemed to experience a dual shear layer mode of one and two. The unsteady characteristics are not so strong as the case 2, but they are surely in the same frequency range as the present computational result, though SPL was quite over-predicted by the present calculation.

The computational results for the case 2 are also presented in figures 11-13. The computational results show a similar value of a Strouhal number close to 0.65 (or 2,080 Hz) and the acoustic wave length of 9.5, which is also quite close to an estimated value of 10. See Fig. 12 for the computed sound pressure field. The SPL of 133 dB inside the cavity left wall was also predicted from the computed result of p' shown in Fig. 13. The frequency and SPL are quite closely compared with experimental data shown in Fig. 14.

Conclusions

Unsteady flow computations of a self-sustained feedback flow are quite sensitive to the mesh size, computational domain, and outflow boundary conditions. Difficulties in keeping the numerical consistency are encountered in these unsteady flow computations and further investigations are in definite need, including the flow calculations with thick turbulent boundary layers.

References

1. Henderson, B.: Third CAA workshop on Benchmark Problems, http://www.math.fsu.edu/~smith/caaw bp99.html, 1999.
2. Hardin, J.C.; Pope, D.S.: Sound Generation by Flow over a Two-Dimensional Cavity, AIAA J. vol. 33, no. 3, 1995, pp.407-412.
3. Hirt, C.W.; Cook, J.L.: Calculating Three-Dimensional Flows around Structures and over Rough Terrain, J. Compt. Phys. Vol. 10, 1972, pp. 324-340.
4. Shen, W.Z.; Sorensen, J.N.: Comment on the Aeroacoustic Formulation of Hardin and Pope, AIAA J. vol. 37, no. 1, 1999, pp.141-143.
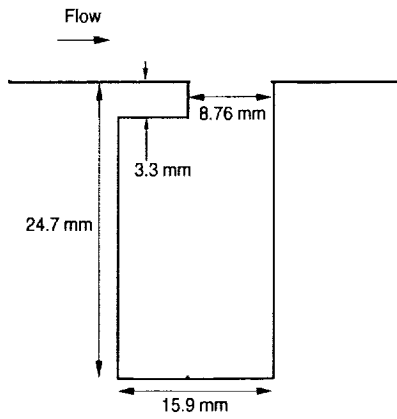
Fig. 1 A schematic of cavity configuration
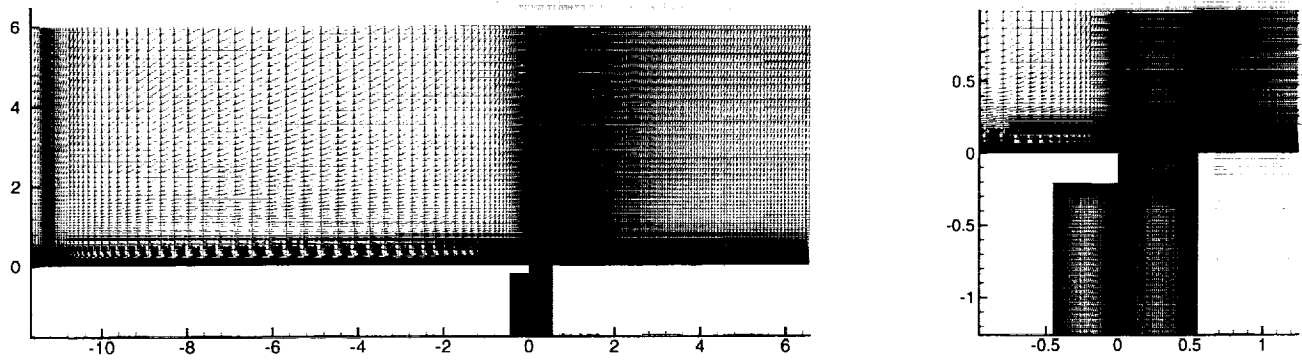
Fig. 2 Computational meshes (11,240 triangular elements): gobal and near cavity views
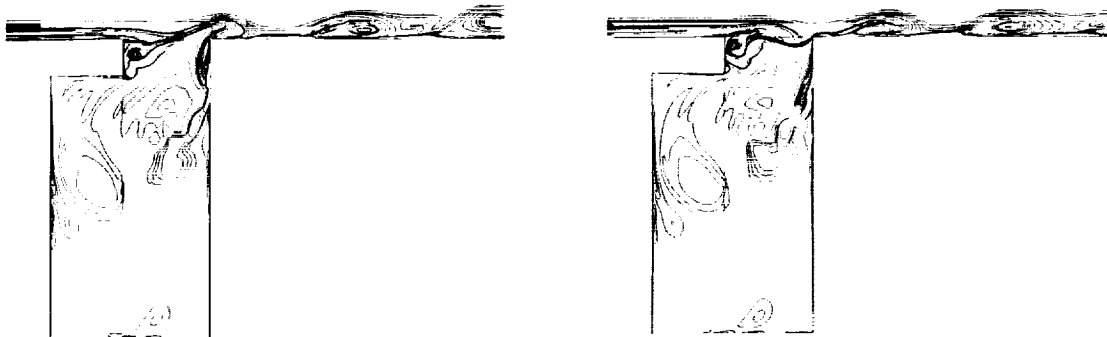
Fig. 3 Vorticity contours at two instants in a period (shear layer mode 1, case 1)
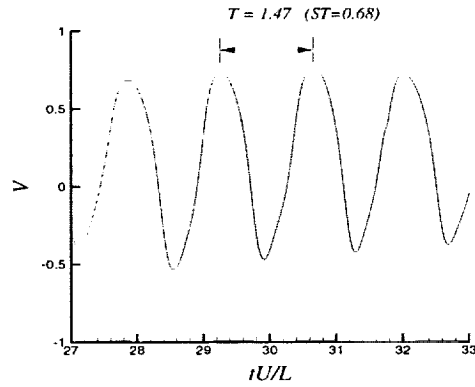
Fig. 4 Oscillating flow in a feedback (v-velocity near the downstream cavity edge, grid-*a*, case 1)
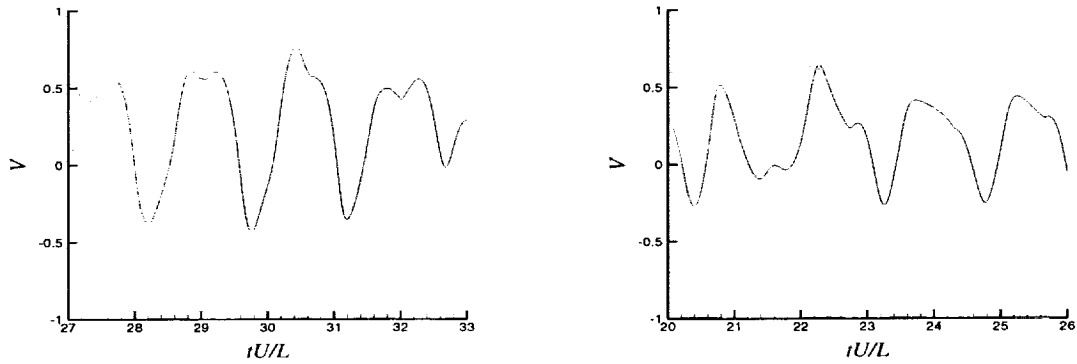
Fig. 5 Grid sensitivity test (grid-*b* & *c*)

(grid-*a*)

(grid-*c*)
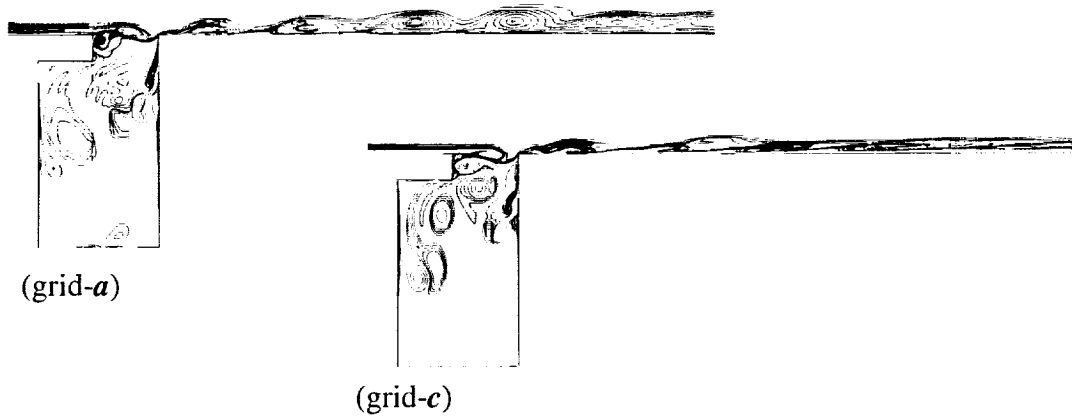
Fig. 6 Comparison of vorticity wave propagation
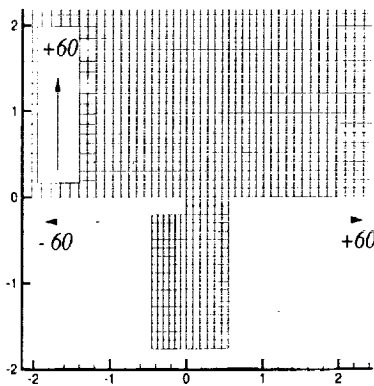
Fig. 7 Grid for acoustic field computation
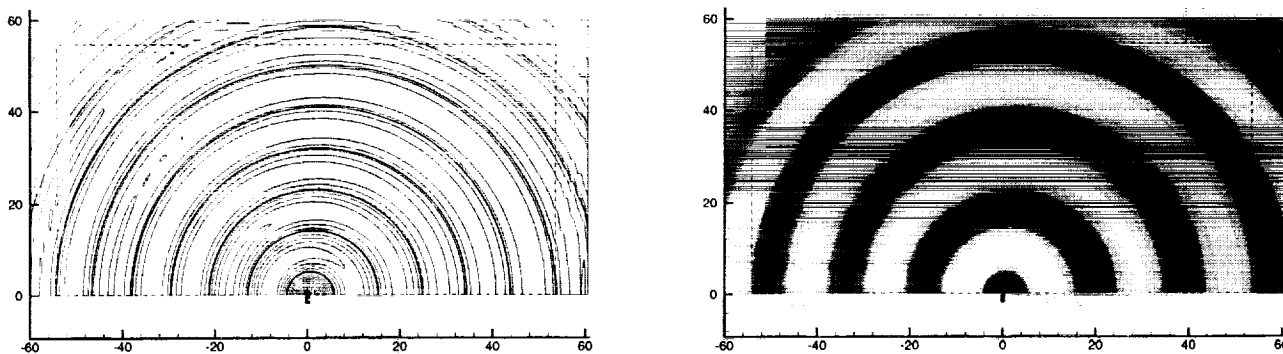
Fig. 8 Sound pressure fields (---: PML zones, case 1)
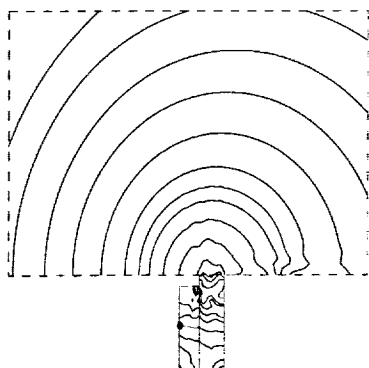
Fig. 9 Sound pressure field near the cavity
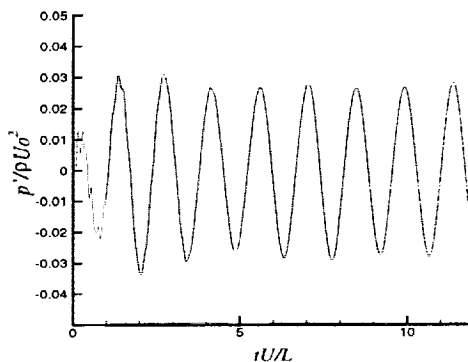
Fig. 10 Time history of p' inside cavity on
a center of the left wall (case 1)
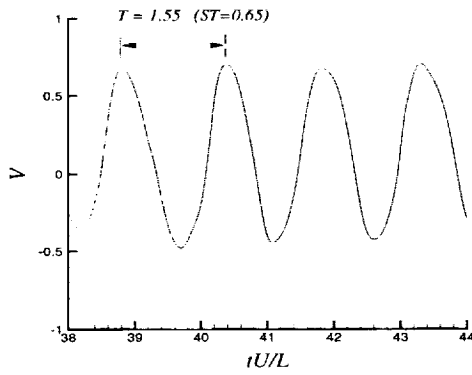
Fig. 11 Oscillating flow in a feedback (v-velocity near the downstream cavity edge, case 2)
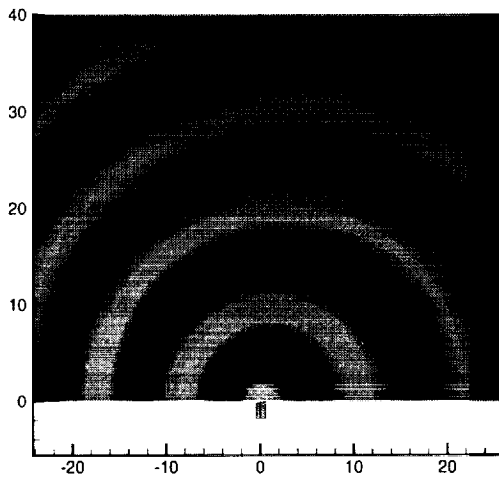
Fig. 12 Sound pressure field (case 2)
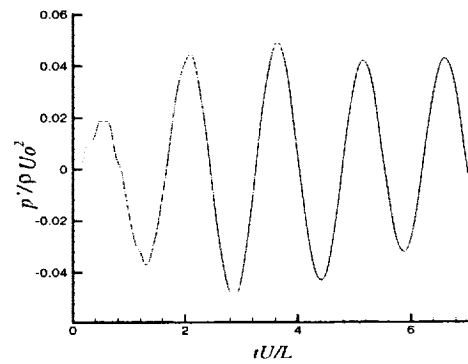
Fig. 13 Time history of p' inside cavity on a center of the left wall (case 2)
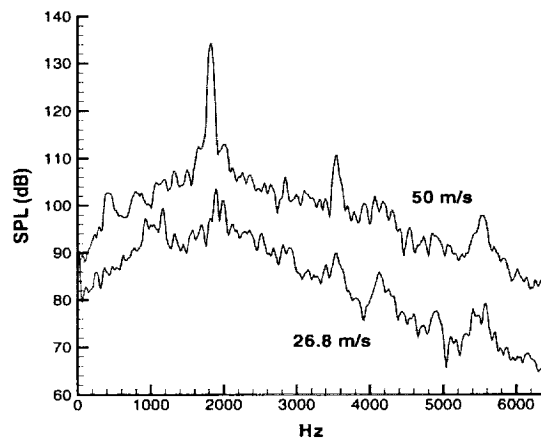
Fig. 14 SPL spectrum (case 1 & 2, Exp.: Henderson)
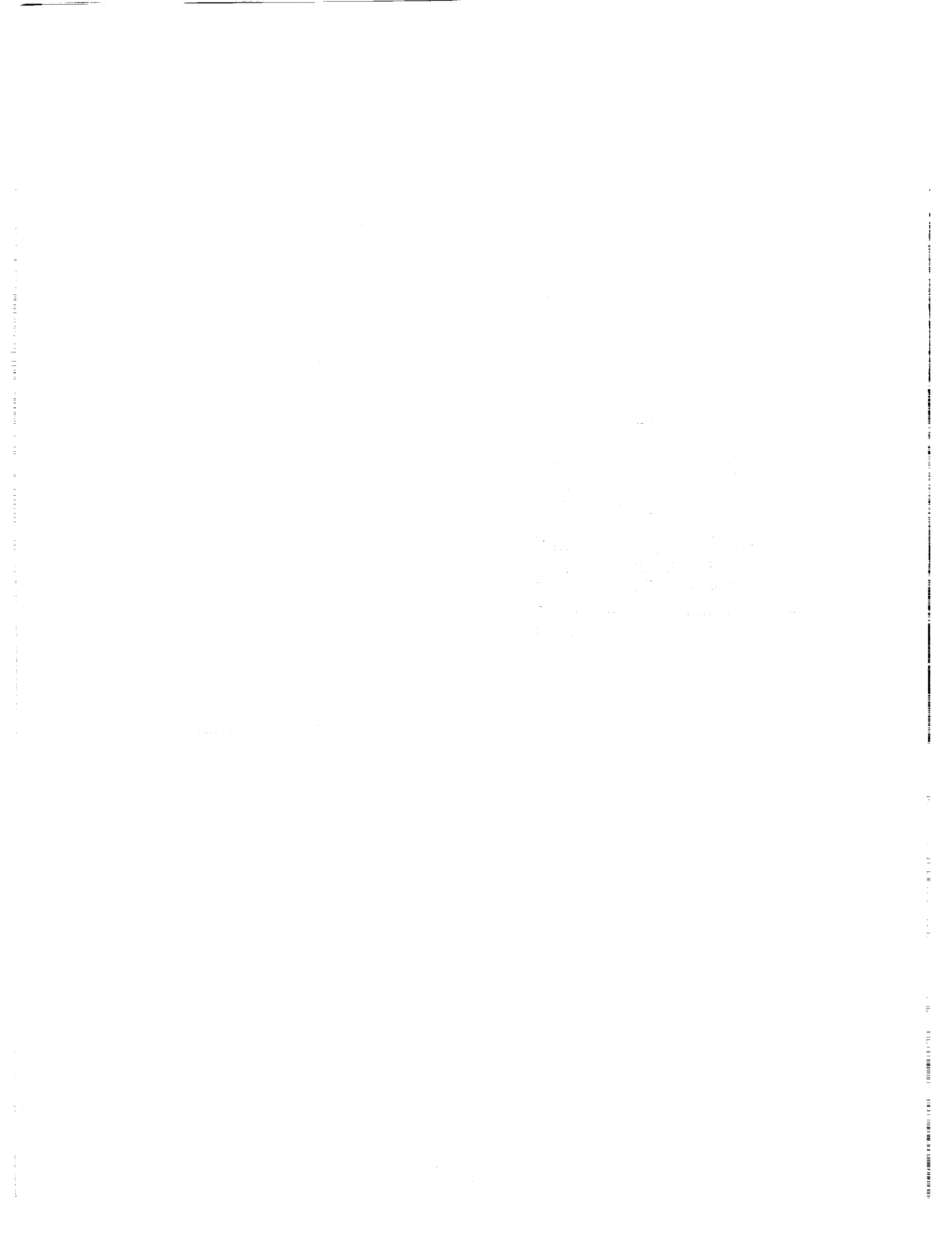
COMPUTATIONS OF SELF-INDUCED OSCILLATORY FLOW IN AN AUTOMOBILE DOOR CAVITY

G. B. Ashcroft, K. TAKEDA and X. Zhang

School of Engineering Sciences

University of Southampton

Southampton SO17 1BJ, UK

E-mail: (G.B.Ashcroft, ktakeda, xzhang)@soton.ac.uk

Abstract

We present results for computing the unsteady flow around a two-dimensional automobile door cavity. The solution of the unsteady, compressible Navier-Stokes equations is performed using the CFL3D code. By using a multi-block strategy, stretched grids refined in regions of high vorticity and small time steps we are able to capture fine vortical structures. A Wilcox k-ω turbulence model is used, which is integrated through to the wall. Simple extrapolation boundary conditions are used at the edge of the computational domain. Results for a flow speed of 50.9 m/s with a thick (2.2 cm at the cavity leading edge) incoming turbulent boundary layer are presented. These agree well with experimental data, although the presence of numerical reflections is of concern.

Problem Description

The benchmark problem, category 6, is representative of the flow around an automobile door cavity [1]. The geometry of the test case specified at the workshop is shown in Figure 1. In this paper we present results for a flow speed of 50.9 m/s with an incoming turbulent boundary layer which is 2.2 cm thick at the leading edge of cavity. A one-seventh power-law velocity profile is assumed,

$$\left\{ \frac{u}{U_0} \right\} = \left(\frac{y}{\delta} \right)^{\frac{1}{7}}, \tag{1}$$

where δ is the boundary layer thickness.

Computational results are non-dimensionalised in time and space with respect to the freestream speed of sound and cavity mouth width (8.76mm).

Solution Strategy

In order to compute the flow over the door cavity we use the CFL3D code (version 5). This is a multi-block, compressible, finite-volume, unsteady RANS solver [4, 5]. In the work presented here the code is configured to use second-order central differencing for both the viscous and inviscid terms. Fluxes at the cell faces are calculated by the flux-differencing-splitting method of Roe. An implicit three-factor approximate factorisation method is used to advance the solution in time. For the results presented here we use

CFL3D's t-TS sub-iteration option [5], with ten sub-iterations per physical time step to obtain second-order temporal accuracy. While CFL3D has not been specifically designed for aeroacoustics problems, it has been shown to be able to resolve flow structures responsible for noise generation processes when suitably fine mesh and time steps are used [2, 3].

For this door cavity test case we have used an eleven-block grid, shown in

Figure 2. A total of 68,736 grid cells are used. The grid is refined significantly along the walls ($\Delta y^+ < 1$ at the wall), and notably along the cavity mouth in order to resolve the shear layer correctly. Grid stretching within the cavity was kept to a minimum, but outside of the cavity grid stretching was used in conjunction with a coarse 'buffer region' to damp disturbances before they encountered the outflow boundary.

Adiabatic, no-slip boundary conditions are imposed on all solid walls in the computation. Along the upstream boundary the three velocity components are fixed describing the approaching turbulent boundary layer profile, together with the two turbulence quantities, k and ω, appropriate to the turbulence model being used. Wilcox's EDDYBL turbulent boundary layer program has been used to ensure that the specified profile provides the correct boundary layer at the cavity lip [6].

At the outflow boundary downstream of the cavity, zeroth-order extrapolation is used. Along the upper computational boundary characteristic 1-D Riemann invariants are solved. The use of these simple boundary conditions does, not surprisingly, lead to reflections, which degrade the solution quality for long-times.

For the results presented here the simulation is run to steady state initially for 1000 iterations. It is then restarted in unsteady mode. Numerical oscillations after the unsteady restart appear to settle down quickly, after around 2000 iterations. For the purposes of this benchmark we output the fluctuating pressure signal on the entire left-wall of the cavity.

All computations were run on Pentium III 450MHz and 500MHz PCs. CFL3D was compiled with Digital Visual FORTRAN (version 6), using aggressive compiler optimisations, under Windows NT 4 Workstation (Service Pack 4). Run times were of the order 24 hours for 2000 iterations (one shedding cycle) on a single 500MHz processor.

Results and Discussion

After several preliminary simulations with different grids, we found that we were able to resolve flow separation, secondary vortex structures, and corner flow within the cavity using the grid described above.

Vorticity contour plots for a single cycle of the cavity mouth shear layer are presented in Figure 3. We show results for the case with a large time step, $\Delta \tau = 0.01$. Refining the time step by an order of magnitude shows no change in the solution, with changes in peak-to-peak pressure amplitude of less than 0.1%. Therefore we are confident that the coarse time-step solution is converged.

A comparison of the measured [1] and calculated spectrum of the pressure signal is shown in figure 4 for the coarse time step, with frequency and amplitude comparisons given in Table 1. The spectrum was obtained by averaging the CFD results over an area equivalent to that covered by the (1/4 inch diameter) microphone in the experiment. A flat-top window was used for the FFT analysis, with a bandwidth of 49 Hz. Note that the experimental results are at a lower speed and with a thinner boundary layer than that specified in the original problem statement (and used in the CFD). This may account for some of the discrepancy between the experimental and computational results. Additionally, in the experiment the flow was seen to randomly switch preferred modes. Henderson [1] states that she does therefore not expect numerical results to be closer than approximately 3-5 dB of experiment.

The CFD results agree well with the experimental observations for the near-field initially. The presence of reflections that appear to be emanating from the upstream computational boundary is cause for serious concern, and is likely to be due to the specification of the inflow boundary condition, and the use of low order extrapolation at the outflow boundary. The use of a larger computational domain with non-reflecting boundary conditions is required for accurate long-time simulations to be run with confidence.

	Frequency (Hz)	Sound Pressure Level
Experiment	1824	134
50m/s, 1.9cm boundary layer	3552	111
Unsteady RANS CFD simulation	1960	141
50.9m/s, 2.2cm boundary layer	3920	111

Table 1. Frequency and sound pressure levels from pressure signal at the centre of the door cavity left wall

Conclusions

In this paper we present unsteady CFD results for an automobile door cavity using a compressible RANS code. With careful grid construction and small time steps the near-field unsteady flow is captured. The spectrum of the pressure signal agrees well. The use of fixed inflow and low-order extrapolation boundary conditions leads to reflections, which degrade the solution. Extending the computational domain and implementing non-reflecting boundary conditions are necessary to carry out longer-time simulations for far-field acoustic calculations. For this problem we have demonstrated that the use of a low-order, unsteady RANS code can give reasonable results for the near-field aeroacoustics and it is the lack of non-reflecting boundary conditions which currently limits the application of this approach.

Acknowledgements

References

1. Henderson, B., "Category 6 Automobile Noise with Feedback Benchmark Problem and Experiment", 3rd Computational Aeroacoustics Workshop, 8-10 November 1999, Ohio Aerospace Institute.

2. Singer, B.A., Brentner, K.S., Lockard, D.P. and Lilley, G.M., 1999, "Simulation of Acoustic Scattering from a Trailing Edge", 37th Aerospace Sciences Meeting and Exhibit, January 11-14, Reno, NV, AIAA Paper no. 99-0231.

3. Singer, B.A., Lockard, D.P., Brentner, K.S., Khorrami, M.R., Berkman, M.E. and Choudhari, M., 1999, "Computational Acoustic Analysis of Slat Trailing-Edge Flow", 5th AIAA/CEAS Aeroacoustics Conference, May 10-12, Greater Seattle, Washington, AIAA Paper no. 99-0231

4. Rumsey, C., Biedron, R. and Thomas, J., "CFL3D: Its History and Some Recent Applications", TM 112861, NASA, May 1997, presented at Godonov's Method for Gas Dynamics Symposium, Ann Arbor, MI.

5. CFL3D User's manual (Version 5.0), Krist, S.L., Biedron, R.T. and Rumsey, C.L., NASA/TM-1998-208444.

6. Turbulence Modelling for CFD, Wilcox, D. C., DCW Industries Inc., ISBN 0-9636051-0-0

Figures

A=15.9mm
B=24.7mm
C=8.76mm
D=3.3mm
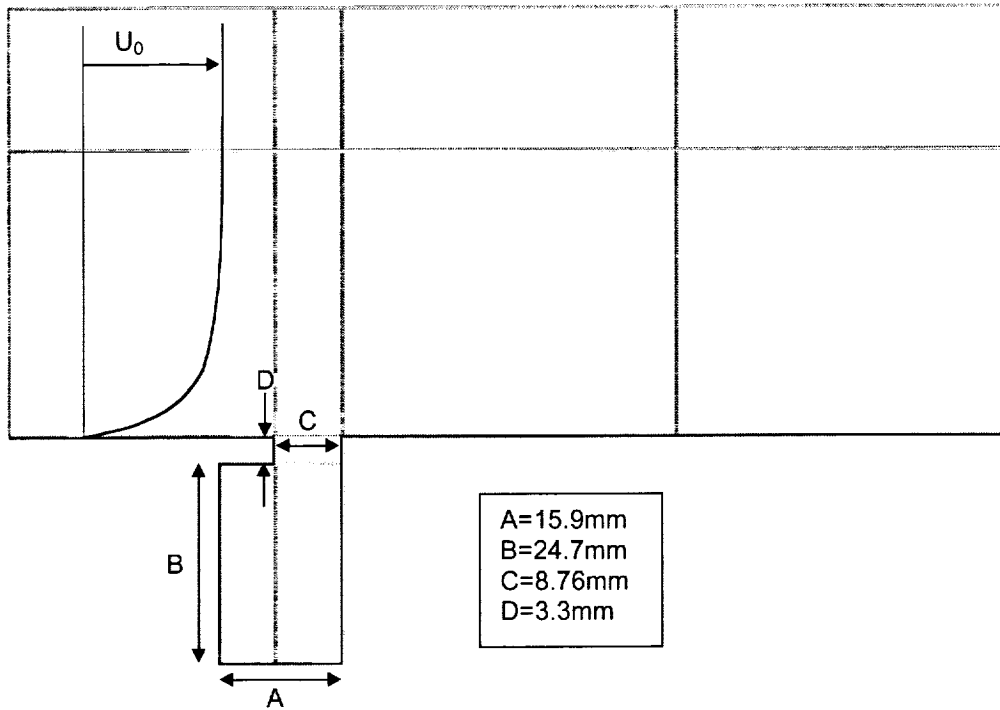
Figure 1: Door cavity geometry with multi-block structure
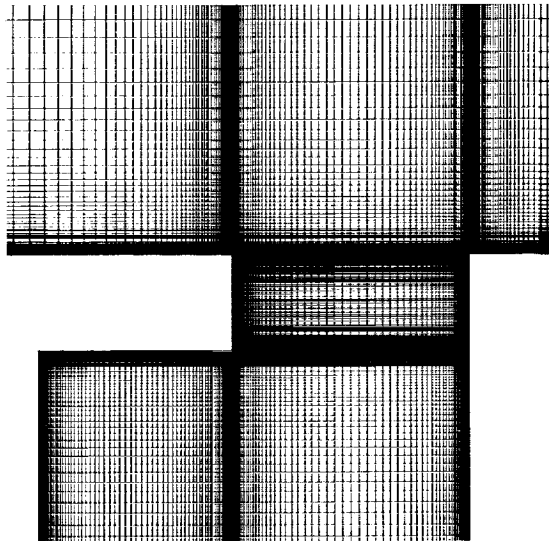
Figure 2: Computational grid around cavity mouth

a) τ=20

b) τ=24

c) τ=28

d) τ=32

e) τ=36
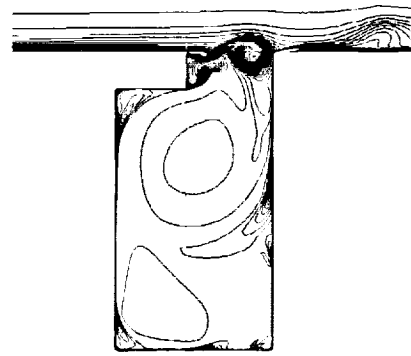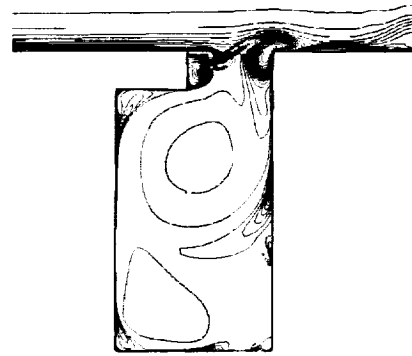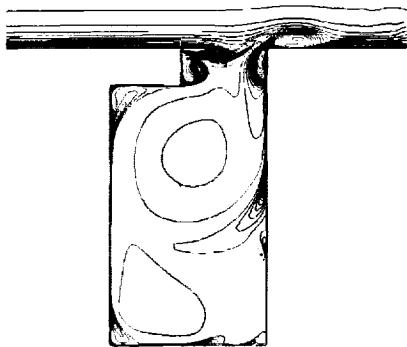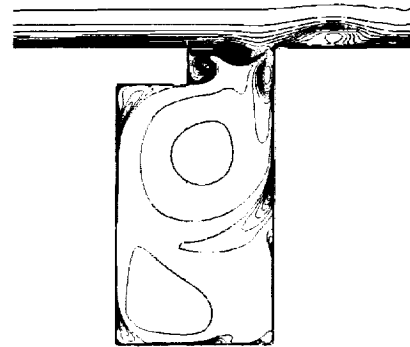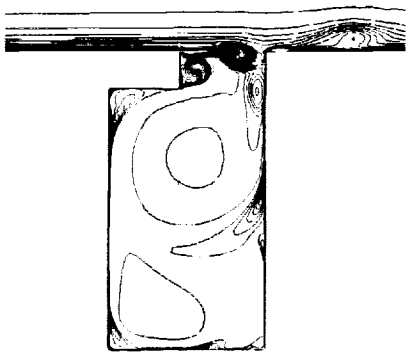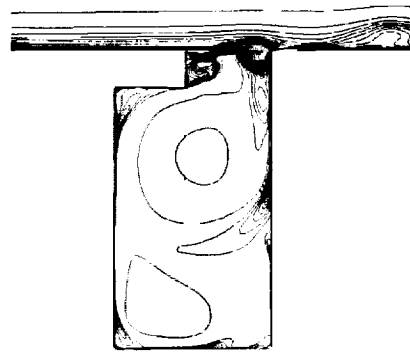
f) τ=40

Figure 3: Vorticity plots at non-dimensional times (τ) 20, 24, 28, 32, 36 and 40
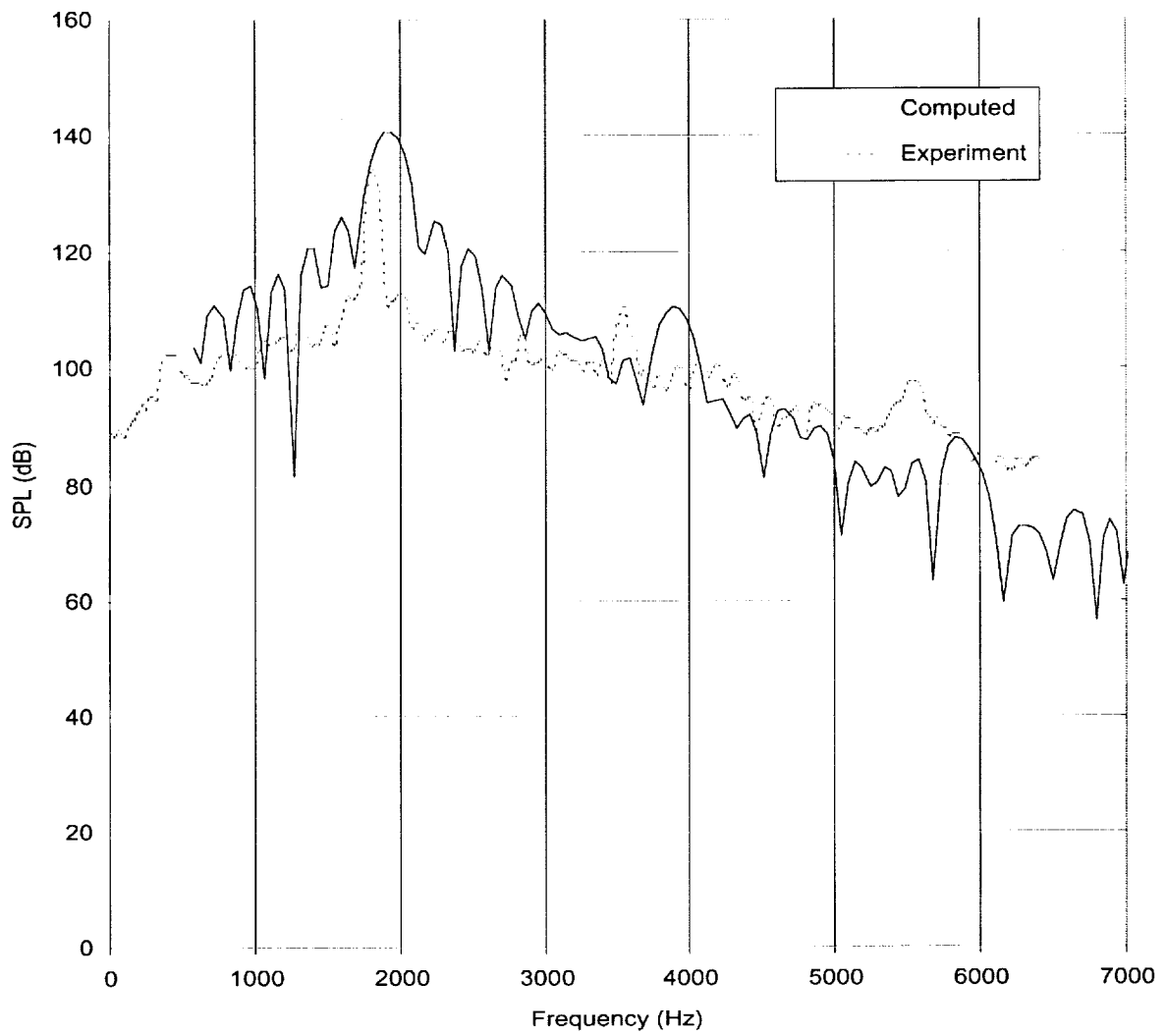
Figure 4: Sound pressure level spectrum

A PARALLEL NUMERICAL SIMULATION OF AUTOMOBILE NOISE INVOLVING FEEDBACK

Chingwei M. Shieh* and PHILIP J. MORRIS[†]
Department of Aerospace Engineering
The Pennsylvania State University, University, PA 16802

Abstract

A parallel numerical simulation of cavity flow and noise at low subsonic Mach number is presented in this paper. The one-equation Spalart-Allmaras model is implemented to simulate the turbulent flow phenomena in two dimensions. In order to prevent excessive numerical dissipation from the turbulence model in separated flow regions, the Detached Eddy Simulation (DES) proposed by Spalart *et al.* [1] is used. Laminar and turbulent simulations have been carried out for a Mach 0.15 flow. An incoming boundary layer thickness of $0.05D$ is selected to insure tone generation. Various phenomena of the cavity flow are examined. Frequencies and sound pressure levels of the tones are calculated and presented in this paper.

1 Introduction

Significant attention has been paid to the reduction of automobile aerodynamic noise in recent years. This is due to a tremendous decrease in the noise generated by engines, tires, transmission, and many other components. Since a major source of automobile aerodynamic noise is due to flow over cavities such as open windows or door gaps and seals, the elimination of cavity noise can offer a commercial advantage in the automobile industry by creating a more comfortable and environmentally friendly vehicle. In this paper, both direct numerical simulations and unsteady Reynolds Averaged Navier-Stokes (RANS) calculations of a subsonic flow over a deep cavity are presented. This research is part of an effort to understand the noise generation mechanisms of deep cavities, and ultimately to minimize this noise source.

2 Numerical Approach

The governing equations that describe the near-field turbulent flow and the far-field acoustics are the compressible Navier-Stokes equations. With the implementation of Favre averaging and the assumption of the

---

*Graduate research assistant
[†]Boeing/A. D. Welliver Professor of Aerospace Engineering

Boussinesq eddy viscosity approximation, the governing equations, using a standard nomenclature, can be written as

$$\frac{\partial \rho}{\partial t} + \frac{\partial \rho u_i}{\partial x_i} = 0 \tag{1}$$

$$\frac{\partial (\rho u_i)}{\partial t} + \frac{\partial}{\partial x_j}(\rho u_j u_i) = -\frac{\partial p}{\partial x_i} + \frac{\partial}{\partial x_j}(\sigma_{ij} + \tau_{ij}) \tag{2}$$

$$\frac{\partial (\rho E_t)}{\partial t} + \frac{\partial}{\partial x_j}\left[\rho u_j \left(E_t + \frac{p}{\rho}\right)\right] = \frac{\partial}{\partial x_j}\left[-q_{L_j} - q_{T_j} + u_i(\sigma_{ij} + \tau_{ij})\right] \tag{3}$$

where σ_{ij} is the laminar viscous stress tensor, τ_{ij} is the Reynolds stress tensor, and q_{T_j} is the turbulent heat flux. Notational differences between Reynolds and Favre averaging have been omitted for simplicity. The Reynolds stress tensor is modeled with the use of the one-equation Spalart-Allmaras turbulence model [2], where the eddy viscosity is determined from

$$\frac{\partial \tilde{v}}{\partial t} + u_j \frac{\partial \tilde{v}}{\partial x_j} = c_{b1}\tilde{S}\tilde{v} - c_{w1}f_w \left(\frac{\tilde{v}}{d}\right)^2 + \frac{1}{\sigma}\frac{\partial}{\partial x_k}\left[(v + \tilde{v})\frac{\partial \tilde{v}}{\partial x_k}\right] + \frac{c_{b2}}{\sigma}\frac{\partial \tilde{v}}{\partial x_k}\frac{\partial \tilde{v}}{\partial x_k} \tag{4}$$

$$v_t = \tilde{v}f_{v1}, \quad f_{v1} = \frac{\chi^3}{\chi^3 + c_{v1}^3}, \quad \chi \equiv \frac{\tilde{v}}{v}. \tag{5}$$

v and v_t are the kinematic laminar and eddy viscosities respectively. A modification to the turbulence production term in Eq. (4), proposed by Edwards and Chandra [3], has been implemented to provide a more stable calculation in modeling near-wall behavior. In order to prevent excessive numerical dissipation from the turbulence model in separated flow regions, a hybrid RANS/LES approach called the Detached Eddy Simulation (DES), proposed by Spalart et. al [1], has been used. In DES, the distance to the closest wall, d, in Eq. (4) is replaced with $\tilde{d} \equiv \min(d, C_{DES}\Delta)$ where $\Delta \equiv \max(\Delta_x, \Delta_y)$ and C_{DES} is an adjustable constant, set to unity in present calculations.

The governing equations are discretized with a fourth-order, seven-point stencil, DRP differencing operator spatially, and are integrated in time explicitly with the use of a fourth-order Runge-Kutta method. A parallel multiblock implementation with pipeline block communication is employed to take advantage of the geometry of the problem. This is an extension to the parallel multiblock implementation proposed by the authors [4]. Solid wall boundaries are assumed to be adiabatic, and the no-slip boundary condition is applied. A small section of the wall upstream of the cavity is assumed to be a slip wall. This allows the flow to trigger the onset of boundary layer growth naturally, while simplifying the implementation of the inflow boundary condition so that a Riemann invariant boundary condition can be employed. For the far-field and the outflow boundaries, the MOC boundary condition is used.

For the laminar calculation, the number of grid points used for the computational meshes are 171×97 and 59×113 for the upper block and the cavity block respectively. The meshes used for the turbulent calculation have 171×113 and 59×135 grid points respectively for the two blocks. Simulations are run on the new PC cluster at Penn State, with 32 dual 500 MHz Intel Pentium III nodes (64 processors) and a fast ethernet network with 100 Mbits/s transfer rate. The equivalent single CPU/grid point/time step of the code is 226 μs, and about 30% of the run time is spent on communication. This is reasonable, since additional communications need to be performed for the block interface. The relative communication time will drop further for three-dimensional calculations or larger problems.

3 Results and Discussions

Initial time-dependent RANS calculations with the splitter plate in the original configuration and an incoming turbulent boundary layer thickness of about 10% of the total cavity depth showed that the flow was not able to maintain a self-oscillatory mode. According to the the experimental study by Sarohia [5], for a thin incoming boundary layer such that $\delta_0/D < 0.5$, the value of the nondimensional length of the cavity $(L_{min}/\delta_0)\sqrt{Re(\delta_0/D)}$ has to be above 290 for a sustained flow oscillation to occur. Therefore, to satisfy this criterion, a new configuration has been set up in which the splitter plate has been removed. This eliminates the difficulty that arises from the multiple scales present in the original configuration, and isolates the investigation to the effects of boundary layer thickness on cavity flow oscillations.

Both laminar and turbulent calculations have been performed for the new configuration, and results are discussed in this section. The Mach number of the flow is 0.15, and the Reynolds numbers based on the cavity depth are 15000 and 335041 for the laminar and turbulent calculations respectively. These Reynolds numbers correspond to an incoming boundary layer thickness δ_0/D of 0.05 in both cases. For the laminar case, the nondimensional cavity length based on Sarohia's analysis is calculated to be 317, so this satisfies the minimum cavity length criterion for flow oscillations. It is still not clear whether the same criterion can be applied to turbulent flows.

(a) $t = 266.02$ (b) $t = 268.02$ (c) $t = 270.02$
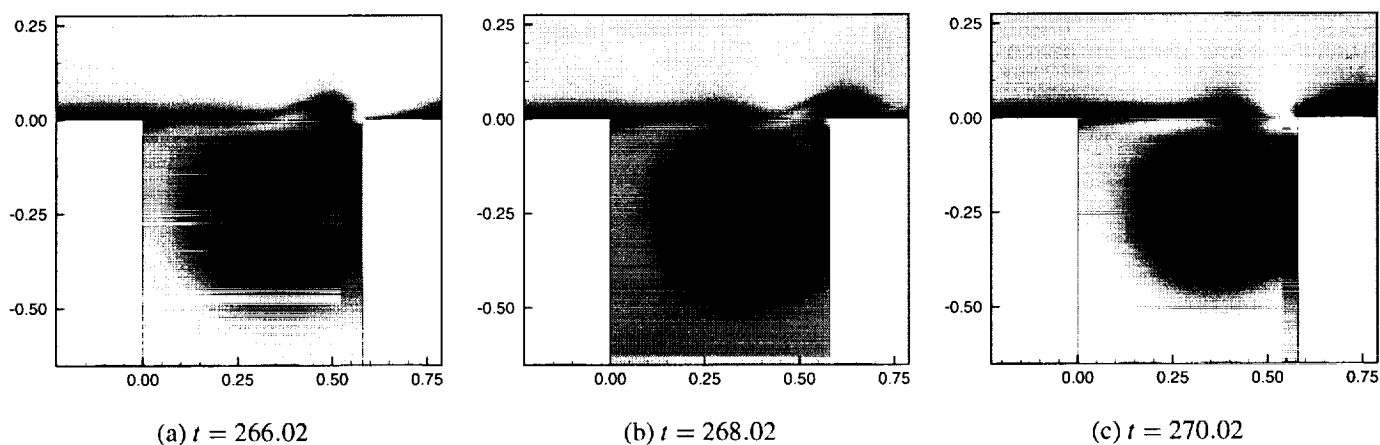
Figure 1: Instantaneous contours of nondimensional density for a laminar, $M = 0.15$, $Re = 15000$, $L/D = 0.58$, $\delta_0 = 0.05D$ cavity flow at different times, corresponding to approximately one period of the large-scale structure oscillation. Contour levels range from 0.995 (dark) to 1.001 (light).

Figure 1 shows the instantaneous contours of nondimensional density (ρ/ρ_0) for the laminar calculation at different nondimensional times that correspond to approximately one period of the large-scale structure evolution inside the shear layer. As the vortical structure impinges on the downstream cavity wall, part of it spills over the cavity and continues to travel downstream, forming smaller vortical structures along the downstream flat plate. The rest of the vortex rolls underneath the downstream cavity edge, creating a recirculating region. The presence of a well-formed, trapped vortical structure is more prominent in deep cavities, and the present calculation agrees qualitatively with the experimental work of Roshko [6] and Maull and East [7]. Unlike shallow cavities, the flow oscillates in a depth mode for deep cavities, more like a Helmholtz resonator. This is shown in Figure 2. The instantaneous pressure is sampled for a nondimensional time of 32 that corresponds

to approximately four periods of the large-scale structure evolution in the shear layer. The sound pressure levels are calculated from this data, and the acoustic field indicates that the sound source due to the flow over the cavity behaves like a monopole, as shown in Figure 3.

(a) $t = 266.02$ (b) $t = 268.02$ (c) $t = 270.02$
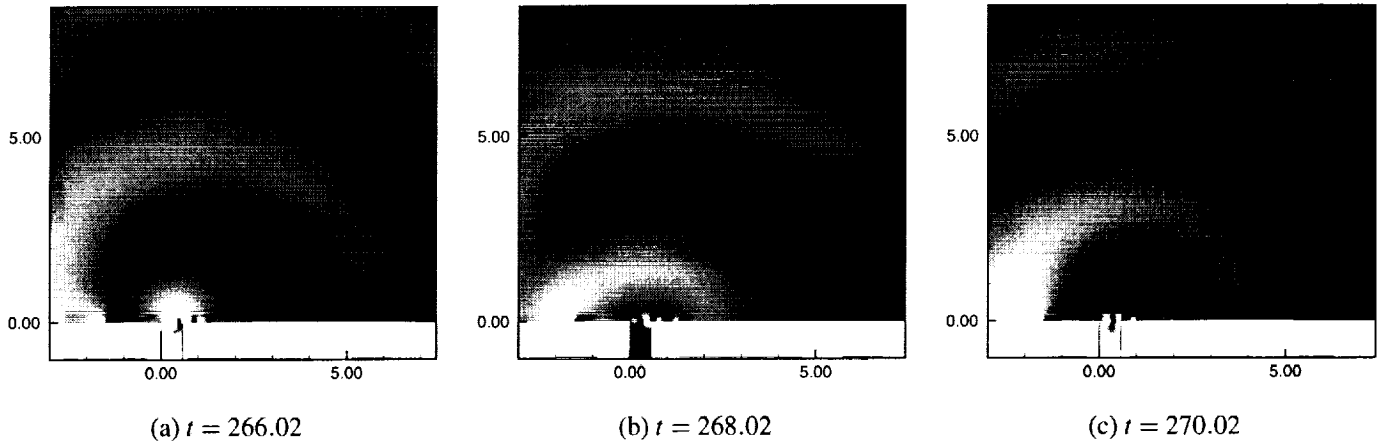
Figure 2: Instantaneous contours of nondimensional pressure for a laminar, $M = 0.15$, $Re = 15000$, $L/D = 0.58$, $\delta_0 = 0.05D$ cavity flow at different times. Contour levels range from 0.71415 (dark) to 0.7147 (light).
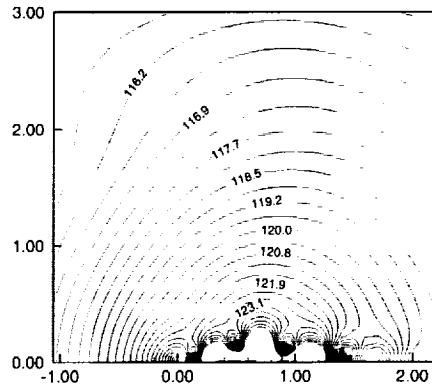
Figure 3: Contour levels of sound pressure level for the laminar calculation.

The far-field noise generation mechanism for the laminar and the turbulent cavity flows is quite similar: however, the main difference lies in the near-field flow solution. Figure 4 shows a series of instantaneous nondimensional density contours at different nondimensional times that correspond to approximately one period of the vortical structure evolution in the turbulent shear layer. It is evident that there are multiple large-scale structures present inside the cavity. The largest large-scale structure undergoes roughly a solid-body rotation, while smaller structures from vortex shedding in the turbulent shear layer are swept up by the main vortex. This results in a stronger recirculation zone, as indicated by the mean shear layer profiles and the streamline contours for the laminar and turbulent case shown in Figures 5 and 6 respectively.

Time history data at position $(0.0, -0.5)$ have been sampled, and an FFT has been used to calculate the power spectral density of the data. This is plotted in Figure 7 for both the laminar and turbulent calculations.

(a) $t = 202$ (b) $t = 204$ (c) $t = 206$
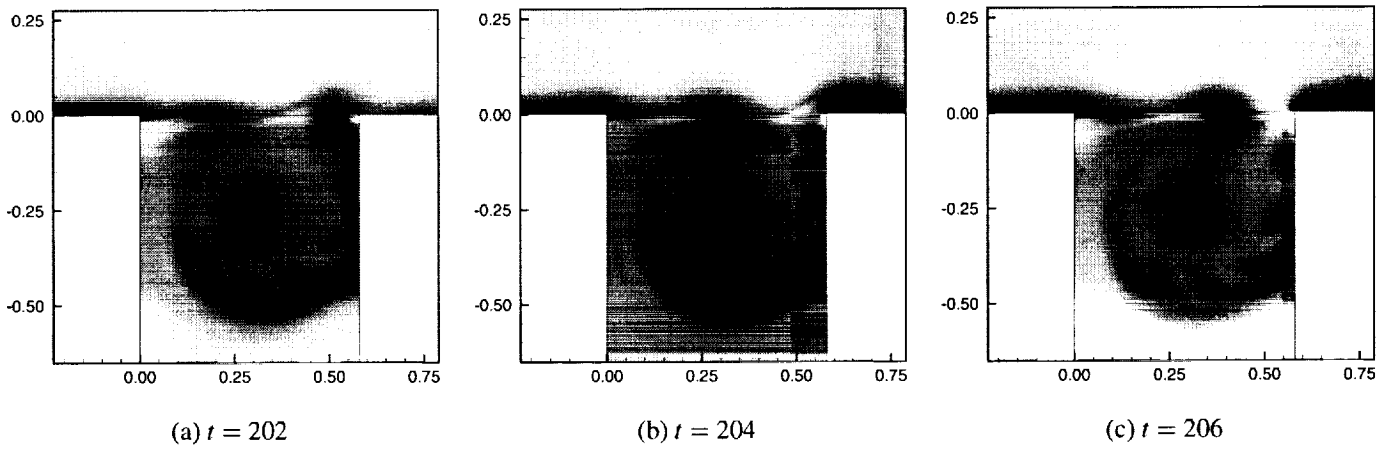
Figure 4: Instantaneous contours of nondimensional density for a turbulent, $M = 0.15$, $Re = 335041$, $L/D = 0.58$, $\delta_0 = 0.05D$ cavity flow at different times, corresponding to approximately one period of the large-scale structure oscillation. Contour levels range from 0.995 (dark) to 1.001 (light).

(a) shear layer profiles (b) streamlines
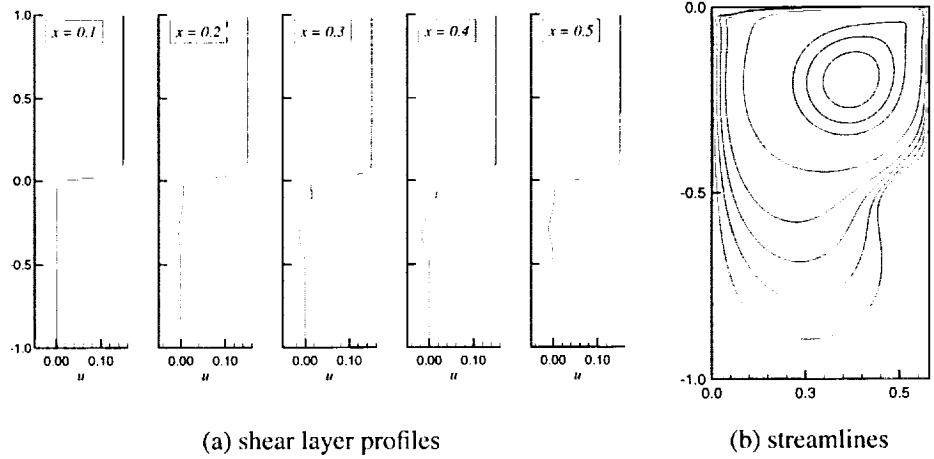
Figure 5: Mean shear layer profiles at various x locations and mean streamlines inside the cavity for the laminar calculation.

(a) shear layer profiles   (b) streamlines
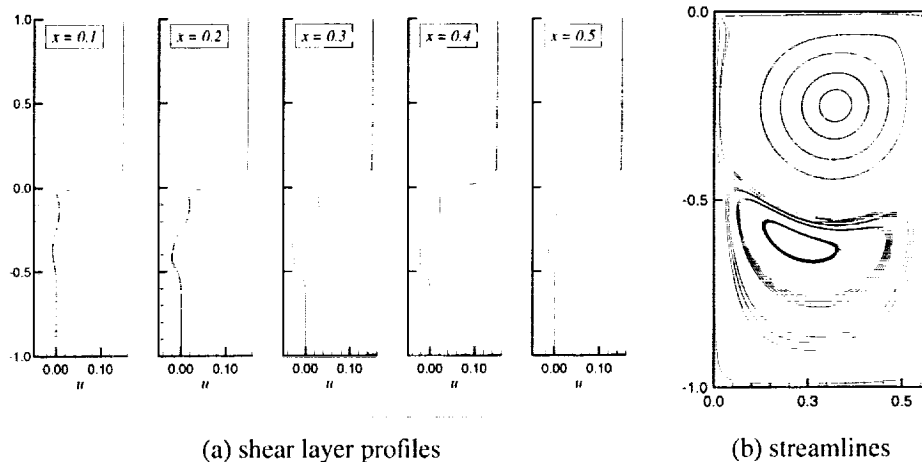
Figure 6: Mean shear layer profiles at various x locations and mean streamlines inside the cavity for the turbulent calculation.

According to the analysis by Tam [8], the lowest normal mode of a $L/D = 0.58$ two-dimensional rectangular cavity has a mode frequency of 2191.32 Hz. Even though this analysis is based on the no flow condition, the model should be a reasonable approximation since the current flow Mach number is only 0.15. For the laminar calculation, the lowest mode frequency from the power density spectrum is 2018.08 Hz. The frequency resolution is $\Delta f = 87.75$Hz. Higher harmonics are also captured in the current calculation. For the turbulent calculation, the fundamental mode has a lower frequency, 1852.61 Hz, than the laminar case, as shown in Figure 7. Besides higher harmonics of the normal mode, there are also higher frequency modes as well as a very low frequency content that is present in the turbulent case. This very low frequency mode can be seen clearly from the time history of the data as shown in Figure 8. Similar observations have been made in the experimental work by Henderson [9], though the cavity configurations are different.

4   Summary and Conclusions

Simulations of low subsonic flow, $M = 0.15$, over a deep cavity, $L/D = 0.58$, are presented in this paper. The splitter plate from the original problem configuration has been removed in the present simulations. The incoming boundary layer thickness is kept at $\delta_0/D = 0.05$ for both the laminar and turbulent calculations. At such a low Mach number, the deep cavity is under a normal resonance, and the frequency of the lowest normal mode for the laminar case compares well with the analytic result. For the turbulent case, the dominant mode has a slightly lower frequency than the laminar case, and there is a very low frequency oscillation that is also observed in the experiment work. More analysis needs to be performed to ascertain the physical nature of the very low frequency oscillation in the turbulent calculation.
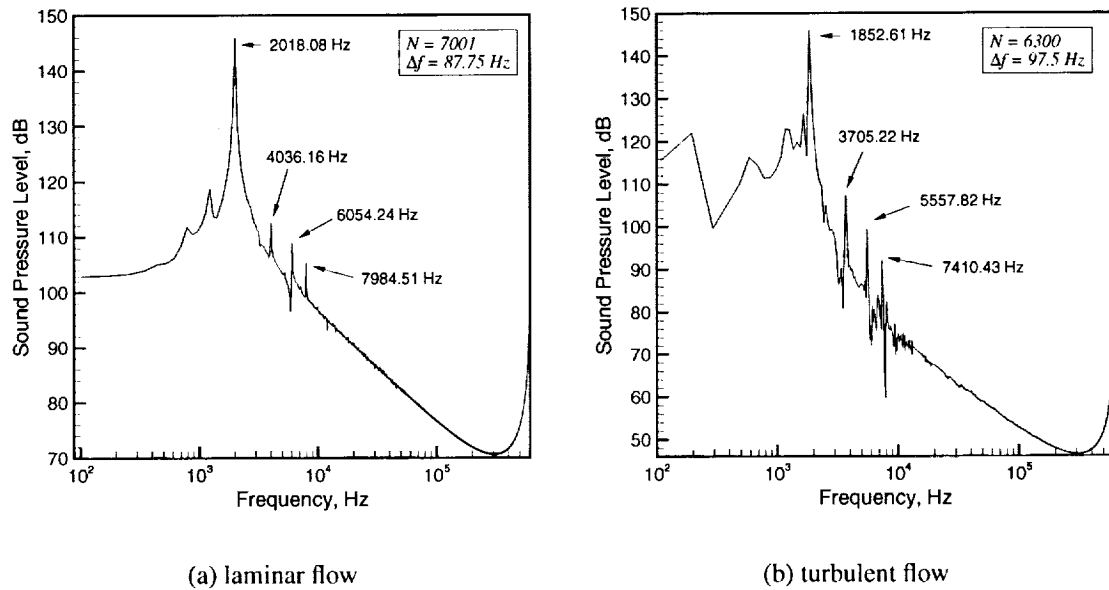
Figure 7: Power spectral density of the sampled data at $(0.0, -0.5)$ for the laminar and turbulent calculations.
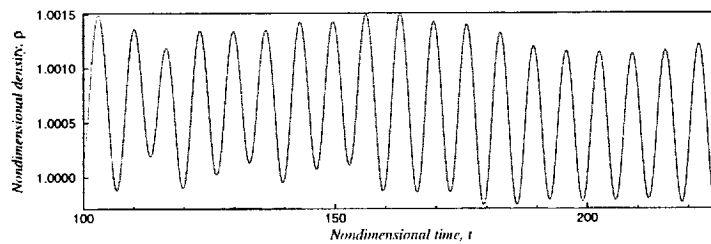
Figure 8: Time history of instantaneous density at $(0.0, -0.5)$ for the turbulent calculation.

References

[1] Spalart, P. R., Jou, W.-H., Streles, M., and Allmaras, S. R., "Comments on the feasibility of LES for wings and on a hybrid RANS/LES approach," *Proceedings of the First AFOSR International Conference on DNS/LES*, Greyden Press, Columbus, OH, Ruston, LA, August 4–8 1997.

[2] Spalart, P. R. and Allmaras, S. R., "A one-equation turbulence model for aerodynamic flows," AIAA–92–0439, 30th Aerospace Sciences Meeting and Exhibit, January 1992.

[3] Edwards, J. R. and Chandra, S., "Comparison of eddy viscosity-transport turbulence models for three-dimensional, shock-separated flowfields," *AIAA Journal*, Vol. 34, No. 4, 1996, pp. 756–763.

[4] Shieh, C. M. and Morris, P. J., "Parallel numerical simulation of subsonic cavity noise," AIAA–99–1891, 5th AIAA/CEAS Aeroacoustics Conference, May 1999.

[5] Sarohia, V., "Experimental investigation of oscillations in flows over shallow cavities," *AIAA Journal*, Vol. 15, No. 7, 1977, pp. 984–991.

[6] Roshko, A., "Some measurements of flow in a rectangular cutout," NACA TN-3488, 1955.

[7] Maull, D. J. and East, L. F., "Three-dimensional flow in cavities," *Journal of Fluid Mechanics*, Vol. 16, 1963, pp. 620–632.

[8] Tam, C. K., "The acoustic modes of a two-dimensional rectangular cavity," *Journal of Sound and Vibration*, Vol. 49, No. 3, 1976, pp. 353–364.

[9] Henderson, B., Private communication, November 1999.

DIRECT NUMERICAL SIMULATION OF AUTOMOBILE CAVITY TONES

KONSTANTIN K. KURBATSKII
Department of Mathematics
Florida State University
Tallahassee, FL 32306-4510

and

CHRISTOPHER K.W. TAM
Department of Mathematics
Florida State University
Tallahassee, FL 32306-4510
Email: tam@math.fsu.edu

Abstract

The Navier Stokes equation is solved computationally by the Dispersion-Relation-Preserving (DRP) scheme for the flow and acoustic fields associated with a laminar boundary layer flow over an automobile door cavity. In this work, the flow Reynolds number is restricted to $R_{\delta^*} < 3400$; the range of Reynolds number for which laminar flow may be maintained. This investigation focuses on two aspects of the problem, namely, the effect of boundary layer thickness on the cavity tone frequency and intensity and the effect of the size of the computation domain on the accuracy of the numerical simulation. It is found that the tone frequency decreases with an increase in boundary layer thickness. When the boundary layer is thicker than a certain critical value, depending on the flow speed, no tone is emitted by the cavity. Computationally, solutions of aeroacoustics problems are known to be sensitive to the size of the computation domain. Numerical experiments indicate that the use of a small domain could result in normal mode type acoustic oscillations in the entire computation domain leading to an increase in tone frequency and intensity. When the computation domain is expanded so that the boundaries are at least one wavelength away from the noise source, the computed tone frequency and intensity are found to be computation domain size independent.

1. Introduction

The benchmark problem specifies a turbulent boundary layer flow over the cavity. To properly model and compute the turbulent boundary layer flow and its interaction with the cavity is a task that will require extensive time and effort. Because of time constraint, we will consider a laminar boundary layer instead. We believe that the cavity tone frequency would most likely be about the same whether the flow is turbulent or laminar.

A boundary layer flow will definitely be laminar if $R_{\delta^*} < 600$. This is the Reynolds number below the stability limit of the Tollmien-Schlichting waves. In modern facilities with low free stream turbulence and sound, a boundary layer may remain laminar if R_{δ^*} is larger than 600 but less than 3400. For a free stream velocity of 50.9 m/s and 26.8 m/s (velocities prescribed by the benchmark problem), this corresponds to a boundary layer thickness of 2.9 mm and 5.5 mm, respectively. In this investigation, we will, therefore, restrict our consideration to a boundary layer thickness less than 3 mm and 5.5 mm for flow velocities of 50.9 m/s and 26.8 m/s.

Cavity tone is a multi-facet problem. A full investigation is beyond the scope of this work. We focus our effort primarily on two aspects of the problem. The first is on the effect of the size of the computation domain on the computed tone frequency and intensity. Specifically, we wish to find out if the size of the computation domain affects the solution. If it does what is the smallest size that will still give accurate simulations. The second is on the influence of the boundary layer thickness on the cavity tones. It has been suggested in Ref. [1] that boundary layer thickness has some influence on the frequency of the tones. The present study offers some quantitative results.

2. The Computation Domain and Grid Design

The computation domain is shown in figure 1. It is designed primarily for the case $U = 50.9$ m/s and a boundary layer thickness $\delta = 2$ mm. In the actual computation, the outside dimensions of the computation domain change somewhat with flow velocity and boundary layer thickness.

In the cavity opening region, viscous effects are important. To capture these effects, a fine mesh is needed. Away from the cavity, the disturbances are mainly acoustic waves. By using the Dispersion-Relation-Preserving (DRP) scheme (Ref. [2]) in the computation, only a very coarse mesh would be necessary in the acoustic region. The mesh design is dictated by these considerations. The computation domain is divided into a number of subdomains as shown in figure 1. The finest mesh with $\Delta x = \Delta y = 0.0825$ mm is used in the cavity opening region. The mesh size increases by a factor of 2 every time one crosses into the next subdomain. The mesh size in the outermost subdomain is

32 times larger than the finest mesh.
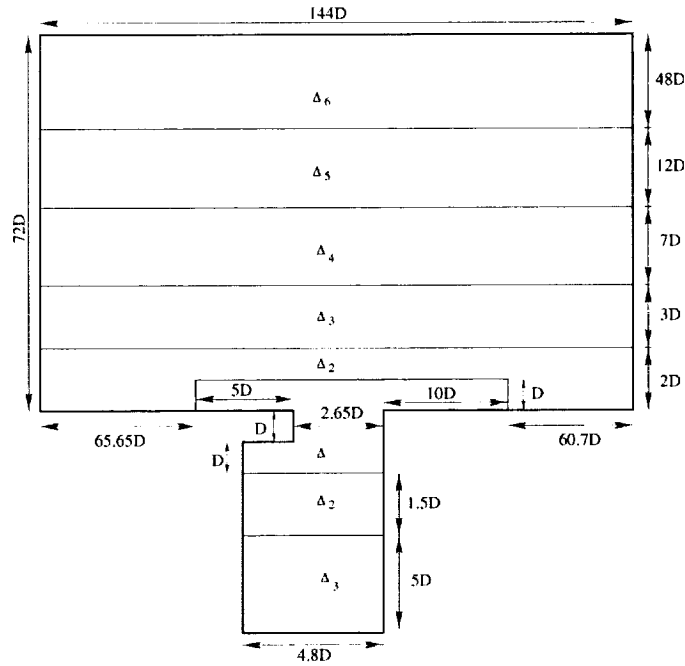
Figure 1. Computation domain showing the division into sub-domains and their mesh sizes.

3. The Governing Equations and the Computational Algorithm

The governing equations are the compressible Navier-Stokes equations in two-dimensions.

$$\frac{\partial \rho}{\partial t} + \rho \frac{\partial u_j}{\partial x_j} + u_j \frac{\partial \rho}{\partial x_j} = 0 \tag{1}$$

$$\frac{\partial u_i}{\partial t} + u_j \frac{\partial u_i}{\partial x_j} = -\frac{1}{\rho}\frac{\partial p}{\partial x_i} + \frac{1}{\rho}\frac{\partial \tau_{ij}}{\partial x_j} \tag{2}$$

$$\frac{\partial p}{\partial t} + u_j \frac{\partial p}{\partial x_j} + \gamma p \frac{\partial u_j}{\partial x_j} = 0 \tag{3}$$

$$\tau_{ij} = \mu \left(\frac{\partial u_j}{\partial x_j} + \frac{\partial u_j}{\partial x_i} \right) \tag{4}$$

In this study, the above equations are solved in time by the multiple-size-mesh multiple-time-step DRP algorithm as described in Ref. [3]. In each subdomain of figure 1, the equations are discretized by the DRP scheme of Ref. [2]. At the mesh size change boundaries, special stencils as given in Ref.

[3] are used. The time-steps of adjacent subdomains differ by a factor of 2 just as the mesh size. By using the multiple-size-mesh multiple-time-step algorithm most of the computation effort and time are spent in the opening region of the cavity where the resolution of the unsteady viscous layers is of paramount importance.

4. Numerical Boundary Conditions and Artificial Selective Damping

Along the solid surfaces of the cavity and the outside wall, the no-slip boundary condition is enforced by the ghost point method (Ref. [4]). Along the external boundary region (3 mesh points adjacent to the boundary), the flow variables are split into a mean flow and a time dependent component. The mean flow, with a given boundary layer thickness, is provided by the Blasius solution. The time dependent part of the solution is the only portion of the solution that is computed by the time marching scheme (for the split variable method, see Ref. [5]). The boundary conditions used for the computation are as follows. Along the top and left external boundaries the asymptotic radiation boundary conditions (Ref. [2]) are imposed. Along the right boundary, the outflow boundary conditions (Ref. [2]) are used.

Artificial selective damping is added to the time marching DRP scheme (see Ref. [6], [7]) to eliminate spurious short waves and to prevent the occurrence of numerical instability. The damping stencil with a damping curve of half-width 0.2π is used for background damping. Near the solid walls or the outer boundaries where a 7-point stencil does not fit, a 5- or 3-point stencil as provided in Ref. [7] is used instead. For general background damping an inverse mesh Reynolds number ($R_\Delta^{-1} = \frac{\nu_a}{(a_\infty \Delta x)}$ where ν_a is the artificial kinematic viscosity and a_∞ is the speed of sound) of 0.05 is used everywhere. Along walls and mesh change interfaces, additional damping is included. The added damping has an inverse mesh Reynolds number distribution in the form of a Gaussian function with the maximum value at the wall or interface and a half-width of four mesh points. On the wall, the maximum value of R_Δ^{-1} is set equal to 0.15. The corresponding value at a mesh size change interface is 0.3. There are three external corners at the cavity opening. They are likely sites at which short spurious waves are generated. To prevent numerical instability from developing at these points, additional artificial selective damping is imposed. Again a half-width of 4 mesh point Gaussian distribution of the inverse mesh Reynolds number centered at each of these points is used. The maximum value of R_Δ^{-1} at these points is set equal to 0.35. By implementing artificial selective damping distribution as described, it is our experience that no numerical instability nor excessive short spurious waves have been found in all the computations.

5. Numerical Results

In this work, the time-marching computation uses the time independent boundary layer solution without the cavity as the initial condition. Computation continues until a time periodic state is reached.
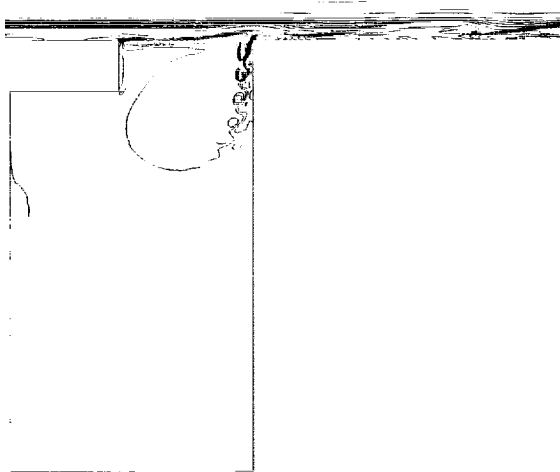
Figure 2. Instantaneous vorticity contours showing the shedding of small vortices at the trailing edge of the cavity. $U = 50.9$ m/s, $\delta = 2$ mm.

The characteristic features of the flow in the vicinity of the cavity opening and the acoustic field can be found by examining the instantaneous vorticity, steamlines and pressure contours. Figure 2 shows a plot of the instantaneous vorticity contours for the case $U = 50.9$ m/s and $\delta = 2.0$ mm. As can easily be seen, vortices are shed periodically at the trailing edge of the cavity. The shed vortices move inside the cavity driven by the circulation of a large vortex (to be described later) located at the opening of the cavity. Vortices are also shed into the flow outside. They are convected downstream by the boundary layer flow. These convected vortices are clearly shown in the pressure contour plot of figure 3. They form the low pressure centers. These vortices persist over a rather long distance and eventually dissipated by viscosity. Figure 4 shows the instantaneous streamline pattern. It is seen that the flow at the mouth of the cavity is completely dominated by that of a single large vortex. Below the large vortex, another vortex of opposite rotation often exists (see figure 4). The position of this vortex changes from time to time and does not always attach to the cavity wall. The far field pressure contour pattern is shown in figure 5. This pattern is the same as that of a monopole acoustic source in a low subsonic stream. That the noise source is a monopole and not a dipole is consistent with the model of Ref. [1]. The sound is generated by flow impinging periodically at the trailing edge of the cavity.
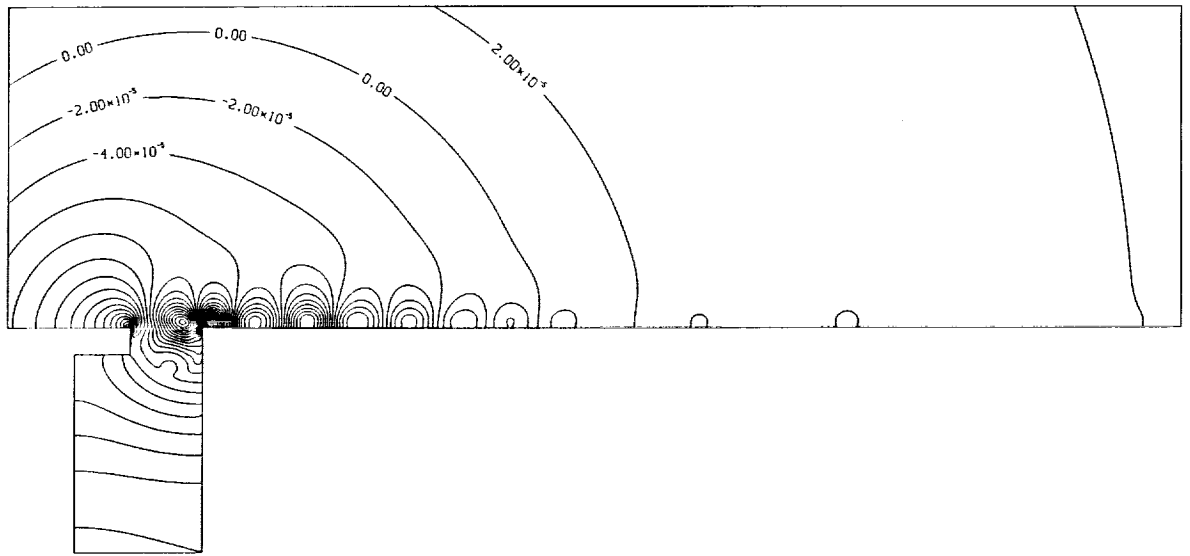
Figure 3. Near field pressure contours showing the convection of shed vortices along the outside wall. $U = 50.9$ m/s, $\delta = 2$ mm
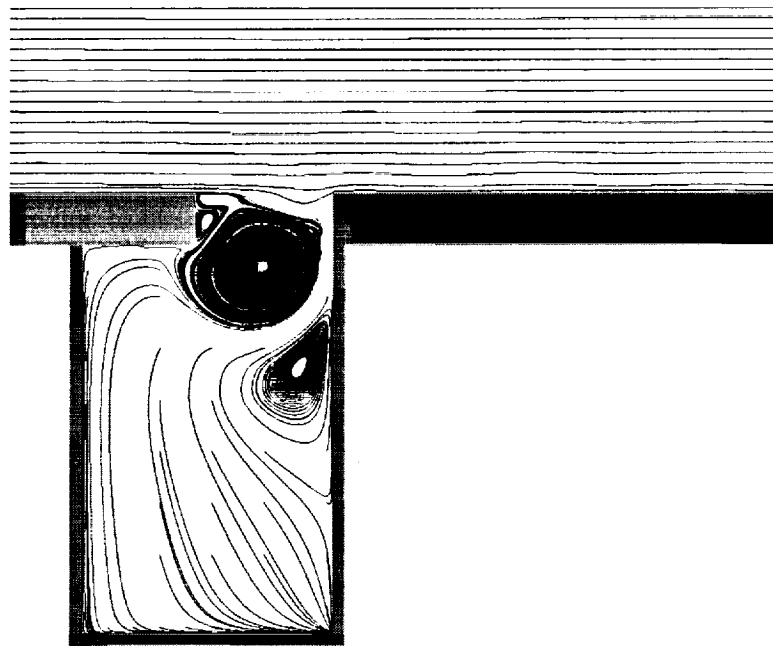
Figure 4. Instantaneous streamline pattern. $U = 50.9$ m/s, $\delta = 2$ mm.
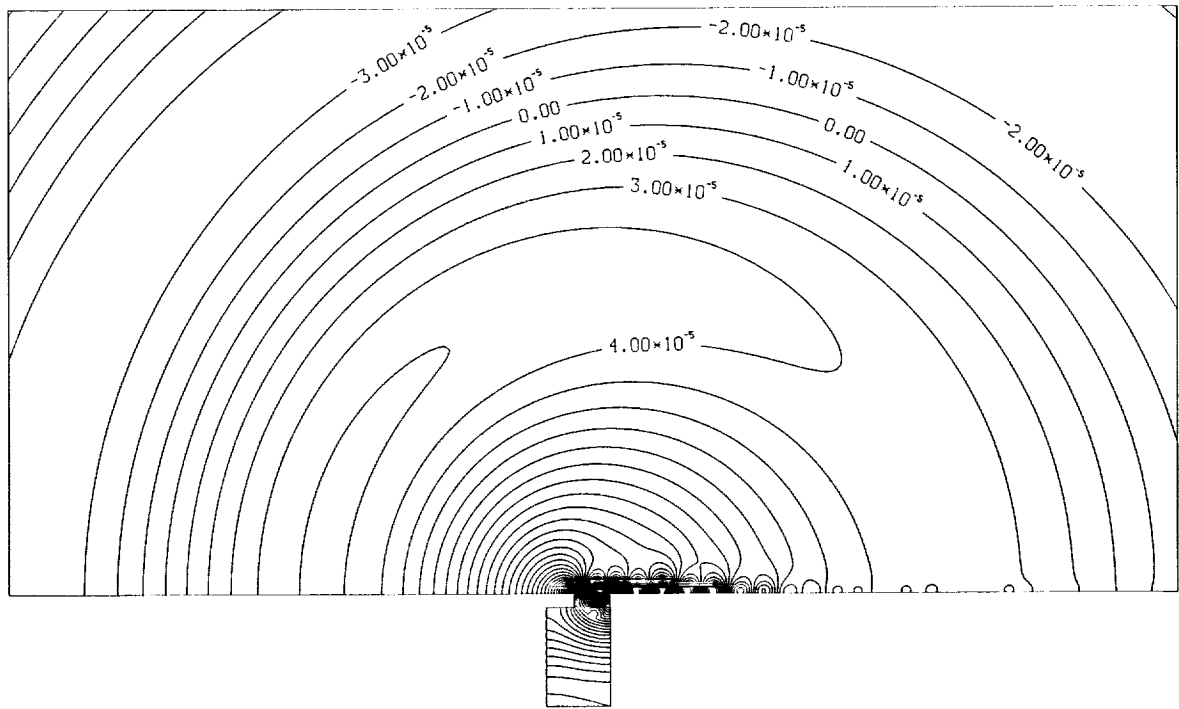
Figure 5. Far field pressure contours showing a monopole acoustic field. $U = 50.9$ m/s, $\delta = 2$ mm.

5.1. The Effect of the Size of the Computation Domain

The effect of the size of the computation domain on the cavity flow and acoustic field is investigated by repeating the same numerical simulation three times each with a different size external domain. At $U = 50.9$ m/s and $\delta = 2.0$ mm the cavity tone frequency is around 2 KHz. Let λ be the acoustic wavelength. The smallest size domain used is 0.3λ by 0.23λ. This small size domain has the advantage that the CPU time required for convergence to a time periodic state is very short. The moderate size domain used is 1.8λ by 0.9λ. In other words, the external boundaries are at approximately 0.9 acoustic wavelength from the trailing edge of the cavity or the noise source. The largest domain used is 2.8λ by 1.4λ. This is a very large domain and requires a long run time for convergence.

Figure 6 shows the pressure variations measured at the center of the left wall inside the cavity for the three simulations. The large and the medium size computation domain give nearly the same result with a tone at 1992Hz and a sound pressure level (SPL) at 125.6 dB. The small computation domain gives a tone frequency at 2193 Hz and SPL = 131.8 dB. Thus the tone is stronger and at a higher frequency. Upon examining the pressure fluctuations at a number of locations inside the computation domain for the small computation domain case, it is found that there are normal mode type oscillations inside the entire domain. It is believed to be caused by partial reflections at the outer

boundaries of the computation domain. The asymptotic radiation boundary conditions presuppose that the boundaries are far from the noise source. The above results suggest that this is reasonably satisfied if the boundaries are, at least, one wavelength away from the noise source.
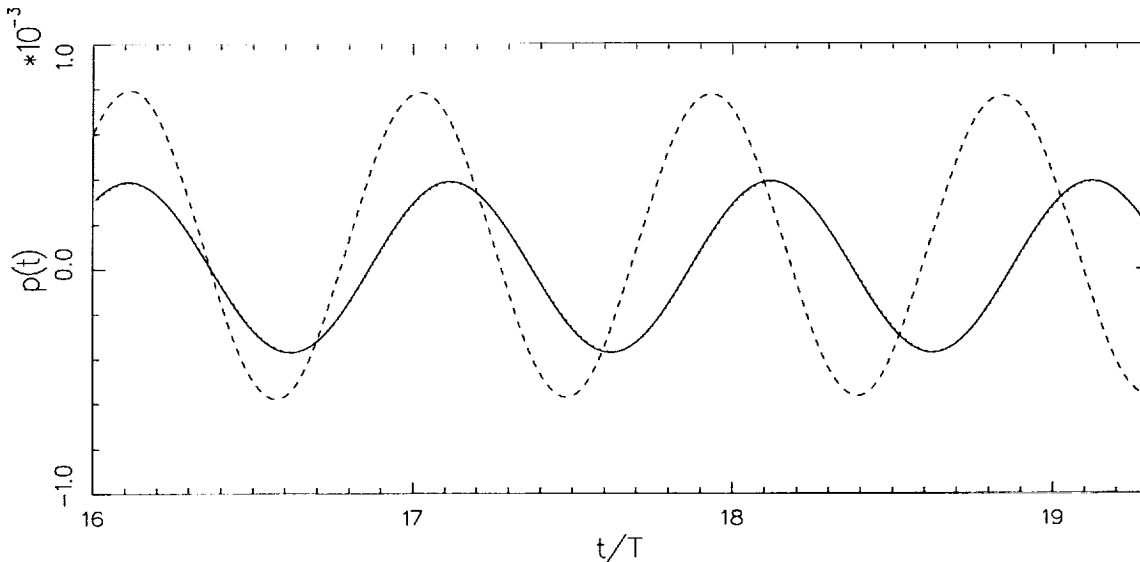
Figure 6. Time variations of the pressure field at the center of the left wall inside the cavity for $U = 50.9$ m/s, $\delta = 2$ mm. —— large size domain, ... medium size domain, - - - small domain.

5.2. The Effect of Boundary Layer Thickness

The effect of boundary layer thickness on the cavity tone frequency and intensity at the two prescribed flow velocities of the benchmark problem, $U = 50.9$ m/s and 26.8 m/s, are investigated. When the boundary layer is thick, it is found that there is no tone. The boundary layer flows smoothly over the cavity opening. In this case, the numerical simulation converges to a time independent state. Figure 7 shows the dependence of the tone frequency on the boundary layer thickness, δ, at $U = 50.9$ m/s. The tone frequency decreases as δ increases. At $\delta = 4$ mm, no tone could be detected. Figure 8 shows the SPL of the tone measured at the center of the left wall inside the cavity as a function of boundary layer thickness. The highest intensity occurs at $\delta = 2$ mm. This suggests that the intensity depends on the instability characteristics of the mean flow profile. It does not vary monotonically with boundary layer thickness. Figures 9 and 10 show the dependence of the dominant tone frequency and SPL on δ at the lower speed of 26.8 m/s. Again the tone frequency decreases with increase in boundary layer thickness.
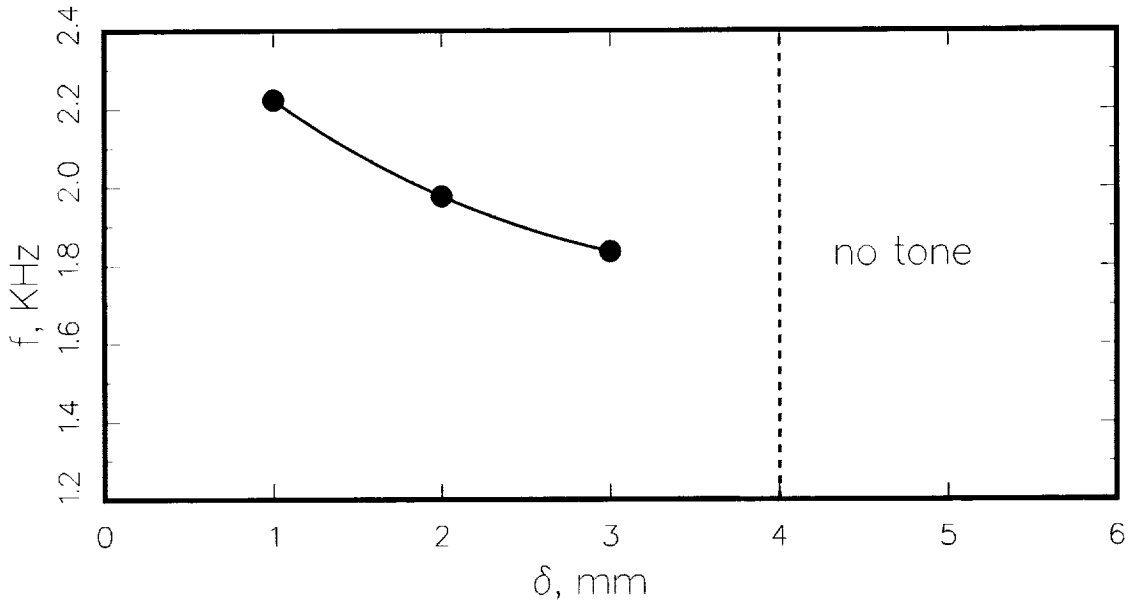
Figure 7. Dependence of the tone frequency on the boundary layer thickness. $U = 50.9$ m/s.
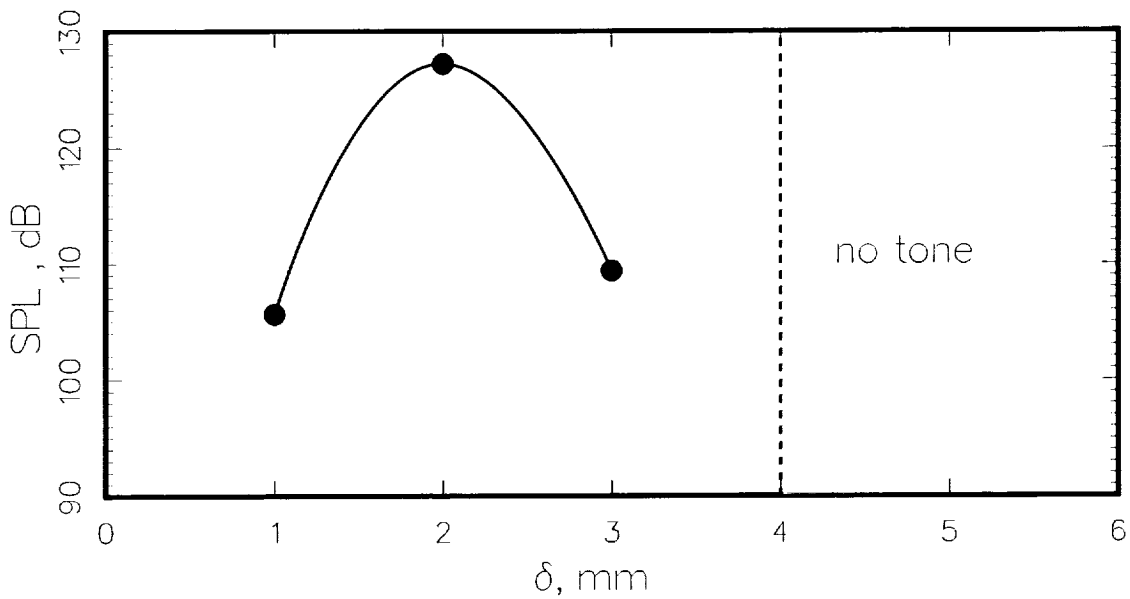
Figure 8. Dependence of the tone SPL on the boundary layer thickness. $U = 50.9$ m/s.
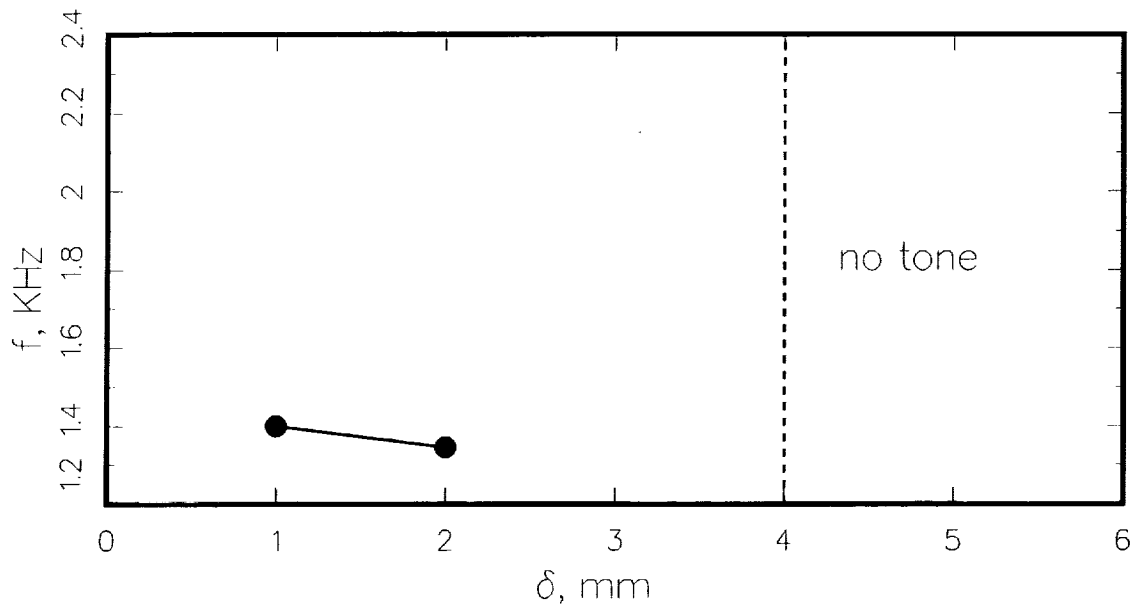
Figure 9. Dependence of the tone frequency on the boundary layer thickness. $U = 26.8$ m/s.
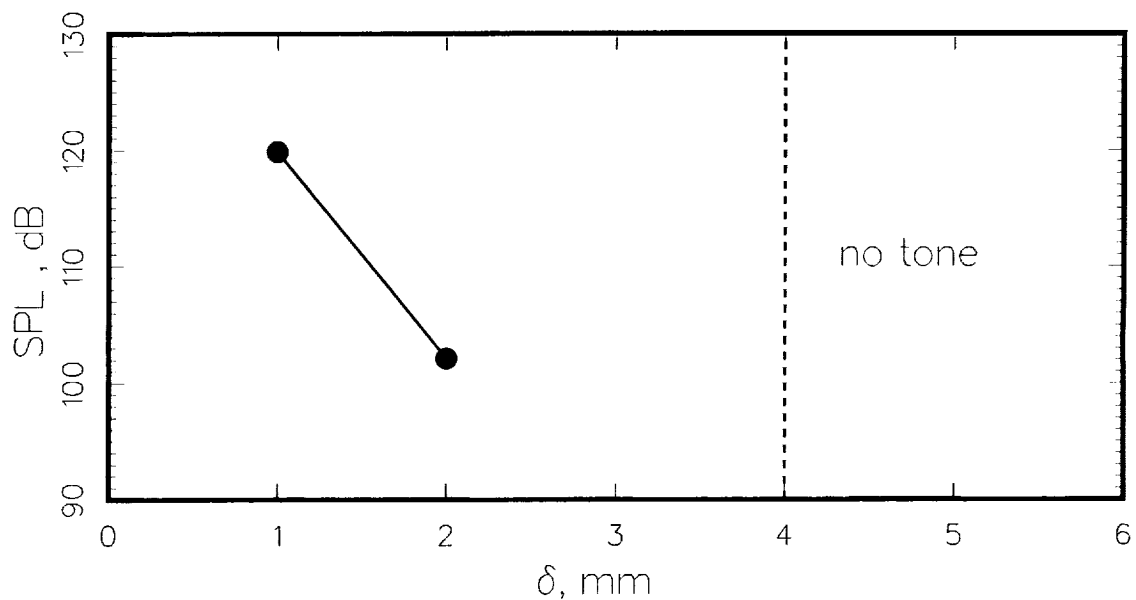
Figure 10. Dependence of the tone SPL on the boundary layer thickness. $U = 26.8$ m/s.

5.3. Noise Spectrum

Experiments indicate that cavity resonance may consist of a single tone or multiple tones. The number of tones found depend on the flow conditions and the cavity geometry. Figure 11 shows the

noise spectrum measured at the center of the left wall of the cavity at $U = 50.9$ m/s, $\delta = 2$ mm (the case of the highest tone intensity). Clearly the spectrum consists of a single tone at 1.99 KHz.
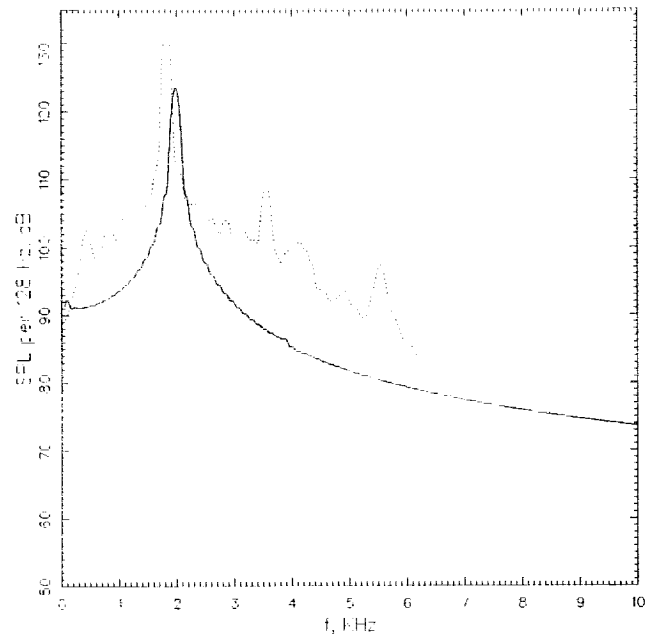
Figure 11. Noise spectrum at the center of the left wall of the cavity.
$U = 50.9$ m/s, $\delta = 2$ mm —— numerical simulation, ...experiment (Henderson, Ref. [8]).
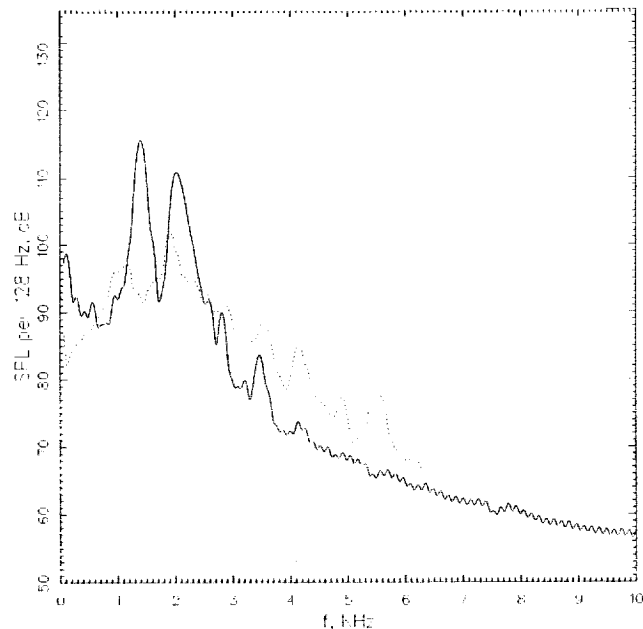
Figure 12. Noise spectrum at the center of the left wall of the cavity.
$U = 26.8$ m/s, $\delta = 1$ mm —— numerical simulation, ...experiment (Henderson, Ref. [8]).

Shown in this figure also is the experimental spectrum measured by Henderson, Ref. [8]. There is good agreement between the tone frequency of the numerical simulation and that of the physical experiment. In the experiment, the boundary layer is turbulent, therefore, we do not expect good agreement in the tone intensity. Figure 12 shows the noise spectrum at the lower speed $U = 26.8$ m/s and $\delta = 1$ mm. In this case, there are two tones. One is at a frequency of 1.32 KHz and the other at 2.0 KHz. This is in agreement with the experimentally measured spectrum. Again, the tone frequencies are well reproduced in the numerical simulation. But the tone intensities are different. Figures 11 and 12 together suggest that as the flow velocity increases, one of the tones disappears. The strength of the remaining tone intensifies with flow speed.

6. Conclusions

The present investigation demonstrates the feasibility of performing direct numerical simulation of automobile cavity tones using the multiple-size-mesh multiple-time-step DRP scheme. It is found that the size of the computation domain is a factor of influence on the accuracy of the numerical simulation. If too small a domain is used, the tone intensity as well as the frequency can be substantially increased due to partial reflections at the boundaries of the computation domain. It is recommended that the outer boundaries should be placed, at least, one acoustic wavelength away from the cavity trailing edge where the tone is generated. In recent years, a number of investigators; e.g., Ref. [9] and [10], had performed numerical simulation of cavity tones at a subsonic Mach number. The study of the size of the computation domain on the accuracy of the numerical simulation has, however, never been done before.

The dependence of the cavity tone frequency and intensity on the boundary layer thickness is also studied. No tone could be detected when the boundary layer is thick. For thin boundary layers, the tone frequency increases with a decrease in boundary layer thickness. The variation of the tone intensity with boundary layer thickness is not monotonic. It appears to be influenced by the instability characteristics of the boundary layer velocity profile.

Acknowledgments

References

1. Tam, C.K.W. and Block, P.J.W.: On the Tones and Pressure Oscillations Induced by Flow over Rectangular Cavities. *J. Fluid Mechanics*, vol. 89, 1978, pp. 373–399.

2. Tam, C.K.W. and Webb, J.C.: Dispersion-Relation-Preserving Finite Difference Schemes for Computational Acoustics. *J. Computational Physics*, vol. 107, Aug. 1993, pp. 262–281.

3. Tam, C.K.W. and Kurbatskii, K.A.: Microfluid Dynamics and Acoustics of Resonant Liners. AIAA Paper 99-1850, May 1999; to appear in the *AIAA Journal*.

4. Tam, C.K.W. and Dong, Z.: Wall Boundary Conditions for High-Order Finite Difference Schemes in Computational Aeroacoustics, *Theoretical and Computational Fluid Dynamics*, Vol. 8, Oct. 1994, pp. 303–322.

5. Tam, C.K.W.: Advances in Numerical Boundary Conditions for Computational Aeroacoustics, *Journal of Computational Acoustics*, Vol. 6, Dec. 1998, pp. 377–402.

6. Tam, C.K.W. Webb, J.C. and Dong, Z.: A Study of the Short Wave Components in Computational Acoustics. *Journal of Computational Acoustics*, vol. 1, Mar. 1993, pp. 1–30.

7. Tam, C.K.W.: Computation Aeroacoustics: Issues and Methods. AIAA Journal, vol. 33, Oct. 1995, pp. 1788–1796.

8. Henderson, B.: Category 6 — Automobile Noise Involving Feedback. 3rd Computational Aeroacoustics Workshop, Nov. 8–10, 1999, Ohio Aerospace Institute, Cleveland, Ohio.

9. Shieh, C.M. and Morris, P.J.: Parallel Numerical Simulation of Subsonic Cavity Noise. AIAA Paper 99-1891, May 1999.

10. Colonius, T., Basu, A.J. and Rowley, C.W.: Numerical Investigation of the Flow Past a Cavity. AIAA Paper 99-1912, May 1999.
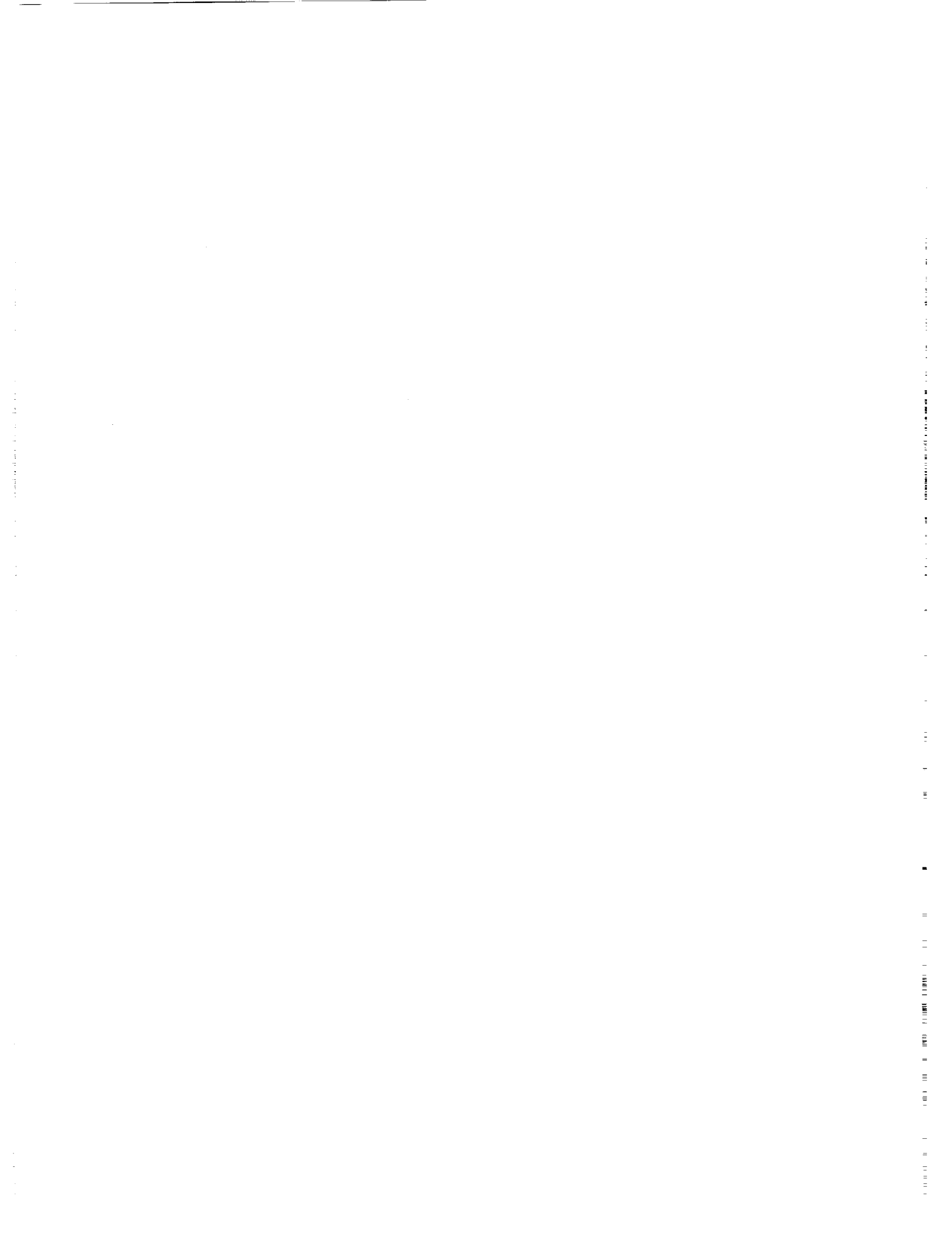
Solution Comparisons

COMPARISONS WITH ANALYTICAL SOLUTION: CATEGORY 1, PROBLEM 1

CHRISTOPHER K.W. TAM and ALEXEI AGANIN
Department of Mathematics
Florida State University
Tallahassee, FL 32306-4510
Email: tam@math.fsu.edu

Altogether, thirteen participants submitted their computed results for comparison with the exact solution. The solution consists of three distinct regions. In the region upstream of the nozzle throat, there is only the transmitted waves. So the maximum pressure envelope is nearly a flat line. Near the nozzle throat region, the pressure increases dramatically. The maximum pressure envelope consists of a sharp spike. In the region downstream of the nozzle throat, the solution comprises of an interference pattern formed by the incoming and reflected waves. In order to compare the above features well, two figures are used. The first compares the transmitted wave amplitude in the region upstream of the nozzle throat and the interference pattern downstream of the nozzle throat. The second compares the location and peak pressure amplitude at and near the nozzle throat.

—·—— solution by Chen and Wang (301 mesh points)
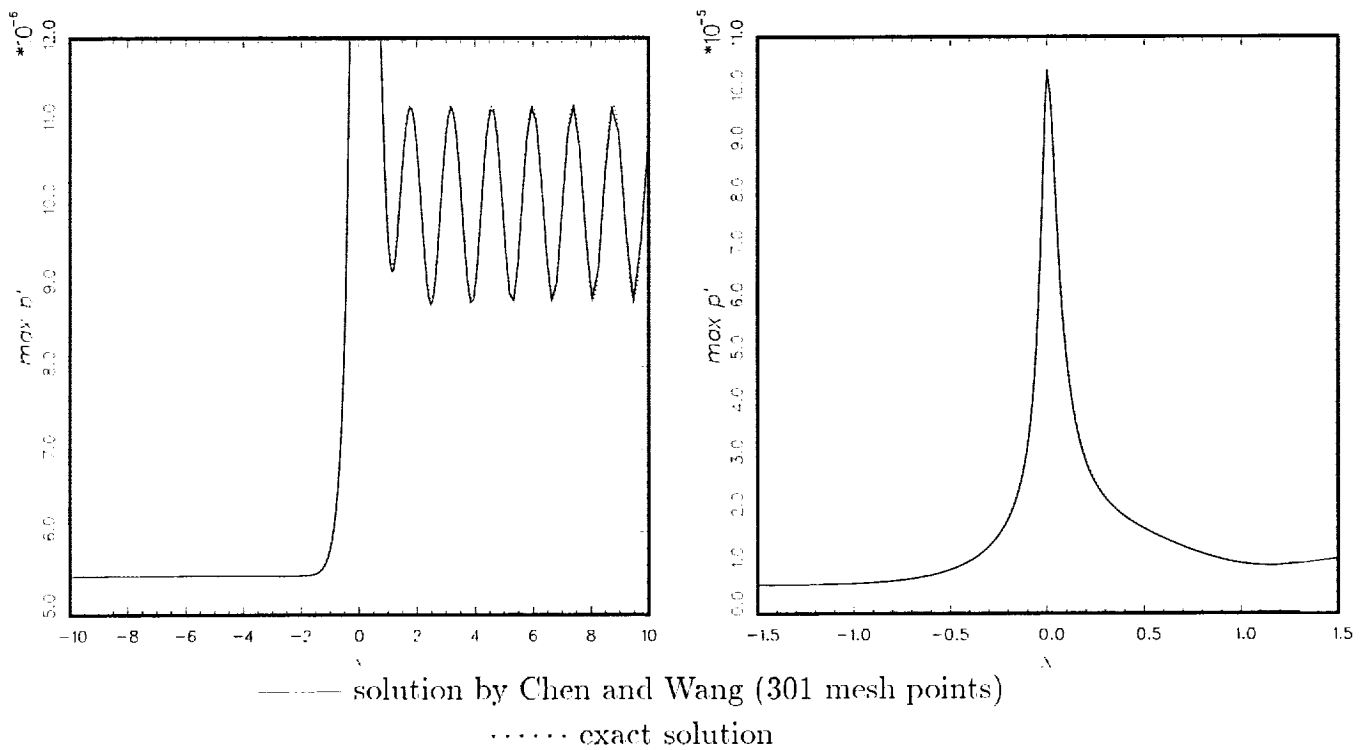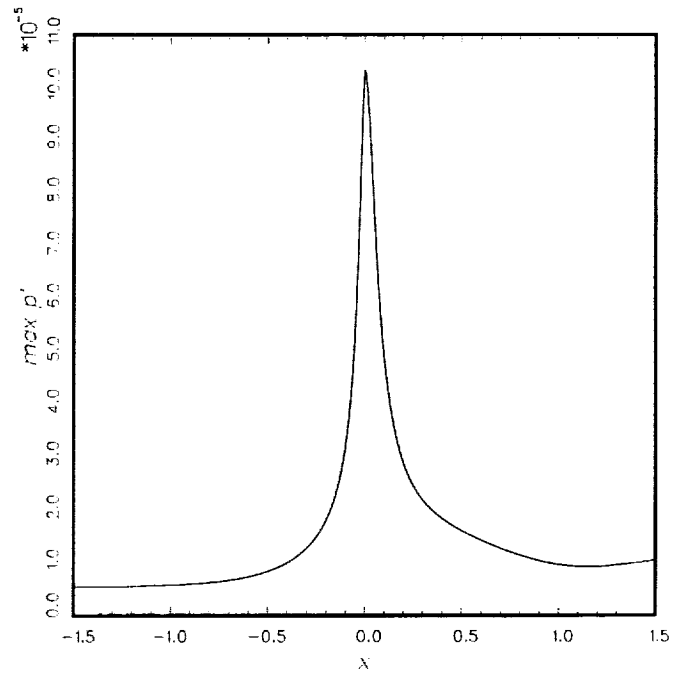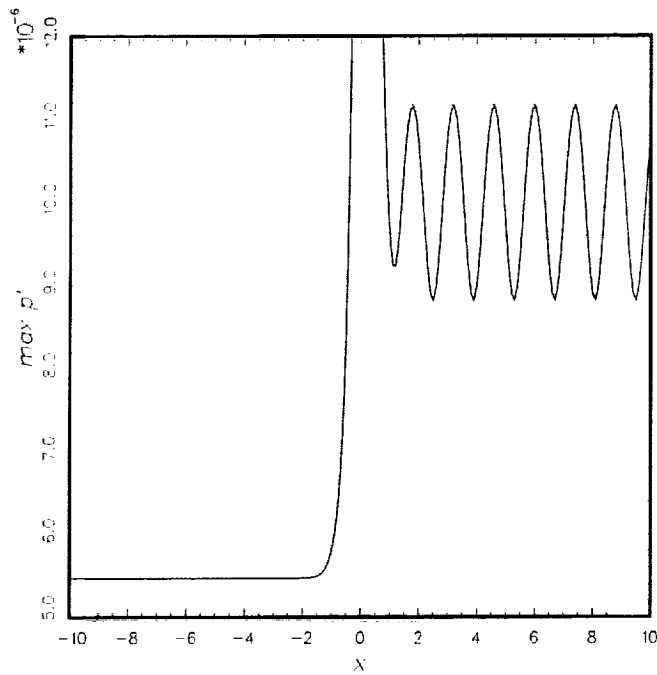
· · · · · · exact solution

—— – solution by Hixon and Mankbadi (251 mesh points)

$\cdots\cdots$ exact solution
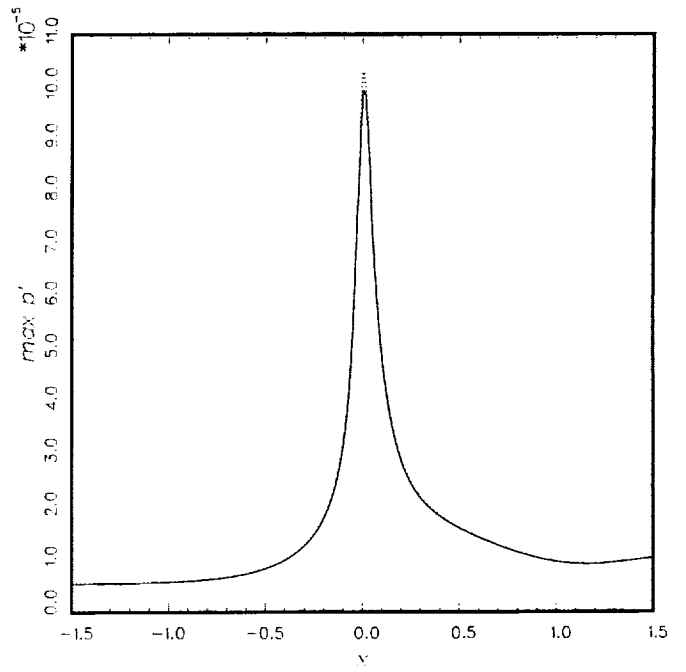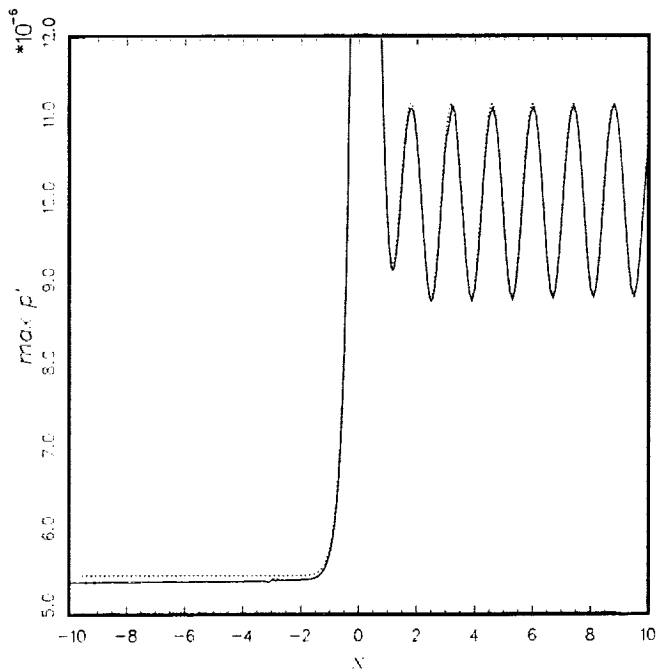
—— solution by Fang Hu (381 mesh points)

$\cdots\cdots$ exact solution
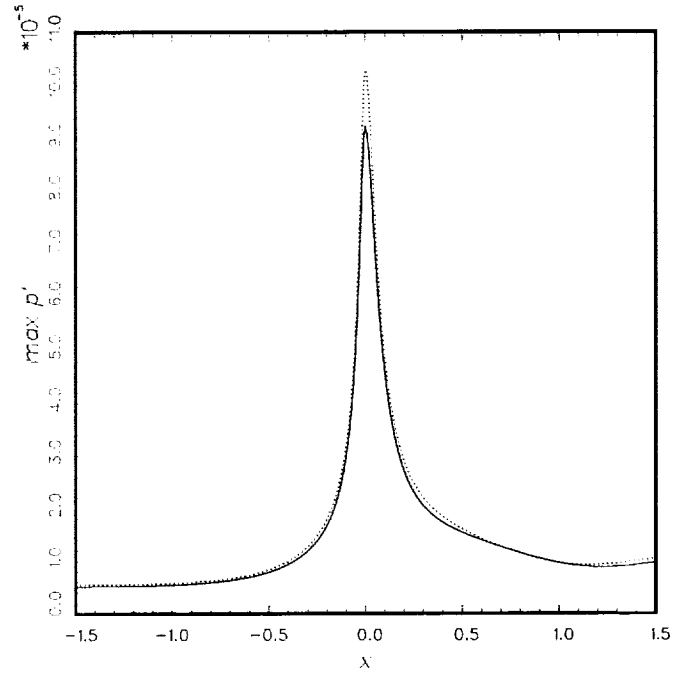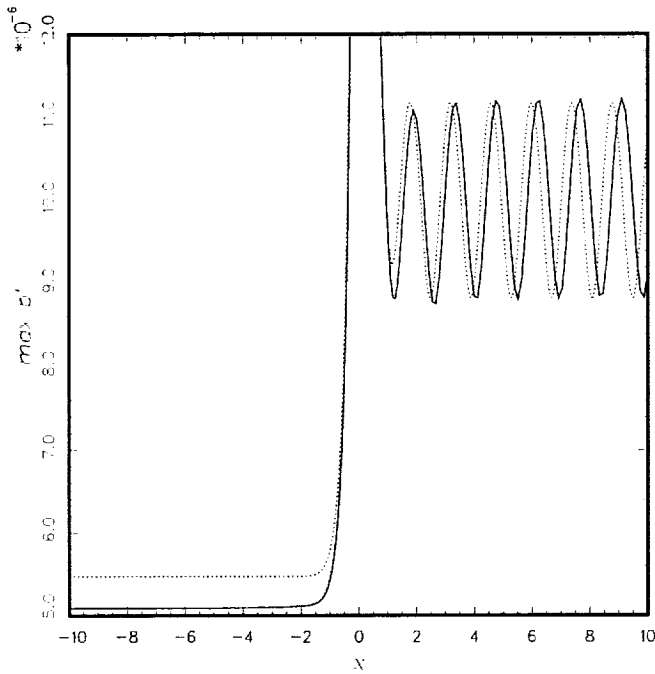
——— solution by J.W. Kim and Lee (301 mesh points)

· · · · · · exact solution
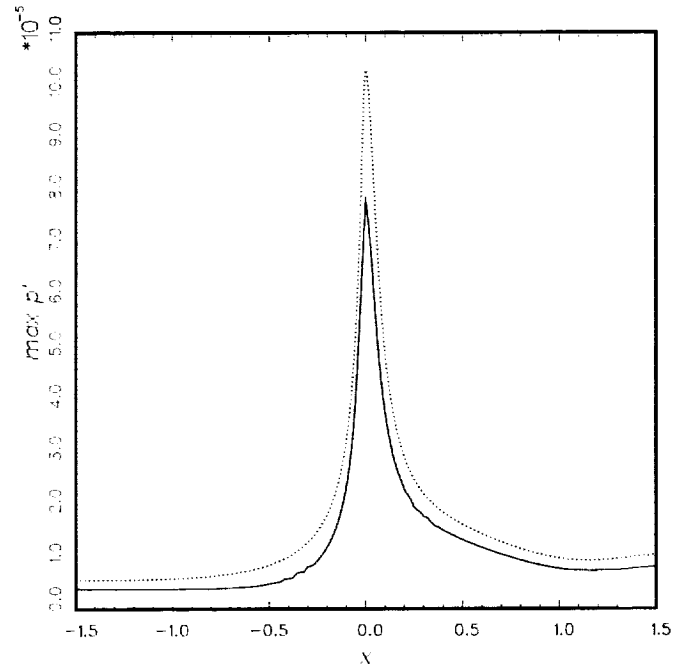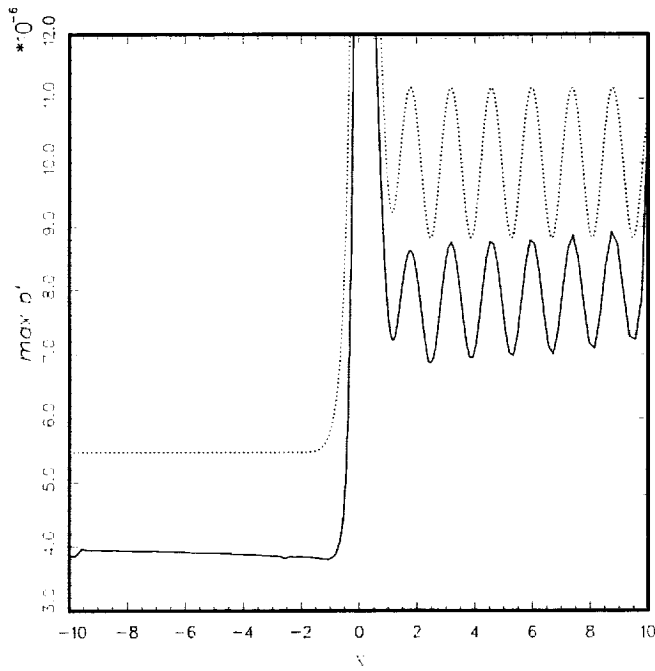
——— solution by Y.S. Kim and Lee (251 mesh points)

· · · · · · exact solution
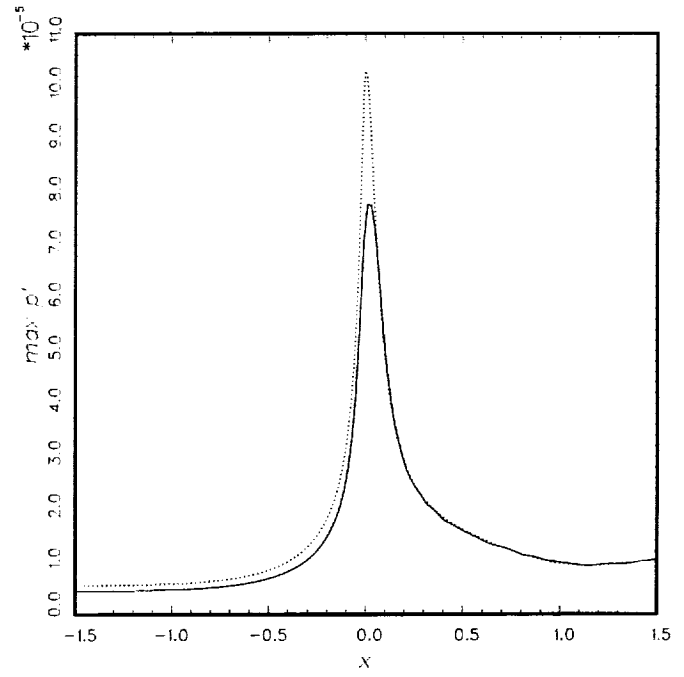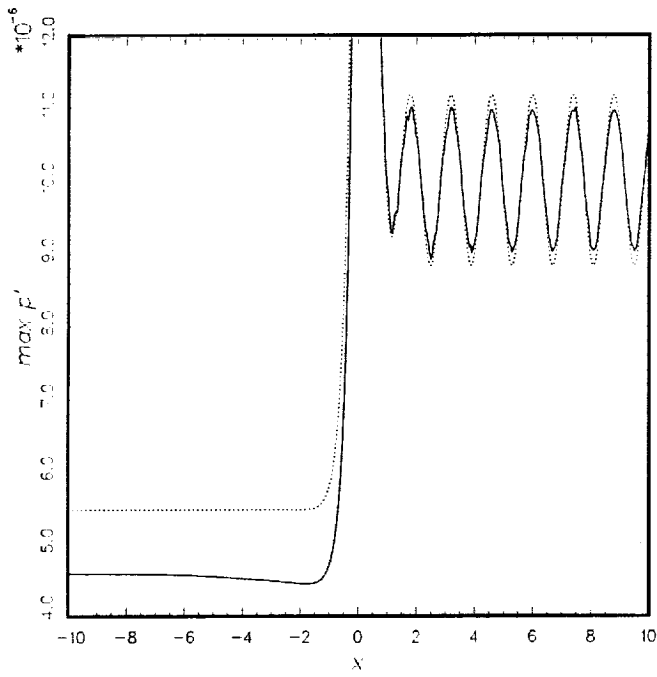
solution by Loh and Lin (999 mesh points)

······ exact solution
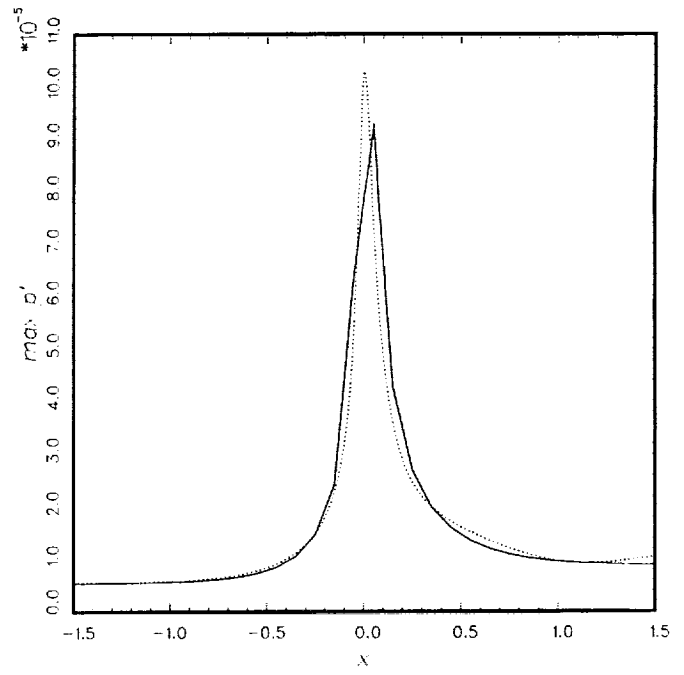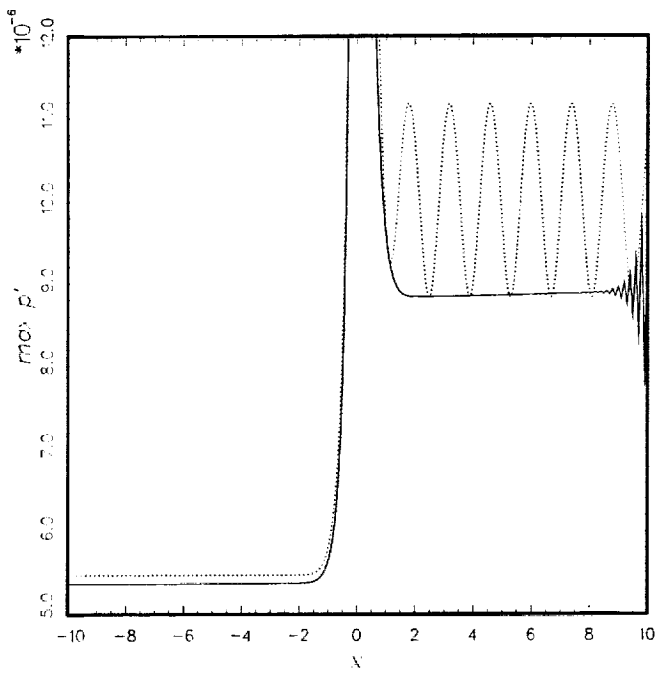
solution by Miles (200 mesh points)

······ exact solution
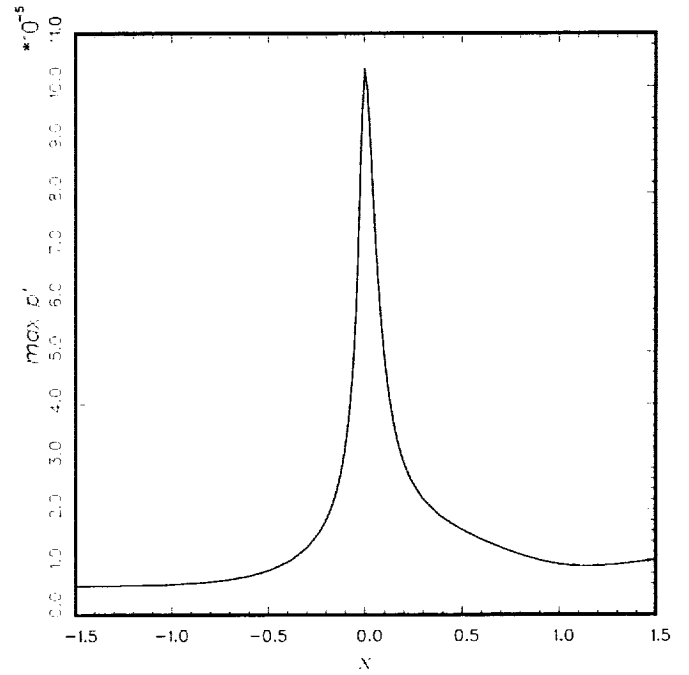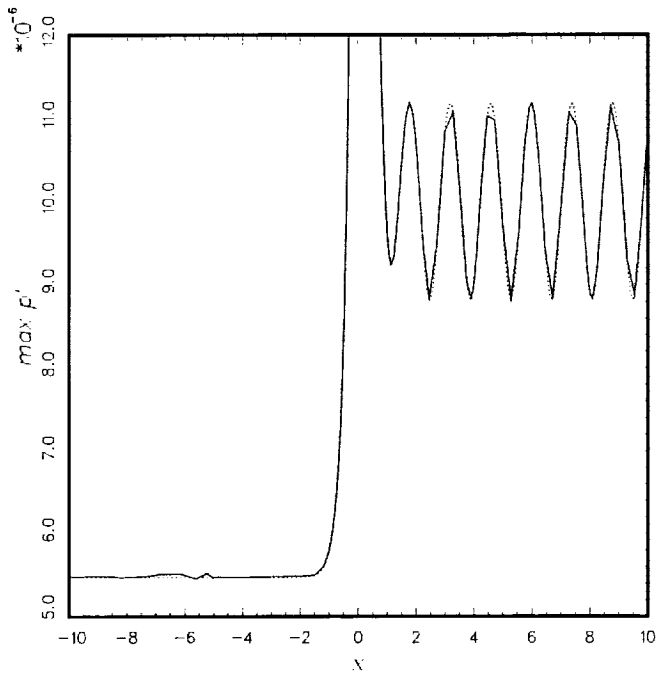
solution by Rasetarinera, Kopriva and Hussaini (132 mesh points)

······ exact solution
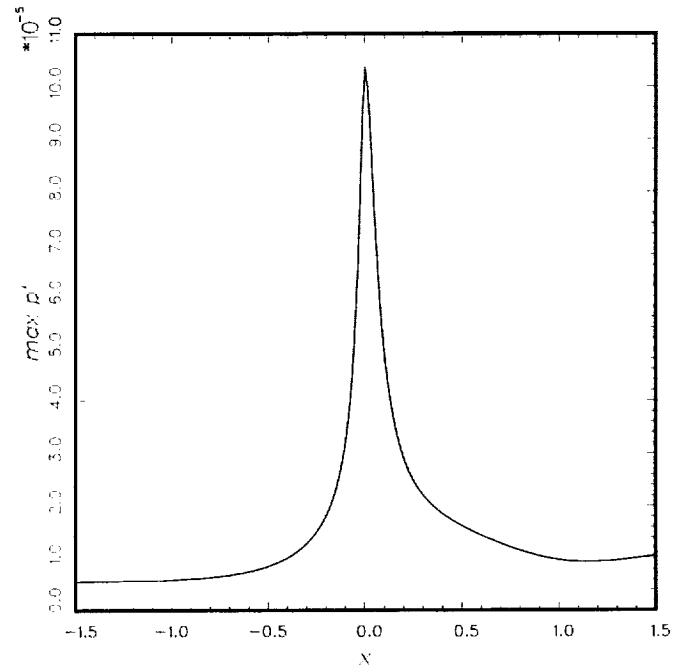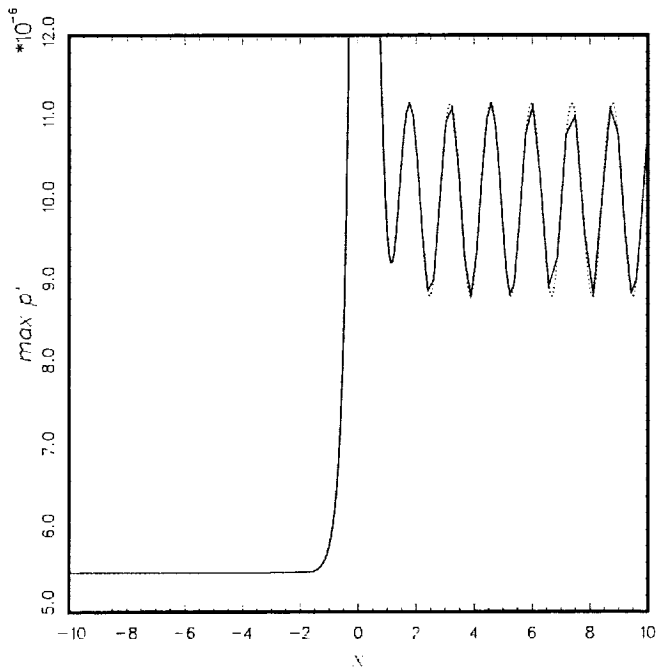
solution by Stanescu and Habashi (multi-domain, 225 mesh points)

······ exact solution
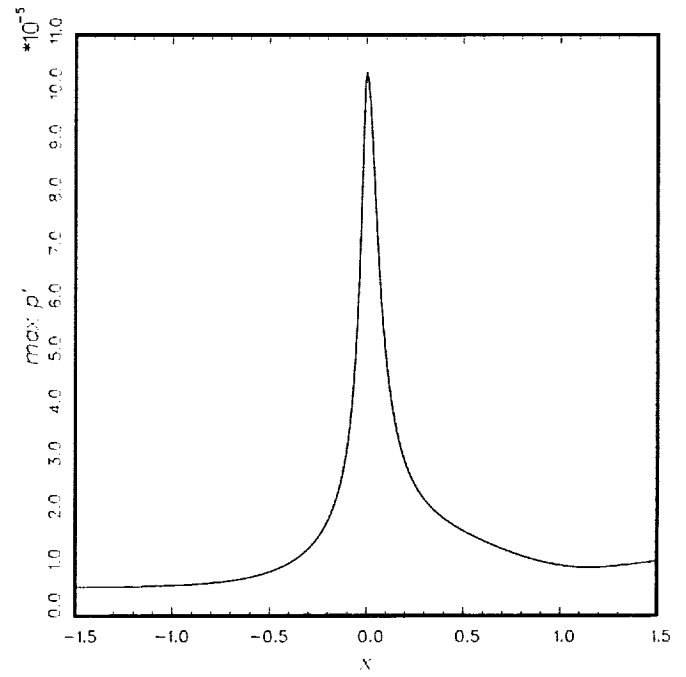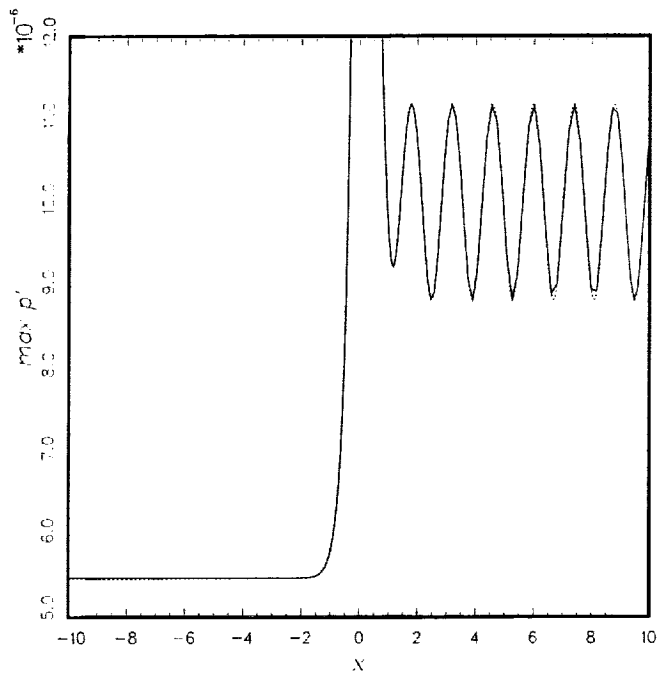
———— solution by Stanescu and Habashi (global, 257 mesh points)

· · · · · · exact solution
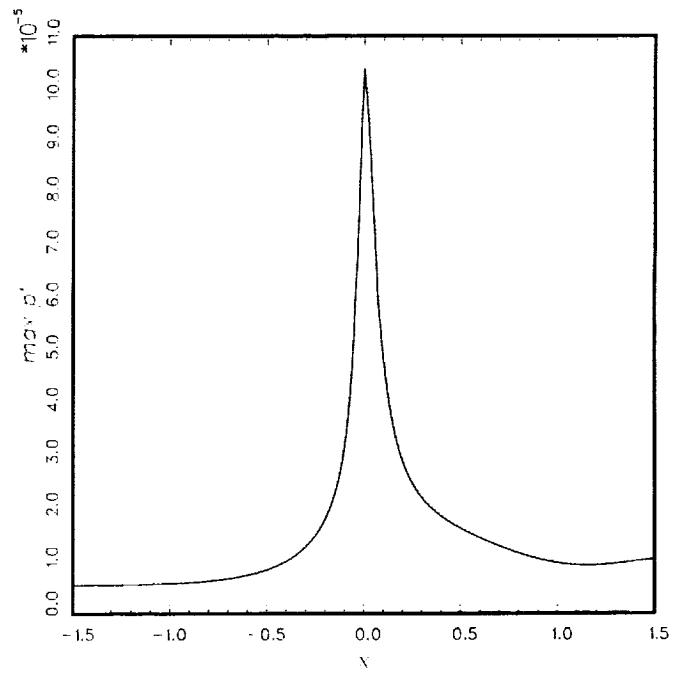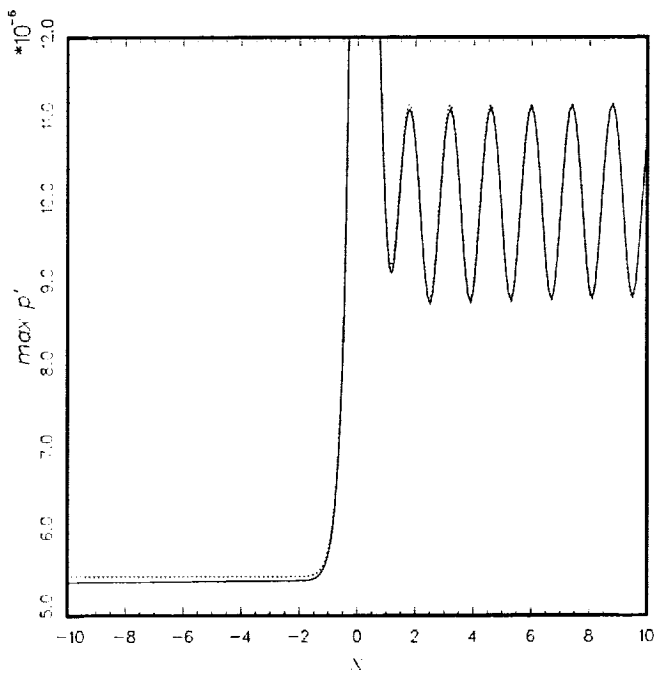
———— solution by Tam and Aganin (359 mesh points)

· · · · · · exact solution
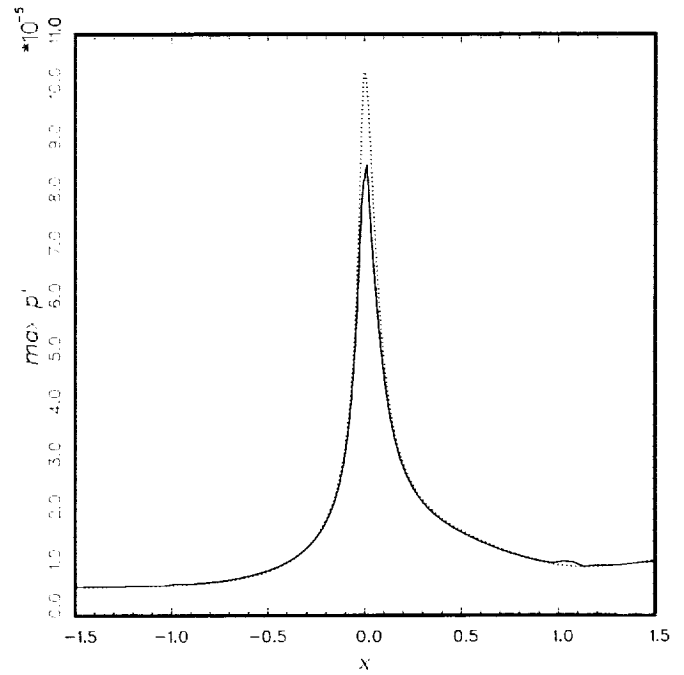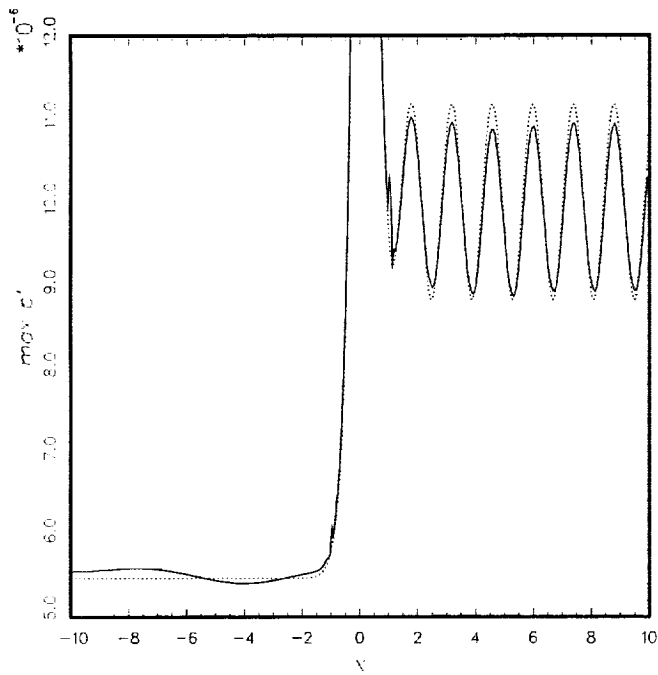
——— solution by Wang, Chang and Jorgenson (400 mesh points)
······ exact solution
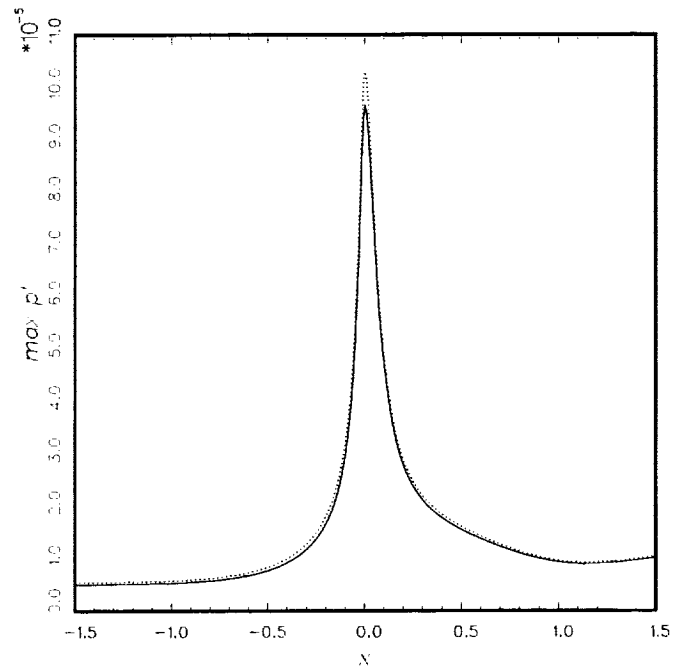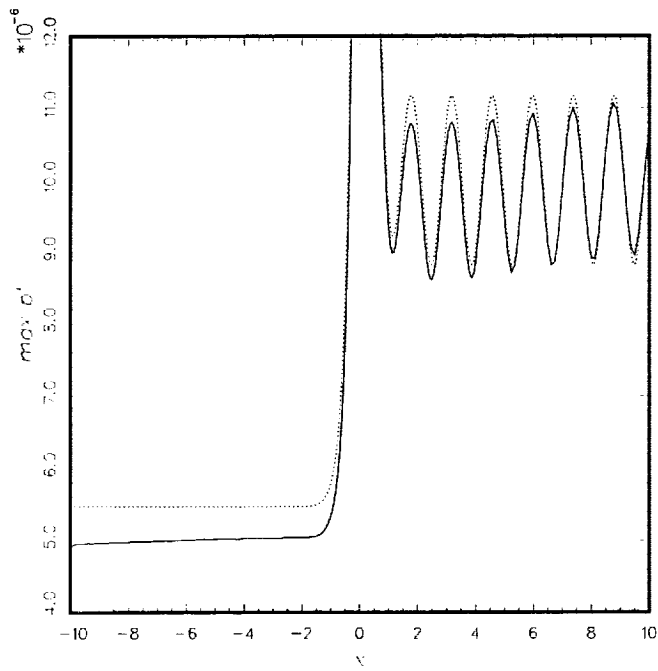
——— solution by Yin and Delfs (321 mesh points)
······ exact solution
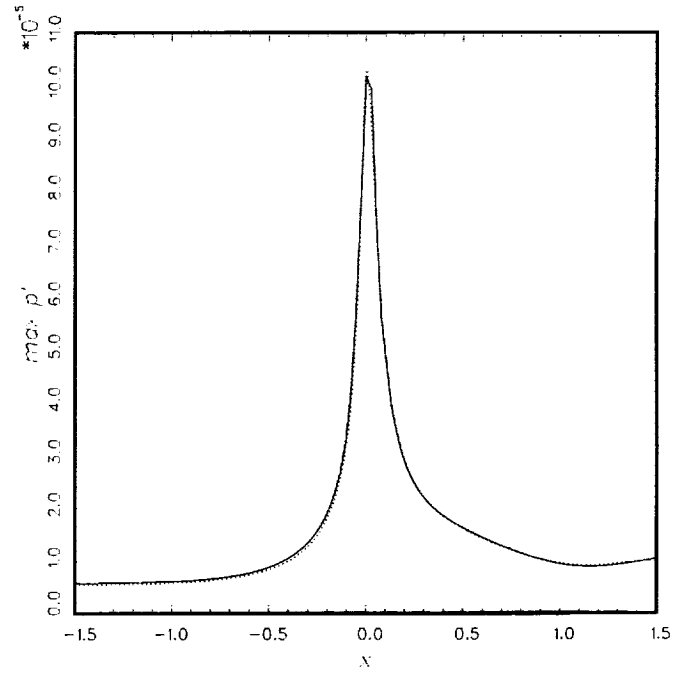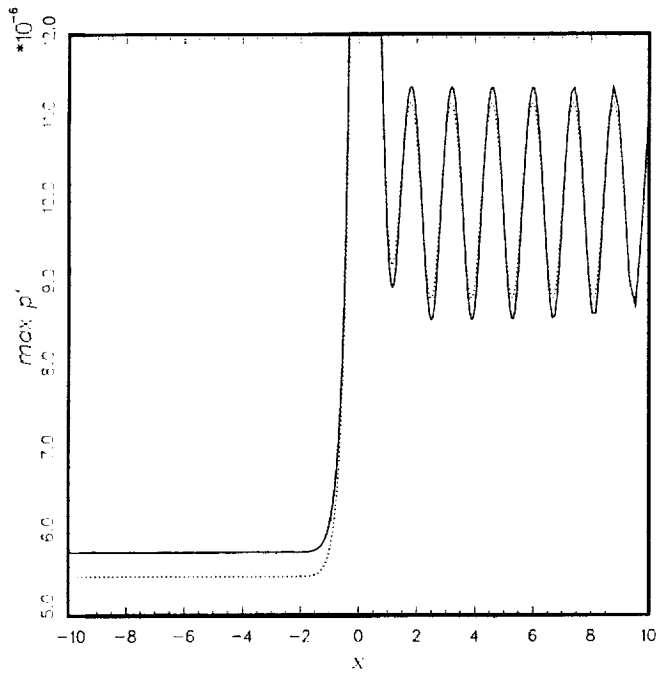
——— solution by Zhuang and Zheng (401 mesh points)

· · · · · · exact solution

394

Solutions to Category 1 Problem 2

Ray Hixon and Reda R. Mankbadi
CAA Group, ICOMP
NASA Glenn Research Center
Cleveland, Ohio 44135

1) Mean Pressure Distribution
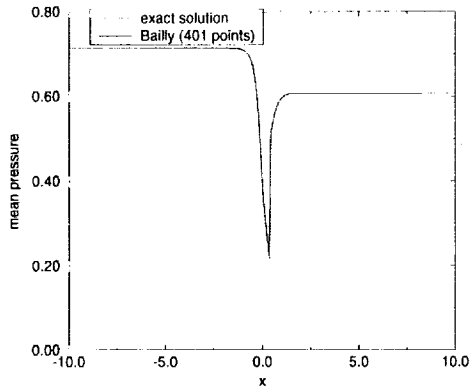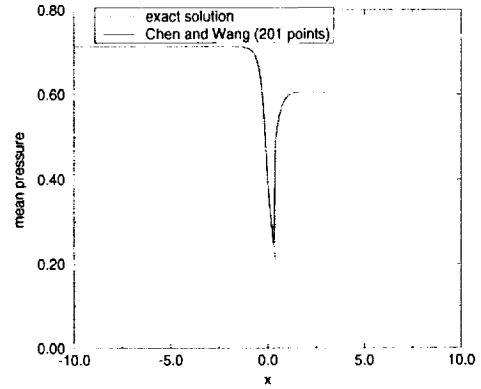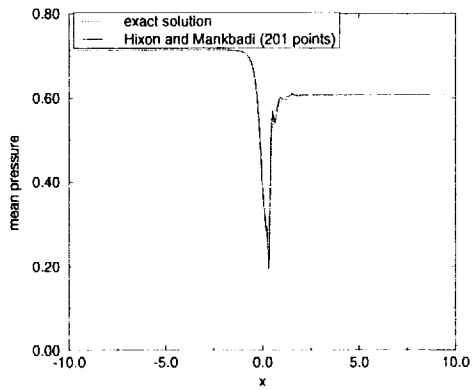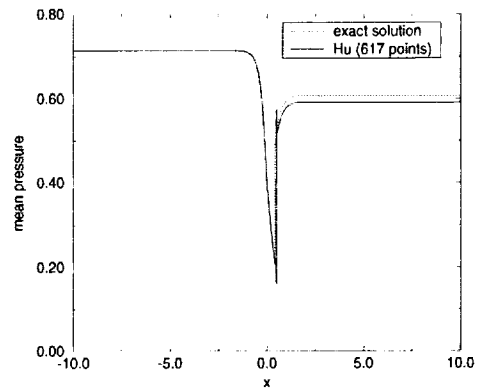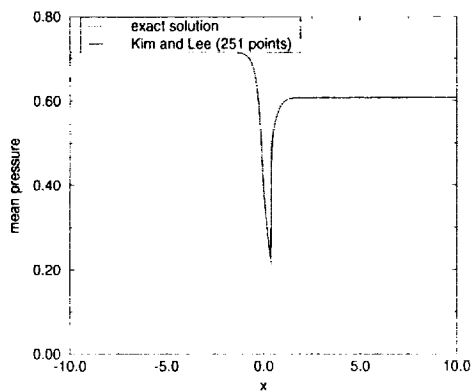
C. Bailly

R. F. Chen and Z. J. Wang

R. Hixon and R. R. Mankbadi

F. Q. Hu
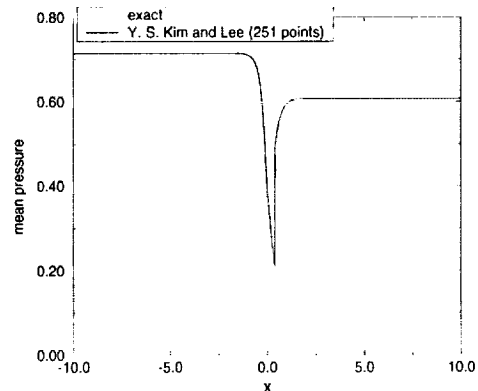
J. W. Kim and D. J. Lee
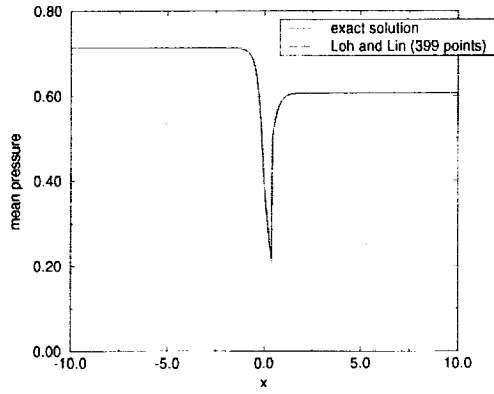
Y. S. Kim and D. J. Lee
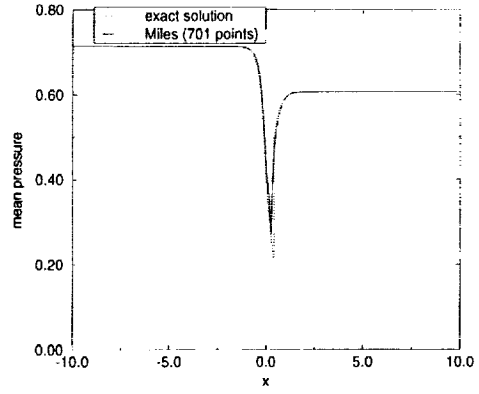
H.-T. Loh and W. H. Lin
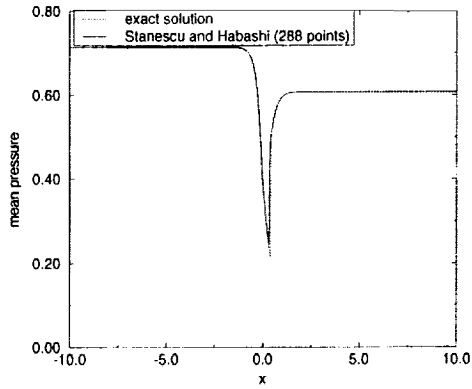
J. H. Miles

D. Stanescu and W. G. Habashi
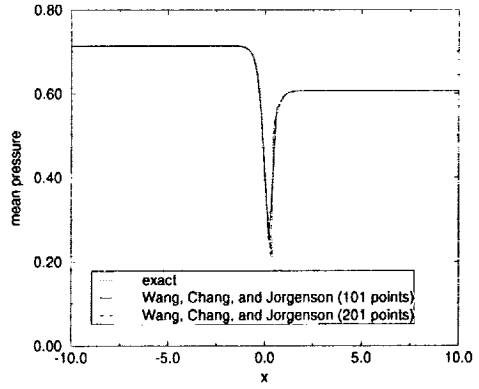
X. Y. Wang, S. C. Chang, and P. Jorgenson
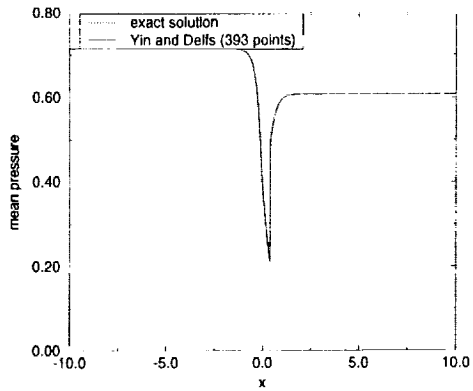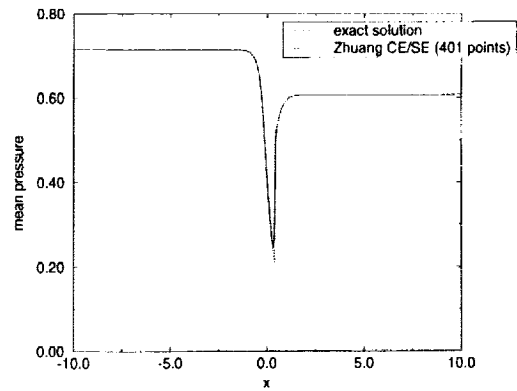
J. Yin and J. Delfs

M. Zhuang and S. Zheng

2) Perturbation Pressure Distribution
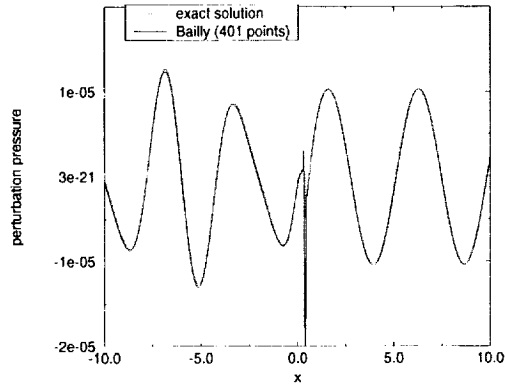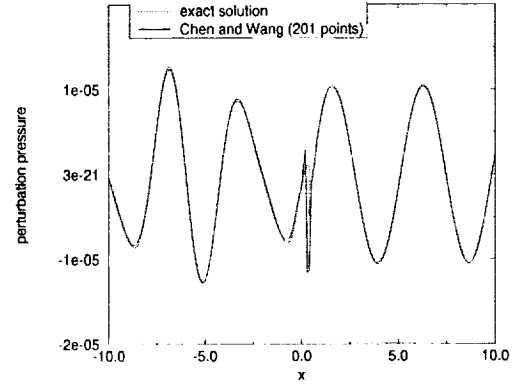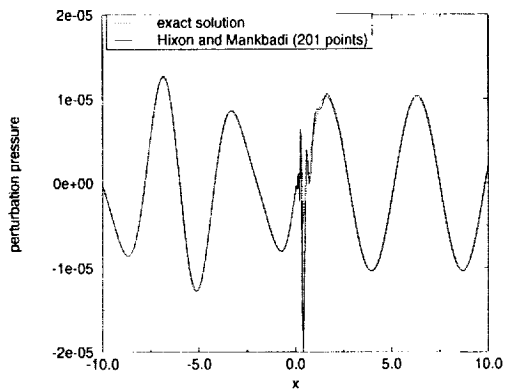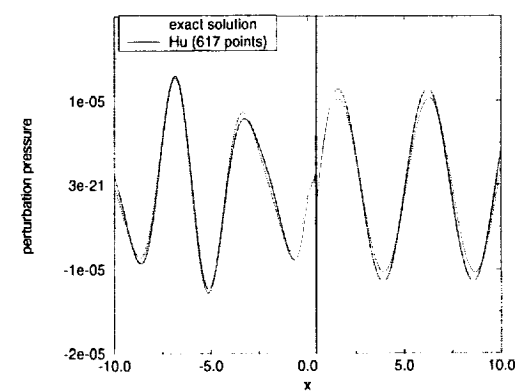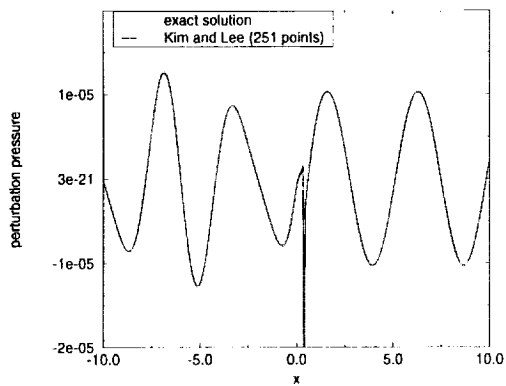
C. Bailly

R. F. Chen and Z. J. Wang

R. Hixon and R. R. Mankbadi

F. Q. Hu
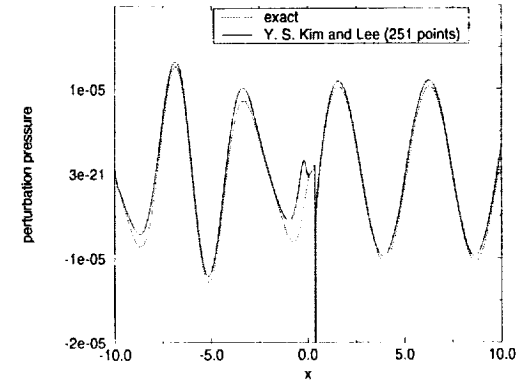
J. W. Kim and D. J. Lee
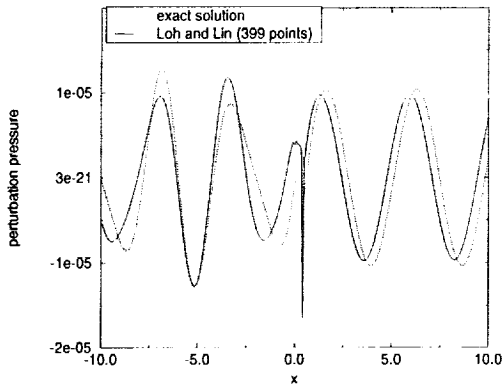
Y. S. Kim and D. J. Lee

H.-T. Loh and W. H. Lin
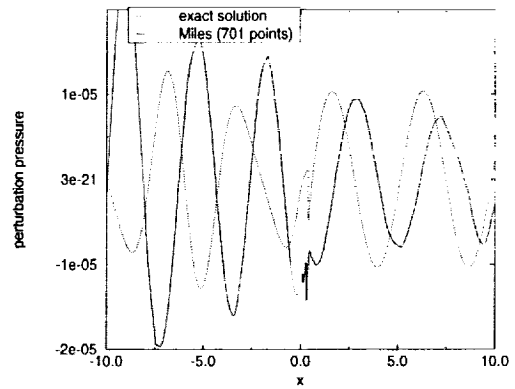
J. H. Miles
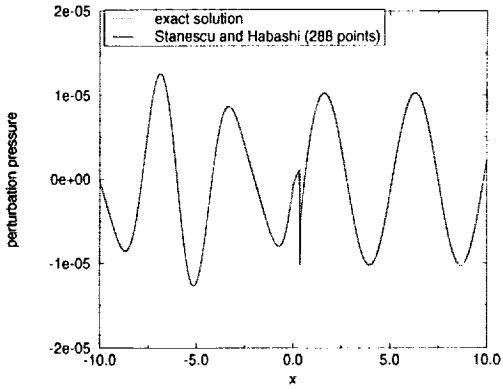
D. Stanescu and W. G. Habashi
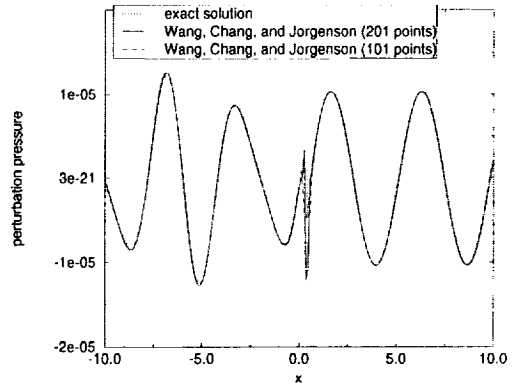
X. Y. Wang, S. C. Chang, and P. Jorgenson
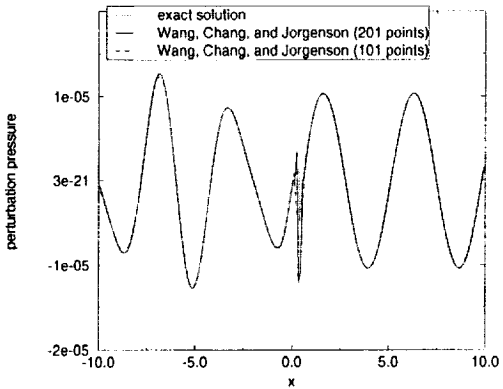
J. Yin and J. Delfs
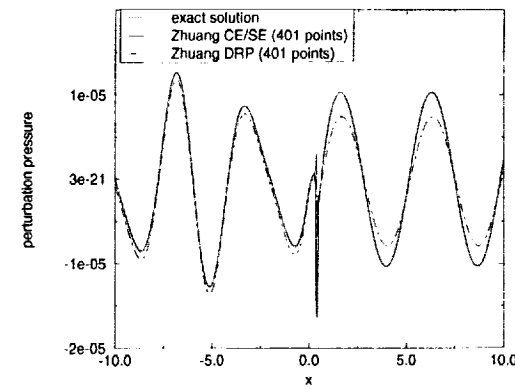
M. Zhuang and S. Zheng

3) Perturbation Pressure History at Exit Plane
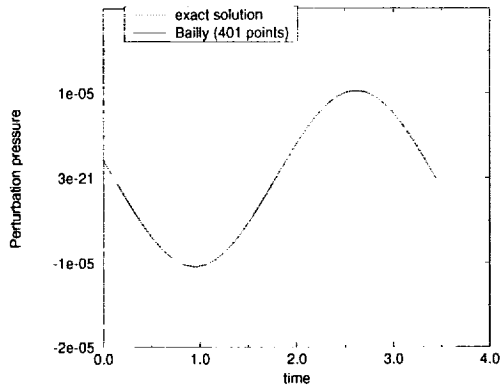
C. Bailly
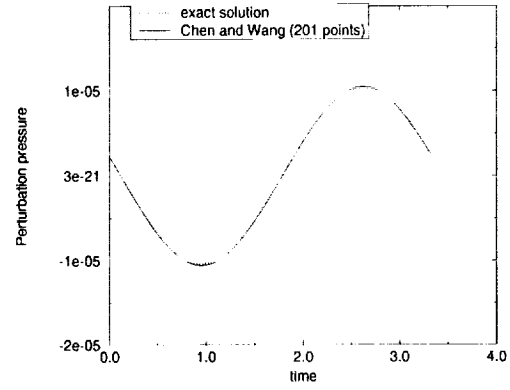
R. F. Chen and Z. J. Wang
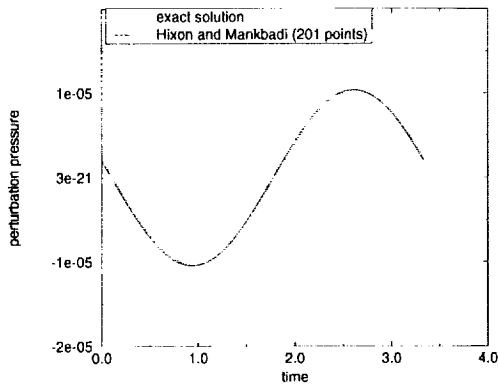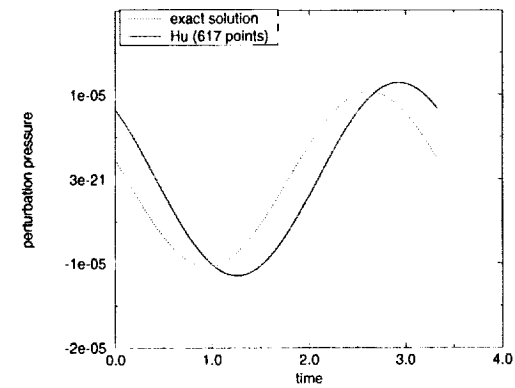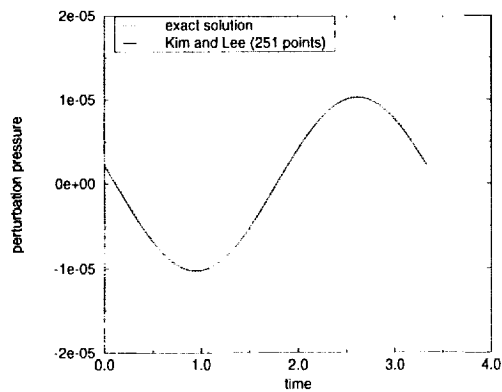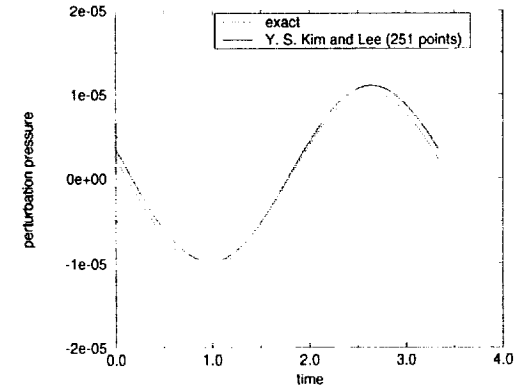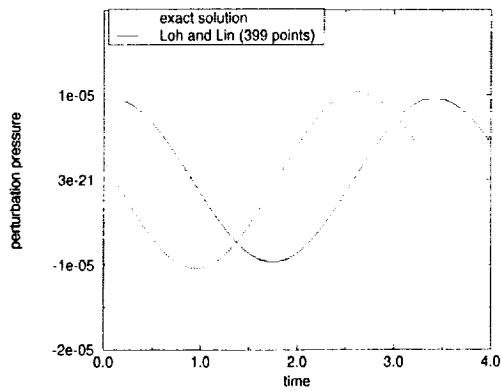
R. Hixon and R. R. Mankbadi

F. Q. Hu

J. W. Kim and D. J. Lee

Y. S. Kim and D. J. Lee

H.-T. Loh and W. H. Lin
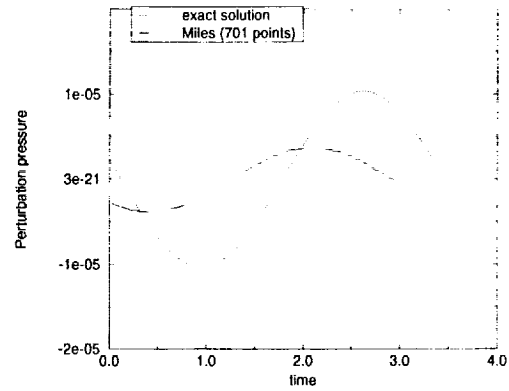
J. H. Miles
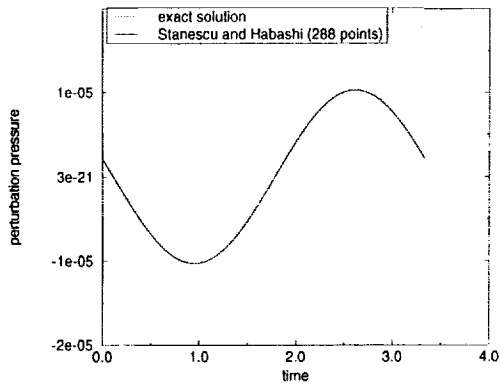
D. Stanescu and W. G. Habashi
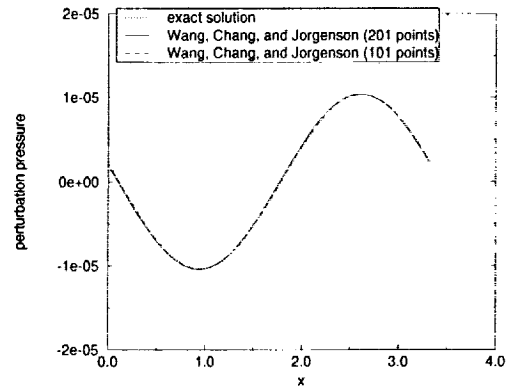
X. Y. Wang, S. C. Chang, and P. Jorgenson
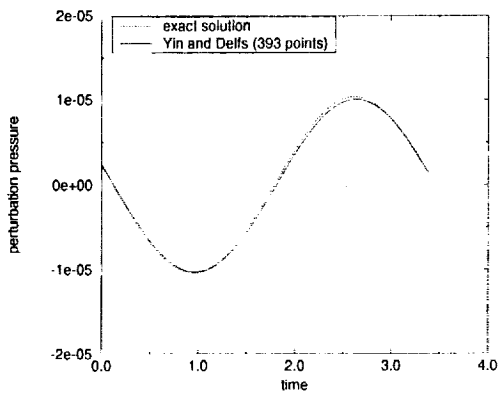
J. Yin and J. Delfs
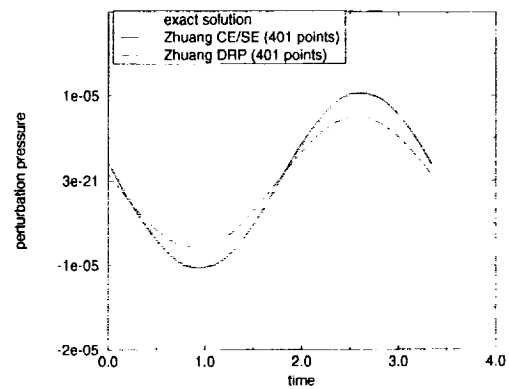
M. Zhuang and S. Zheng

COMPARISONS WITH ASYMPTOTIC SOLUTION: CATEGORY 2

CHRISTOPHER K.W. TAM and ALEXEI AGANIN
Department of Mathematics
Florida State University
Tallahassee, FL 32306-4510
Email: tam@math.fsu.edu

Only two participants submitted computed results for comparison with analytical solutions. The analytical solutions are asymptotic solutions valid for large distances from the rotor. The computed results, on the other hand, are measured at finite distances away. One should take this difference into account when judging the comparisons.

There are two parts to this benchmark problem; the open rotor and the ducted rotor problems. The blade passage frequencies of the ducted rotor, as prescribed by the benchmark problem, are below the cut-off frequency of the duct. Therefore, effectively there is very little acoustic radiation. Accordingly, no comparison is presented.

——— solution by solution by Fang Hu

· · · · · · asymptotic solution
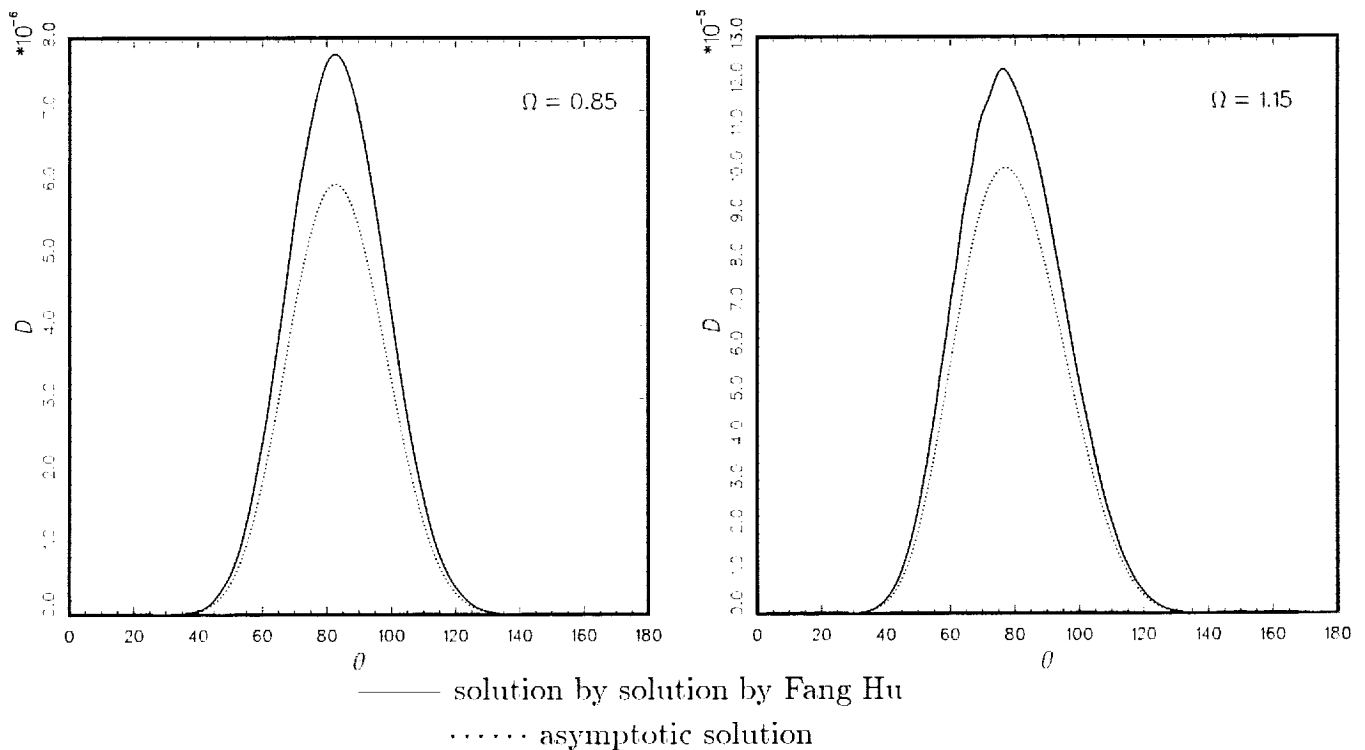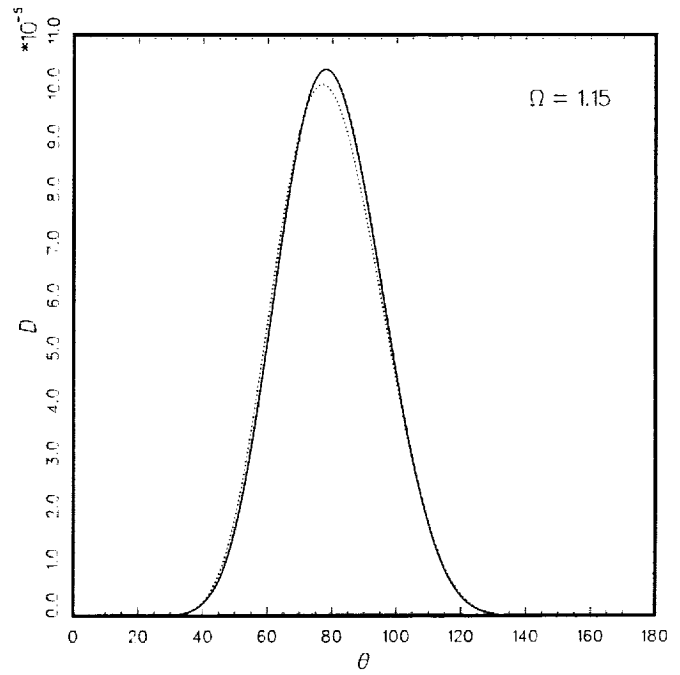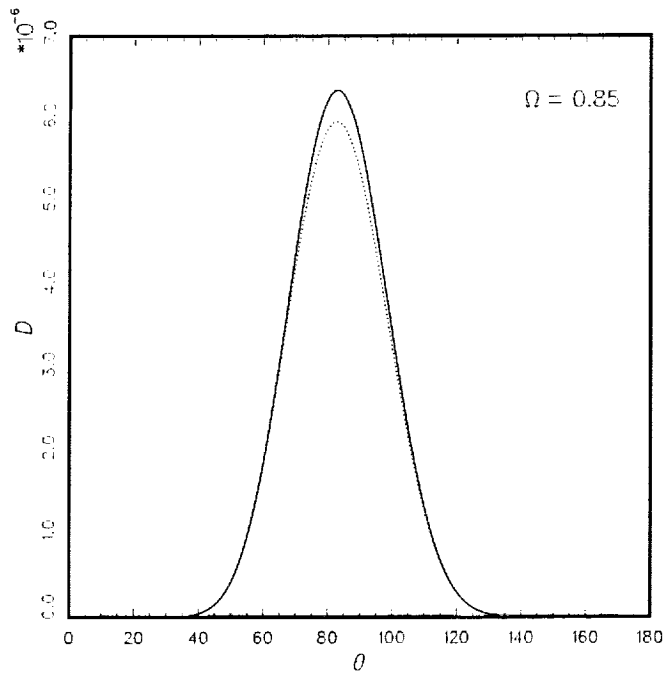
solution by Tam and Aganin

asymptotic solution

COMPARISON OF ANALYTICAL AND CAA SOLUTIONS
CATEGORY 3, BENCHMARK PROBLEM 1

James R. Scott
NASA Glenn Research Center
Cleveland, Ohio 44135
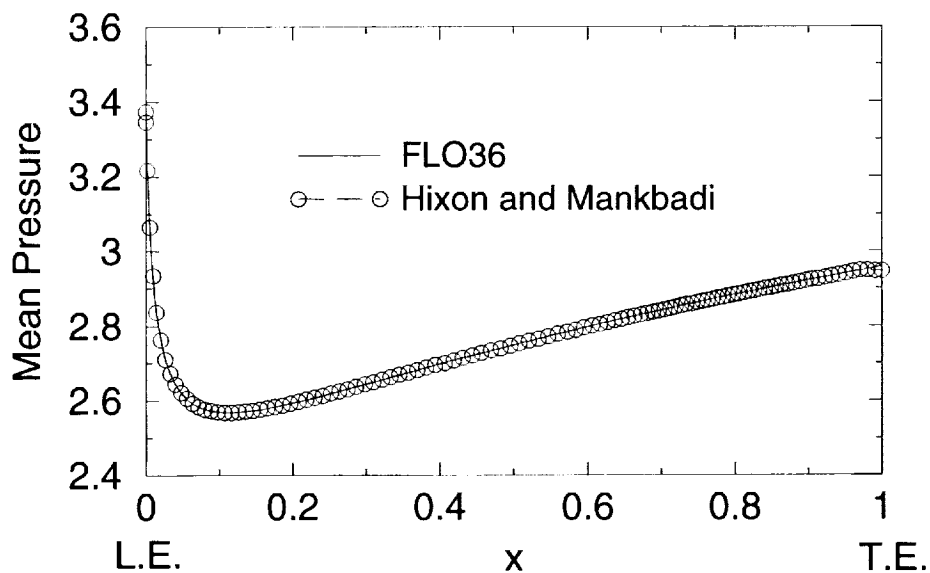
Mean pressure on airfoil surface, Case 1, k1=k2=0.1
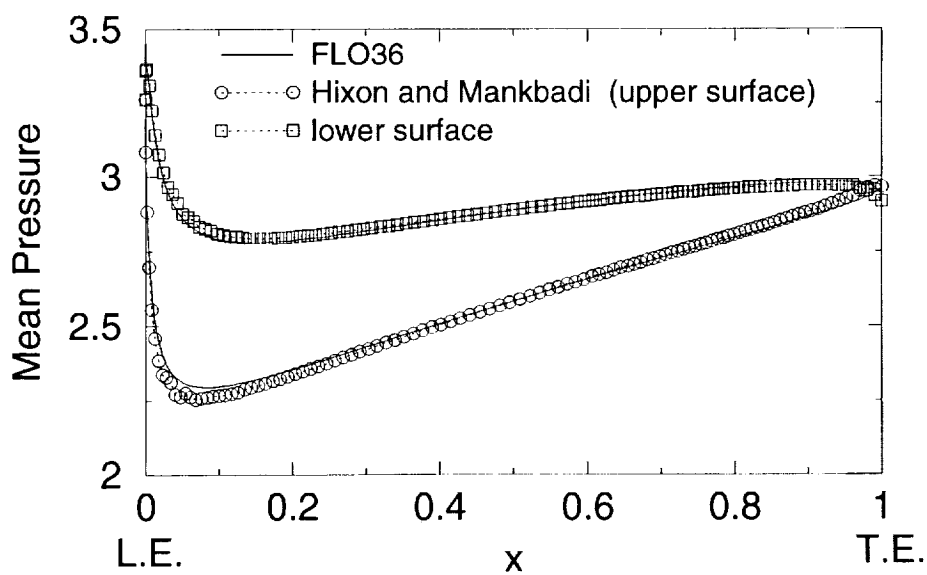
Mean pressure on airfoil surface, Case 2, k1=k2=1.0
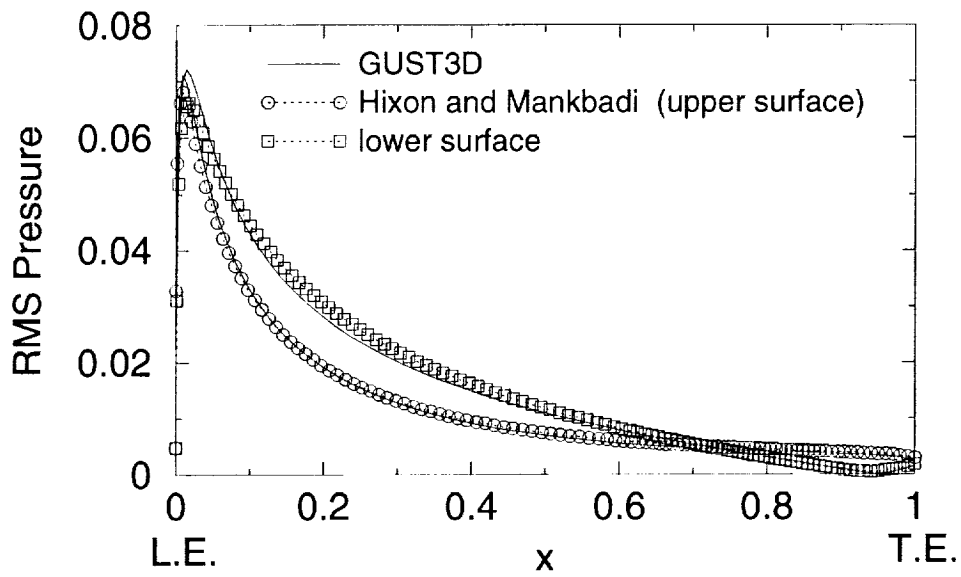
RMS pressure on airfoil surface, Case 1, k1=0.1
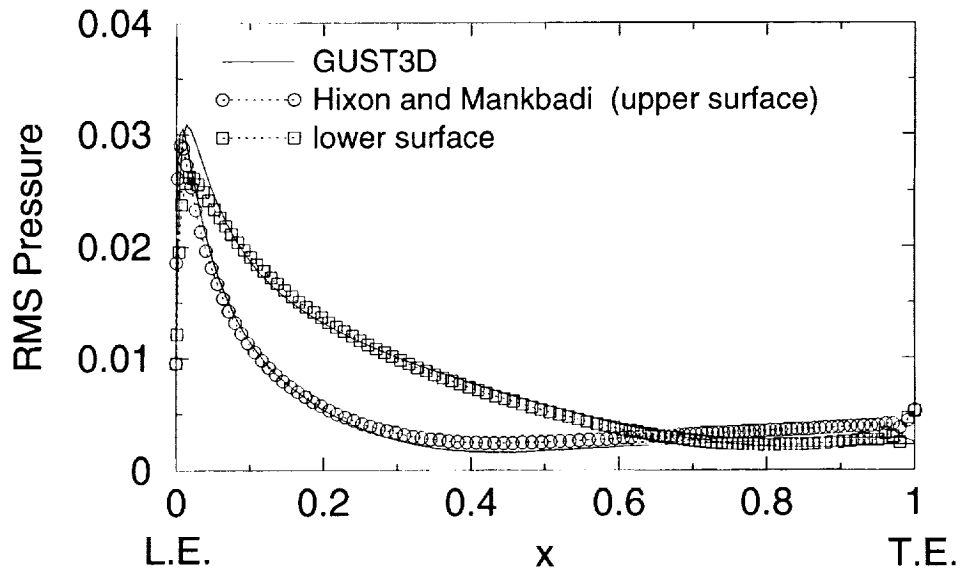
RMS pressure on airfoil surface, Case 1, k1=k2=1.0
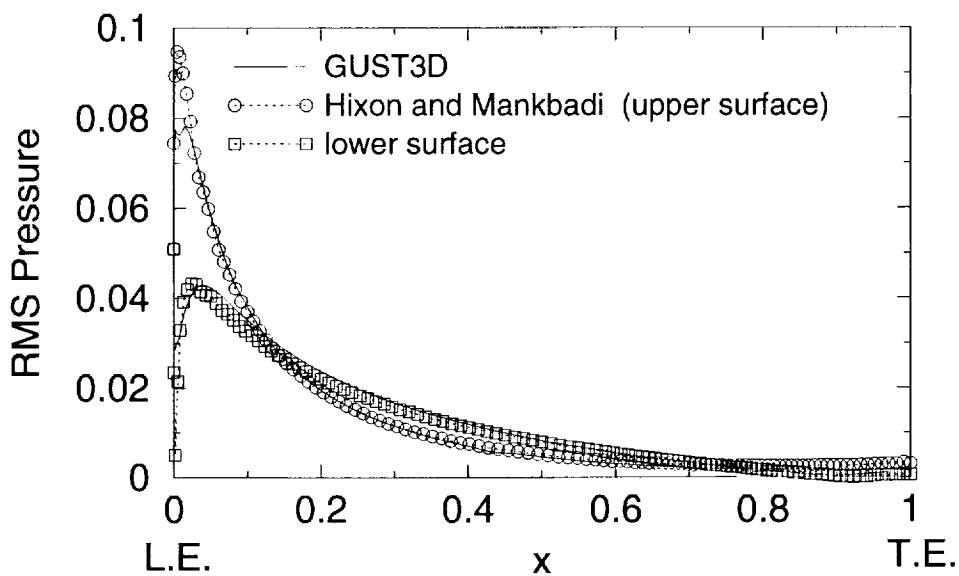
RMS pressure on airfoil surface, Case 2, k1=k2=0.1
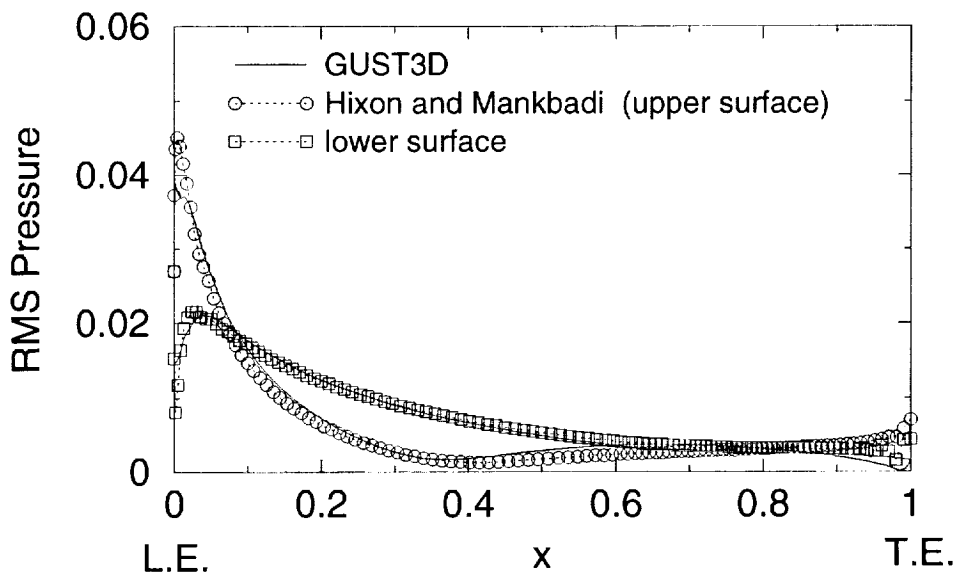
RMS pressure on airfoil surface, Case 2, k1=k2=1.0
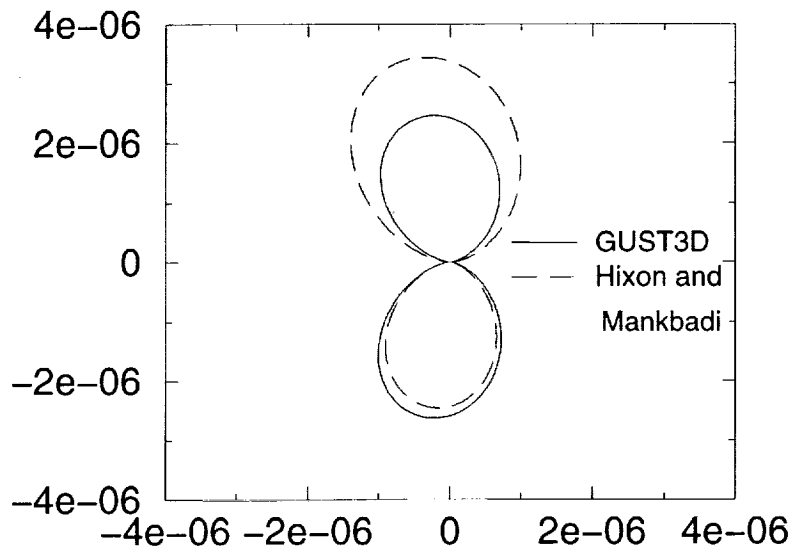
Acoustic intensity, Case 1, k1=k2=0.1

Acoustic intensity, Case 1, k1=k2=1.0
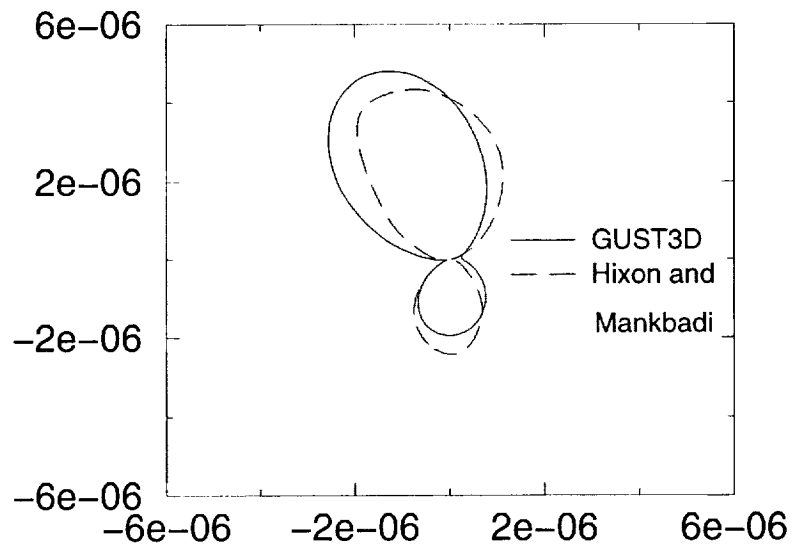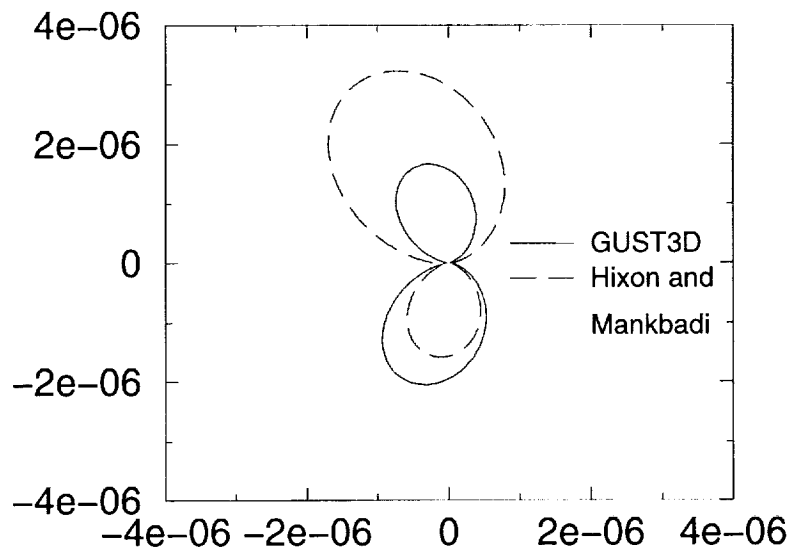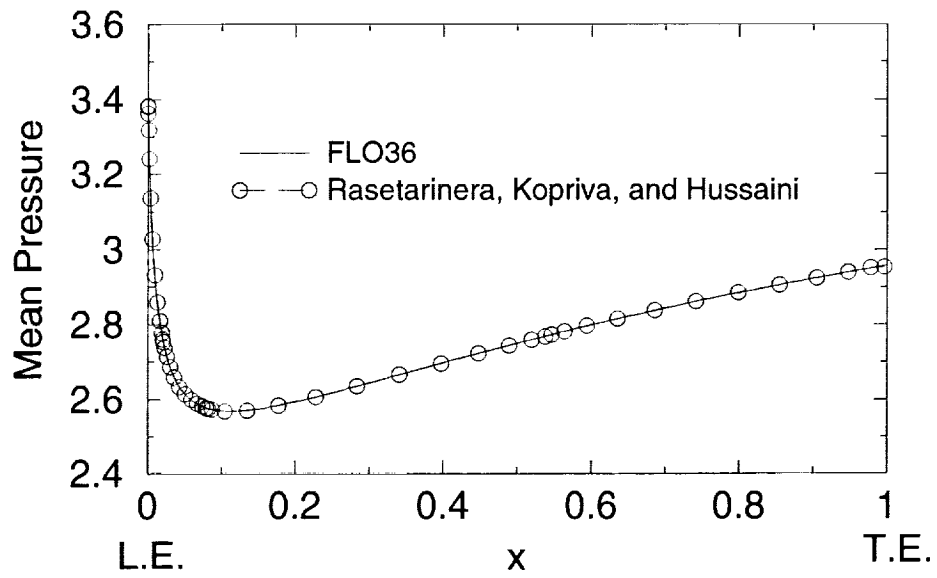
Acoustic intensity, Case 2, k1=k2=0.1

Acoustic intensity, Case 2, k1=k2=1.0

Mean pressure on airfoil surface, Case 1, k1=k2=3.0
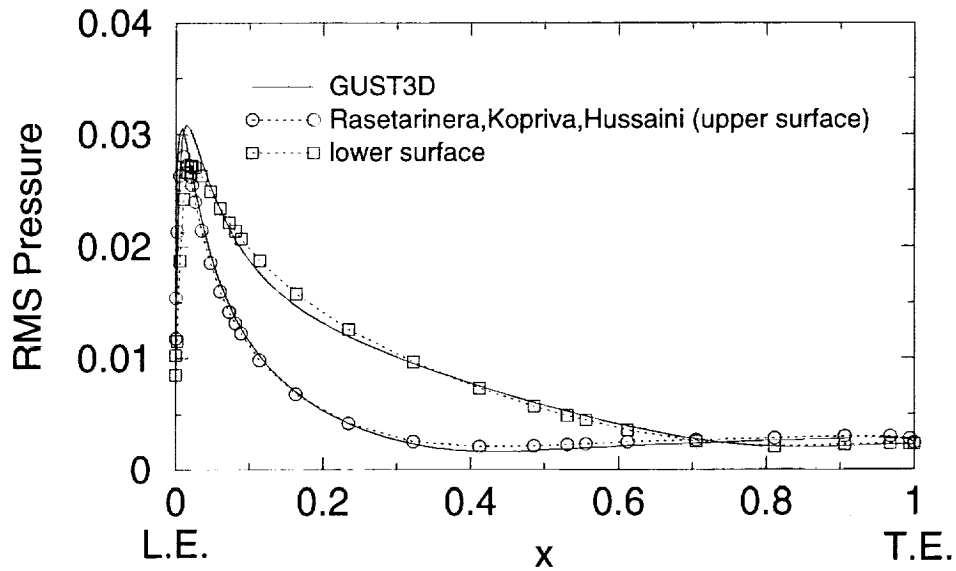
RMS pressure on airfoil surface, Case 1, k1=k2=1.0
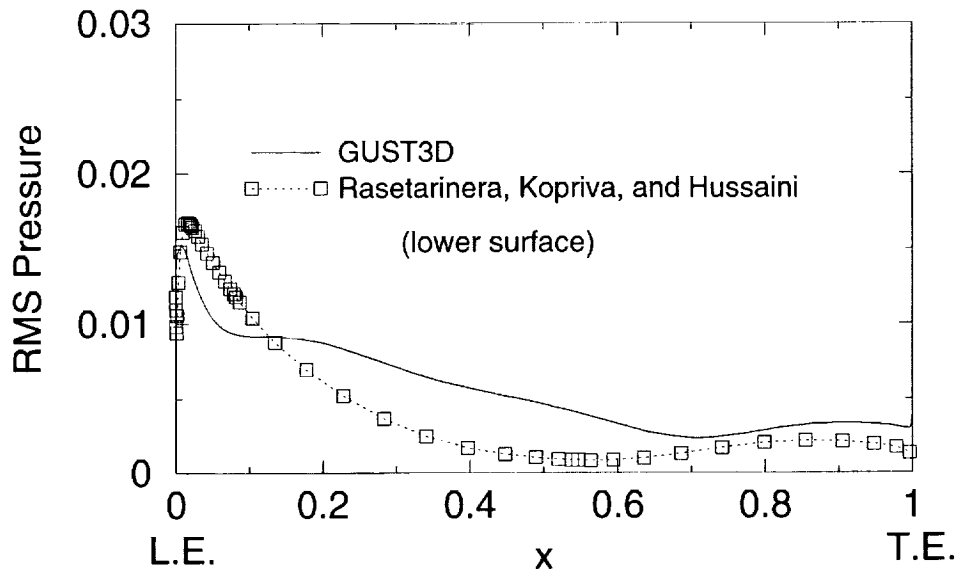
RMS pressure on airfoil surface, Case 1, k1=k2=3.0
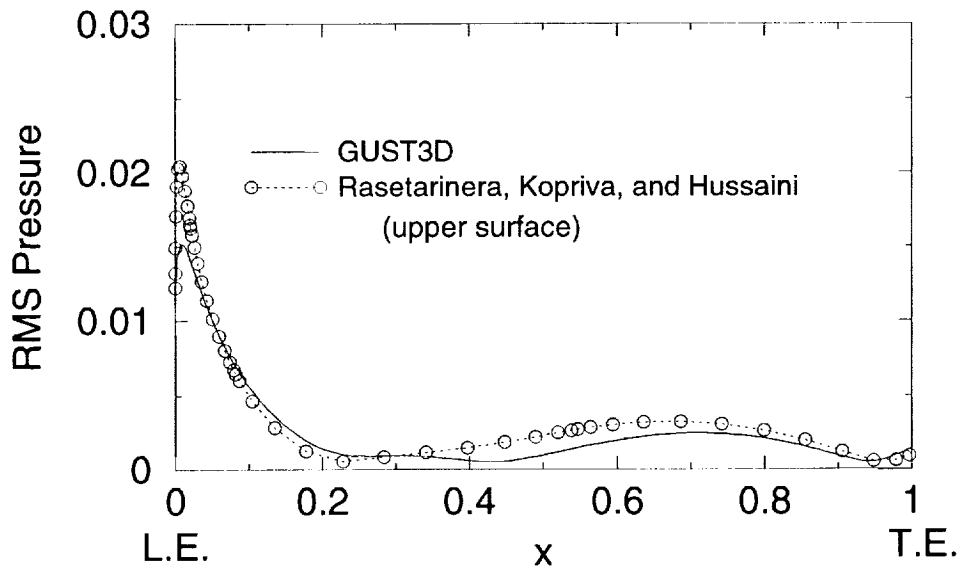
RMS pressure on airfoil surface, Case 1, k1=k2=3.0
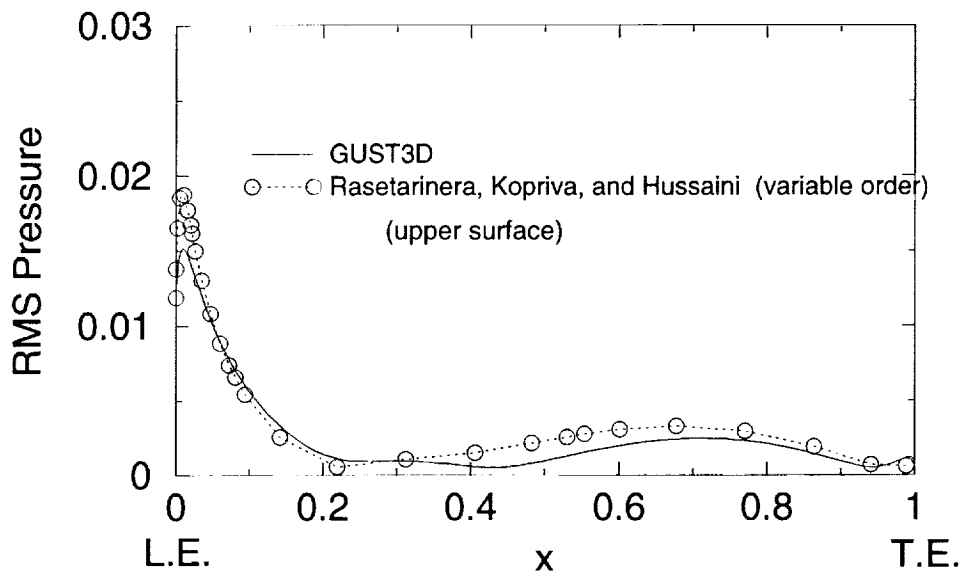
RMS pressure on airfoil surface, Case 1, k1=k2=3.0
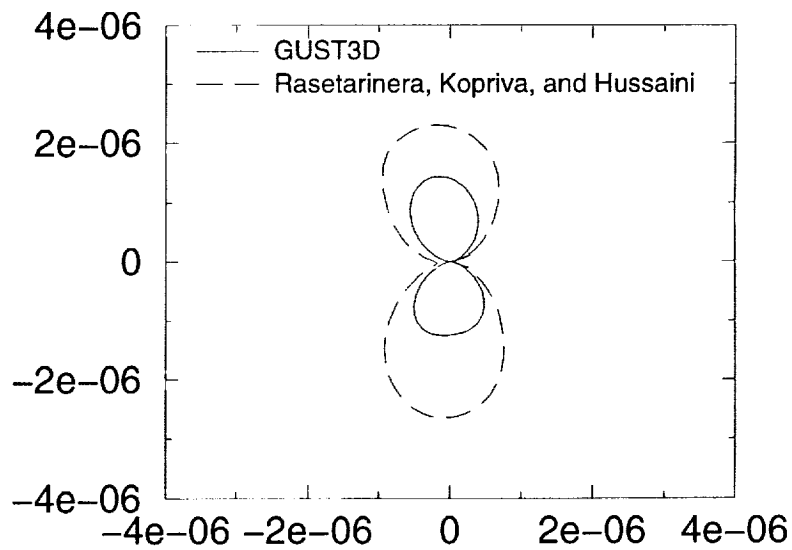
Acoustic intensity, Case 1, k1=k2=1.0

COMPARISON OF ANALYTICAL AND CAA SOLUTION(S) CATEGORY 3, BENCHMARK PROBLEM 3

Edmane Envia
NASA Glenn Research Center
Cleveland, Ohio 44135
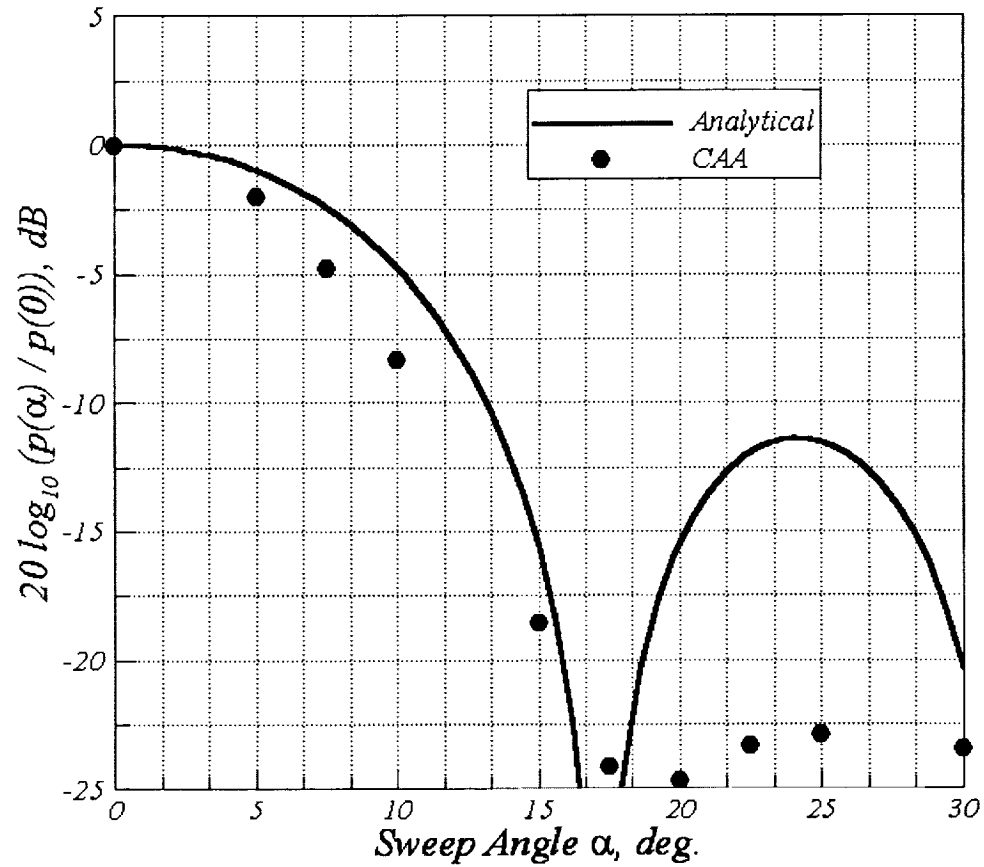
Sound pressure level reductions at the upstream location $(-5c, 0, \ell/2)$ due to the introduction of sweep. Solid line is analytical solution and the symbols denote the CAA-based solution due to Wang, et. al.
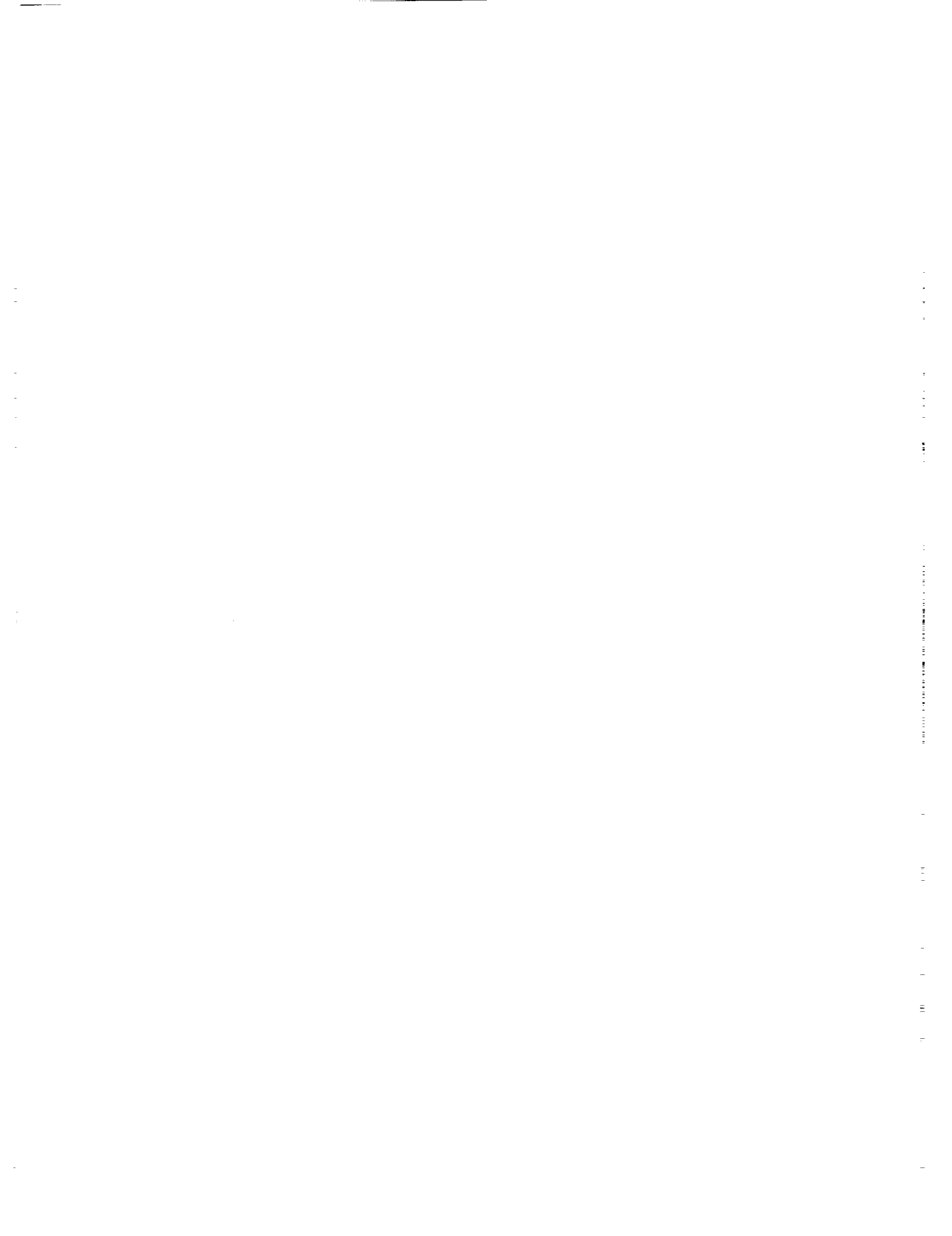
COMPARISONS WITH ANALYTICAL SOLUTION: CATEGORY 5

MILO D. DAHL
NASA Glenn Research Center
Cleveland, OH

**Bailly**

Hu

Li and Thiele

Lockard and Atkins

414
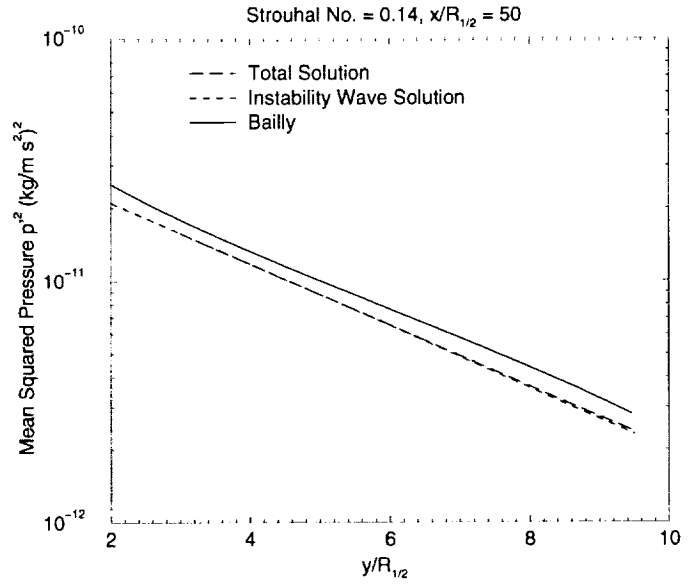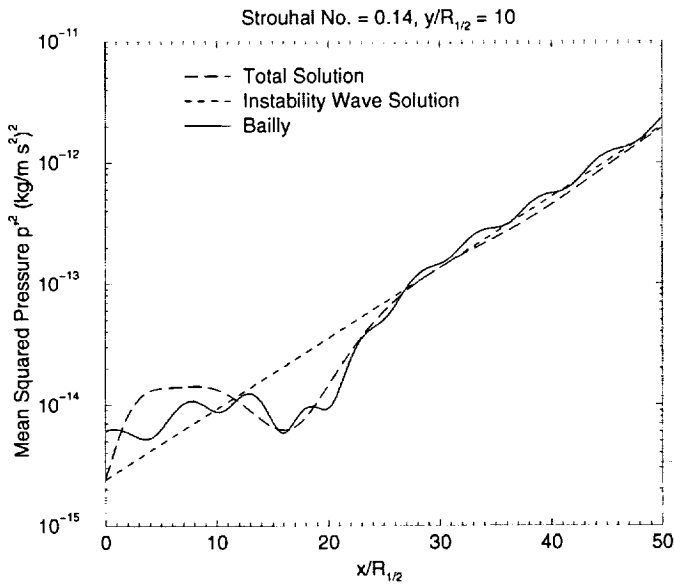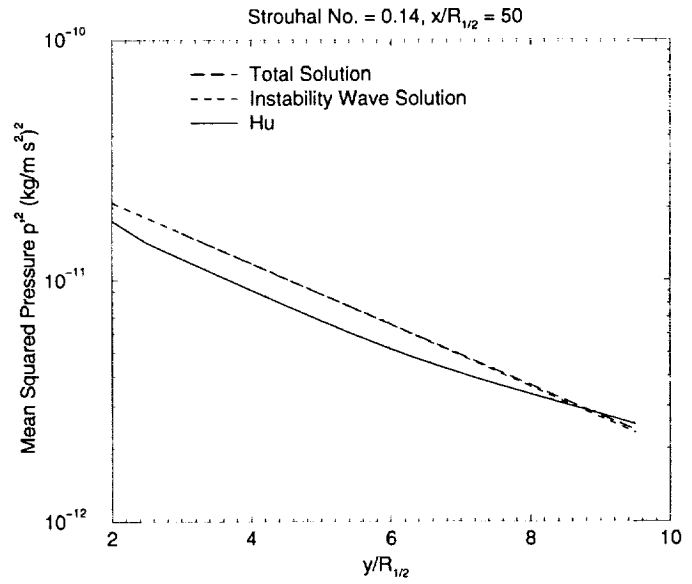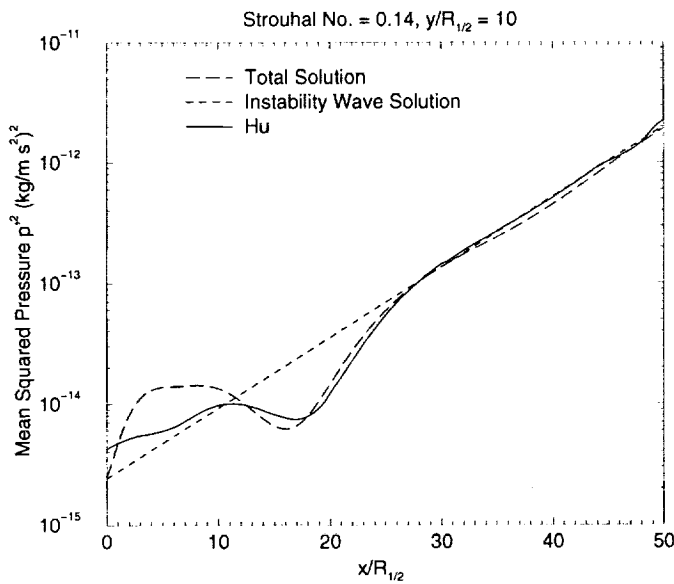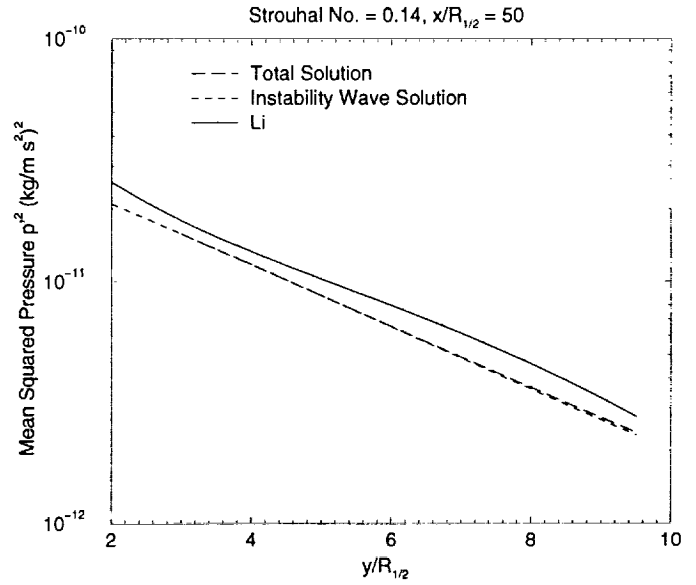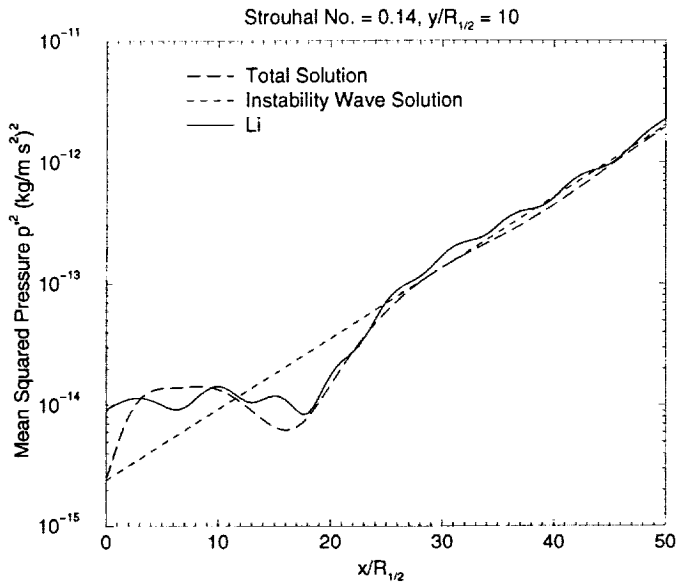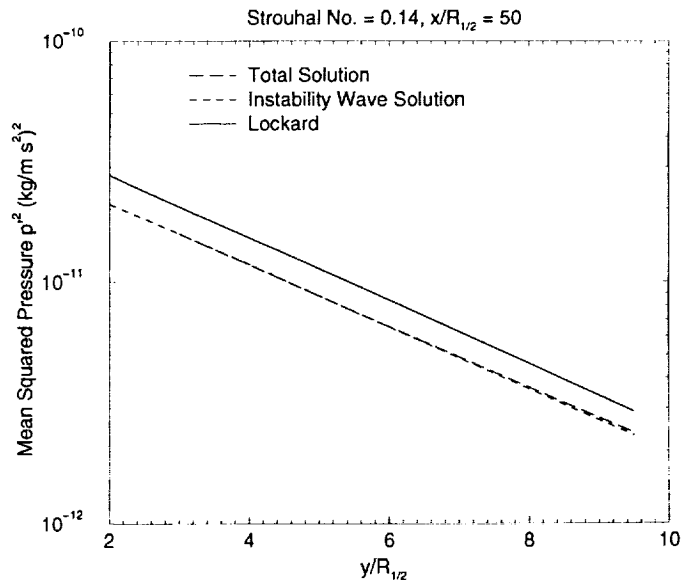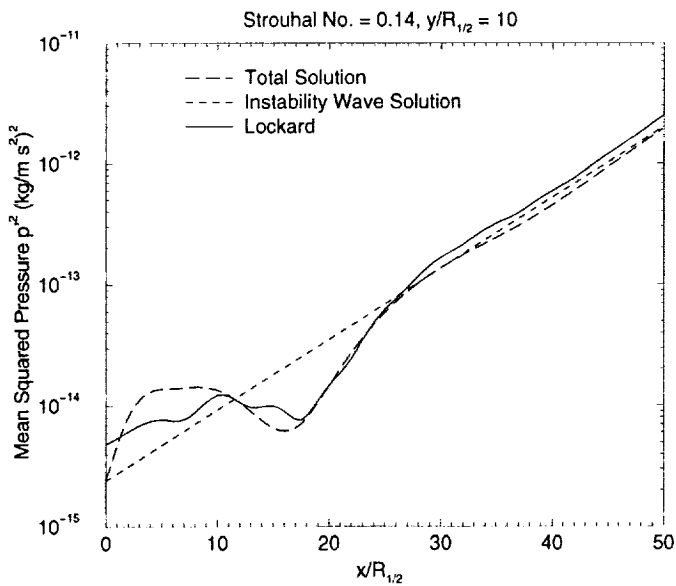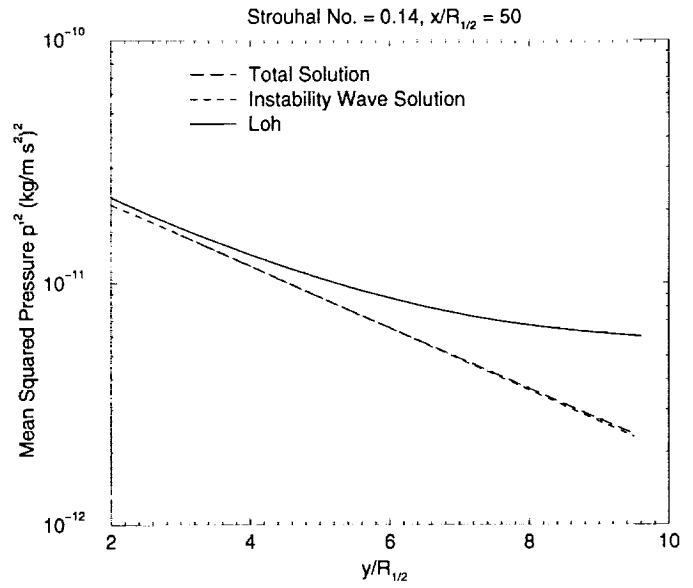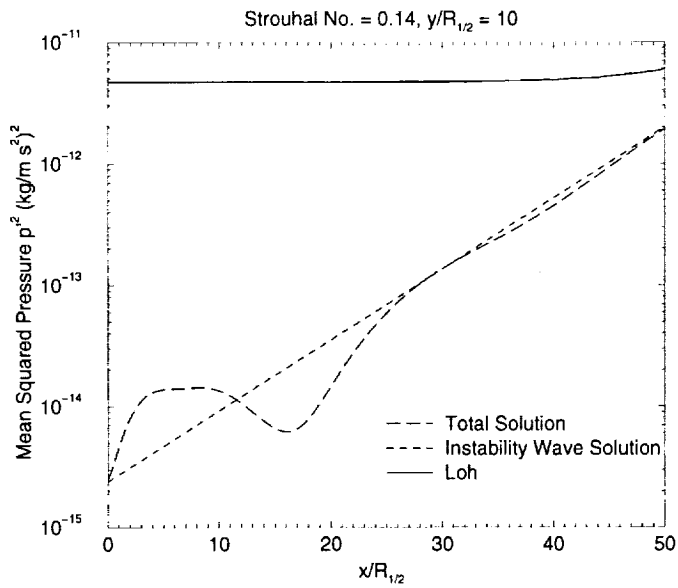
Loh, Wang, Chang, and Jorgenson

Scheidegger and Morris

Strouhal No. = 0.14, $y/R_{1/2}$ = 10

Strouhal No. = 0.14, $x/R_{1/2}$ = 50

Stanescu, Ait-Ali-Yahia, and Habashi

Strouhal No. = 0.60, $y/R_{1/2}$ = 10

Strouhal No. = 0.60, $x/R_{1/2}$ = 50

Bailly

Strouhal No. = 0.60, $y/R_{1/2} = 10$

Strouhal No. = 0.60, $x/R_{1/2} = 50$

Hu

Strouhal No. = 0.60, $y/R_{1/2} = 10$

Strouhal No. = 0.60, $x/R_{1/2} = 50$

Li and Thiele

Strouhal No. = 0.60, $y/R_{1/2}$ = 10

10^{-13}

Mean Squared Pressure p'^2 $(kg/m\ s^2)^2$

10^{-14}

10^{-15}

10^{-16}

10^{-17}

--- Total Solution
—— Lockard

0   10   20   30   40   50

$x/R_{1/2}$

Strouhal No. = 0.60, $x/R_{1/2}$ = 50

10^{-14}

Mean Squared Pressure p'^2 $(kg/m\ s^2)^2$

10^{-15}

10^{-16}

--- Total Solution
—— Lockard

2   4   6   8   10

$y/R_{1/2}$

Lockard and Atkins

Strouhal No. = 0.60, $y/R_{1/2}$ = 10

10^{-13}

Mean Squared Pressure p'^2 $(kg/m\ s^2)^2$

10^{-14}

10^{-15}

10^{-16}

10^{-17}

--- Total Solution
Scheidegger, Wasistho BC
Scheidegger, Tam and Dong BC

0   10   20   30   40   50

$x/R_{1/2}$

Strouhal No. = 0.60, $x/R_{1/2}$ = 50

10^{-14}

Mean Squared Pressure p'^2 $(kg/m\ s^2)^2$

10^{-15}

10^{-16}

--- Total Solution
Scheidegger, Wasistho BC
Scheidegger, Tam and Dong BC

2   4   6   8   10

$y/R_{1/2}$

Scheidegger and Morris

Strouhal No. = 0.60, $y/R_{1/2} = 10$

Strouhal No. = 0.60, $x/R_{1/2} = 50$

**Stanescu, Ait-Ali-Yahia, and Habashi**

Strouhal No. = 0.14, $y/R_{1/2} = 1$

Strouhal No. = 0.14, $y/R_{1/2} = 1$

Bailly

Hu

Li and Thiele

Lockard and Atkins

Agarwal and Morris

Scheidegger and Morris

Strouhal No. = 0.14, $y/R_{1/2} = 1$

- - - Instability Wave Solution
—— Stanescu

Stanescu, Ait-Ali-Yahia, and Habashi

Strouhal No. = 0.14, $y/R_{1/2} = 1$

- - - Instability Wave Solution
—— Loh
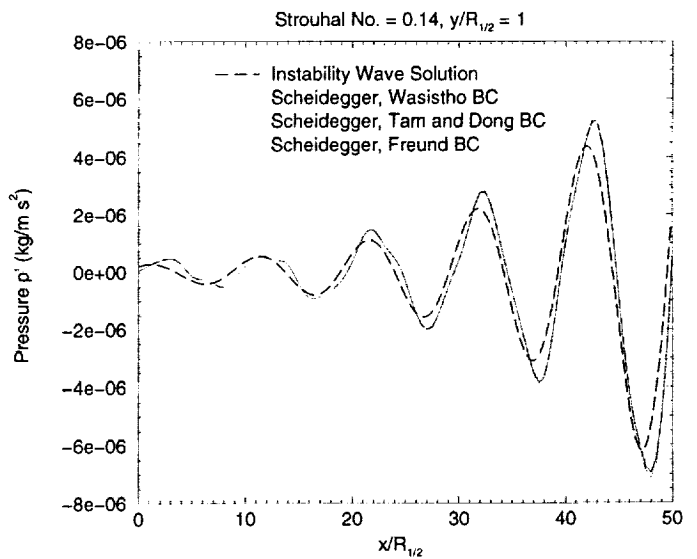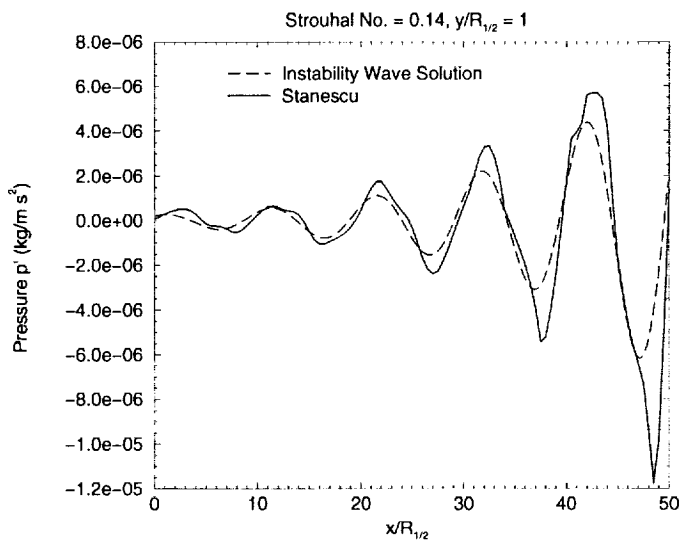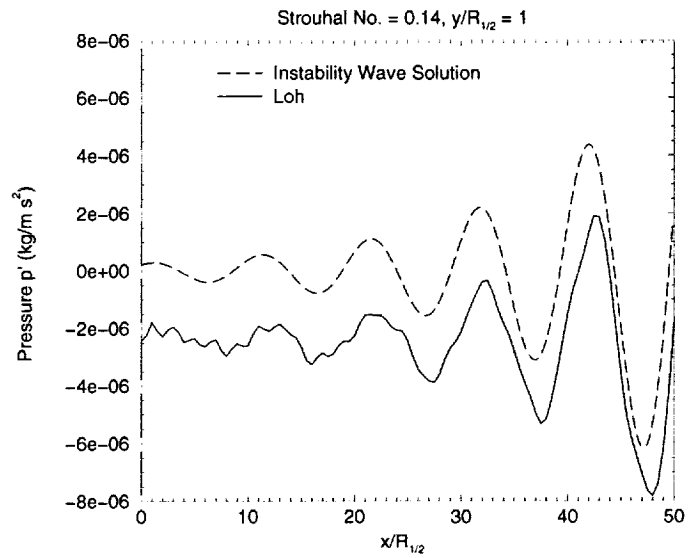
Loh, Wang, Chang, and Jorgenson

Computational Aeroacoustics Workshop Industry Panel Discussion

Computational Aeroacoustics Workshop
Industry Panel Discussion

A panel discussion was held, comprising representatives from industry, and each panel member gave a prepared presentation on their views and interests in Computational Aeroacoustics (CAA). The panel members were asked to address one or more of the following issues or questions:

1. What is the status of CAA as it applies to your business and product line?
2. How has CAA helped solve problems for your business in the past?
3. How are you implementing CAA in your organization?
4. What direction would you like CAA to go to provide tools useful to your business?

The following panel members participated:

1. Don Weir, AlliedSignal
2. Wesley Lord, Pratt & Whitney Aircraft
3. Mahendra Joshi, Boeing Company
4. Bill Dalton, Rolls Royce-Allison
5. Tom Dong, Lockheed-Martin
6. Phil Gliebe, GE Aircraft Engines

The participants gave approximately 20-minute presentations, followed by questions from the audience. The paragraphs below summarize the highlights and significant points made by the panel participants. The Appendix to this summary contains the presentation charts provided by each presenter.

Phil Gliebe – GE Aircraft Engines
Areas where CAA can help include (1) turbomachinery noise analysis, (2) jet noise analysis, and (3) combustor noise analysis. CAA has the potential to help in resolving physical modeling issues which seemingly escape resolution by analytic and/or classical numerical methods. Specific examples include (1) the relative roles of dipole and quadrupole sound sources in noise generated by gust-blade row interaction, (2) flight effects on jet noise and attendant wind tunnel or free-jet corrections of scale model jet test data to the flight condition, (3) duct propagation with flow gradients, variable wall geometries and bifurcations, and (4) duct wall liner impedance modeling and duct inlet and exit transmission/reflection effects. There is also a need for additional benchmark experiments for validating CAA methods and codes, as the codes become capable of analyzing more complex problems for which no simple analytical or classical numerical solutions exist. Finally, there is concern about the ability of industry to implement, train users, and deploy into the design community CAA tools, which are by nature very complex. Issues that need to be addressed include compatibility with existing design tools, grid generation, geometry modeling, CFD codes, etc. These tools must be robust and cost effective, and have to be consistent with available computing capacity.

Don Weir – AlliedSignal
The acoustic design of aircraft engines has several objectives for noise reduction. These include community noise certification, guarantees to airline customers, noise complaints from the community, local airport rules and aircraft interior passenger and crew noise exposure. Testing of various design options can be very expensive. CAA tools potentially can reduce the amount of testing required if they can be used to down-select the options with confidence. With a good

analysis tool, a full matrix Design of Experiments (DOE) evaluation can be made to develop the optimum design. Specific areas where CAA tools may be able to contribute are (1) mixed-flow jet exhaust noise, (2) fan multiple-pure-tone (MPT) noise, and (3) auxiliary power unit (APU) noise. APU systems have unique inlet and exhaust configurations, which are prone to flow distortions and unsteady flows and separations, and therefore have the potential for creating additional noise. As a final note, CAA codes and methods are very complex, and therefore are difficult to import and deploy in a typical product design environment.

Wesley Lord – Pratt & Whitney Aircraft

Future aircraft engines are envisioned to have much higher bypass ratio cycles than current fleet engines, and thus fan noise is likely to be the dominant noise source. Thus CAA development in fan noise modeling would be most useful. In the narrow view of CAA, i.e., actual time-accurate computation of the sound field using discretized formulations of the basic fluid dynamic equations, there has not yet been an impact of CAA on aircraft engine product design. In the broader view, however, where CFD tools, and in particular unsteady CFD tools such as the LINFLUX code are used to model acoustic phenomena, there has been significant utilization of CAA in product development. The current paradigm for turbomachinery acoustic design (especially fan design) is as follows:

$$\text{Geometry} \rightarrow \text{3DCFD} \rightarrow \text{Noise Model} \rightarrow \text{Computed Noise}$$

This paradigm has been used to successfully predict fan tone noise characteristics.

Areas where CAA could help quantify important noise-generation phenomena include the following: (1) airfoil self noise, (2) noise from 3-dimensional nozzle geometries, (3) realistic airfoil shapes and high Mach number simulation for blade row noise analysis, and (4) fan rotor tip clearance effects on noise.

Mahendra Joshi – Boeing Company

CAA could be a useful tool for analysis of aircraft landing gear noise, auxiliary air system exhaust valve noise, and "unexpected" tones from various aircraft surfaces, cavities, joints, protuberances, control surfaces on the wings and stabilizers, etc. There is not always a need to evaluate far field noise, as many aircraft noise problems are near field problems, and resolution of the problem in the near field also solves any associated far field problem.

Bill Dalton – Rolls Royce-Allison

CAA is today where CFD was 15 years ago, a promising technology that is just beginning to show potential. Today, CFD is now a standard analysis tool in aircraft and engine product design, and it can be speculated that 15 years from now, CAA will also be a standard analysis tool. Specific technology areas where CAA in the "broader view" has helped include (1) inlet shape effects, (2) fan blade shape effects on MPT noise, and (3) installation effects on propeller noise. Relative to the usefulness of CAA methods in the "narrow view," this depends on the problem being addressed. Whether CAA is an appropriate tool for problem solving depends on how long you have to solve the problem, how serious is the problem, and how good is the answer going to be with the tool used. The problem itself (and its consequences if not solved) dictates the level of sophistication of the tools used to address it. It would be useful to quantify the domain of applicability of linear vs. nonlinear CAA methods, so that some guidance may be provided for the complexity of the method required to address specific problems. Two specific technical areas where CAA may be useful are (1) non-axisymmetric duct geometries and (2) shear layer propagation.

Tom Dong – Lockheed-Martin

Lockheed-Martin is actively pursuing development of the Tam DRP scheme for product applications using multi-domain, multiple-time step approaches. Improvements in computational efficiency are felt to be very important. Some problem applications of interest for utilization of CAA methods are jet screech, and payload and weapons bay cavity noise and acoustic response.

Summary:

The industry panel consensus was that CAA has made significant progress in developing codes and solution methods, which can address flow conditions and geometries of interest to the industry community. The CAA research and development community is encouraged to continue development of this important and potentially fruitful technology area. Key technical issues are computational efficiency, correct modeling of boundary conditions for a high fidelity simulation of a small amplitude of acoustic waves, and the capability to model high frequencies and complex geometries. Eventually, preferably sooner than later, CAA codes and tools need to recognize and deal with the issues of compatibility with industry design systems, and must embody robustness so that generating accurate, believable solutions do not always require that a CAA expert be the only user. It is also important to recognize and appreciate that CAA still holds out the promise that it can provide quantitative evaluations of acoustic phenomena that defy useful analysis by existing methods and techniques.

Appendix

1. "Industry Panel Session – Aircraft Engine Acoustics," P.R. Gliebe and R.E. Kraft, GE Aircraft Engines, November 9, 1999.
2. "Relevance of CAA to Regional and Business Aircraft Engine Design," Donald S. Weir, AlliedSignal Engines and Systems, November 9, 1999.
3. "An Industry View of CAA," W.K. Lord, Pratt & Whitney, November 9, 1999.
4. "Use of Computational Methods for Noise/Vibration Problems," K. Viswanathan and M.K. Joshi, Boeing Commercial Airplane Group, November 8-10, 1999.
5. "Industry Panel Discussion," William N. Dalton, Rolls-Royce Allison, November 9, 1999.
6. "Industrial Applications of CAA," Tom Dong, Lockheed Martin Aeronautical Systems, 11/09/1999.

Philip R. Gliebe
GE Aircraft Engines
December 10, 1999

Industry Panel Session
Aircraft Engine Acoustics

Philip R. Gliebe
Robert E. Kraft
GE Aircraft Engines

Areas Where CAA Can Help

- **Turbomachinery Noise Analysis**

- **Jet Noise Analysis**

- **Combustor Noise Analysis**

Resolving Physical Modeling Issues Which Seemingly Escape Resolution By Analytic and/or Classical Numerical Methods:

Example:

The Roles And Contributions Of "Dipole" Sound and Quadrupole" Sound Sources in the Noise Generated By Blade Rows In Response To An Incident Gust

Can a "CAA" Analysis of a Model Problem of This Type Identify, decompose, resolve, etc., the existence of "dipole" and "quadrupole" sound sources? What is the real blade row unsteady response - effective "Sears Function" - vs. Mean Flow-Gust Interaction?

Develop A Better Understanding of Acoustic Phenomena Which Defy Analytic Treatment Without Employing Severely Limiting Approximations or Simplifications:

Example 1:

Flight Effects On Jet Noise . . . . .
- **Wind Tunnel Data and Free-Jet Corrections for Distributed Source Jet Noise Measurements**
- **Correcting Static Engine Jet Noise Data To Flight**

Can a "CAA" Model Problem be Constructed To Develop A More Accurate Method For Extrapolating Static Data and Wind Tunnel Data To Flight?

Develop A Better Understanding of Acoustic Phenomena Which Defy Analytic Treatment Without Employing Severely Limiting Approximations or Simplifications, Cont'd.:

Example 2:

Duct Propagation With Complex Geometry and Flow Gradients . . . . .
- **Variable Inner and Outer Wall Radius**
- **Radial Bifurcations and Struts**
- **Radial and Axial Flow Velocity and Pressure Gradients**

Can A "CAA" Model Problem be Constructed To Quantify and Understand Complex Duct Modal Pattern Behavior? Is "Duct Modes" the Right Physical Paradigm?

Develop A Better Understanding of Acoustic Phenomena Which Defy Analytic Treatment Without Employing Severely Limiting Approximations or Simplifications, Cont'd.:

Other Examples:

Duct Treatment Impedance Predictions - Time-Domain Models

Inlet and Exhaust Nozzle Transmission and Reflection Phenomena

Component Resonance and Instability Phenomena
- **Combustors**
- **Cavities**
- **Rotating Disk Spaces**

Define Benchmark Experiments Which Can Be Used To:

- **Validate CAA Methodologies**

- **Provide Key Insights into "Sticky" Modeling Issues - e.g., Boundary Conditions, etc.**

- **Complement Benchmark Exact Solutions**

- **Extend The Validation Range To Problems Where Exact Solutions Do Not Exist**

Industry, Universities and Government (NASA) Need to be thinking about Providing Resources to Execute These Benchmark Experiments

Issues Related To Commercial Application of CAA Tools In Industry (Implementation, Training and Deployment):

- Compatibility with Existing Tools – CFD, Grid Generation, Geometry Modeling, etc.

- Complex Design Problems Often Require Solution In Short Time Frame, CAA Tools May Require More Time To Use Than Is Available

- Robustness – Minimize "Tweaking" and Iteration of Solutions

- In-House vs. Outside Expertise – Designers May Not Have The Expertise To Use Tools If They Are "Fussy" – Require Pampering To Get The Correct Solutions – May require Outsourcing or Consulting Expertise

- Cost Effectiveness – Can CAA Replace Costly Testing? Is the Technical Advantage Relative To Standard Methods Worth the Investment?

- Will Computing Capacity Limitations Constrain Use As A Standard Tool?

Relevance of CAA to Regional and Business
Aircraft Engine Design

Donald S. Weir
AlliedSignal Engines & Systems

Why is CAA Relevant?

- Noise is an important design objective
  - Customer guarantees
  - Certification
  - Operator complaints
- Testing is expensive
  - trial and error doesn't always give expected results
  - limited in number of configurations
- Computational models are a key element of design
  - Makes "Design of Experiments" techniques feasible
  - Obtain insight into root causes of problems

Want to use CAA tomorrow like we use CFD today!

Three Examples

- Turbofan Engine Jet

- Turbofan Engine Fan
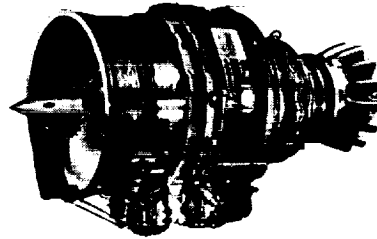
- APU installation
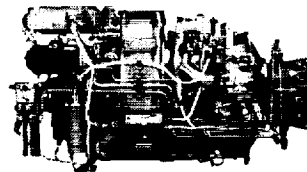

Full Scale Mixer Demonstration

- 18 Lobes
- 75% penetration
- 5% porosity
- lobed centerbody
- cutback core mixing lobes
- highly cutback centerbody lobes

Three Test Configurations

TFE731-40 nozzle baseline
Advanced Solid Mixer
Advanced Porous Mixer

AlliedSignal
San Tan
Acoustic
Test
Facility

120 degrees relative to inlet centerline

- Porous Mixer, 96263PN086
- Solid Mixer, 96263SN086
- Compound Nozzle, 96263RN089

SPLs at Fn = 4,000 lbs

Sound Pressure Level, dB re 20 µP₂

10 dB

1/3 Octave Band Center Frequency, Hz

50 80 125 200 315 500 800 1250 2000 3150 5000 8000
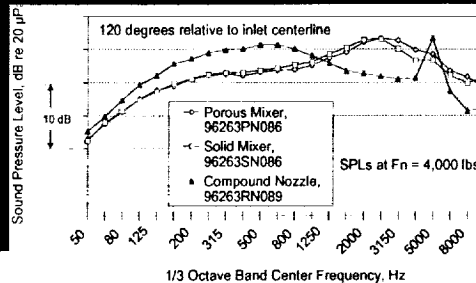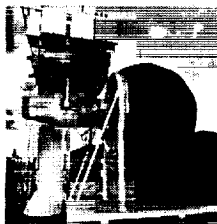
MGB Analysis of Full Scale Mixer

Comparison of Measured Exhaust PWL (90-160 deg) and
Predicted Jet Plume Noise (20-160 deg)

Plume Solution

Legend:
— Measured Reference
- - - Measured Solid Mixer
—•— Predicted Reference
•• Predicted Solid Mixer

10 dB

Freq (Hz)

Mixer Nozzle

Compound Nozzle

Acoustic Power

Internal Solution

Legend:
—◆— Bypass Mixer
—■— Core Mixer
••• Sum
━━ Reference
— • Ref. - Core

Acoustic Power

10 dB

50 100 200 400 800 1600 3150 6300 12500

Frequency (Hz)
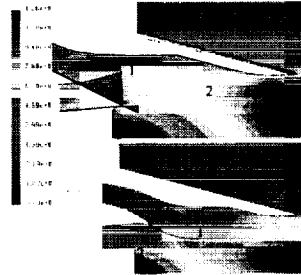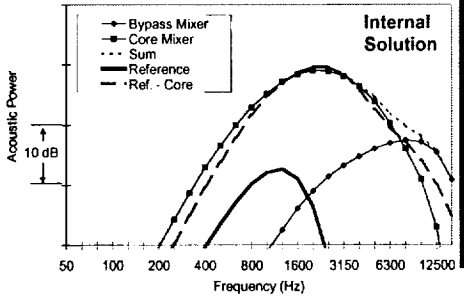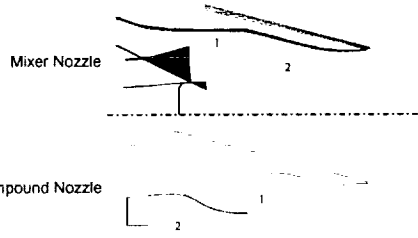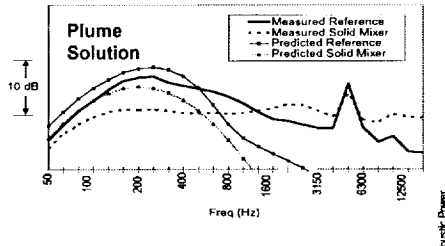
Fan Noise Prediction

- Rotor Alone Tone Noi se
- Multiple Pu

- Rotor/Stator Interaction Noise
- Broadband Noise

1.6
1.4
1.2
1.0
0.8
0.6
0.4

Relative Mach Number Contours

Tone Nois

Narrow Band Spectrum

Sound Power Level (dB)

10 dB

0.   2000.   4000.   6000.   8000.   10000.   12000.

Frequency (Hz)

1/3 Octave Band Spectrum

Sound Power Level (dB)

10 dB

200   400   800   1600   3150   6300   12500

Frequency (Hz)
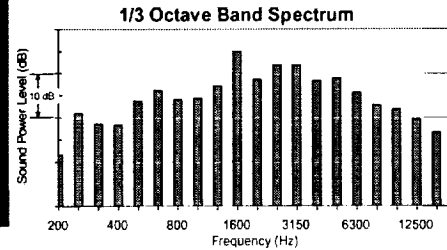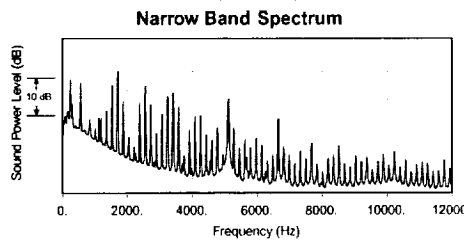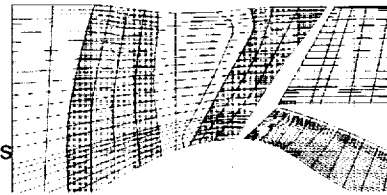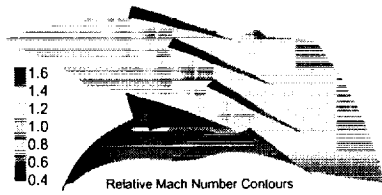
Some Fan Prediction Results

Baseline Fan
Contours of Relative
Total Pressure (psi)
◆ V072 Predicted Wake Traces

19
18
17
16
15
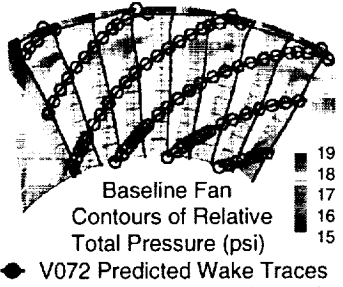
- Rotor/Stator Interaction Noise
- Far Field Propagation

- Inlet 2BPF
- Inle 3BPF
- Exit 2BPF
- Exit 3BPF

PWL (leaned) -
PWL (Straight), dB

Angle of Tangential Lean
(deg, "+" against rotation)
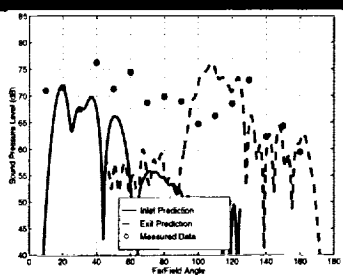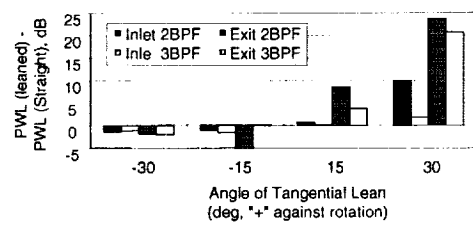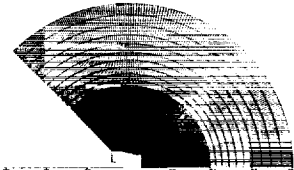
Flow Through APU Inlet Ducting Has Significant Effect On Installed Noise

Plenum
Diffuser
Baffle
FOD Screen
Load Compressor Inlet   Core Compressor Inlet

High Mach
Number at
Lip Increases
Noise

Axial and Lateral
Distortion Affect
Compressor Noise
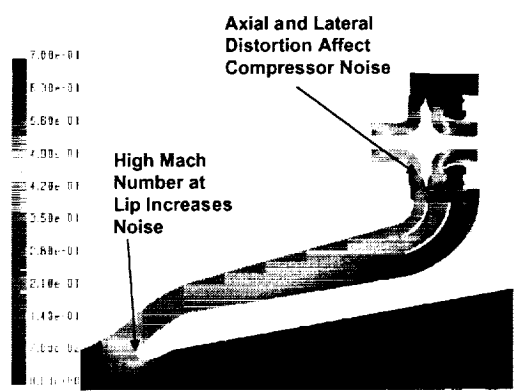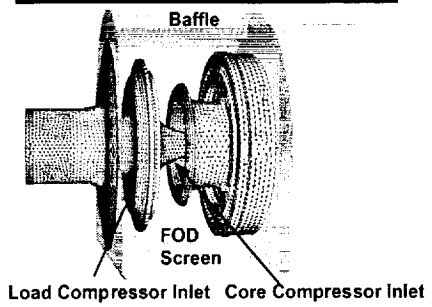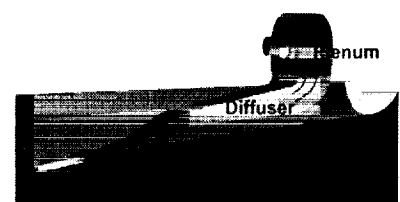
Measured Effect of Inlet Mach Number and Distortion
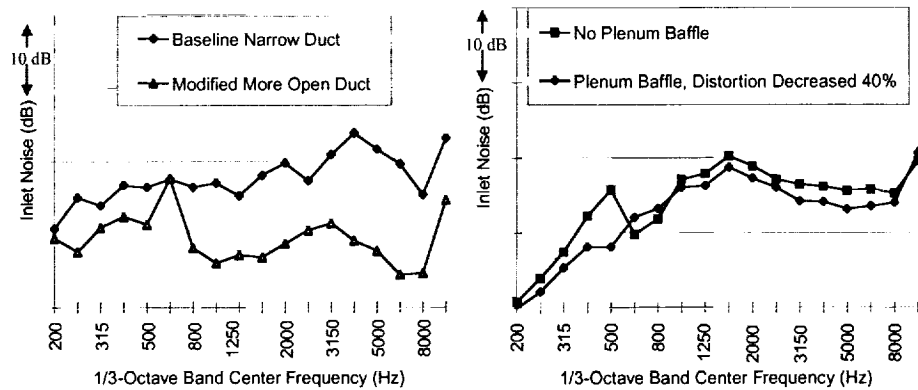
CFD gives qualitative comparisons but
quantitative prediction not currently available

Conclusions

- Noise is an important design objective
- Computational models are a key element of design
- **Want to use CAA tomorrow like we use CFD today!**
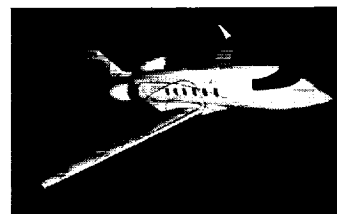
An Industry View of CAA

W. K. Lord
Pratt & Whitney

Subsonic-transport engine noise

fan tone noise
fan broadband
jet noise
other turbomachinery noise (LPC,LPT)
combustor noise
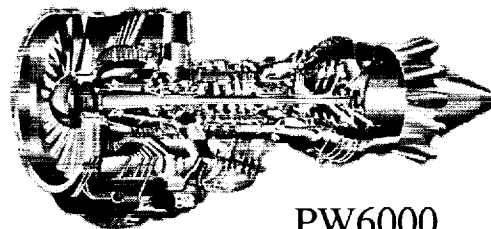
PW6000

Design Trends

higher BPR cycles
swept fan rotor or geared fan
swept FEGV
mixed-flow exhaust
    or separate-flow with tabs/chevrons
extensive use of computational methods for 3D aero,structures,noise
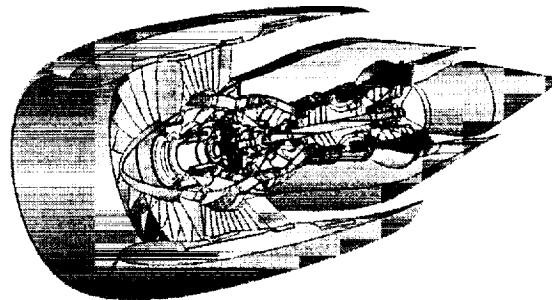
PW8000

What is CAA?

Narrow Definition: compute unsteady pressure
at every point in the field

Examples: linearized-Euler for fan tone
LES for jet

Impact on design: none to date
still in development phase

What is CAA? #2

Broad definition:

component geometry + 3D CFD + noise model = component
noise

Examples: V072/TFANS fan tone
BFANS fan broadband
KMGB, Tam, Morris jet noise models

Impact on design: set blade/vane airfoil counts
contributed to development of swept FEGV
TFANS/BFANS initial design studies '99

Fan Rotor/Stator Interaction Tone Noise

First-generation models in place (V072/TFANS)
Linearized Euler results look promising (LINFLUX)

Acoustic Modal Analysis at 2 BPF Compared to Fan Rig Data

	Inlet PWL(dB)		Exit PWL (dB)	
Mode	Predicted		Predicted	Data
1,0	112.3		121.2	122.1
1,1	106.9		120.4	121.4
1,2	114.9		119.2	119.4
1,3	105.2		112.5	110.1
1,4	--		--	
Total PWL(dB)	*117.5*		*125.4*	*126*
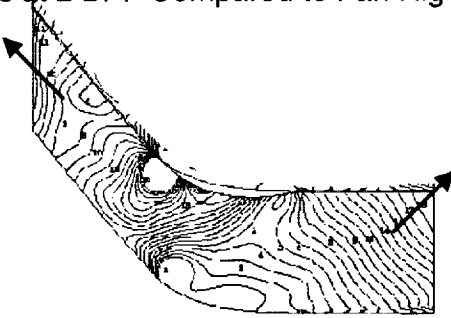
- potential for FEGV airfoil shape aero/acoustic optimization

Fan Broadband Noise Sources
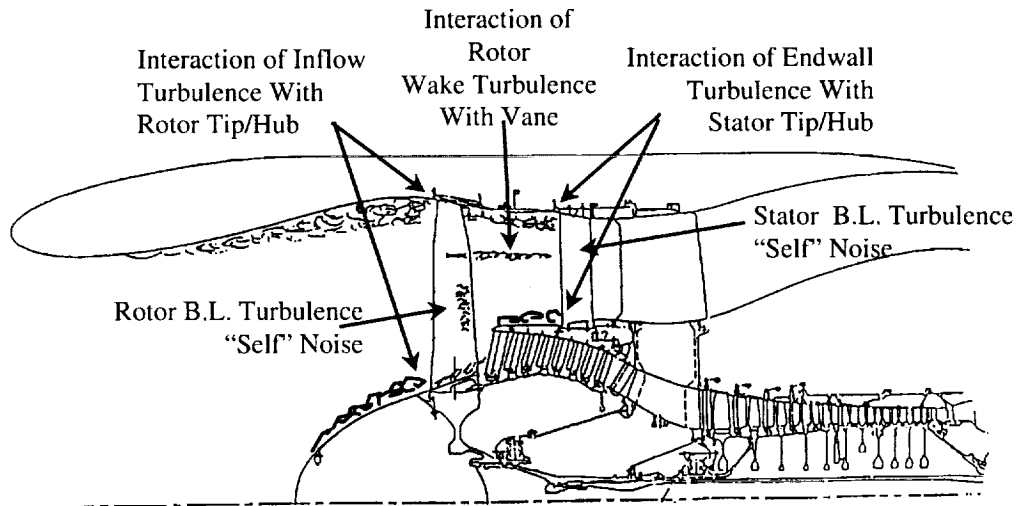
BFANS modeling
noise due to turbulence inflow: CFD turbulence +airfoil
acoustic response model
airfoil self noise: empirical model (need help here!)

Can LES of trailing edge flow
help develop improved self noise models?

Ref:

M. Wang
"Progress in large-eddy simulation of trailing-edge
   turbulence and aeroacoustics"
Center for Turbulence Research
Annual Research Briefs 1997

Jet Noise
methods for 3D mixing devices
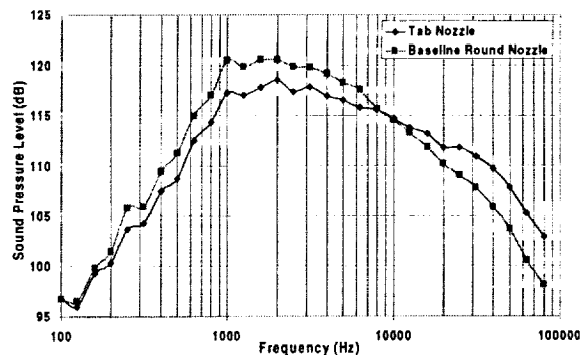
Near term: RANS CFD + noise model

Longer term: large-eddy simulation

CAA Direction

Expectation is that acoustics design tools will be merged into component design systems

First-generation tools based on 3D CFD + noise modeling

Industry likes real airfoil shapes better than flat plates

Work needed on understanding/modeling airfoil self noise

Jet methods for design of 3D mixing devices, including assessment of high-frequency mixing noise
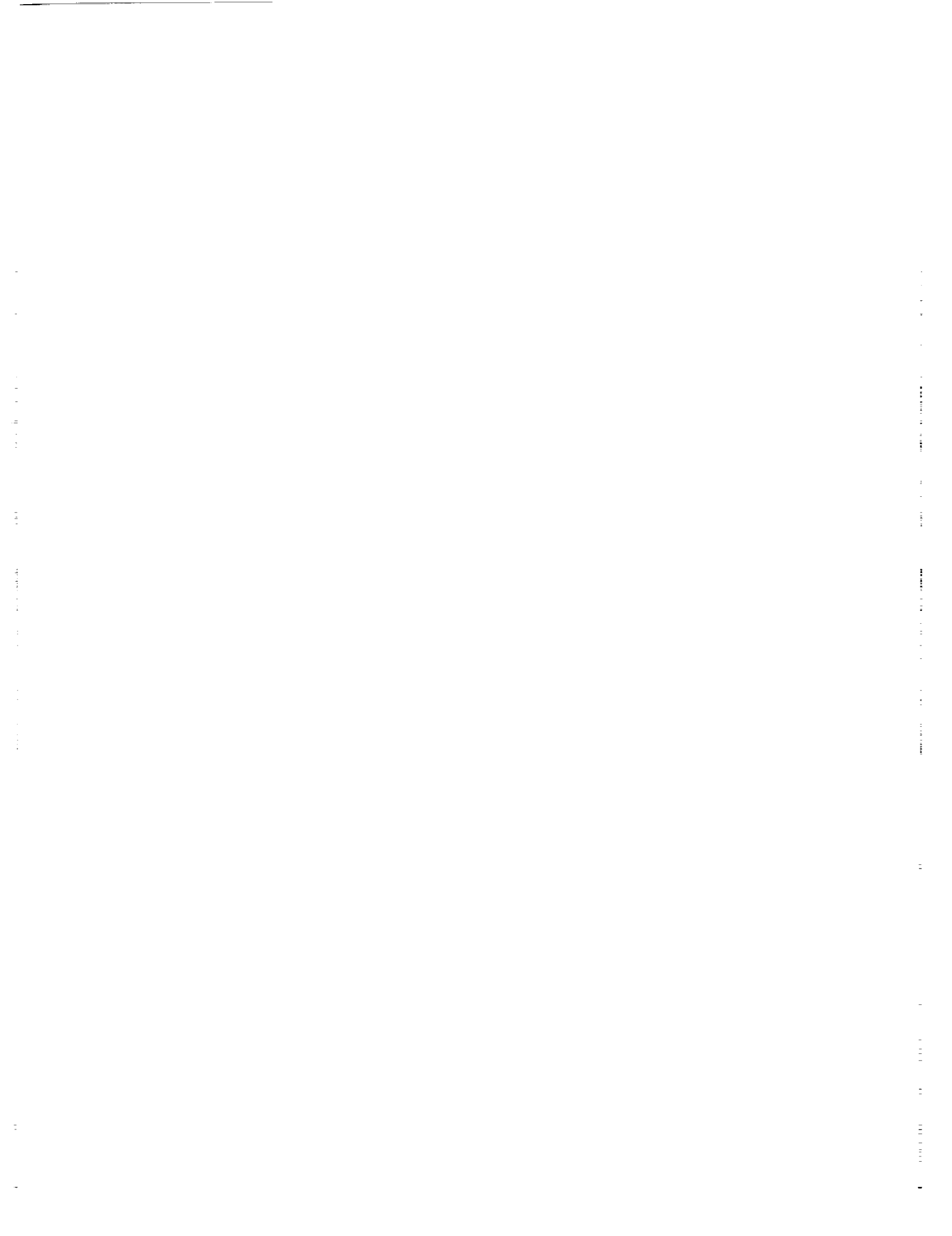
Use of Computational Methods for Noise/Vibration Problems

K. Viswanathan & M. C. Joshi
Boeing Commercial Airplanes Group

What does CAA mean to Boeing?

- **How has CAA helped solve problems in the past?**

- **How is CAA being implemented?**

- **What direction should CAA take to provide useful tools?**

- **What types of problems should be tackled?**

- **Provide guidance to CAA community**

Problems of interest to Boeing
(Noise modeling & control activities underway)

- **Community noise**
  - airframe noise
  - jet noise
  - fan noise
  - acoustic liners

- **Cabin noise**
  - turbulent boundary layer noise
  - engine vibration related noise
  - shock-associated noise
  - equipment noise and noise squawks

Flow field computations

- **Directed at understanding the physics**

- **Use unsteady CFD to gain insights**

- **Develop & implement suitable solutions**

- **Typical examples**

Preliminary DES: surface pressure & streamwise vorticity
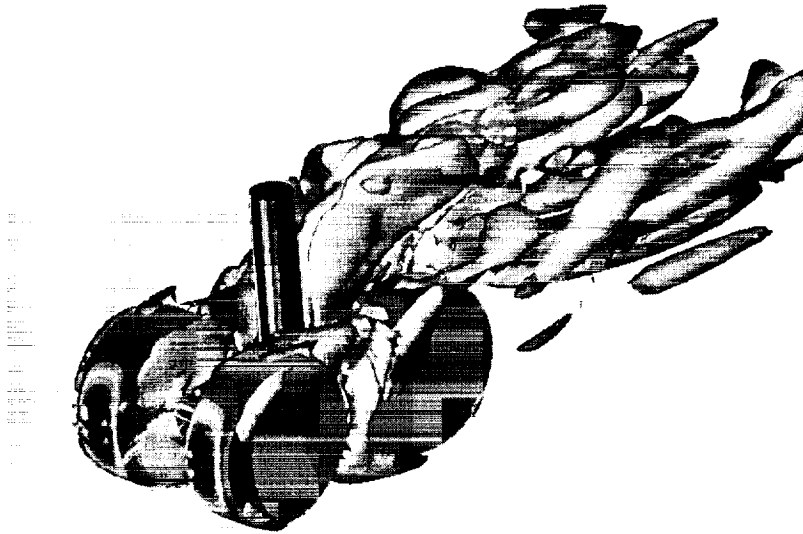
- **Unsteady flowfield & surface pressures from CFD**

- **Radiated noise from acoustic analogy**

NASA ASCOT Airframe Noise Research

Landing gear experimental flow physics research
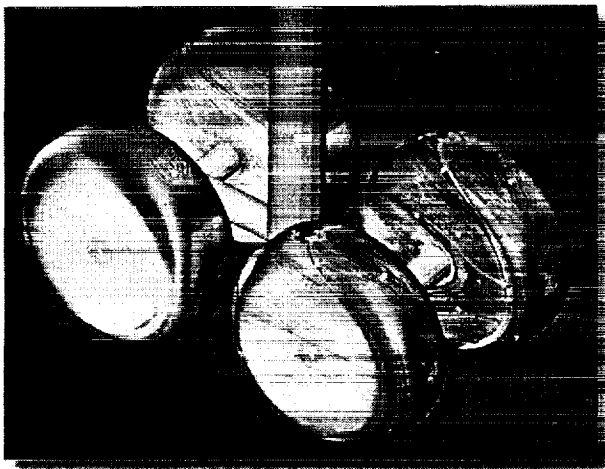
Experimental pressures and surface streamlines

Approach
- Flow field study around 4-wheel landing gear model to identify the flow physics associated with noise generation
- Establish landing gear noise reduction methodology

Accomplishments
- Completed static pressure measurements and oil flow visualization on fore and aft wheels
- Identified strong wake inflow regions and separation zones likely responsible for significant noise generation
- Began extensive PIV mapping of flow field above and below the wheels

Shock-cell noise

- **Emphasis on interior noise**

- **Current method: Tam's model with empirical corrections**

- **CAA approach: (Dr. S. Lele, Stanford U.)**
  - **detailed flow field with RANS**
  - **characterization of large structures with PSE**
  - **shock-cell/turbulence interaction with DNS**

- **Ongoing data analysis:**
  - **evaluate/interpret surface pressure data**
  - **develop prediction procedure for pressure field**
  - **develop cross-spectra input for FEM analysis**

Equipment noise / Noise squawks

- **Observed in product testing/pre-delivery flights**

- **Frequently, aero tones due to flow instabilities in on-board equipment, airframe components, etc. (vortex shedding, cavity tones, valve & pump noise)**

- **Annoyance & acoustic loads on nearby structures**

- **Potential application of computational tools**
  - **diagnose problem**
  - **provide design changes to eliminate problem**
  - **define "noise-free" design space/guidelines**

- **Typical examples**

Aeroacoustic Analysis: Outflow Valve
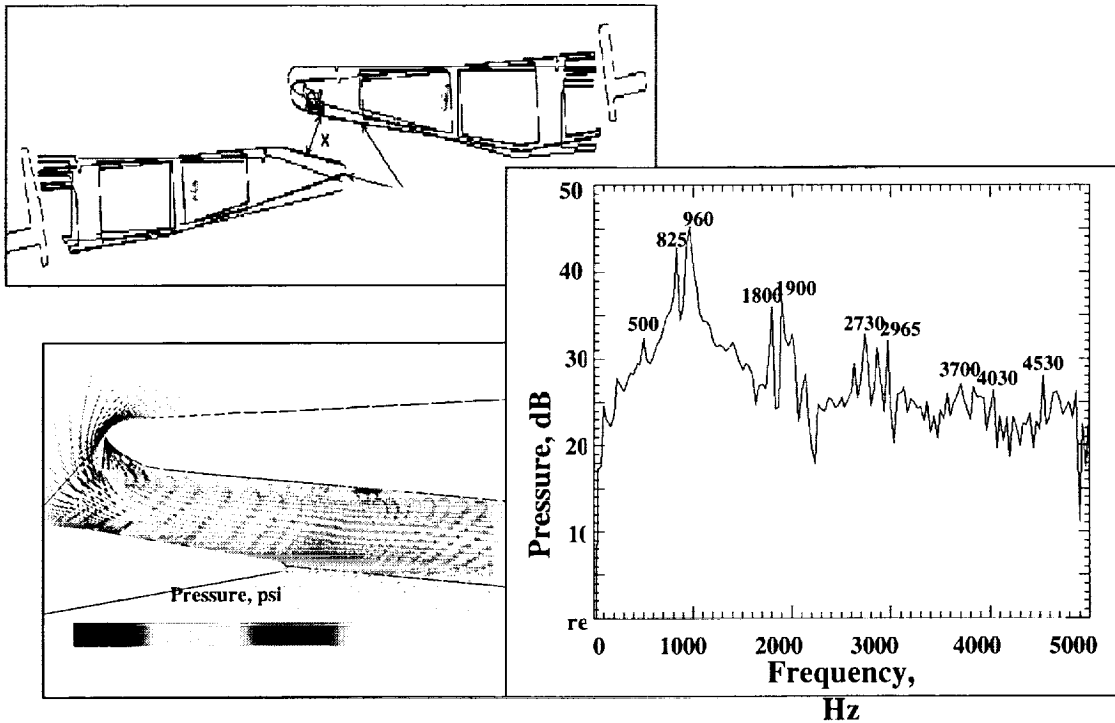
Requirements of computational tools for noise squawks

- **Accurate prediction of amplitudes not always necessary; ability to determine if a design change can eliminate/reduce noise more important**

- **Near field unsteady pressures provide useful info.; far field solutions not always required**

- **Many problems are tonal & may be more suitable for advanced computational methods**

- **Rapid turn-around (overnight including grid generation) required for squawk problems**

- **Validation necessary**

Rudder "tone" problem
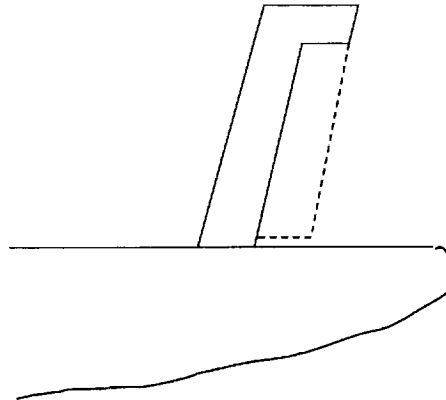
- **Unsteady CFD established vortex shedding**

- **Installed rubber 'boot' to eliminate problem**

Concluding remarks

- **CAA has made impressive strides**

- **Absolute predictions - not possible in near term**

- **Acceptable/realistic expectation:**
  - **ability to assess change in noise due to change in geometry**
  - **gain insights to the physics**

- **Use CFD/CAA as diagnostic tools**

Third CAA Workshop on Benchmark Problems

Industry Panel Discussion

William N. Dalton
Rolls-Royce Allison

- Current predictive technology status- gas turbine engines

  Continuing reliance on empirical data base

  Limited application of numerical methods to tones
  diagnostics
  evalution of nonconventional control concepts

- Computation of broad band noise requires significant progress to reach application stage
- Goal- Integration of numerical methods into the overall strategy of noise prediction

- In a gas turbine engine, methods must capture:

  1.Mean Flow Aerodynamic environment

  2. Time dependent flows associated with the acoustic process of interest

     Existence multiple wave numbers

     Resolution of high frequencies

     Complex internal geometry and flow field

     Existence of both bounded(internal) and unbounded(external) domains

     Existence of convected and propogating disturbance fields

     Presence of relative motion between adjacent domains

- Examples of Rolls-Royce Allison applications of CAA

  1. Effects of inlet geometry on tone radiation- diagnostic

  2. Reduction in fan rotor generated shock noise- predictive

  3. Installation effects on turbopropeller noise- evaluation of corrective action for existing problem

- Effects of inlet geometry on fan tone radiation
    Substitution of flight configured inlet for bellmouth inlet
    produced reductions in fan BPF tone level and directivity in
    forward quadrant during static engine testing

    Both inlets were hardwall (no acoustic treatment)

    Directivity shifts consistent with change in duct spinning
    mode content radiated to far field

    Sensitivity to rotational speed

- Numerical solution for radiation field used to determine spinning
  order content by matching radiation pattern
    linearization of full potential equation about nonuniform
    mean flow
        Acoustic/flow interaction within duct
        Diffraction around inlet leading edge
        Limited to axisymmetric mean flow

- Reduction in fan rotor generated shock noise

  Buzzsaw noise increase at part speed result of shock spillage from fan rotor

  Rotor sweep can be used to control rotational speed at which shock moves out of passage

  Solution of 3-D RANS Equations for rotor passage coupled to potential flow radiation solver to determine far field sensitity of shock induced noise to rotor sweep
    Restricted to harmonics of BPF

- Evaluation of installation effects on turbopropeller noise

  Penetration of BPF harmonic tones into cabin exceeded customer requirements. Levels incident on fuselage not symmetric.

  Installation effects produce assymetry in propeller noise
    Propeller angle of attack
    Propeller interaction with nacelle, wing, fuselage

  Solution of 3-D unsteady flow around one half of the airplane used to diagnose problem

- CAA is already used to solve development problems
    Diagnostics
    Assessment of new component configurations
    Solution of field problems
- Examples illustrate that problem dictates level of model sophistication
    Small perturbation approximations
    Full non-linear fluid equations
    Mixture

- Need: Accelerate the transition from research to application

- Areas for technical effort important to engine applications
    Improve existing models for tone radiation through a shear layer
        Downstream fan tone radiation

    Application and refinement of methods to non-axisymmetric geometries
        drooped and scarfed inlets
        ducts of non-circular cross section

    Propagation in lined ducts
        Modeling of segmented and non-axisymmetric liner

Integration of linear and nonlinear solution methods

Establish domains and parameter ranges within which small perturbation methods applicable

Clearly determine where differences result from numerical implementations and physics

Improved boundary methods at interfaces

Proper transfer of convecting and radiating energy in both directions

Relative motion between interfaces

Industrial Applications of CAA

BY

Tom Dong

Lockheed Martin Aeronautical Systems
Marietta, Georgia

CAA Code Development by LMAS/FSU

(1) High Accuracy <u>DRP</u> Finite Difference Algorithm

(2) Euler Computations <u>(Navier-Stokes</u> Capability Is Under Development)

(3) A Large Set of <u>BC</u>s for Acoustics Computations

(4) Multi-block Grid Capability Interfaced w/ *<u>Gridgen</u>* for Complex Geometry

(5) Multi-domain, Multiple Time-Step (<u>MDMT</u>) Method to Enhance Efficiency

(6) Implementation of <u>MPI</u> for Parallel Calculations

APPLICATION OF DRP/CAA CODE -

## Airframe Noise Source Mechanism Analyses (NASA AST)

Flap Side-edge Noise

Acoustics Contours

Wing

Slat/Wing Noise
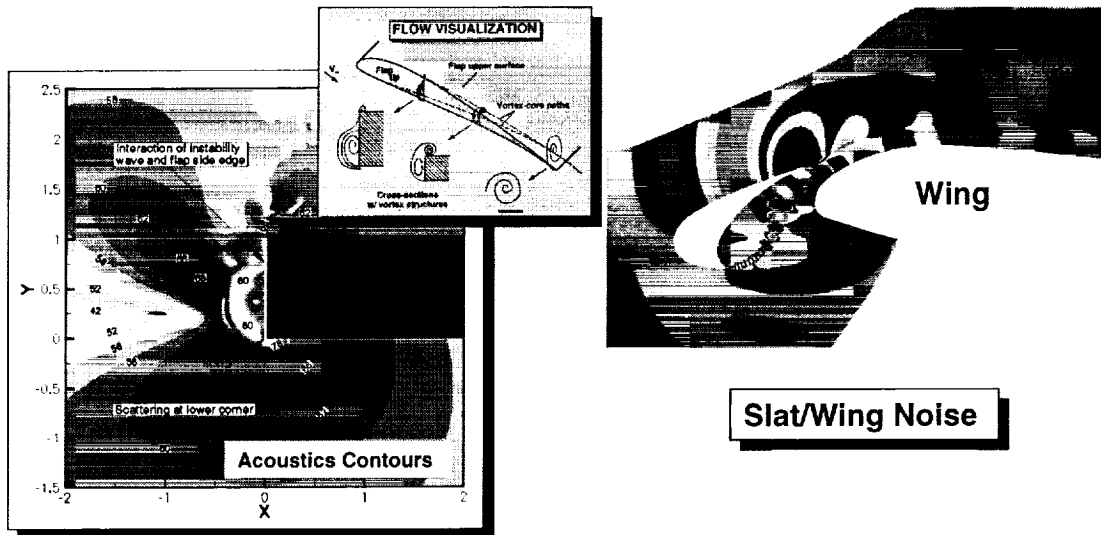
APPLICATION OF DRP/CAA CODE -

Screech Tones From Supersonic Jets (FSU)
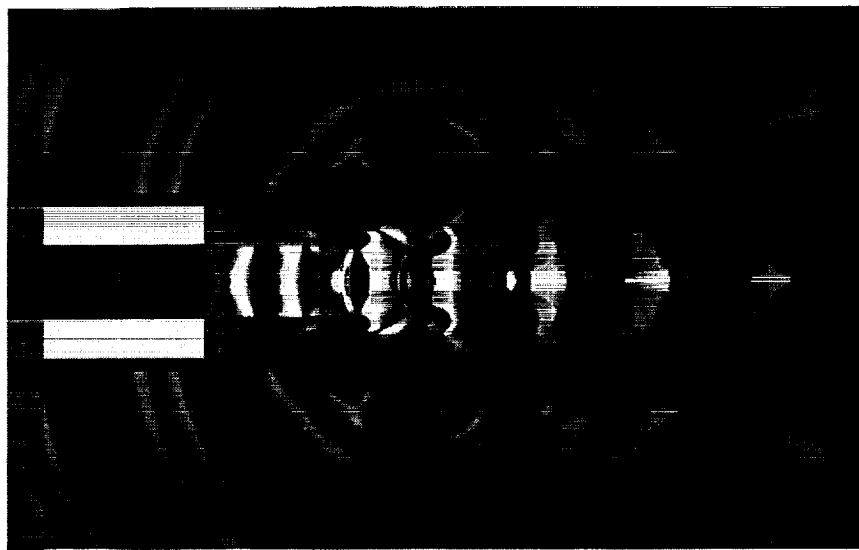
Unsteady RANS Simulation w/ DRP

Potential Aeroacoustics Applications

(a) Prediction - Acoustic loads and far-filed noise
from engines, airframes, and propellers.

(b) Reduction - Source mechanism investigation

Potential Aerodynamics Applications

(a) **Flow separation control w/acoustics for high-lift
systems** (e.g. Seifert and Pack AIAA J.Sept. 1999).

(b) **Unsteady flow environment around open payload
bays (store separation, cavity)**

*Acoustics is, a critical part of the unsteady
phenomena, not necessarily the end product*

Industrial Needs:

We Need **CAA CODES** with:

      (1) Current CAA Accuracy (Algorithms, BCs)

      (2) Current CFD Grid and Turbulence Capability

      (3) All The Efficiency Enhancing Techniques:

            Multi-domain, Multiple Time-Step Method

            Parallel Computing

            Multi-grid Technique

            Good Programming Skills

      (4) Flexibility For Future Modification (Modules)

Difficulty:

Block Communication:

      The large stencils associated with CAA algorithms make the communication at block interface difficult

      Most CFD Algorithms Have Reduced Time Accuracy At Interfaces

Suggestions:

- Develop Modular CAA Codes using the Currently Existing and Well-tested Methods w/ a coordinated effort among Government, Industry, Academia, Research Institutes.

- Validate Various CAA Techniques

- Define the Needs For Future CAA Development

REPORT DOCUMENTATION PAGE

Public reporting burden for this collection of information is estimated to average 1 hour per response, including the time for reviewing instructions, searching existing data sources, gathering and maintaining the data needed, and completing and reviewing the collection of information. Send comments regarding this burden estimate or any other aspect of this collection of information, including suggestions for reducing this burden, to Washington Headquarters Services, Directorate for Information Operations and Reports, 1215 Jefferson Davis Highway, Suite 1204, Arlington, VA 22202-4302, and to the Office of Management and Budget, Paperwork Reduction Project (0704-0188), Washington, DC 20503.

1. AGENCY USE ONLY (Leave blank)	2. REPORT DATE	3. REPORT TYPE AND DATES COVERED
	August 2000	Conference Publication

4. TITLE AND SUBTITLE

Third Computational Aeroacoustics (CAA) Workshop on Benchmark Problems

5. FUNDING NUMBERS

WU–522–81–11–00

6. AUTHOR(S)

Milo D. Dahl, editor

7. PERFORMING ORGANIZATION NAME(S) AND ADDRESS(ES)

National Aeronautics and Space Administration
John H. Glenn Research Center at Lewis Field
Cleveland, Ohio 44135–3191

8. PERFORMING ORGANIZATION REPORT NUMBER

E–12078

9. SPONSORING/MONITORING AGENCY NAME(S) AND ADDRESS(ES)

National Aeronautics and Space Administration
Washington, DC 20546–0001

10. SPONSORING/MONITORING AGENCY REPORT NUMBER

NASA CP—2000-209790

11. SUPPLEMENTARY NOTES

Proceedings from the Third Computational Aeroacoustics (CAA) Workshop on Benchmark Problems sponsored by the NASA Glenn Research Center, Cleveland, Ohio, November 8–10, 1999. These proceedings are available on CD-ROM in the PDF document format. In addition, the CD-ROM contains information related to all 6 categories of the benchmark problems including the numerical results from the calculations of the analytical solutions and the experimental data for the Category 6 problem. See the README file in the CD-ROM directory entitled "caawksp3data" for further details. Responsible person, Milo D. Dahl, organization code 5940, (216) 433–3578.

12a. DISTRIBUTION/AVAILABILITY STATEMENT

Unclassified - Unlimited
Subject Category: 71   Distribution: Nonstandard

This publication is available from the NASA Center for AeroSpace Information, (301) 621–0390.

12b. DISTRIBUTION CODE

13. ABSTRACT (Maximum 200 words)

The proceedings of the Third Computational Aeroacoustics (CAA) Workshop on Benchmark Problems cosponsored by the Ohio Aerospace Institute and the NASA Glenn Research Center are the subject of this report. Fan noise was the chosen theme for this workshop with representative problems encompassing four of the six benchmark problem categories. The other two categories were related to jet noise and cavity noise. For the first time in this series of workshops, the computational results for the cavity noise problem were compared to experimental data. All the other problems had exact solutions, which are included in this report. The Workshop included a panel discussion by representatives of industry. The participants gave their views on the status of applying computational aeroacoustics to solve practical industry related problems and what issues need to be addressed to make CAA a robust design tool.

14. SUBJECT TERMS

Aeroacoustics; Numerical methods; Wave propagation; Sound sources; Acoustic boundary conditions

15. NUMBER OF PAGES

473

16. PRICE CODE

A20

17. SECURITY CLASSIFICATION OF REPORT	18. SECURITY CLASSIFICATION OF THIS PAGE	19. SECURITY CLASSIFICATION OF ABSTRACT	20. LIMITATION OF ABSTRACT
Unclassified	Unclassified	Unclassified	

NSN 7540-01-280-5500

Standard Form 298 (Rev. 2-89)
Prescribed by ANSI Std. Z39-18
298-102